FE-2341-8
Distribution Categories UC-90g and UC-93

Topical Report

on

AXIAL FIELD LIMITATIONS IN MHD GENERATORS

NOTICE
This report was prepared as an account of work sponsored by the United States Government. Neither the United States nor the United States Department of Energy, nor any of their employees, nor any of their contractors, subcontractors, or their employees, makes any warranty, express or implied, or assumes any legal liability or responsibility for the accuracy, completeness or usefulness of any information, apparatus, product or process disclosed, or represents that its use would not infringe privately owned rights.

by

William C. Unkel

Stanford University
Stanford, California 94305

Date Published

April 1978

Prepared for the United States
Department of Energy

Under Contract No. EX 76-C-01-2341

MASTER

DISCLAIMER

This report was prepared as an account of work sponsored by an agency of the United States Government. Neither the United States Government nor any agency thereof, nor any of their employees, makes any warranty, express or implied, or assumes any legal liability or responsibility for the accuracy, completeness, or usefulness of any information, apparatus, product, or process disclosed, or represents that its use would not infringe privately owned rights. Reference herein to any specific commercial product, process, or service by trade name, trademark, manufacturer, or otherwise does not necessarily constitute or imply its endorsement, recommendation, or favoring by the United States Government or any agency thereof. The views and opinions of authors expressed herein do not necessarily state or reflect those of the United States Government or any agency thereof.

DISCLAIMER

Portions of this document may be illegible in electronic image products. Images are produced from the best available original document.

Blank Page

Foreword

This report forms the basis of the Ph.D. thesis of the author who was advised by Professors C. H. Kruger, R. H. Eustis and S. A. Self. The work was started under Contract AFAPL F-33615-72-C-1088 from the Air Force Aero Propulsion Laboratory, continued under National Science Foundation Grant NSF AER-72-03487 and completed under Department of Energy Contract EX 76-C-01-2341.

Blank Page

ABSTRACT

The results of an experimental and analytical investigation of axial field breakdown in non-slagging wall, combustion-driven MHD generators are presented. Some experiments and analysis were performed for a segmented Faraday generator, however more detailed studies were performed for a simplified configuration in which a voltage was applied to a pair of adjacent electrodes in the absence of a magnetic field. Plasma conditions for both types of experiments were typical of expected central station power plant MHD applications. Breakdown was characterized by a rapid decline in axial voltage and a change in the mode of current transport from a relatively diffuse mode to a highly constricted and extremely destructive mode. Cine-photographic records obtained for the simplified configuration demonstrated that breakdown could be initiated in the plasma or in the inter-electrode insulator; however, for breakdown initiated in the plasma, the insulator became the dominant breakdown current carrier within a few seconds. Plasma initiated and insulator initiated breakdown resulted only when a threshold voltage was exceeded, the threshold voltage increasing with increased insulator gap size. For the electrode wall configuration studied, the threshold voltage for plasma initiated breakdown was significantly higher than the threshold voltage for insulator initiated breakdown. Both threshold voltages were considerably in excess of the voltage maintained after breakdown was well developed. Insulator initiated breakdown observed in the generator experiments was qualitatively similar to the insulator initiated breakdown observed in the simplified configuration, although the threshold voltage for a particular insulator gap size was somewhat reduced in the generator experiments. No qualitative differences in the development of breakdown on an anode wall and on a cathode wall were observed.

Simple consideration indicated that an electro-thermal instability was responsible for the behavior observed in the experiments. A computer model was developed to predict the non-breakdown and incipient breakdown behavior for the inter-electrode insulator region for the simplified configuration. The two-dimensional model for the plasma included a solution of the unsteady

(in the mean) turbulent boundary layer equations including the electron-continuity equation and a solution for the distribution of current. A separate analytical solution was obtained for the electrical behavior in the region near the anode where space-charge effects are important; similar effects in the region near the cathode could be treated only in an empirical fashion. The insulator was modeled by the heat conduction equation with the Joule heating evaluated using an electrical conduction model. The analytical model predicts most of the qualitative features leading up to axial field breakdown and predicts threshold voltages for plasma initiated and insulator initiated breakdown comparable to the threshold voltages measured in the experiments. Detailed comparisons of theory and experiment indicate that even with the relatively sophisticated model utilized, only moderately good agreement is obtained. In particular, the model consistently under-predicted the effect of Joule heating in the plasma. A quasi-one-dimensional performance code well modeled the generator behavior for non-breakdown conditions. Moderate success in simulating the effect of isolated breakdowns on generator performance was achieved through the use of a coarse grid current distribution model.

Simple considerations show that significant improvements in generator performance can result from prevention of breakdown. The present study indicates that for non-slagging wall generators careful thermal design of the inter-electrode region should alleviate the problem of insulator initiated breakdown. The results also indicate that for both plasma and insulator initiated breakdown reducing the electrode pitch at fixed average current density to the electrode increases the resistance of channel to breakdown.

TABLE OF CONTENTS

TABLE OF CONTENTS

TABLE OF CONTENTS

TABLE OF CONTENTS

LIST OF TABLES

LIST OF FIGURES

LIST OF SYMBOLS

English Letter Symbols

A	area
B	magnetic field strength
C_e, C_i	electron and ion mean thermal speed
c_c	electron concentration
c_p	specific heat at constant pressure
c_v	specific heat at constant volume
D_a	ambipolar diffusion coefficient
D_e, D_i	electron and ion diffusion coefficient
E_x, E_y	components of electric field
F	force
h	heat transfer coefficient, channel height, static enthalpy
I	current
J_x, J_y	components of current density
k	thermal conductivity
ℓ	electrode length
M_e	electron mass
N_e, N_i	electron and ion number density
p'''	power output per unit volume
p	electrode pitch, pressure
P_e	electrode pressure

LIST OF SYMBOLS

English letter Symbols

$\dot{q}'''_{rad}$	volumetric radiation loss from plasma
$\bar{Q}_{eH}$	average electron-heavy collision cross-section
R	Reynolds number, electric Reynolds number, radius, resistance, gas constant
t	time
T	temperature
u, U	axial velocity component
v	transverse velocity component
V	voltage
w	width, non-dimensional potential

Greek Letter Symbols

β	ratio of ion mobility to electron mobility, function used in simple breakdown model
β_e	Hall parameter
γ	ratio of specific heats, function used in simple breakdown model
Γ_e, Γ_i	electron and ion fluxes
δ	boundary layer thickness, inelastic energy loss factor
δ_1	boundary layer displacement thickness
ε	ratio of ion temperature to electron temperature

LIST OF SYMBOLS

Greek Letter Symbols

ε_E	eddy diffusivity for species transfer
ε_H	eddy diffusivity for heat transfer
ε_M	eddy diffusivity for momentum transfer
ζ	fraction of ideal Hall field
η	non-dimensional boundary layer coordinate
θ	non-dimensional temperature, coverage fraction of adsorbant on substrate
λ_D	Debye length
λ_{mfp}	mean free path
λ	wavelength
μ_e, μ_i	electron and ion mobility
ν_e, ν_i	surface electron and ion emission flux
$\bar{\nu}_{eH}$	average electron heavy particle collision frequency
ξ	departure from charge neutrality
ρ	density
ρ_c	charge density
σ	electrical conductivity
τ	time constant, transmittance
ϕ	electric potential
ψ	current stream function

LIST OF SYMBOLS

Miscellaneous Symbols

$\langle\ \rangle$	denotes spatial average
$*$	denotes equilibrium value or reference condition
$\hat{}$	denotes dimensional quantity
$\tilde{}$	denotes vector quantity
∞	denotes freestream quantity

CHAPTER 1
INTRODUCTION

Magnetohydrodynamic (MHD) power generation is a direct energy conversion technique which, when used as a topping cycle for a conventional central station steam cycle, has been shown to be economically attractive. The basic concept of MHD has been long accepted, however several important engineering problems need to be solved before MHD can be fully developed. In particular, experiments with MHD generators have indicated that at the high axial electric fields at which MHD is most attractive, "breakdown" or "arcing" between adjacent electrodes in the generator can occur [1,2,3,4]. In addition to degrading the electrical performance of the generator by local shorting of the Hall (or axial) field, the arcing can cause enough damage to force a shutdown of the facility. Although this problem had received considerable attention prior to the present study and some engineering solutions have been effected, little detailed experimental data had been obtained for combustion plasmas and no direct comparison of theory and experiment had been made. The overall goal of the present investigation was to produce and study axial voltage breakdown in MHD generators specifically to identify the mechanisms responsible for the breakdown. Theoretical models developed in the course of the work were then applied toward a preliminary evaluation of possible solutions to the problem of breakdown.

1.1 Background

The basic MHD generator system consists of a channel through which a conducting fluid is passed perpendicular to an externally maintained magnetic field, as shown schematically in Figure 1. A variety of working fluids can be used, however the present study will consider only the products of combustion of a clean hydrocarbon fuel and oxygen, with nitrogen added as a diluent and potassium added to enhance the electrical conductivity. In the MHD generator, the Lorentz force acting on the moving charged particles provides the motive force for driving a current through an external circuit. The maximum power density extracted from an ideal device (neglecting for the moment the Hall effect) can be shown to be given as

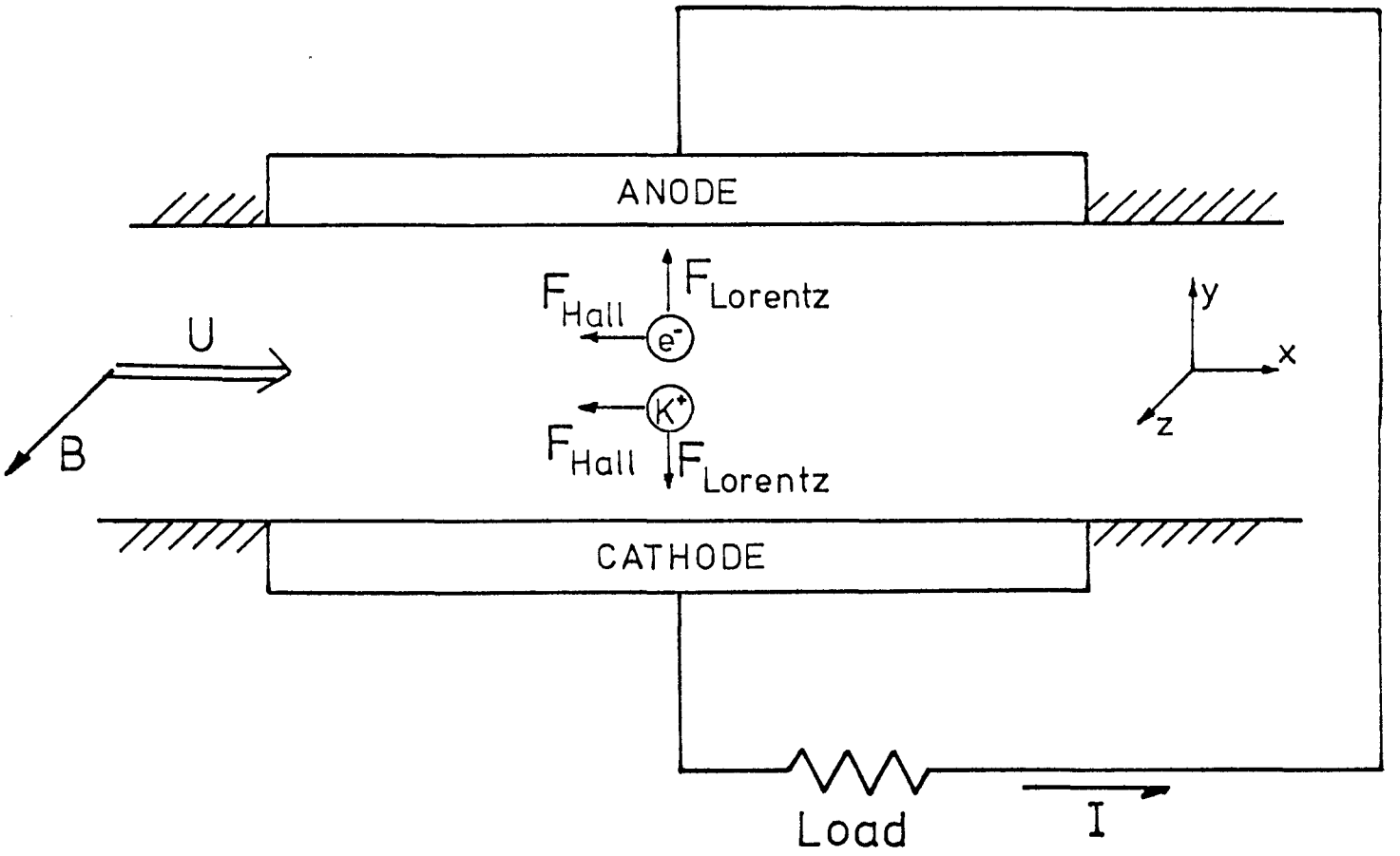

Figure 1. Schematic of continuous-electrode Faraday configuration MHD generator.

$$P'''_{\substack{max \\ (\text{no Hall effect})}} = \frac{1}{4}\sigma u^2 B^2$$

where, σ is the electrical conductivity of the fluid, u is the axial velocity of the fluid and B is the magnetic field strength. For typical conditions, ($\sigma \simeq 10$ mho/m, $u \simeq 1000$ m/sec, $B \simeq 6$ tesla) an ideal power density of $P''' \simeq 90$ Mw/m^3 is indicated. To the extent that a high power density represents lower surface losses (thermal, electrical and frictional) and smaller required magnet volume, the power density can be viewed as a simple economic yardstick for comparison of particular generator devices.

As shown in Figure 1, the net drift of charged particles forming the main (Faraday) current through the generator is perpendicular to the imposed magnetic field, inducing forces on the charged particles in the axial (Hall) direction. With continuous electrodes no field can build up in the axial direction and the charged particles drift in the Hall direction, resulting in longer current paths and higher internal impedence. For a combustion plasma, where electrons, by virtue of their high mobility, are the predominant current carriers the power density of an ideal continuous electrode device with Hall effect can be shown to be given by

$$\left(P'''_{\substack{max \\ \text{continuous electrodes} \\ \text{with Hall effect}}}\right) = \frac{1}{4}\sigma u^2 B^2 \left(\frac{1}{1+(\mu_e B)^2}\right)$$

where μ_e is the electron mobility and the product $\mu_e B \equiv \beta_e$ is termed the electron Hall parameter. Thus for typical conditions ($\mu \simeq 0.5$ Tesla^{-1}, $B \simeq 6$ Tesla) the Hall effect results in an order of magnitude reduction in power density for a continuous electrode device.

To reduce the influence of the Hall effect, the electrodes can be segmented in the axial direction, as shown in Figure 2, with each electrode pair electrically isolated from the others. In this way the axial current is forced toward zero and an electric field is established in the axial direction. For an ideal generator with infinitely segmented electrodes the power density can be shown to be given as

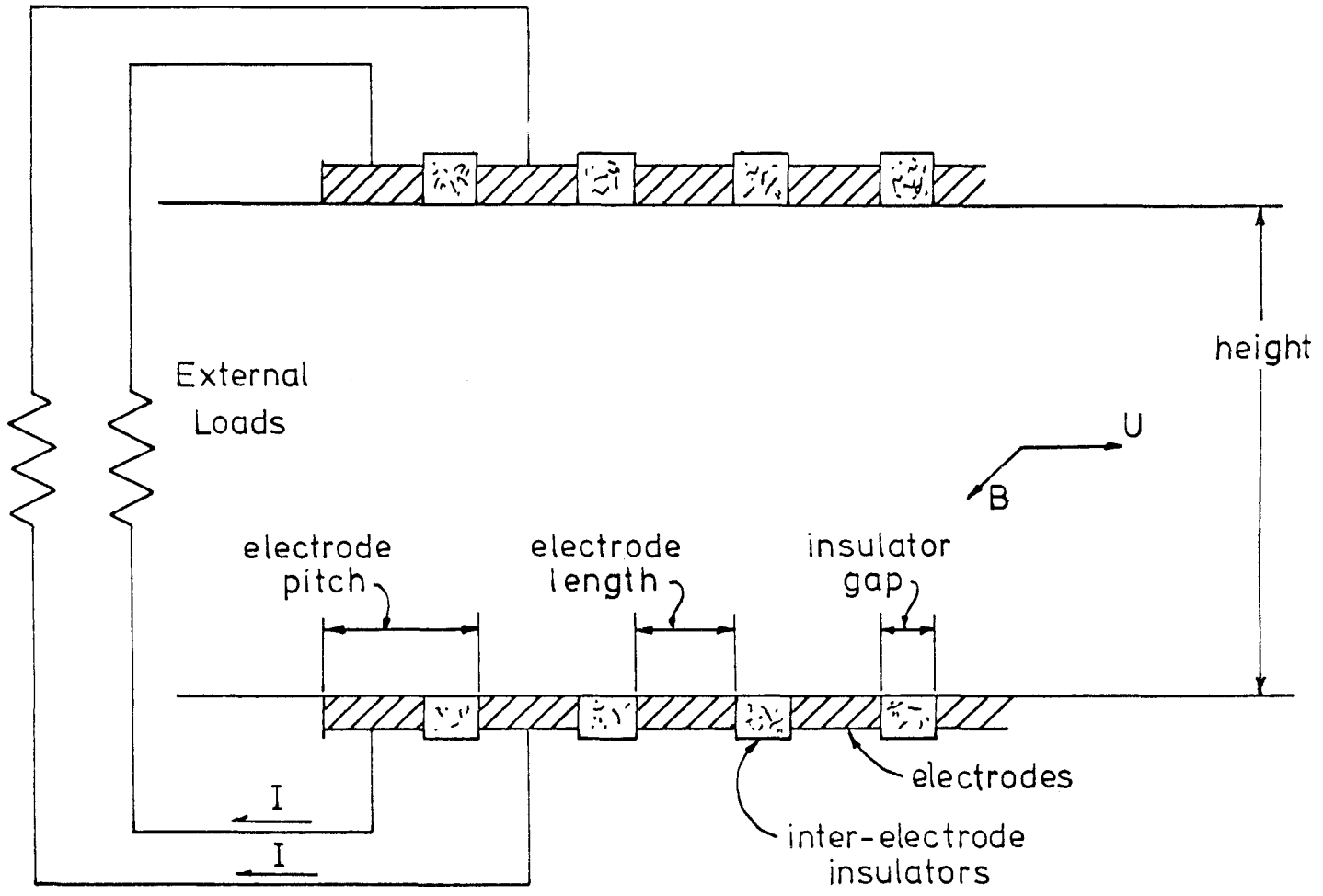

Figure 2. Schematic of segmented-electrode Faraday configuration MHD generator identifying several important dimensions.

$$\left(\begin{array}{c} p'''_{max} \\ \text{infinite segmentation} \\ \text{with Hall effect} \end{array}\right) = \frac{1}{4}\sigma u^2 B^2$$

which is identical to the expression obtained when the Hall effect was neglected. The axial field built up in the generator, at maximum power density conditions can be shown to be

$$\left(\begin{array}{c} E_{x_{max.\ power}} \\ \text{infinite segmentation} \\ \text{with Hall effect} \end{array}\right) = -\frac{uB}{2}\beta e = -\frac{uB^2}{2}\mu_e$$

$$= -\frac{2\mu_e}{\sigma u}\ p'''_{\substack{max \\ \text{infinite segmentation} \\ \text{with Hall effect}}}$$

If the non-ideal effects of an actual generator result in a degradation of the axial field to a fraction ζ of the ideal axial field, the appropriate expression for the power density is

$$p'''_{\substack{\text{actual generator} \\ \text{with Hall effect}}} = \frac{1}{4}\sigma u^2 B^2 \left(\frac{1 + \zeta \beta_e^2}{1 + \beta_e^2}\right)$$

This indicates that significant gains in power density will result from increases in magnetic field strength only if the Hall field can be maintained at a level close to the ideal level.

The electrode wall of a practical MHD device is composed of alternating, finite-length, electrode and insulator elements as shown schematically in Figure 2. Each pair of opposite electrodes is externally isolated from the others such that under normal conditions the net axial current inside the generator would be forced toward zero. Local shorting of the Hall field by the finite length electrodes and effects of non-uniform conductivity through the electrode wall boundary layer, introduce regions of non-zero axial current flow as shown schematically in Figure 3a. For some conditions, notably for high Hall parameter, substantial current flow over the inter-electrode insulator and even internal "leakage" of current between adjacent electrodes can result. As shown schematically in Figure 3b, the return path for the leakage current may be through either the plasma or the inter-electrode insulator. Internal leakage in the near electrode-wall

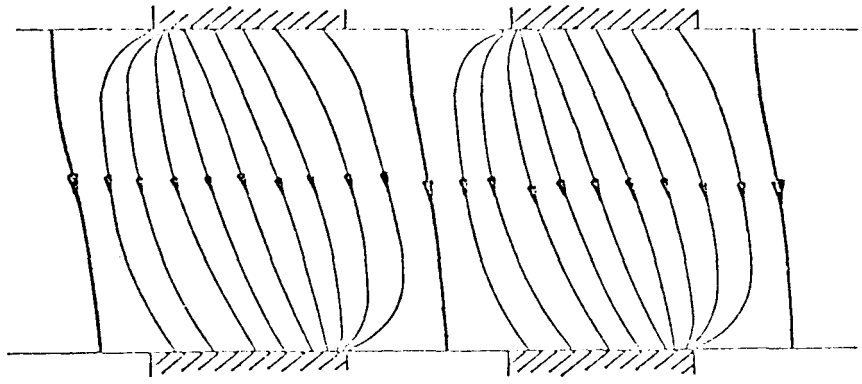

Figure 3a. Schematic of current streamlines for 'normal' generator conditions. All current from the top electrode passes directly to the corresponding opposing electrode.

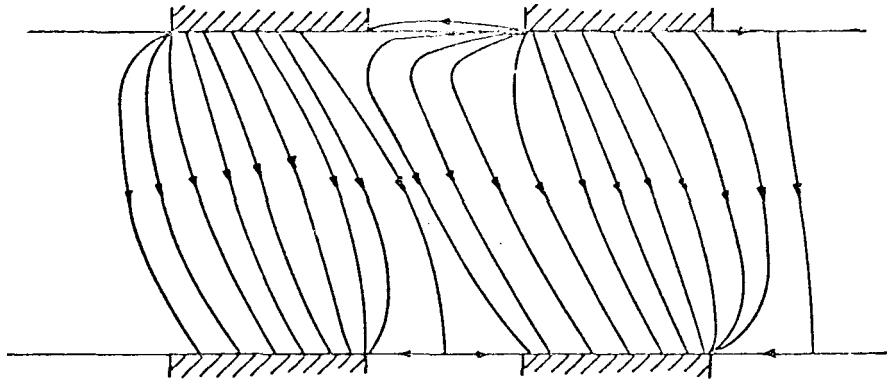

Figure 3b. Schematic of current streamlines with diffuse leakage in the top inter-electrode insulator region: leakage can occur either through the plasma or through the inter-electrode insulator. A portion of the current from the top right electrode passes to the adjacent electrode prior to entering the opposite electrode.

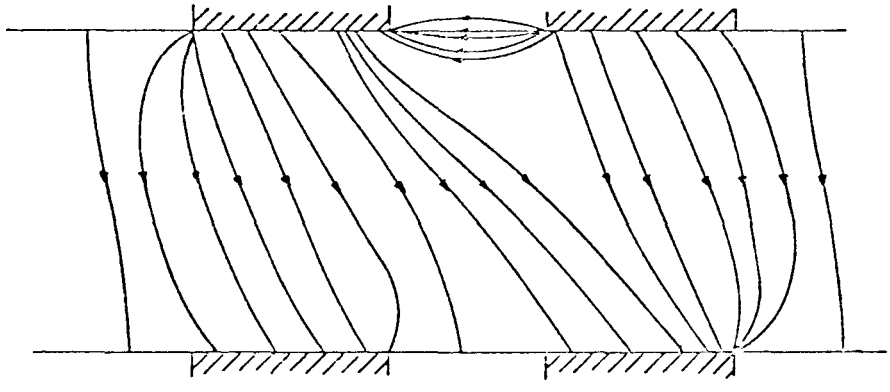

Figure 3c. Schematic of current streamlines with constricted leakage or arcing between the upper adjacent electrodes. This arcing can occur through the plasma or through the inter-electrode insulator and takes the form of a constricted (three-dimensional) discharge.

region permits a larger net axial current flow in the bulk of the generator, resulting in a degradation of the Hall field and the electrical performance of the device, Diffuse, two-dimensional leakage through the plasma has been predicted in several analytical studies [5,6] and measured in at least one experimental study [7]. In several experiments, constricted three-dimensional discharges formed between the adjacent electrodes as shown schematically in Figure 3c. This constricted discharge can represent a more substantial current leakage path than the diffuse path and, of more significance, the constricted discharge can cause substantial damage to the electrode wall of the generator. It is in this latter respect that this phenomenon, termed Hall voltage breakdown, has been established as a major problem in the implementation of MHD power generation.

1.2 Review of Previous Work

Although the literature contains a few references to Hall voltage breakdown in a particular generator, the principal experimental results, prior to the present work, were obtained at AVCO, and their experience with Hall voltage breakdown in combustion MHD generators will be discussed in some detail. In addition, some comment will be made concerning the recently initiated efforts at the Soviet High Temperature Institute to study the phenomenon of breakdown. Although no breakdown was observed, the work of Cutting is also summarized since his work represents the only prior detailed theoretical and experimental work relating to breakdown. A brief discussion of the analytical modeling of Oliver relating to breakdown is included, although detailed discussion of his work is defered to a later section.

1.2.1 AVCO Everett Research Laboratory

The existence and importance of inter-electrode arcing was established in early experiments at AVCO, where extensive damage to the electrode walls by such arcing was observed [1,2,3,4]. Experience at AVCO established that for their electrode wall design, steady arcing could occur only for voltages in excess of $\simeq$40 volts per electrode pair and that damage to the wall would result when the power available to the arc was in excess of $\simeq$200 watts. The most severe damage occurred on the anode wall, where the

Lorentz force acting on the high current arc drives the arc into the wall; considerable damage, however, has also been observed on the other walls of the generators. Although experiments at AVCO have shown that voltages as high as 120 volts can be maintained over some of the insulator gaps, efforts at AVCO have been primarily directed toward maintaining a relatively uniform Hall voltage at levels below 40 volts per pair, toward limiting the power which can be coupled to the arc and toward other controls of the arc after it has formed [7]. Little effort has been directed toward an identification of the breakdown mechanism. While some success has been achieved by their approach, the problems of leakage and breakdown have been present in the most recent experiments at AVCO [8].

1.2.2 Cutting

In the experiments by Cutting [9] using a noble gas plasma with nitrogen added to reduce non-equilibrium effects, Hall voltages in excess of 40 volts per electrode pair were maintained over a .65 cm gap at high Hall parameter. Leakage of as much as 50% of the total transverse current was measured on the cathode wall; however the leakage was always diffuse and well predicted by a numerical solution of the two-dimensional current distribution and energy equations. Measured leakage on the anode wall was less than the predicted leakage and no arcing was observed for any experimental condition. Unfortunately, the electrode wall construction was such that the electrodes were separated by a plasma gap rather than a ceramic insulator; this factor and the large differences in experimental conditions make comparisons with the combustion generator experiments of AVCO and others difficult. The results of this work do stress that current leakage does not imply breakdown and that in the absence of breakdown, reasonable predictions of the plasma behavior can be performed using a two-dimensional fluid and electrical model.

1.2.3 Oliver

Oliver has obtained a solution of the two-dimensional boundary layer-core flow equations appropriate for combustion MHD generator conditions and used the model to make some predictions relating to the problem of breakdown [10]. The fluid mechanical model is well developed, including the effects of the Lorentz body forces in both the axial and transverse momentum equations; however the electrical solution is based upon a very

coarse finite element analysis and equilibrium electrical conductivity is assumed. Although the model functions used in the finite element analysis satisfy the electrical equations globally, it is questionable whether the details of the coupling between the fluid and electrical state of the plasma are well modeled. Further, the present study suggests that the assumption of equilibrium conductivity limits the wall temperature to above ≈2000°K, as will be discussed later. Periodic boundary conditions are applied to a single electrode pair, imposing the condition that a breakdown, should it occur, must occur at every inter-electrode gap. Finally, the thermal and electrical behavior of the inter-electrode insulator is not included in the analysis, although the inter-electrode insulator surface temperature can be varied in the model. Since a detailed evaluation of this work requires, among other things, a comparison with experimental data, further discussion is deferred to Chapter 5, where the theoretical results of the present work are presented and compared with experiment.

1.2.4 High Temperature Institute

Experiments using the Soviets actually was done as part of the U.S.-USSR cooperation. U-25 and U-02 facilities have yielded some evidence of axial field limitations [11]. At the time of writing this thesis, an experiment specifically designed to study the problem of breakdown was performed on the Soviet U-02 facility [12]. This experiment was similar to the induced field experiments performed in the present study, the results of which are described in Chapter 3. The Soviets studied inter-electrode gaps of 5 mm and 15 mm, obtaining high Hall voltages through augmentation of the Faraday current and through increases of their normal electrode pitch. Photographs were taken of the inter-electrode region during operation with current to augment the time records taken for the overall electrical parameters. No breakdown was observed in these experiments. Some experimental data from this experiment is compared to results from the present investigation in Chapter 3.

1.3 Objectives of the Present Investigation

The purpose of this research was to produce and study axial voltage breakdown under non-slagging, combustion MHD conditions. While

focusing on slag-free conditions may be somewhat restrictive, the understanding and predictive ability gained in studying breakdown along non-slagging walls presents, at the least, a beginning for the understanding of the slagging wall behavior. Specifically the objectives of the investigation were:

a) to identify the mechanisms responsible for axial voltage breakdown and to identify the parameters of importance,

b) to propose and to verify a theoretical model capable of predicting whether breakdown will occur,

c) to use the theoretical models and the experience gained to propose and evaluate possible solutions to the problem of breakdown.

1.4 Organization of the Thesis

The remainder of the thesis is organized into five chapters, with detailed description of some of the experimental apparatus and some of the numerical techniques deferred to the appendix. Chapters 2 and 3 summarize the experimental work, describing the apparatus and presenting the most important results. A description of the analytical model is contained in Chapter 4, which also presents the general characteristics of the results of the model. Direct comparison of theoretical predictions and experimental results are made in Chapter 5 and the areas of agreement and disagreement are discussed. Chapter 6, the final chapter, presents a summary of the entire investigation and outlines the main conclusions of the study.

CHAPTER 2

EXPERIMENTAL APPARATUS AND PROCEDURES

2.1 Introduction

In this chapter, an overview of the experimental approach is first given, with emphasis on describing the purpose of each type of experiment performed and on describing the specific purpose of each of the diagnostic measurements employed in the experiment. A detailed description of the two basic experimental set-ups and of the diagnostic techniques is then given. Experimental procedures are also discussed.

2.2 Overall Experimental Approach

Initial generator experiments were performed with the Stanford MHD generators to determine if breakdown would occur for their normal operating conditions. Hall voltages well in excess of the steady arcing value of 40 volts per pair observed at AVCO were maintained over insulator gaps of 0.9 cm, with no evidence of arcing or abnormal behavior [13]. Detailed diagnostic measurements were limited by access problems, and systematic variation of the important parameters limited by the fixed geometry of the generator. Further, detailed calculations for the generator configuration were expected to be extremely time consuming due to the slow convergence of current distribution algorithms, even at moderate Hall parameter. To facilitate a rapid development of the diagnostic and calculation techniques, experimental and analytical efforts were directed toward a simplified configuration, shown schematically in Figure 4, where an external voltage is applied to a pair of adjacent electrodes, rather than being induced by the Hall effect. Although the magnetic field is absent in this configuration, the important features of Joule heating in the plasma and thermal and electrical conduction in the inter-electrode insulator are retained, suggesting that strong similarities, at least of a qualitative nature, should exist between the two cases. Breakdown was first observed in the applied field experiments and the understanding of the breakdown process gained through the applied field work was used to determine conditions favorable for breakdown in the subsequent induced field experiments. Further, the diagnostic techniques developed

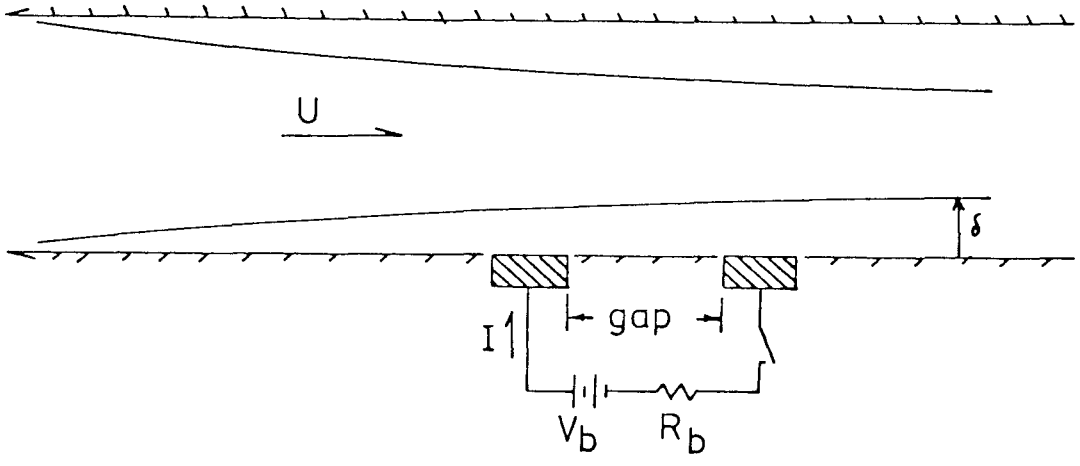

Figure 4. Schematic of Applied Field Configuration

in the applied field experimental work were used in the final induced field experiments with only relatively minor modifications required.

Several diagnostic techniques were developed with the overall goal of identifying the mechanisms responsible for breakdown, providing detailed measurements for comparison with the calculations and yielding general information helpful to the modeling process. A dual-filter cinephotographic technique was used to monitor the inter-electrode region and to provide separate records of the plasma and the insulator behavior. In particular, with this technique it was possible to monitor the formation of current constrictions and deduce whether the dominant current transfer was through the plasma or the insulator. The insulator record was calibrated such that an estimate of the surface temperature could be obtained. The photographic record of the plasma response was not calibrated to yield plasma temperature; however, a semi-quantitative measurement of the plasma temperature in the region above the inter-electrode insulator was provided by a simple measurement of the total emission intensity of a spectral line. A quantitative measurement of the current distribution at the electrode was provided by a subdivided electrode. Voltage probes were used to determine the behavior of the near anode and near cathode voltage drops during pre-breakdown and post-breakdown times, to determine whether variations in these quantities might be important in the breakdown process. Finally, large scale fluctuations in plasma temperature or seed fraction were monitored by optical emission techniques to determine if these fluctuations played a role in the breakdown process.

2.3 Applied Field Experimental Apparatus and Procedures

In this section the experimental apparatus used in the simplified configuration is described. The basic combustion system is first considered and then the test section and basic instrumentation techniques are discussed. A description of each of the advanced instrumentation techniques is then given and finally the experimental procedures are set down.

2.3.1 Basic Combustion System

The basic combustion system, referred to as the M-2 combustor, consists of a swirl-stabilized, liquid fuel burner feeding a plenum

chamber which exhausts through a subsonic nozzle as shown schematically in Figure 5. The M-2 combustor components are of stainless-steel, water cooled construction, with the majority of the interior surfaces lined with refractory brick (MgO) to reduce the heat loss. In the present experiments, the working fluid was obtained by the combustion of ethanol (C_2H_5OH) with oxygen, and nitrogen was added to reduce the combustion products temperature to a level typical of expected commercial MHD applications. Potassium seed was introduced to the system by dissolving potassium hydroxide in the ethanol, with a typical seeding fraction of 1% potassium by weight. Sodium hydroxide was also added to the ethanol for experiments where sodium emission techniques were to be used; typically ≈0.01% sodium by weight was added. Reactant flow rates and component heat losses are routinely measured such that an energy balance could be performed for the combustor system. Nominal operating conditions for the M-2 combustor are given in Table 1 and further details can be found in reference [14] and in Appendix H. Actual combustor operating conditions for each run will be presented when experimental results are cited.

2.3.2 Test Section and Basic Instrumentation

The test section for the applied field experiments, a constant area extension of the M-2 combustor, was formed by lining a copper walled shell with MgO bricks. The electrodes and inter-electrode insulator were mounted on a special section, described below, which was inserted in the center of the bottom wall of the test section. Cooling was provided to the test section walls by copper cooling tubes soldered to the external surfaces, thereby allowing easy modification as access requirements changed. A double layered MgO liner was used, with the layers overlapped to provide good electrical insulation between the copper test section and the conducting plasma. The brick thicknesses were chosen such that the interior surface temperature would be in the range of ≈1800°K to 2200°K for the flow conditions of interest. A sketch of the test section, showing the important dimensions is given in Figure 6; a photograph of the partially assembled test section is shown in Figure 7. In some experiments, thermocouples were inserted at two locations in the outer MgO brick such that the heat flux and the surface temperature could be deduced. Surface temperature measurements were also made using an optical pyrometer sighted

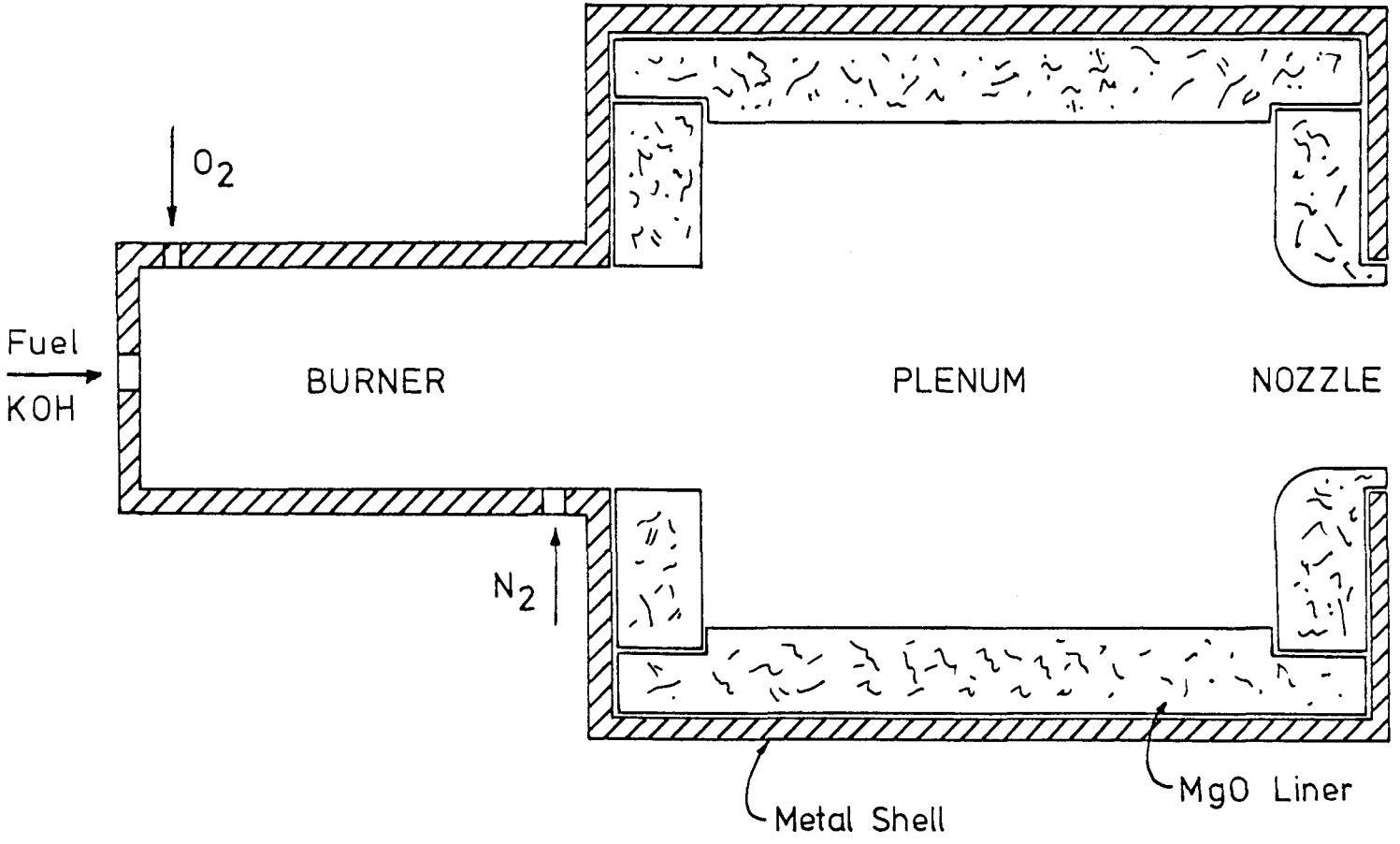

Figure 5. Schematic of the Stanford M-2 combustor system.

Table 1. Nominal flow conditions of the M-2 Combustor.

Mass flow rate	=	.15 - .3 kg/sec
Pressure	=	1 atm.
Temperature	=	2700 K
Electrical Conductivity	=	10 mho/m
Core Velocity	=	600 m/sec

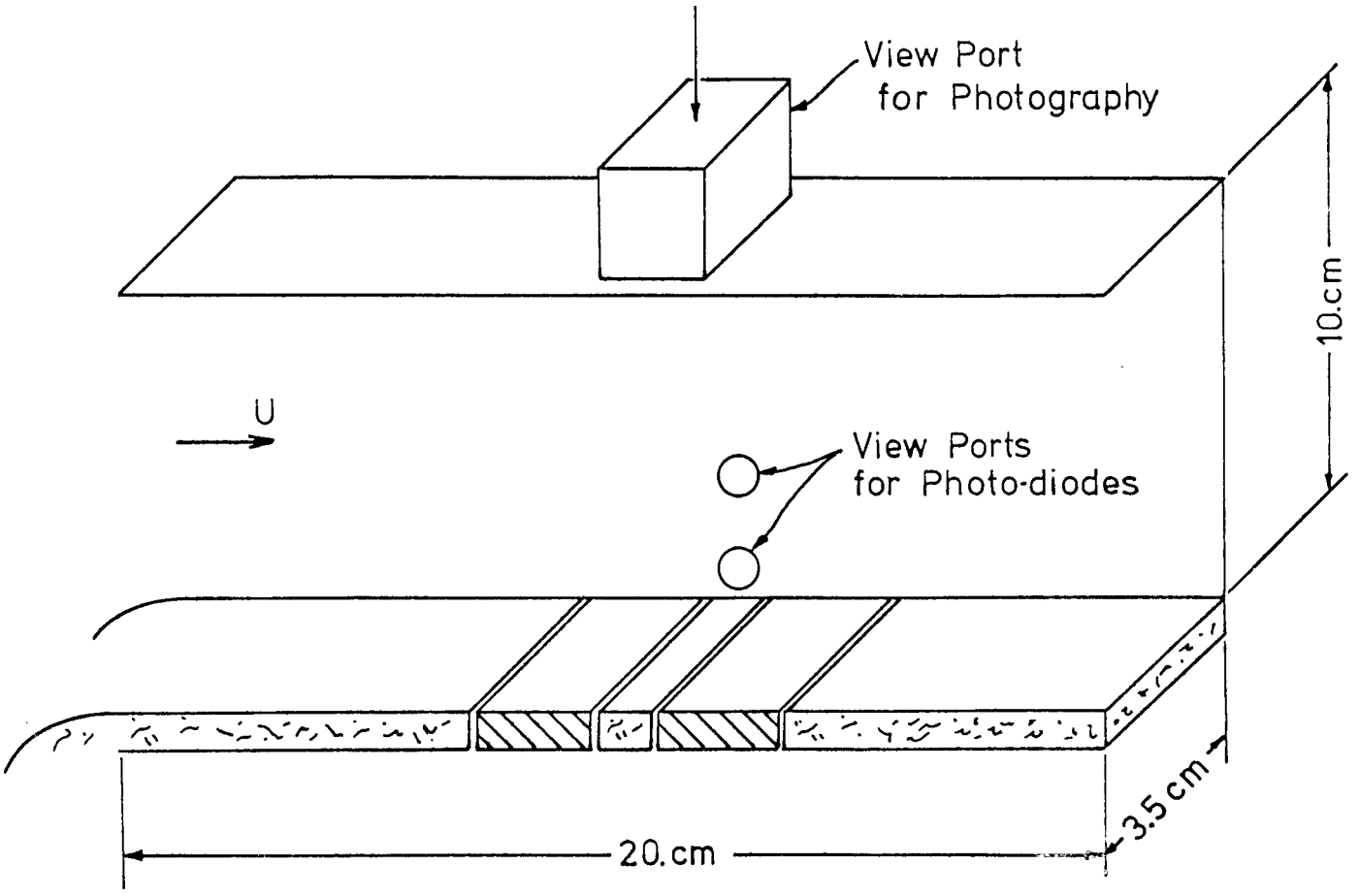

Figure 6. Sketch of the test section used in applied field experiments.

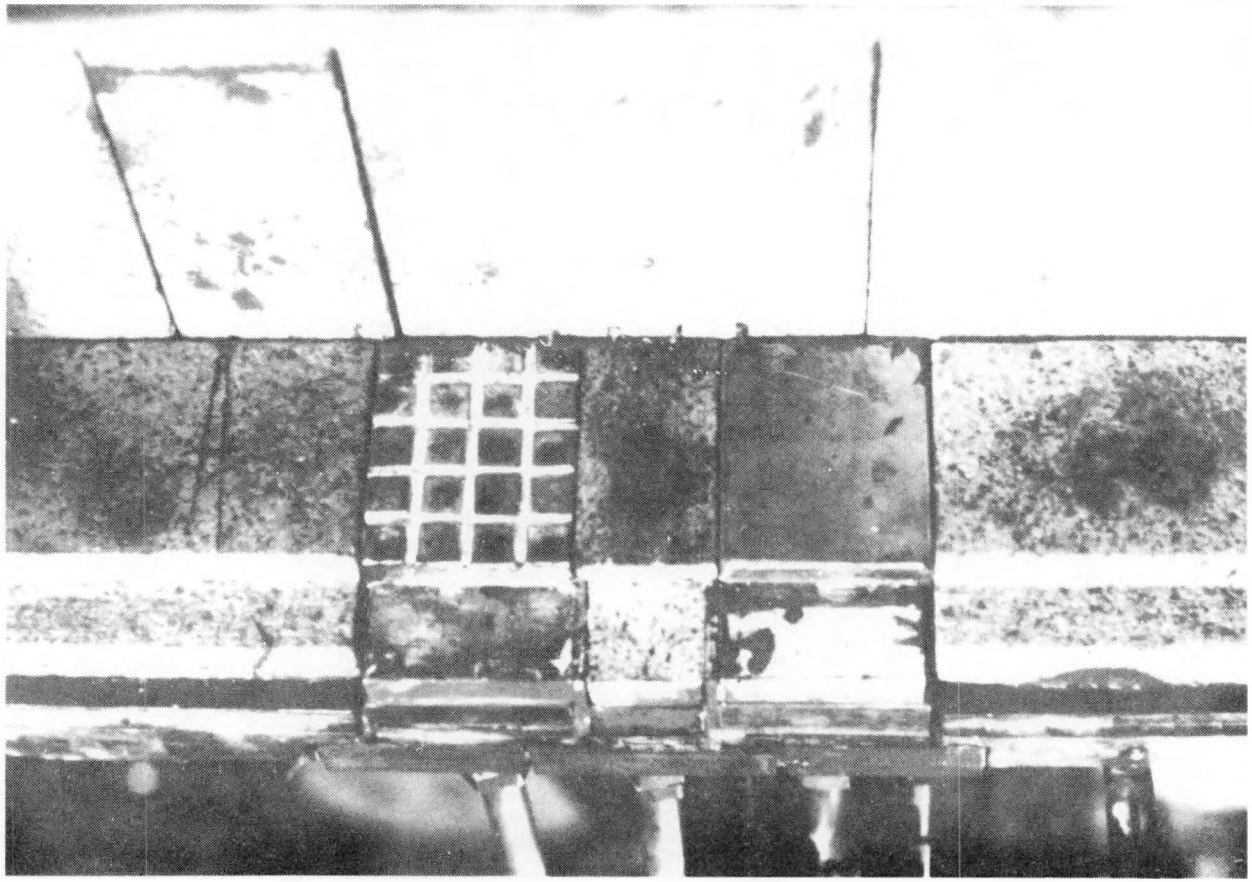

Figure 7. Photograph of electrode wall of applied field test section.

through the downstream end of the channel. Static pressure measurements at the burner, plenum, and test section inlet were made and recorded using pressure transducers. The pressure at the test section exit, which exhausted into the ambient air, was assumed to be atmospheric.

The two electrodes and the inter-electrode insulator were mounted on a phenolic support piece, such that the electrode/insulator module could be completely assembled independent of the test section. Variation of the important parameters, such as insulator gap and insulator thickness, was accomplished by modifying or replacing the appropriate components of the electrode module. A schematic of the electrode module and the various components, is shown in Figure 8. The stainless-steel surface of the non-segmented electrode was designed to operate at a temperature in excess of ≈1000°K, to avoid the formation of highly resistive surface coatings of seed oxide condensate [15]. Surface temperature uniformity was maintained by furnace brazing a water-cooled copper-backing piece to the stainless-steel electrode head. To keep the overall thickness of the electrode reasonably small, the stainless-steel piece was thermally choked by milling slots into the rear face. Chromel/alumel thermocouples, inserted to within ≈1/32" of the surface, were used to monitor the electrode temperature. Due to reflected radiation from the considerably hotter sidewalls, measurement of the surface temperature with an optical pyrometer was not possible.

Some cooling of the inter-electrode insulator is effected by conduction to the adjacent electrodes, however for these experiments additional cooling was supplied in the form of a water-cooled copper-backing piece for the insulator. In most experiments, thermal contact between the copper and the insulator was provided by RTV-60, a silicon-rubber sealant and a thermocouple inserted slightly into the back face of the insulator was used to determine whether good contact remained throughout the experiment. Thermocouples were not used to measure the surface temperature of the inter-electrode insulator, for fear that they would significantly alter the breakdown characteristics. Surface temperature measurements were made with the optical pyrometer, however the accuracy of readings obtained for low surface temperatures are questionable due to the reflections from the hot side walls.

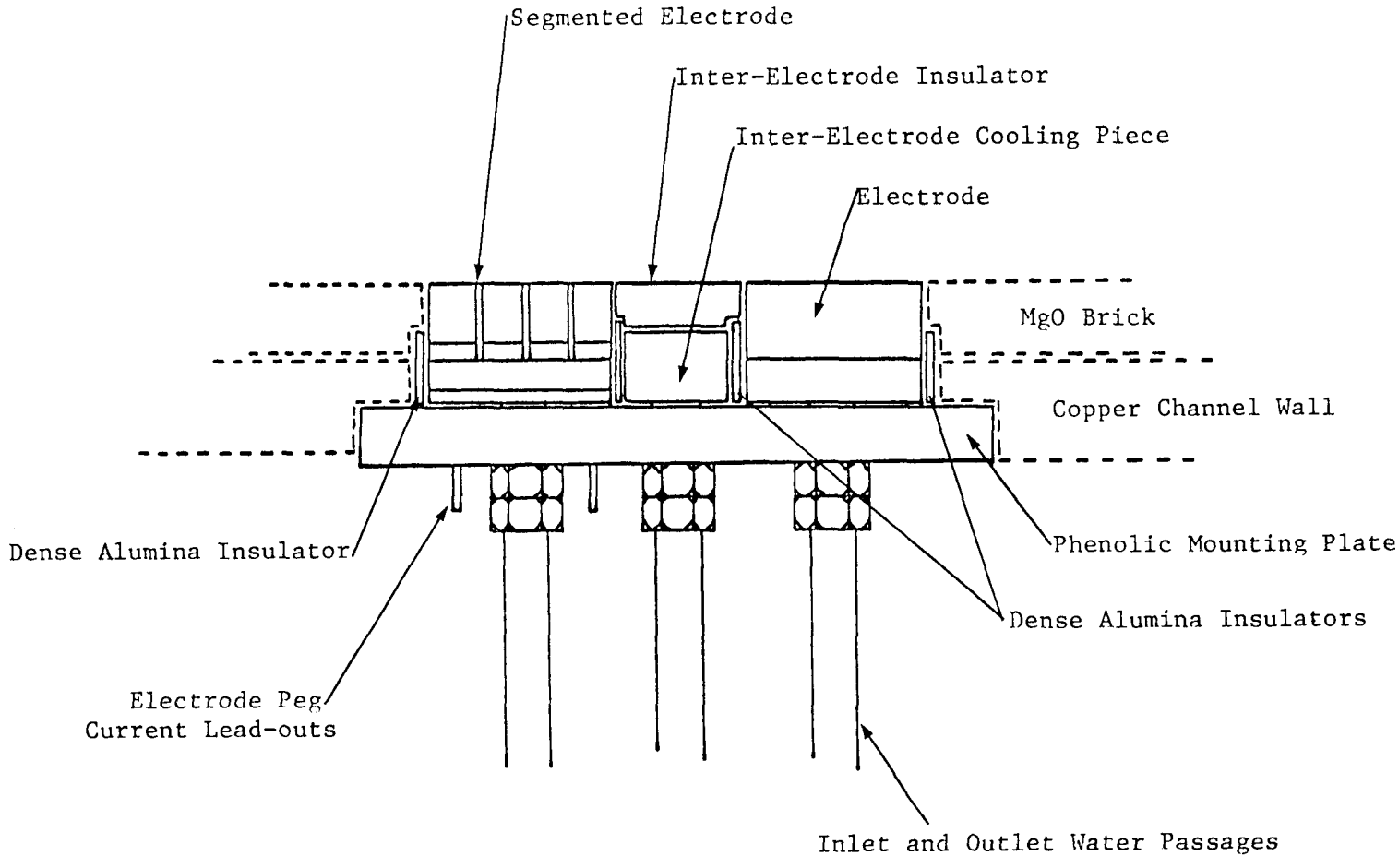

Figure 8. Schematic of electrode module which allowed pre-assembly of the inter-electrode wall.

A schematic of the external circuit for powering the electrode pair is shown in Figure 9. Groups of 10 automotive batteries were connected in series to provide a low impedence supply voltage at discrete levels up to 720 volts. In series with the batteries was an adjustable ballast resistor, which could be varied (in discrete increments) from $\simeq 1\Omega$ to $> 100\Omega$. This combination of supply voltages and ballast resistors was adequate to produce acceptable load lines for all experiments. A silicon controlled rectifier (SCR) was used to switch on the circuit with a characteristic rise-time of $\simeq 10\mu$ sec. The circuit was turned off using a conventional relay.

Several instruments were used for recording the response of the important parameters. Key thermocouple outputs were displayed on a strip chart recorder to allow adjustment of the flow parameters (and thus the heat flux) to obtain acceptable component temperatures. Slowly varying parameters were measured by a VIDAR scanning, integrating, digital voltmeter controlled by an HP-2100 computer, with on-line reduction of the data performed as seemed appropriate. The behavior of 15 to 20 parameters were recorded with a time response of $\tau_{min} \simeq 1$ msec using 2 CEC high speed oscillographs, with appropriate amplifier and galvanometer control circuits interfacing the transducers to the galvanometers. A few parameters were recorded with fast time response ($\tau_{min} < 1$ msec) using oscilloscopes.

2.3.3 Advanced Diagnostics

Dual-Filter Cine-Photography. Optical access was provided to the channel looking down on the inter-electrode region and movies were taken during operation with current. The field of view provided by the window assembly extended far enough in the flow direction to observe the edges of both electrodes and the entire inter-electrode insulator, and extended across the entire channel width. Details of the optical port design, including the window protection techniques, are presented in Appendix G. The inter-electrode region was viewed through a special optical set-up, shown schematically in Figure 10, which formed a dual image of the region on each frame of the film. One of the images was formed through a red cutoff filter which, together with the spectral sensitivity of the film (Kodak, High Speed Ektachrome) isolated a relatively narrow wavelength

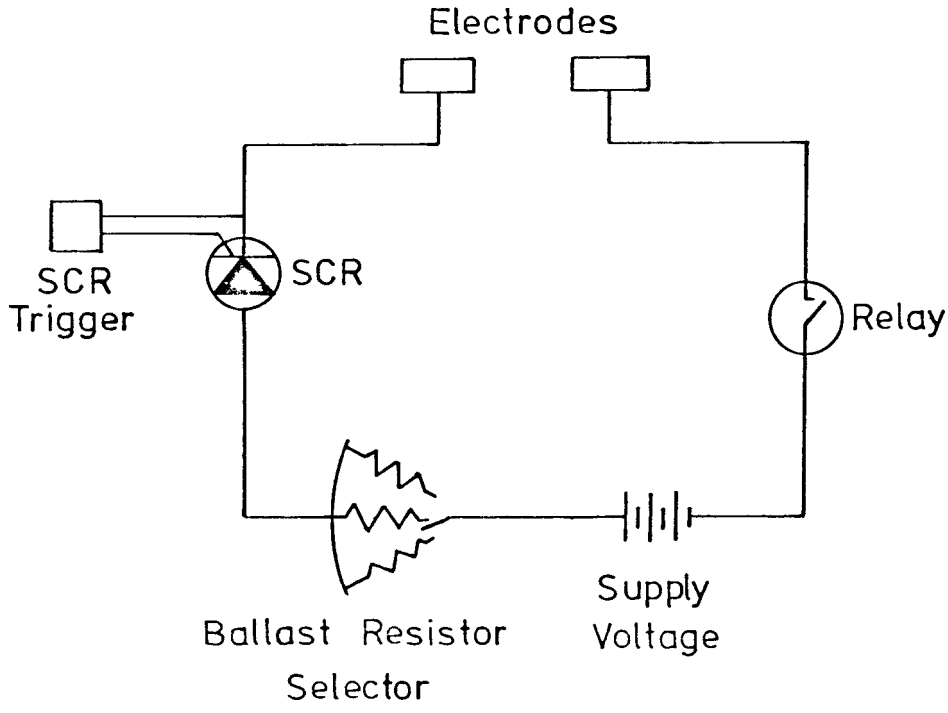

Figure 9. Schematic of the external circuit used for the applied field experiments.

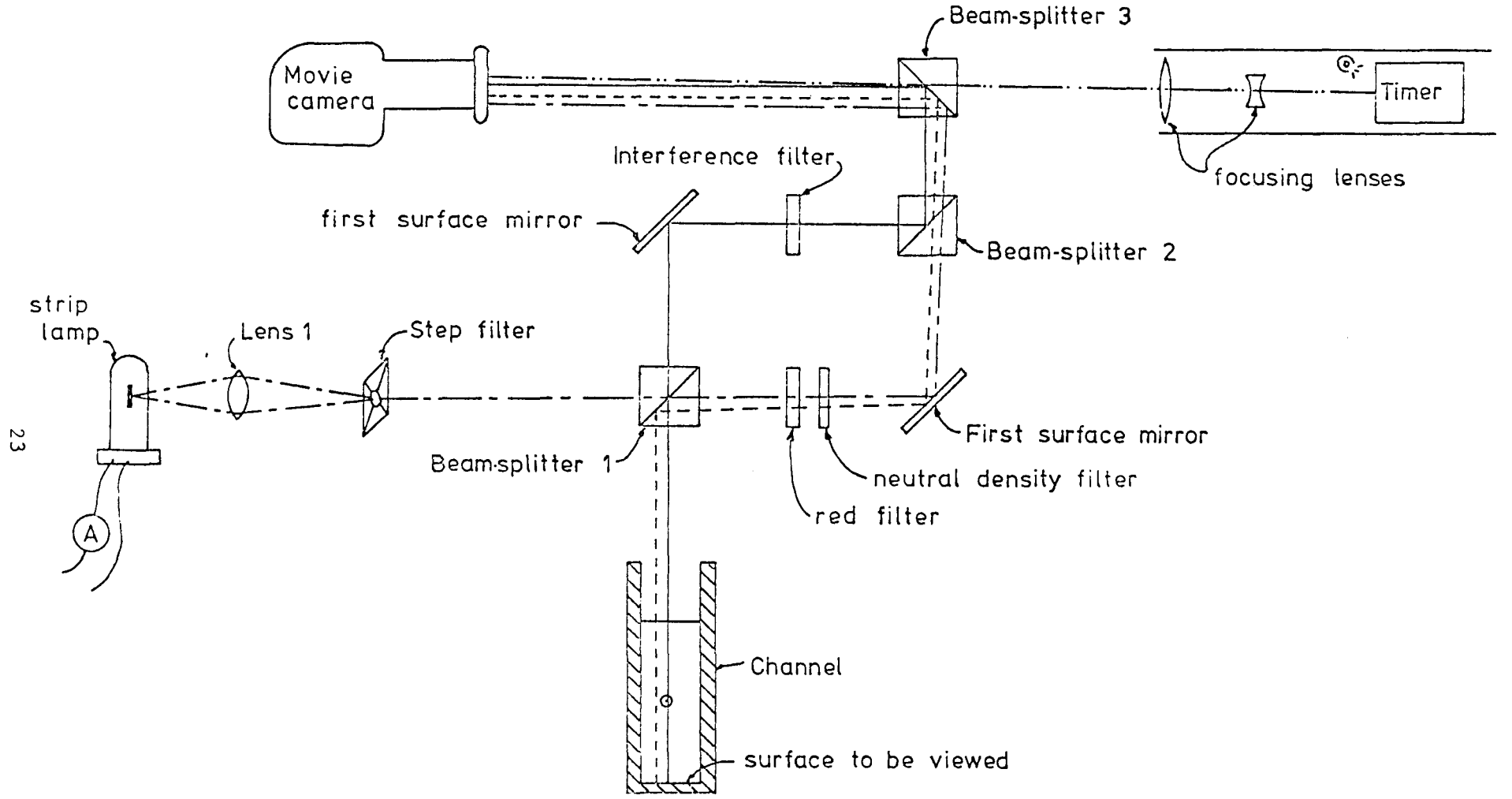

Figure 10. Schematic of dual-filter photographic device, detailing the various light paths and components. A detailed description is contained in Appendix B.

region from ≃6500 Å to ≃7000 Å . No strong spectral lines are observed from the plasma in this spectral range, so the film exposure from this image responds primarily to the intensity of radiation emitted by the wall. The second image was formed through a bandpass filter centered near the potassium doublet at 4044-4047 Å . Exposure from this image, which appears blue on the film, responds strongly to the intensity of radiation from the plasma, although significant sensitivity to radiation emitted by the wall will result if the bandpass of the filter is too broad or the surface temperature very high.

A calibration technique was used to allow the determination of insulator surface temperature from the red image as formed on the film. The image of a five region neutral density step filter, illuminated from the rear by a tungsten lamp, was formed on the film through the main optical train. The transmittance of each of the regions was determined by calibration, such that a knowledge of the brightness temperature of the lamp and the emissivity of MgO allowed a determination of the "effective MgO temperature" for each region of the step filter. For a typical tungsten lamp current, the five regions represented surface temperatures from ≃2500°K to 1700°K. Comparison of the exposure of a region of the insulator on the red image, with the regions of the step filter as seen through the red filter, allowed a determination of the surface temperatures. An image of the step filter was also formed through the blue filter, as an indicator of the sensitivity of this image to wall emission. It was found that a very narrow bandpass filter (≃10 Å Band width) was required to reduce the interference to acceptable levels. No attempt was made to obtain quantitative measurement of plasma temperature using the films. Further details of the photographic method and of the calibration techniques used is given in Appendix B.

The movie camera used was a Beaulieu 4008 M3 super-8mm camera capable of framing speeds up to 70 frames per second, with an exposure of ≃4 milliseconds at that speed. A brightly lit clock, with resolution to ≃0.1 second was imaged onto the film to give an indication of the framing speed and to provide a positive identification of the footage corresponding to each set of experimental conditions. Significant attenuation of the light results from the three beam splitters (and the various filters), such that even though the radiation from the plasma and the wall are

intense, a "fast" film was required to keep the f/# high and the depth of field long. To avoid over exposure of the film when breakdown occurred, exposure conditions were frequently chosen such that frames with no breakdown were considerably underexposed. Properly exposed sequences for no current conditions were taken periodically to allow examination of the inter-electrode region for damage. A typical frame for no current conditions and a sketch identifying the various images on the frame are given in Figure 11.

Electrode Current Distribution Measurements. The upstream electrode was segmented in the flow direction and in the direction perpendicular to the flow, to facilitate the measurement of the current distribution at the electrode surface. The electrode surface was composed all, or in part, of rows (across the channel width) of 1/4" by 1/4" stainless steel pegs, as shown schematically in Figure 12; where only part was composed of pegs, the remainder was similar in design to the electrode described in Section 2.3.2. To avoid regions of high electric field which might affect the current distribution patterns, all edges of the pegs and other electrode parts exposed to the plasma, were rounded to a radius of 1/32". The pegs were electrically insulated from each other and from the water-cooled copper piece on which they were supported and by which they were cooled. Each peg had a current lead-out stem, which was attached to an external current shunt. The total current to each row of pegs and the current to the entire electrode were also measured. The main cooling of the pegs was through the alumina insulator, with the necessary good thermal contact required maintained by metallizing both surfaces of the alumina and brazing it to both the stainless and the copper. Further details of the electrode design, including the special techniques required to produce reliable alumina to metal braze joints are given in Appendix A.

Near-Electrode Voltage Drop Measurements

The near-anode and near-cathode voltage drops were measured by inserting voltage probes through the side-wall of the channel, approximately 2-4 mm above the electrode surfaces. Typically a 25 mil platinum wire, insulated up to the interior brick surface by an alumina sleeve, was inserted approximately 1/16" into the flowing plasma and the potential was measured relative to the appropriate electrode. Since voltage

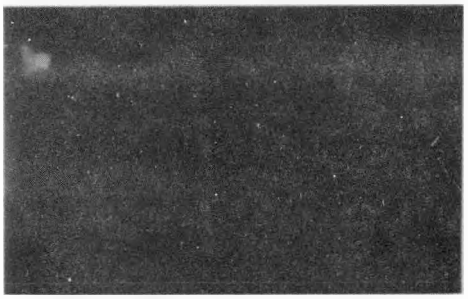

Figure 11a. Frame of the movies taken in the applied field experiments, showing the region when no current is flowing. Sketch below identifies the various features of the photograph.

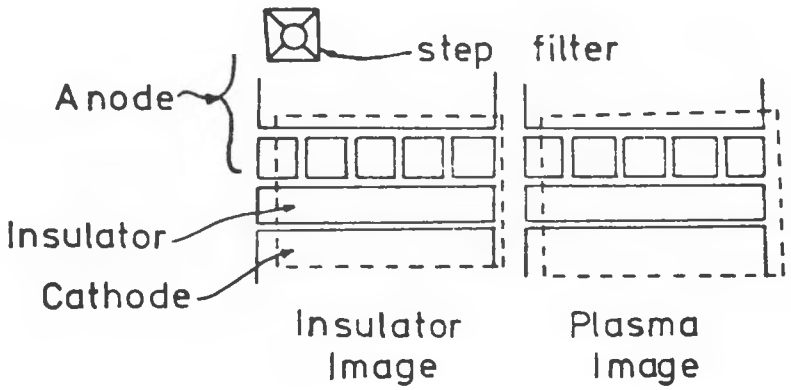

Figure 11b. Sketch of view into the camera, identifying the features of the photograph. The dashed lines show the region recorded on the film. The right image, formed through an interference filter, is designated "plasma"; the left image, formed through a red filter, is designated " wall".

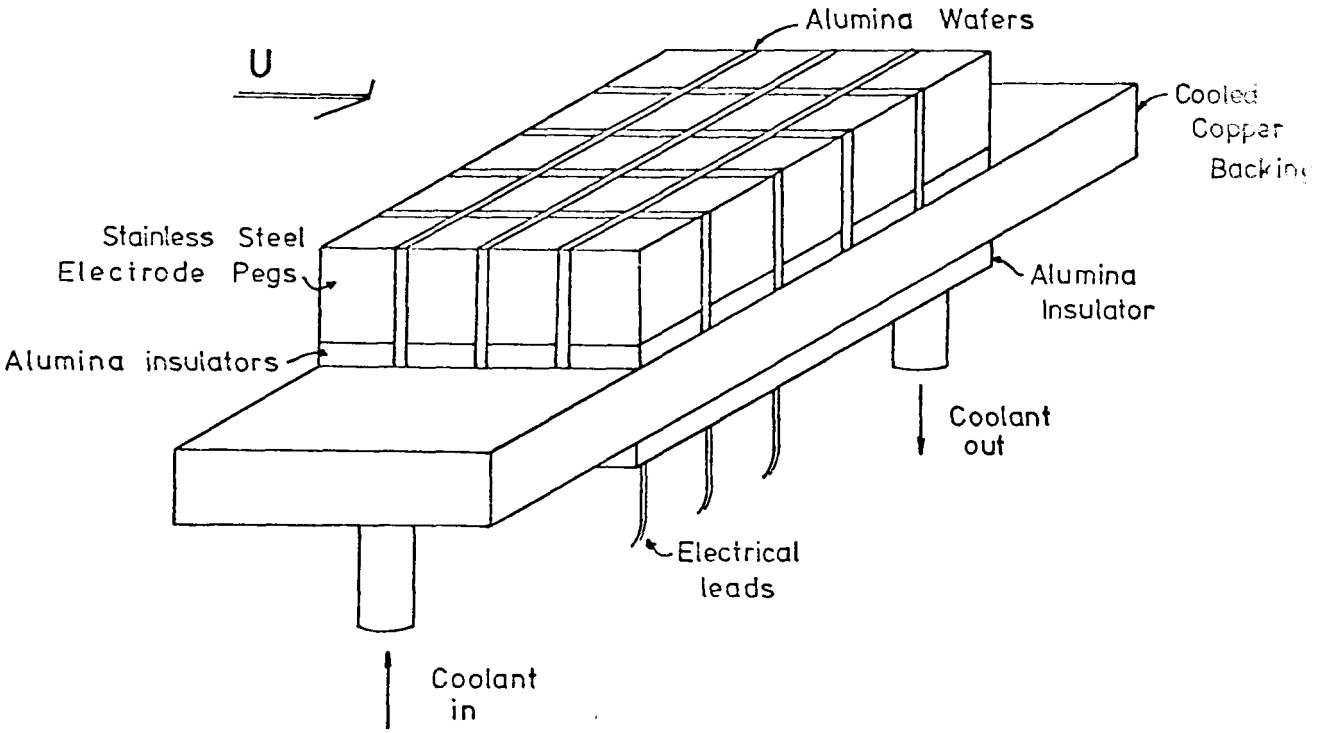

Figure 12a. Sketch of overall design of segmented electrode used in the applied field experiments.

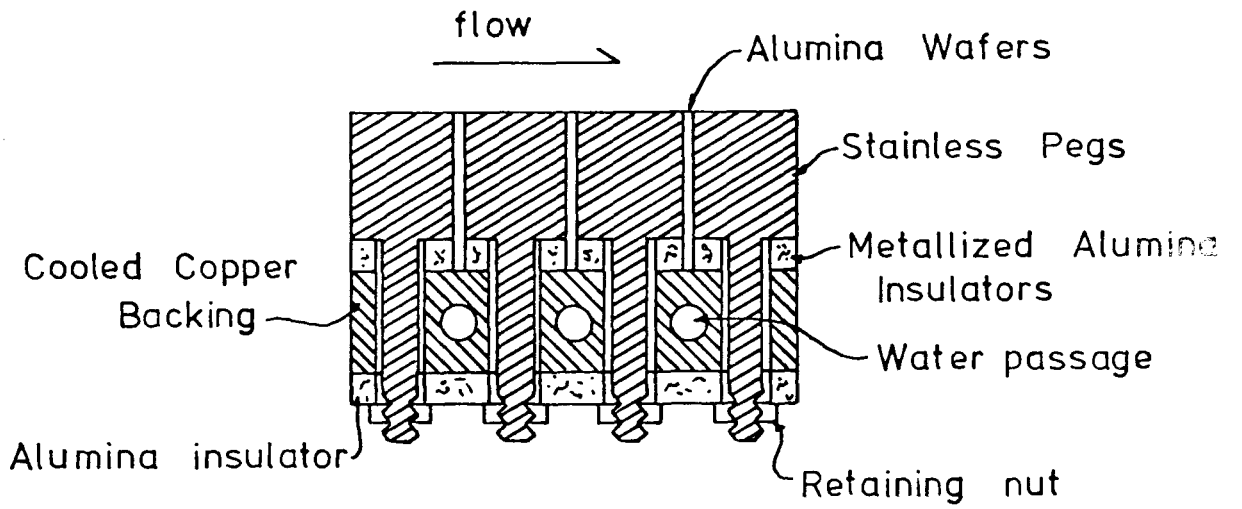

Figure 12b. Sketch detailing the construction of the segmented electrodes. Further details are indicated in Appendix A.

differences were greater than a few volts for all but the lowest currents, sheath effects at the probe surface could be neglected and standard voltmeters could be used to measure the potential difference. In some experiments, probes were also inserted in the region over the inter-electrode insulator.

Relative Temperature Measurement. Optical access was provided through the sidewalls to allow measurement of the total emission intensity of the potassium line (4044 Å) or sodium D-line (5890 Å) radiation. For this purpose, photo-diode detectors with appropriate electronics were used, with the spatial region of view defined by a lens-aperature arrangement. Spectral filtering was provided by band-pass interference type filters; a 40 Å band width filter centered at 4040 Å was used to isolate radiation from the potassium lines and a 12 Å band width filter centered at 5888 Å was used to isolate radiation from the sodium lines. The influence of radiation from the opposing brick sidewall was reduced by locally cooling those regions of the wall in view of the detector. A sketch of the view into the channel is shown in Figure 13. Further details of the optical access port and of the detection optics and electronics are given in Appendix G and Appendix C respectively.

For the case of a spatially non-uniform plasma, the problem of relating the total intensity to the population temperature of the emitting species is not straight forward. Even in the simple case of an optically thin gas and a non-emitting wall, the intensity depends on the line-of-sight averaged population temperature. If for example it is desired to determine the core temperature from intensity measurements looking through the cold boundary layer region, the form of the temperature variation through the boundary layer must be known. If the gas is not optically thin to the radiation, as is the case for the sodium and potassium lines, accurate determination of the total intensity leaving a spatially non-uniform plasma would require an integration of the radiative transfer equation. Again the variation of temperature along the line of sight would have to be known. Hohnstreiter [16] has shown that for the developing turbulent boundary layer flows typical of the present work, the relative intensity along two lines of sight (or along the same line of sight at two different times) could be related to the respective core temperatures by the optically thin relations, with an error of only a few

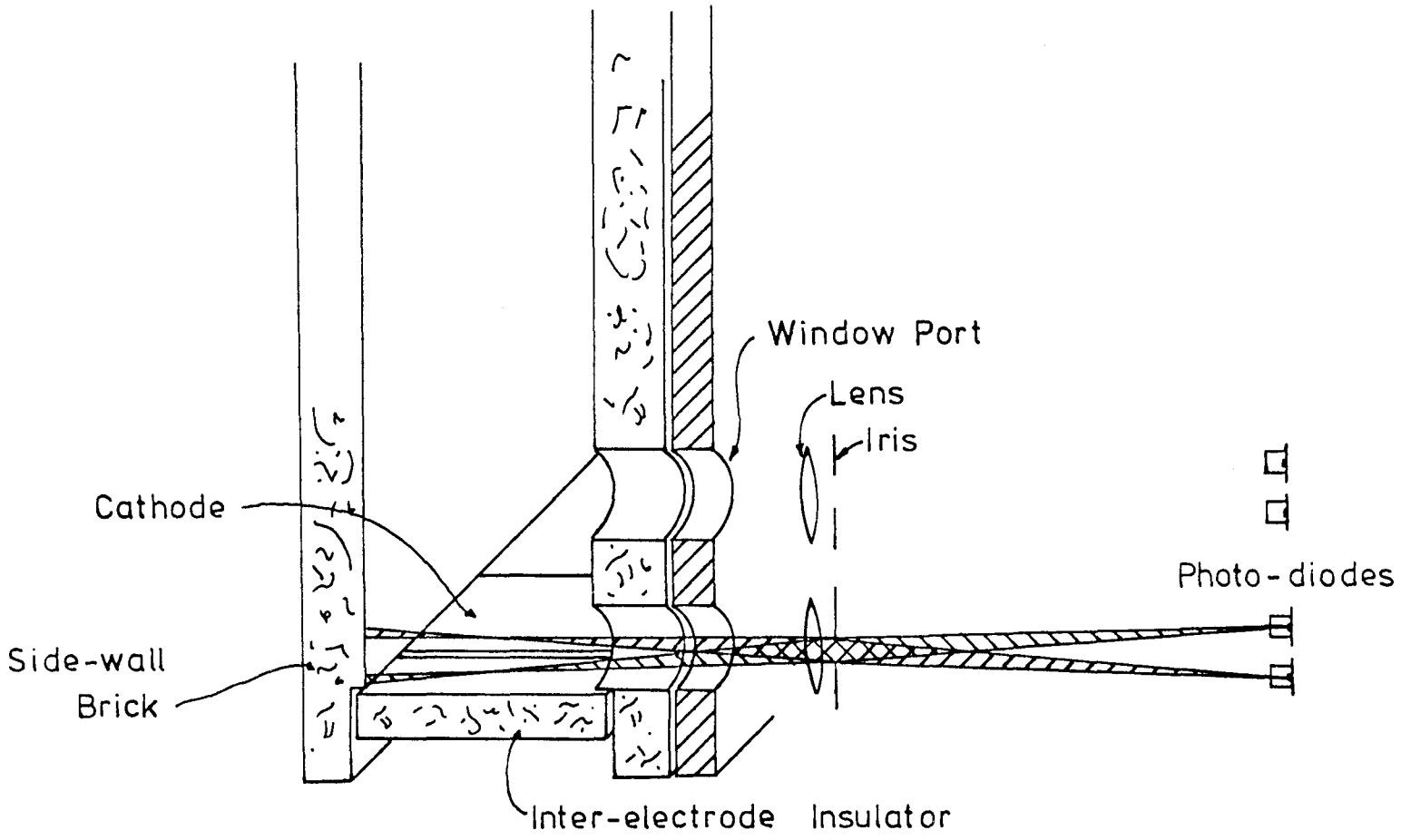

Figure 13. Sketch of view of the side-view photo-diodes. As many as four photo-diodes were used, each sighted at different heights above the inter-electrode insulator surface.

percent. Thus, if the absolute temperature of a reference condition can be determined in some manner, the relative intensity measurements can be used to determine the temperature at another location or another time. For more severe temperature variations, such as would result from a constricted discharge region, the optically thin formula would not be expected to be of sufficient accuracy and solution of the radiative transfer equation would be required even to make the relative temperature measurements. Further details of the calculation methods and background theory are given in reference [16].

The technique was applied to monitor the gas flow and detect hot (or high seed fraction) slugs of plasma which were observed in several experiments with the combustor system. For this purpose two diodes, filtered to detect radiation from the sodium D lines, were sighted across the channel width away from the electrode wall boundary layer, as shown schematically in Figure 13. Assuming the variations to be slug-like, the optically thin formula should be sufficiently accurate to relate the temperature (or seed number density) of the hot gas bursts to the normal conditions. A second application of the technique was to monitor the formation of current constrictions in the region above the inter-electrode insulator. For this purpose, two diodes were sighted across the center-line of the inter-electrode insulator $\simeq$2 mm and $\simeq$8 mm from the insulator surface as shown in Figure 13. In this way an estimate of the location above the insulator and the spatial extent of the constriction can be made. Further, if the location relative to the sidewalls and the width of the constriction were determined by the photographs taken from above, a rough determination of the temperature in the constricted discharge region could be made. In addition to responding to the formation of constricted discharges, the diodes also respond to the slug-like fluctuations and to any diffuse, but relatively large, changes in temperature in the near-wall region which might occur when the discharge is first initiated.

2.3.4 Experimental Procedures

The long preparation time of the experiments, the overall complexity of the experimental apparatus and diagnostics and the limited run time (due to fuel and oxidizer storage capacity) dictated that a well planned

and conservative experimental strategy be adopted. For this purpose, each experiment was performed in two parts--a checkout experiment followed within a day or so by the actual experiment. Further, the experimental conditions to be run were specified before the experiment and detailed instruction sheets were prepared for each of the 8 to 12 persons helping with the experiment. Although not strictly adhered to, the detailed run plan allowed the majority of the runs to be performed quickly and efficiently, leaving more time for making extra runs which the on-line data analysis indicated would be useful.

Overall Experimental Run Plan. The checkout and main experiments were structured in four parts: a preheat phase, a thermal and flow checkout phase, an electrical powered phase and finally a post-heat phase. The preheat stage, which was the same for both experiments, was used to slowly heat the ceramic liners and reduce the possibility of damage from thermal shock. For this purpose, the combustor was operated with propane rather than alcohol and the gas temperature was increased in steps over a period of about 40 minutes. Key thermocouples were monitored and the combustor and channel inspected for abnormal behavior. With preheat sucessfully completed, the alcohol flame was ignited, with the temperature and total flowrate kept relatively low. Unseeded alcohol was used for this portion of the experiment. For the checkout experiment, with some components were being tested for the first time, this phase was usually the most important and the most time-consuming. The response of key thermocouples was monitored and the channel components inspected for abnormal behavior. After the components had reached steady-state, the nitrogen to oxygen ratio was reduced and/or the total flow rate increased and the response carefully followed. This process was repeated until the desired condition was reached, some component approached its thermal limit or some other problem was encountered. Problems of a less serious nature were resolved at the time, perhaps returning to preheat to avoid using too much fuel and oxygen, and the run was continued. More serious problems were often handled in a cautious manner, especially when they arose during the checkout run. If, for example, it seemed likely that some repair could be made in the day separating the checkout and main experiments, the decision was usually made not to risk damage to the component, and the remainder of the experiment was performed at the

flow condition which was safe. After the desired or the most severe possible flow setting was reached, final alignments and checkouts of the diagnostics and of the electrical circuits were made, and the personnel were readied for the electrical powered phase. Seeded fuel was then introduced into the combustor. The procedures during this phase, described in more detail below, were the same for the checkout and the main experiments, although in the checkout experiment only a few electrical conditions were run, and the voltage was always kept well below the level expected to produce breakdown. The postheat stage was designed to flush the potassium from the combustor and test section bricks and to cool the bricks somewhat, before the flame was extinguished. Usually the combustor was operated for several minutes on unseeded alcohol at a high temperature and flowrate and then the flowrate and temperature were reduced slowly over a period of minutes. A fast shutdown was then effected, to prevent the condensation of water on the channel walls. Following the checkout experiments the channel exit was capped and a slight positive pressure of nitrogen maintained in the combustor and channel. This prevented moisture from being absorbed into the bricks where it could combine with any potassium left in the brick and result in deterioration of the brick.

Computer Control. Coordination of the various instruments driving the electrically powered phase was performed by an HP-2100 mini-computer. For this purpose a programmable relay register card, with 16 low current ($\lesssim$100 ma) relays was interfaced with an external relay box equipped with 16 large current ($\lesssim$10 a) relays and with override switches and status lights. With the appropriate software the computer-relay system would switch on the instruments, trigger the SCR to initiate current, switch off the current after a specified time and switch off the instruments. In addition, the computer controlled the operation of the scanning digital voltmeter system, storing the data and performing several types of on-line data reduction.

Detailed Procedures for Current Runs. After establishing the desired flow conditions, a series of electrical runs were made. For each run, the test personnel adjusted the manually operated controls of their instruments to the specified settings for that run. Typically, this included selection of the proper supply voltage and ballast resistance, proper camera film speed and f/#, oscilloscope sensitivities and sweep speeds

and input of the proper control parameters to the computer program. When the run coordinator was satisfied that all personnel were ready, he initiated the run by pressing a button. The computer then assumed control until all the data for that set of conditions were taken, at which time control was returned to the test personnel. Table 2 presents a flow chart of the operations performed by the computer and indicates the operations which were performed manually by the test personnel.

2.4 Induced Field Experimental Apparatus and Procedures

In this section, the experimental apparatus used in the induced field experiments is discussed. When appropriate, reference is made to descriptions made in the previous section. The basic combustion system, the test section and basic instrumentation are first discussed. A description of the advanced diagnostics used is then made and finally the experimental procedures are detailed.

2.4.1 Basic Combustion System

As in the applied field experiments, these experiments utilized the Stanford M-2 combustor operating roughly at the same operating conditions listed in Table 1. The reader is referred to Section 2.3.1 and to reference [14] and Appendix H for more details.

2.4.2 Test Section and Basic Instrumentation

The induced field experiments utilized the Stanford M-2 MHD generator, with electrode pairs installed at seven of the possible thirteen electrode locations. An adapter section equipped with an optical port was placed between the M-2 channel and the M-2 combustor nozzle to allow observation of the upstream portion of the bottom wall of the generator. The adapter section was a simple water-cooled copper shell lined with MgO bricks to form a constant area flow channel. The main test section, the M-2 generator, was constructed of a double-walled, water-cooled silicon-bronze shell. Except for the active portion of the electrode wall, the metallic shell was lined with a double layer of overlapping MgO bricks. The upstream (active) region of the test section was bricked to present a constant 10 cm x 3.2 cm flow area to the plasma, while the downstream portion was divergent and in fact formed the initial portion of the subsonic diffuser. After exhausting from the diffuser, the seeded combustion products

Table 2. Table displays sequence of events for a single experimental set point, indicating the functions performed by the computer using relay control.

Manual	Computer
Select Supply Voltage and Ballast Resistance	
Set Oscillograph speed and sensitivity	
Set movie camera framing speed and f/#	
Set Oscilloscope sensitivities and sweep speed	
Enter run identification into computer	
--- when coordinator determines all is ready computer is triggered.	
	Activate SCR circuits
	Turn on Oscillograph
	Turn on Movie Camera
	Reset single sweep of oscilloscopes
Manual abort anytime during run if necessary	Trigger SCR, oscilloscopes
	Start scanning digital voltmeter
	Terminate current after specified time.
	Turn off oscillograph
	Turn off movie camera
	Print Reduced data to console
	--- Return control to operator
Pull oscilloscope film and mark run identification	
Check film in movie camera and change as necessary	
Ready for next run	

were quenched by a water spray, scrubbed and exhausted to the atmosphere. A simplified sketch of the apparatus is shown in Figure 14 and the pertinent dimensions are given. Using previously obtained heat transfer data, the MgO brick thicknesses were chosen to give an operating surface temperature around 2000°K; no measurements of insulator surface temperature were made in the present experiments. Static pressure measurements were made at locations in the burner, plenum and at several locations as indicated in Figure 14.

The magnet used in the experiments was a conventional, iron yoke copper-coil magnet, with water cooling provided to allow continuous operation at a magnetic induction of 2.6 Tesla. Soft iron pole pieces located flush with the test section sidewalls helped produce a relatively uniform magnetic field over the entire active region of the generator. The magnetic field direction was reversed during the experiment and the bottom wall, which could be observed, was thus operated both as the anode wall and as the cathode wall of the generator.

The electrode walls of the M-2 generator were constructed with thirteen 7/8" diameter electrode access holes located on a pitch of 1 1/2". All water-cooling connections, current leads and thermocouple leads for the electrodes were made through these holes, and electrical insulation was provided to prevent shorting to the metallic test-section shell. As in the applied field experiments, the electrode surface was stainless steel and the electrodes were designed to operate at surface temperatures in excess of 1000°K. The surface temperature was maintained reasonably uniform by furnace brazing a copper-backing piece to the stainless steel head. Cooling of the copper backing piece was possible only in a small region at the center and care was required to prevent film boiling of the water coolant. To keep the overall thickness of the electrode small, the stainless steel head was thermally choked by milling slots into the rear-face. For some of the electrodes, chromel/alumel thermocouples, inserted to within ≈3/64" of the surface, were used to monitor the electrode surface temperature.

The desired inter-electrode gap was obtained by adjusting the electrode length, the pitch being fixed by the generator shell. For all gaps, excepting the two which could be viewed through the view port, the

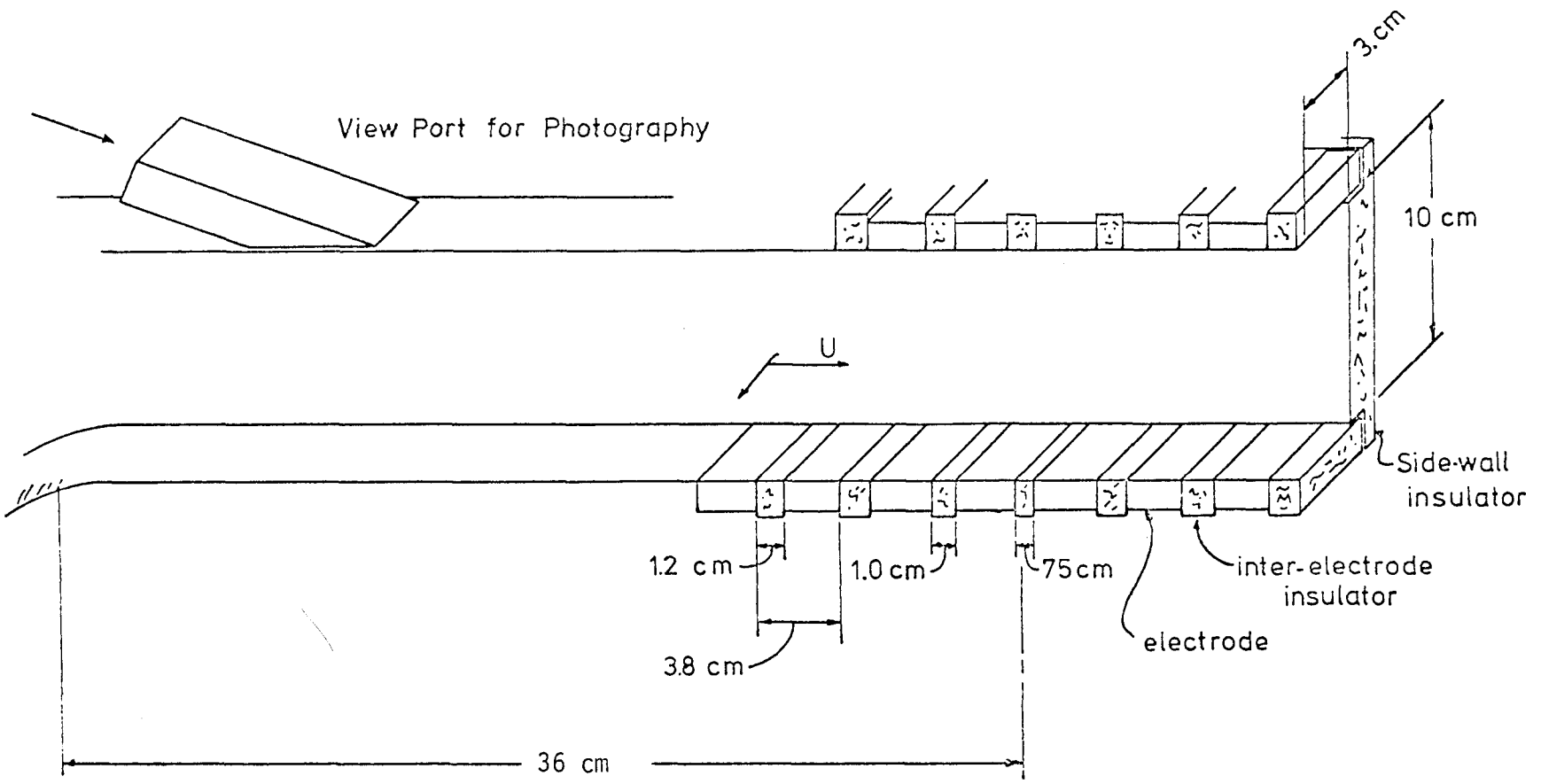

Figure 14. Sketch of the test section used in the induced field experiments, identifying the important dimensions and indicating the port through which the photographs of the inter-electrode region were taken.

insulator gaps were set at 1.2 cm. The remaining gaps were set at 1.0 cm and .75 cm. The material used for all gaps was dense MgO. Cooling of the inter-electrode insulators was effected partly by lateral conduction to the adjacent electrodes and partly by conduction to the test section wall.

In the present experiments, the generator was operated in the segmented-Faraday mode, with each electrode pair connected to a separate circuit via an external patch panel. As shown schematically in Figure 15, each circuit consisted of a series connection of an adjustable resistor, a solid state (SCR) switch and a conventional contact switch. Four of the six circuits normally used were provided with a 360 volt d.c. power supply. Pairing of the electrodes of the generator to increase the electrode pitch was effected using an additional patch panel. To prevent momentary over-voltages of the inter-electrode gaps and to allow examination of the early-time behavior, all circuits were switched on within $\simeq$10-20 μsec, by simultaneously triggering the solid state switches. The circuits were switched off using the contact relays. Continuous monitoring of the generator performance was provided by meters displaying the current and voltage for each Faraday circuit and a meter displaying one of the Hall voltages.

The instrumentation used for recording the response of the important parameters was essentially the same as for the applied field experiments.

2.4.3 Advanced Diagnostics

Dual Filter Photography. The dual filter photographic setup used in the applied field experiments was adapted for use in the induced field experiments. Optical access was provided by a port in the test-section upstream of the active region of the generator and the view of the inter-electrode region was at an angle of $\simeq$25° with respect to the electrode wall. The region of view extended far enough to observe the .75 cm and 1.0 cm gaps, but the entire width of the channel could not be viewed. A typical frame for no current conditions and a sketch identifying the images on the frame are shown in Figure 16.

Electrode Current Distribution Measurements. The electrodes bordering the .75 cm gap and the 1.0 cm gap were sub-divided in the flow direction and in the magnetic field direction to facilitate a measurement of the current distribution at the electrode surface. The edges of these

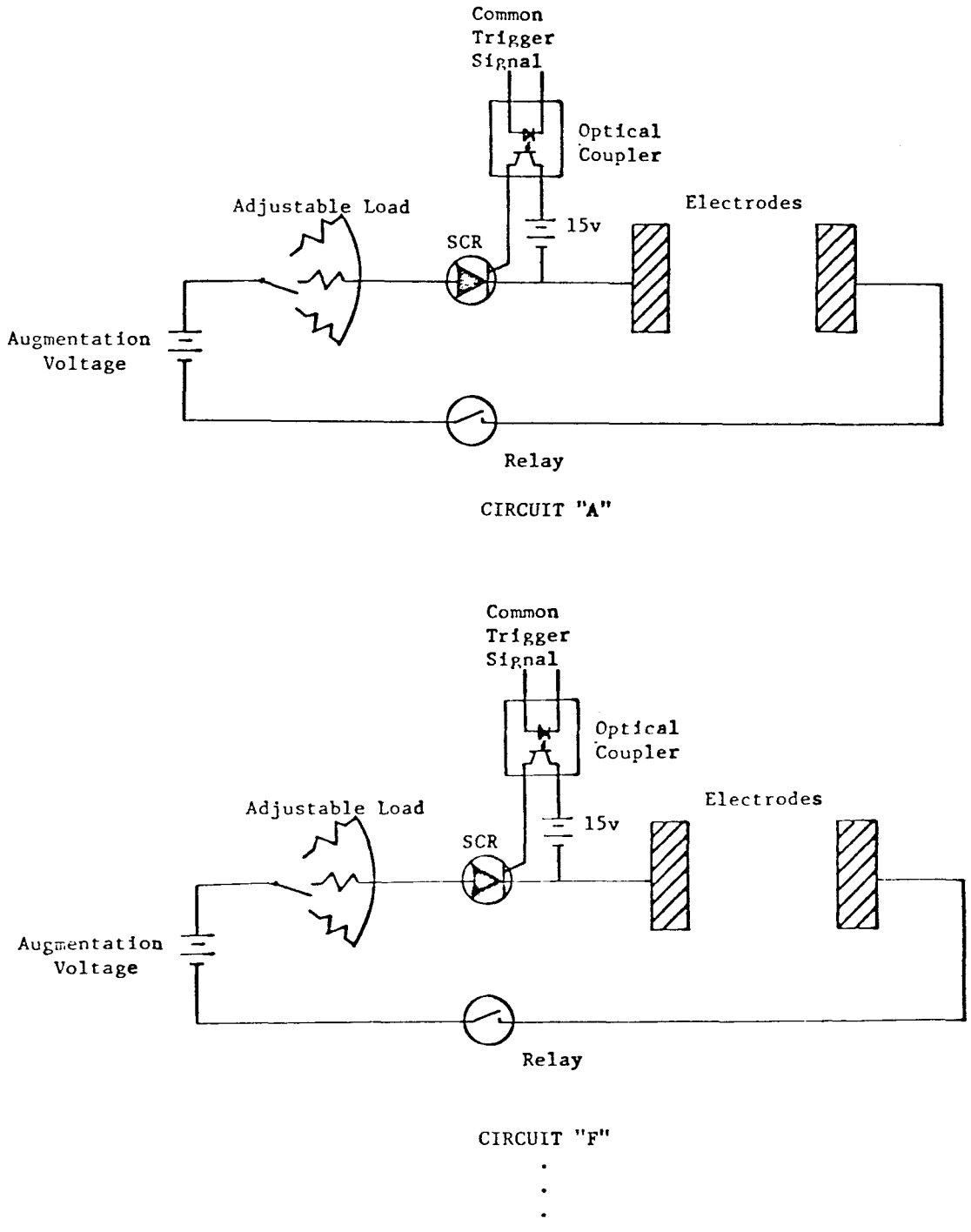

Figure 15. Schematic of external circuit for the generator experiments. Up to six such circuits were utilized in the experiments.

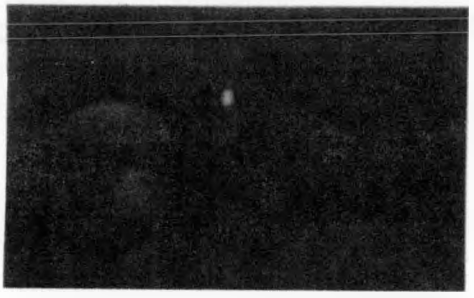

Figure 16a. Frame of the movies taken in the induced field experiments, showing the region when little current is flowing. Sketch below identifies the various features of the photograph.

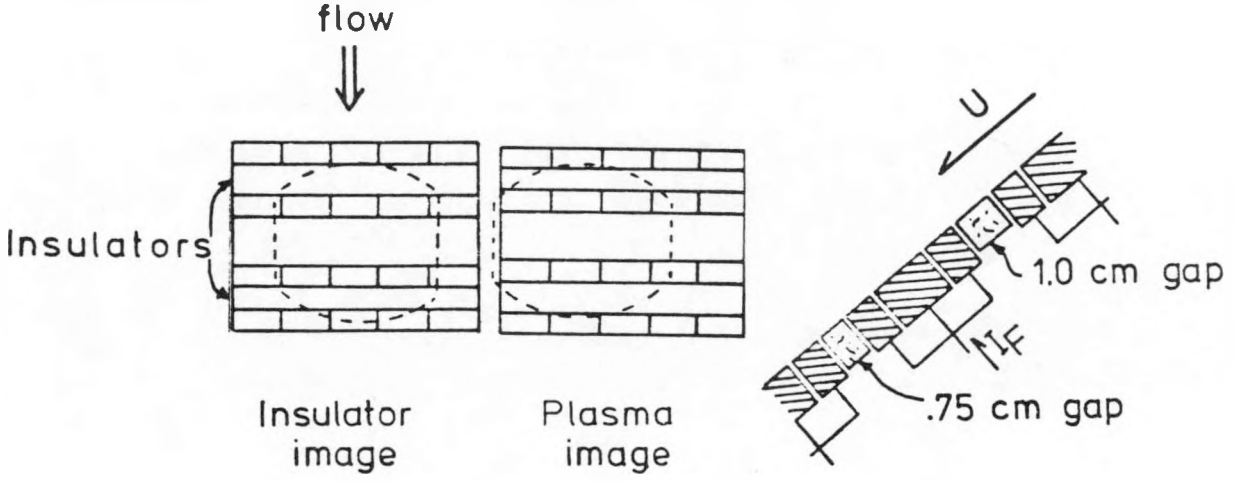

Figure 16b. Sketch of the view into the camera identifying the important features and indicating the angle at which the movies were taken. The right image, formed through an interference filter, is designated "plasma"; the left image, formed through a red filter, is designated "insulator". The dashed lines indicate the approximate field of view of the camera.

electrodes adjacent to the gaps were formed by rows of 1/4" x 1/4" stainless steel pegs as shown in Figure 12. The basic design of the electrodes was similar to the design of the sub-divided electrodes for the applied field experiments. Each peg of the electrode had a separate current lead which was attached to an external current shunt. The total current to each row of pegs was also measured.

Near-Electrode Voltage Drop Measurements. The near-electrode voltage drop was measured at two top wall electrodes and two bottom wall electrodes. A 25 mil platinum wire was inserted through the sidewall brick approximately 2 mm above the electrode surface. The wires were located at the electrode centerline and penetrated about 1/16" into the plasma. Standard voltage measuring devices were used to measure the potential of the probe relative to the appropriate electrode.

2.4.4 Experimental Procedures

The same overall experimental strategy used in the applied field experiments was adopted for the induced field experiments. In particular, the strategy included the use of a shake-down experiment, the specification of experimental conditions prior to the experiment and the use of the computer to coordinate the operation of various instruments. Section 2.3.4 gives a more complete description of the overall strategy and details of operation.

CHAPTER 3
EXPERIMENTAL RESULTS

3.1 Introduction

In this chapter the important results of the induced field and applied field experiments are presented and discussed. The applied field experiments are treated first, with a presentation of the experimental conditions followed by a discussion of the non-breakdown behavior and then the breakdown behavior. The induced field experimental results are then discussed and finally a comparison of induced field and applied field breakdown is made.

3.2 Applied Field Results

Inter-electrode insulator gaps from 1 mm to 19 mm were studied in the several applied field experiments; however, detailed measurements were made only in three of the experiments and only results from those experiments are discussed. Two of these experiments employed an inter-electrode insulator width of 19 mm while the other employed an inter-electrode insulator width of 7.5 mm. Dense MgO was used as the insulator material for these experiments. The effects of plasma flow conditions and of electrode polarity were studied in two of the experiments. Attempts at operating the inter-electrode insulator cold were apparently unsuccessful and the insulator surface temperatures (as measured by an optical pyrometer) approached or exceeded 2000°K in all experiments.

The presentation of results is made in several sections, beginning with a detailed list of experimental conditions for the various experimental runs. The non-breakdown behavior of the inter-electrode region is then discussed, followed by a discussion of the early time transient behavior and of the non-breakdown fluctuation data. The characteristics of breakdown are described, and finally the behavior of the discharge after the breakdown is well developed is presented.

3.2.1 Experimental Conditions

The applied field experiments are divided into eight separate run series, representing the various inter-electrode gap and plasma flow

conditions for which data was taken. The combustor operating conditions and the computed plasma "core" conditions for the ten run series are presented in Table 3. A brief description of the calculation procedure for obtaining the core conditions is given in Appendix D. Pertinent test-section and electrode wall dimensions, measured surface temperatures and other relevant data are presented for each run series in Table 4. The voltage probe locations for the different run series are detailed in Figure 17. Location of the total emission intensity detectors and miscellaneous data relating to the dual-filter photographic device are presented in Table 5.

3.2.2 Non-Breakdown Behavior

The overall behavior of the inter-electrode region can be characterized by the steady-state (or non-breakdown) total axial voltage versus total axial current curve, shown for each run series in Figures 18a-18h. In cases where breakdown occurred (or would have, provided the discharge remained on longer) only the pre-breakdown level is shown. As expected, the qualitative behavior for all experimental conditions is similar, although both plasma flow conditions and insulator gap size influence the detailed response. Little effect is observed when the electrode polarities are reversed. Two regions of operation can be identified for the pre-breakdown behavior. As will be shown more directly, later in this section, a relatively large voltage drop is required in the very near-cathode region if appreciable current is to flow, resulting in the rapid rise of voltage with current observed in all the experimental results. For voltages in excess of this cathode voltage drop, the voltage rises at a moderate rate with current, the slope decreasing with increasing current for some cases. Joule heating of some portion of the inter-electrode region is likely to be the cause of the declining slope at the higher currents.

The photographic records, current distribution measurements and the near wall emission intensity measurements show that in the regions away from the cathode the discharge is relatively diffuse. For example, the axial distribution of current is represented in Figures 19a-19h, where the fraction of current passing through the downstream quarter of the upstream electrode is plotted as a function of total axial current. As expected, the small distance to the downstream electrode results in a higher than average current density at this edge, however, as observed

Table 3. Combustor and channel flow conditions for each applied field experimental run series. Nitrogen to oxygen ratio, N_2/O_2, is by mass. Stoichometry expressed in terms of ϕ, the fuel-air ratio divided by fuel-air ratio for stoichiometric combustion. The seed fraction, q, is the fraction by mass of potassium in the combustion products.

Date	Run Designation	Combustor Conditions				Computed Core Conditions			
		$\dot{m}$ (kg/sec)	N_2/O_2	Φ	q	U (m/s)	P (n/m^2)	T (°K)	σ (mho/m)
3/10/76	1.9-A	.112	0.7	1.0	.91%	250	1.018×10^5	2627	9.1
7/22/76	1.9-B	.117	0.58	.95	.92%	256	1.04×10^5	2264	10.8
7/22/76	1.9-C	.171	1.1	1.06	.81%	383	1.04×10^5	2560	7.1
7/29/76	1.9-D	.108	0.6	.97	.92%	265	1.01×10^5	2651	10.2
7/29/76	1.9-E	.171	1.05	1.03	.80%	420	1.02×10^5	2568	7.2
10/28/76	.75-A	.112	0.6	1.0	.95%	281	1.013×10^5	2660	11.1
10/28/76	.75-B	.112	0.8	1.0	.86%	275	1.013×10^5	2593	8.2
10/28/76	.75-C	.180	1.1	1.0	.76%	428	1.013×10^5	2542	6.7

Table 4. Channel construction parameters for each applied field experimental run series.

	Inter-Electrode Construction				Surface Temperatures						Electrodes
Run Designation	Gap (cm)	Thickness (cm)	Method of Thermal Contact	Probe Config.	Upstream Insulator (K)	Side-wall Insulator (K)	Upstream Electrode (K)	Inter-Electrode Insulator (K)	Downstream Electrode (K)	Downstream Insulator (K)	Length (cm)
1.9-A	1.91	0.79	air	a	n.a.	n.a.	n.a.	∿2000 fc	∿1200 t	n.a.	2.74
1.9-B	1.91	1.28	RTV	b	2190 ts	2100 pc	1130 t	1990 pc	811 t	1950 pc	2.74
1.9-C	1.91	1.28	RTV	b	∿2090 tc	2130 pc	1160 t	2050 pc	830 t	2050 pc	2.74
1.9-D	1.91	1.28	RTV	b	2190 ts	2100 pc	1130 t	1990 pc	811 t	1950 pc	2.74
1.9-E	1.91	1.28	RTV	b	∿2090 ts	2130 pc	1160 t	2050 pc	830 t	2050 pc	2.74
.75-A	.75	1.28	RTV	c	2060 ts	2000 pc	1170 t	2000 pc	1100 t	n.a.	2.74
.75-B	.75	1.28	RTV	c	1900 ts	1900 pc	980 t	n.a.	970 t	n.a.	2.74
.75-C	.75	1.28	RTV	c	2030 ts	1970 pc	1100 t	n.a.	1122 t	n.a.	2.74

c = corrected for MgO emissivity
f = from top view photographs
p = from optical pyrometer
s = corrected to surface
t = thermocouple

Table 5. Optical related conditions for each applied field experimental run series.

Top View Photography							Side View Emission Measurements distance from surface/band pass (line)			
Run Designation	Band Pass of Blue filter	Step filter - Equivalent MgO Temperatures (K) #1	#2	#3	#4	#5				
1.9-A	160Å	2430	2280	2070	2910	1840	2mm/80Å(Na)			
1.9-B	10Å	2420	2290	2130	1960	1870	2mm/40Å(K),	8mm/40Å(K),	40mm/40Å(K),	46mm/40Å(K)
1.9-C	10Å	2420	2290	2130	1960	1870	2mm/40Å(K),	8mm/40Å(K),	40mm/40Å(K),	46mm/40Å(K)
1.9-D	10Å	2420	2290	2130	1960	1870	2mm/40Å(K),	8mm/40Å(K),	40mm/40Å(K),	46mm/40Å(K)
1.9-E	10Å	2420	2290	2130	1960	1870	2mm/40Å(K),	8mm/40Å(K),	40mm/40Å(K),	46mm/40Å(K)
.75-A	10Å	2440	2310	2150	1980	1890	2mm/40Å(K),	8mm/40Å(K),	40mm/8Å(Na),	46mm/8Å(Na)
.75-B	10Å	2440	2310	2150	1980	1890	2mm/40Å(K),	8mm/40Å(K),	40mm/8Å(Na),	46mm/8Å(Na)
.75-C	10Å	2440	2310	2150	1980	1890	2mm/40Å(K),	8mm/40Å(K),	40mm/8Å(Na),	46mm/8Å(Na)

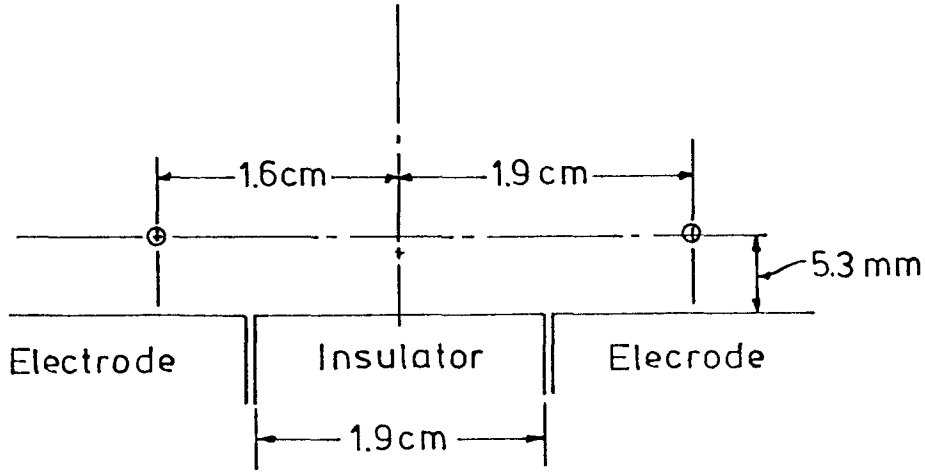

Figure 17a. Location of voltage probes for Run series 1.9-A.

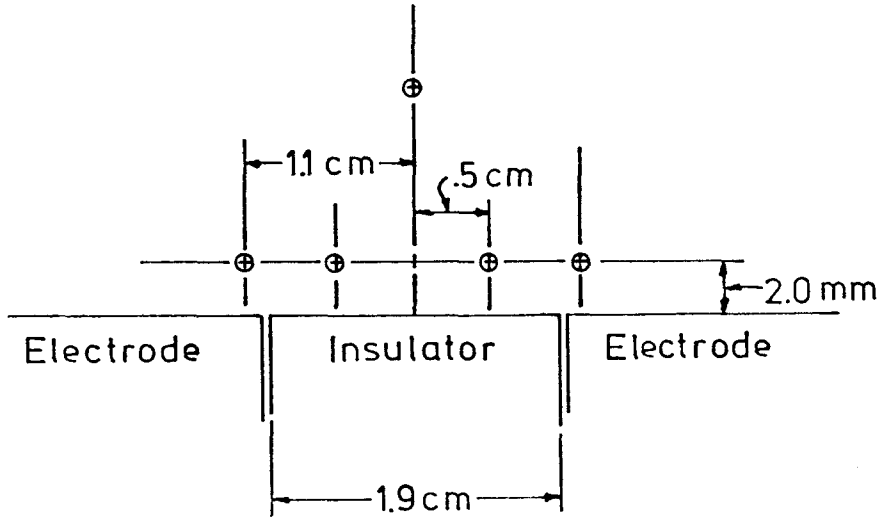

Figure 17b. Location of voltage probes for Run series 1.9-B, 1.9-C, 1.9-D, and 1.9-E.

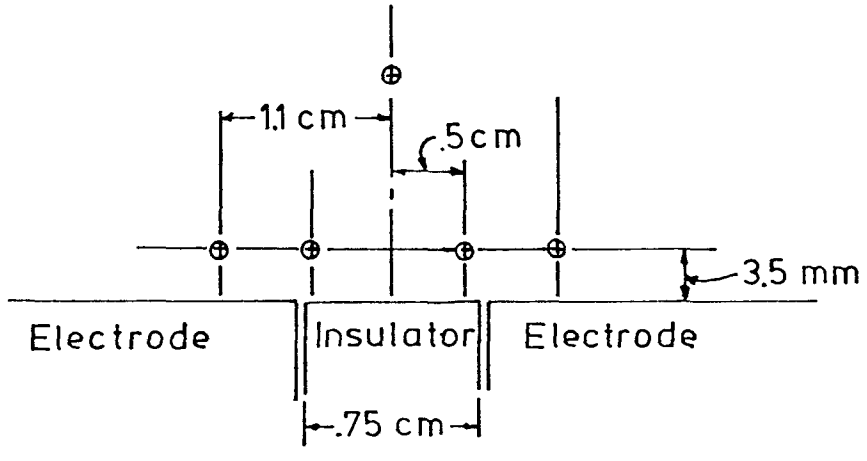

Figure 17c. Location of voltage probes for Run series .75-A, .75-B, and .75-C.

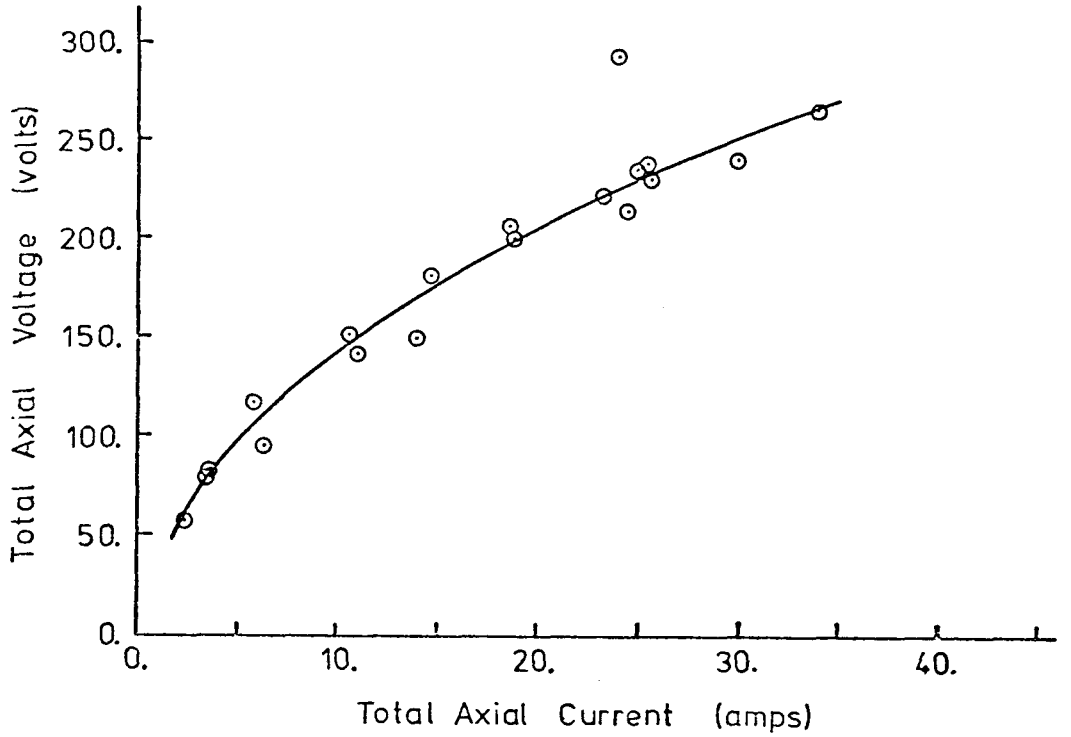

Figure 18a. Total axial voltage versus total axial current for non-breakdown conditions. Data taken from Run 1.9-A.

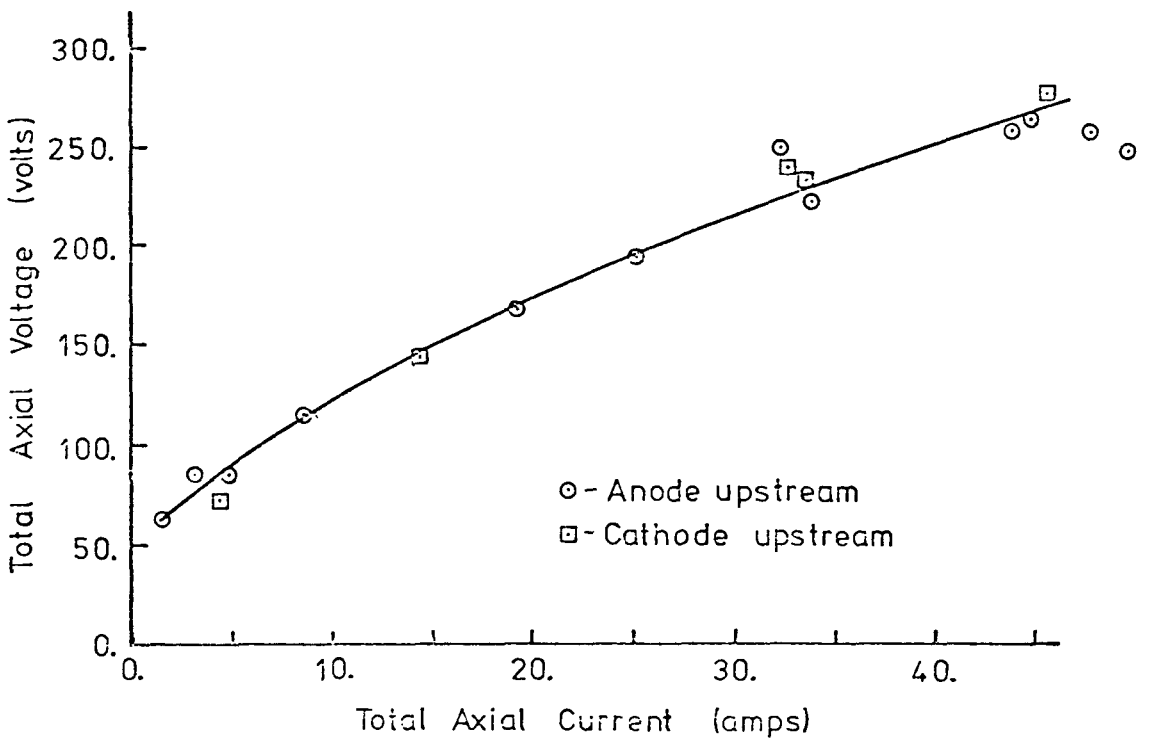

Figure 18b. Total axial voltage versus total axial current for non-breakdown conditions. Data taken from Run 1.9-B.

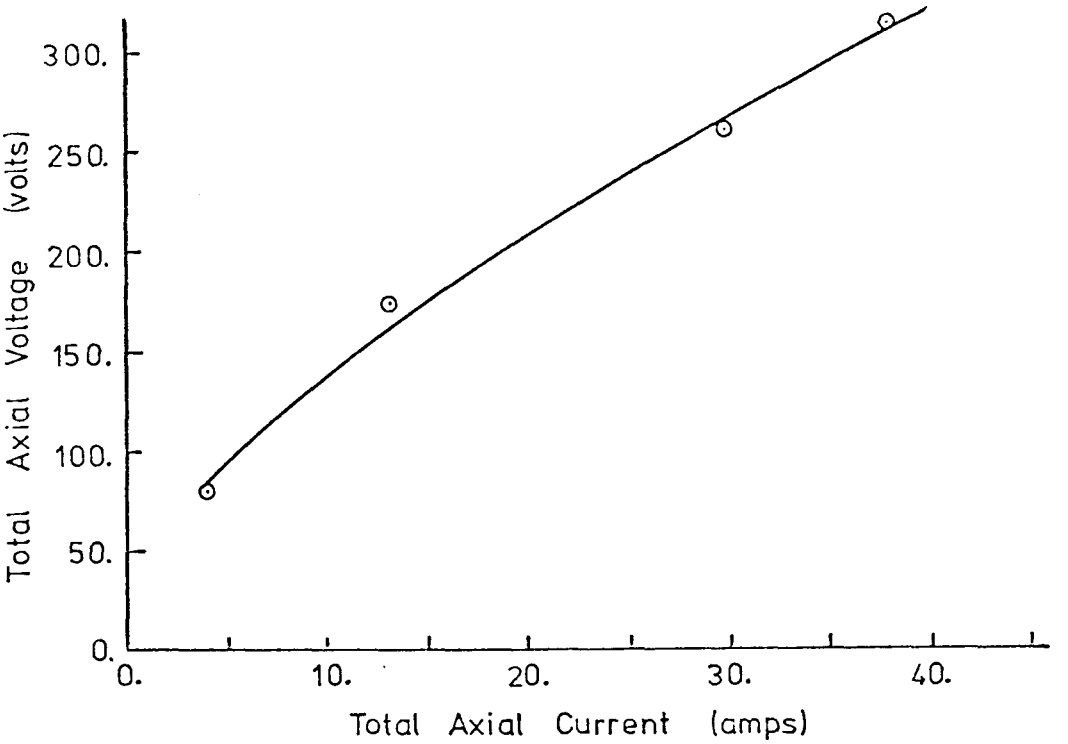

Figure 18c. Total axial voltage versus total axial current for non-breakdown conditions. Data taken from Run 1.9-C.

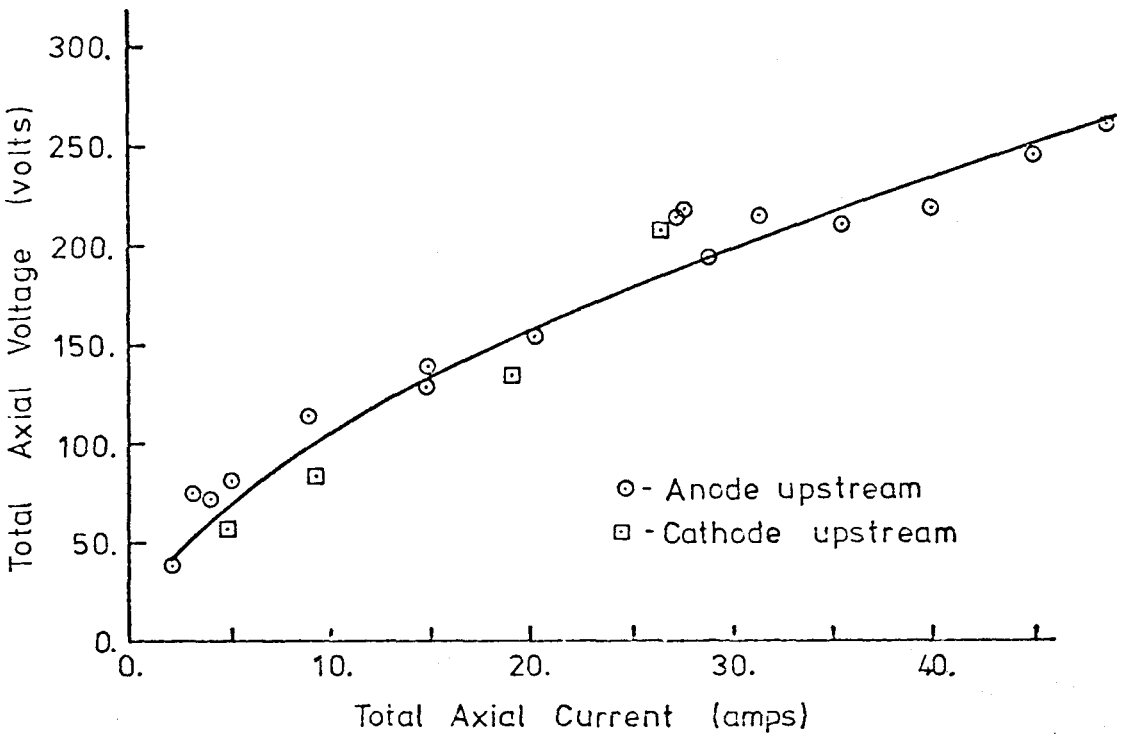

Figure 18d. Total axial voltage versus total axial current for non-breakdown conditions. Data taken from Run 1.9-D.

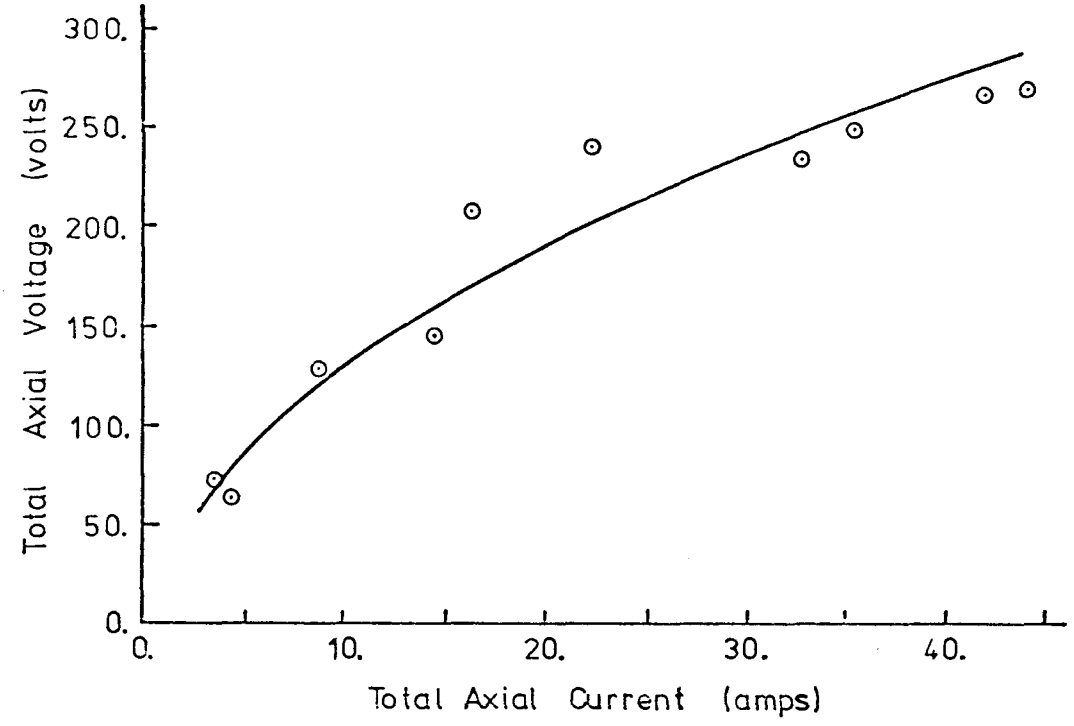

Figure 18e. Total axial voltage versus total axial current for non-breakdown conditions. Data taken from Run 1.9-E.

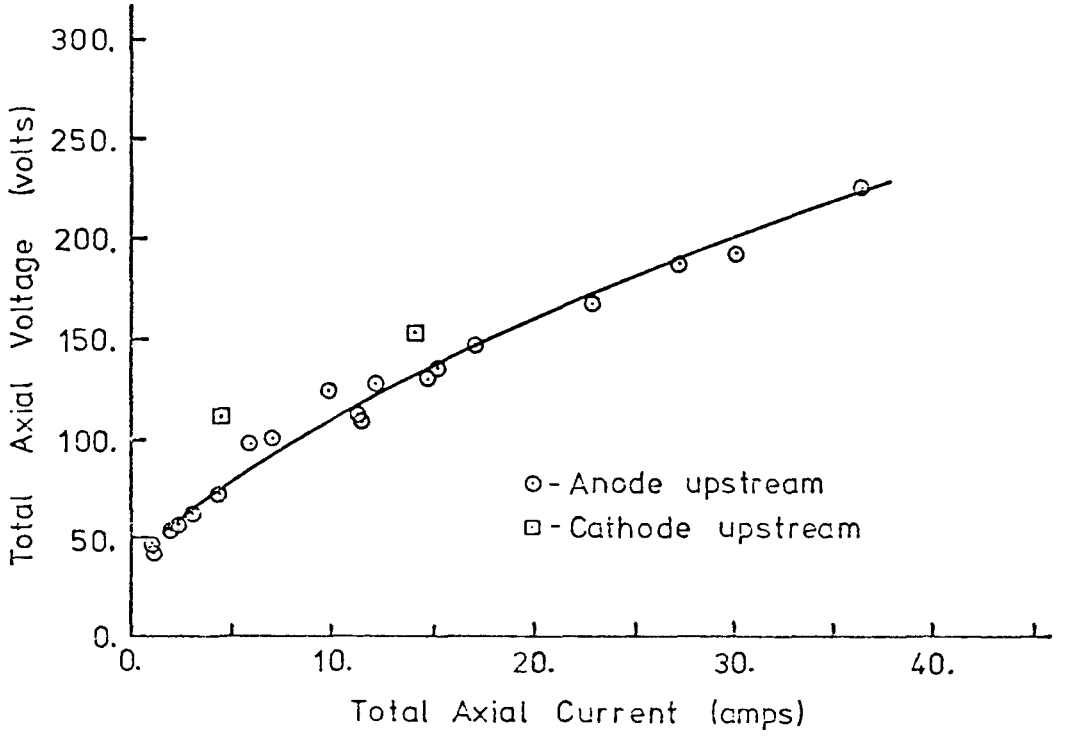

Figure 18f. Total axial voltage versus total axial current for non-breakdown conditions. Data taken from Run .75-A.

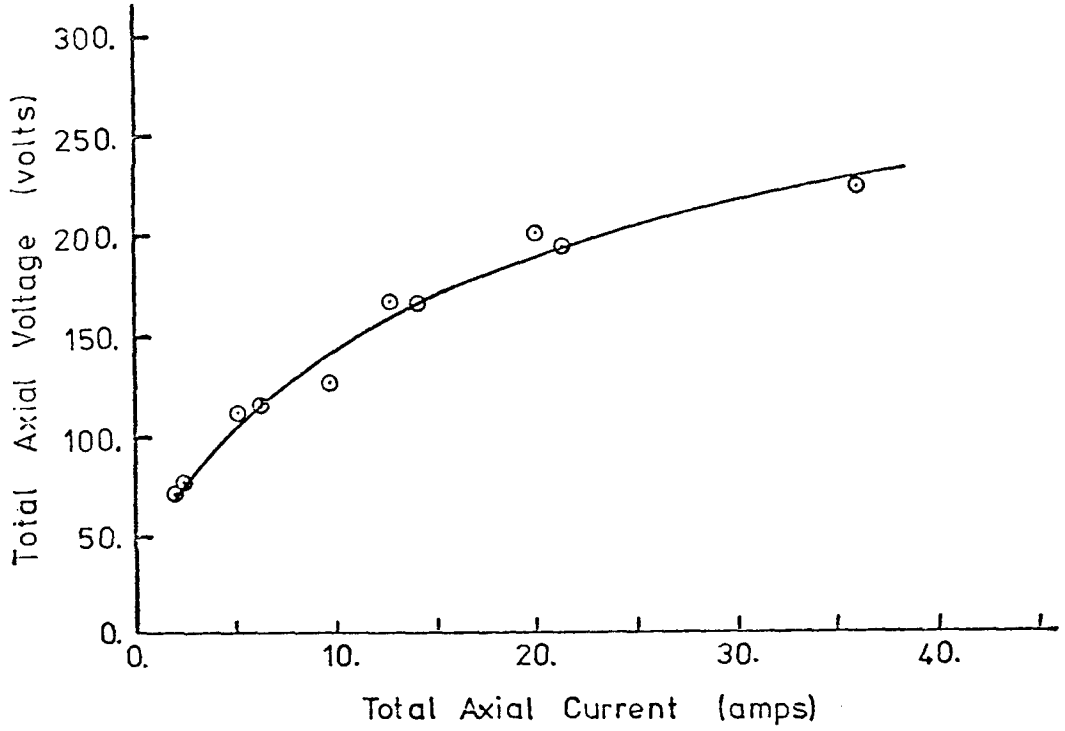

Figure 18g. Total axial voltage versus total axial current for non-breakdown conditions. Data taken from Run .75-B.

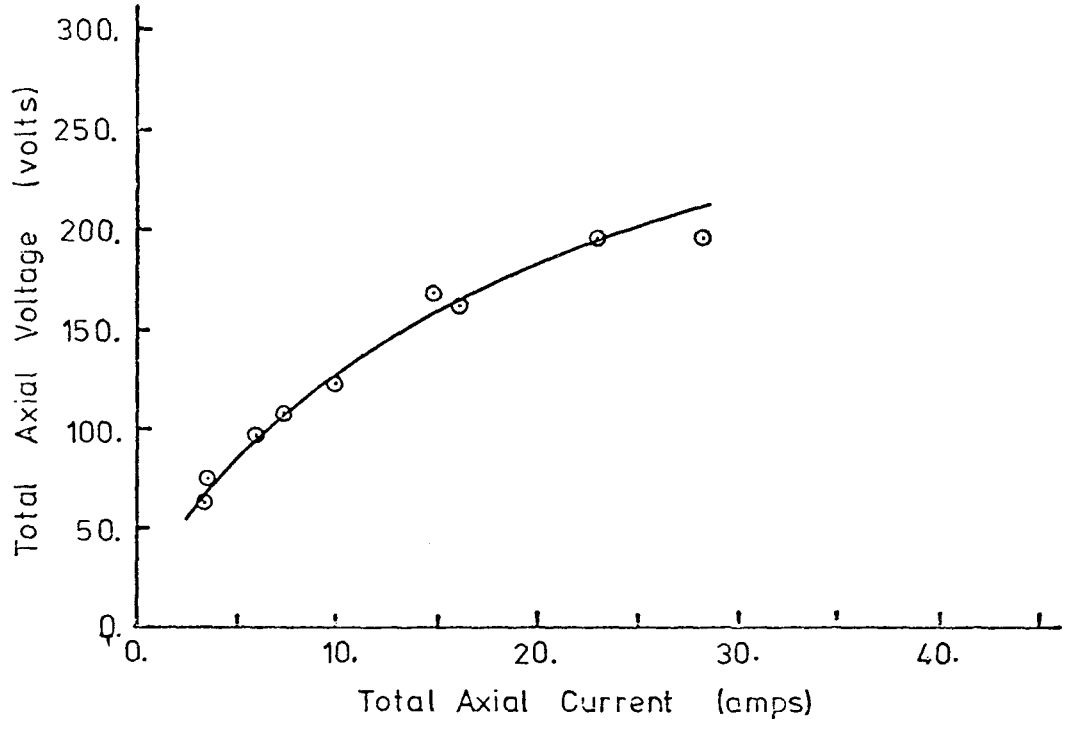

Figure 18h. Total axial voltage versus total axial current for non-breakdown conditions. Data taken from Run .75-C.

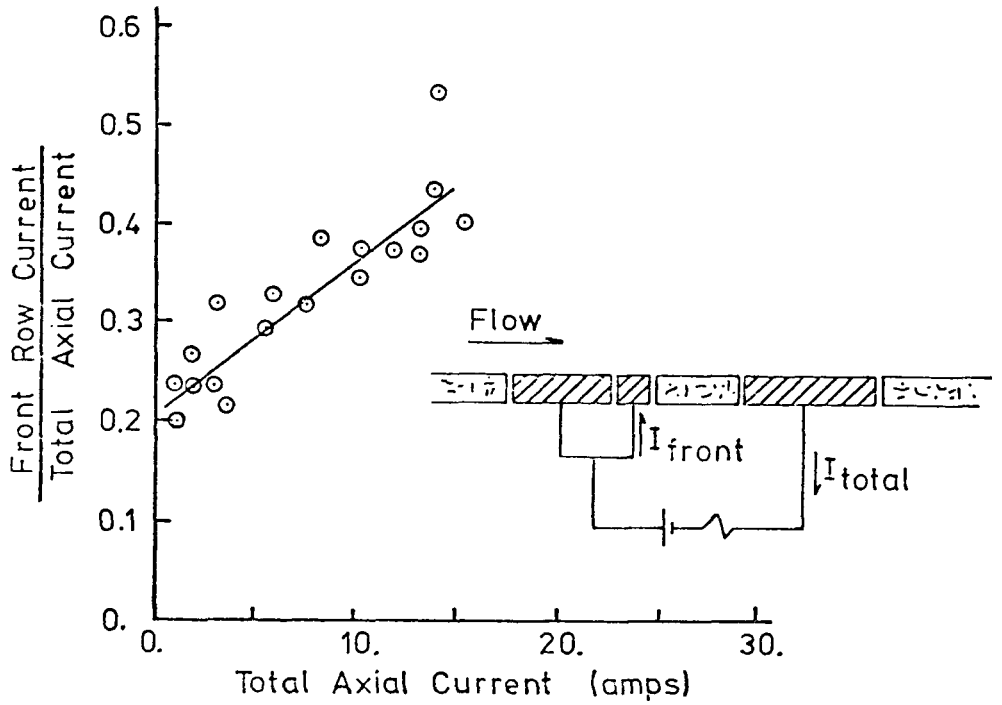

Figure 19a. Current distribution in axial direction as a function of total axial current. Fraction of current leaving the downstream edge of the upstream electrode is used to represent the axial current distribution. Data taken from Run 1.9-A.

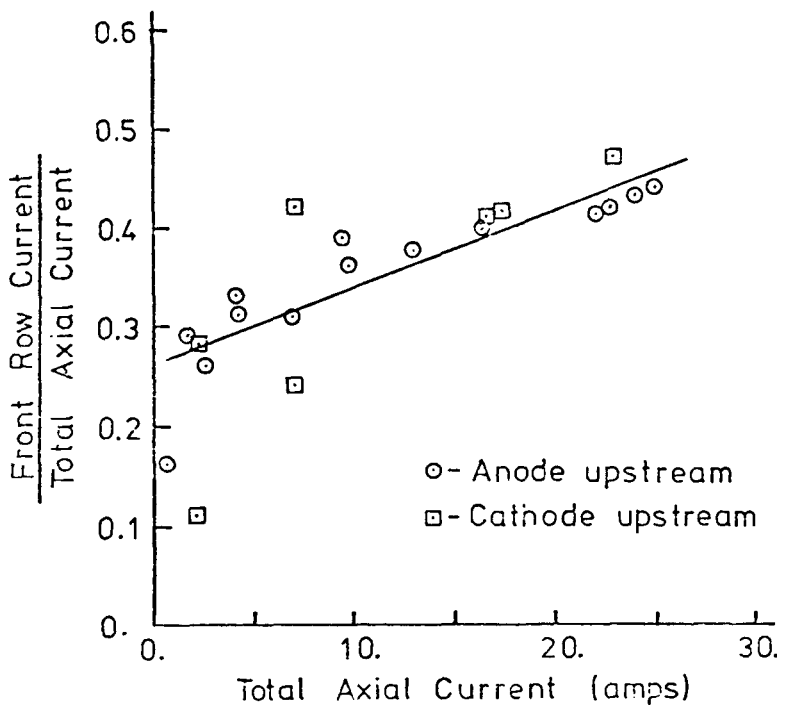

Figure 19b. Current distribution in axial direction as a function of total axial current. Fraction of current leaving the downstream edge of the upstream electrode is used to represent the axial current distribution. Data taken from Run 1.9-B.

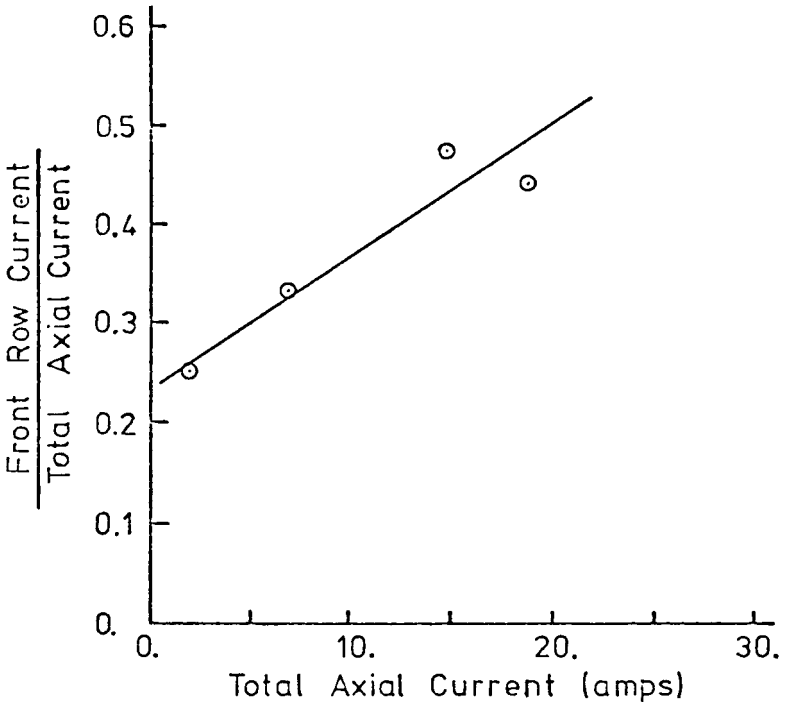

Figure 19c. Current distribution in axial direction as a function of total axial current. Fraction of current leaving the downstream edge of the upstream electrode is used to represent the axial current distribution. Data taken from Run 1.9-C.

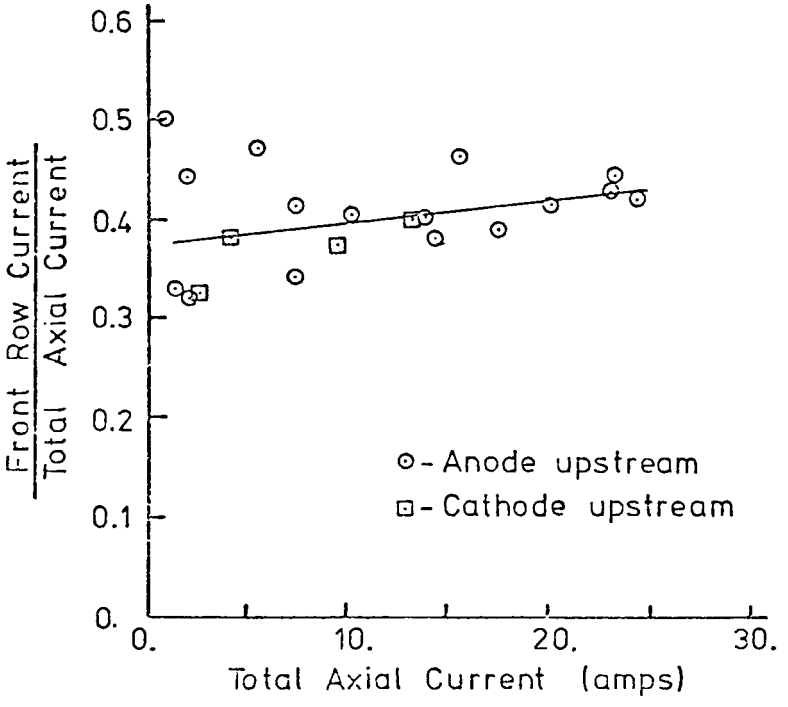

Figure 19d. Current distribution in axial direction as a function of total axial current. Fraction of current leaving the downstream edge of the upstream electrode is used to represent the axial current distribution. Data taken from Run 1.9-D.

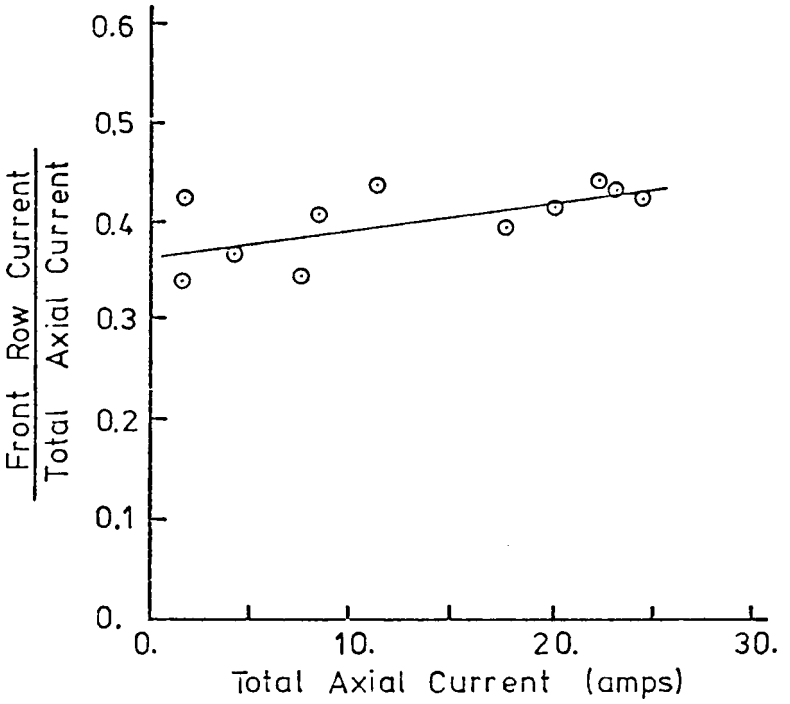

Figure 19e. Current distribution in axial direction as a function of total axial current. Fraction of current leaving the downstream edge of the upstream electrode is used to represent the the axial current distribution. Data taken from Run 1.9-E.

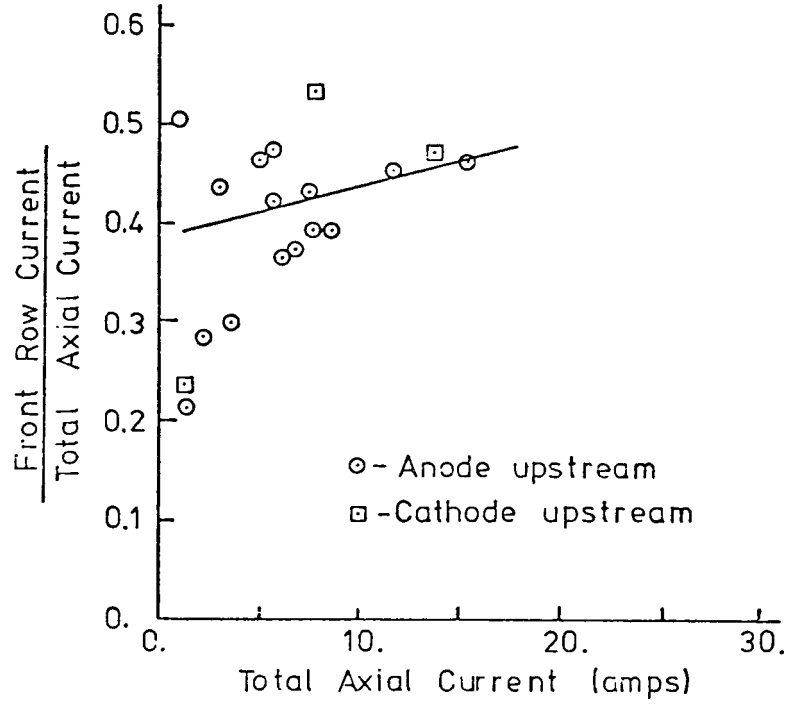

Figure 19f. Current distribution in axial direction as a function of total axial current. Fraction of current leaving the downstream edge of the upstream electrode is used to represent the axial current distribution. Data taken from Run .75-A.

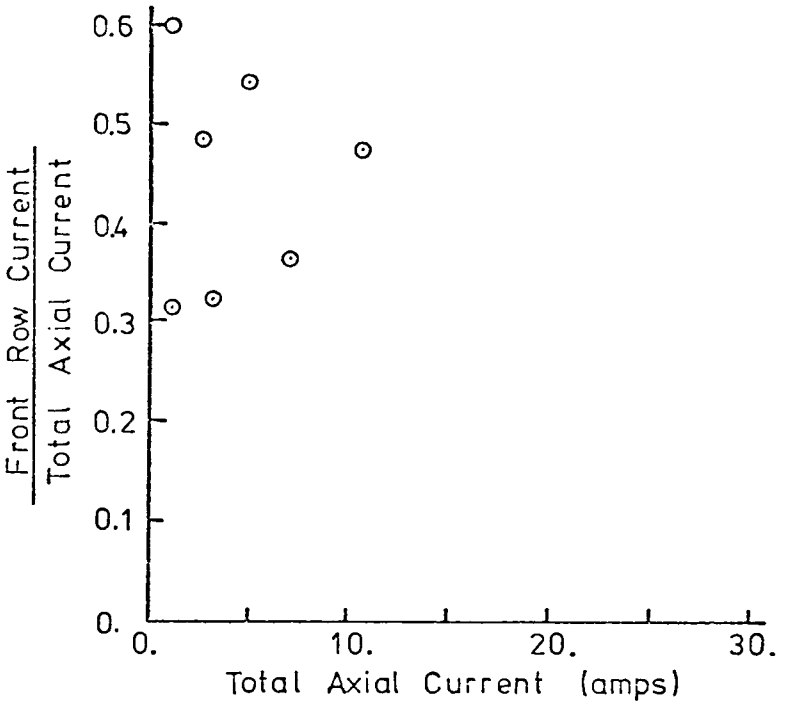

Figure 19g. Current distribution in axial direction as a function of total axial current. Fraction of current leaving the downstream edge of the upstream electrode is used to represent the axial current distribution. Data taken from Run .75-B.

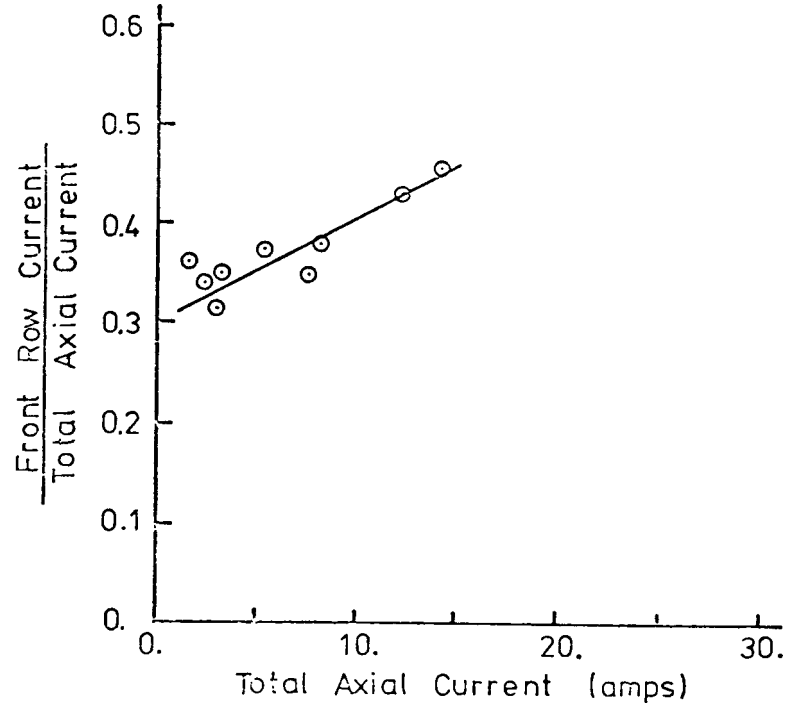

Figure 19h. Current distribution in axial direction as a function of total axial current. Fraction of current leaving the downstream edge of the upstream electrode is used to represent the axial current distribution. Data taken from Run .75-C.

in the figures this concentration is not severe. While the scatter in the data is somewhat high, a trend toward increased current density with increased total current is observed for some experimental conditions. Such a trend might be expected to result from increased Joule heating of the inter-electrode region. The distribution of current across the channel width is represented in Figures 20a-20h, by a plot of the fraction of current passing through each peg in the row closest to the inter-electrode insulator, for all current levels of each run series. Although the scatter in the data is relatively high and some anomolous results were obtained, in general the data indicate a low current density near the sidewalls as would be expected to result from the low conductivity boundary layers existing along the cold sidewalls. It is interesting to note that the current distribution measured when the electrode was operating as a cathode was not dramatically different from that when the electrode was operated as an anode (see Figures 20b and 20d). The photographic records for the non-breakdown runs display little activity except at the cathode where small hot spots can be observed to form and to slowly migrate downstream. A few frames of the movies, typical of the non-breakdown conditions are shown in Figures 21a-21c. The radiation emission intensity records display little activity during the non-breakdown runs, although as discussed in Section 3.2.3, some increase in intensity was detected close to the wall for the higher currents.

Additional understanding of the discharge structure can be obtained by examining the behavior of different regions as measured using the voltage probes. Direct quantitative comparison of the voltage probe data is possible only between data taken with the same probe locations, and it should be kept in mind that in measurements referenced to either of the electrodes the voltage drop associated with the electrode surface is included. One region of interest is the near cathode region, where a large voltage drop and severe current constriction are required to provide the required flux of electrons. The steady-state (non-breakdown) behavior of the near-cathode voltage drop is displayed for various experimental conditions in Figures 22a-22c. For all the experiments a high voltage drop ($\simeq$30-50 volts) is observed even at the smallest current densities ($J_{average} \simeq .2$ amps/cm^2) drawn in the experiments. For most conditions, the cathode voltage drop rises with current up to a current of

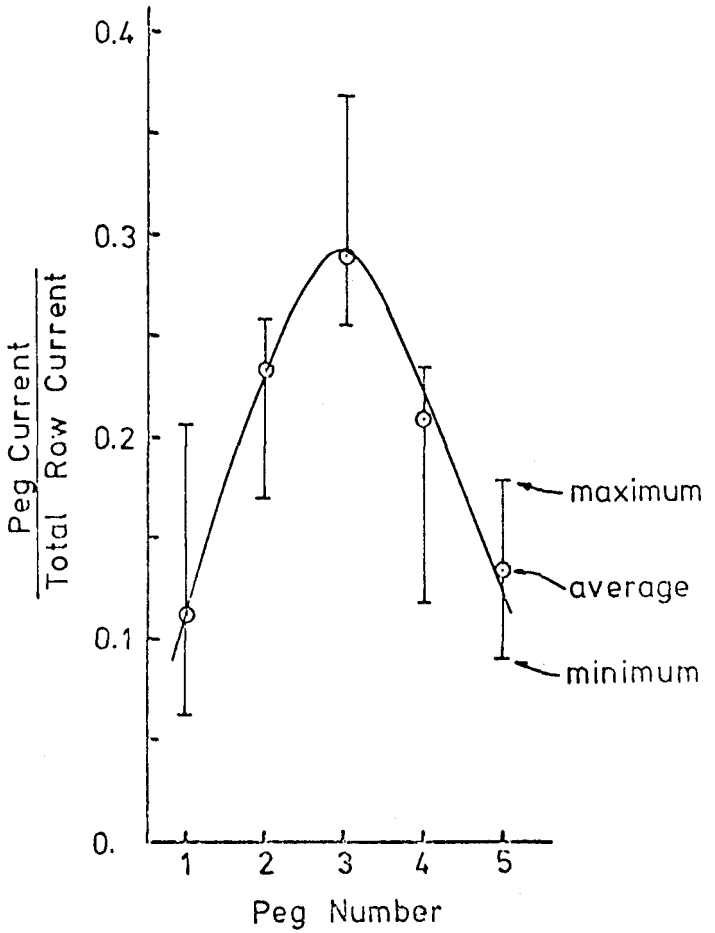

Figure 20a. Current distribution in transverse direction for non-breakdown conditions. Current from individual pegs plotted as a fraction of the total current to the row of pegs. All data from Run 1.9-A are represented in the figure. Electrode was operating as an anode.

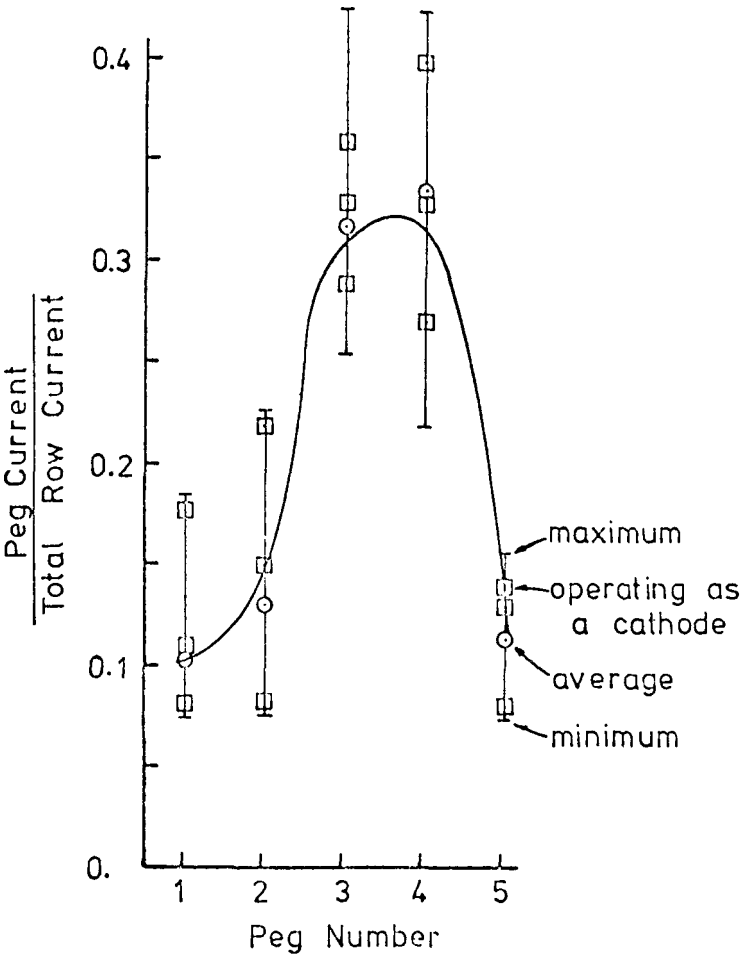

Figure 20b. Current distribution in transverse direction for non-breakdown conditions. Current from individual pegs plotted as a fraction of total current to the row of pegs. All data from Run 1.9-B are represented in the figure. As indicated the electrode was operated as an anode and as a cathode.

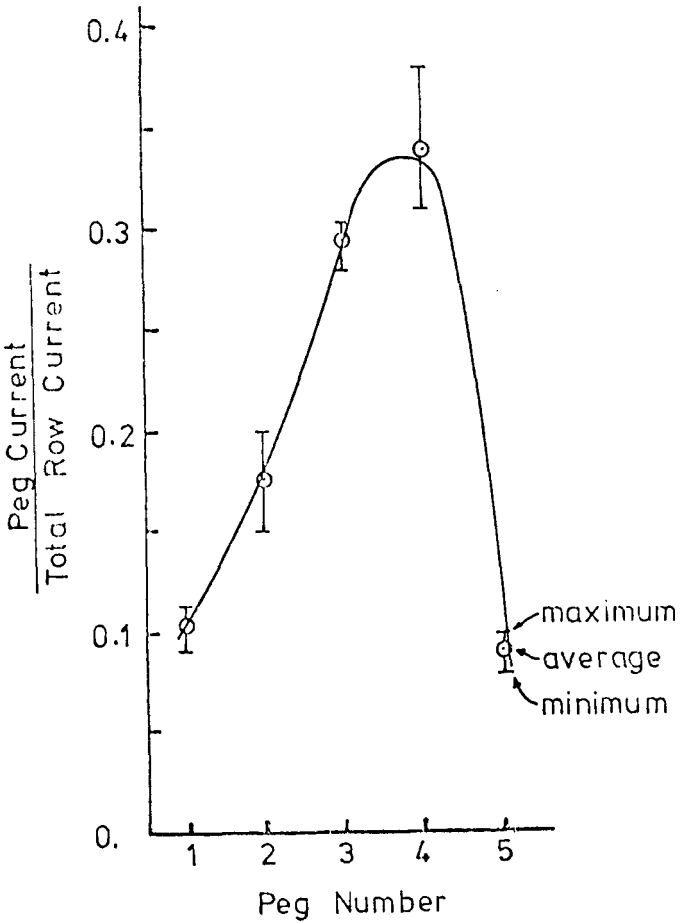

Figure 20c. Current distribution in transverse direction for non-breakdown conditions. Current from individual pegs plotted as a fraction of total current to the row of pegs. All data from Run 1.9-C are represented in the figure. Electrode was operating as an anode.

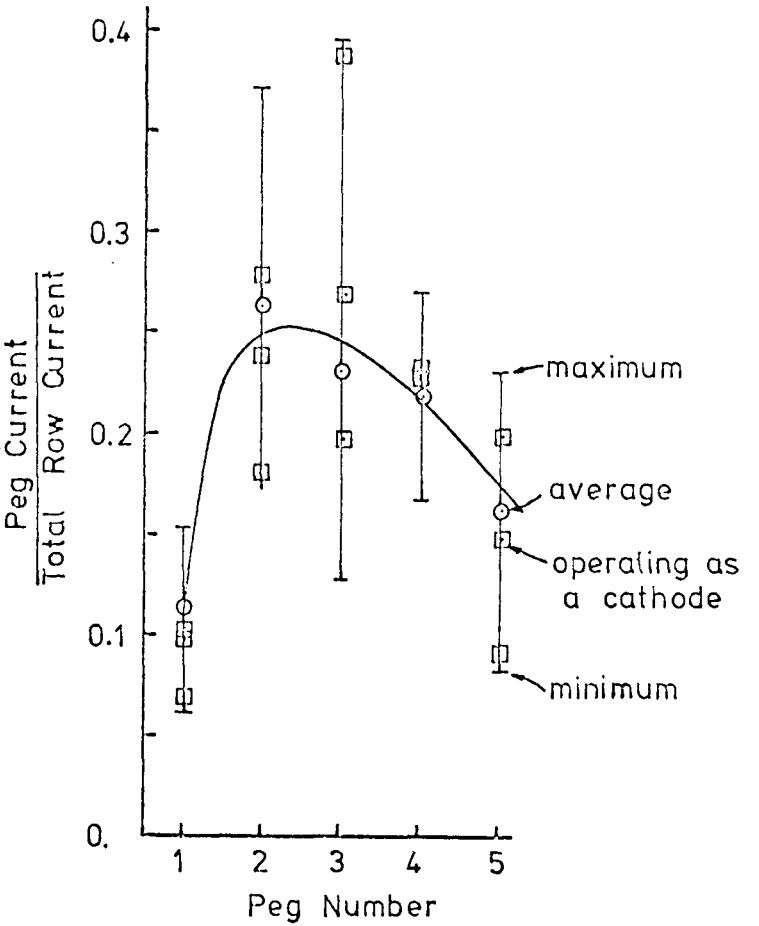

Figure 20d. Current distribution in transverse direction for non-breakdown conditions. Current from individual pegs plotted as a fraction of total current to the row of pegs. All data from Run 1.9-D are represented in the figure. As indicated the electrode was operated as an anode and as a cathode.

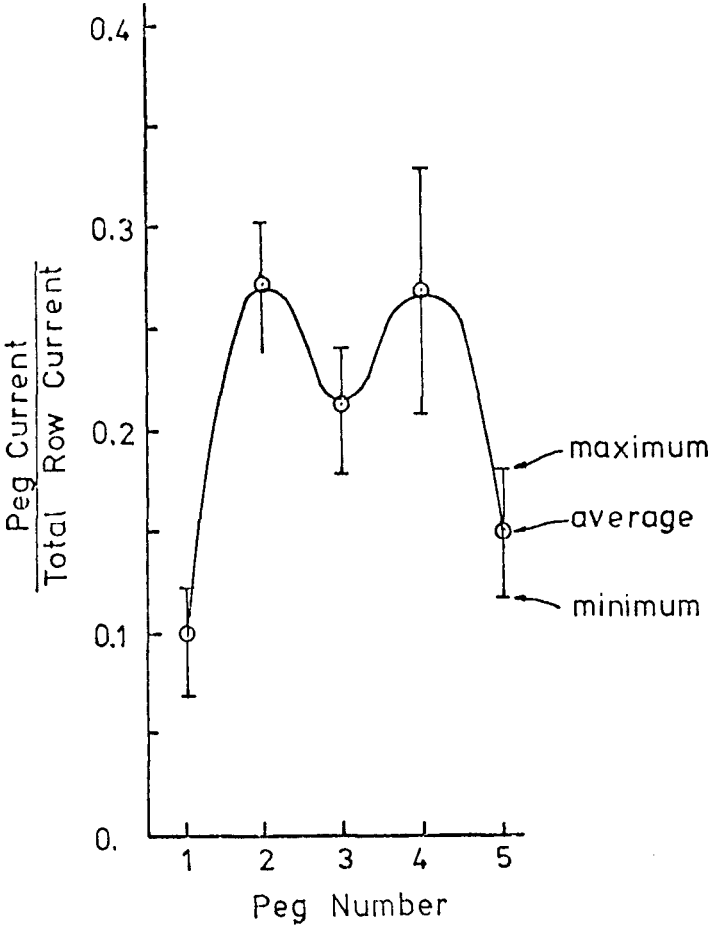

Figure 20e. Current distribution in transverse direction for non-breakdown conditions. Current from individual pegs plotted as a fraction of total current to the row of pegs. All data from Run 1.9-E are represented in the figure. Electrode was operating as an anode.

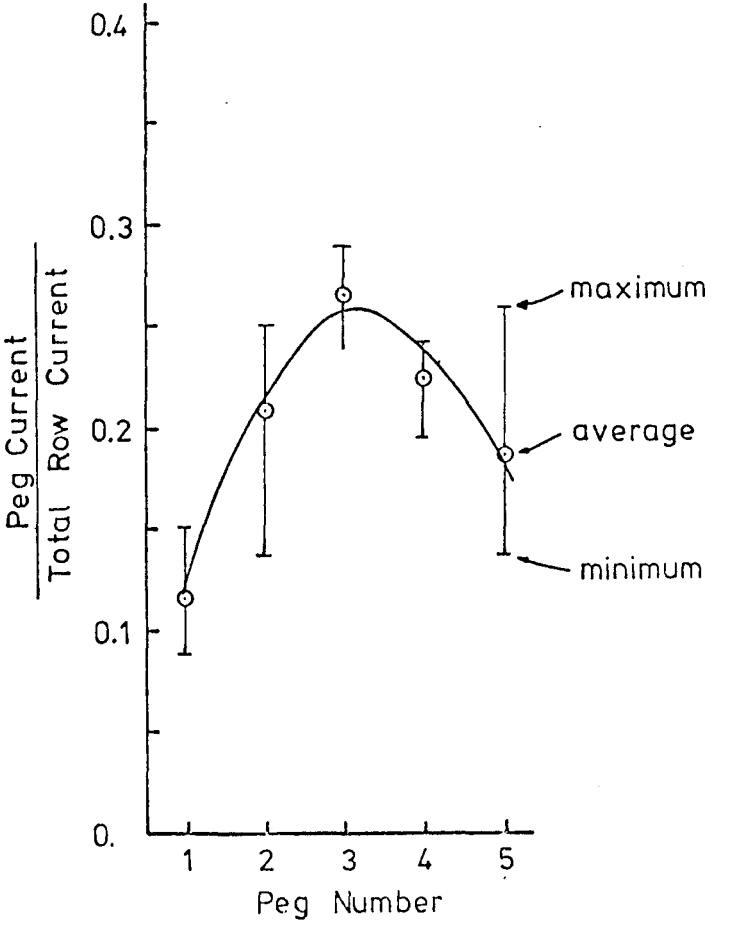

Figure 20f. Current distribution in transverse direction for non-breakdown conditions. Current from individual pegs plotted as a fraction of total current to the row of pegs. All data from Run .75-A are represented in the figure. Electrode was operating as an anode.

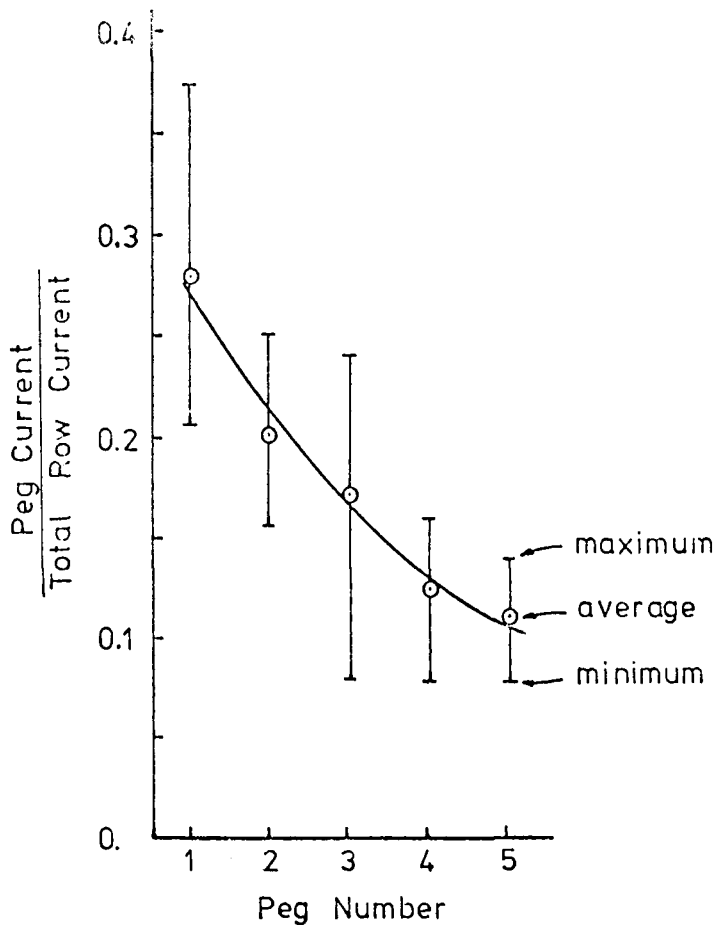

Figure 20g. Current distribution in transverse direction for non-breakdown conditions. Current from individual pegs plotted as a fraction of total current to the row of pegs. All data from Run .75-B are represented in the figure. Electrode was operating as an anode.

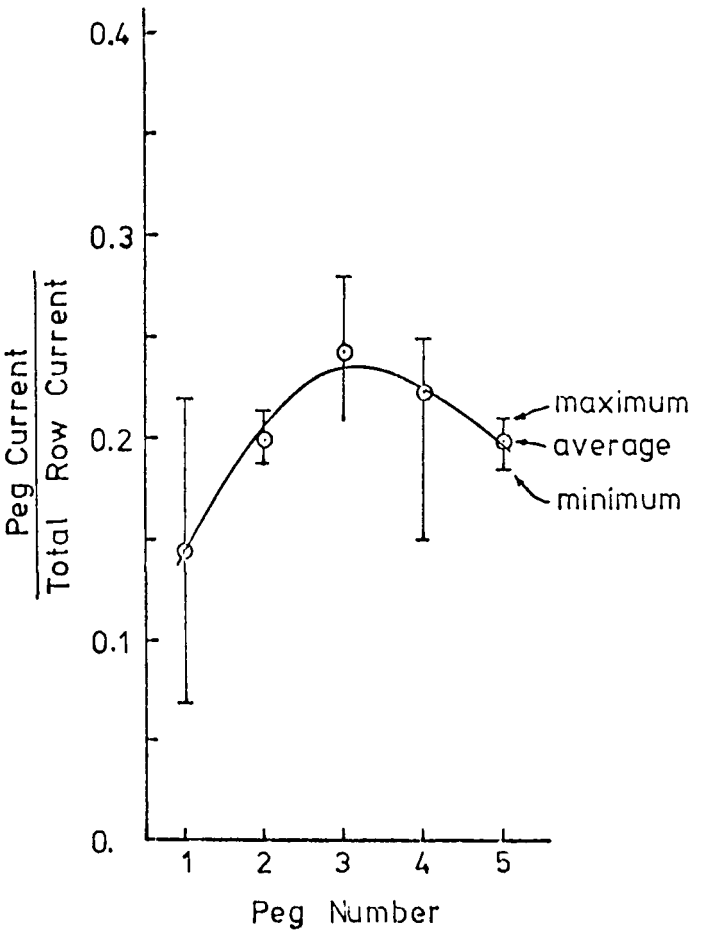

Figure 20h. Current distribution in transverse direction for non-breakdown conditions. Current from individual pegs plotted as a fraction of total current to the row of pegs. All data from Run .75-C are represented in the figure. Electrode was operating as an anode.

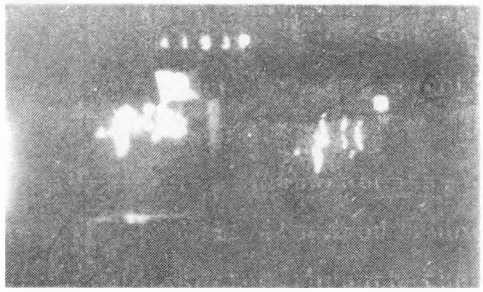

Figure 21a. Photograph of inter-electrode region for non-breakdown conditions. Taken from Run series 1.9-A.

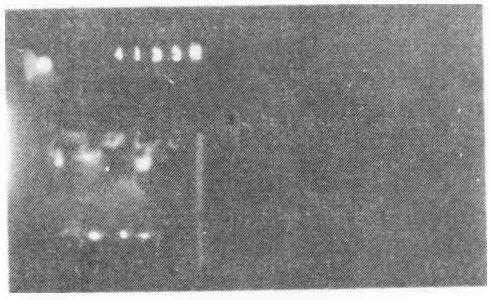

Figure 21b. Photograph of inter-electrode region for non-breakdown conditions. Taken from Run series 1.9-C.

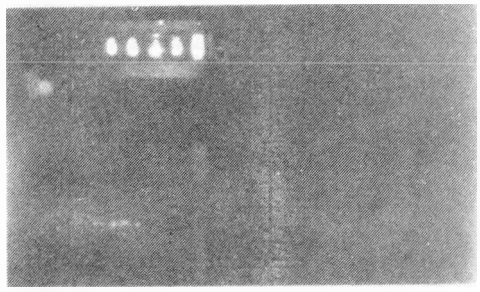

Figure 21c. Photograph of interelectrode region for non-breakdown conditions. Taken from Run series .75-A.

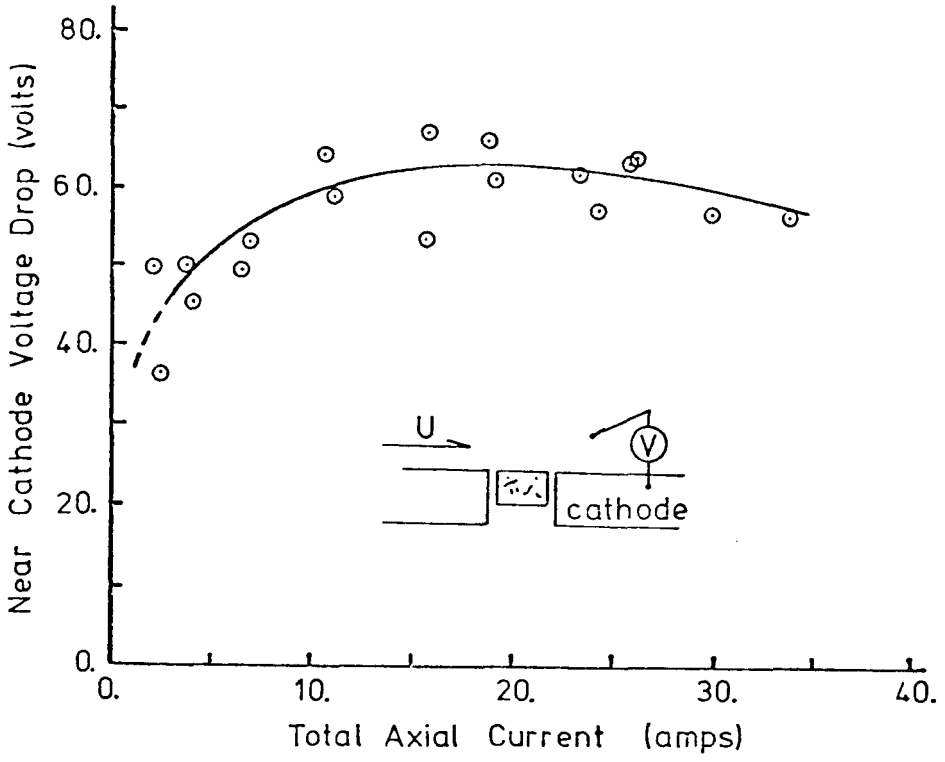

Figure 22a. Near cathode voltage drop as a function of total axial current. Cathode was downstream electrode and probe was located ~5 mm from the electrode surface. Data taken from Run 1.9-A.

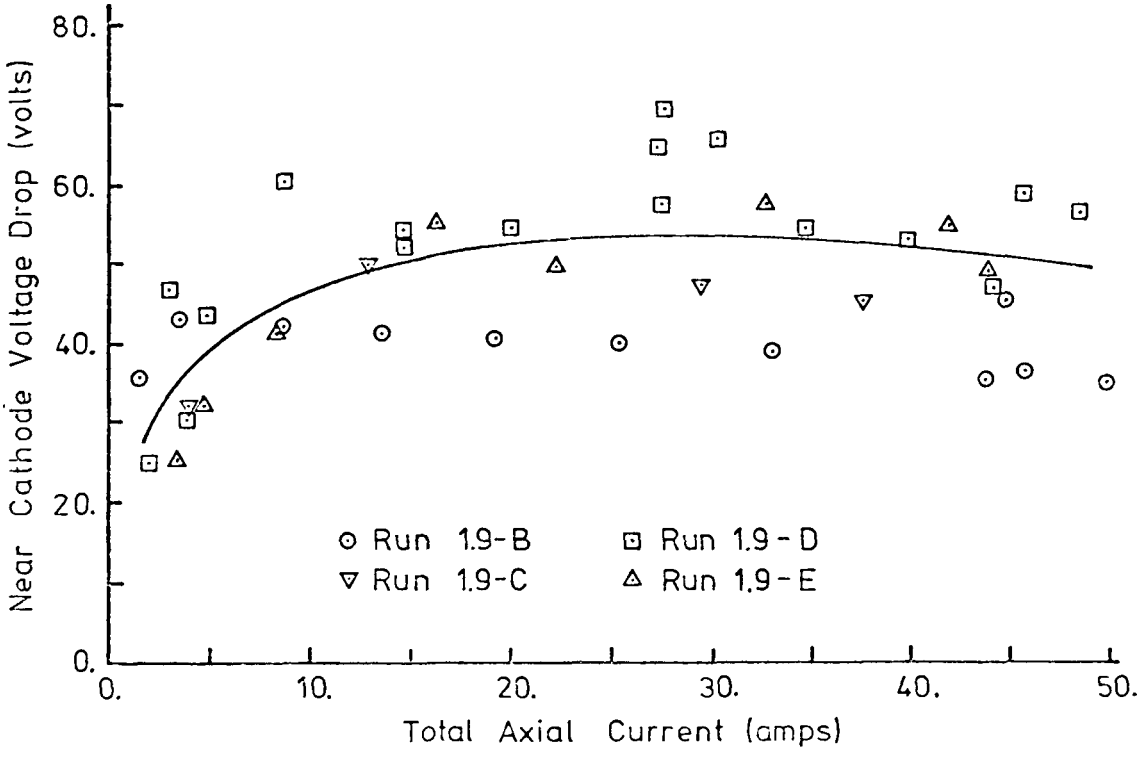

Figure 22b. Near cathode voltage drop as a function of total axial current. Cathode was downstream electrode and probe was located ~2 mm from the electrode surface. Data taken from Runs 1.9-B, 1.9-C, 1.9-D and 1.9-E.

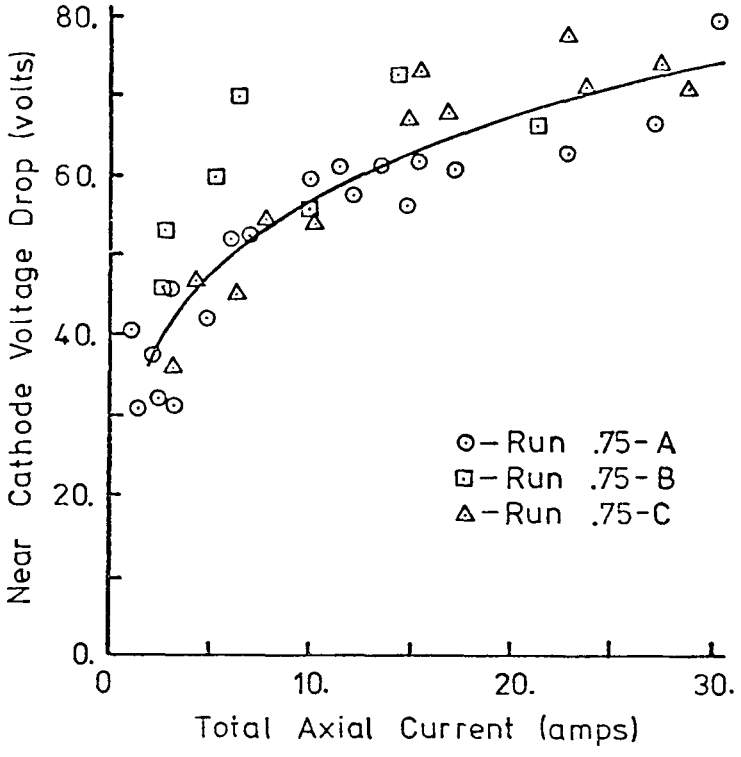

Figure 22c. Near cathode voltage drop as a function of total axial current. Cathode was downstream electrode and probe was located ~3.5 mm from the electrode surface. Data taken from Runs .75-A, .75-B and .75-C.

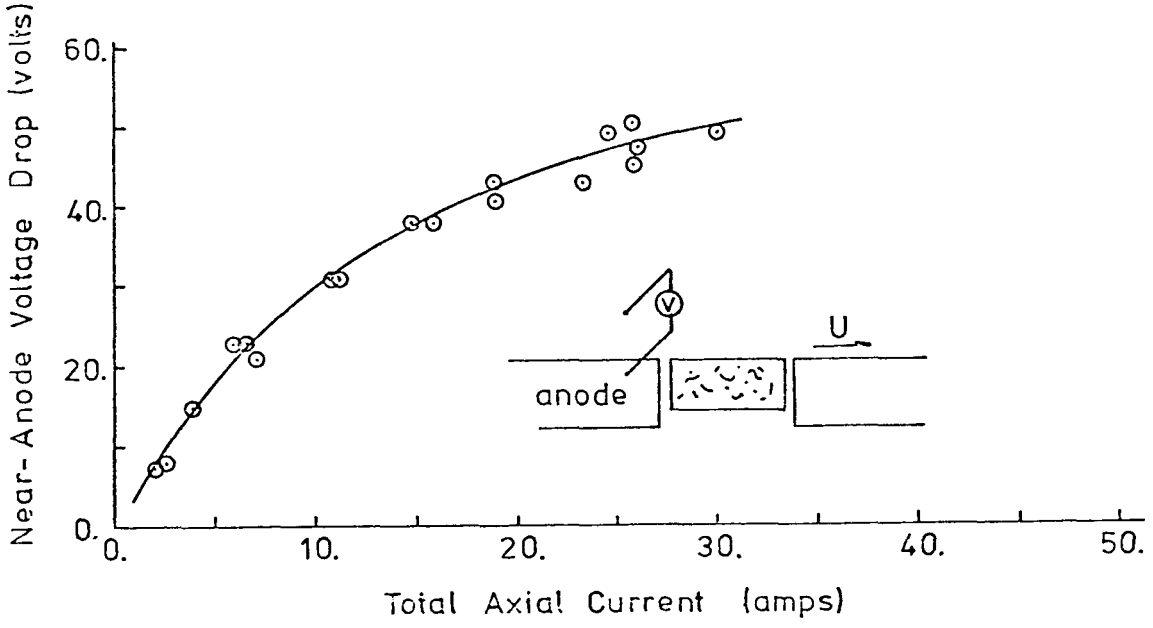

Figure 23a. Near anode voltage drop as a function of total axial current. Anode was upstream electrode and probe was located ~5 mm from the electrode surface. Data taken from Run 1.9-A.

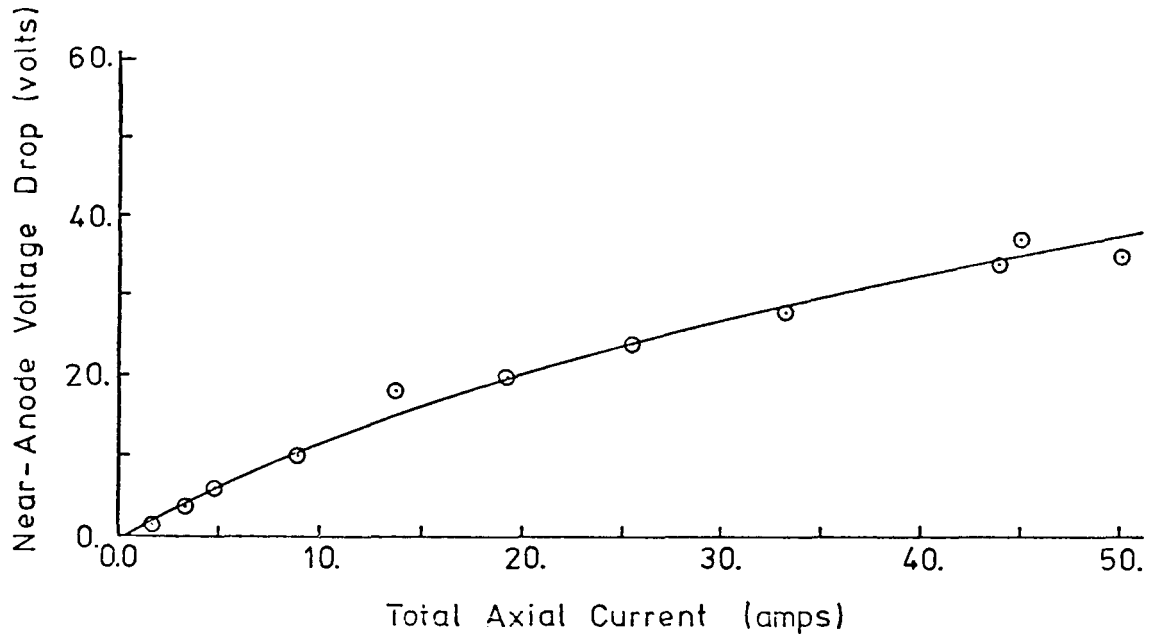

Figure 23b. Near anode voltage drop as a function of total axial current. Anode was upstream electrode and probe was located ~2 mm from the electrode surface. Data taken from Run 1.9-B.

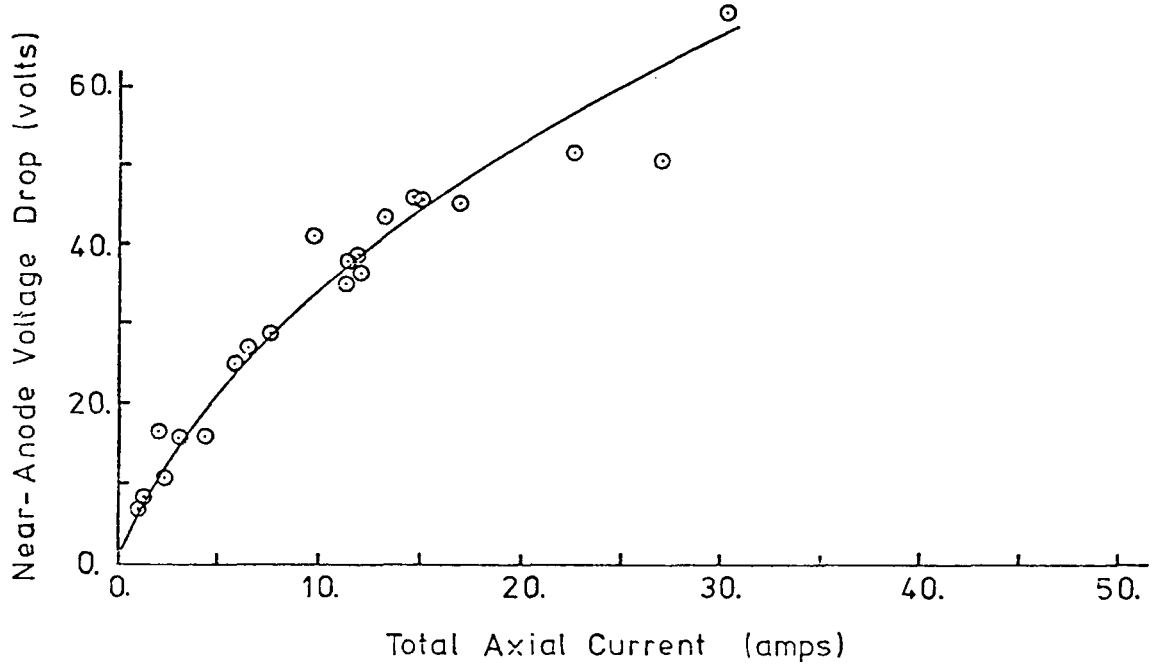

Figure 23c. Near anode voltage drop as a function of total axial current. Anode was upstream electrode and probe was located ~3.5 mm from the electrode surface. Data taken from Run .75-A.

≈10-15 amps and then levels out or declines slightly. Any effect of plasma flow condition lies within the scatter of the data. In contrast to the behavior near the cathode, the near-anode voltage drop increases steadily with current from effectively zero voltage at zero current. The behavior of the near-anode voltage drop with total axial current is shown for three of the experimental conditions in Figures 23a-23c. As would be expected to result from increased Joule dissipation, the slope decreases with increasing current, whether the heating effect is a surface related effect or a plasma related effect cannot be determined from the measurements. The results for all experimental conditions are summarized in Table 6, where the near anode dynamic resistance (dV/dI evaluated at a particular current level) for low current (≤10A) and for high current (≈30A) are tabulated. Although considerable scatter is introduced in determining the slope, the results generally indicate an increased resistance with decreased freestream conductivity. Further and more detailed discussion is deferred to Chapter 5. The behavior of the region away from the electrodes is displayed for three of the experimental conditions in Figures 24a-24c, where the voltage difference between the two probes is plotted as a function of total axial current. In these curves the voltage rises linearly with current out to the highest currents, indicating little overall effect of Joule heating in this region. The indicated resistance for each experimental condition is displayed in Table 6 and again a general trend of increased resistance with decreased free-stream conductivity is observed. An attempt to correlate all the data on the basis of an equivalent resistance per unit area [$R/A|_{equivalent} = (1/\sigma_\infty) \times gap$] is displayed in the table and can be seen to be only mildly successful. Comparison of the data with more detailed predictions is deferred to Chapter 5.

The preceeding data indicate that the non-breakdown discharge can be characterized as a relatively diffuse discharge (except close to the cathode surface) with the major effect of Joule Heating confined to the region close to the electrodes and perhaps to the electrode surfaces themselves. The complexity of the near-cathode region indicates that modeling of that region would prove difficult, so for later comparison with calculations, it is useful to eliminate the behavior that is peculiar to the near-cathode region. For this purpose the experimental data were used to

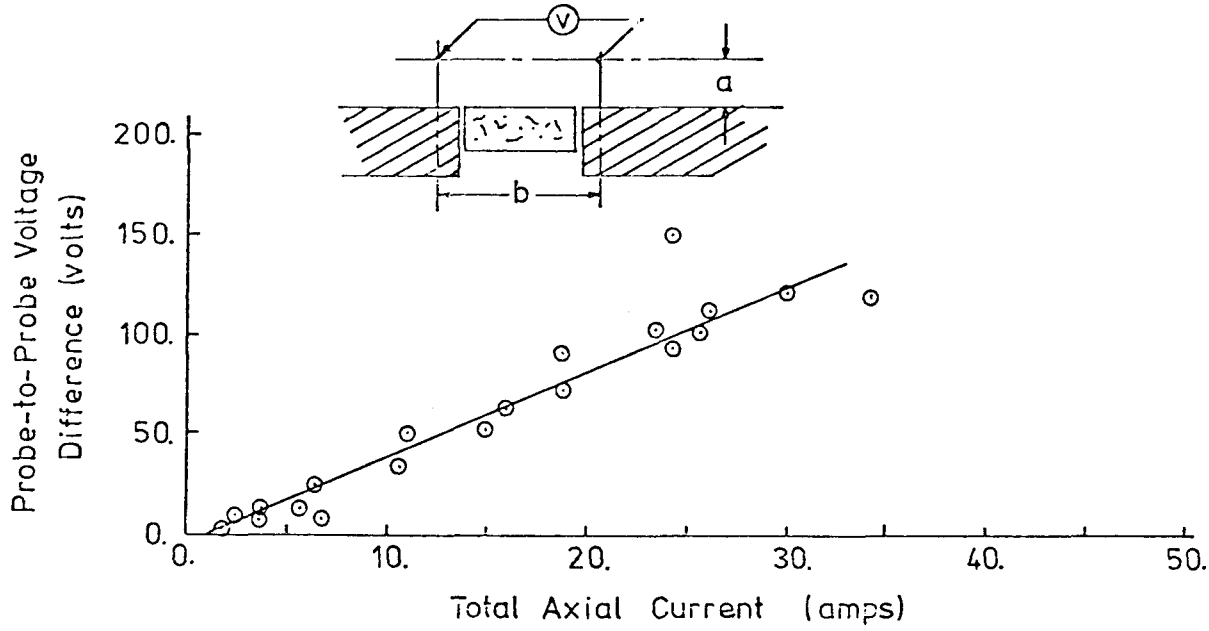

Figure 24a. Voltage difference between probe located above anode and probe located above cathode as a function of total axial current. Anode was upstream electrode. Probes located ~5 mm from electrode surface. Data taken from Run 1.9-A.

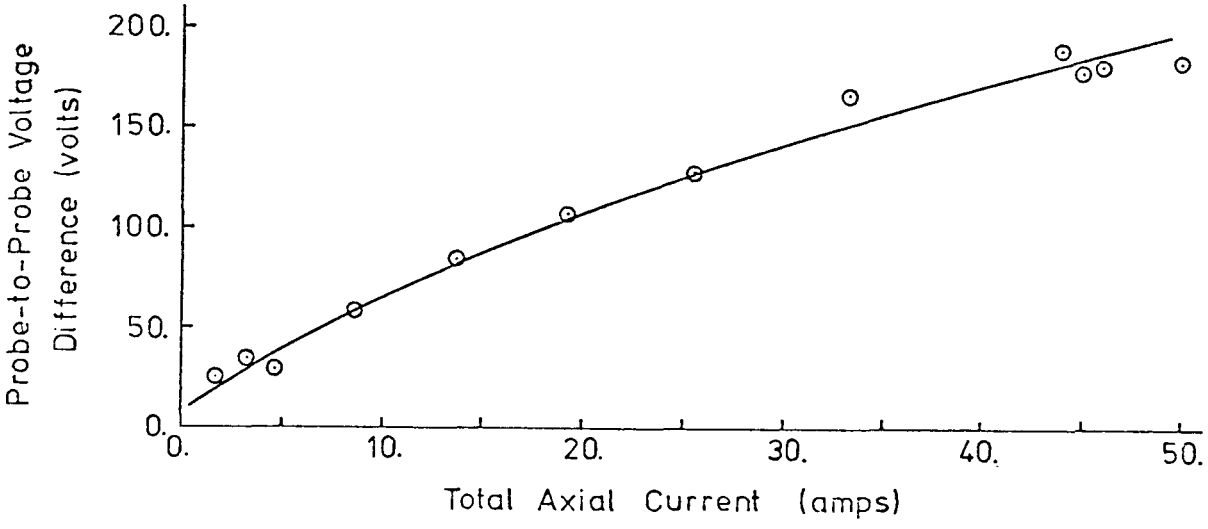

Figure 24b. Voltage difference between probe located above anode and probe located above cathode as a function of total axial current. Anode was upstream electrode. Probes located ~5 mm from electrode surface. Data taken from Run 1.9-B.

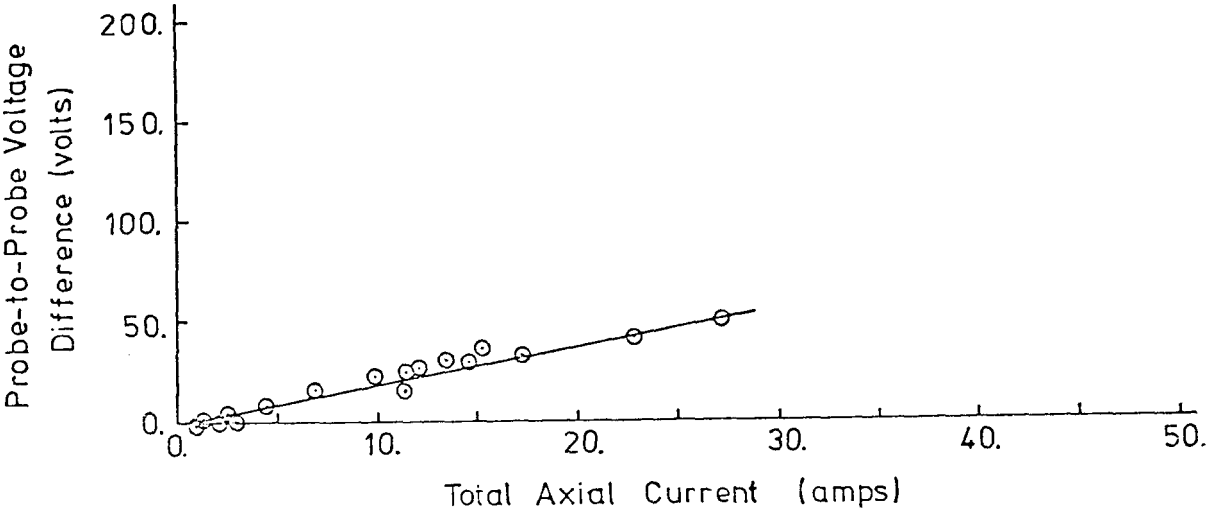

Figure 24c. Voltage difference between probe located above anode and probe located above cathode as a function of total axial current. Anode was upstream electrode. Probes located ~5 mm from electrode surface. Data taken from Run .75-A.

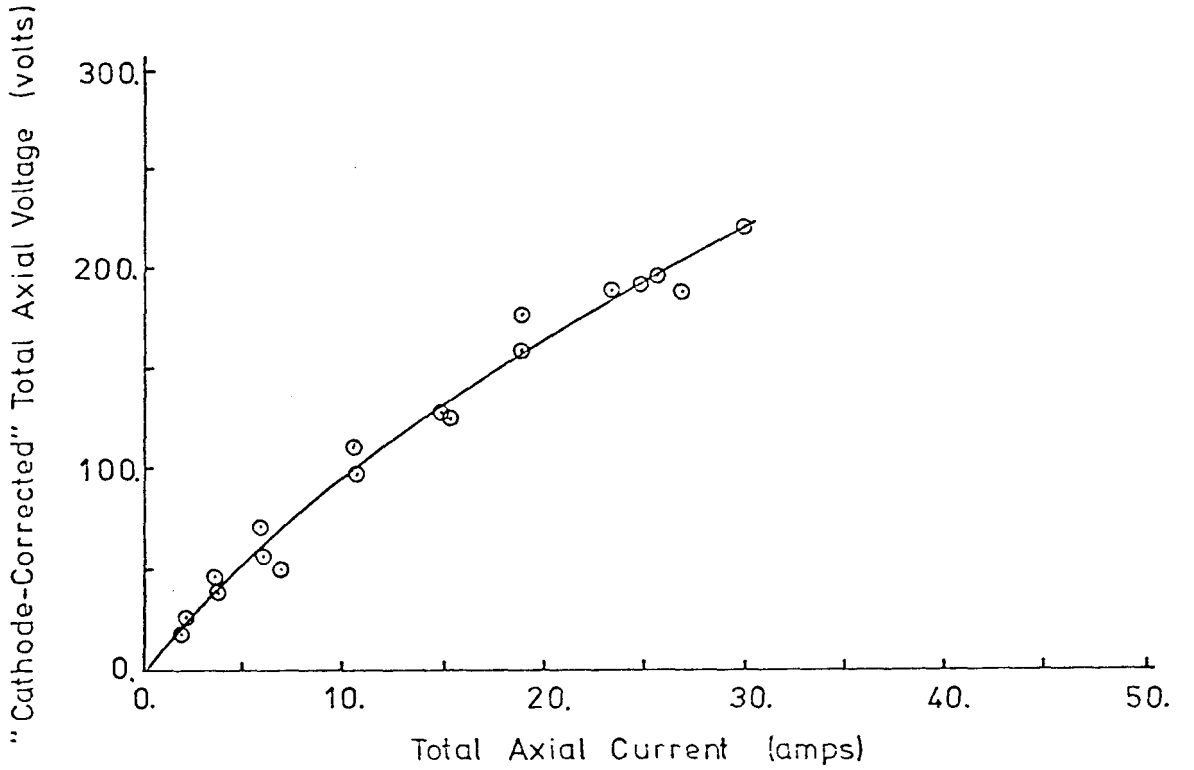

Figure 25a. "Cathode-corrected" total axial voltage versus total axial current. Curve constructed from experimental data with the near-cathode voltage drop replaced by the near-anode voltage drop. Data taken from Run 1.9-A.

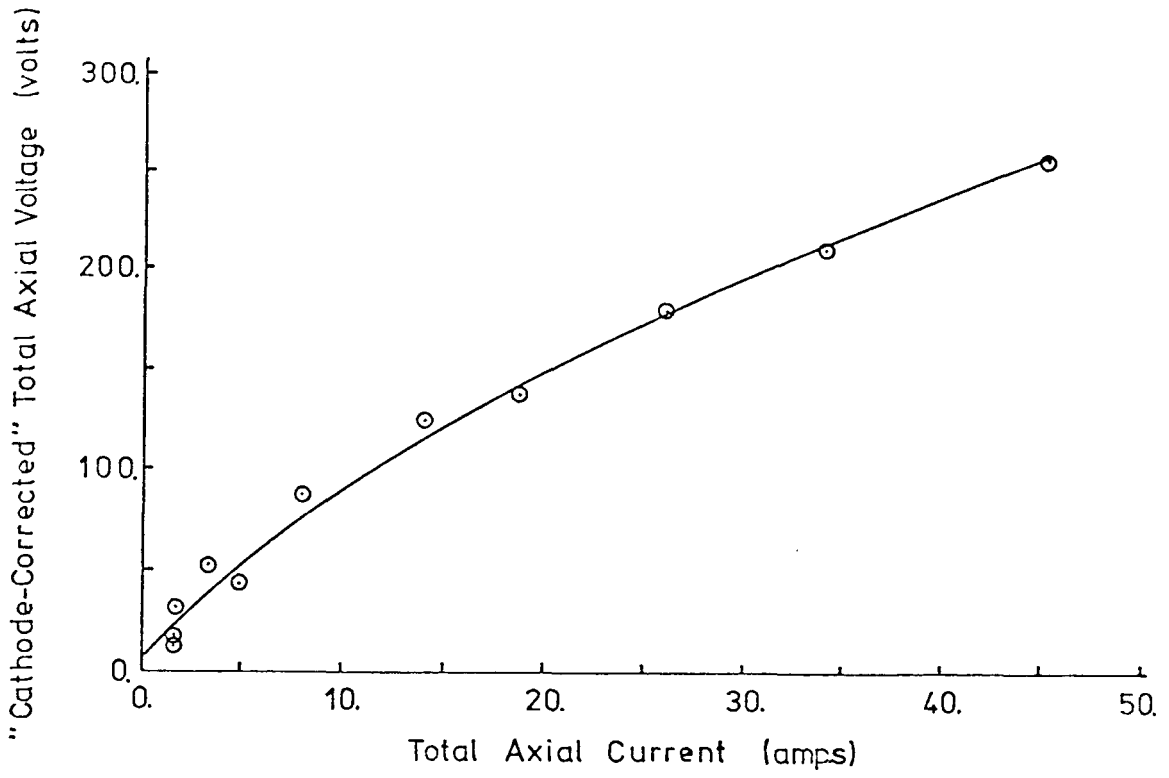

Figure 25b. "Cathode-corrected" total axial voltage versus total axial current. Curve constructed from experimental data with the near-cathode voltage drop replaced by the near-anode voltage drop. Data taken from Run 1.9-B.

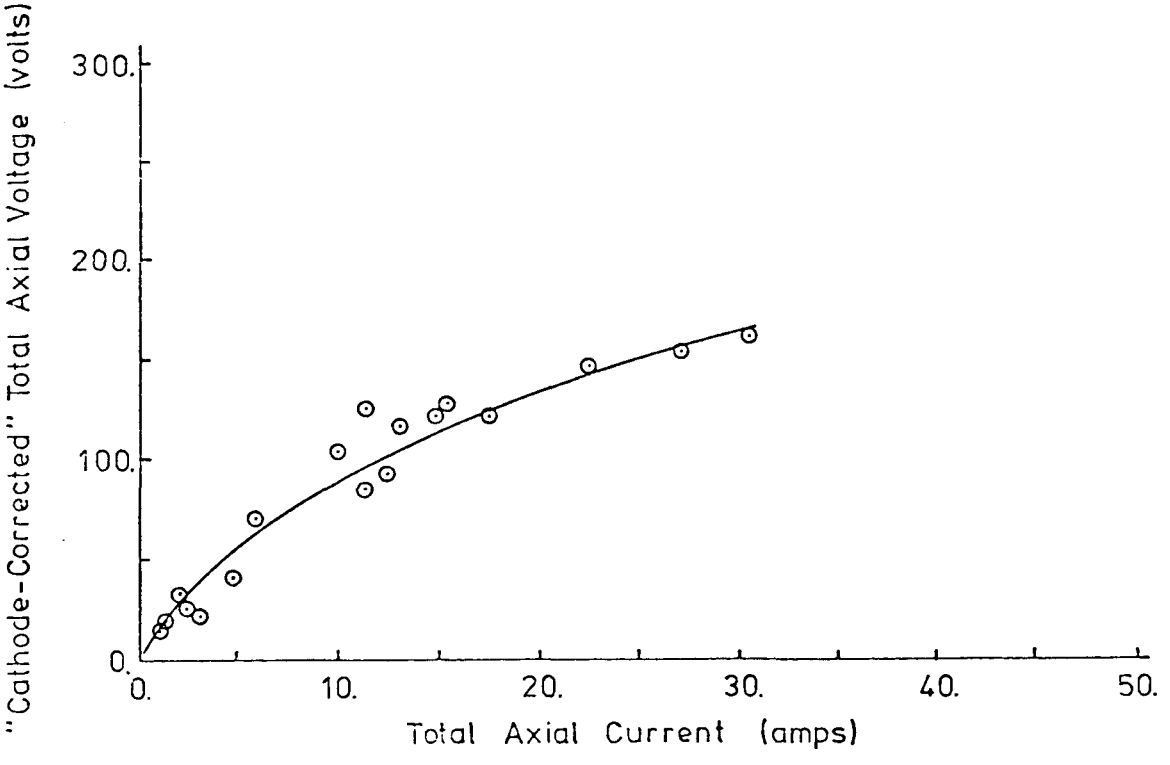

Figure 25c. "Cathode-corrected" total axial voltage versus total axial current. Curve constructed from experimental data with the near-cathode voltage drop replaced by the near-anode voltage drop. Data taken from Run .75-A.

form a voltage-current characteristic for a hypothetical situation where the near-cathode region behaves the same as the near-anode region; that is, a "cathode-corrected" total voltage at a particular current is computed as the sum of the far-electrode voltage drop measured by the voltage probes plus twice the near-anode voltage drop. Such "cathode-corrected" curves are shown for three of the experimental conditions in Figures 25a-25c. The low current and high current dynamic resistances for all experimental conditions are given in Table 6.

3.2.3 Transient Behavior for Non-Breakdown Conditions

The transient response of the inter-electrode region to an impulsive switching on of the circuits was measured. The most pronounced variation in electrical behavior was observed in the near-cathode region, where a significant decline in voltage drop was observed. As can be seen in Figure 26, the near-cathode voltage drop declines by as much as 30 volts in the initial millisecond, and in the subsequent seconds relaxes to its steady-state level approximately 10-15 volts lower. This decline in near-cathode voltage drop results in an increase in total axial current; however no other significant variations in electrical behavior were observed for non-breakdown conditions. The lack of change in near-anode voltage drop is unexpected considering the non-linear character of the steady-state voltage drop; this behavior will be discussed in Chapter 5. The total emission intensity at a distance ≃2 mm above the inter-electrode insulator surface increased with increasing axial current. The ratio of intensity after the application of current to the intensity prior to the application of current is plotted as a function of total axial current in Figure 27. While the scatter is high, the data indicate an increase in intensity of ≃25% at a current of ≃20 amps. This intensity increase corresponds to an increase in plasma temperature of ≃150°K.

The fluctuation level for the electrical parameters was approximately constant for all non-breakdown runs at a level of ≃10% peak-to-peak, except for the near-cathode voltage drop which was typically 15-20% peak-to-peak. In all experiments, large magnitude, momentary changes in the electrical parameters were observed. The behavior of the total axial voltage and total axial current for these "bursts" is displayed in Figure 28. The bursts occurred at random and in all cases the discharge returned

Table 6. Indicated dynamic resistances for different regions for each applied field experimental run series.

Run Designation	$\dot{m}$ (kg/sec)	N_2/O_2	Gap (cm)	σ (mho/m)	Near Anode Dynamic Resistance (ohm) Low Current	Near Anode Dynamic Resistance (ohm) High Current	Probe to Probe Dynamic Resistance (ohm)	$\frac{R_D \cdot \sigma_\infty}{g}$ (l/cm^2)	"Cathode Corrected" Total Dynamic Resistance (ohm) Low Current	"Cathode Corrected" Total Dynamic Resistance (ohm) High Current
1.9-A	.11	0.7	1.9	9.1	3.3	.6	4.4	2.1	11.0	5.6
1.9-B	.12	0.58	1.9	10.8	1.1	.5	4.6	2.6	6.8	5.6
1.9-C	.17	1.1	1.9	7.6	1.9	.7	5.4	2.0	9.2	6.8
1.9-D *	.11	0.6	1.9	10.9	.8	.3	3.4	1.8	5.0	4.0
1.9-E *	.17	1.05	1.9	7.6	.6	.3	4.4	1.7	5.6	5.0
.75-A	.11	0.6	0.75	11.1	3.0	1.3	1.9	2.8	7.9	4.5
.75-B	.11	0.8	0.75	8.2	3.5	2.0	3.3	3.6	10.3	7.3
.75-C	.18	1.1	0.75	6.7	3.6	1.7	2.6	2.3	9.8	6.0

* Data indicates possibility of probe coating affecting the readings

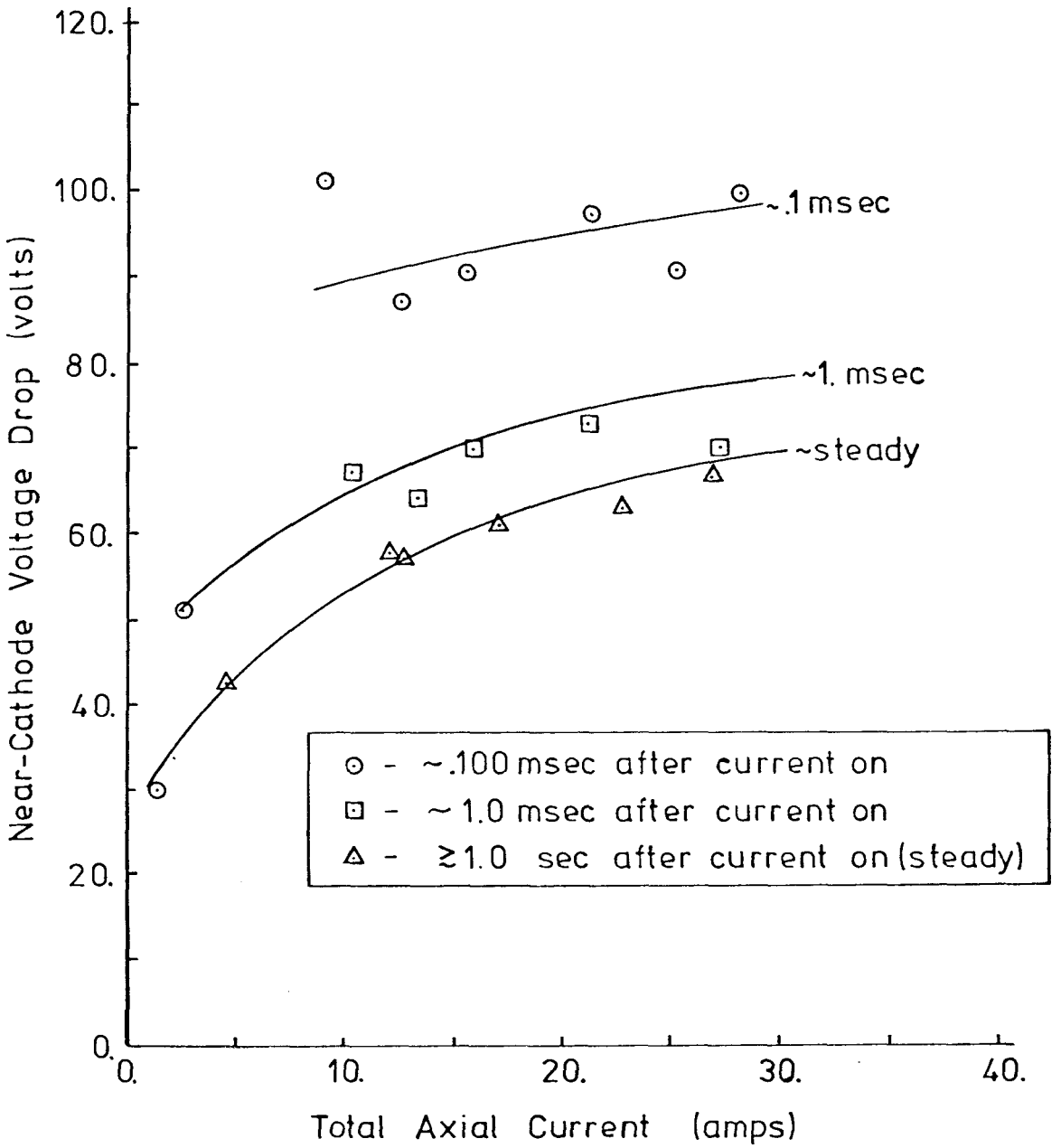

Figure 26. Time response of near-cathode voltage drop as a function of total axial current. Data taken from Run .75-A. The cathode was the downstream electrode.

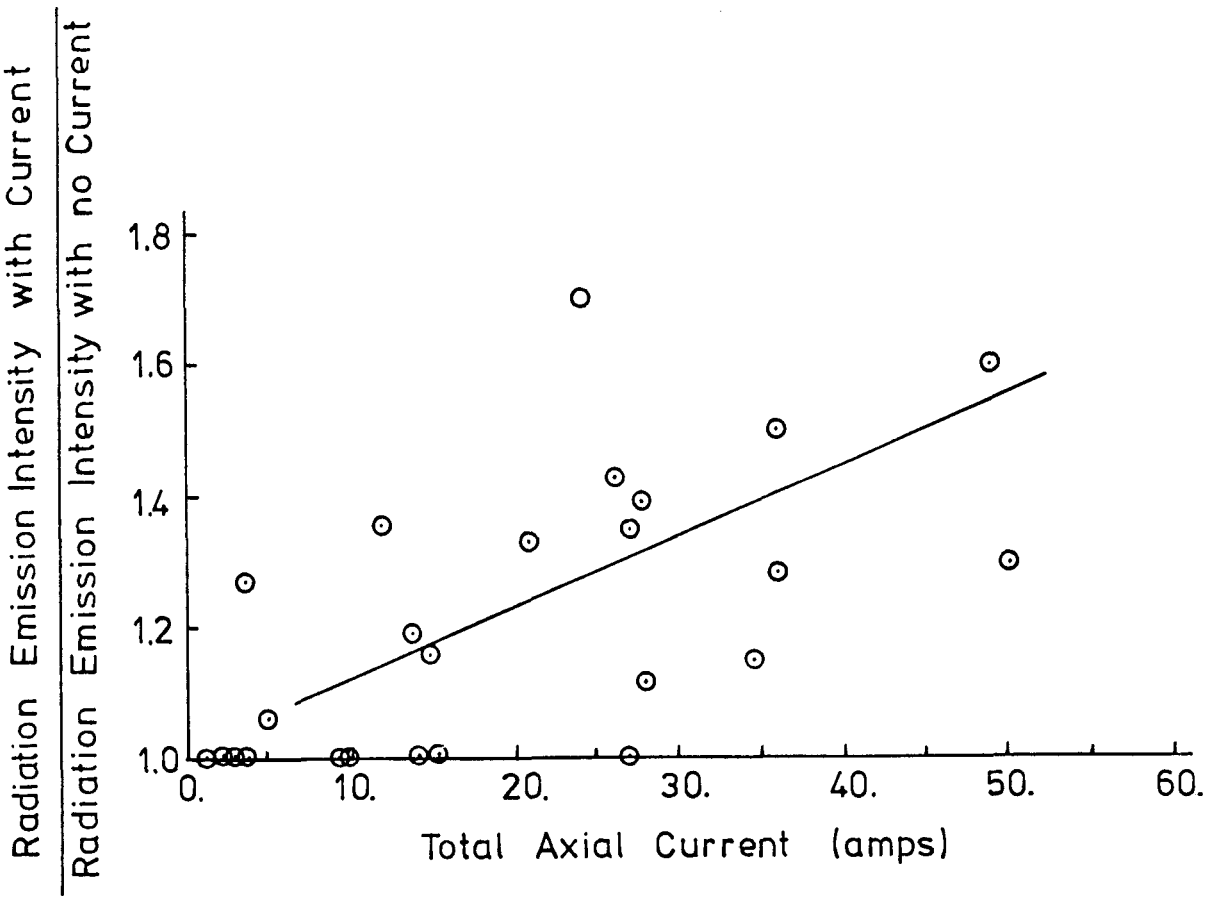

Figure 27. Increase in radiation intensity at a position ~2mm above the inter-electrode insulator as a function of total axial current. Increase is expressed as a ratio of the intensity just prior to the application of current to the intensity measured a few milli-seconds after initiation of current. Data taken from Run .75-A.

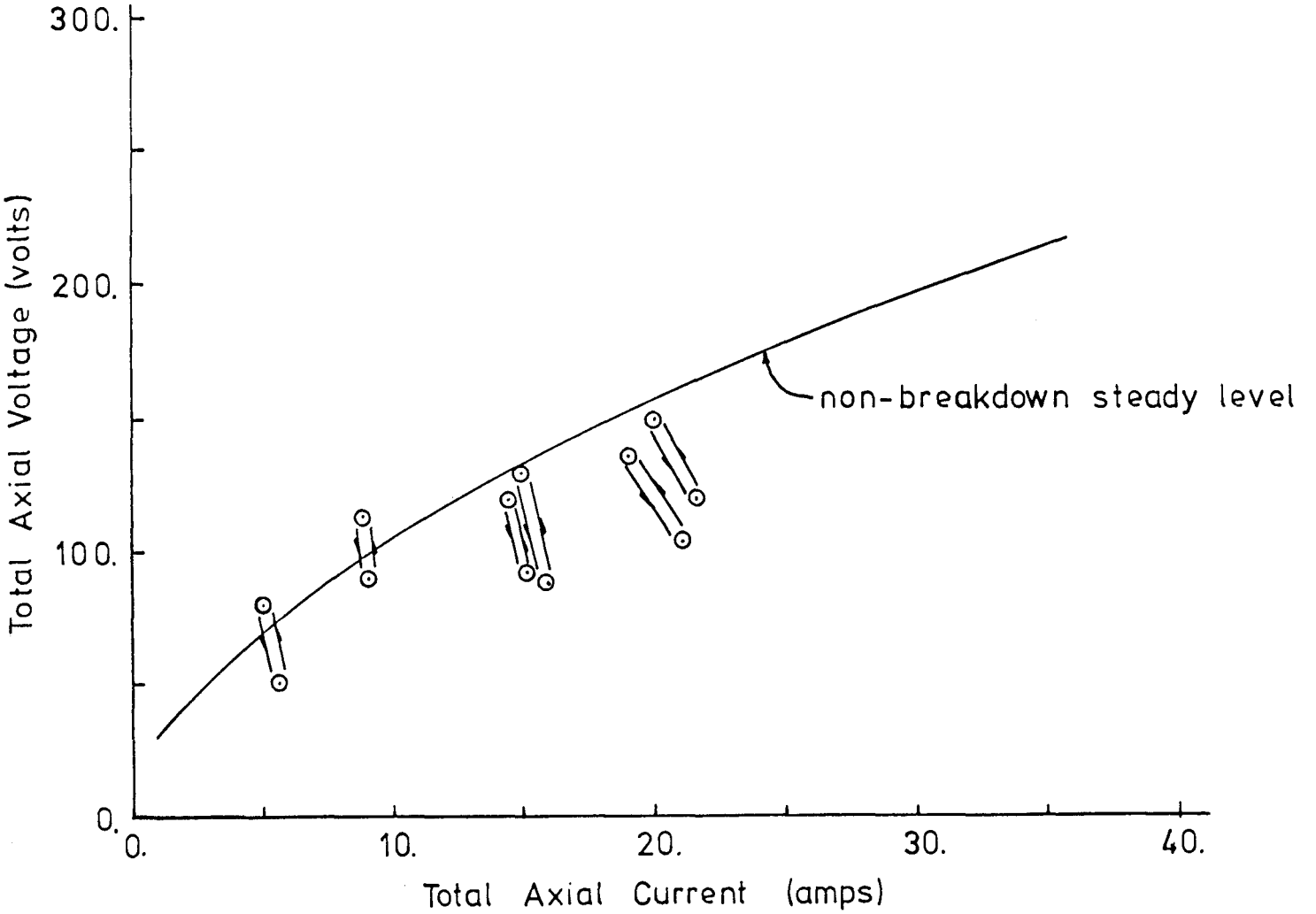

Figure 28. Voltage-current characteristics of "bursts" observed in applied field experiments. Non-breakdown steady level is represented by the solid curve.

to its original state. The photo-diode emission intensity measurements indicated that the majority of these momentary changes were accompanied by an increase in intensity at all probe locations. For such cases, the voltage probe measurements showed that the near-electrode and far-electrode regions were all affected. From the above observations it is concluded that slugs of high seed fraction and/or high temperature plasma are responsible for the bulk of these bursts. For some of the bursts, no change in emission intensity was observed and a decline in near-cathode voltage drop was found to be responsible. The cause of such momentary drops in near-cathode voltage are not known, however, in all cases the discharge returned to its original state.

3.2.4 Plasma Breakdown

For voltages exceeding a threshold level the discharge was not steady, and following a delay period a rapid and significant decline in voltage was observed. This behavior was termed axial voltage breakdown. While many characteristics were common to all the breakdowns, the experiments distinguished between two types of breakdown and these types are discussed separately. In this section, the breakdowns characterized by a very short delay time are described, with evidence presented to establish that this type of breakdown is dominated by events in the plasma.

The total voltage versus total current characteristics showing the behavior during breakdown are displayed in Figures 29a-29h, with breakdowns of both types shown and identified. The non-breakdown behavior is represented by a solid line on each of the figures. As can be observed in the figures, breakdown occurs only for voltages exceeding a threshold level and has the main characteristic of a significant reduction in voltage. The transient behavior for two breakdowns of the plasma type are presented in Figures 30 and 31. These breakdowns are representative of plasma type breakdown observed for all experimental conditions. In both cases the timescale over which the majority of the breakdown occurs is less than a milisecond; however, the time separating the initiation of current and the breakdown is considerably different for the two cases. The cause of the delay time is not well understood, although the delay time did appear to be shorter for the higher applied voltages. Delay times as short as a few milliseconds and as long as a few hundreds

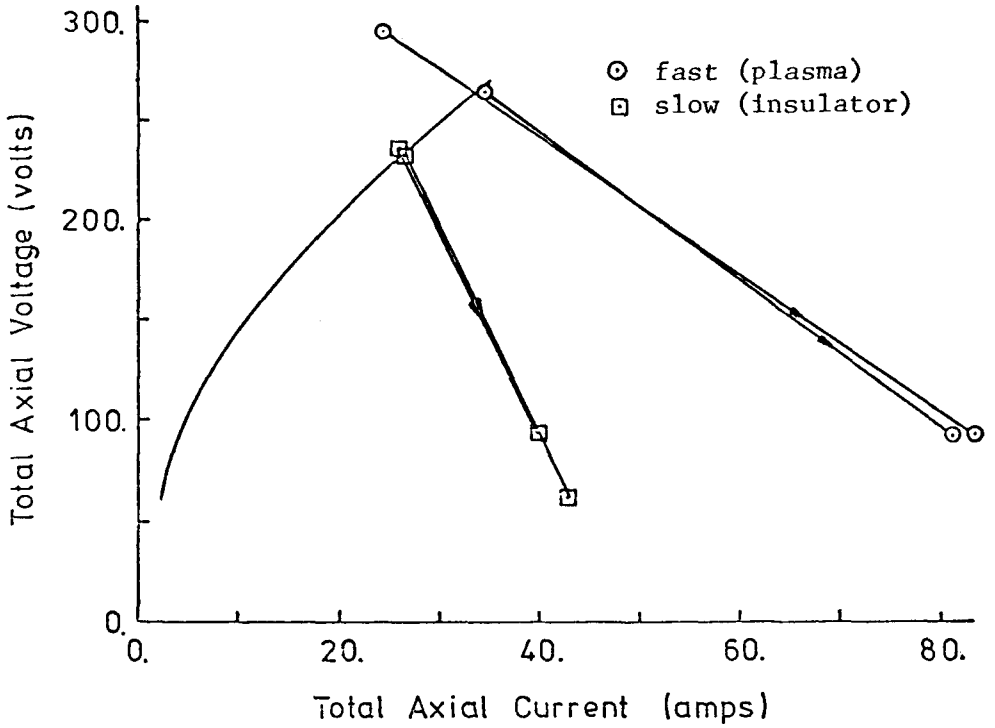

Figure 29a. Voltage-current characteristic displaying behavior for axial breakdown. Both types of breakdown are shown and labeled. Solid line represents non-breakdown behavior. Data taken from Run 1.9-A.

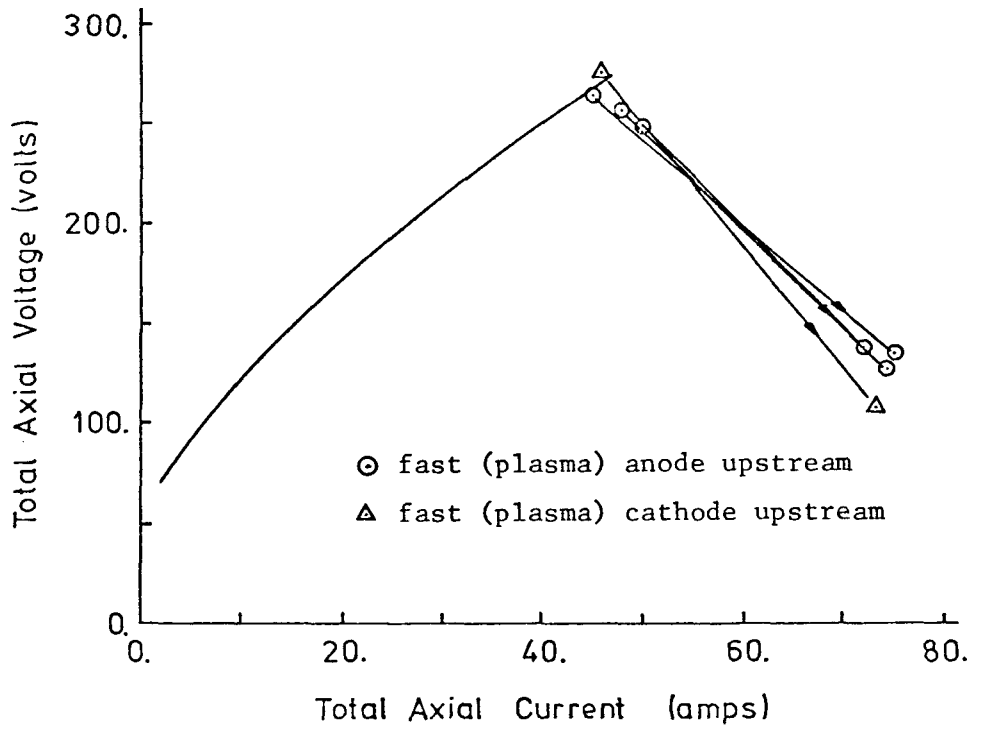

Figure 29b. Voltage-current characteristic displaying behavior for axial breakdown. Both types of breakdown are shown and labeled. Solid line represents non-breakdown behavior. Data taken from Run 1.9-b.

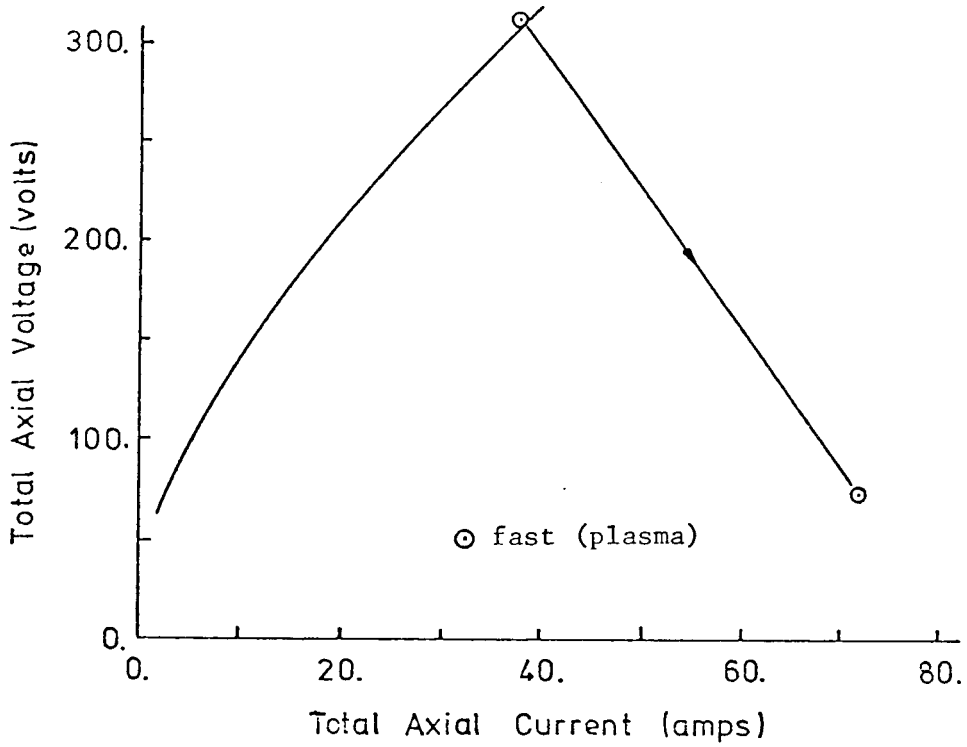

Figure 29c. Voltage-current characteristic displaying behavior for axial breakdown. Both types of breakdown are shown and labeled. Solid line represents non-breakdown behavior. Data taken from Run 1.9-C.

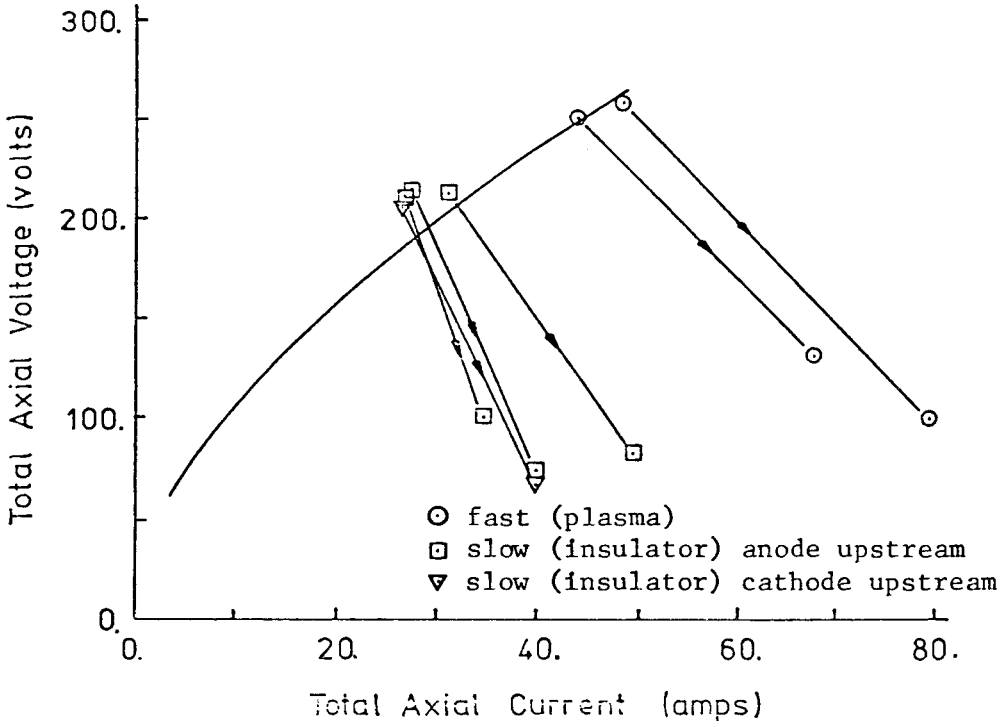

Figure 29d. Voltage-current characteristic displaying behavior for axial breakdown. Both types of breakdown are shown and labeled. Solid line represents non-breakdown behavior. Data taken from Run 1.9-D.

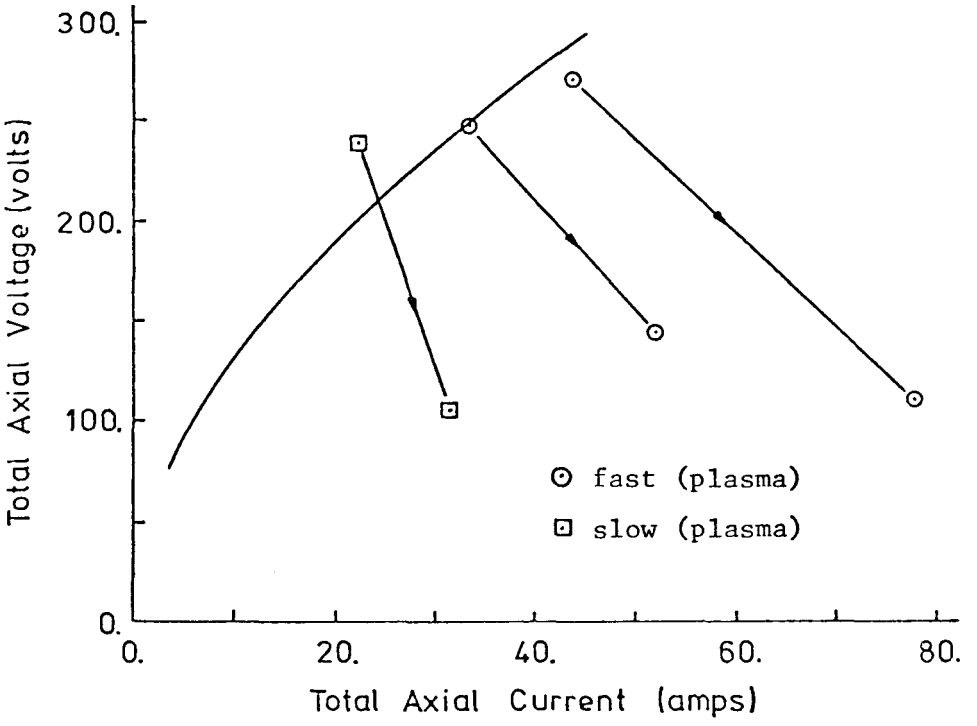

Figure 29e. Voltage-current characteristic displaying behavior for axial breakdown. Both types of breakdown are shown and labeled. Solid line represents non-breakdown behavior. Data taken from Run 1.9-E.

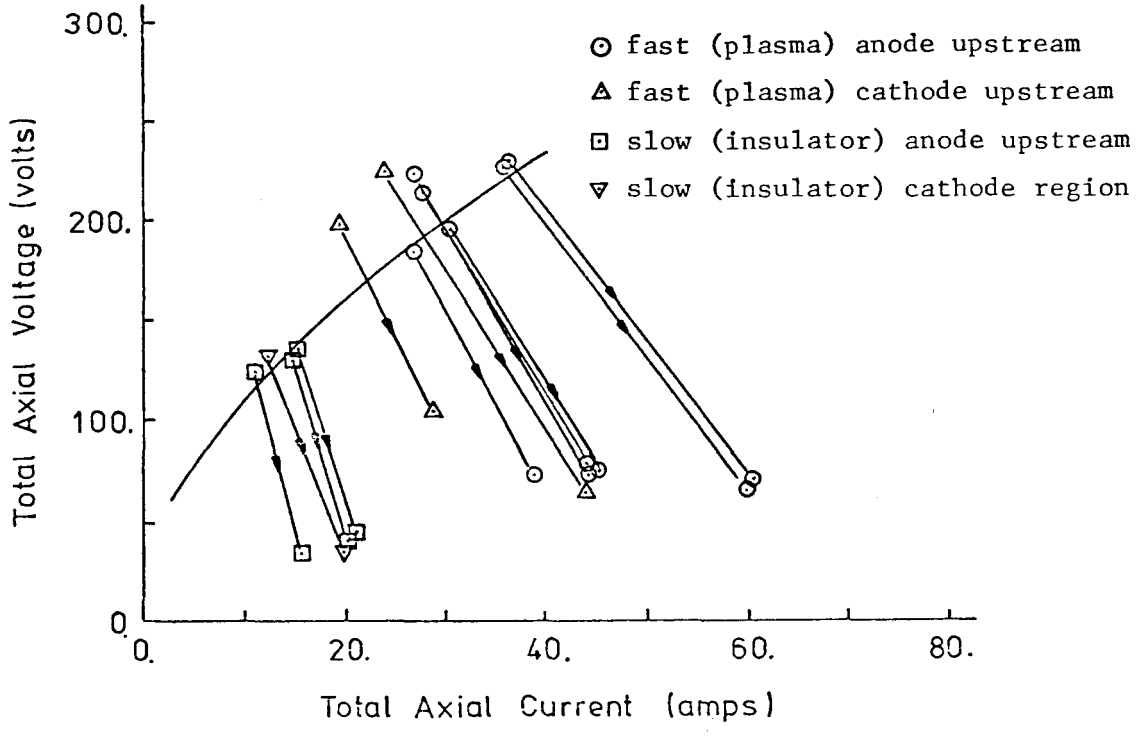

Figure 29f. Voltage-current characteristic displaying behavior for axial breakdown. Both types of breakdown are shown and labeled. Solid line represents non-breakdown behavior. Data taken from Run .75-A.

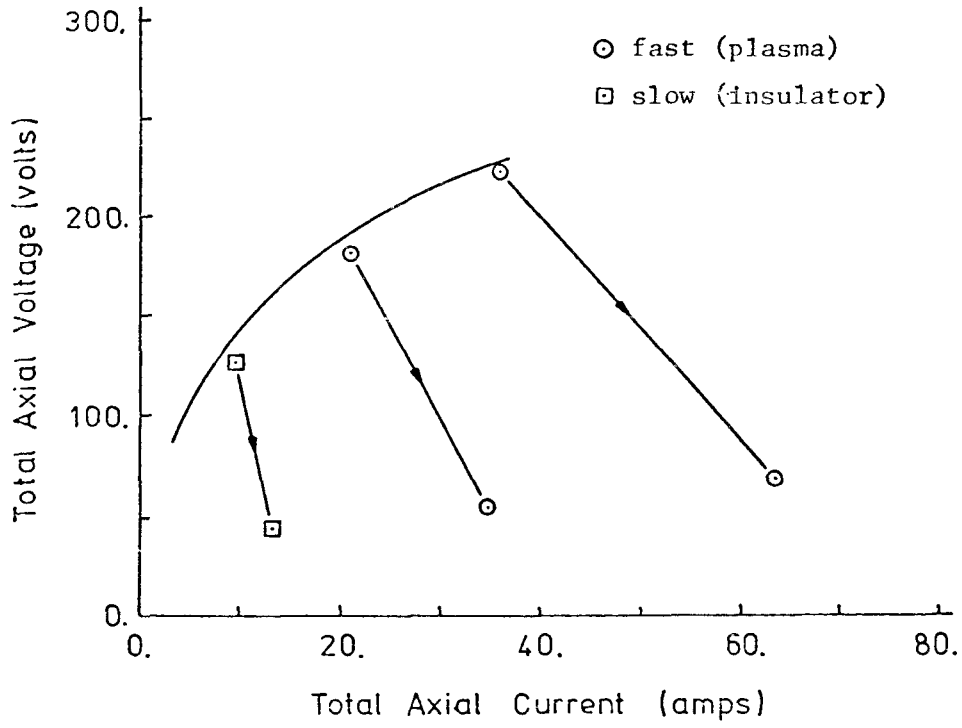

Figure 29g. Voltage-current characteristic displaying behavior for axial breakdown. Both types of breakdown are shown and labeled. Solid line represents non-breakdown behavior. Data taken from Run .75-B.

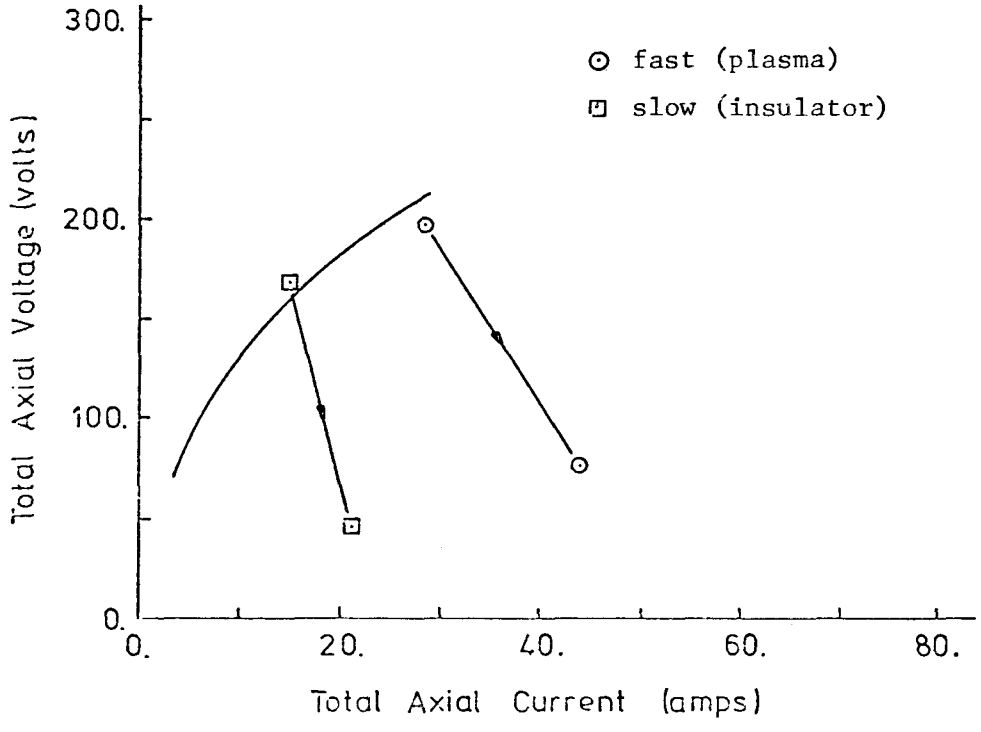

Figure 29h. Voltage-current characteristic displaying behavior for axial breakdown. Both types of breakdown are shown and labeled. Solid line represents non-breakdown behavior. Data taken from Run .75-C.

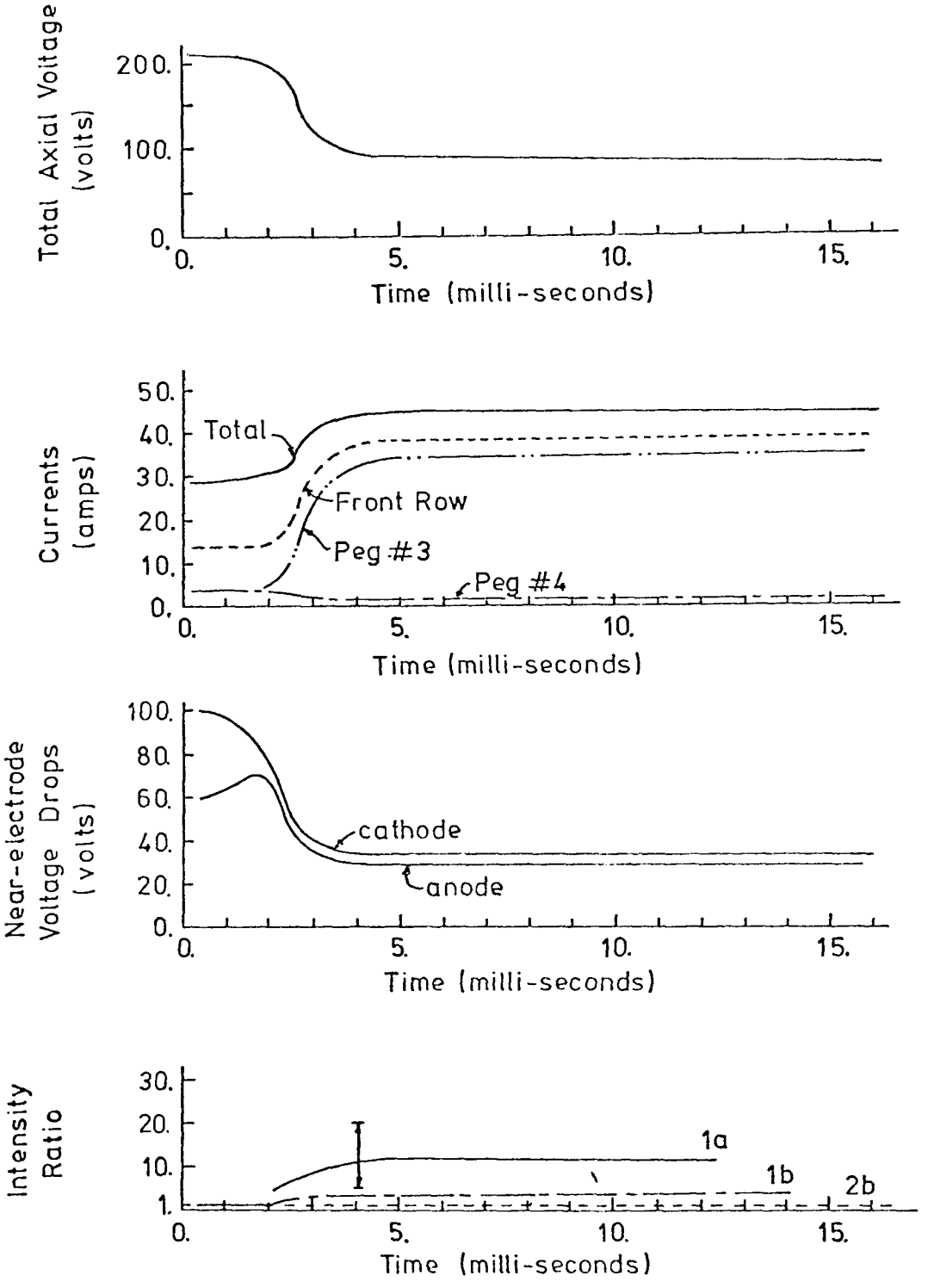

Figure 30. Time response of various parameters for a "fast" (plasma) breakdown. Data taken from Run .75-A.

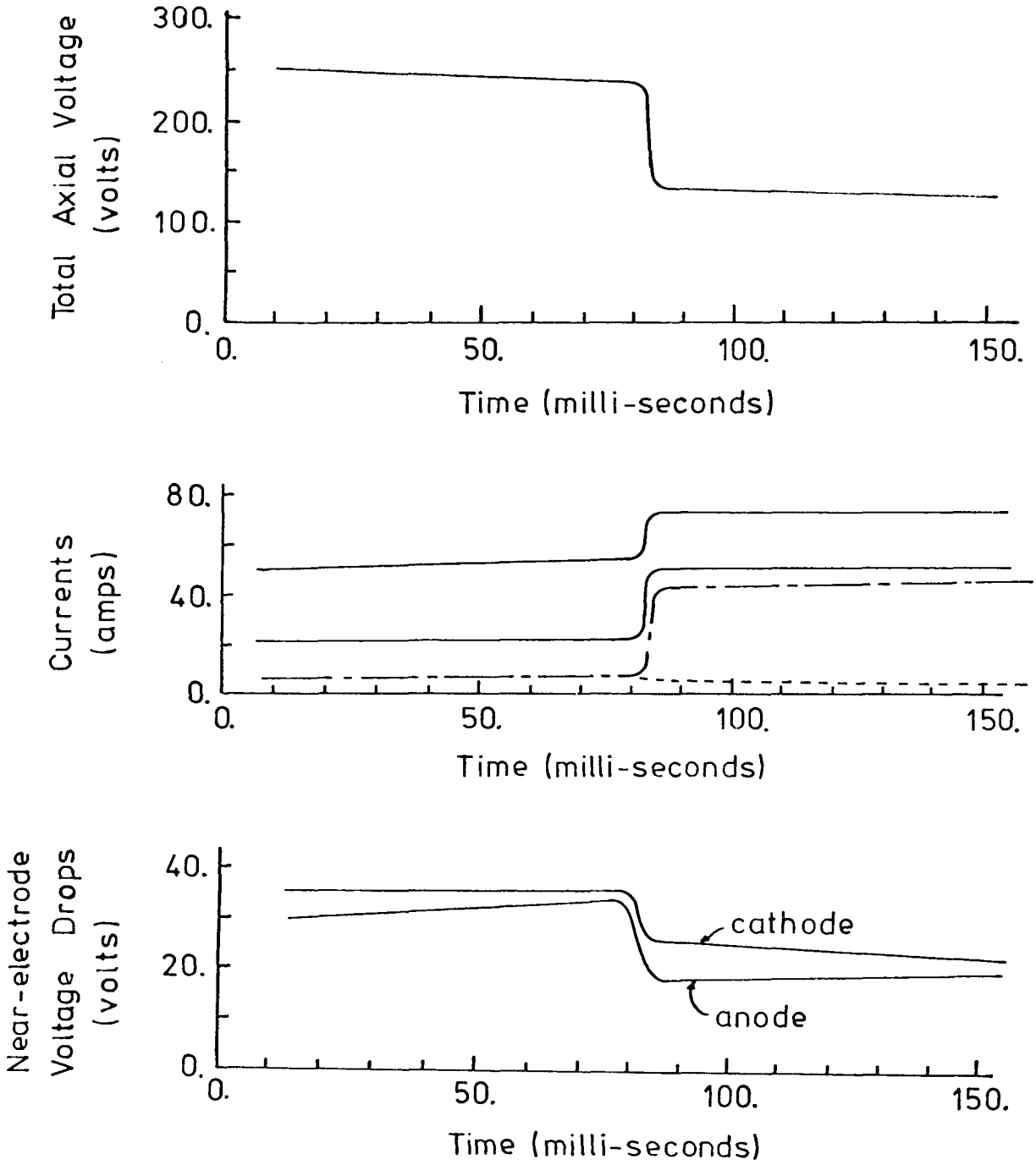

Figure 31. Time response of various parameters for a "fast" (plasma) breakdown. Data taken from Run 1.9-B.

of milliseconds were observed for breakdowns of the plasma type. The data presented in Figures 30 and 31 demonstrate that the breakdown is accompanied by a constriction of the current, such that after breakdown a small portion of the electrode carries the majority of the current passing between the two electrodes. As can also be observed in the figures, both near-electrode voltage drops decline significantly as the breakdown develops. The photo-diode emission intensity measurements indicate extremely high temperatures in the plasma region close to the inter-electrode region, while the emission intensity in the region away from the inter-electrode region does not change.

A qualitative, overall understanding of the breakdown process may be obtained by examination of the photographic records taken during a run in which breakdown occurred. A few frames taken from runs in which plasma breakdown occurred are displayed in Figures 32 and 33; the sequence of frames in Figure 32 corresponds to the transient response shown in Figure 30. Details of the diagnostic technique are given in Section 2.3.3. In the first frame of Figure 32 taken just after the breakdown, an intense region bridges the gap from anode to cathode in the plasma image and the insulator beneath the discharge is significantly heated. As can be observed the insulator beneath the discharge heats up considerably more with time and when the current is stopped the intense region in the plasma image is immediately extinguished while the insulator slowly cools. The intense region in the plasma is extremely mobile as can be observed in Figure 33. Long-time effects resulting from the heating of the insulator are discussed in Section 3.2.7.

The above data clearly establish that this type of breakdown is caused by a constriction of the current passing through the plasma in the region directly above the inter-electrode insulator.

3.2.5 Insulator Breakdown

Many of the breakdowns observed were characterized by a delay time greater than a second and by a timescale of about 1 second for the breakdown itself. As with plasma breakdown, this type of breakdown is characterized by a significant decline in voltage, and breakdown occurs only when a threshold voltage is exceeded. The total axial voltage versus total axial current behavior for breakdowns of this type are shown in

Photograph taken ≳ 15 msec after initiation of current.

Photograph taken ≳ 30 msec after initiation of current.

Photograph taken ≳ 60 msec after initiation of current. Frame immediately prior to stopping of current.

Photograph taken just after current stopped.

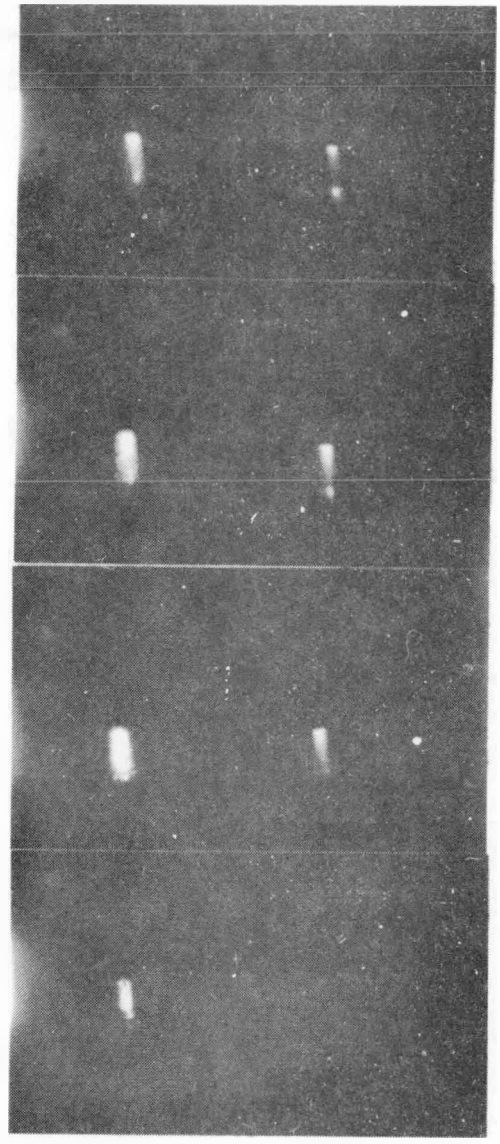

Figure 32. Sequence of frames of the movies showing the behavior of the inter-electrode region for a fast breakdown. Data is taken for Run series .75-A; the gap is 7.5 mm. The time response of the important parameters for the run are shown in Figure 30. A descriptive sketch of the camera view is given in Figure 11. Note that the plasma image shows an intense region bridging the gap in the first frame and the intense region disappears as soon as the current is stopped. The insulator beneath, however, remains heated for a considerable time.

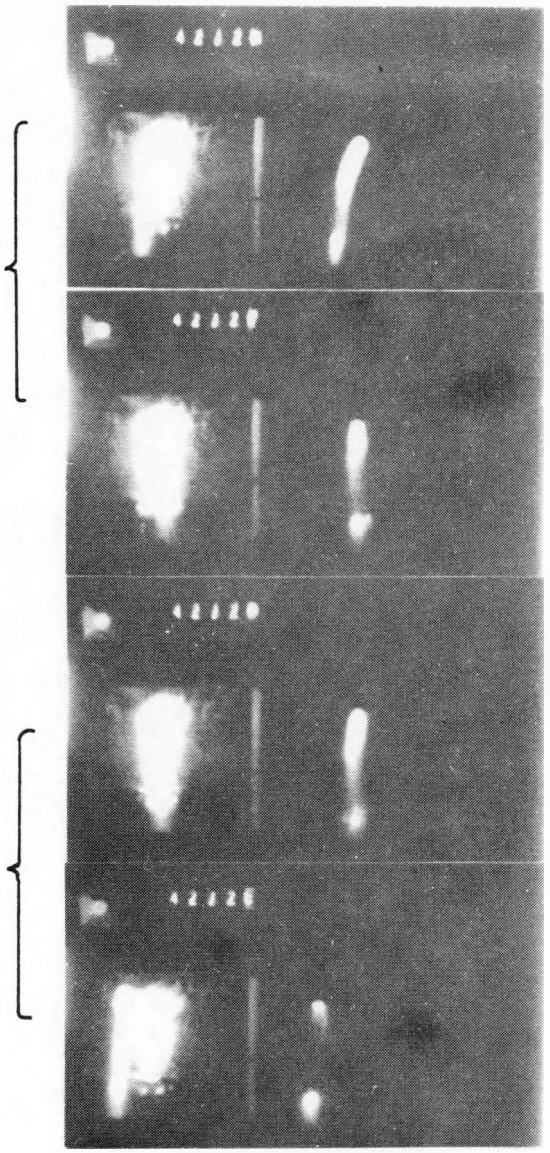

Figure 33. Sequence of frames of the movies showing the behavior of the inter-electrode region for a fast breakdown and displaying the high mobility of the intense region in the plasma. Data is taken from Run series 1.9-C; the gap is 19. mm. A descriptive sketch of the view into the camera is given in Figure 11.

Figures 29a-h. The transient response of the important parameters for two insulator breakdowns is displayed in Figures 34 and 35. For these runs the total voltage and total current remain constant over a period of 5-17 seconds after which breakdown is observed. As can be observed in the figures, breakdown is accompanied by a constriction of the current such that after breakdown a small region of the electrode carries most of the total current passing between the electrodes. As in the case of plasma breakdown, both near-electrode voltage drops decline significantly when breakdown occurs. For this type of breakdown, little or no increase in emission intensity was observed for any of the locations monitored by the photo-diode.

A qualitative, overall understanding of the insulator breakdown process may be obtained by an examination of the photographic records taken during the breakdowns described above. Several frames from the movies are reproduced in Figures 36 and 37. A descriptive sketch of the view through the camera is shown in Figure 11. The early frames for both sequences show little activity other than a few hotspots on or near the cathode. The later frames in the sequences show the formation of relatively broad heated regions in the insulator image at one or both edges of the inter-electrode insulator. These regions slowly grow in the axial direction and breakdown is observed when the gap is bridged by a narrow channel in the insulator. Temperatures well in excess of 2500°K are indicated by comparison of the channel region and the intensity standards in the photographs. As the breakdown develops further, the channel widens and molten insulator material is observed to flow downstream. As can be observed in the figures, no activity is recorded in the plasma image on the film during the development of the breakdown.

The above data clearly indicate that this type of breakdown results from the formation of a constricted current path through the inter-electrode insulator.

3.2.6 Breakdown Threshold Voltage

As demonstrated in the previous sections a stable and diffuse discharge was observed for total axial voltage below a threshold level; however, when this threshold voltage was exceeded breakdown resulted. When plasma and insulator breakdown were observed in the same experiment, the threshold voltage for plasma breakdown was higher. A summary of the

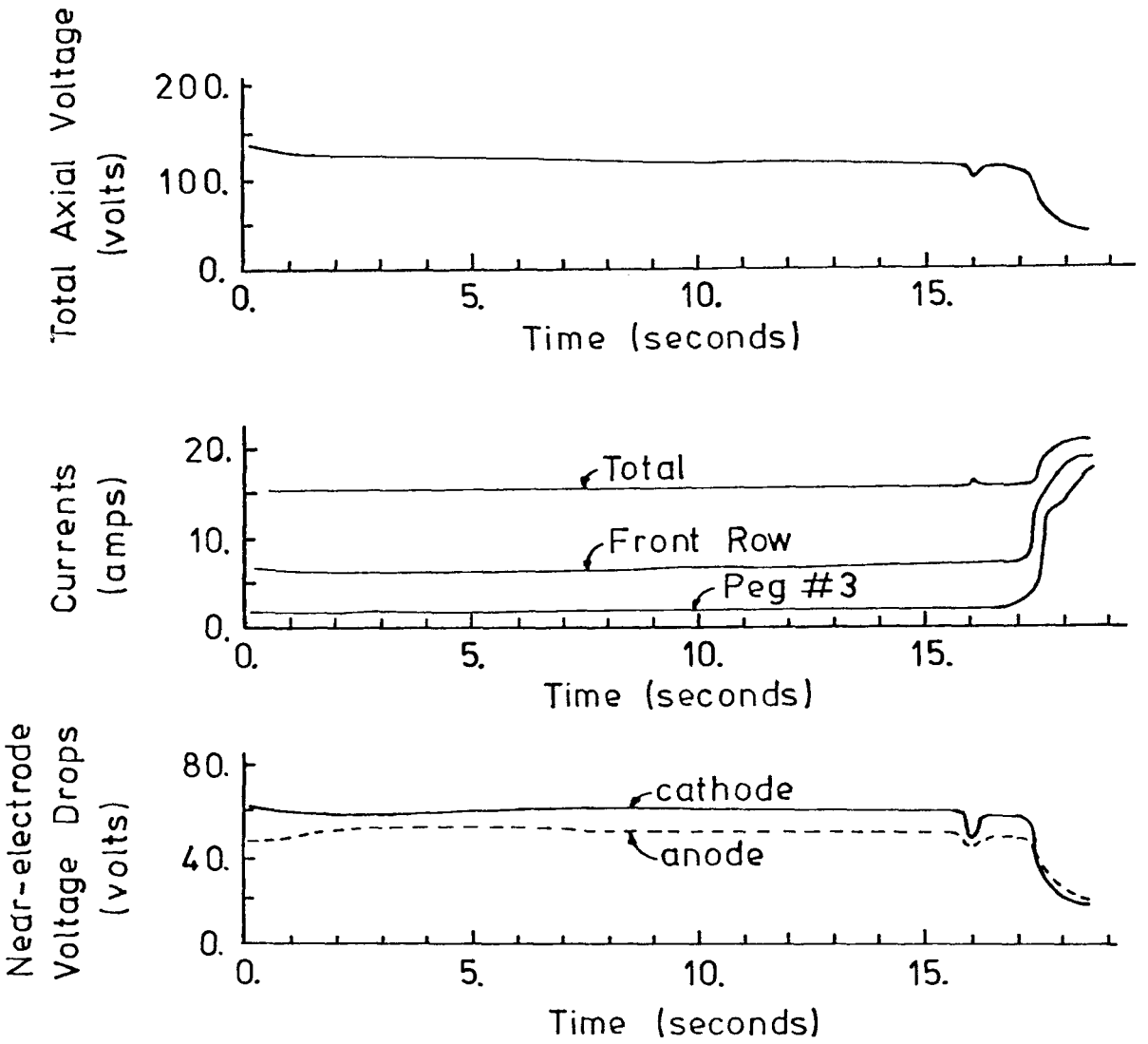

Figure 34. Time response of various parameters for a "slow" (insulator) breakdown. Intensity measurements show no increase when insulator breakdown occurs. Data taken from Run .75-A.

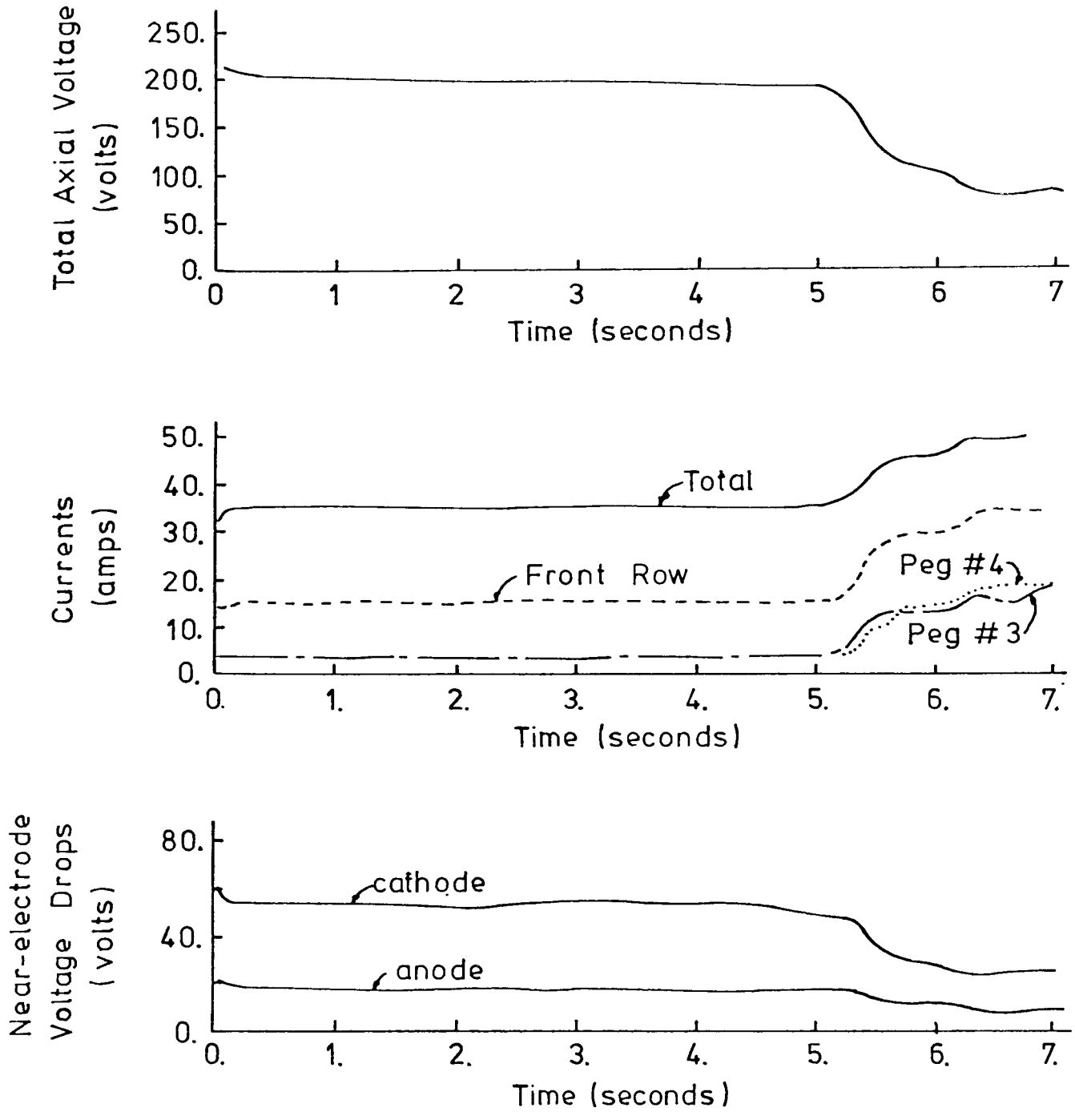

Figure 35. Time response of various parameters for a "slow" (insulator) breakdown. Data taken from Run 1.9-D.

Photograph taken ∿13.5 seconds after initiation of current.

Photograph taken ∿16.4 seconds after initiation of current.

Photograph taken ∿17.4 seconds after initiation of current.

Photograph taken ∿17.7 seconds after initiation of current.

Photograph taken ∿18.2 seconds after initiation of current.

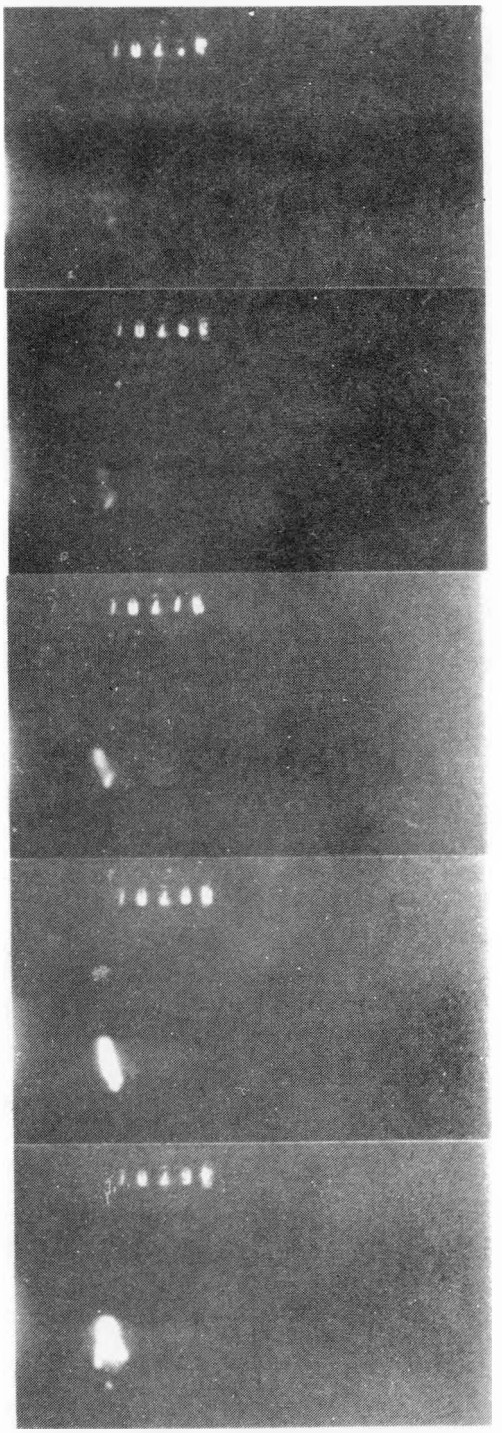

Figure 36. Sequence of frames of the movies showing the development of a slow (insulator) breakdown. Data is taken from Run series .75-A; the gap is 7.5 mm. The time response of the important parameters for the run are shown in Figure 34. A descriptive sketch of the camera view is given in Figure 11. Note that no activity is observed in the "plasma" image.

Photograph taken ∿.5 seconds after initiation of current.

Photograph taken ∿1.8 seconds after initiation of current.

Photograph taken ∿4.7 seconds after initiation of current.

Photograph taken ∿5.5 seconds after initiation of current.

Photograph taken ∿5.7 seconds after initiation of current.

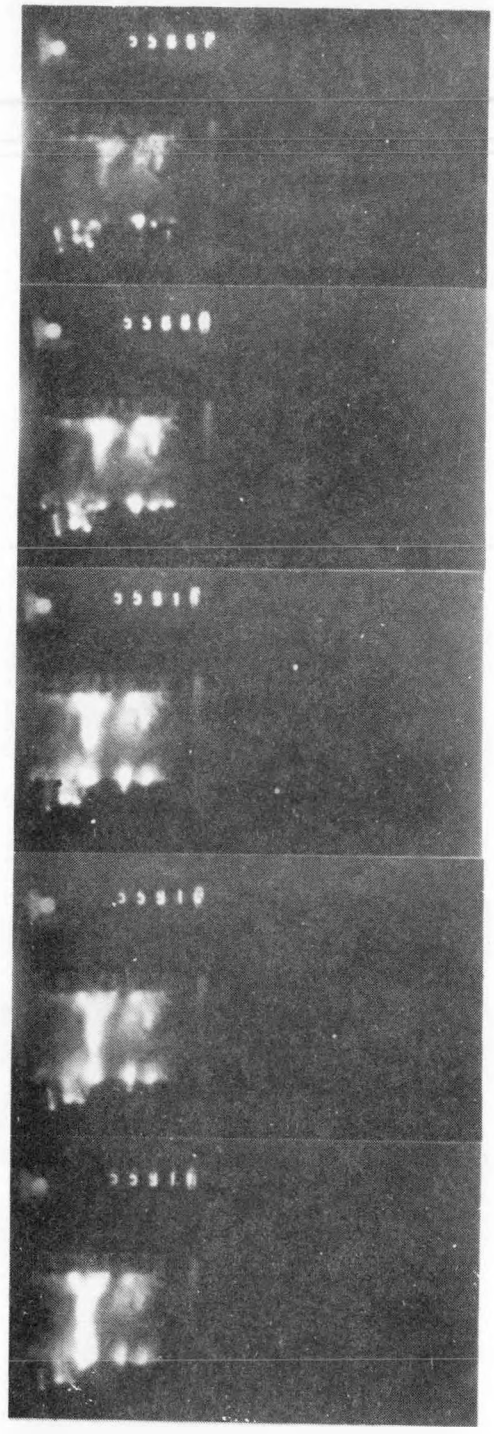

Figure 37. Sequence of frames of the movies, showing the development of a slow (insulator) breakdown. Data is taken from run series 1.9-D; the gap size is 19.1 mm. The time response of the important parameters for the run are shown in Figure 35. A descriptive sketch of the camera view is given in Figure 11. Note that except for a brief flash well after the breakdown is well-developed, no activity is observed in the "plasma" image.

breakdown behavior for the experiments described in detail is made in Table 7. In the table, the lowest voltage for which breakdown was observed and the highest voltage for which breakdown was not observed are given for plasma and insulator breakdown. These points identify the breakdown regimes displayed in Figure 38, where the threshold voltage is plotted as a function of insulator gap size. Experimental data from earlier runs is also shown in the figure [17]. The data indicate a region of insulator breakdown, with threshold voltage increasing roughly linearly with gap size and above that a region of plasma breakdown again with the threshold voltage increasing with gap size. As can be observed in Table 7, little variation of the threshold voltage with plasma flow conditions was observed and little effect of electrode polarity was evident in the experiments. It is interesting to note that the threshold voltages for both plasma and insulator breakdown extrapolate to non-zero voltages at small gap size. Following the discussion in Section 3.2.2, Figure 39 displays the behavior of the "cathode-corrected" threshold voltage for plasma and insulator behavior as a function of insulator gap size. With the effect of the cathode removed, somewhat lower voltage levels are observed, however, extrapolation to small gap size still indicates a non-zero threshold voltage for both types of breakdown.

3.2.7 Post-Breakdown Behavior

Experimental data from the experiments can be used to make rough estimates of the electrical conductivity and temperature of the constricted plasma discharge region and of the electrical conductivity of the constricted insulator discharge region at times subsequent to the breakdown. The conductivity of the plasma discharge region was estimated using the axial voltage and breakdown current measurements, with the photographic records used to define roughly the spatial extent. For the values shown in Table 8, the constricted discharge region was assumed to be cylindrical in shape with a length equal to the inter-electrode gap and a diameter equal to the width of the discharge as determined by the photographs. Also shown in the table are the equilibrium plasma temperatures corresponding to the indicated conductivity, the power density and the power dissipated per unit surface area. Average electrical conductivities of as high as 800 mho/m and temperatures approaching 4000°K are indicated.

Table 7. Summary of breakdown threshold behavior for experiments discussed in Table. Shows highest value with no breakdown observed and lowest voltage where breakdown was observed. Data for plasma and insulator breakdown are both given.

Run Designation	Gap (cm)	$\dot{m}$ (Kg/sec)	N_2/O_2	Threshold Voltage (volts)			
				"Slow" (insulator) breakdown		"Fast" (plasma) breakdown	
				High No Bkd'n	Low Bkd'n	High No Bkd'n	Low Bkd'n
1.9-A	1.9	.11	0.7	195	220	232	264
1.9-B	1.9	.12	0.58	--	--	250	249
1.9-C	1.9	.17	1.1	--	--	260	310
1.9-D	1.9	.11	0.6	150	193	240	235
1.9-E	1.9	.17	1.05	190	240	246	264
.75-A	.75	.11	0.6	114	110	164	185
.75-A	.75	.11	0.8	100	130	166	194
.75-C	.75	.18	1.1	115	125	162	196

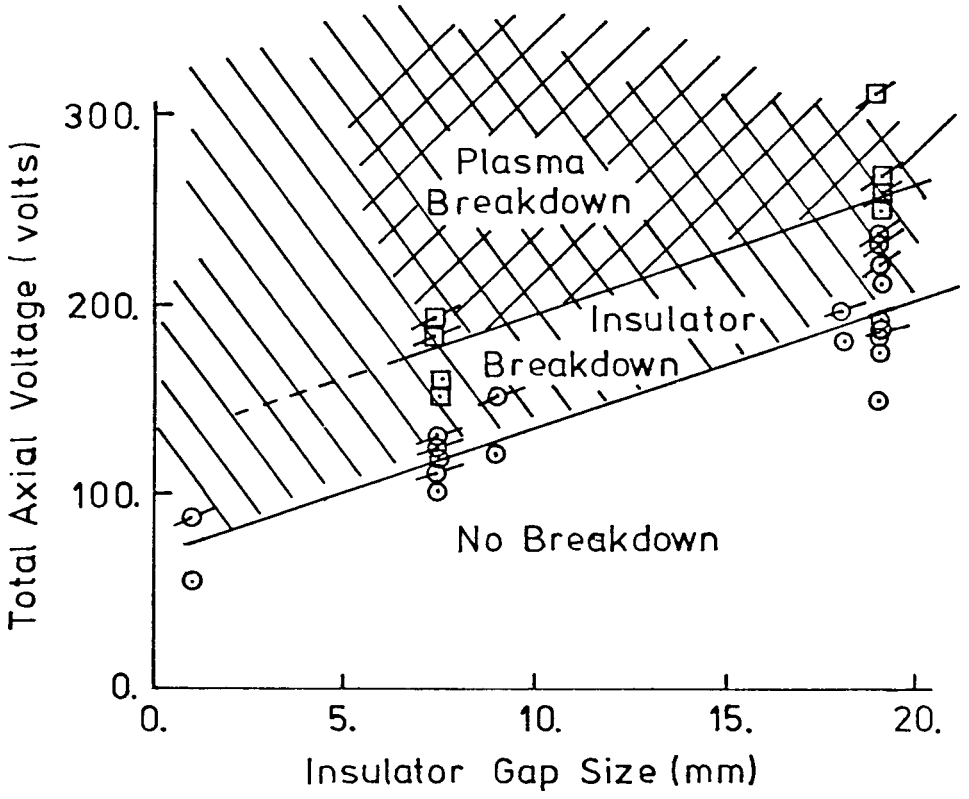

Figure 38. Threshold voltage as a function of insulator gap size. Figure shows the highest voltage for which no breakdown occurred and the lowest voltage for which breakdown occurred, thus establishing the breakdown threshold for plasma and insulator breakdown. Data for 1mm, 9mm and 18mm gaps taken from experiments described in reference [17]. All insulators were MgO except the 1mm gap, which was dense alumina.

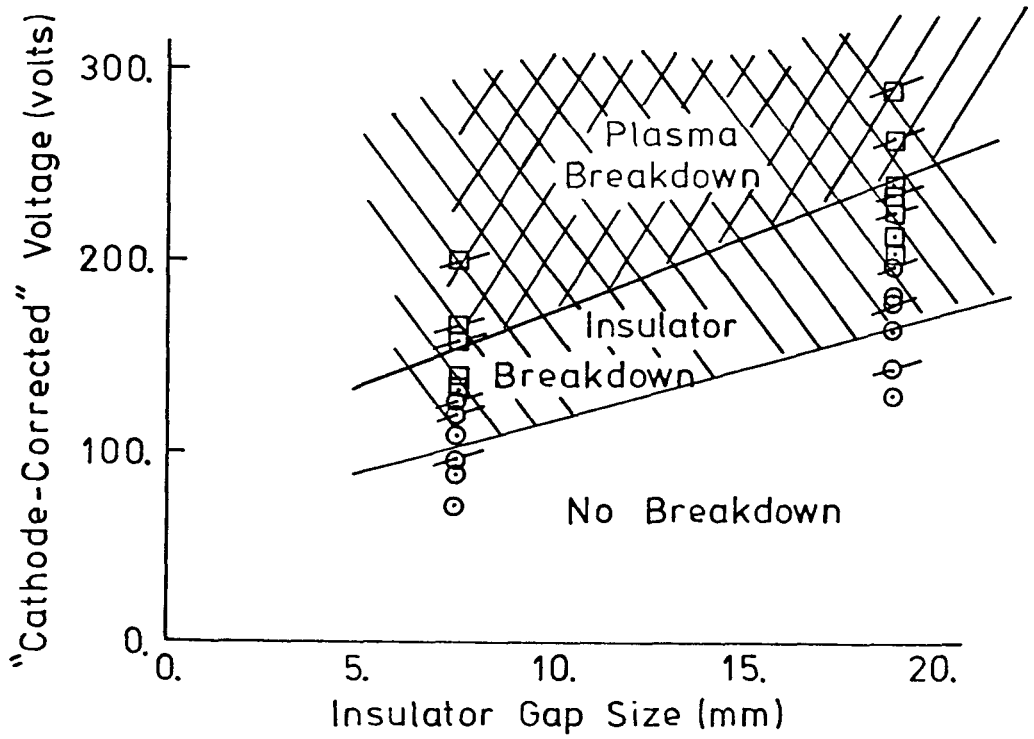

Figure 39. "Cathode-corrected" threshold voltage as a function of insulator gap size. Figure shows the highest voltage for which no breakdown resulted and the lowest voltage for which breakdown occurred thus distinguishing the breakdown threshold region for plasma and insulator breakdown. The "cathode-corrected" threshold voltage is formed to remove the effect of the cathode-voltage drop as was discussed in Section 3.2.2.

Table 8. Rough determination of average electrical conductivity of the breakdown region for several conditions. For plasma breakdown, the average conductivity was computed assuming the breakdown region to be a circular cylinder of diameter equal to the width of the discharge as indicated by the photographs and a length equal to the inter-electrode gap. Insulator conductivity computed assuming the discharge region to have a square cross-section with a width as indicated by the photographic records and a depth as determined by post test examination of the inter-electrode insulator. Discharge power density and power per unit surface area are also tabulated.

Gap (cm)	Type of Breakdown	Total Voltage (volts)	Breakdown Current (amps)	Current Density (amp/cm^2)	Approx. Discharge Dimension	Indicated Conductivity (mho/m)	Indicated Temperature (K)	Discharge Power Density (Gw/m^3)	Discharge Power per Unit Area (Mw/m^2)
1.9	plasma	95	75	382	5mm dia.	800	3800	19	24
1.9	plasma	125	48	245	5mm dia.	400	3600	16	20
.75	plasma	106	23	325	3mm dia.	230	3400	28	21
.75	plasma	76	39	550	3mm dia.	550	3700	56	42
.75	plasma	47	62	490	4mm dia	800	3800	31	31
1.9	insulator	95	30	250	4mm x 3mm	950	---	60	30
.75	insulator	60	18	450	2mm x 2mm	350	---	92	23

Estimates of the temperature in the constricted discharge region using the total emission intensity measurements also indicate temperatures in excess of 3600°K. The extremely high current densities and power densities in this discharge region indicate that many phenomena not of importance for the pre-breakdown discharge would need to be considered in a modeling of the constricted discharge region. The voltage-current characteristic for the constricted plasma discharge region is displayed in Figure 40, where the axial voltage has been normalized with respect to the inter-electrode gap. The data for each gap size are plotted without reference to the plasma flow conditions and are seen to exhibit a negative dynamic resistance. The results from the two gap sizes can be extrapolated to large gap size under the assumption that the anode and cathode voltage drops are the same for the two gap sizes at a particular level of current and that these voltage drops occur over a small distance. The resultant voltage-current curve is also shown in Figure 40. A combined anode plus cathode drop of ≈20 volts at 40 amps and a far-electrode field of ≈50 volts/cm are indicated for the above assumptions.

Estimates of the electrical conductivity in the constricted insulator discharge region can also be made using the axial voltage and breakdown current measurements, with the photographic records determining the width of the region and post-test examination of the inter-electrode insulator indicating the depth of the region. Results for two representative cases are displayed in Table 8, with the power density and power dissipated per unit surface area shown also. The voltage-current characteristic for the constricted discharge region is shown in Figure 41, where the axial voltage has been normalized with respect to the inter-electrode spacing. The data indicate an axial field of ≈40 volts/cm at 40 amps with small near-electrode voltage drops.

Some experimental runs were included where the constricted discharge was maintained for a considerable time after the breakdown was established. For the insulator breakdowns, no qualitative change in behavior was observed, although a widening or a shifting of the discharge region was sometimes observed. For the plasma breakdowns, the insulator region beneath the discharge was observed to heat up and, when the gap was bridged by a heated insulator region, the plasma image flashed out. Several frames from the movies taken during such a run are displayed in Figure 42. A

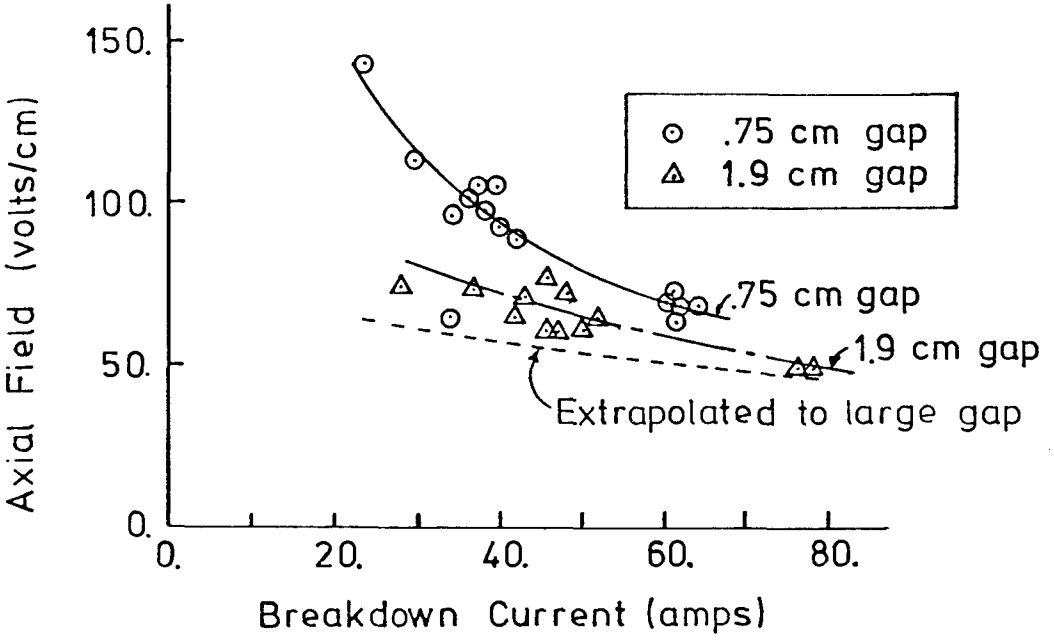

Figure 40. Axial field versus breakdown current for conditions of plasma breakdown. Breakdown current determined from current distribution measurements. Data distinguished only as to gap size. Data from both gaps used to extrapolate to large gap size as shown on the figure.

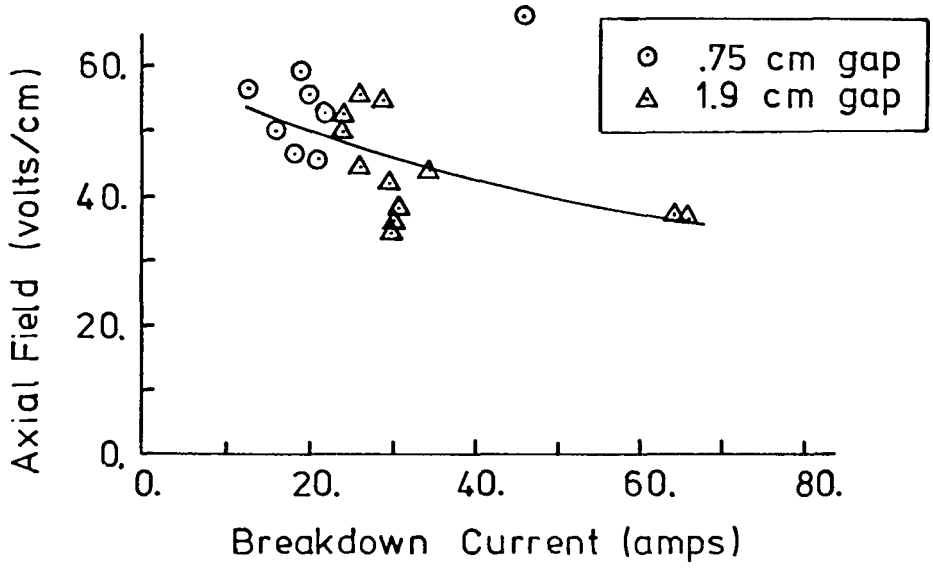

Figure 41. Axial field versus breakdown current for conditions of insulator breakdown. Breakdown current determined from current distribution measurements. Data distinguished only as to gap size.

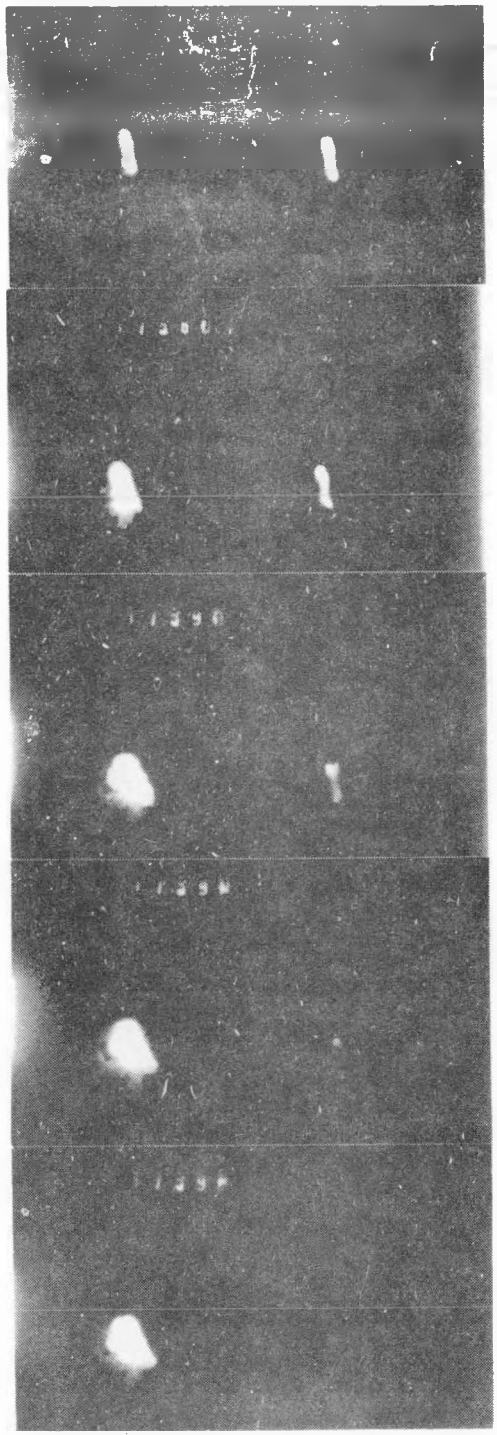

Photograph taken $\leq$15 m seconds after initiation of current.

Photograph taken $\sim$.5 seconds after initiation of current.

Photograph taken $\sim$1.0 seconds after initiation of current.

Photographs showing plasma discharge being extinguished.

Figure 42. Sequence of frames of the movies showing the long term behavior of the inter-electrode region following a plasma breakdown. Data is taken for the same conditions as Run series .75-A.

moderate decline in voltage and a significant drop in fluctuation level accompanies the flashing out of the plasma discharge and it appears that the insulator has become the dominant current carrier. The discharge remained on for several seconds after the plasma image first flashed out and excepting for occasional flashes in the plasma image the plasma appears to be inactive. The photo-diode emission measurements corroborate the information obtained by the photographic records.

3.3 Induced Field Experiments

Inter-electrode insulator gaps from 2.5 mm to 19 mm were studied in the induced field experiments, however breakdown was observed in only two experiments and in only one of these were photographic records obtained. Although data from the experiment studying a 2.5 mm dense alumina insulator will be presented, the main emphasis will be on the experiment studying 7.5 mm, 10 mm and 12 mm MgO insulators. Other data will be used only in relation to the voltage threshold curve. No systematic variation of flow conditions or of inter-electrode cooling were performed; however the behavior of anode wall insulator gaps and of cathode wall insulator gaps were investigated.

The presentation of results is made in several sections beginning with a detailed list of experimental conditions. A discussion of the steady-state (non-breakdown) behavior of the generator is then made and that is followed by a description of the transient and fluctuating behavior for non-breakdown conditions. The final sections discuss the breakdown behavior and the breakdown threshold voltage.

3.3.1 Experimental Conditions

The induced field experiments are divided into five run series, representing the different experimental conditions. The combustor operating conditions and the computed plasma "core" properties for each run series are listed in Table 9, The MHD channel was operated subsonically with the mass flow to the burner fixed. For these conditions the effect of the MHD braking force is to increase the plenum pressure and alter the flow properties at the inlet to the active region of the generator. The conditions reported in Table 9 are for the open circuit case. Calculated values were obtained as described in Appendix D. Pertinent test-section and electrode wall dimensions, surface temperatures and other

Table 9. Combustor and channel flow condition for each main induced field experimental run series. All conditions are for the open circuit case. Nitrogen to oxygen ratio, N_2/O_2, is by mass. Stoichiometry expressed in terms of ϕ, the fuel-air ratio divided by fuel-air for stoichiometric combustion. The seed fraction, q, is the fraction by mass of potassium in the combustions products.

Combustor Conditions						Computed Core Conditions			
Date	Run Designation	$\dot{m}$ (kg/sec)	N_2/O_2	ϕ	q	U (m/s)	P (nt/m^2)	T (K)	σ (mho/m)
1/6/77	.75-A	.157	0.5	1.0	1%	450	10^5	2725	14.4
1/6/77	.75-C	.157	0.5	1.0	1%	450	10^5	2725	14.5
1/6/77	1.0-AP	.157	0.5	1.0	1%	450	10^5	2725	14.5
1/6/77	1.0-CP	.157	0.5	1.0	1%	450	10^5	2725	14.5
1/6/77	.75-CP	.157	0.5	1.0	1%	450	10^5	2725	14.5

data are summarized in Table 10. The MHD generator was run in the segmented-Faraday configuration for all runs. Only limited measurement of surface temperature was possible, so many of the surface temperature values presented in Table 10 are estimates based on data from other experiments with the MHD channel.

3.3.2 Non-Breakdown Generator Behavior

The overall electrical behavior of the generator can be characterized by the generator load line (Faraday voltage versus Faraday current curve) and the Hall voltage versus Faraday current curve. The load lines for non-breakdown conditions are shown in Figures 43a and 43b. As shown schematically in the sketches accompanying the figures the data represented in Figure 43a was obtained for electrode circuits connected at the normal electrode pitch, while the data represented in Figure 43b was obtained for circuits connected such that the electrode pitch was doubled. The rapid decline in voltage at small current levels exhibited by both figures is associated with the near-cathode voltage drop required to produce the necessary electron emission at the cathode. For currents greater than two or three amps the load line is relatively linear, although some change in slope is evident at high currents for the outer electrode circuits, presumably due to end effects. Data shown in the figures was taken from runs with the top wall electrodes operating as cathodes and from runs with the top wall electrodes operating as anodes. The large negative Faraday voltages result from the heavy augmentation of the electrode circuits. The near-electrode voltage drops for four electrodes are displayed in Figure 44 and provide some insight regarding the nature of the discharge in those regions. Data for the two near-anode regions show the voltage drop increasing with Faraday current, with a tendency toward saturation observed for one of the regions. In contrast to the anode behavior, where the voltage drop approaches zero at low Faraday current, the near-cathode voltage drop remains high even at very low Faraday currents and varies little with current at the higher Faraday current levels.

While not a sensitive indicator of the generator performance, the pressure drop across the active region of the generator as a function of total current through the generator is shown for all experimental conditions in Figure 45. As expected the pressure drop rises roughly linearly with total current out to the highest levels.

Table 10. Channel conditions of each main experimental run series for the induced field experiments. A 10Å blue filter was used to isolate the potassium radiation in the top view photographs. The temperature standard corresponds to an equivalent MgO temperature of ∿2300 K.

	Data for main gap studied			Electrodes			Surface Temperatures		
Run Designation	Gap (cm)	Generator Wall	Electrodes Paired?	Length (cm)	Pitch at Main Gap (cm)	Pitch elsewhere (cm)	Side-wall Insulators (K)	Electrodes (K)	Inter-Electrode Insulators (K)
.75-A	.75	anode	no	≅ 3	3.8	3.8	∿2200 e	1050-1160 t	2000 e
.75-C	.75	cathode	no	≅ 3	3.8	3.8	∿2200 e	1050-1160 t	2000 e
1.00-AP	1.0	anode	yes	≅ 3	7.6	3.8	∿2200 e	1050-1160 t	2000 e
1.00-CP	1.0	cathode	yes	≅ 3	7.6	3.8	∿2200 e	1050-1150 t	2000 e
.75-CP	.75	cathode	yes	≅ 3	7.6	3.8	∿2200 e	1050-1150 t	2000 e

t = thermocouple

e = estimate from other experiments

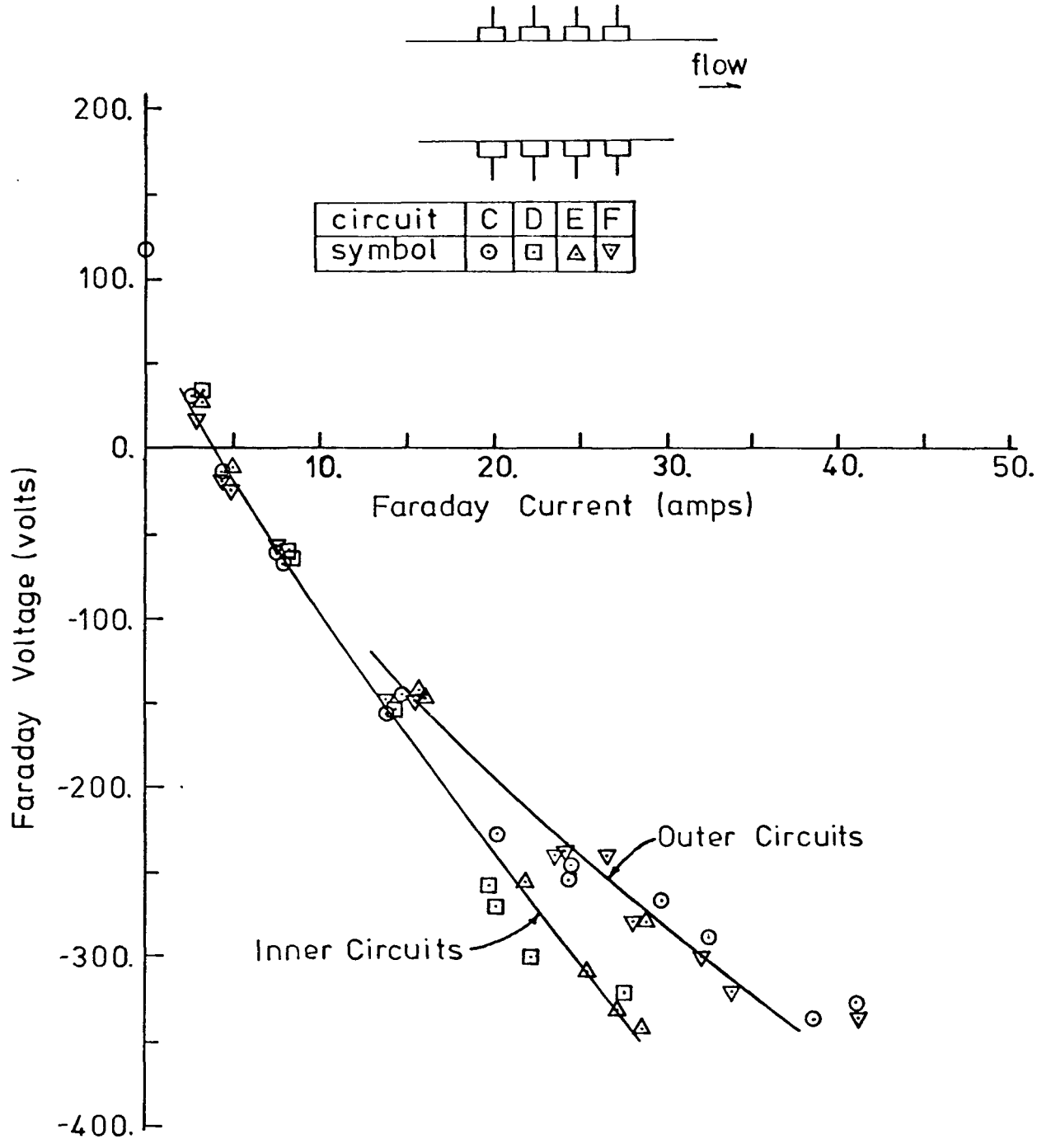

Figure 43a. Faraday voltage versus Faraday current for unpaired circuits and for non-breakdown conditions. Data taken from Runs .75-A and .75-C. Sketch identifies circuits and symbols.

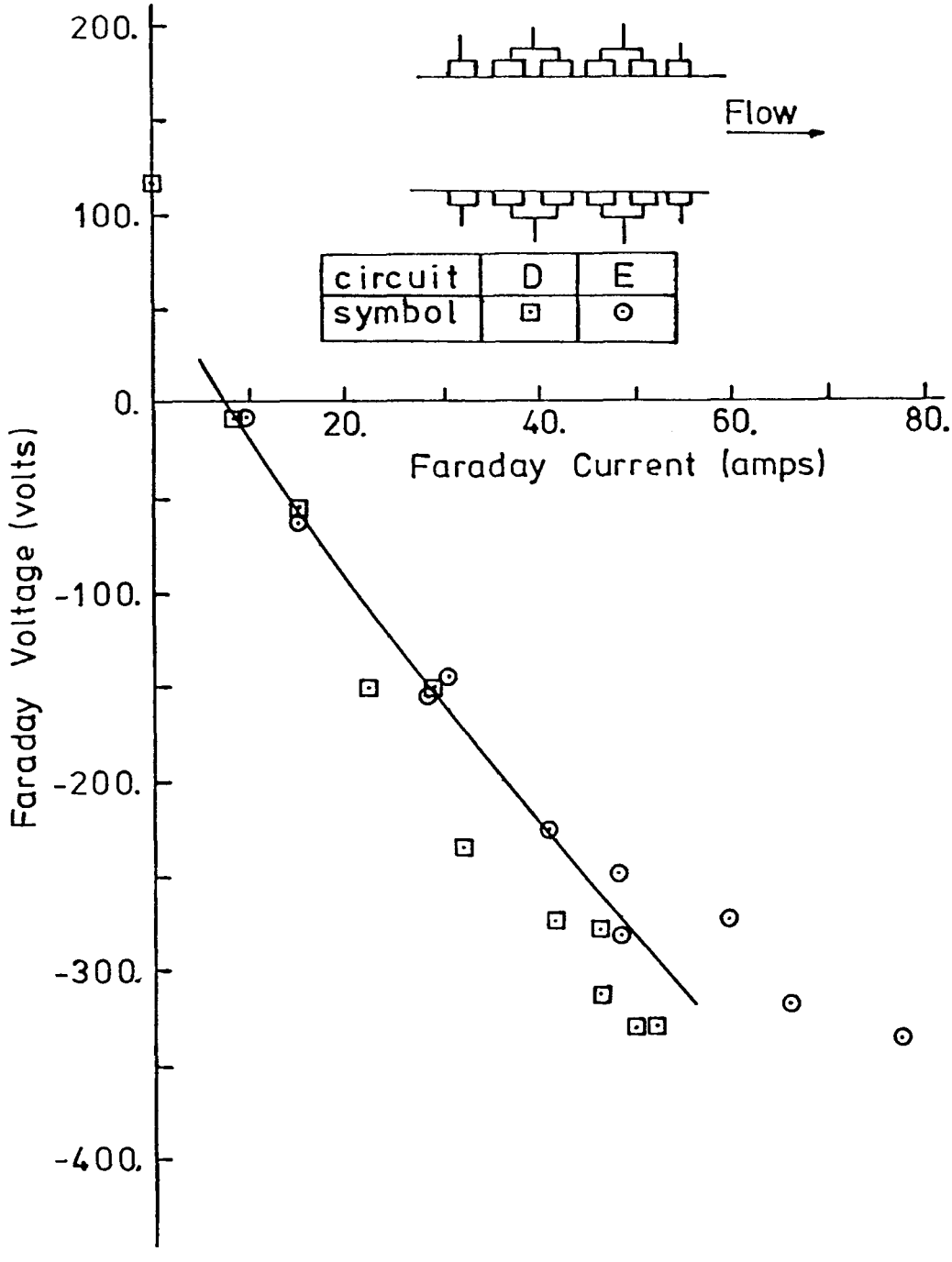

Figure 43b. Faraday voltage versus Faraday current for paired circuits and for non-breakdown conditions. Data taken from Runs 1.0-AP and 1.0-CP. Sketch identifies circuits and symbols.

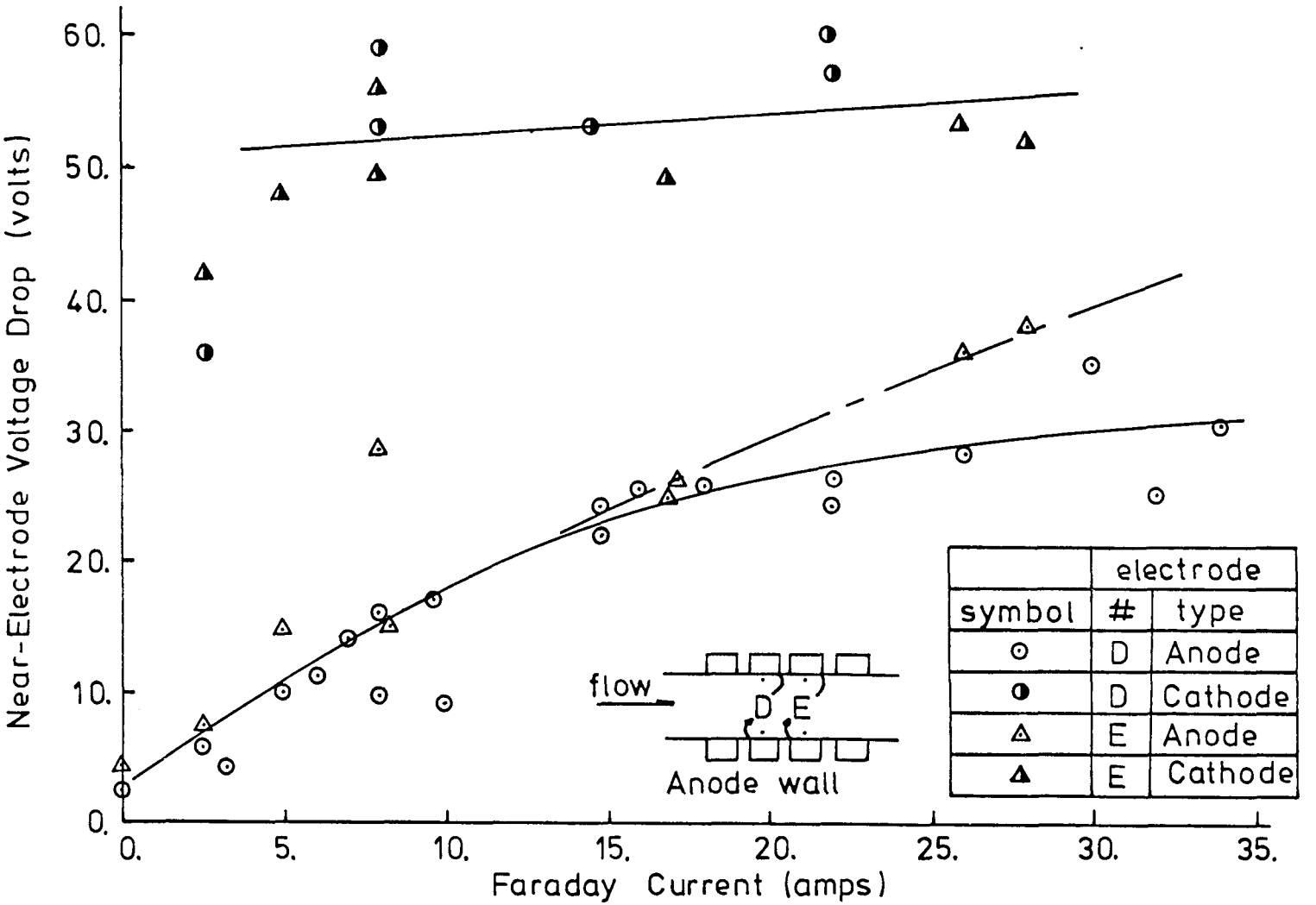

Figure 44. Near-Electrode voltage drop for four different electrodes as a function of Faraday current. Data taken from Run .75-A.

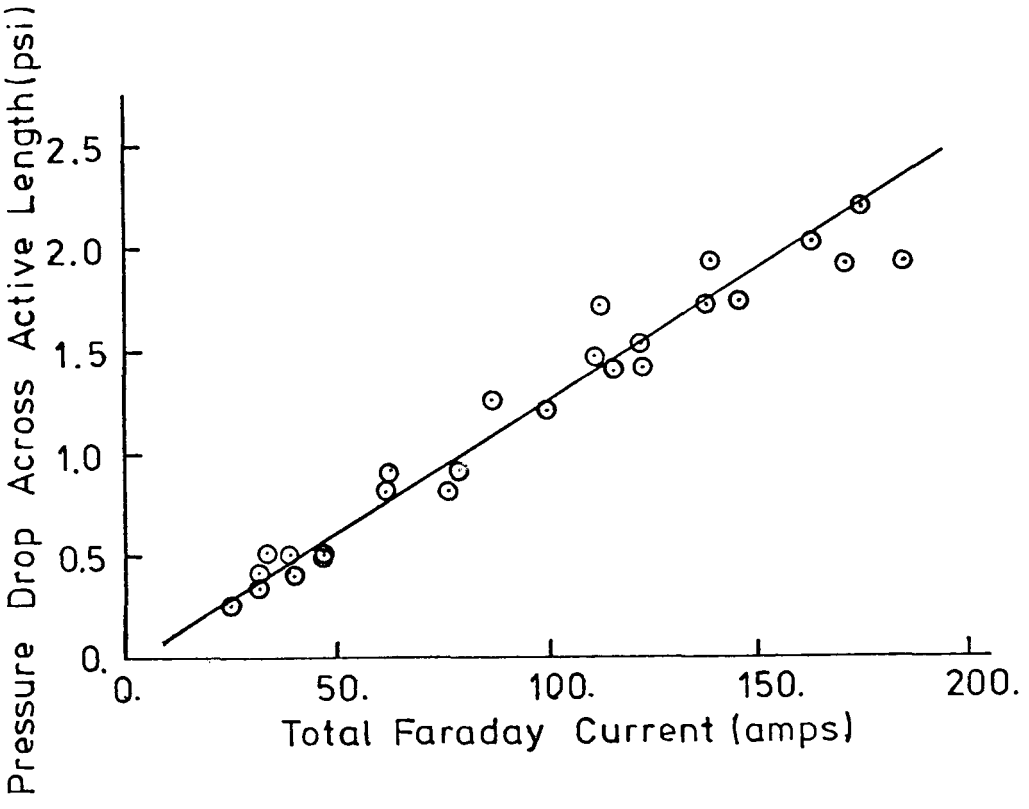

Figure 45. Pressure drop across active length of the generator as a function of total Faraday current from the generator. Data taken from Runs .75-A, .75-C 1.0-AP and 1.0-CP.

The non-breakdown behavior of Hall voltage with Faraday current for the different experimental conditions is shown in Figures 46a-d. In cases where breakdown occurred only the pre-breakdown level is shown. A sketch accompanying each figure identifies the gaps for which results are presented and identifies the Faraday current used for each gap in the preparation of the figure. Although the Hall voltage depends on the average current passing through the electrode circuits adjacent to the particular gap, the figures were prepared using the upstream circuit current for gaps on the cathode wall and using the downstream circuit current for gaps on the anode wall. In this way the Hall voltage for a gap is plotted as a function of the current which passes most closely to the gap. As is evident in the figures the Hall voltage rises non-linearly with Faraday current in most cases, with a tendency toward saturation deserved for the smaller inter-electrode spacings. Increases in electrode pitch did not produce a significantly higher Hall voltage at a given current density than was observed at the normal electrode pitch, indicating that the influence of the Hall effect on the current patterns is quite severe for the high pitch to height ratios of this experiment. The non-zero Hall voltage intercept exhibited in some of the plots is the result of axial gradients in the Faraday field caused by variations in augmentation voltage and load resistance.

Despite the tendency toward saturation of the Hall voltage, and the current concentrations due to the Hall effect, the current distribution measurements and the photographic records indicate no severe current constrictions or axial leakage. The axial current distribution for non-breakdown conditions is represented in Figure 47a by the fraction of current to the electrode edge where the Hall effect concentrates the Faraday current, and in Figure 47b by the fraction of current to the edge away from the current concentration. As expected the Hall effect causes a higher than average current to pass through the upstream edges of the anodes and the downstream edges of the cathodes, however the fraction remains roughly constant with increasing Faraday current. The fraction of current to the edge away from the current concentration declines with increasing Faraday current; however the current is always in the same direction as the average current for the non-breakdown runs. The abnormally high fractions observed in Figure 47a for run .75-A and in Figure 47b for run .75-C,

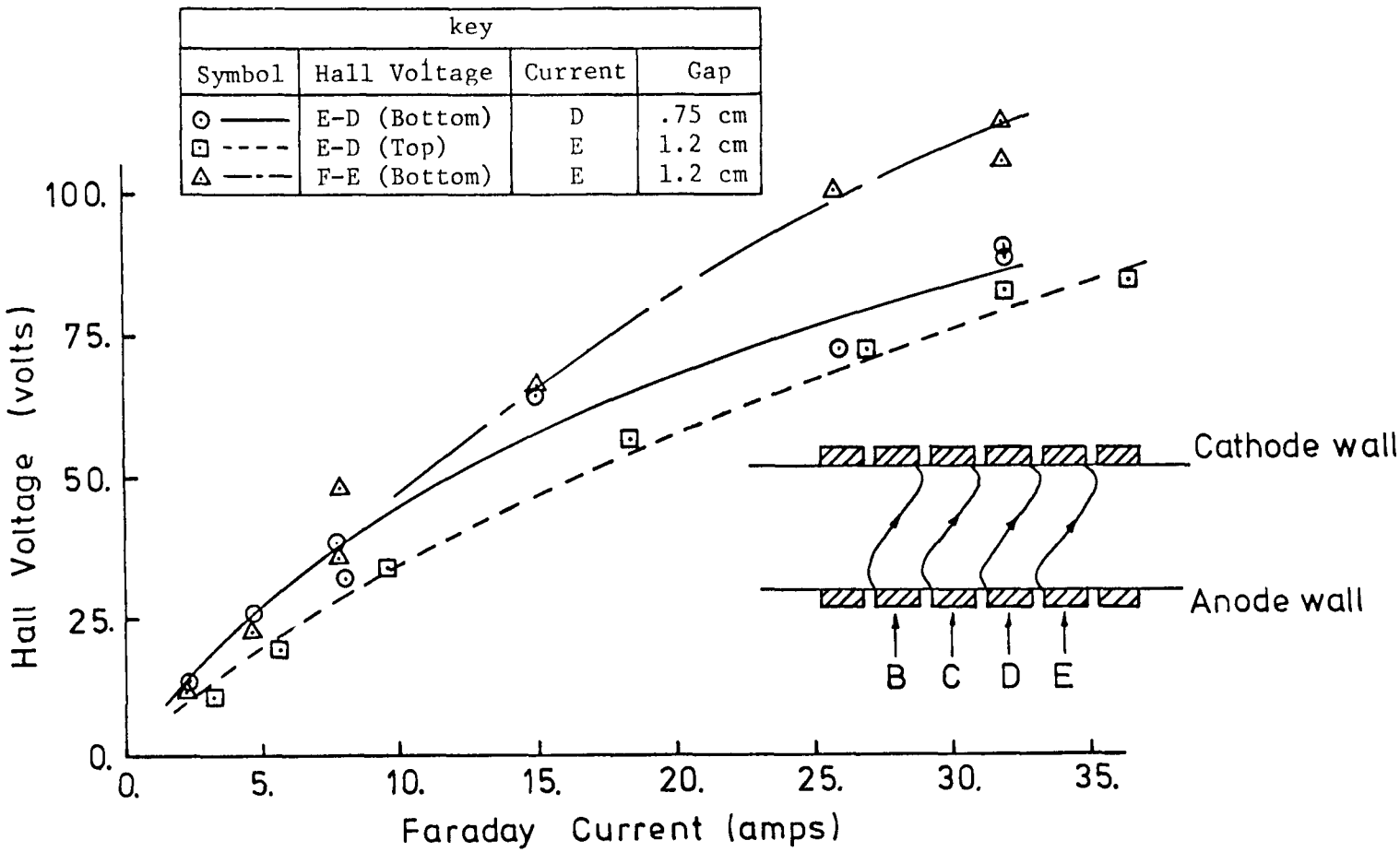

Figure 46a. Non-breakdown response of Hall voltage with Faraday current for three inter-electrode insulator gaps for experimental Run .75-A. Sketch and Table identify the gap voltages and the currents used in preparing the figure.

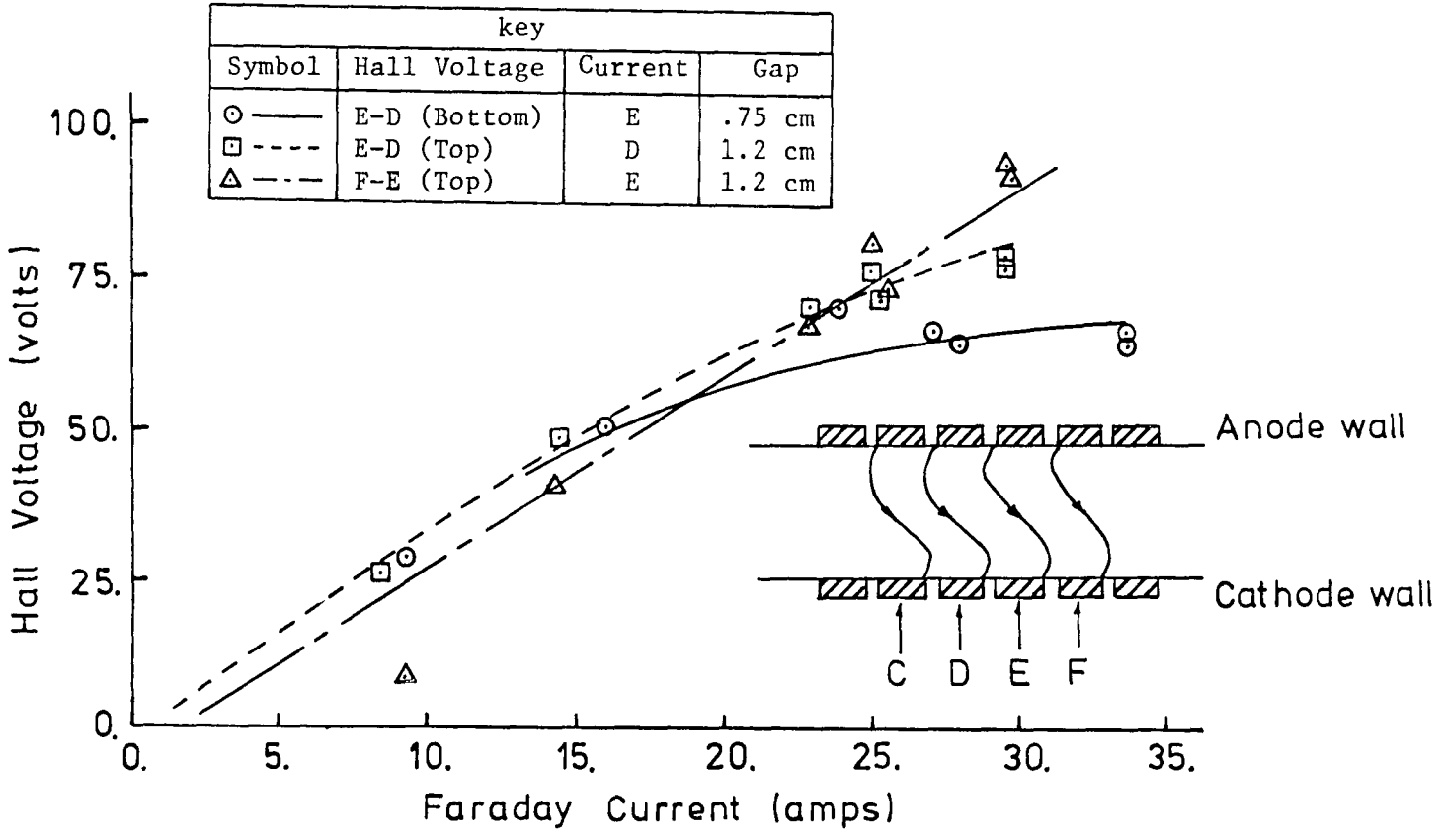

Figure 46b. Non-breakdown response of Hall voltage with Faraday current for three inter-electrode insulator gaps for experimental Run .75-C. Sketch and Table identify the gap voltages and the currents used in preparing the figure.

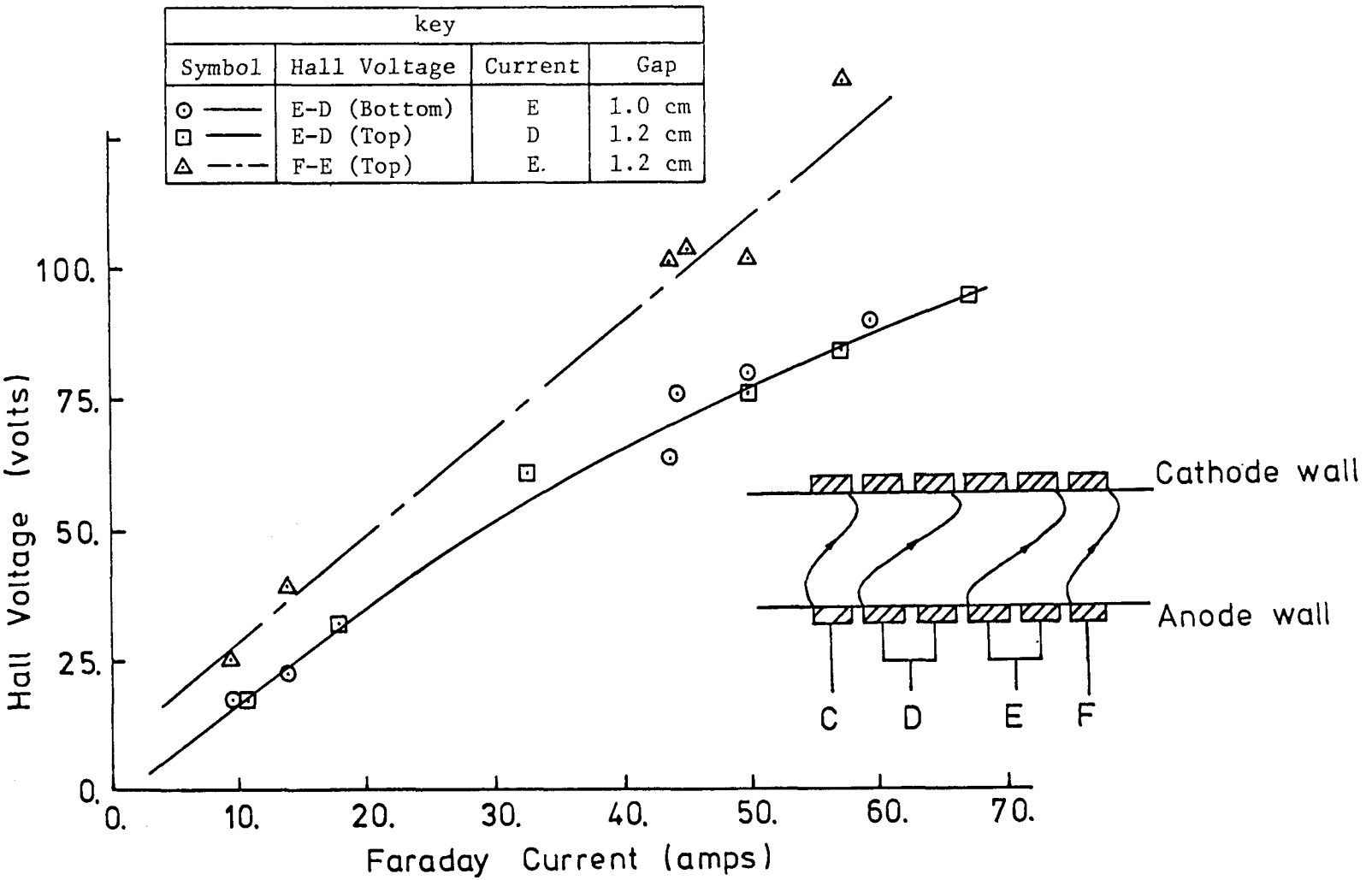

Figure 46c. Non-breakdown response of Hall voltage with Faraday current for three inter-electrode insulator gaps for experimental Run 1.0-AP. Sketch and Table identify the gap voltages and the currents used in preparing the figure.

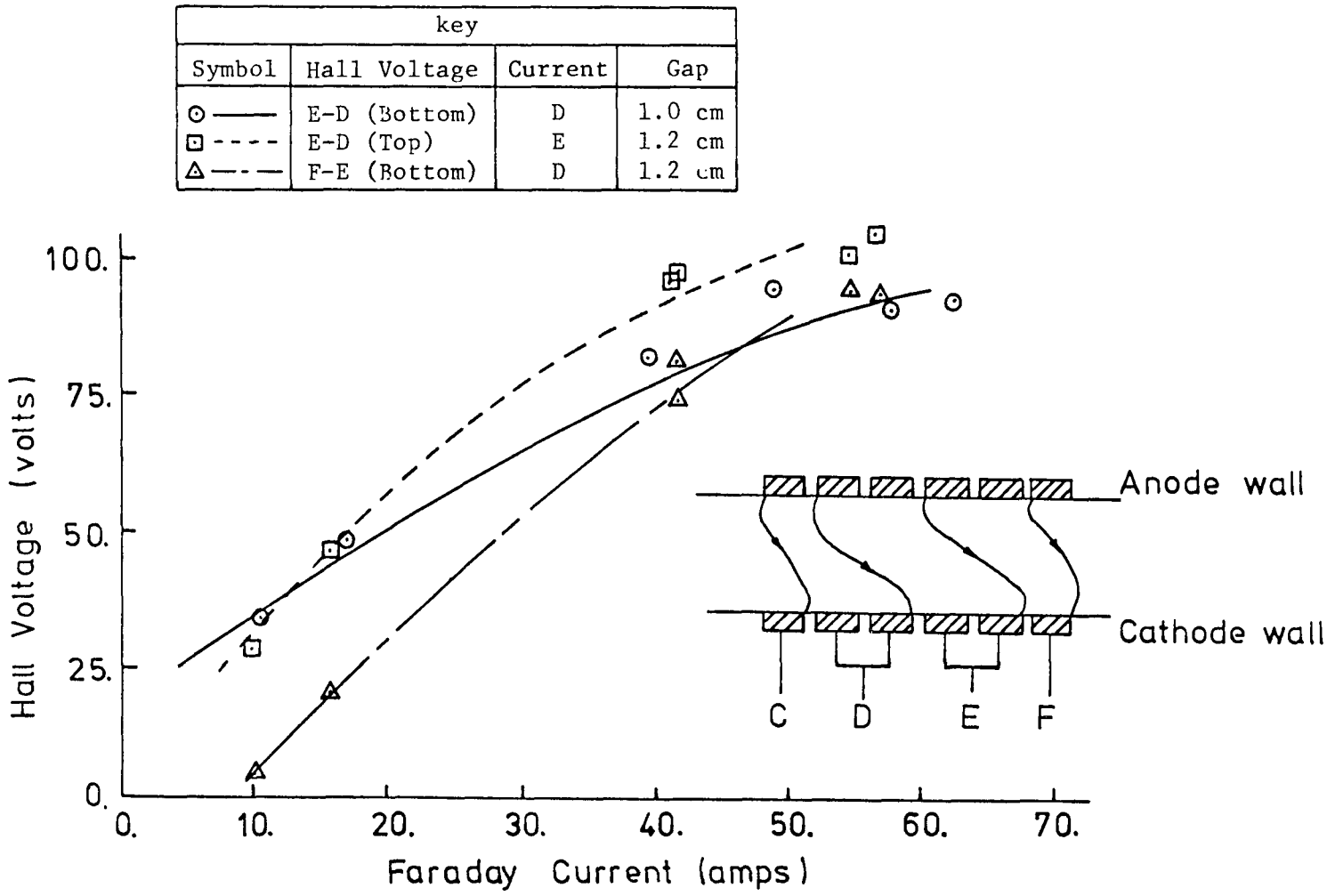

Figure 46d. Non-breakdown response of Hall voltage with Faraday current for three inter-electrode insulator gaps for experimental Run 1.0-CP. Sketch and Table identify the gap voltage and the currents used in preparing the figure.

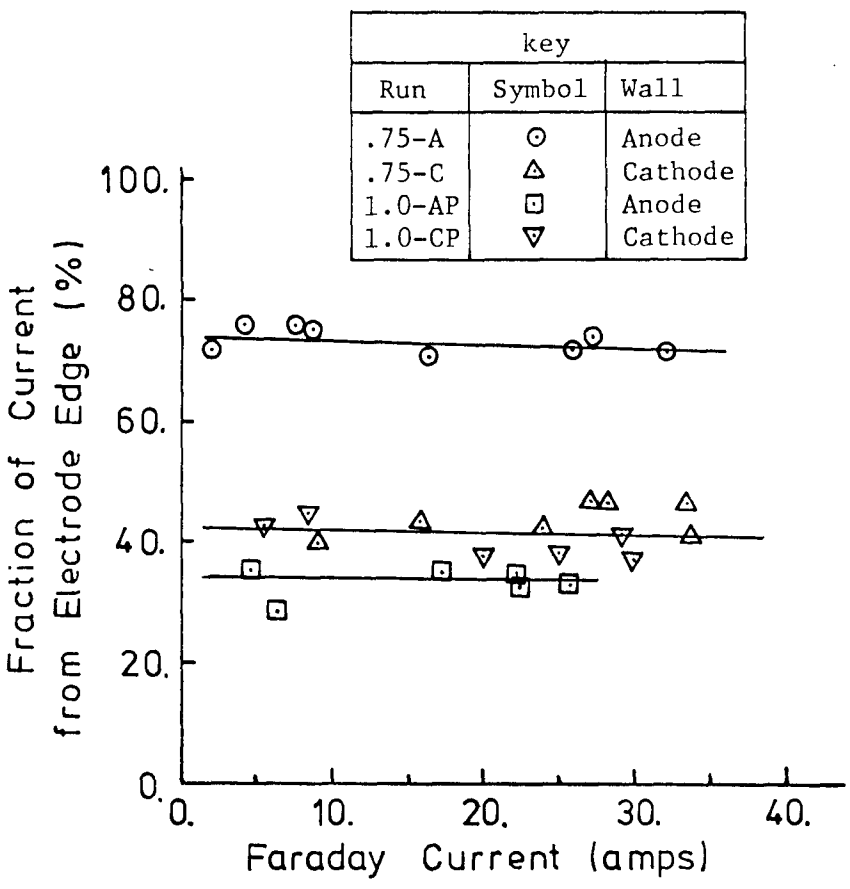

Figure 47a. Fraction of current leaving 1/4" strip on edge of electrode where the current is concentrated due to the Hall effect. Key identifies the conditions for each set of data. The 1/4" strip represents approximately 20% of the total electrode surface area.

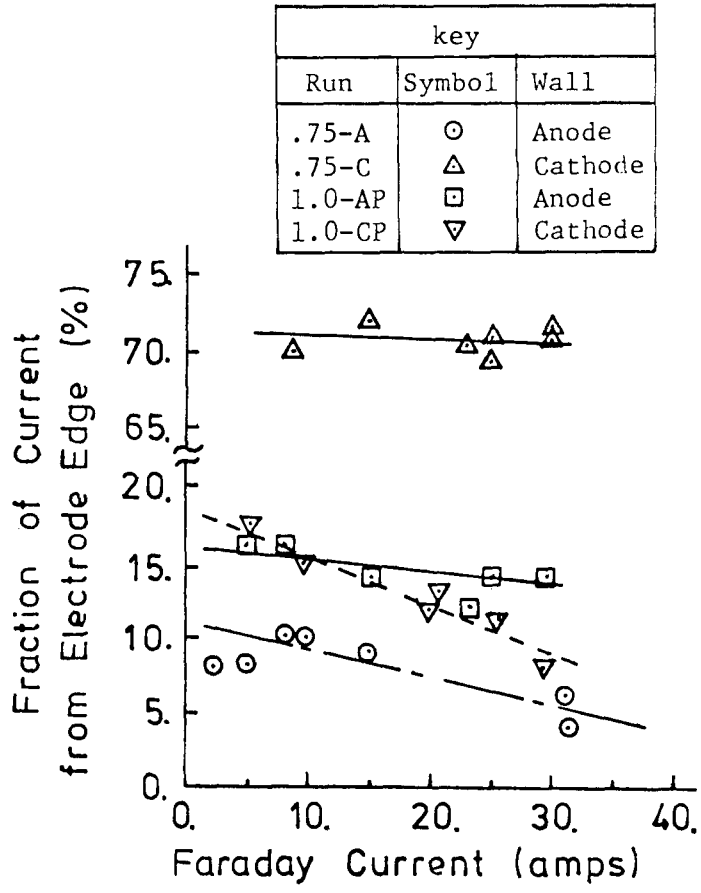

Figure 47b. Fraction of current leaving 1/4" strip on edge of electrode where the current is not concentrated due to the Hall effect. Key identifies conditions for each set of data. The 1/4" strip represents approximately 20% of the total electrode surface area.

appears to result from the electrode edge operating considerably hotter than the remainder of that electrode. The distribution of Faraday current across the channel width is displayed in Figures 48a-c, where the fraction of current leaving each peg of the electrode edge toward which the current concentrates is shown for all levels of Faraday current. For the earlier runs the current is concentrated toward the center of the channel as might be expected to result from the cold side-wall boundary layers. However, in later runs it appears that other factors, perhaps surface temperature or surface coating variations, have become important and the distributions no longer have a strong peak at the center of the channel. Nevertheless, even in the later runs, no severe constrictions of the Faraday current are observed for the non-breakdown runs. The photographic records display some heating of the inter-electrode insulator for the higher current, but indicate no severe heating for the non-breakdown runs. Several frames taken during such runs are displayed in Figure 49.

The above data indicate that the non-breakdown electrical discharge in the generator can be characterized as a steady, relatively diffuse discharge except close to the cathode. The effects of Joule heating are evidenced by the saturation of the Hall voltage across some of the inter-electrode gaps, a slight shift in the current pattern and a saturation of the near-anode voltage drop.

3.3.3 Transient Behavior for Non-Breakdown Conditions

For all conditions the generator was impulsively loaded, both as a precaution against momentary overvoltage across individual gaps and to provide information regarding the early time response of the generator. In general the Hall voltage declined over the first few milliseconds; unfortunately signal conditioning problems prevented the reliable measurement of the corresponding Faraday current, so the behavior cannot be compared with the steady-state Hall voltage curves. No systematic change over the initial seconds was observed in the electrical parameters for the non-breakdown conditions. The fluctuation level was approximately constant for all non-breakdown conditions at approximately 15% peak-to-peak. As in the applied field experiments, large magnitude, momentary changes in the electrical parameters were observed. The bursts occurred at random and in all cases the discharge returned to the original state. Measurements

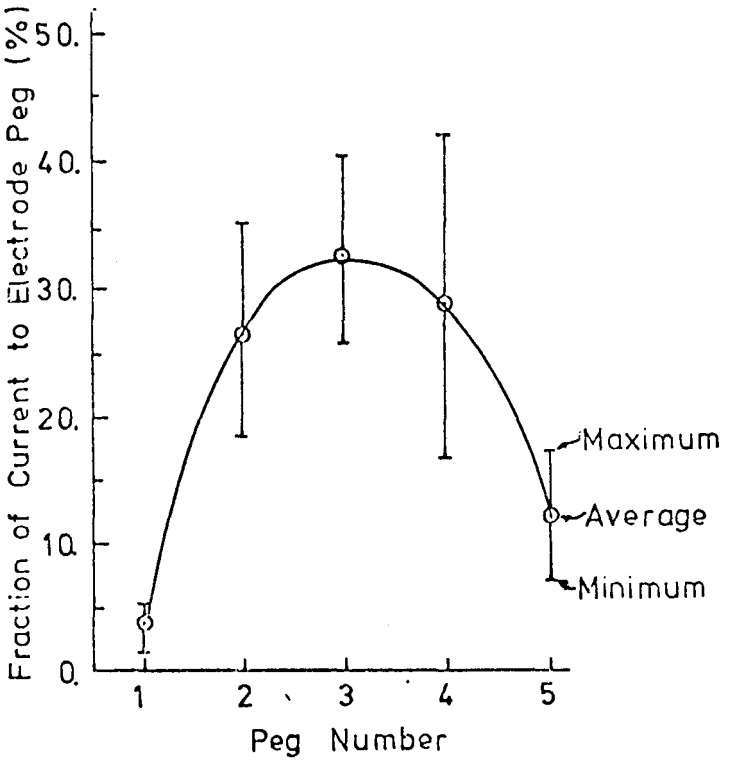

Figure 48a. Distribution of Faraday current in the magnetic field direction for non-breakdown conditions. Figure shows the fraction of current leaving individual pegs along the electrode edge where the current concentrates due to the Hall effect. Data is taken from Run .75-A. Average Faraday currents as high as 4 A/cm^2 are represented for this anode.

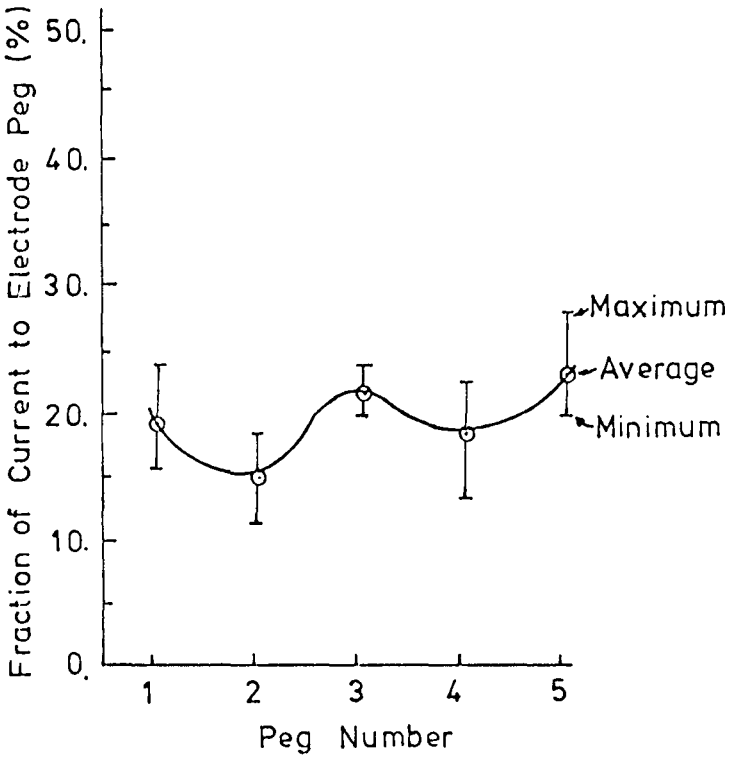

Figure 48b. Distribution of Faraday current in the magnetic field direction for non-breakdown conditions. Figure shows the fraction of current leaving individual pegs along the electrode edge where the current concentrates due to the Hall effect. Data is taken from Run 1.0-AP. Average Faraday currents as high as 2 A/cm^2 are represented for this anode.

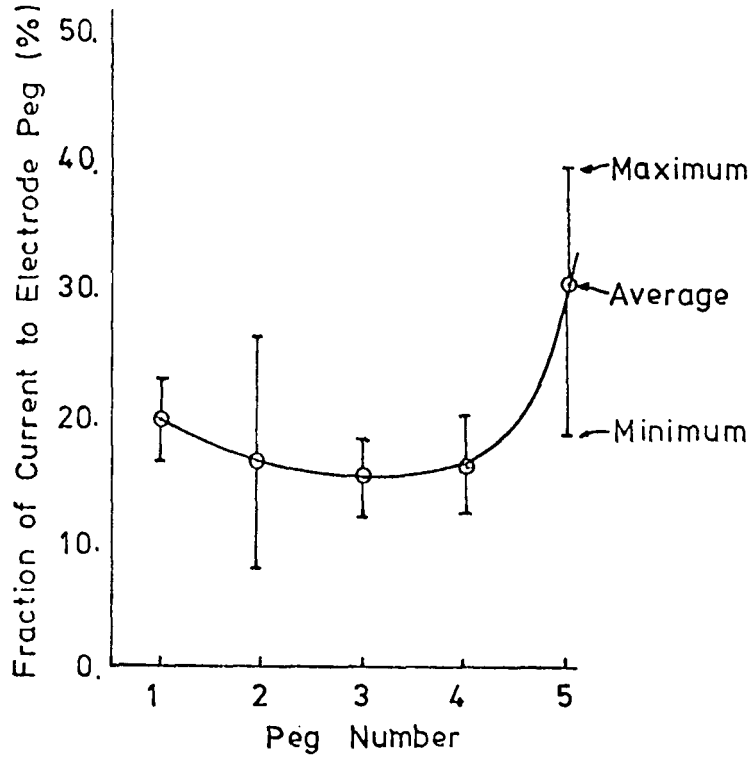

Figure 48c. Distribution of Faraday current in the magnetic field direction for non-breakdown conditions. Figure shows the fraction of current leaving individual pegs along the electrode edge where the current concentrates due to the Hall effect. Data is taken from Run 1.0-CP. Average Faraday currents as high as 2 A/cm^2 are represented for this cathode.

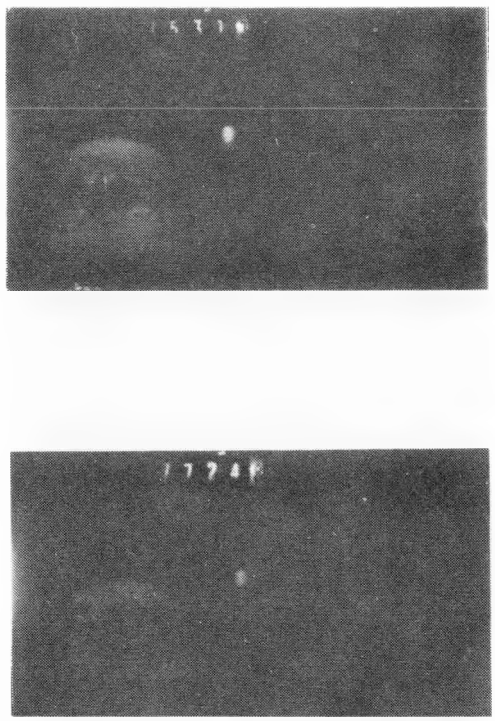

Figure 49. Frames of the photographs from the induced field experiment for non-breakdown and pre-breakdown conditions.

indicated a substantial increase in Faraday current and a decline in Faraday and Hall voltages at all locations monitored. In most cases the near-cathode voltage drop declined significantly and the near-anode voltage drop indicated a reduction in resistance of that region also. It is concluded that, as in the applied field experiment, slugs of high seed fraction and/or high temperature plasma are responsible for these bursts.

3.3.4 Breakdown Behavior

For Hall voltages exceeding a threshold level, the electrical behavior of the generator was not steady in time and following a delay period a rapid and significant decline in Hall voltage across one or more of the insulator gaps was observed. In general, the delay time was at least a second and the timescale of the breakdown itself was on the order of a second. In addition to the decline in Hall voltage, a change in the output terminal behavior (Faraday voltage and current) usually occurred when more than one gap suffered breakdown. Some care is required in interpreting the data for the multiple breakdown cases since changes in Faraday current resulting from breakdown of one gap may be the cause of the change in Hall voltage across another gap. The Hall voltage and Faraday current behavior for breakdown are displayed in Figures 50a-d. The non-breakdown behavior is represented by a solid curve, and to avoid confusion these figures show only the data for the principal inter-electrode gap being studied. For the 7.5 mm gap operating on the cathode wall breakdown was observed only with the electrode pitch doubled; a full load line was not obtained for this configuration and the breakdown data is compared in the figure to non-breakdown data for the normal electrode pitch. Although all breakdowns result in a decline in Hall voltage, the response of the generator depends on the response of all the insulator gaps and as can be observed in the figures, the response of the Faraday current is different for the several breakdowns represented. The transient response of the electrical parameters for three breakdowns are presented in Figures 51-53 and serve to display the main characteristics common to all the breakdowns as well as behavior peculiar to particular breakdowns.

The transient response for a run in which breakdown was observed only for the main test gap is shown in Figure 51, where the main test gap was a 7.5 mm gap operating on the anode wall of the generator. For this case the Hall voltage across the 7.5 mm gap remains constant over a period of

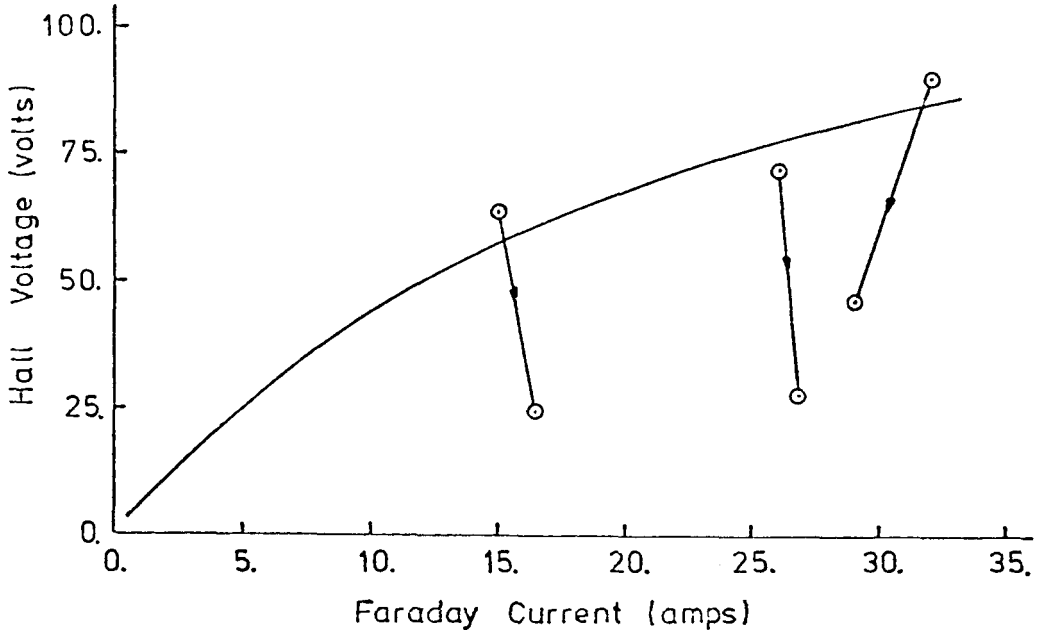

Figure 50a. Hall voltage versus Faraday current behavior for breakdown. Non-breakdown data is represented by the solid line. Data is taken from Run .75-A, for the .75 cm gap operating on the anode wall of the generator.

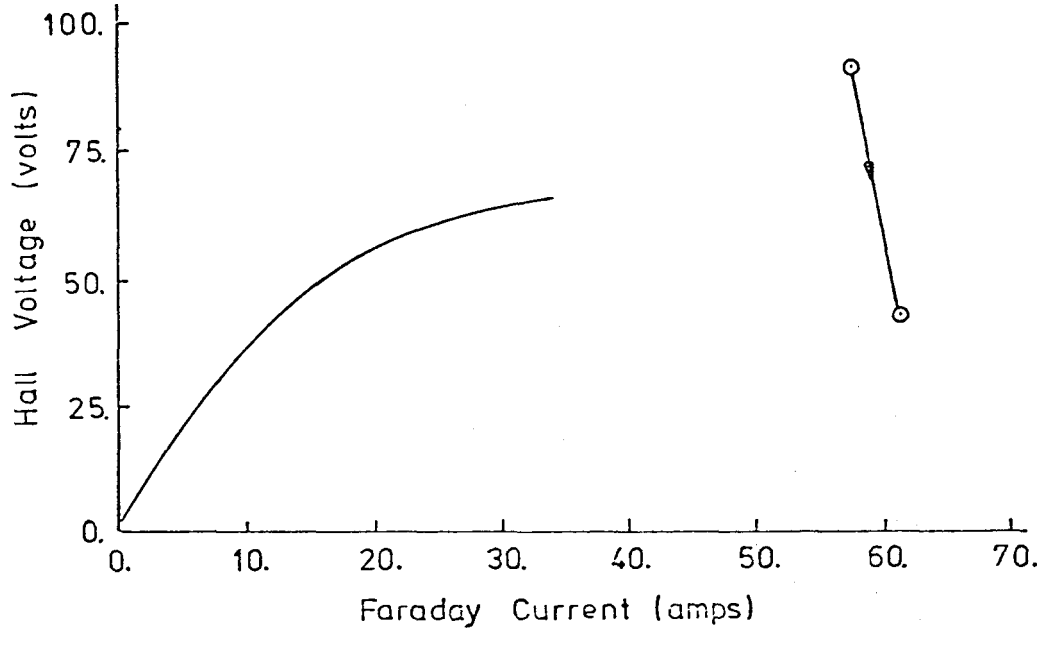

Figure 50b. Hall voltage versus Faraday current behavior for breakdown. Non-breakdown data, represented by the solid line, is for a .75 cm gap operating on the cathode wall of the generator with no pairing of the electrode circuits. Breakdown data is taken from Run .75-CP, for the .75 gap operating on the cathode wall, with electrode pitch increased by pairing of the electrodes.

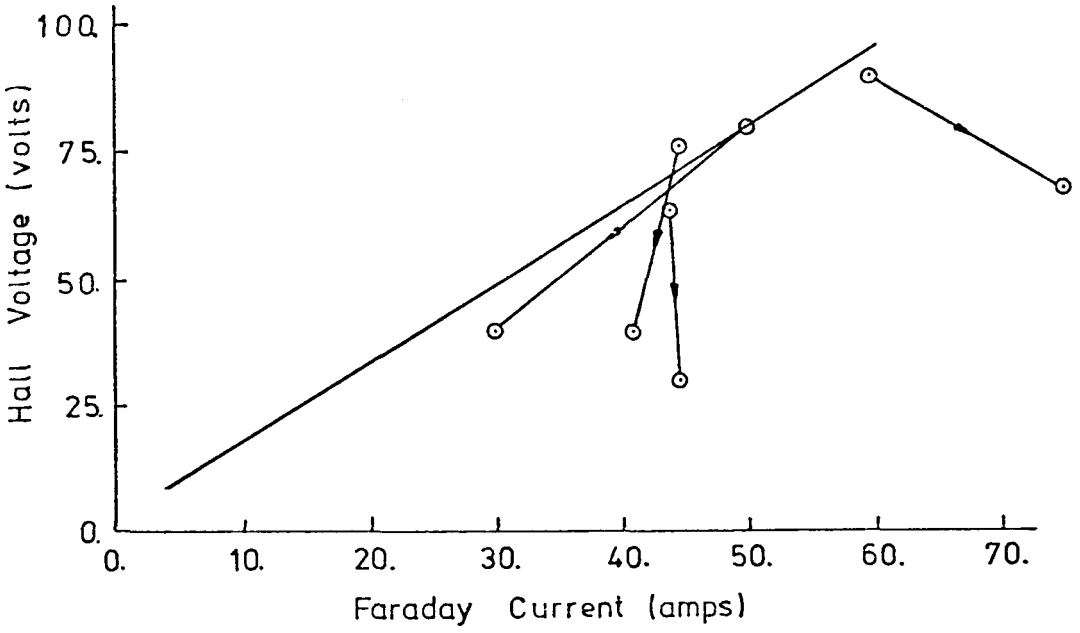

Figure 50c. Hall voltage versus Faraday current behavior for breakdown. Non-breakdown data is represented by the solid line. Data is taken from Run 1.0-AP, for the 1.0cm gap operating on the anode wall of the generator.

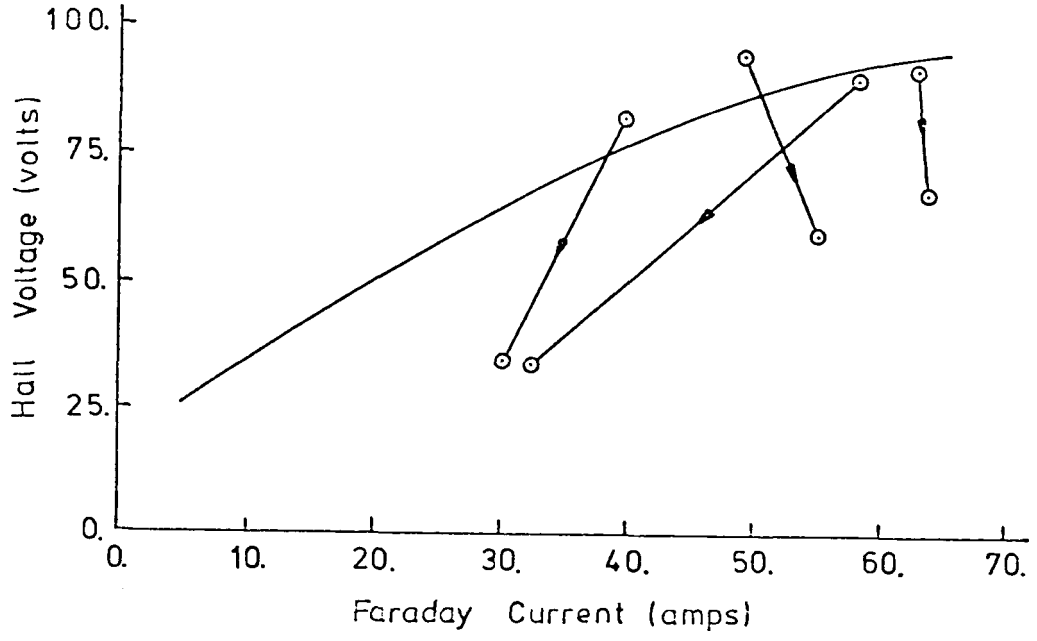

Figure 50d. Hall voltage versus Faraday current behavior for breakdown. Non-breakdown data is represented by the solid line. Data is taken from Run 1.0-CP, for the 1.0cm gap operating on the cathode wall of the generator.

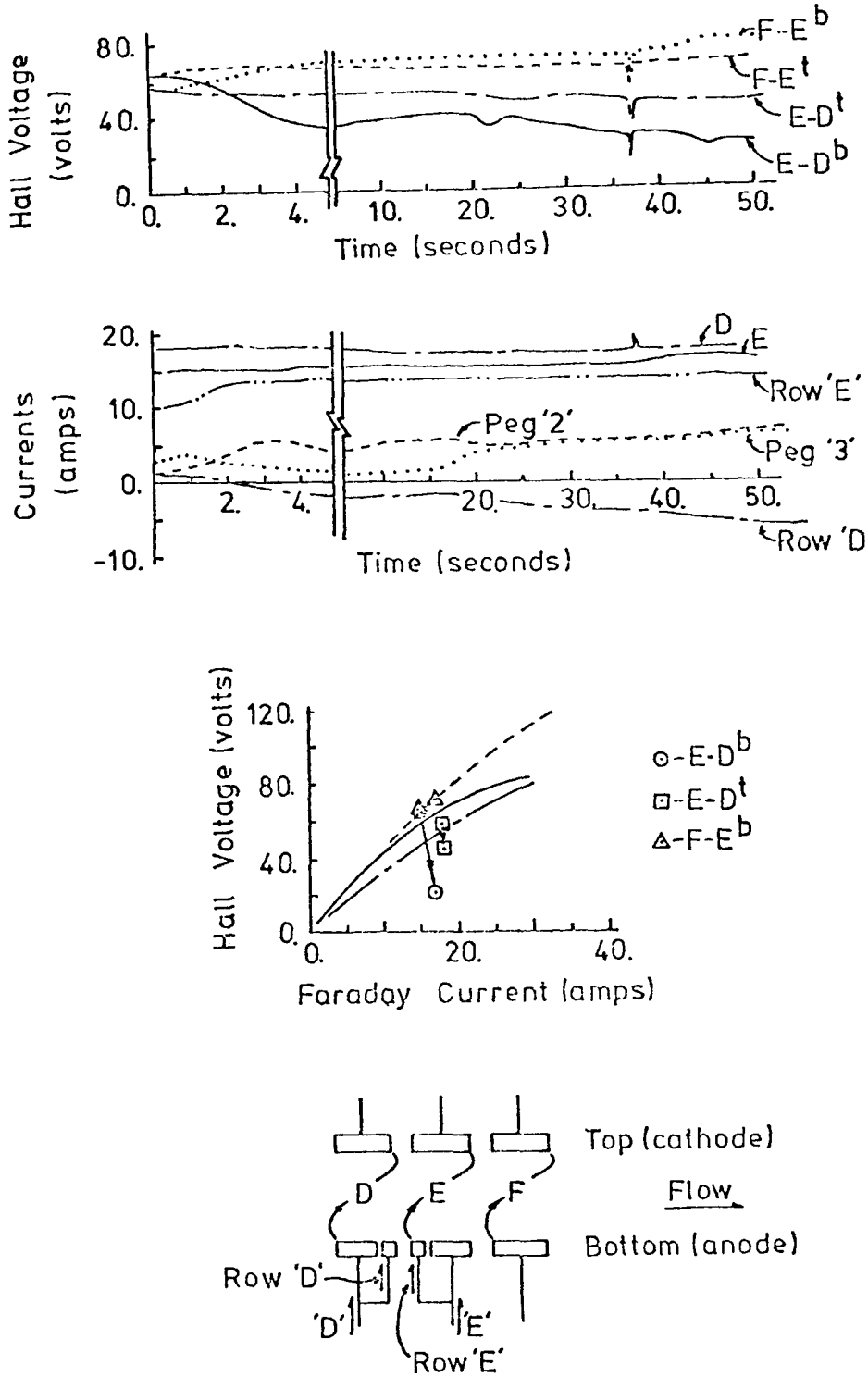

Figure 51. Transient response of Hall voltages and various currents for a run in which breakdown occurred. Main test gap is a .75cm gap operating on the anode wall of the generator. Sketch identifies the various Hall voltages and currents plotted; peg "2" and peg "3" are located along row "E".

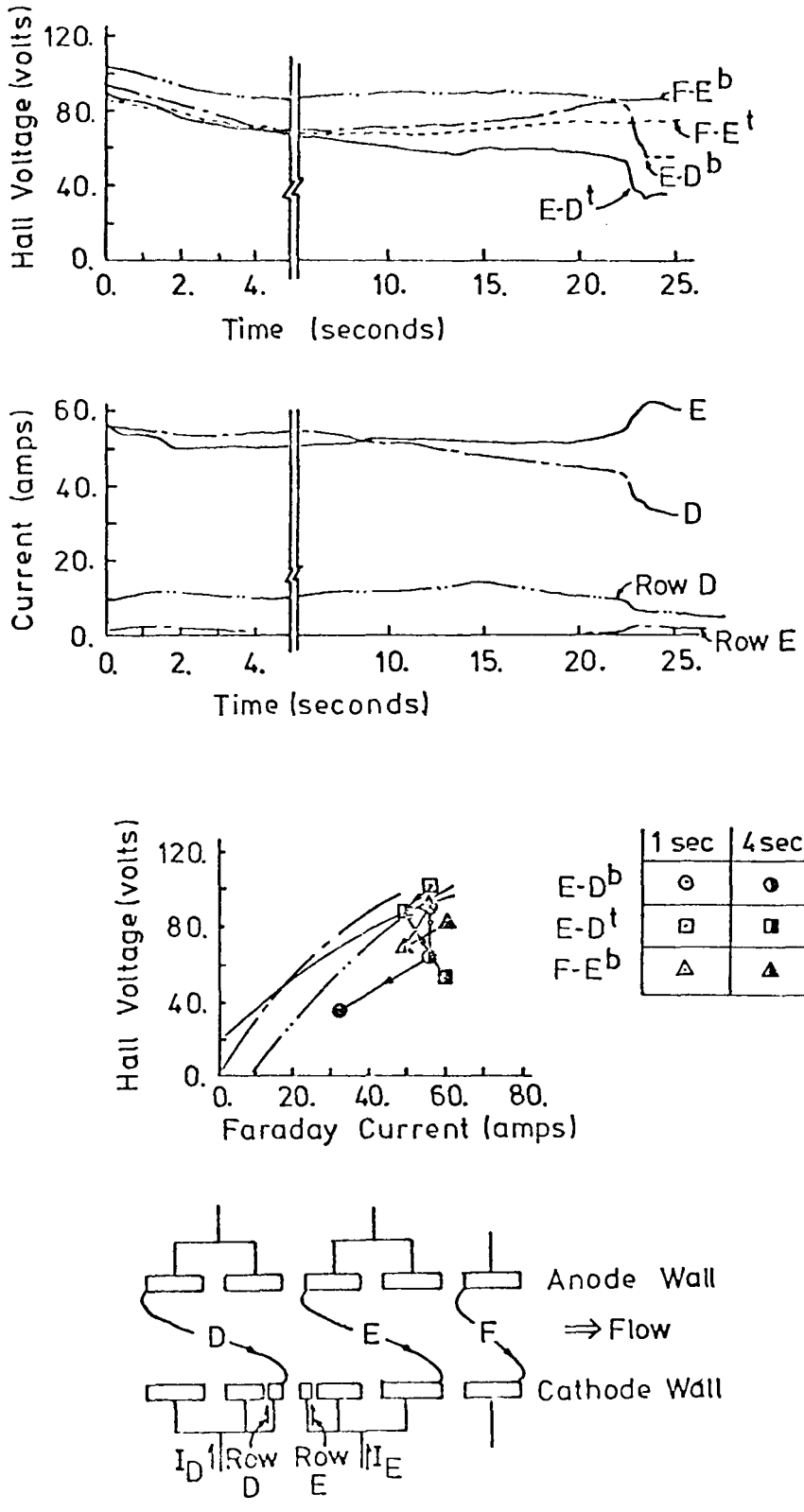

Figure 52. Transient response of Hall voltages and various currents for a run in which breakdown occurred. Main test gap was a 1.0 cm gap operating on the cathode wall. Sketch identifies the various voltages and currents.

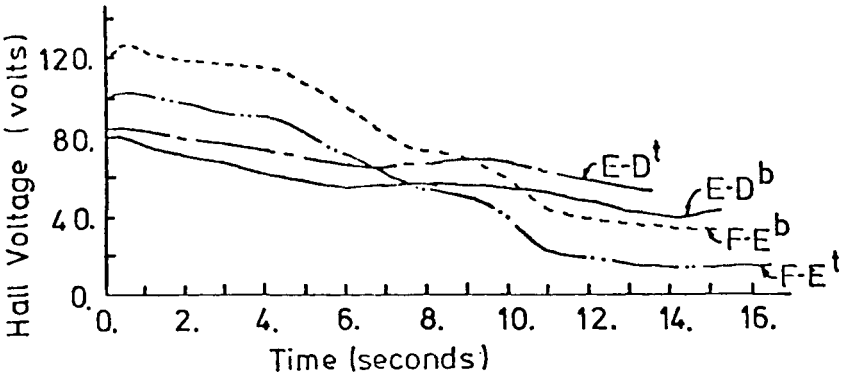

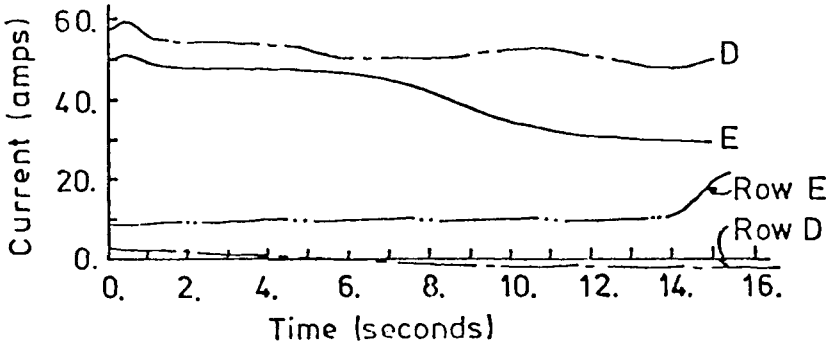

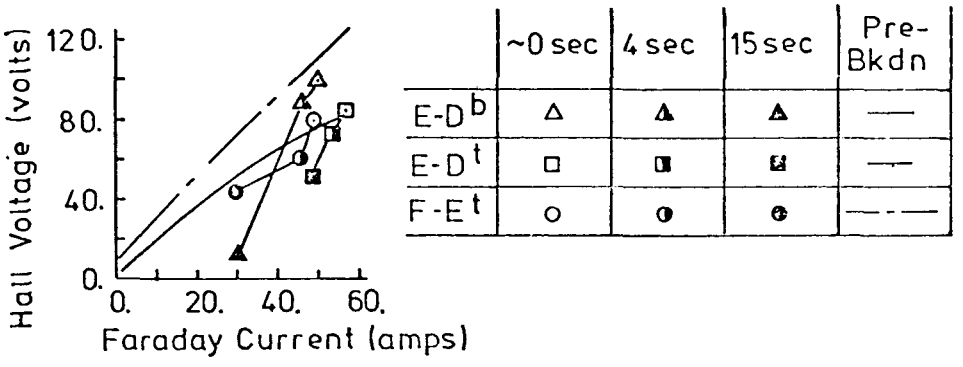

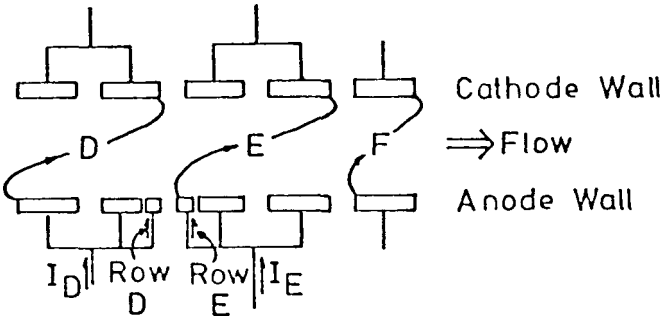

Figure 53. Transient response of Hall voltages and various currents for a run in which breakdown occurred. Main test gap was a 1.0 cm gap operating on the anode wall. Sketch identifies the various voltages and currents.

≈1 second after which breakdown develops over a time period of a few seconds. During this period the Faraday currents change only slightly, the Hall voltages of the gap opposite the 7.5 mm gap declines somewhat and the Hall voltages across the adjacent gaps rise to accommodate the decline at the main test gap. Although the overall change in Faraday current is small, the current to one of the pegs of electrode row 'E' rises dramatically as breakdown develops and the breakdown is accompanied by a current reversal in the downstream edge of the electrode upstream of the gap. Several frames of the movies taken for this run provide a good overall understanding of the breakdown process and are displayed in Figure 54. The initial frame taken soon after the initiation of current shows some heating of the inter-electrode insulator. In the second frame, taken ≈0.5 second after initiation of current, a local heated region can be observed near the downstream edge of the insulator. In subsequent frames this region grows and breakdown occurs when the gap is bridged by a narrow channel in the insulator. It should be noted that no activity is observed in the plasma image during breakdown. Subsequent to the breakdown, the heated region widens with a moderate, further decline in Hall voltage across the test gap.

The transient response for a run in which two breakdowns were observed is shown in Figure 52, where the main test gap was a 10 mm gap operating on the cathode wall of the generator. The main test gap suffers breakdown in the first few seconds, with the Hall voltage of the opposite and adjacent gaps declining with the breakdown. As can be seen in the Hall voltage versus Faraday current plot in Figure 52, this initial breakdown of the Hall voltage to the gap opposite the main test gap does not move far off the non-breakdown curve for that gap, while the Hall voltage for the main test gap drops well below its non-breakdown level. Although the total Faraday current is not affected, the current to two of the pegs (outside the view of the camera) on the electrode edge where the Faraday current concentrates rises and the current from the electrode edge to the other side of the inter-electrode insulator declines to zero. Following a delay of about 15 seconds a second breakdown is observed, the Hall voltages across the main test gap and the insulator gap opposite the main test gap declining dramatically, while the Hall voltages for the adjacent gaps rise somewhat. In this case the Faraday currents change considerably.

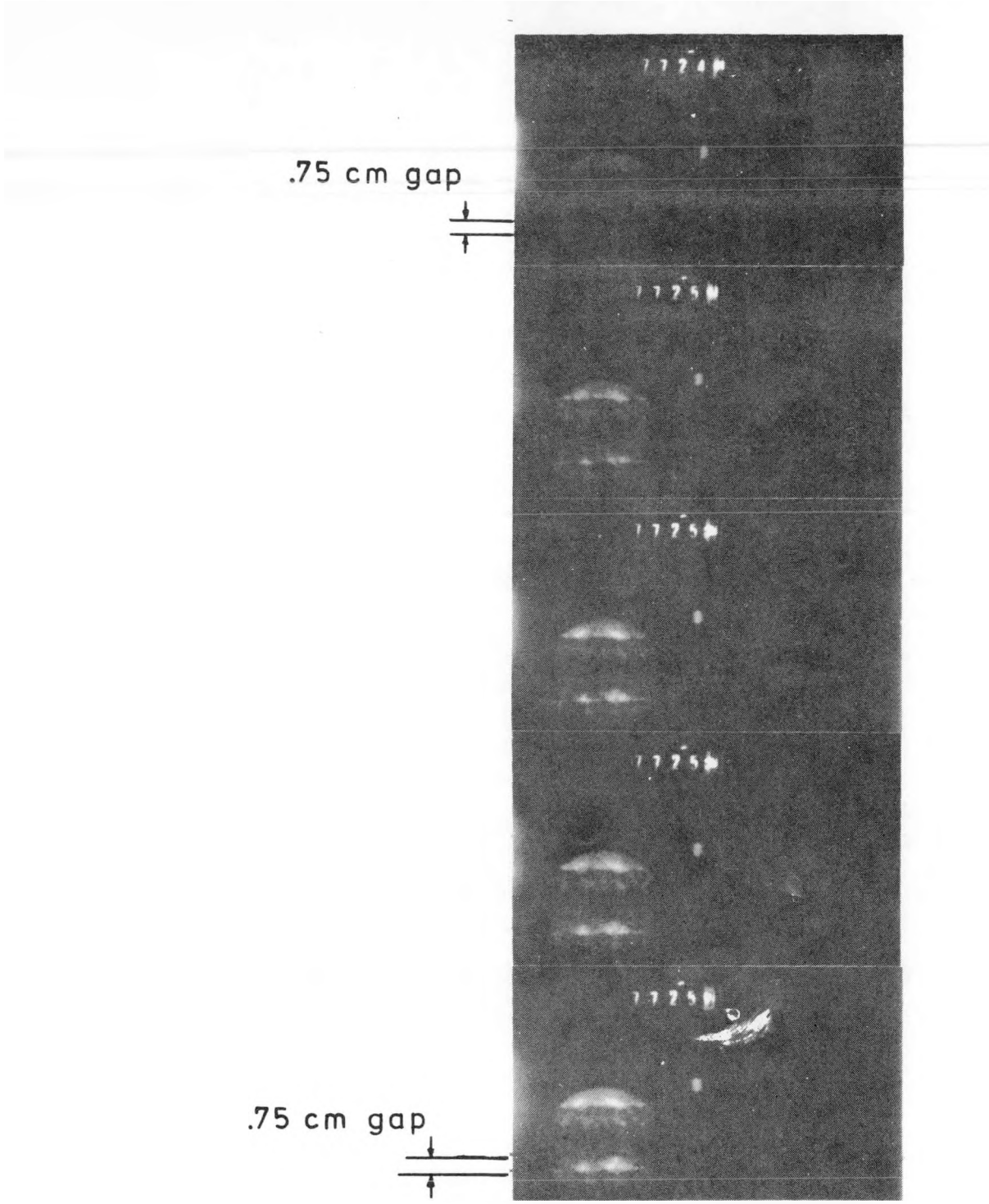

Figure 54. Sequence of the frames of the movies showing the development of a slow (insulator) breakdown. Data taken from induced field Run Series .75-A; the gap suffering breakdown is 7.5 mm. The time response of the important parameters for the run are shown in Figure 51. A descriptive sketch of the camera view is given in Figure 11. The times appearing on the photograph are approximate. Note that no activity is observed in the "plasma" image.

The Hall voltage versus Faraday current response for this second breakdown is shown in the figure and indicates that this breakdown occurs at the gap opposite the main test gap and that a decline in Faraday current is responsible for the decline in Hall voltage across the main test gap.

The transient response for a run in which the main breakdown occurs for a gap other than the main test gap is displayed in Figure 53, where the main breakdown occurs for a 12 mm gap operating on the cathode wall of the generator. In this case a relatively mild decline in Hall voltage across the main test gap occurs in the first few seconds and is accompanied by a mild increase in current from two pegs in the row downstream of the main test gap and a decline in current leaving the row upstream of the main test gap. Whether or not this behavior should be considered breakdown is unclear. During the initial four seconds, the Hall voltage across the gaps downstream of the main test gap remain roughly constant; however, about five seconds after the initiation of current the Hall voltages across two of these gaps decline dramatically as breakdown occurs at one or both of these gaps. As is evident in the Hall voltage versus Faraday current curve accompanying Figure 53, the Faraday currents are significantly affected and the decline in Faraday current is responsible for the decline in Hall voltage across the main test gap.

Photographic records were obtained of breakdown for the 7.5 mm gap operating on the cathode wall of the generator and several frames are displayed in Figure 55. In the second frame two arc spots are observed near the downstream edge of the upstream electrode. Although somewhat difficult to observe due to the angle in which the photographs were taken, the heated insulator region corresponding to the breakdown can be observed in the final frame. As in the photographic records for the breakdown on the anode wall, no activity is observed in the plasma image for this cathode wall insulator breakdown.

The evidence presented above indicates that the Hall voltage breakdowns, observed for three gap sizes and for gaps on both walls of the generator, were caused by a constriction of the current passing through the inter-electrode insulator. No breakdown of the plasma type was observed for these experiments.

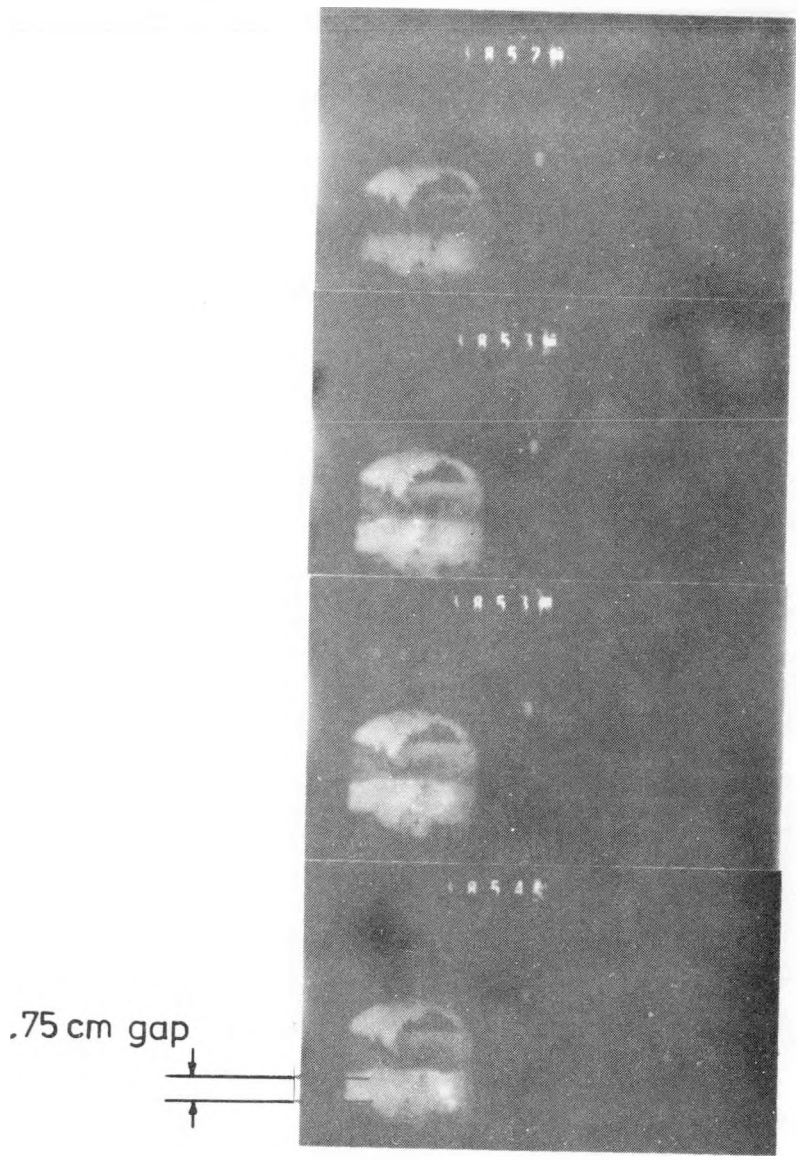

Figure 55. Sequence of frames of the movies showing the formation of a slow (insulator) breakdown. Data is taken from induced field Run series .75-A; the gap suffering breakdown is 7.5 mm and is on the cathode wall of the generator. A descriptive sketch sketch of the camera view is given in Figure 11. The times appearing on the photographs are approximate. Note that no activity is observed in the plasma image.

3.3.5 Breakdown Threshold Voltage

As demonstrated in the previous section the generator electrical parameters remained steady only when the Hall voltages were below a threshold level. A summary of the breakdown behavior as determined by the induced field results described above and by previously reported induced field experiments is presented in Figure 56. Data from the Soviet experiments using their U-02 facility are also shown, although no breakdown was observed in those experiments. In the figure the lowest Hall voltages which resulted in breakdown for particular conditions and the highest voltages not resulting in breakdown are plotted as a function of inter-electrode gap size. While the separation between breakdown and non-breakdown conditions is not as distinct as it was for the applied field experiments a non-breakdown region is identified in the figure. Inter-electrode gap size appears to be an important parameter although the figure indicates that other factors are most likely of importance as well. It should be noted that the Soviet data was obtained at considerably lower current density levels than the data reported here and the electrode wall construction was considerably different. In interpreting the presently reported data is should be kept in mind that several of the breakdowns observed involved breakdown at more than one gap and were obtained under conditions of extremely high transverse currents.

3.3.6 Post-Breakdown Behavior

In several cases the current was left on for a considerable time after breakdown had occurred with the main result being a widening of the breakdown channel. Unfortunately it is not possible to accurately measure the current passing between the adjacent electrodes after breakdown has occurred and it is therefore difficult to make estimates of the temperature or conductivity of the breakdown region in the insulator.

3.4 Comparison of Induced Field and Applied Field Breakdown

The overall manifestation of breakdown for both configurations is a rapid and significant reduction in axial voltage accompanied by the formation of a constricted current path joining the adjacent electrodes. Current distribution measurements and photographic records show that in the induced field configuration a portion of the transverse current passes to

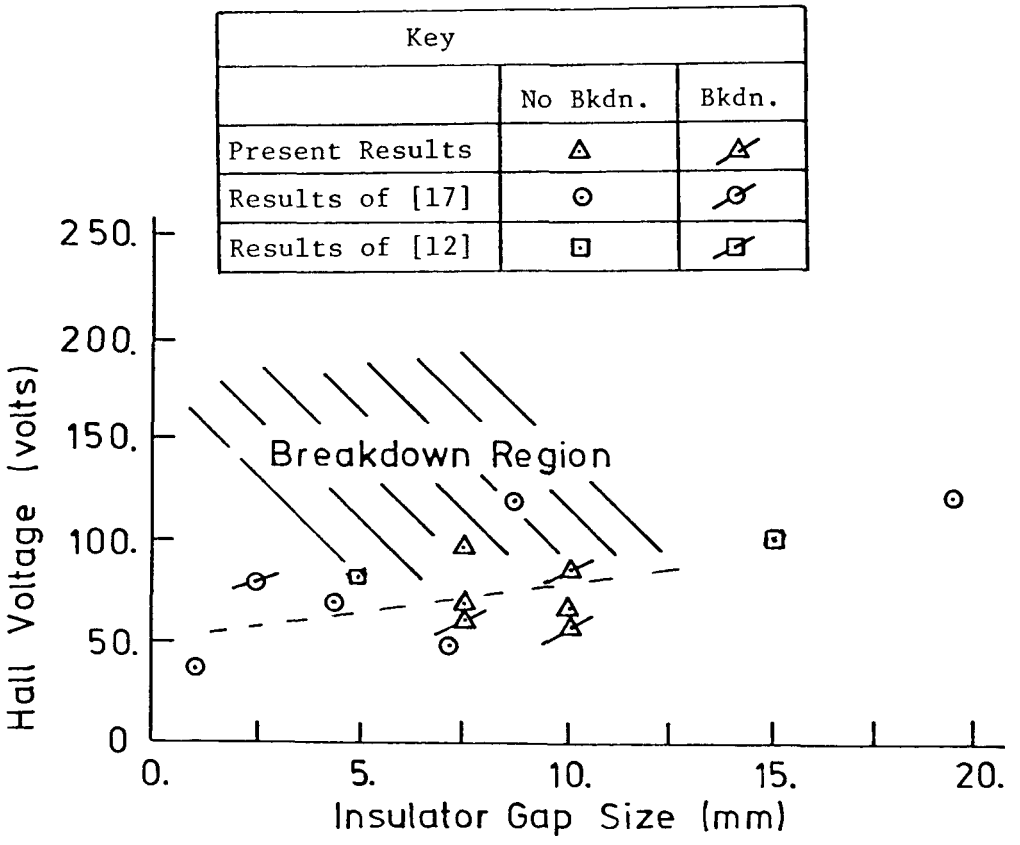

Figure 56. Plot of breakdown threshold voltage for induced field configuration versus inter-electrode gap size. Figure shows highest voltage for which breakdown did not occur. Data from references 12 and 17 ahso shown.

to the adjacent electrode prior to passing to the opposite electrode. For both configurations breakdown occurred only when a threshold level was exceeded and the insulator gap size was an important parameter affecting the threshold voltage. Applied field experiments demonstrated that the constricted current path could form either in the plasma or in the inter-electrode insulator, with a somewhat higher threshold voltage indicated for breakdown through the plasma. Induced field breakdowns for present conditions were of the insulator type and displayed characteristics close to the insulator breakdown observed in the applied field experiments. In particular, for both configurations of a delay of about 1 second or more separated the initiation of current and the insulator breakdown. The photographic records show that small hotspots originally located on the insulator edges grow during this delay period and breakdown is observed when the insulator gap becomes completely bridged by a heated channel in the insulator. The majority of the voltage decline occurs over a period of $\simeq$1 second. The threshold voltage for insulator breakdown for the induced field configuration is somewhat lower than those observed for the same gap size for the applied field configuration as is displayed in Figure 56, however the trend of increased threshold voltage with increased gap size is evident in both cases. The absence of breakdown of the plasma type in the induced field experiments is not surprising considering the significantly higher threshold voltages required for plasma breakdown in the applied field experiments.

The good qualitative similarity between induced field and applied field breakdown indicates that the understanding and successful modeling of the applied field behavior would represent a significant step toward the solution of the problem of Hall voltage breakdown.

CHAPTER 4

ANALYTICAL MODELING

4.1 Introduction

The initial sections of this chapter describe the scope of the modeling performed and discuss, in general terms, the phenomenon of breakdown. A much simplified model is also presented and is used to illustrate the most important qualitative features of one type of breakdown. The remainder of the chapter describes the models developed for the inter-electrode region and discusses the predicted behavior for conditions typical of the experiments. Direct comparison of the analytical and experimental results is deferred to chapter 5.

4.1.1 Scope of the Modeling

Analytical effort was directed toward the modeling of the inter-electrode region for the non-breakdown and incipient breakdown regimes of operation. Modeling was performed for the induced field configuration and the applied field configuration, with the applied field models considerably more detailed. Overall characteristics exhibited in the experiments were used to guide the modeling process, indicating simplifications appropriate for each region of operation. A single model for the applied field configuration was employed to predict the non-breakdown behavior and to predict the conditions for which breakdown would occur. Modeling for the induced field configuration is limited to the non-breakdown and well-developed breakdown regimes of operations.

4.2 Introduction to Breakdown Phenomena

The gross characteristic of breakdown established by the experiments described in the previous chapter is a reduction in effective resistence of the inter-electrode region resulting from the formation of a channel of high conductivity material joining the electrodes. In discussing the possible mechanisms leading to such a breakdown it is useful to classify breakdown into the somewhat imprecise categories of thermal breakdown and field-induced breakdown. Both types are similar in that a strong positive feedback between the energy transferred from the electric field and the conduction properties of the material is responsible for the breakdown;

however there are significant differences in behavior between the two types due to differences in the energy coupling characteristics of the material. In the discussion which follows, electrons by virtue of their high mobility are assumed to be the predominant charged particle carriers. For completeness field-induced breakdown phenomena are considered, although it is concluded that this mechanism does not control the breakdown phenomena observed in the experiment. Thermal breakdown phenomena are then discussed.

4.2.1 Field-Induced Breakdown

If the electron-electron and electron-heavy gas mean free paths are large, as might be expected for low electron number density and low gas densities, electrons can be accelerated by the electric field to extremely high velocity before transferring their energy to the heavy particles by collision. For sufficiently high electric fields a significant number of electrons acquire kinetic energies high enough that ionization can result from collision with the neutral species. Breakdown, referred to in this case as an electron avalanche, results when the electric field reaches a level where on the average electrons leaving the cathode produce more electrons in their passage to the anode by ionization than are lost by recombination, lateral diffusion and other loss mechanisms. Spark breakdown in gaseous conductors and breakdown in dielectric solids results from this process. Analytical models, of varying degrees of sophistication, have been advanced to predict the threshold or critical electric field which results in breakdown. Typical values of $\gtrsim 10^4$ v/cm are required to produce a spark breakdown between parallel plates separated by air at S.T.P., and similar fields are required to cause breakdown in an insulator such as alumina at room temperature [18,19]. For spacings less than several centimeters and electric fields not too close to the critical electric field, spark breakdown through a gas will develop in a time-scale on the order of a two microseconds or less [18]. Similar or shorter time scales would be expected for field-induced breakdown of a dielectric material [19].

If the electron velocity distribution is maintained close to equilibrium by a relatively high electron-electron collision frequency the avalanche type breakdown is suppressed; however, breakdown can again result if the energy coupling between the electrons and the heavy species

is weak. Breakdown results when the electric field reaches a level for which electrons gain energy at a rate faster than can be removed by convection and conduction of electrons and by transfer to the heavy species. The formation of current streamers in noble gas MHD generators is an example of such a breakdown and display characteristic formation times on the order of microseconds [20]. Theoretical predictions of this type of breakdown in dielectric materials have not been confirmed experimentally.

Average electric fields which resulted in breakdown in this experimental investigation ($\lesssim$ 200 v/cm) are at least an order of magnitude lower than the critical electric fields for avalanche type breakdown in either an insulator or in air and the time scale for development of breakdown by electron avalanche is considerably shorter than the breakdown time scales displayed in the experiments. Further, for the conditions of the experiments (excepting the regions very close to the wall) estimates show that the energy distribution of the electrons in the plasma is closely Maxwellian and that the electron temperature is maintained close to the heavy gas temperature (see Appendix F). The high near-cathode voltage drop at low currents and the formation of hot spots at the cathode surface indicate that field-induced mechanisms may be important in establishing the discharge near the cathode; however, all indications are that this is a very localized effect. Similarly, the effects of electron temperature elevation are confined to the regions very close to the electrodes, at least prior to the breakdown. For these reasons it seems unlikely that field-induced mechanisms could be responsible for the breakdown over the majority of the distance separating the electrodes. The insulator breakdowns experienced in the experiments formed in regions of relatively high temperature, where it is again likely that an equilibrium distribution should well describe the state of the charged particles, and electronic breakdown mechanisms are not likely to govern the development of breakdown over the majority of the separation distance.

4.2.2 Thermal Breakdown

If the energy coupling between the electrons and the heavy species is very strong, the explicit dependence of the electrical conductivity on the electric field is suppressed such that if formation and recombination of electron-ion pairs is relatively fast, the electrical conductivity can be expressed simply as a function of the material temperature. If the conductivity is a strong increasing function of temperature, thermal breakdown can result if the rate of energy transfer to the electrons is faster than can possibly be transferred from the material by the processes of conduction, convection and radiation. The time scale for the breakdown is then related to the thermal response time of the material and, as will be shown below, typical critical fields can be estimated to be of the same order of magnitude as those for which breakdown was observed in the experiments described in the previous chapter.

The general characteristics of thermal breakdown can be illustrated, and an estimate of the electric field required to produce breakdown obtained through the steady-state thermal and electrical analysis of a much simplified problem. Consider a substance bounded by plane parallel-plates which are maintained at fixed temperature and perpendicular to which an electric field is applied, as shown in Figure 57. Neglecting radiation and convection, energy will be transferred to the plates only by conduction and the steady-state behavior is governed by the one-dimensional heat conduction equation including the Joule dissipation resulting from the current transfer. For this discussion, the electrical conductivity is assumed to vary as temperature to the exponent n, and the thermal conductivity is assumed to be constant. The resultant equations can be non-dimensionalized and universal solutions obtained for the average current density as a function of electric field as indicated in Figure 57.

The steady-state, non-dimensional electric field versus average current density per unit depth is displayed for several values of n in Figure 58. Also shown on the figure are contours of constant maximum temperature. For values of n greater than 1, the electric field rises with current only until a critical electric field is reached; with further increases in current density resulting in a decline in electric field. The steady-state operating point for the region is dependent on the nature of the external circuit as well as the steady-state electric field-current density characteristic of the medium. For the case of an external circuit

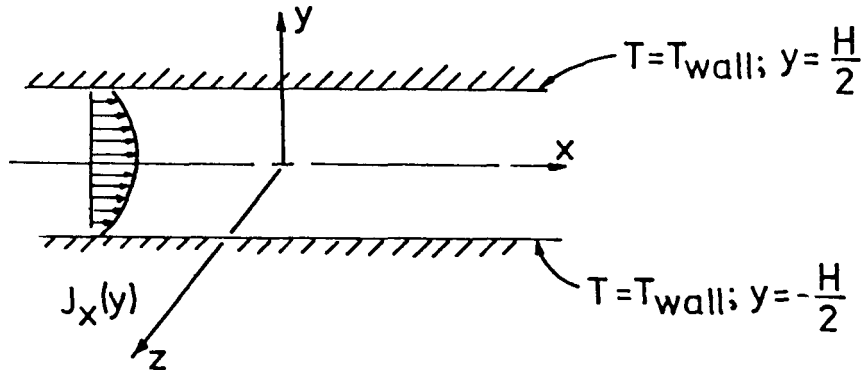

Equations and boundary conditions:

$\frac{d}{dy} k \frac{dT}{dy} = - J_x E_x$ — 1-D Heat conduction

$\frac{dT}{dy}(y=0) = 0$ — Symmetry condition

$T(y=H/2) = T_w$ — Constant wall temperature

$\bar{E} = E_x \underline{i} = \text{constant}$ — 1-D current flow

$J_x(y) = E_x \sigma(y)$ — Ohm's Law

$\sigma(T) = \alpha T^n$ — Assumed conductivity dependences

$k(T) = k = \text{constant}$

$\langle J_x \rangle = \frac{1}{H} \int_{-H/2}^{H/2} J_x(y)\, dy$ — Average current density per unit width in z.

Introducing $T_c = T(y=0)$ the solution for $\langle J_x \rangle$ can be obtained as

$$\frac{w}{2} \sqrt{\frac{\sigma_w T_w}{k}} \langle J_x \rangle = \sqrt{\frac{2}{n+1}} \left[\frac{1}{\theta_w^{n+1}} - 1 \right]^{1/2} \qquad \theta_w = T_w / T_c$$

$$\frac{w}{2} \sqrt{\frac{\sigma_w}{k T_w}} E_x = \sqrt{\frac{n+1}{2}}\, \theta_w^{\frac{n-1}{2}} \int_1^{\theta_w} \frac{d\theta}{(1 - \theta^{n+1})^{1/2}}$$

Figure 57. Schematic of geometry, formulation of equations and outline of solution for simple illustrative example of planar thermal breakdown.

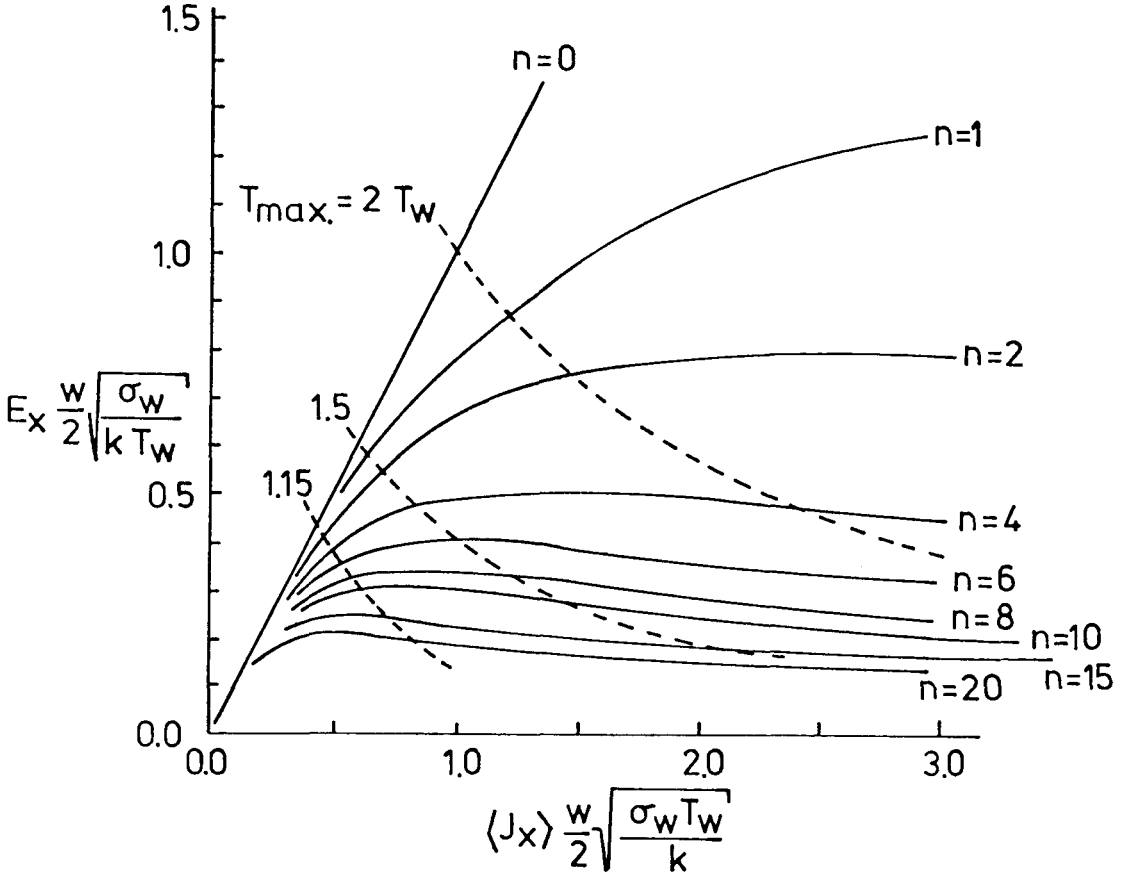

Figure 58. Non-dimensional electric field versus average current density for simplified configuration shown in Figure 57. Results are shown for several values of n, the exponent in the assumed conductivity variation. Also shown are lines of constant T_{max}/T_w.

of maintaining a constant electric field for all current density levels (zero source impedance) a steady operating condition can be realized only for electric fields less than the maximum, or critical field. For applied electric fields in excess of the critical field there is no steady-state solution, and the temperature and current grow indefinitely. This behavior is identified as thermal breakdown. For the case where the external circuit provides a fixed current density (infinite source impedance), a steady operating condition can be obtained for all current density levels; however for average current densities greater than the level corresponding to the critical electric field, extremely high centerline temperatures and current densities result. This behavior is displayed in Figure 59, where the current density is plotted as a function of distance from the centerline for an average current density less than the critical level and greater than the critical level. The conventional concepts of striking voltage and of discharge stability for the case of a finite impedance external voltage supply, such as are discussed in Cobine [18] can be applied to this simplified configuration.

From the foregoing solution, the critical electric field for thermal breakdown can be expressed as

$$E_x\Big|_{critical} = \frac{1}{w/2}\sqrt{\frac{k\,T_{wall}}{\sigma_{wall}}}\,\gamma(n) \quad ,$$

where $\gamma(n)$ is displayed in Figure 60 and the other terms are defined in Figure 57. The function $\gamma(n)$ decreases with increasing n as shown in Figure 60 and, as expected, the critical electric field is lower when the conductivity is more strongly dependent on temperature. Increased thermal conductivity and decreased plate separation result in increases in critical electric field as would be expected. Recalling that the conductivity varies as T^n, the critical electric field can be expressed as

$$E_x\Big|_{critical} \propto 1./T_{wall}^{\frac{n-1}{2}} \quad ,$$

displaying explicitly the great importance of the wall temperature. The assumption of no variation of temperature in the x or z direction renders the critical electric field independent of the depth and electrode separation of an actual sample.

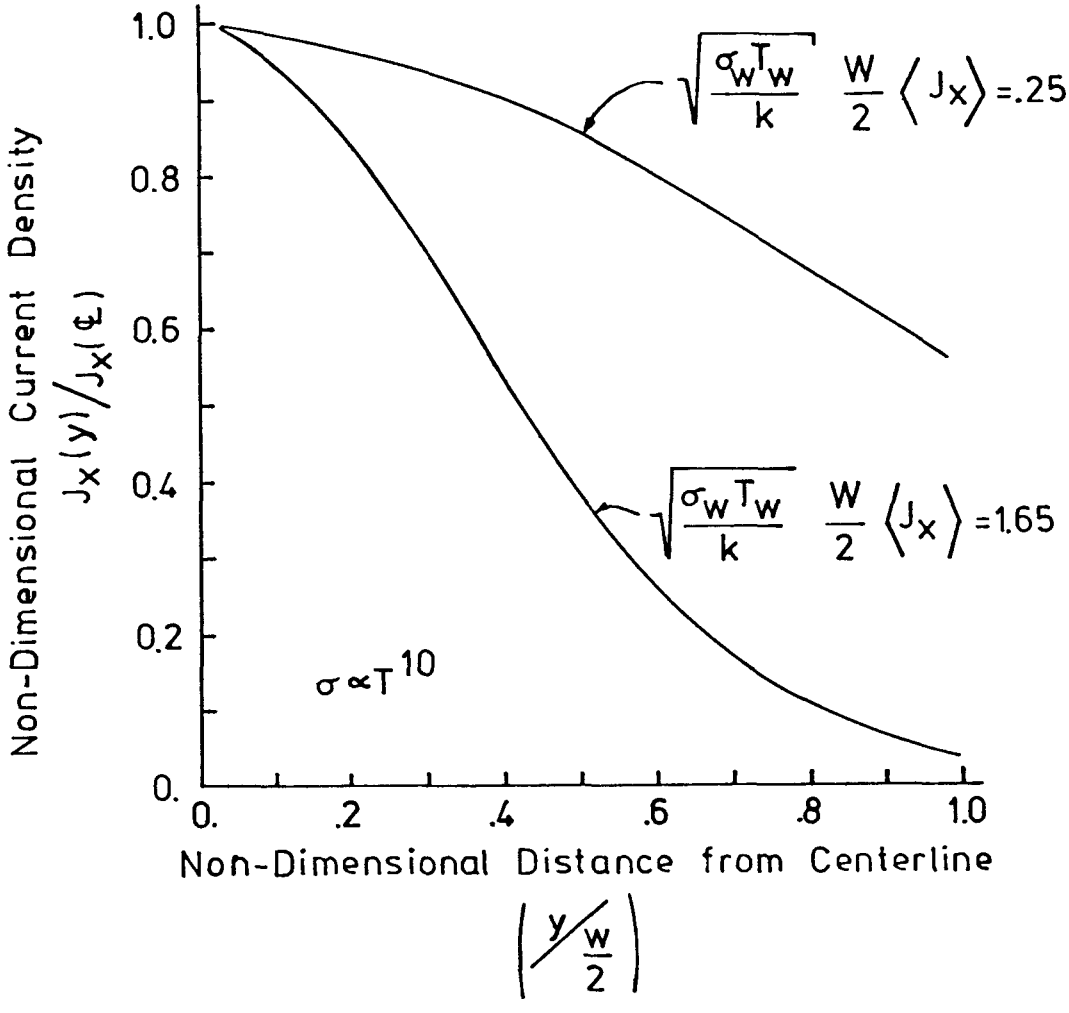

Figure 59. Non-dimensional current density as a function of non-dimensional distance from the centerline for two values of non-dimensional average current density. Conductivity varies as $\sigma \propto T^{10}$.

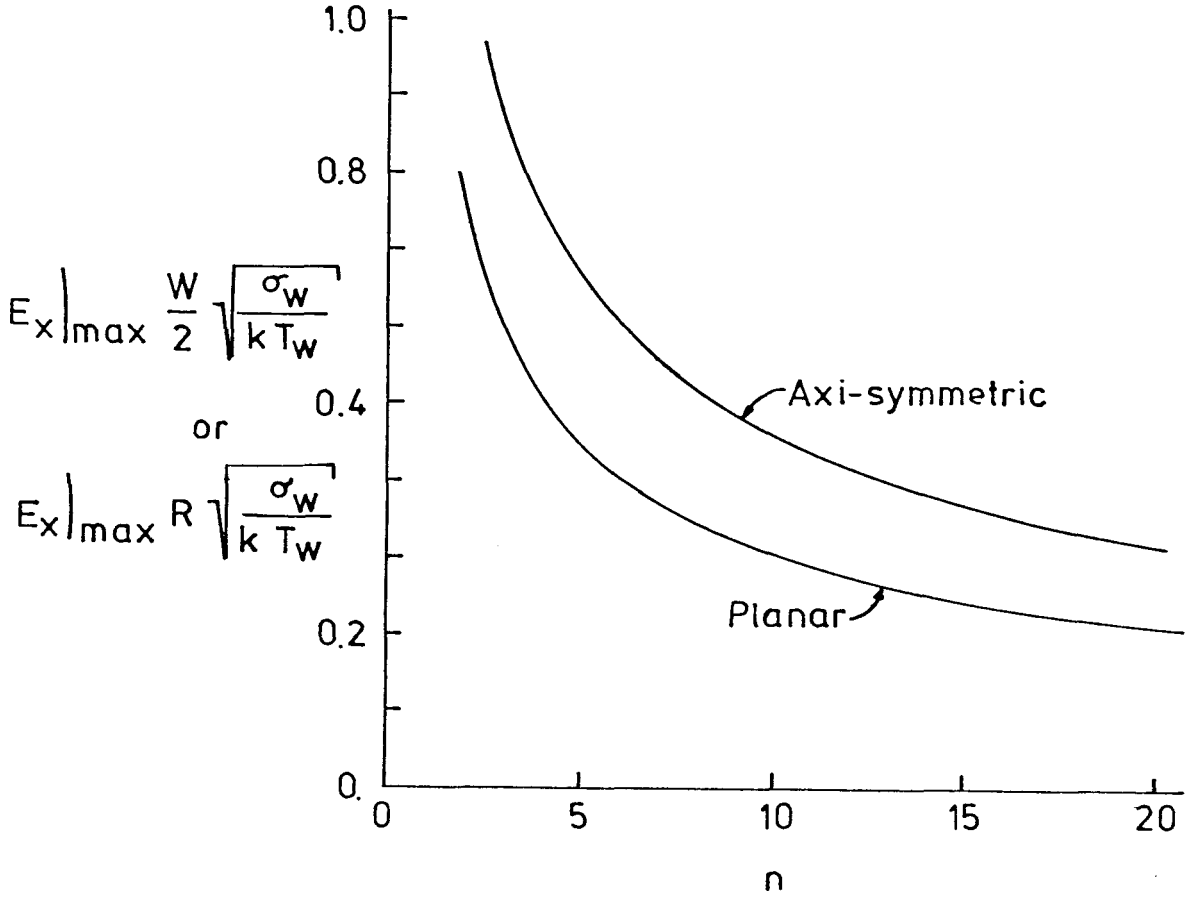

Figure 60. Normalized critical electric field for planar and axi-symmetric thermal breakdown as a function of the exponent, n, in the assumed conductivity dependence on temperature ($\sigma \propto T^n$). Configurations and terms defined in Figure 56 and 61. Note that W and R represent distances perpendicular to the direction of the electric field, such that a limiting axial field, rather than voltage, results.

While the model just described does not include several important features of the experimental investigation, it is useful to compare the critical field indicated by the simple model with the threshold fields determined in the experiments. For conditions representative of the inter-electrode insulators (alumina or magnesia) used in the experiments ($w \simeq 1$ cm, $k \simeq 7$ w/m-K, $T_{wall} \simeq 1800$ K and $\sigma \simeq 0.25 \times (T/1600)^{10}$ mho/m) a critical electric field of $\simeq 80$ volts/cm is indicated. Adjusting the thermal conductivity to reflect in an approximate manner the energy transport of the plasma in the near insulator region and choosing other conditions to represent the plasma ($w \simeq .4$ cm, $k \simeq 5\ k_{molec} \simeq 1$ w/m-K, $T_{wall} = 1800$ K and $\sigma \simeq 1 \times (T/2300)^{10}$) a critical field of $\simeq 230$ volts/cm is indicated. These estimates compare quite favorably with the threshold voltage of $\simeq 200$ volts for a 1.9 cm/gap ($\simeq$100 volts/cm) typical of the experiments and strongly support the position that thermal mechanisms, rather than field induced mechanisms, are responsible for the development of breakdown over the majority of the distance separating the electrodes.

Before proceeding to the description of the model developed to describe the inter-electrode region, it is useful to mention briefly the results obtained for a problem similar to the one just discussed except that the material is constrained within a cylinder maintained at T_{wall} as shown schematically in Figure 61. Electric field versus average current density curves obtained are similar to those of the planer case with the critical electric field given by

$$E_x\Big|_{critical} = \frac{1}{R}\sqrt{\frac{k\ T_{wall}}{\sigma_{wall}}}\ \beta(n) \quad ,$$

where $\beta(n)$ is displayed in Figure 60, R is the radius and the remaining terms retain the same meaning as in the planar case. As can be observed in Figure 60, the critical levels for planar and axisymmetric thermal breakdown are comparable, although the critical level is higher for the axisymmetric case where increased cooling is provided. This comparison indicates that reasonable estimates of three-dimensional breakdown threshold levels can be obtained using planar models.

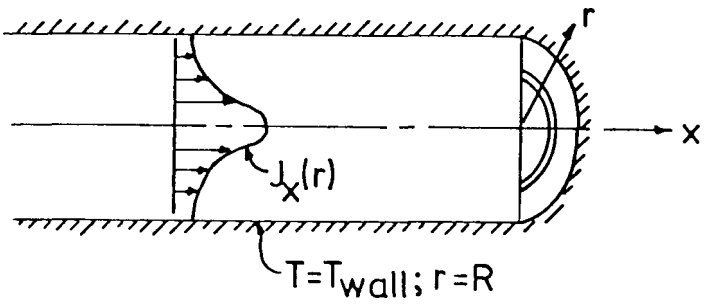

Equations and Boundary Conditions:

$\frac{1}{r}\frac{d}{dr} k\, r \frac{dT}{dr} = - E_x^2 \sigma$	Radial Heat Conduction
$\frac{dT}{dr}(r = 0) = 0$	Symmetry condition
$T(r = R) = T_{wall}$	Fixed Wall Temperature
$\vec{E} = \hat{E}_x \vec{1}$	1-D current flow
$J_x(r) = \hat{E}_x \sigma(r)$	Ohm's Law
$\sigma(T) = a\, T^n$	Assumed conductivity dependences
$k(T) = k$	
$\langle J_x \rangle = \frac{1}{\pi R^2} \int_{r=0}^{r=R} 2\pi r\, J_x(r)\, dr$	Average current density

By suitable scaling, a "universal" equation can be formed and solved numerically for a desired value of n. This yields the non-dimensional electric field as a function of the non-dimensional average current density, and non-dimensional temperature profiles. Solutions can be expressed as

$$E_x = \frac{1}{R}\sqrt{\frac{T_w\, k}{\sigma_w}}\; X_w\, \theta_w^{\frac{n-1}{2}}$$

$$\langle J_x \rangle = \frac{1}{R}\sqrt{k\, \sigma_w\, T_w}\,(2\, J_w)/(X_w\, \theta_w^{\frac{n+1}{2}})$$

where $J_w = J_w(X_w)$ and $\theta_w = (T_{wall})/T_a = \theta_w(X_w)$ are provided from the numerical solution.

Figure 61. Schematic of geometry, formulation of equations and outline of solution for simple illustrative example of axi-symmetric thermal breakdown.

4.3 Pre-Breakdown and Incipient Breakdown Model for the Applied Field Configuration

In this section the model for the pre-breakdown and incipient breakdown behavior is described. Section 4.3.1 discusses the basic assumptions and presents the overall electrical circuit and calculation procedure. The details of the plasma and inter-electrode insulator models are discussed separately in the two sections that follow. In the final section results for typical conditions are presented and the sensitivity of the results to certain parameters is discussed.

4.3.1 General Considerations and Overall Assumptions

Description of the pre-breakdown and incipient breakdown behavior of the inter-electrode region, shown schematically in Figure 62, is provided by a time-dependent thermal and electrical model of the plasma and the inter-electrode insulator. The characteristic response time of the plasma to changes in wall temperature (τ_{plasma} is approximately the flow time: $\ell/u \simeq .05m/100\ m/s = 5 \times 10^{-4}$ sec) relative to the time characterizing changes in wall temperature (τ_{wall} is a thermal inertia term: for typical conditions $\tau_{wall} \simeq 100$ milliseconds) allows the plasma to be considered in quasi-equilibrium with the wall temperature. The further assumption that the interface between the plasma and the inter-electrode insulator is perfectly electrically insulating allows the solution of the plasma response to proceed separately from that of the inter-electrode insulator. The plasma and insulator solutions interact only through the plasma heat flux/inter-electrode insulator surface temperature boundary condition and as parallel current paths in the overall electrical circuit.

The solution for a particular inter-electrode spacing proceeds by first employing the plasma model to compute the steady-state total axial voltage and the average inter-electrode insulator heat flux for a range of total axial currents and inter-electrode insulator surface temperatures. In the model the electrode temperature and the upstream and downstream insulator temperatures are assumed to be fixed in time. The initial response ($\tau \simeq 1$ millisecond) of the inter-electrode region to the application of a voltage is determined using the plasma model since the inter-electrode insulator surface temperature is effectively constant for that time. The total response of the region is determined using the second portion of the model which considers the response of the inter-electrode

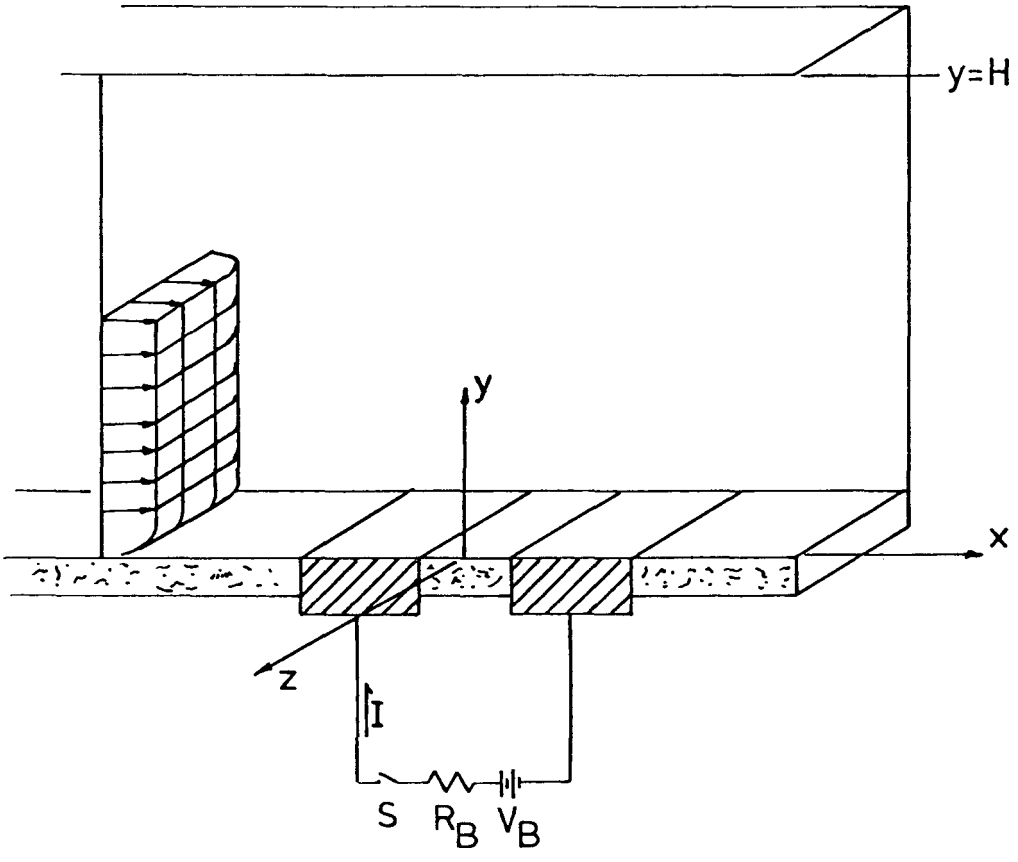

Figure 62. Schematic of applied field configuration, showing the geometry, the inlet profile and the external circuit.

insulator with the plasma behavior described by the steady-state results of the plasma model. The plasma is described fully by the steady-state plasma resistance and heat transfer coefficient as a function of total plasma current and insulator surface temperature. The plasma and insulator currents are determined at a particular time by consideration of the overall circuit, shown schematically in Figure 63. With the above approach, calculations can be made for a variety of insulator thicknesses, initial surface temperatures, applied voltages, etc. without repeating the time consuming plasma response calculations for each set of conditions.

4.3.2 Plasma Modeling

This section describes the model developed to predict the thermal and electrical response of the plasma. The fluid mechanical aspects are discussed first and then the electrical aspects are treated. Some discussion is made regarding the calculation of the thermal and electrical fluid properties used in the modeling. Although some mention is made of the numerical techniques employed, detailed discussion is deferred to Appendix E.

Fluid Behavior. For the conditions of the present experiments an inviscid core exists at the center of the channel and a standard core-flow boundary layer approach is employed in the modeling of the fluid flow. Although the length Reynolds numbers typical of the experiments ($\simeq 4 \times 10^4$ to 8×10^5) are somewhat low for turbulent flow, it is assumed that the high freestream turbulence level resulting from the combustion process insures that the boundary layer flow is turbulent. The flow in the corners of the channel is not treated in detail but rather the fluid properties are assumed to behave as $\gamma(x,y,z) = \gamma_1(x,y) \cdot \gamma_2(x,z)$ where the functions γ_1 and γ_2 are determined by applying the standard two-dimensional boundary layer approach to the flow along each wall. Time-dependent calculations are performed only for the main wall of interest with the required average properties across the channel width determined by integrating the appropriate function $\gamma_2(x,z)$ across the channel width for a specific axial location, usually chosen to be the centerline of the inter-electrode insulator.

The flow over the electrode wall of interest is described by the time-dependent turbulent boundary layer equations for the mean flow. The axial momentum equation and the energy equation are solved for the axial velocity component and the static enthalpy, with the continuity equation used to

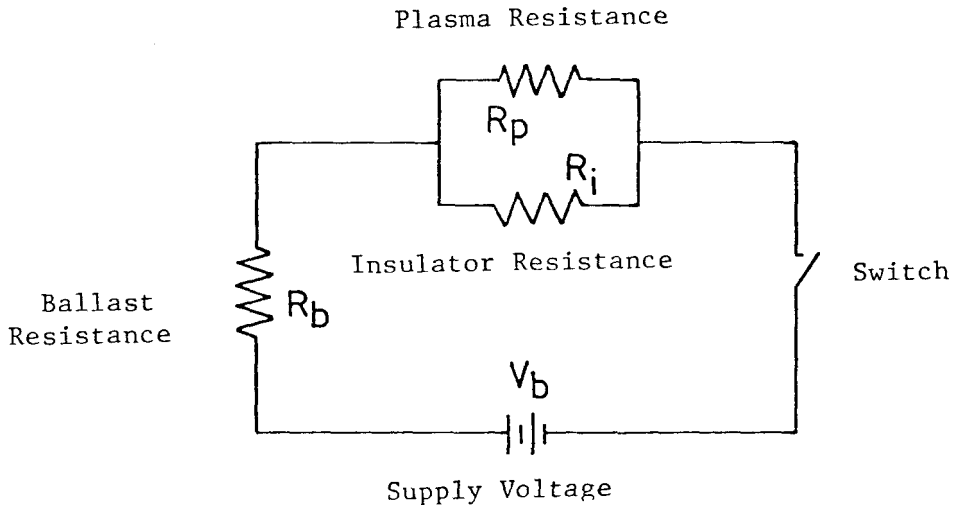

Figure 63. Simplified schematic of overall electrical circuit used in applied field model.

compute the transverse velocity component. The transverse pressure gradient is assumed small and the transverse momentum equation used only to check if this assumption is valid. The Joule heating source term in the energy equation is evaluated from the conductivity distribution as discussed later in the section. To obtain accurate results for the low wall temperatures typical of the experiments, finite electron-ion reaction effects are included by employing the electron-ion continuity equation to determine the electron number density. In formulating the electron-ion continuity equation it has been assumed that for distances far from the wall electric field gradients and translational energy per molecule are low enough that the flow is quasi-neutral and the boundary conditon $n_e = n_e^*$ at the wall (the * denotes equilibrium) is adequate. The region near the wall is considered in detail as described later in the section and in Appendix F. The electron-ion reaction rate of Curry is used in the calculation [21]. The effects of turbulent transport of momentum, energy and species (electrons and ions) are modeled using the mixing length concept, following the work of Kays [22] and many others. Measurements of velocity, temperature and electron number density profiles for boundary layer flow typical of the present experiments have been performed by Daily [23], Rankin [24] and compared with calculated profiles. Unfortunately, recommendations for improvement of the modeling (for example an adjustment of the turbulent mixing parameters to better represent the experimental state) were not available at the time of the calculations; these effects should be considered when the result from those studies are completed.

The calculation procedure for the core-flow through the channel is described in Appendix D. The axial pressure gradient in the time dependent calculations is assumed to be fixed in time and the value calculated from the core-flow model is used. The region modeled extends well upstream of the inter-electrode insulator and the profiles at that location are assumed to be constant in time. The required upstream profiles are calculated using a steady-flow boundary layer computer program as described in reference [23]. As discussed in Section 4.2.1 the wall temperature is assumed to be constant over the plasma response time period. Solutions are sought for an impulsive application of current, so the appropriate initial condition is the steady-state distribution for no Joule heating. The initial condition is computed using the computer program, seeking a

steady-state solution starting with an initial estimate of the profile shape throughout the region.

The equations, boundary conditions and initial conditions appropriate within the above assumptions are given in Figure 64. The solution of the equations is obtained by a finite-difference technique. The finite difference scheme is organized such that transverse derivatives (including the second-order diffusion terms) are handled implicitly, while the axial derivatives, the properties and the Joule heating source terms are handled explicitly. To keep the number of grid points low, fine spacing in the desired regions is accomplished through coordinate transformation. To verify the method and the computer code, steady-state predictions from the program were compared against solutions obtained using well established boundary layer codes. For all cases, including cases with uniform and variable source terms the agreement was good. Further details of the numerical method, coordinate transformations and computer code verification are contained in Appendix E.

Electrical Behavior. A detailed electrical solution was performed to determine the total voltage and total current for the discharge, and to provide the spatial distribution of the current density from which the energy source term is evaluated. Separate solutions are obtained for the near-electrode behavior and the far-electrode behavior in order that major simplifications possible for each region can be fully exploited. The solution for the far-electrode, or outer, region is discussed first and then the near-electrode, or surface-sheath, model is treated. A more detailed discussion and quantitative check of the validity of the many assumptions is contained in Appendix F, where the general problem of computing the voltage drop in the vicinity of an electrode is discussed.

For the conditions of interest, the electric field gradient and the translational energy per molecule are relatively low in the outer region and only small differences between the electron and ion number densities can be supported. The current density and the electric field in the entire region are first calculated from the Faraday relation ($\bar{\nabla} \times \bar{E} = 0$) and the Ohm's law relation between the electric field and the current density for a charge neutral region. The density evaluated with Poisson's equation using the charge neutral solution provides a check on the assumption of charge neutrality, in particular yielding an estimate of the distance from the wall where space charge effects become important. Even for the

Axial Momentum:

$$\frac{\partial u}{\partial t} = - u \frac{\partial u}{\partial x} - v \frac{\partial u}{\partial y} - \frac{1}{\rho} \frac{dp}{dx} + \frac{1}{\rho} \frac{\partial}{\partial y} (\mu + \rho \varepsilon_m) \frac{\partial u}{\partial y}$$

$$\left.\begin{aligned} u(x,0,t) &= 0 \\ U(x,H,t) &= U_\infty(x) \\ p(x,y,t) &= p(x) \end{aligned}\right\} \quad - \frac{dp}{dx} = \frac{\rho}{2} \frac{dU_\infty^2}{dx}; \; p(x) \text{ specified.}$$

$$U(x,y,0) \quad \text{specified}$$

Energy:

$$\frac{\partial h}{\partial t} = \frac{J^2}{\rho\sigma} - u \frac{\partial h}{\partial x} - v \frac{\partial h}{\partial y} + \frac{1}{\rho} \frac{\partial}{\partial y}\left(\frac{k}{c_p} + \rho \varepsilon_H \right) \frac{\partial h}{\partial y} + \frac{u}{\rho} \frac{dp}{dx} + \left(\frac{\mu + \rho \varepsilon_H}{\rho} \right) \left(\frac{\partial u}{\partial y} \right)^2 + u \left(\varepsilon_H + \varepsilon_m \right) \frac{\partial^2 u}{\partial y^2} + \frac{u}{\rho} \frac{\partial u}{\partial y} \frac{\partial}{\partial y} \left(\rho \varepsilon_H - \rho \varepsilon_m \right.$$

$$h(x,0,t) = h_{wall}(x); \text{ specified}$$

$$h(x,H,t) = h_\infty(x); \text{ specified}$$

$$h(x,y,0) \text{ specified}$$

$$J(x,y,t) \text{ given from electrical solution}$$

Continuity:

$$v(x,y,t) = - \frac{1}{\rho} \int_0^y \left\{ \frac{\partial}{\partial t} \rho(x,\xi,t) + \frac{\partial}{\partial x} [\rho(x,\xi,t) \cdot u(x,\xi,t)] \right\} d\xi$$

Electron-Ion Continuity:

$$\frac{\partial c_e}{\partial t} = - u \frac{\partial c_e}{\partial x} - v \frac{\partial c_e}{\partial y} + \frac{1}{\rho} \frac{\partial}{\partial y} \left(\rho D_a + \rho \varepsilon_E \right) \frac{\partial c_e}{\partial y} + \frac{m_e}{\rho} \dot{n}_e$$

$$c_e(x,0,t) = c_e^*(x) \simeq 0$$

$$c_e(x,H,t) = c_e^*(x)$$

$$c_e(x,y,b) \text{ specified}$$

$$\dot{n}_e = 2.52 \cdot 10^{-33} \, n_e \exp\left[-2.98 \cdot 10^{-3} \cdot T \right] \left\{ n_e^{*2} - n_e^2 \right\} \qquad [22]$$

where the * denotes equilibrium.

Figure 64. Summary of equations, boundary and initial conditions used in modeling of the pre-breakdown and incipient breakdown plasma response. Geometry is shown in Figure 62. Fluid properties used are given in Table 11. (This figure is continued on next page.)

Transverse Momentum:

$$\frac{1}{\rho}\frac{\partial p}{\partial y} \simeq -u\frac{\partial v}{\partial x} - v\frac{\partial v}{\partial y} - \frac{\partial v}{\partial t} + \frac{1}{\rho}\frac{\partial}{\partial y}\,u\frac{\partial v}{\partial y}$$

$v(x,y,t)$, $u(x,y,t)$ from solution of above equations

Turbulence Modeling [21]:

Momentum Transport

$$\varepsilon_m = \ell_m^2\, D^2\, \left|\frac{\partial u}{\partial y}\right|$$

$$\ell_m = \begin{cases} Ky & \text{for } Ky \le \lambda_m \delta \\ (K\lambda_m \delta) & \text{for } Ky > \lambda_m \delta \end{cases}$$

$$D = 1 - \exp(-y^+/A_o^+)$$

where:

$$y^+ = y\sqrt{\rho\tau_w/\mu}$$

$$\tau_w = \mu \left.\frac{\partial u}{\partial y}\right|_{wall}$$

and $K = .41$, $A_o^+ = 24$, $\lambda_m = .085$ [21] or $= 1.0$ [23]

Energy and Species Transport

$$\varepsilon_e = \varepsilon_H = \ell_H^2\, D^2\, \left|\frac{\partial u}{\partial y}\right|$$

$$\ell_H = \begin{cases} Ky & \text{for } Ky \le \lambda_H \delta \\ (K\lambda_H \delta) & \text{for } Ky > \lambda_H \delta \end{cases}$$

D given above

and $K = .41$, $\lambda_H = .085$ [21]

Figure 64. Summary of equations, boundary and initial conditions used in modeling of the pre-breakdown and incipient breakdown plasma response. Geometry is shown in figure 62. Fluid properties used are given in Table 11.

more severe conditions, the estimates indicate that the electron and ion number densities differ by less than ≃10% at a distance from the electrode surface of $\simeq 5 \times 10^{-5}$ m.

Under the assumption of charge neutrality, the electron and ion continuity equations can be combined to form the current continuity equation

$$\bar{J} = (\mu_e + \mu_i)\, e\, n_e \left[\bar{E} + \frac{\bar{\nabla} P_e}{n_e} \right] ,$$

where μ_e and μ_i are the electron and ion mobilities respectively. If the further approximation that $\mu_i << \mu_e$ is made, and advantage is taken of the fact that in the outer region $\bar{\nabla}P/n_e$ is small relative to $\bar{E}$ for the conditions of interest, the simple Ohm's law results

$$\bar{J} = \sigma_e \bar{E} = e\, \mu_e\, n_e \bar{E} .$$

The electron number density in the region of interest is known from the fluid solution. The electron mobility is determined from the known gas temperature distribution with the assumption that the electron temperature is maintained close to the heavy gas temperature. For the two-dimensional region of interest, shown in Figure 65, the Faraday relation and Ohm's law are solved for the current density through the introduction of the current stream function ψ . For the outer solution, charge neutrality is assumed to hold across the thin inner region to the electrode surface and the electrodes are assumed to be perfect electrical conductors. The insulators on the main wall are assumed to be perfect and the opposite wall of the channel is also assumed to be perfectly insulating. The region considered extends well upstream and downstream of the inter-electrode insulator and these boundaries are also assumed to be insulating. The current density is determined from the solution for the stream function and the electric potential is determined by integration of the electric field, which is related through the Ohm's law to the current density. An inner region, or surface sheath, solution, rather than the outer solution is used to determine the voltage difference from the estimated point of failure of charge neutrality to the electrode surface.

The equations and boundary conditions for the outer region are presented along with a sketch of the region of interest in Figure 65. The solution to the elliptic boundary valued problem for the current stream

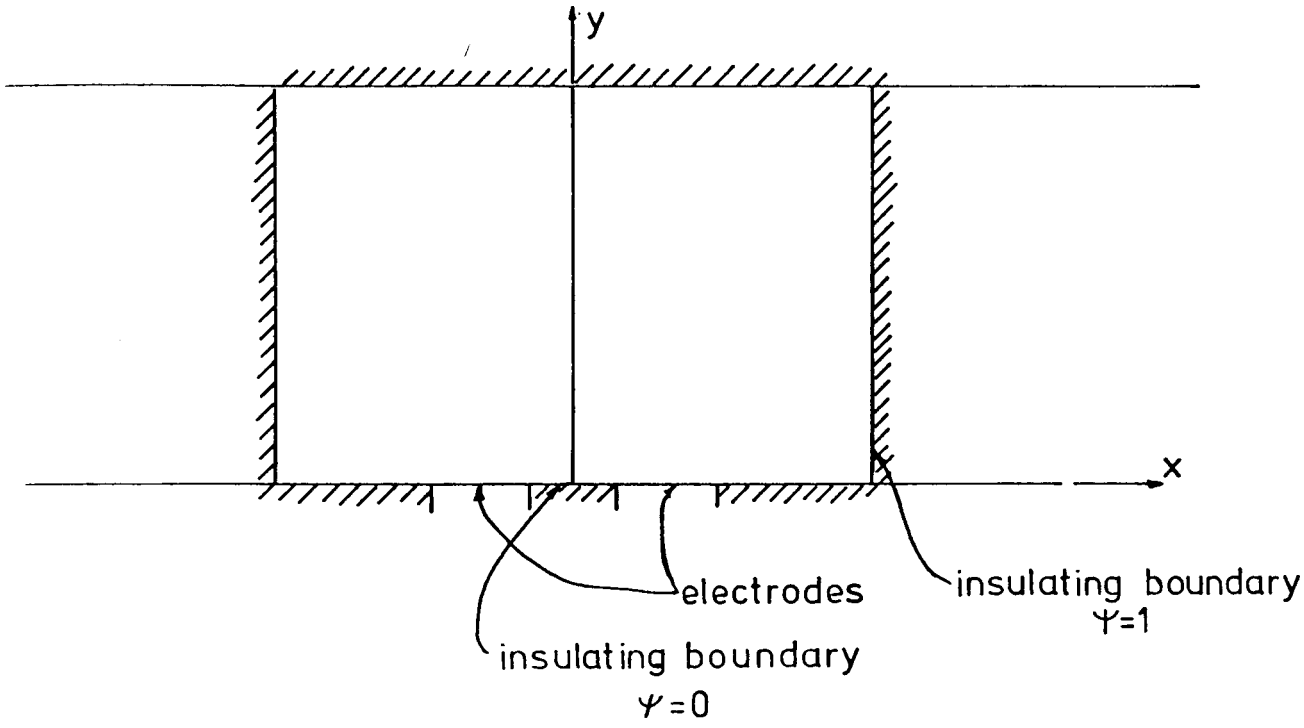

Maxwell's equations:

$$\vec{\nabla} \cdot \vec{J} = 0 \quad \text{(implies existance of 2-D stream function } \psi\text{)}$$

$$\vec{\nabla} \cdot \vec{E} = 0 \quad \text{(implies existance of potential } \phi\text{)}$$

Ohm's Law:

$$\vec{J} = \sigma \vec{E}$$

Definition of stream function:

$$J_x \equiv \frac{\partial \psi}{\partial y} ; \qquad J_y \equiv - \frac{\partial \psi}{\partial x}$$

Definition of potential:

$$E_x = - \frac{\partial \phi}{\partial x} ; \quad E_y = - \frac{\partial \phi}{\partial y}$$

Boundary value problem for stream function:

$$\frac{\partial^2 \psi}{\partial x^2} - \frac{\partial (\ell n\ \sigma)}{\partial x} \frac{\partial \psi}{\partial x} + \frac{\partial^2 \psi}{\partial y^2} - \frac{\partial (\ell n\ \sigma)}{\partial y} \frac{\partial \psi}{\partial y} = 0$$

with

$$\frac{\partial \psi}{\partial y} = 0 \quad \text{at electrodes,}$$

$$\psi = 0,1 \quad \text{on insulators as indicated above,}$$

and

$$\sigma(x,y) \quad \text{specified from fluid solution.}$$

Figure 65. Summary of geometry, equations and boundary conditions for two dimensional current distribution solution in outer region.

function was obtained by an iterative finite-difference technique. An iterative technique is advantageous since the fluid solution requires a sequence of solutions for the current distribution, with only a small alteration of the conductivity distribution between each solution. The particular technique utilized is to introduce a dummy time-dependence to the problem and then seek the steady-state solution. The resulting parobolic problem is solved using a "time-splitting" technique. For simplicity, a Locally-One-Dimensional (LOD) splitting scheme is used and each of the split equations is differenced using the Crank-Nicolson implicit difference operators. To keep the number of grid points small, fine spacing in the regions of large spatial gradients is provided through coordinate transformation. For convenience the same grid is used for both the fluid and electrical solution. To verify the method and the computer code, computed results were compared with analog results obtained using electrically resistive (Teledeltos) paper and the code was used to approximate source-sink flow in constant and variable conductivity regions. Computed and analog results were in close agreement, excepting the regions close to the singularities. Computed results for the source-sink configuration compared favorably with analytical results. Further details of the numerical method, coordinate transformations and computer code verification are contained in Appendix E.

Near the electrodes, the electric field gradient and the concentration gradients become large, necessitating a more complete consideration of the state of the plasma than is required for the outer solution. Space charge effects become important and the continuum assumptions fail very close to the wall. Further, the electron temperature may become elevated significantly above the heavy particle temperature and under some conditions the electron velocity distribution may become significantly non-Maxwellian. Charged particles must enter and leave the electrode material itself and the gas-solid interface must be considered in any complete model. Although the one-dimensional model developed for the surface-sheath considers several of the above aspects of the problem, the approach is relatively elementary and the results should be considered first order, at best. In fact, many of the aspects are poorly understood and others are exceedingly difficult to model in a more precise manner than included in the present

model. Description of the model is deferred to Appendix F, since even for this simple model the details become rather involved.

Thermal and Electric Properties and Curve-fits. The equilibrium thermal and electrical properties used in the plasma calculations were provided by an equilibrium chemical composition and properties computer program EQUIPROP developed by Pepper [25]. For convience and speed of calculation curve-fits of the required properties as a function of enthalpy and pressure were developed and used in the calculations. The functional form of the property curve-fits are given in Table 11.

4.3.3 Insulator Modeling

This section describes two models developed to predict the thermal and electrical response of the inter-electrode insulator for pre-breakdown and incipient breakdown operation. In both models the insulator conductivity is considered to depend only on temperature, and the heat conduction equation including Joule heating effects is used to describe the insulator behavior. Description of the insulator behavior for the full range of inter-electrode gap sizes of interest and account of the spatial distribution in gas-side heat flux would require a three-dimensional heat conduction and electrical current distribution solution. While such a solution is certainly possible, computations would be extremely expensive and the complexity most likely unjustified, considering the uncertainty in the high temperature insulator properties and in the gas-side heat transfer rates. A one-dimensional model, discussed first, is used to describe approximately the insulator behavior for relatively large gaps. Experience with the simple conduction models suggests that the overall features will be well modeled, and that a reasonable estimate of the critical field will be obtained using the one-dimensional model. A two-dimensional model, discussed second, is used to approximate the behavior for relatively small insulator gaps and to refine the breakdown threshold prediction for large insulator gaps by removing the restriction that current constrictions must be planar.

One-Dimensional Model for Large Gaps. For relatively large insulator gap size and depth, heat conduction to the rear-face is most important and an approximate model, neglecting heat conduction to the electrodes and side-walls and using a spatially averaged gas side heat transfer coefficient, can be employed. Within these approximations, the one-dimensional heat

Table 11. Functional form of fluid property curvefits used in fluid solution for plasma response. Curvefits are intended for relatively small pressure range (within ~10-20% of p_{ref}). Two ranges in enthalpy usually utilized to yield more accurate results.

Density:

$$\rho = (a^{\rho} + b^{\rho}\, h + c^{\rho}\, h^2 + d^{\rho}\, h^3)\; p/p_{ref}$$

Viscosity:

$$\mu = (a^{\mu} + b^{\mu}\, h + c^{\mu}\, h^2 + d^{\mu}\, h^3)$$

Prandtl Number:

$$Pr = (a^{Pr} + b^{Pr}\, h + c^{Pr}\, h^2 + d^{Pr}\, h^3)$$

Temperature:

$$T = (a^{T} + b^{T}\, h + c^{T}\, h^2 + d^{T}\, h^3)$$

Equilibrium Electrical Conductivity:

$$\sigma_e^* = (p_{ref}/p)^{f(\hat{h})}\; \exp\,(a^{\sigma} + b^{\sigma}\, h + c^{\sigma}\, h^2 + d^{\sigma}\, h^3)$$

where

$$\hat{h} = \frac{h_{ref} - h}{h - h(0\ K)}$$

with h_{ref} chosen as the enthalpy at the highest temperature of interest and h(T = 0 K) obtained by extrapolation, and usually

$$f(\hat{h}) = e^{\sigma} + f^{\sigma}\, \hat{h}$$

Electron Mobility:

$$\mu_e = (a^{m} + b^{m}\, h + c^{m}\, h + d^{m}\, h)\; (p_{ref}/p)^{n}$$

Equilibrium Electron number Density:

$$\eta_e^* = \sigma_e^*/\, e\, \mu_e$$

conduction equation, including the Joule heating source term, will describe the behavior. The gas-side convective heat transfer rate is obtained from the plasma solution and an "equivalent conductance" added to account approximately for radiation from the plasma and hot side walls. The rear-face of the insulator is assumed to conduct heat through a known thermal resistance to a fixed temperature wall. Solutions are obtained for an impulsive application of current, so the appropriate initial condition is the temperature distribution with no Joule heating. This solution is obtained by using the model to calculate the steady-state profile starting from a cold insulator, with the rear-face thermal resistance adjusted to yield the desired surface temperature. A constant axial electric field is assumed such that the current density varies simply as $J_x(y) = \sigma(y)E_x$. Electrical contact resistance between the electrode and insulator is neglected and the total resistance of the region is computed by averaging the electrical conductivity across the insulator.

The equations, boundary conditions and initial conditions for the problem are presented together with a sketch in Figure 66. The solution for the equations was obtained by an implicit finite difference technique.

Two-Dimensional Model. For small gaps an approximate solution, including heat transfer to the electrodes but assuming the temperature of the insulator is constant in the axial direction, can be employed. A sketch of the configuration displaying the important features is shown in Figure 67. Within this framework, a two-dimensional heat conduction solution with a lateral heat loss (that is heat loss to the electrodes) and a Joule heating source term should adequately describe the behavior. The model can also be used as an improved model for large gaps, still requiring an averaging in the axial direction, but allowing current constrictions to form in two dimensions. Conduction from the insulator to the electrodes is assumed to be the dominant lateral heat transfer mechanism, with the thermal resistance evaluated from an estimated percentage contact and surface roughness dimension. The gas-side heat transfer rate is assumed to vary only in the transverse (z) direction, with the plasma solution providing the heat transfer rate (averaged across the insulator gap) as a function of surface temperature and transverse position. The insensitivity of plasma resistance to insulator surface temperature (for temperatures $\lesssim 2400$) allows the current per unit width to be assumed constant over the

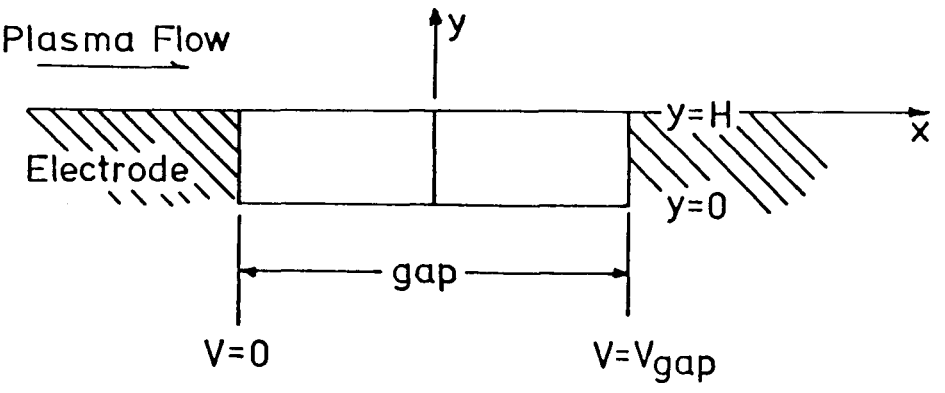

One-Dimensional Heat Conduction for insulator

$$\rho c \frac{\partial T}{\partial t} = \frac{\partial}{\partial y} k \frac{\partial T}{\partial y} + \bar{J} \cdot \bar{E}$$

$$k \frac{\partial T}{\partial y}(H,t) = h_{plasma}\left[T(H,t),\ I_{plasma}(t)\right]\left[T_{\infty} - T(H,t)\right]$$

$$k \frac{\partial T}{\partial y}(0,t) = h_{coolant}\left[T(0,t) - T_{coolant}\right]$$

with $h_{plasma}(T, I_{plasma})$ specified by the plasma solution

$\bar{J} \cdot \bar{E}$ specified from the electrical solution

$T(y,0)$ specified

One-Dimensional Current Distribution for insulator

$$\bar{J} = J_x(y,t)\underline{i}\ ,\ \bar{E} = E_x(t)\underline{i} = \frac{V_{gap}(t)}{gap}$$

with $J_x(y,t) = \sigma(y,t)\, E_x(t)$

with $\sigma(y,t)$ given from the thermal solution.

$$R_{ins}(t) = \frac{gap}{width} \Big/ \int_0^H \sigma(y,t)\, dy$$

with V_{gap}, I_{plasma} evaluated by consideration of the overall electrical circuit

Figure 66. Summary of geometry, equations, boundary and initial conditions for one-dimensional model of inter-electrode insulator pre-breakdown and incipient breakdown behavior. Material properties given in Table 12.

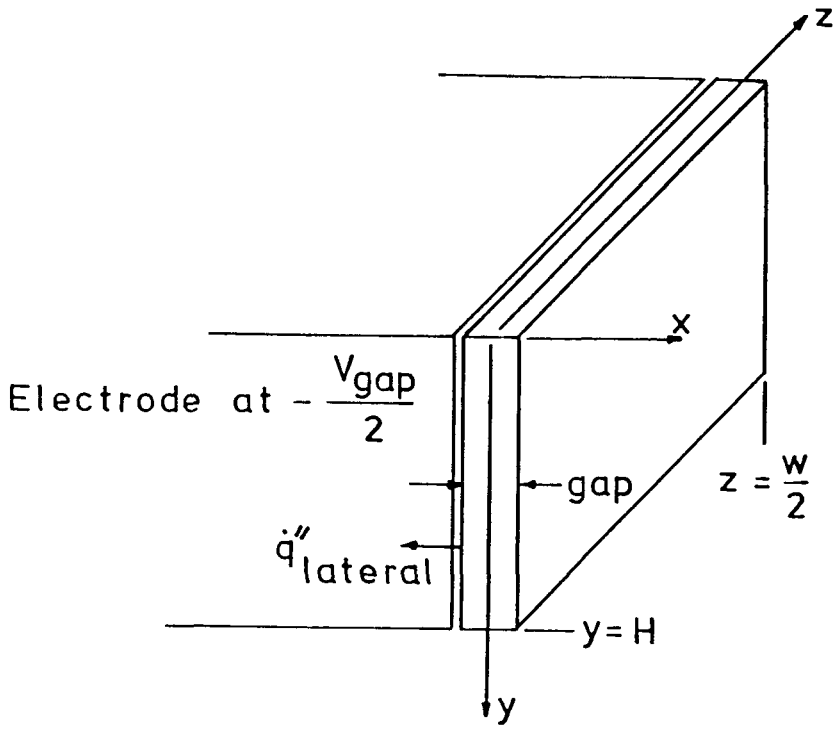

Two-Dimensional Heat Conduction with lateral losses.

$$\rho c \frac{\partial T}{\partial t} = \frac{\partial}{\partial y} k \frac{\partial T}{\partial y} + \frac{\partial}{\partial z} k \frac{\partial T}{\partial z} + \bar{J}\cdot\bar{E} + 2\, h_{contact}\left[(T_{electrode}-T)\right]$$

$$-k\frac{\partial T}{\partial y}(0,z,t) = h_{plasma}\left(T(0,z,t), I_{plasma}(t), z\right)\left[T_{\infty}(z)-T(0,z,t)\right]$$

$$-k\frac{\partial T}{\partial y}(H,z,t) = h_{coolant}\left[T(H,z,t) - T_{coolant}\right]$$

$$\frac{\partial T}{\partial z}(y,0,t) = 0$$

$$+k\frac{\partial T}{\partial z}(y,w/2,t) = h_{coolant}\left[T(y,w/2,t) - T_{coolant}\right]$$

$$T(y,z,0) \text{ specified}$$

$$T_{electrode} = T_{electrode}(y) = T_{surf.\ electrode} - \frac{y}{H}(T_{surf}-T_{coolant})$$

Current Distribution for insulator

$$\bar{E} = E_x(t)\underline{i} = \frac{V_{gap}(t)}{gap}\,\underline{i}\ ;\ J_x(y,z,t) = \sigma(y,z,t)\ E_x(t)$$

with $\sigma(y,z,t)$ given from the thermal solution.

The insulator resistance is

$$R_{ins}(t) = gap \Big/ \int_{w/2}^{w/2}\int_{0}^{H} \sigma(y,z,t)\, dy\ dz$$

Figure 67. Summary of geometry, equations, boundary and initial conditions for two dimensional model of inter-electrode insulator pre-breakdown and incipient breakdown behavior. Material properties given in Table 12.

Table 12. Property variations for insulator materials used in calculations for applied field configuration.

Magnesium Oxide

Thermal Conductivity (w/m-K):

$T<2100$ K $\quad k = a + bT + cT^2 + dT^3 + eT^4 \quad$ (T in K)

$a = 78.43$

$b = -.1703$

$c = .160 \times 10^{-3}$

$d = -.7182 \times 10^{-7}$

$e = .1276 \times 10^{-10}$

$T \geq 2100 \quad k = 10.53 + (T - 2100) * .017 \quad$ (T in K)

Specific Heat (J/kg-K):

$c = 886 + .432 * T \quad$ (T in K)

Density (kgm/m^3):

$\rho = 1700/(1 + 3\alpha * T) \quad$ (T in K)

$\alpha = 13 \times 10^{-6}$

Electrical Conductivity:

$\sigma = .12 \exp [\ 21.5\ (1 - 1900/T)] \quad$ (T in K)

Melting Point: 3200 K (pure)

Aluminum Oxide (96% Al_2O_3)

Thermal Conductivity (w/m-K):

$k = 34.4 - 6.6 \times 10^{-2}\ T + 3.76 \times 10^{-5}\ T^2 \quad$ (T in K)

Specific Heat (J/kg-K):

$c = 1084 + .11 \times T \quad$ (T in K)

Density $= 3700./(1 + 3\alpha * T) \quad$ (T in K)

$\alpha = 8 \times 10^{-6}$

Electrical Conductivity (mho/m):

$\sigma = 3 \times 10^{-5} \exp\ (7.7\ (1 - 1000/T)) \quad$ (T in K)

channel width. The rear-face and side edges of the insulator are assumed to conduct heat through a known thermal resistance to a fixed temperature wall. The temperature of the electrodes is assumed to drop linearly from the surface temperature to the coolant temperature, with the surface temperature assumed constant in the transverse direction. The electrode temperature distribution is fixed in time. Solutions are obtained for an impulsive application of current, so the appropriate initial condition is the temperature distribution with no Joule heating. This solution is obtained by using the model to calculate the steady-state distribution starting from a cold insulator.

A constant axial field is assumed so variations in the current density simply reflect variations in the two-dimensional temperature field. The total resistance is calculated from the spatial average of electrical conductivity for the insulator. An electrical contact resistance between the insulator and the electrode can be included in a manner similar to the thermal contact resistance; the contact characteristics assumed for the calculations will be presented when the results are discussed.

The equations, boundary conditions and initial conditions for the problem are presented in Figure 67. The temperature distribution was assumed to be symmetric about the centerline of the channel and a solution for the half-region was obtained using a finite-difference technique. An alternating-direction implicit technique was used to obtain the solution and a coordinate transformation used to obtain suitable resolution in regions of large gradients while keeping the number of grid points small. The computer code was verified by comparison of predicted transient and steady-state results with analytical solutions.

Thermal and Electrical Properties for Insulator Materials. Thermal properties of magnesium oxide are available in standard handbooks [26] for temperatures up to ≃ 2200 K. These properties and extrapolations for the higher temperatures are employed in the present calculations. Electrical conductivity measurements for magnesium oxide have been performed by Norton (a manufacturer), Pratt and Whitney [27], by Sonju [28], and are reported in part in standard handbooks [26] for temperatures as high as ≃ 2375 K. The results are summarized in Figure 68, a replot of the summary figure presented by Sonju with data from reference 26 added. Good agreement is observed between the data of Norton, Pratt and Whitney and the oven tests

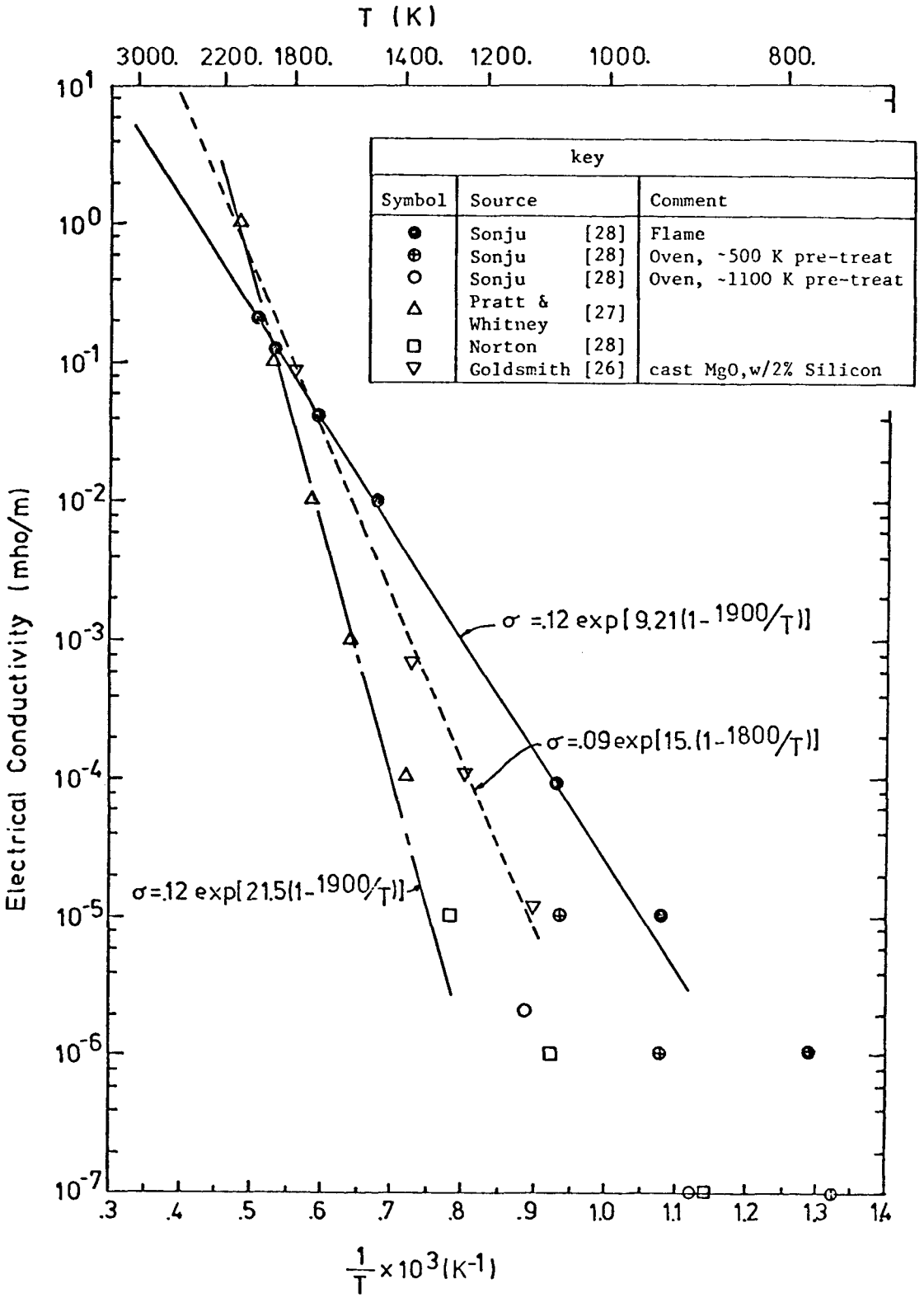

Figure 68. Electrical conductivity data for Magnesia, taken from Sonju [28] and Goldsmith et al. [26].

of Sonju for which high temperature pre-testing was performed. The remainder of the data display considerably different conductivity dependences, although all indicate that the functional form

$$\sigma = \sigma_{ref.} \exp A(1 - T_{ref.}/T)$$

should well represent the data except at low temperatures. This functional form is in accord with simple analytical results for solid dielectrics and the trend at lower temperatures indicated by the data is similar to that exhibited by several dielectric materials [19]. Sonju attributes the discrepancy between his flame data and the Pratt and Whitney data to non-uniformities in temperature existing in his experiments; however the discrepancy is larger at lower temperatures, which does not seem consistent with that explanation. Further, the importance of pre-treating temperature was demonstrated in Sonju's oven tests and it seems equally plausible that differences in pre-treating conditions and in material preparation are responsible for the discrepancy. For this study the electrical conductivity is assumed to obey the foregoing functional form with the constants chosen to represent the Pratt and Whitney and Norton data. The sensitivity of the predicted results to the values of the constants is discussed later.

Thermal and electrical properties for alumina can be obtained from standard handbooks [26] and from manufacturers handbooks [29].

The property dependances used in the calculations are summarized in Table 12.

4.3.4 Presentation of Results

In this section the general characteristics of the pre-breakdown and incipient breakdown model are presented. Results for fixed insulator temperature are first discussed, so that the behavior of the plasma can be directly observed. The total voltage versus total current curve is discussed first, and then the predicted characteristics of breakdown itself are discussed. The influence of several parameters on the voltage-current characteristic curve and on the predicted breakdown threshold voltage is then presented. The discussion of the results including the insulator response is developed in the same manner.

Behavior for Fixed Insulator Temperature. This section discusses the behavior of the inter-electrode insulator region over a time period during which the inter-electrode insulator temperature can be assumed to be fixed. The results for the outer region are represented in Figure 69, by a typical voltage-current characteristic for the region. The results displayed were obtained for a 1.5 cm inter-electrode insulator at a surface temperature of 1800°K and for plasma flow conditions and insulator wall geometry typical of the experiments. Additional conditions are listed in Table 13. As can be observed in Figure 69, the voltage rises roughly linearly with current for currents less than $\simeq$ 30 amps, with a low current resistance of $\simeq$ 5.8 ohms. At approximately 60 amps, the voltage reaches a maximum of $\simeq$ 240 volts and increases in current beyond this level result in a decline in voltage. The maximum represents a threshold level for planar thermal breakdown of the plasma and this behavior will be discussed later in the section.

The voltage-current characteristic for the inner region, under conditions where diffuse operation is possible, are shown in Figure 70; pertinent conditions are shown in the figure. The cathode surface-sheath voltage drop predicted using the one-dimensional model becomes extremely large at a very small current level ($I_{total} \lesssim .5$ amps). This indicates that breakdown to an arc mode across the very small inner region must occur if reasonable current levels are to be extracted from the cathode. This prediction is consistent with the experimental data, however, no quantitative results can be obtained for the cathode with the model. The surface-sheath voltage drop for the anode is slightly negative at zero current and increases monotonically to the highest current. The voltage drop leveling out at the higher currents.

The current streamlines for a moderate current level (I $\simeq$ 30 amps) are plotted in Figure 71 and give a good overall view of the current distribution. A plot of the current density as a function of position along the electrode for a moderate current level ($I_{total} \simeq$ 25 amps) is shown in Figure 72. As expected there is a concentration of current at the electrode edge closest to the other electrode. The effect of total current on the current distribution in the axial direction is shown in Figure 73, where the fraction of current leaving the downstream quarter of the upstream electrode is plotted as a function of total current. As can be observed

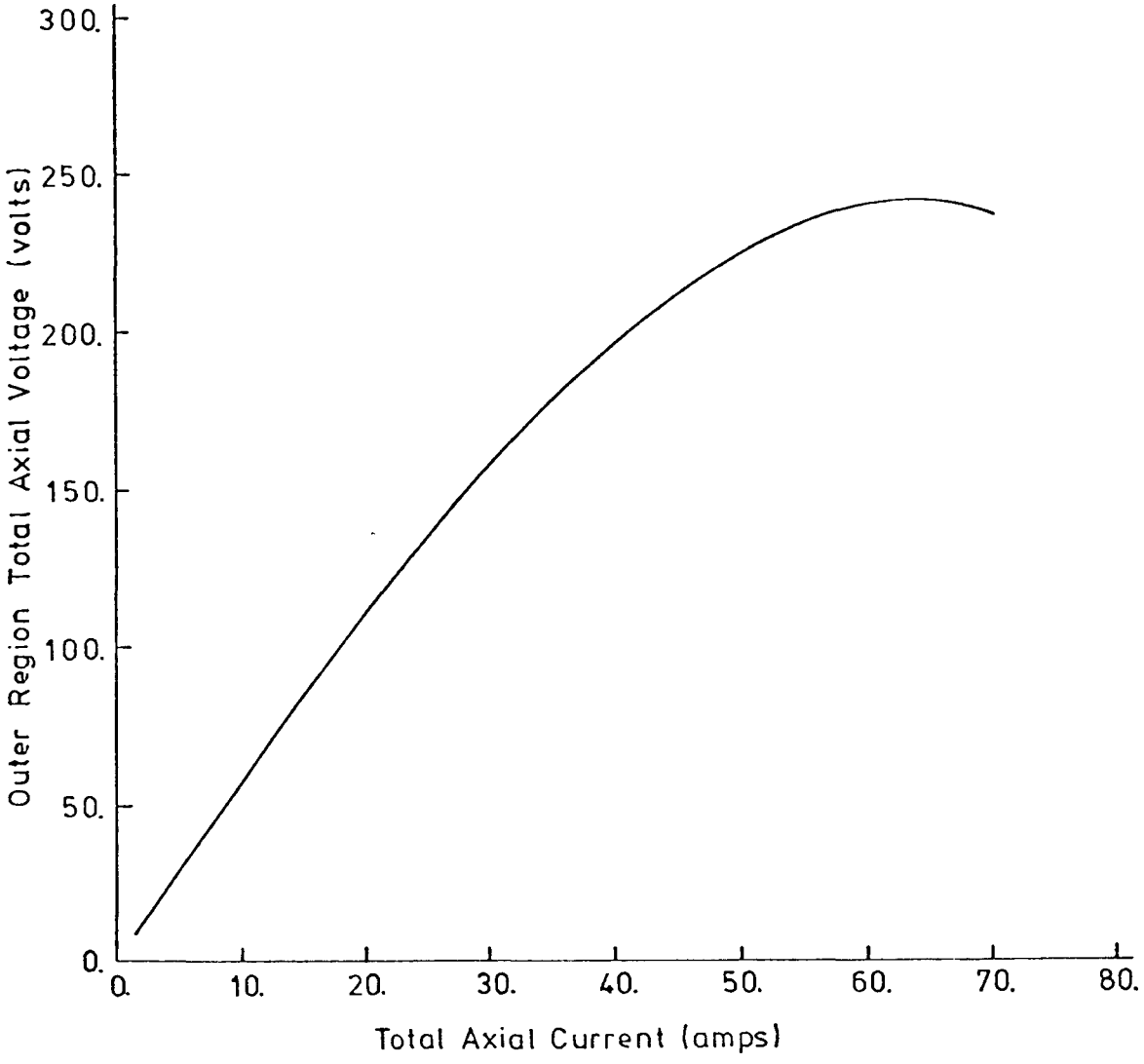

Figure 69. Steady-state total axial voltage versus total axial current for fixed wall temperature. Anode and cathode surface-sheath voltage drops are not included in the calculation. Conditions used in the calculations are specified in Table 13.

Table 13. Base conditions for calculations presented in figures 69-87. Conditions altered for particular calculations are stated.

Flow Conditions:

Velocity - 250 m/sec

Pressure - 1 bar

Temperature - 2630 K

Conductivity - 9.8 mho/m

Boundary Layer Thickness - $\sim$0.8 cm

Channel Dimensions:

Nozzle Exit to Insulator Centerline - 24.9 cm

Channel Height - 10.0 cm

Effective Channel Width - 3.1 cm

Electrode Wall Dimensions:

Electrode Length - 2.8 cm

Inter-Electrode Insulator Width - 1.5 cm

Electrode Wall Conditions:

Upstream and Downstream Insulator Temperature - 1800 K

Electrode Temperature - 1400 K

Inter-Electrode Insulator Temperature - 1800 K

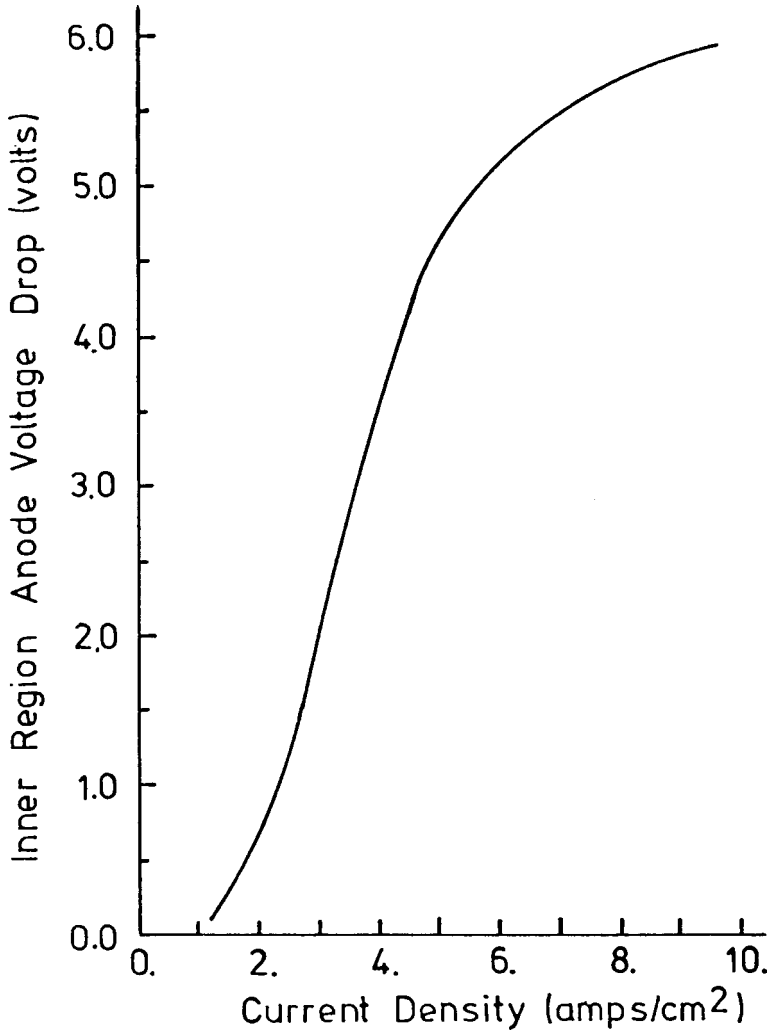

Figure 70. Inner-region anode voltage drop as a function of current density. Calculation method and conditions are discussed in detail in Appendix F.

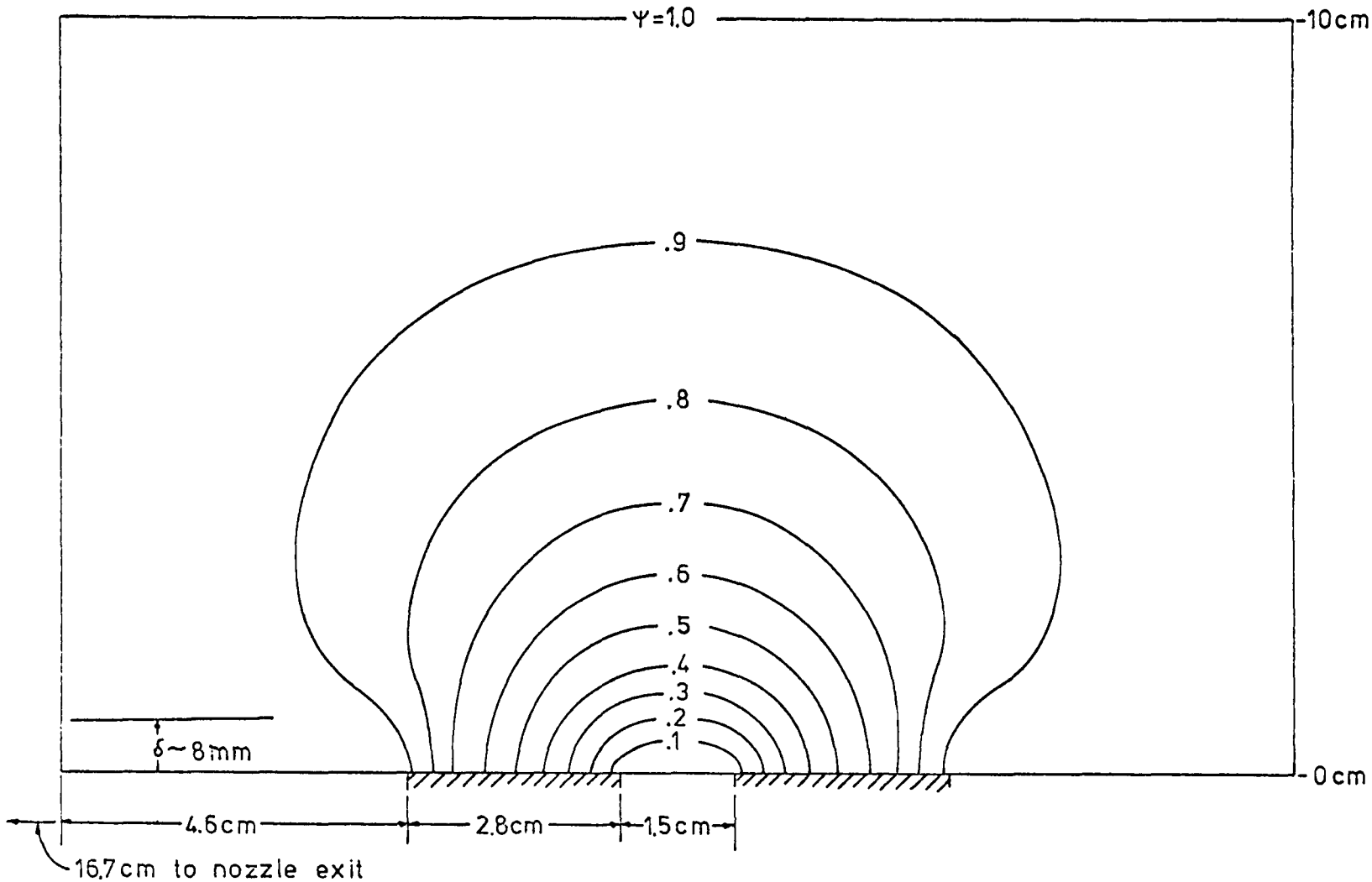

Figure 71. Current streamlines for moderate current (I = 30 amps) level and conditions as specified in Table 13.

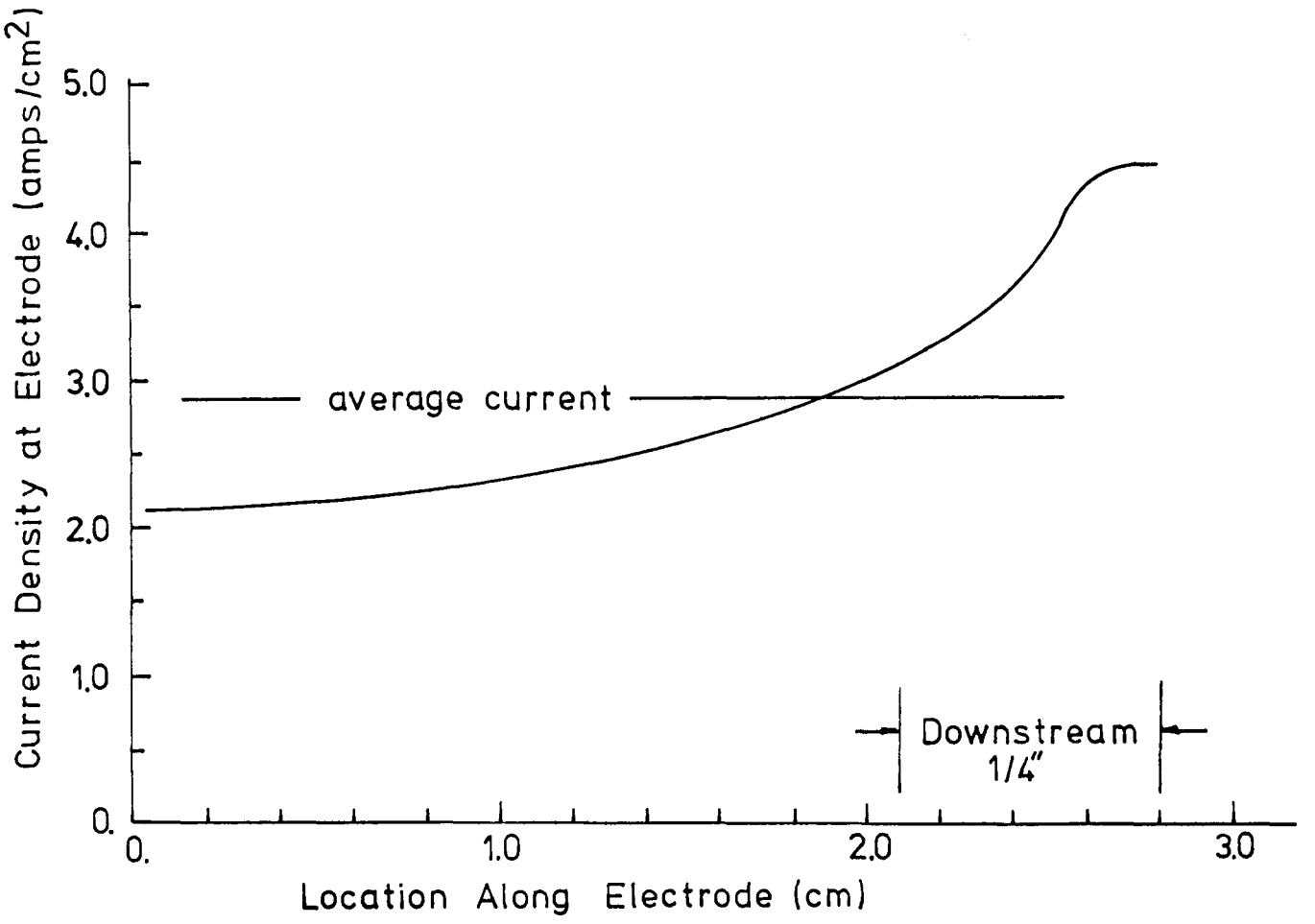

Figure 72. Current density leaving electrode as a function of position along the electrode. Conditions as specified in Table 13, with a total axial current of 25 amps.

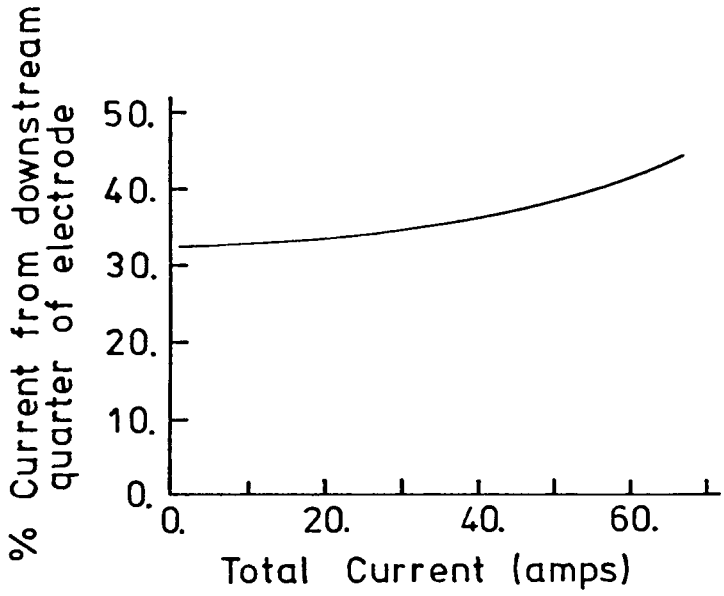

Figure 73. Fraction of current leaving downstream quarter of upstream electrode as a function of total axial current. Conditions as specified in Table 13.

in the figure, a moderate shift in current is predicted with increased total current. The distribution of current across the channel width is represented in Figure 74 and shows the mild concentration of current toward the channel centerline resulting from the sidewall boundary layers.

The potential distribution in the general vicinity of the electrodes is represented in Figure 75a, where the voltage difference between a point near the upstream electrode and the upstream electrode surface is plotted as a function of total current. Results are presented for different distances from the electrode surface and as can be seen in the figure the voltage drop increases linearly with total current to current levels of $\simeq$ 30 amps after which a leveling out occurs. The potential distribution as a function of distance from the wall for a total current of $\simeq$ 30 amps is displayed in Figure 75b. The average electric field is also shown in the figure and, as expected, the electric field decreases with distance from the wall, with a level of $\simeq$ 10 volts/mm indicated at a distance from the wall of $\simeq$ 2 mm. The potential distribution for the region away from the electrodes is displayed in Figure 76a, where the axial electric field as determined by dividing the voltage difference between two axial locations by their separation, is plotted as a function of total current. The electric field increases roughly linearly with current indicating that little effect of Joule heating results in the far electrode region. The influence of separation on the electric field determination is displayed in Figure 76b and indicates that the calculated electric field is little affected by spacing provided the spacing is not too much greater than the insulator gap. Distance of the measurement points from the wall has a more significant effect on the electric field inferred, as is shown in Figure 76c, with higher fields resulting when the measurement points are closer to the electrodes and thus more of the near-electrode voltage drop is included in the measurement. The above observations indicate the difficulty of comparing electric field measurements of different experiments when the probe locations are different.

Gas temperature, electron number density, axial current density and axial velocity profiles at the inter-electrode insulator centerline are presented in Figures 77a-d for three levels of total axial current. As can be observed in the figures, the gas temperature declines from the core level to the wall level, indicating the equilibrium electron number density

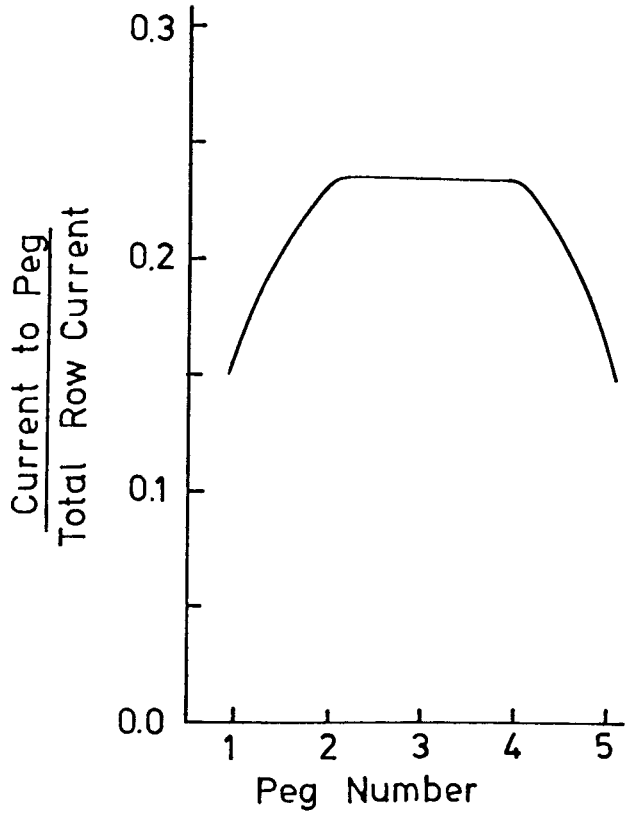

Figure 74. Calculated distribution of current across channel width. Distribution represented as fraction of current collected by five equal segments across the channel width. Conditions for calculations specified in Table 13.

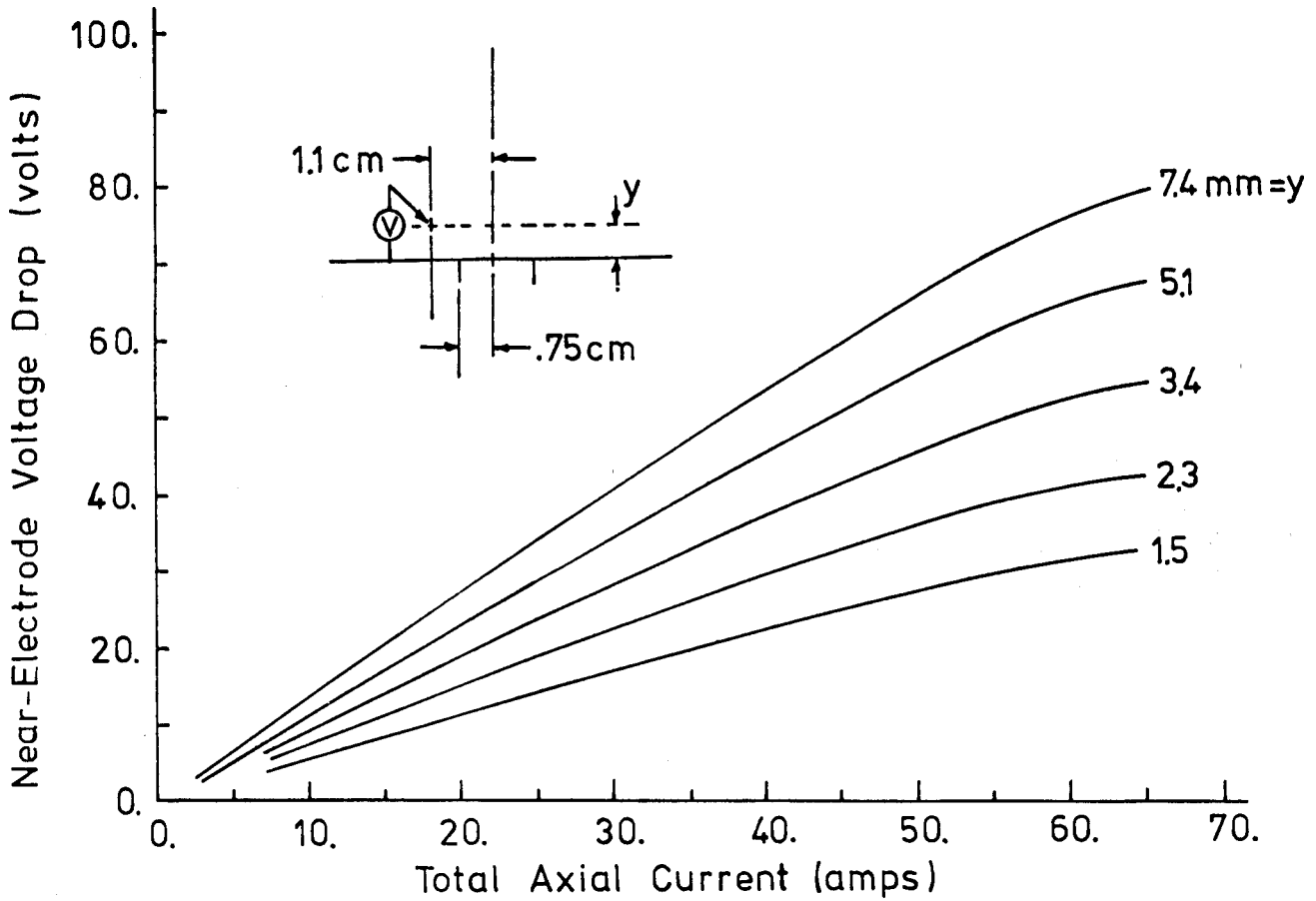

Figure 75a. Near-electrode voltage drop as a function of total axial current, for different locations above the electrode surface. Surface-sheath voltage drop not included. Conditions as specified in Table 13.

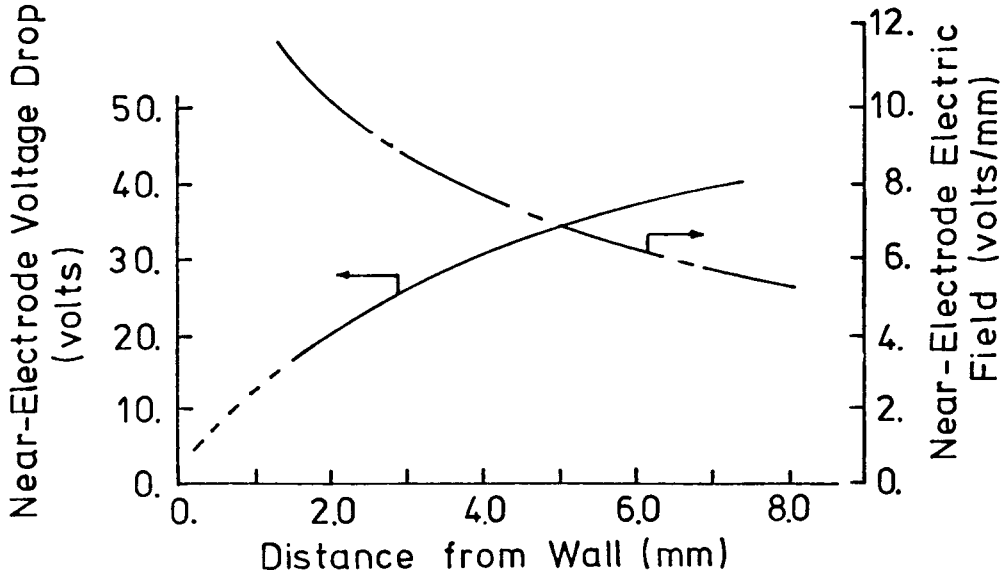

Figure 75b. Near-electrode voltage drop and average near-electrode electric field as a function of distance from the wall. Surface-sheath voltage drop is not included. Conditions as specified in Table 13, with a total current of 30 amps.

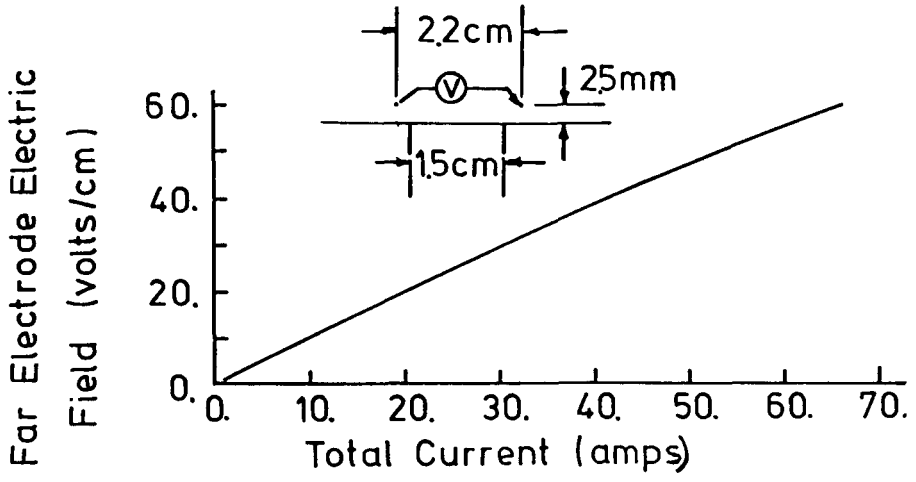

Figure 76a. Electric field in region away from the electrodes as a function of total current. Sketch identifies the location of the voltage measurements.

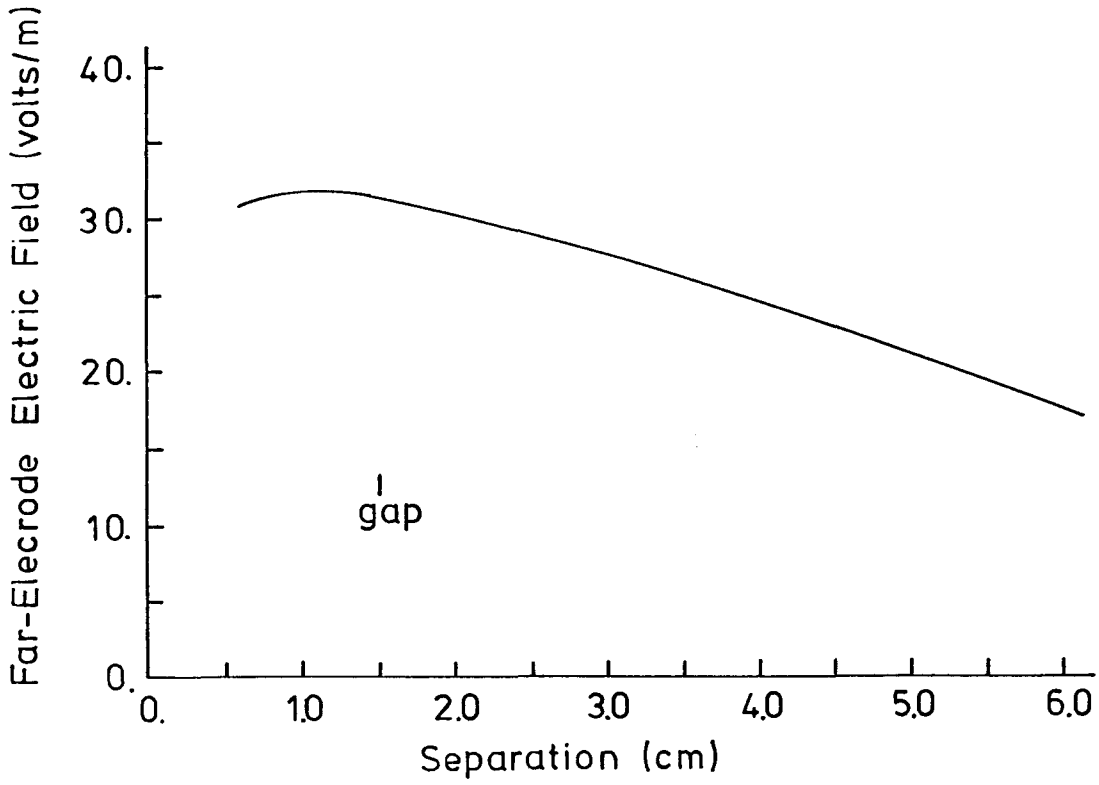

Figure 76b. Axial electric field as a function of separation of locations across which the voltage difference is measured. Measurements made 7.4 mm from electrode surface. Conditions as specified in Table 13, with a total current of 30 amps.

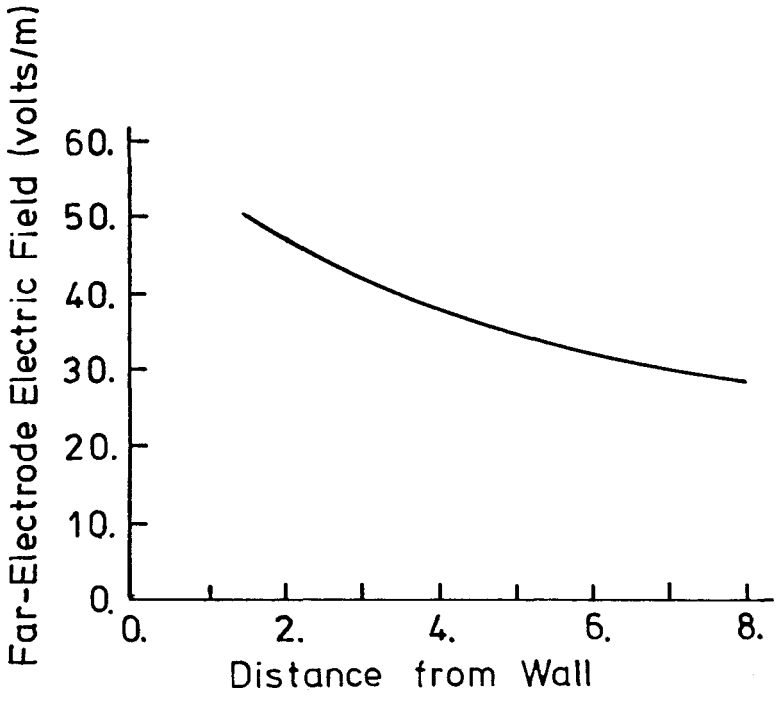

Figure 76c. Axial electric field as a function of distance from the wall. Electric field computed as voltage difference divided by axial spacing of voltage probes (= 2.2 cm). Conditions as specified in Table 13, with a total current of 30 amps.

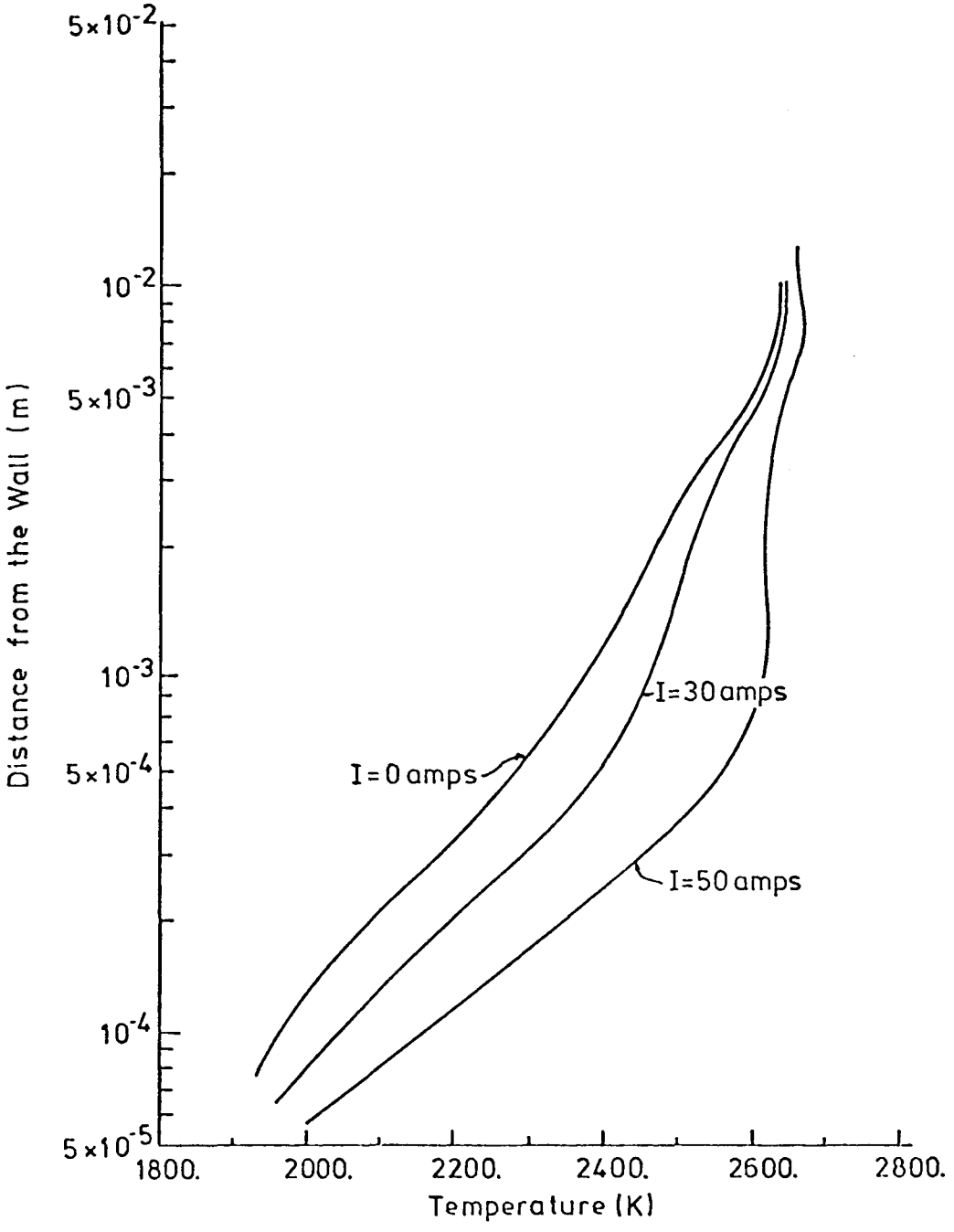

Figure 77a. Temperature profile at inter-electrode insulator center-line for three levels of total axial current. Conditions for calculations specified in Table 13.

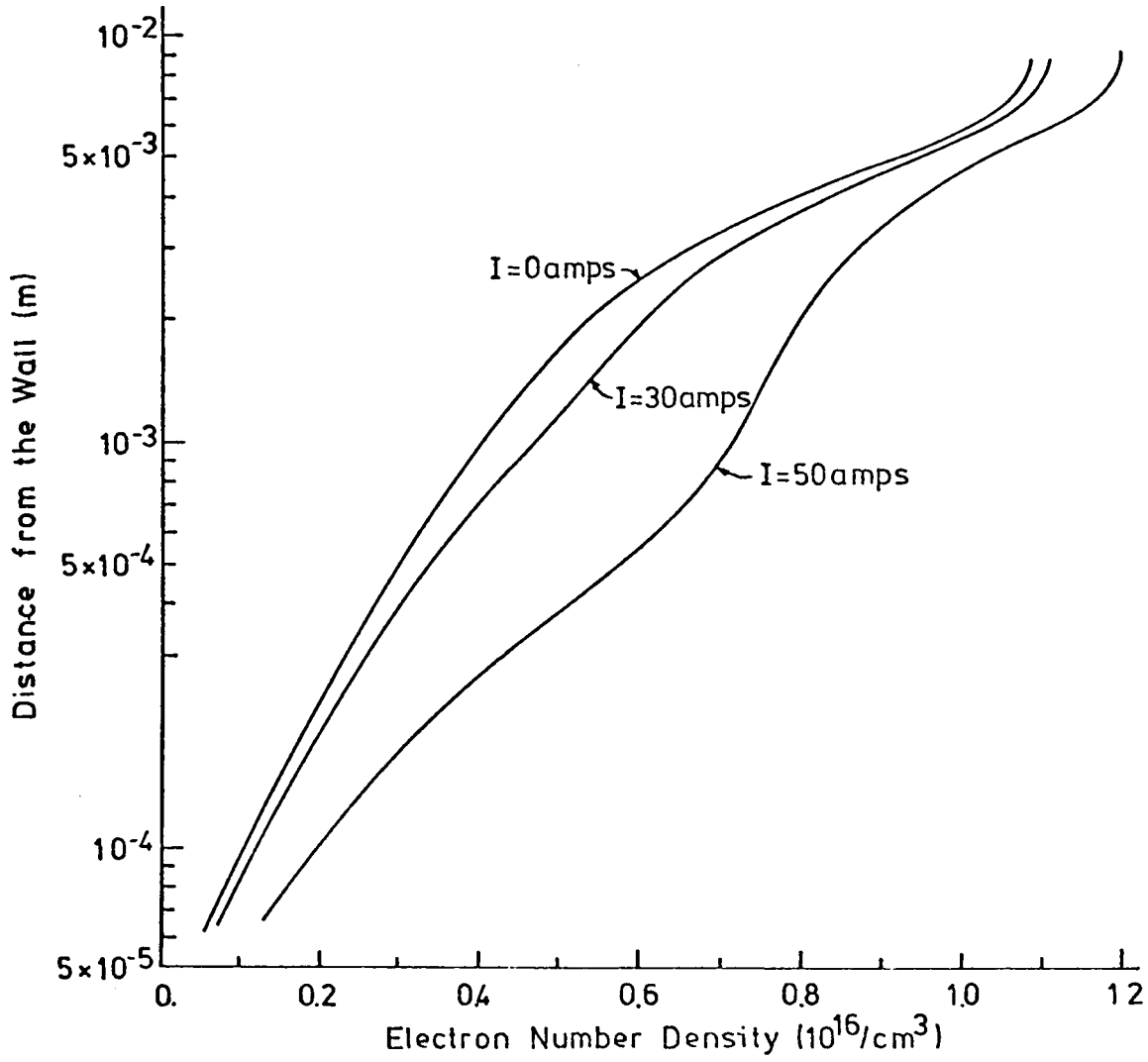

Figure 77b. Electron number density profile at inter-electrode insulator center-line for three levels of total axial current. Conditions for calculations specified in Table 13.

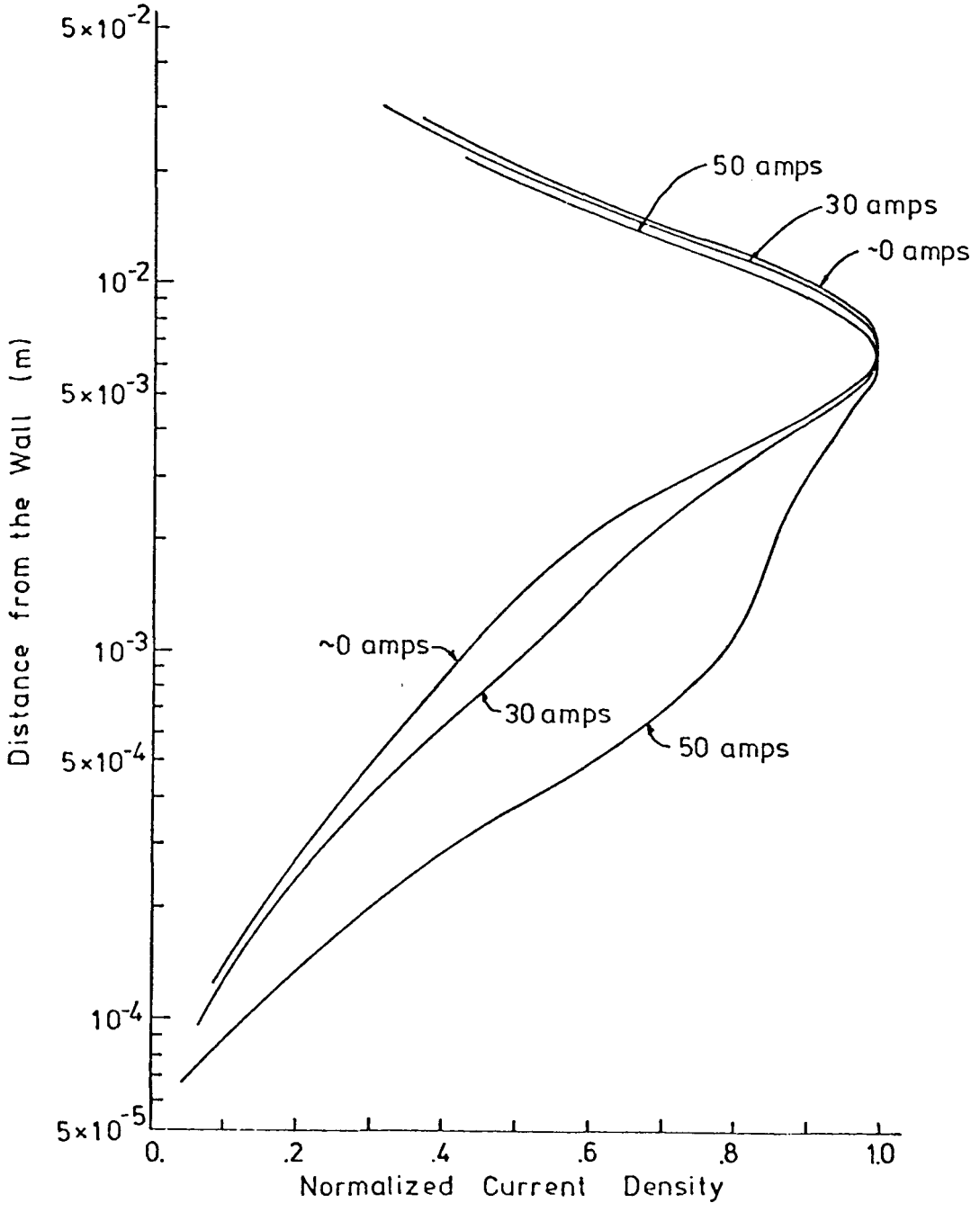

Figure 77c. Profiles of axial current density (normalized by the maximum) at inter-electrode insulator center-line for three total axial current levels. Conditions for calculations specified in Table 13.

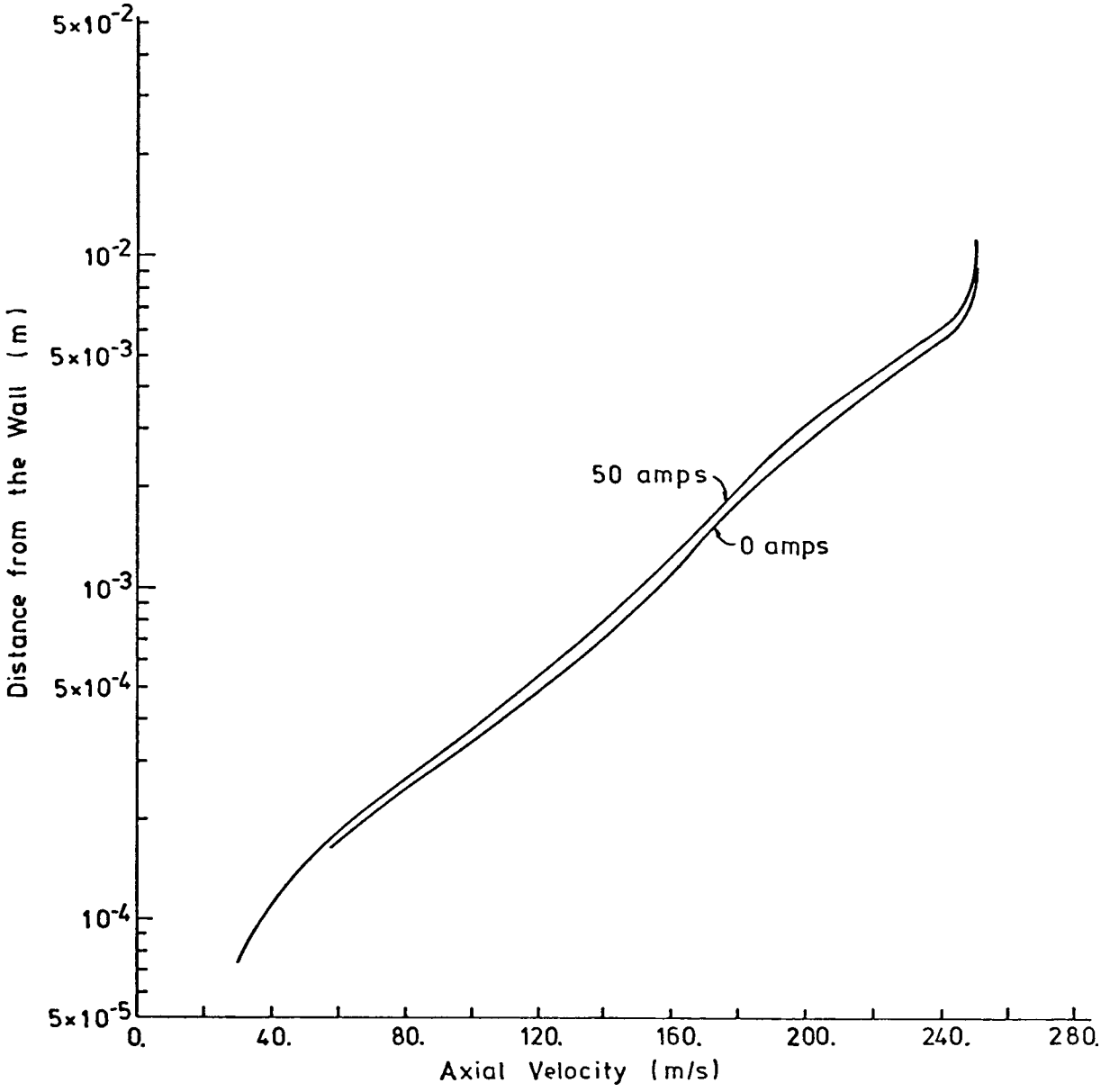

Figure 77d. Profiles of axial component of velocity at inter-electrode insulator centerline for two levels of total axial current. Conditions for calculations specified in Table 13.

will drop quite rapidly as the wall is approached. The calculated, or kinetic, electron number density follows the equilibrium level only to $y \simeq 1$ mm , with the electron number density in the region closer to the wall controlled predominantly by convection and diffusion. The current density peaks at about 6 mm from the wall, a distance corresponding roughly to the edge of the boundary layer. As expected Joule heating of the plasma results in an increase in the gas temperature, the electron number density and the axial current density in the near wall region. The axial component of velocity is little affected by increases in current. The variation of gas temperature with total current is displayed in Figure 78 for three locations above the inter-electrode insulator at the centerline. At a distance of 1.2 mm from the wall the temperature rises by $\simeq$ 150 K over the no current level when a total current of $\simeq$ 45 amps is passed between the electrodes. Smaller changes are observed for locations more distant from the wall and no significant change is observed at the boundary layer edge.

The significance of the voltage maximum in the voltage-current curve can be illustrated by comparing the transient response of the inter-electrode region for two combinations of supply voltage and load resistance. The transient response of total voltage, total current and gas temperature at a distance of $\sim$ 1 mm above the inter-electrode insulator surface are shown in Figure 79, with the steady-state voltage-current characteristic and the external load lines shown for reference. The dashed curves, obtained for a supply voltage of 450 volts and a ballast resistance of 6.5 ohms become steady after $\sim$ .3 milliseconds at levels not extremely different from their initial levels. The solid curves, obtained for a supply voltage of 400 volts and a ballast resistance of 2.0 ohms, do not reach a steady-state but rather display a runaway behavior. The axial current density and gas temperature profiles at the inter-electrode insulator centerline are displayed for three different times in Figure 80, and show that this second combination of supply voltage and ballast resistance results in the formation of a planar current sheet at a distance of $\sim$ 1 mm above the inter-electrode insulator. The model predicts a timescale for the breakdown of $\lesssim$ 1 millisecond and predicts that no delay separates the initiation of current and the breakdown. For an external circuit capable of providing a fixed voltage at all current levels, thermal breakdown will

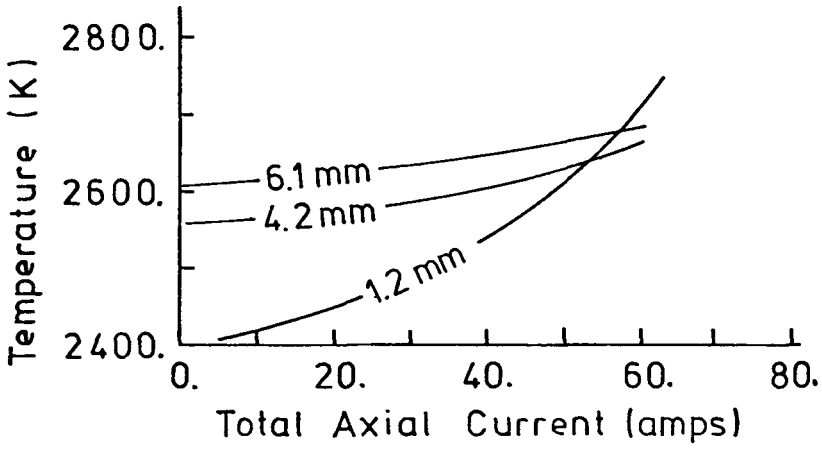

Figure 78. Temperature at the inter-electrode centerline as a function of total axial current for several distances from the wall. Conditions for calculations specified in Table 13.

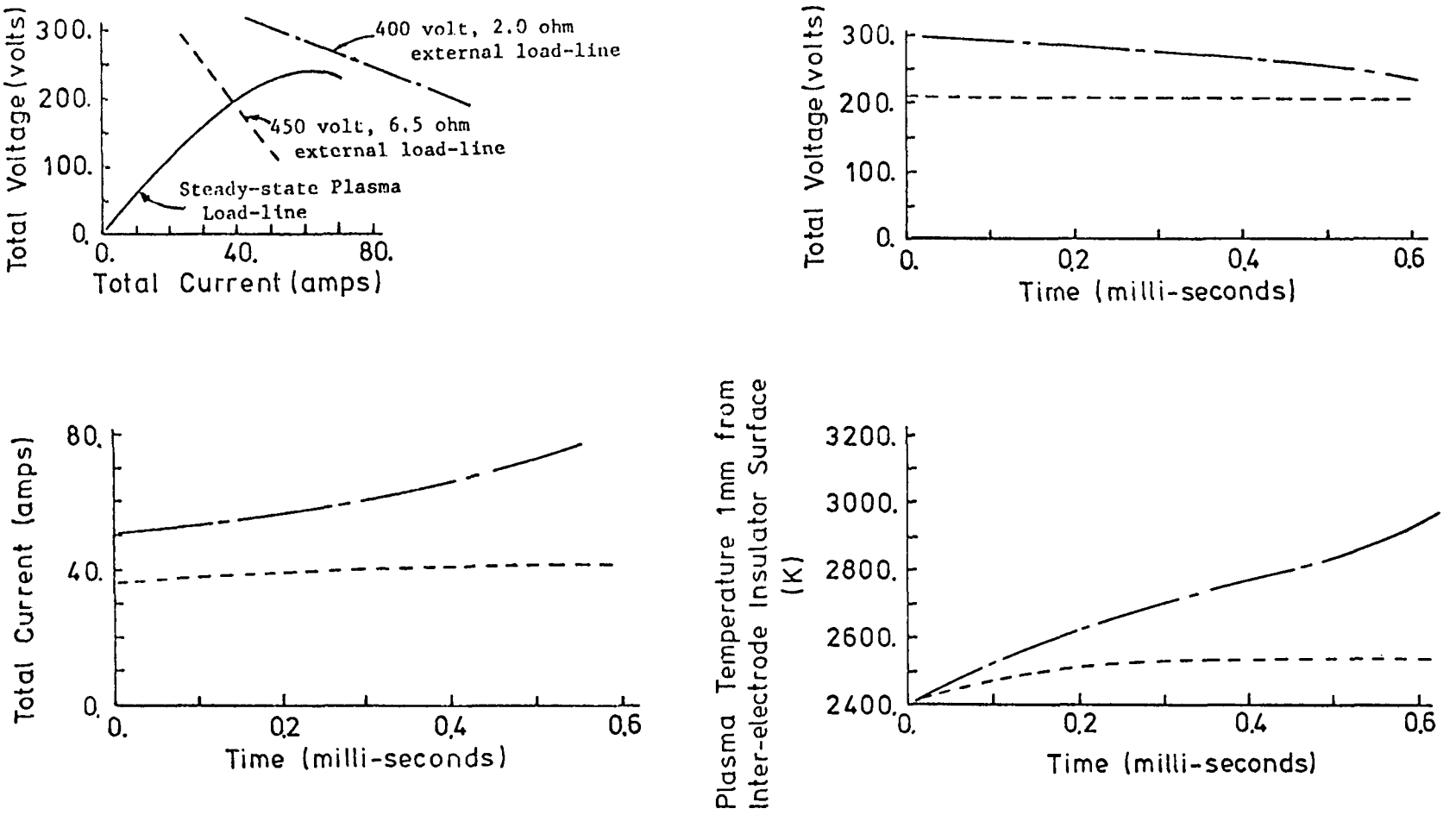

Figure 79. Transient response of inter-electrode region for two combinations of supply voltage and ballast resistance. Total voltage, total current and plasma temperature at the inter-electrode insulator centerline 1.15 mm from the surface are plotted as a function of time. Conditions for calculations specified in Table 13.

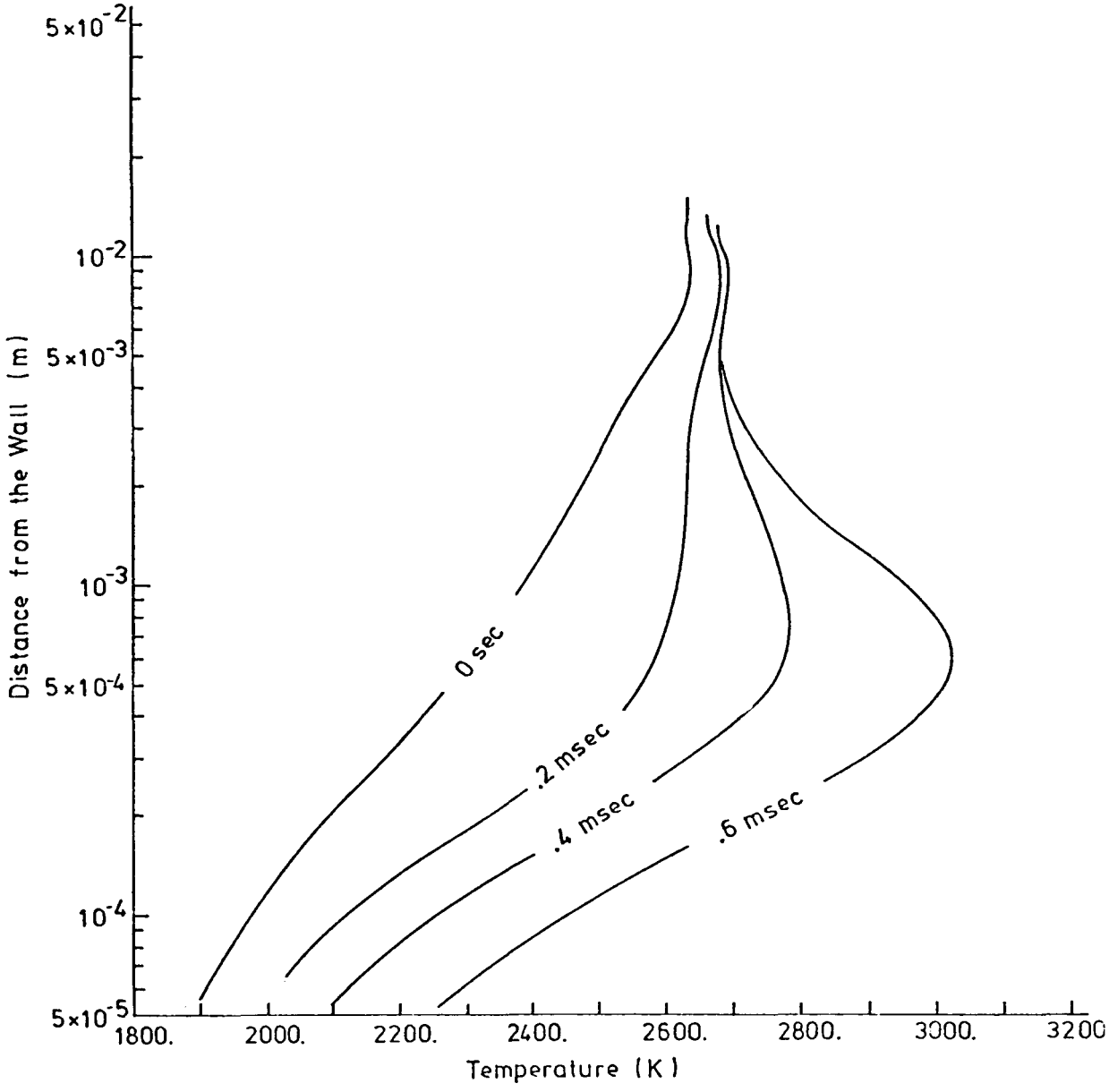

Figure 80a. Plasma temperature profile at inter-electrode insulator centerline as a function of time, showing the formation of a high temperature region approximately 1 mm from the insulator surface. Conditions for the calculation are given in Table 13. Supply voltage of 400 volts and a ballast resistance of 2 ohms were assumed.

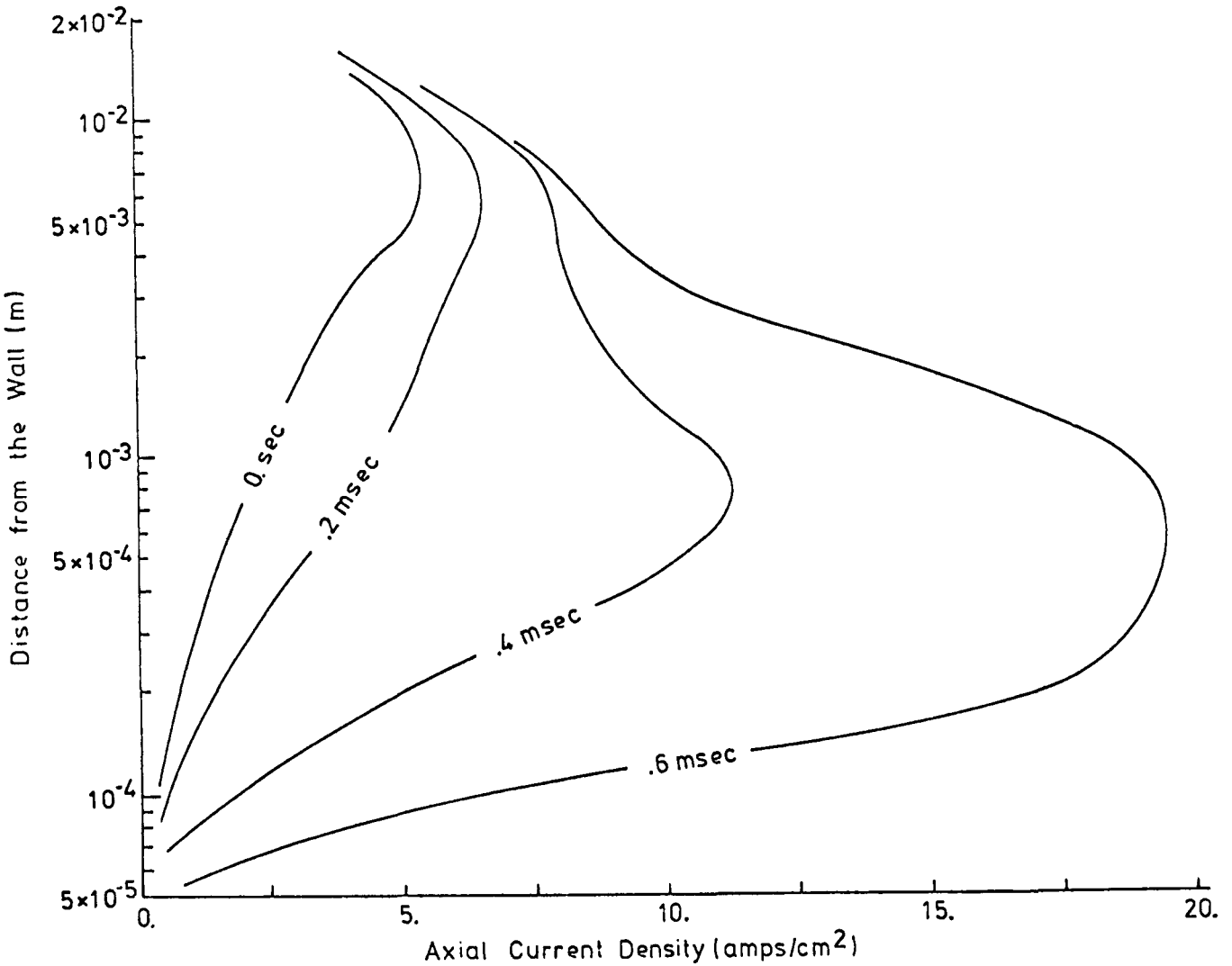

Figure 80b. Axial current density profile at inter-electrode insulator centerline as a function of time, showing the formation of a high current density region approximately 1 mm from the insulator surface. Conditions for the calculations are given in Table 13. Supply voltage of 400 volts and a ballast resistance of 2 ohms were assumed.

result for all supply voltages greater than the voltage maximum displayed in the steady-state voltage current characteristic and the maximum can be considered to be the breakdown threshold voltage.

The influence of various parameters on the behavior of the inter-electrode region can be characterized by the change in low current resistance and the change in threshold voltage resulting from changes in the particular parameter. The most important parameter is the inter-electrode gap size, the influence of which can be observed in Figures 81a and 81b. Neglecting the slight non-linearity, the low current resistance can be expressed approximately as

$$R = 4.2\ \Omega + 1\ \frac{\Omega}{cm} \times \text{gap}\ ,$$

for gap spacing between 2 mm and 20 mm. The relatively large resistance at small gaps is indicative of the fact that current must pass through the cold region adjacent to the electrodes regardless of the gap size. A nearly linear dependence of threshold voltage on insulator gap size is also indicated, and over the gap size range from 2 mm to 20 mm the threshold voltage can be expressed approximately as

$$V_{threshold} = 140\ \text{volts} + 70\ \frac{\text{volts}}{cm} \times \text{gap size.}$$

The large non-zero threshold voltage indicated at small gap size again reflects the fact that the current must pass through the region close to the electrodes.

The influence of inter-electrode insulator surface temperature is of potential importance and is displayed in Figures 82a and 82b. Only small changes in low current resistance or threshold voltage result from changes in surface temperature from ~ 1800°K to ~ 2400°K, however when the surface temperature exceeds a level of ~ 2450°K the threshold voltage and low current resistance drop rapidly. The insensitivity of the inter-electrode region to surface temperature changes at the lower temperatures results from the electron number density being effectively frozen in the near insulator region; increases in surface temperature result in little change in electron number density profiles over the insulator until the insulator temperature is high enough that electron-ion reactions become of importance.

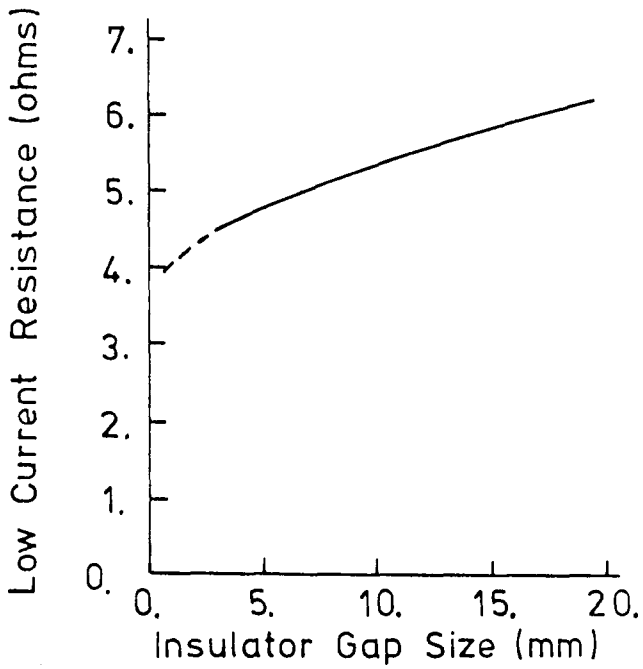

Figure 81a. Low current resistance as a function of insulator gap size. Conditions as specified in Table 13, except insulator gap size.

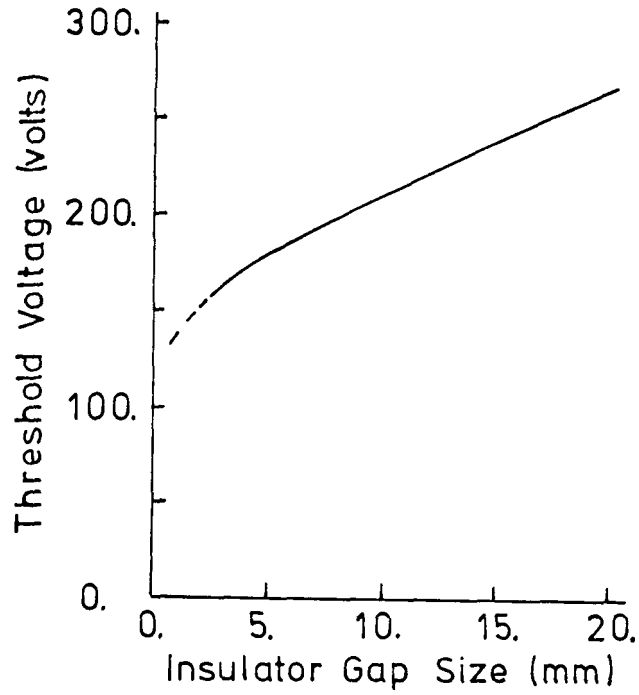

Figure 81b. Threshold voltage for planar breakdown as a function of insulator gap size. Conditions as specified in Table 13, except insulator gap size.

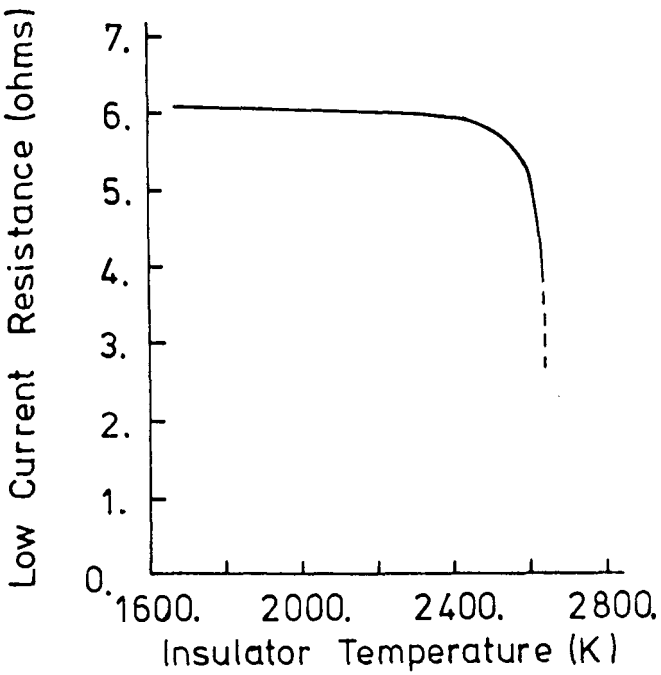

Figure 82a. Low current resistance as a function of inter-electrode insulator surface temperature. Conditions as specified in Table 13, except inter-electrode insulator surface temperature and insulator gap gap size (= 1.91 cm).

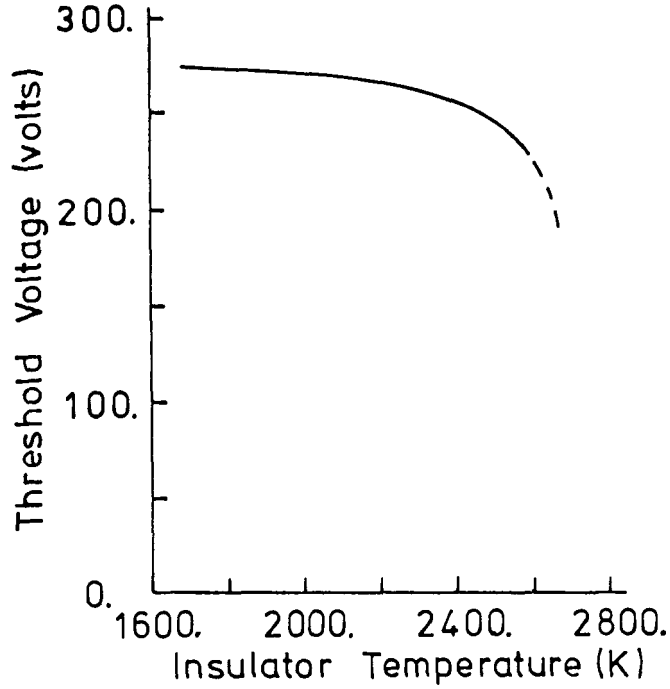

Figure 82b. Threshold voltage for planar breakdown as a function of inter-electrode insulator surface temperature. Conditions as specified in Table 13, except inter-electrode insulator surface temperature and insulator gap size (= 1.91 cm).

Similar arguments apply to the influence of electrode temperature and as shown in Figure 83a and 83b low current resistance and threshold voltage are little affected by changes in electrode temperature from 1300°K to 1800°K. Change in upstream wall temperature from 1800 - 2100 K results in a significant change in low current resistance, as can be observed in Figure 84a, but only a small change in the threshold voltage as can be observed in Figure 84b. The greater sensitivity to this surface temperature results from the significant time the flow has to respond to the surface condition. The effect of the ionization-recombination rate on the response of the inter-electrode region was investigated by increasing or decreasing the Curry rates (see Figure 64); no attempt was made to consider effects of recombination processes other than the three-body electron type. The influence of recombination rate on low current resistance and on the threshold voltage is displayed in Figure 85a and Figure 85b and is seen to be relatively small over the range considered.

The effects of freestream velocity and freestream temperature on the response of the inter-electrode region are displayed in Figures 86 and 87 respectively. Increase in freestream velocity from 250 m/sec to 500 m/sec decreases the low current resistance by ~ 15% and increases the threshold voltage by ~ 100 volts. The decline in low current resistance results primarily from a thinning of the boundary layer and this thinning results in less current passing through the boundary layer region directly above the inter-electrode insulator. The increase in threshold voltage results primarily from increased convective cooling and from a reduced flow time (for ionization) in the region above the insulator. Change in freestream temperature over the range from 2560°K to 2700°K results in a decline in low current resistance from 8.1 Ω to 4.4 Ω and a decline in threshold voltage from 300 volts to 200 volts. It should be noted that increases in threshold voltage are not proportional to the increases in low current resistance as increased resistance leads to increased dissipation which results in an earlier breakdown.

Behavior for Variable Insulator Temperature - One-Dimensional Results. This section discusses the behavior of the inter-electrode insulator region over a time period during which the inter-electrode insulator temperature can change. The results using the one-dimensional model are represented in Figure 88, by a typical steady-state voltage current characteristic for

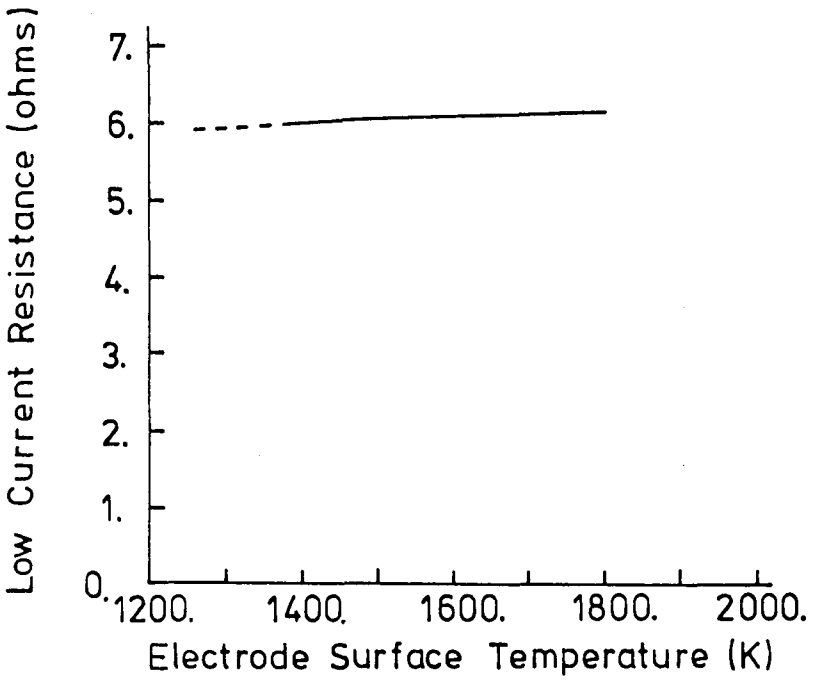

Figure 83a. Low current resistance as a function of electrode surface temperature. Conditions as specified in Table 13, except electrode surface temperature and insulator gap size (= 1.91 cm).

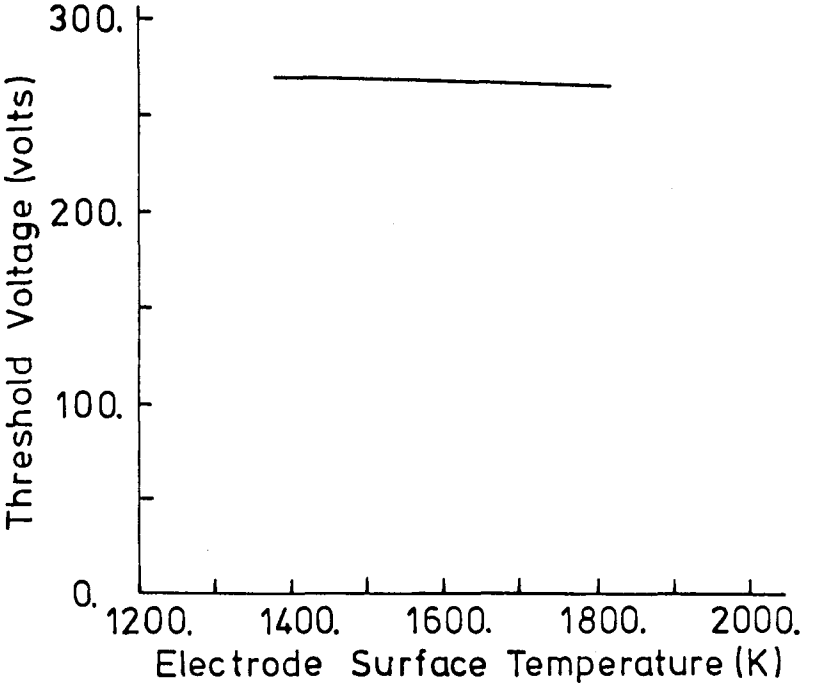

Figure 83b. Threshold voltage for planar breakdown as a function of electrode surface temperature. Conditions as specified in Table 13, except electrode surface temperature and insulator gap size (= 1.91 cm).

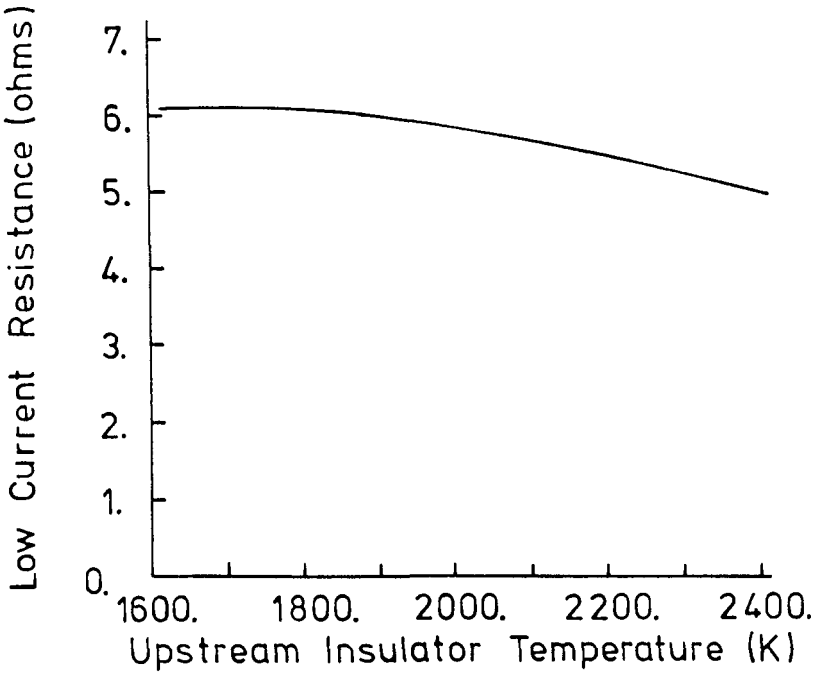

Figure 84a. Low current resistance as a function of upstream insulator surface temperature. Conditions as specified in Table 13, except upstream insulator surface temperature and insulator gap size (= 1.91 cm).

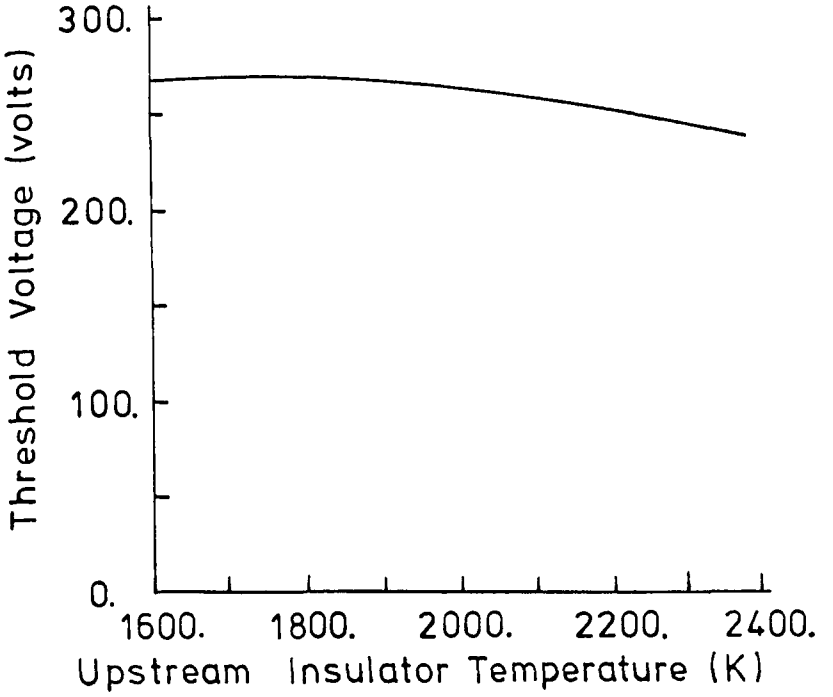

Figure 84b. Threshold voltage for planar plasma breakdown as a function of electrode surface temperature. Conditions as specified in Table 13, except upstream insulator surface temperature and insulator gap size (= 1.91 cm).

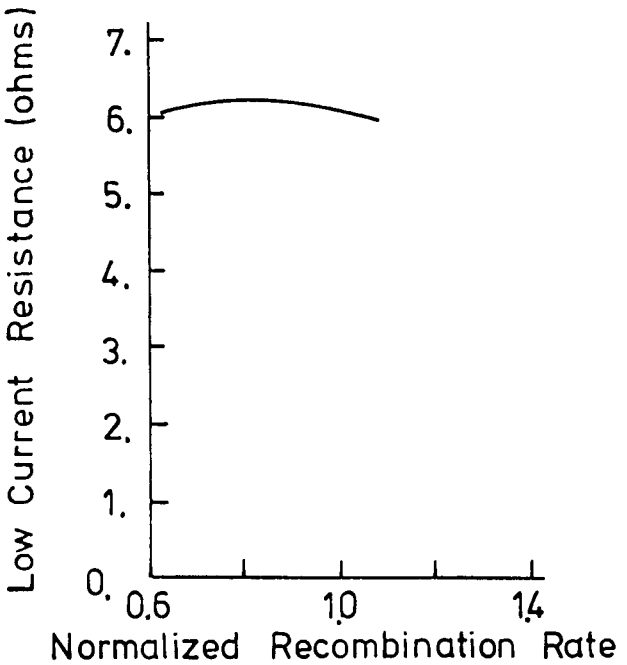

Figure 85a. Low current resistance as function of electron-ion recombination rate. Curry [21] rates multiplied by the abscissa. Conditions as specified in Table 13, except recombination rate and insulator gap size (= 1.91 cm).

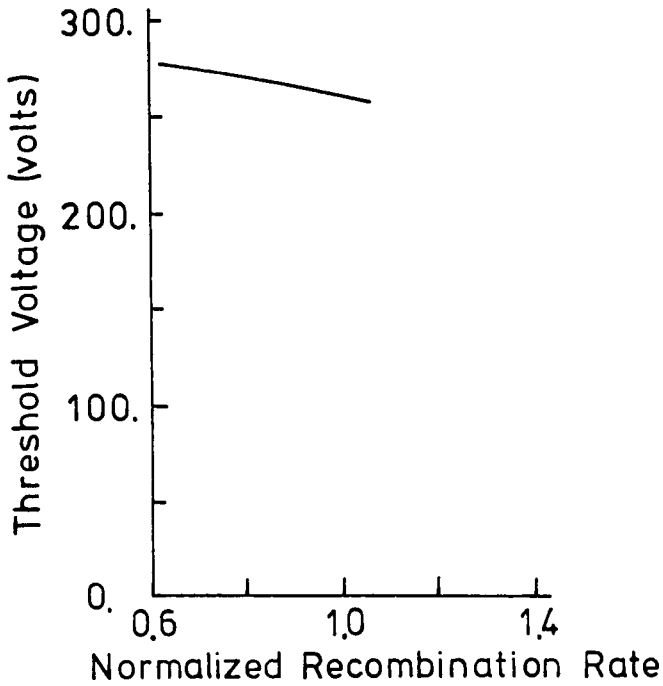

Figure 85b. Threshold voltage for planar plasma breakdown as a function of electron-ion recombination rate. Curry [21] rates multiplied by the absiccsa. Conditions as specified in Table 13, except recombination rate and insulator gap size (= 1.91 cm).

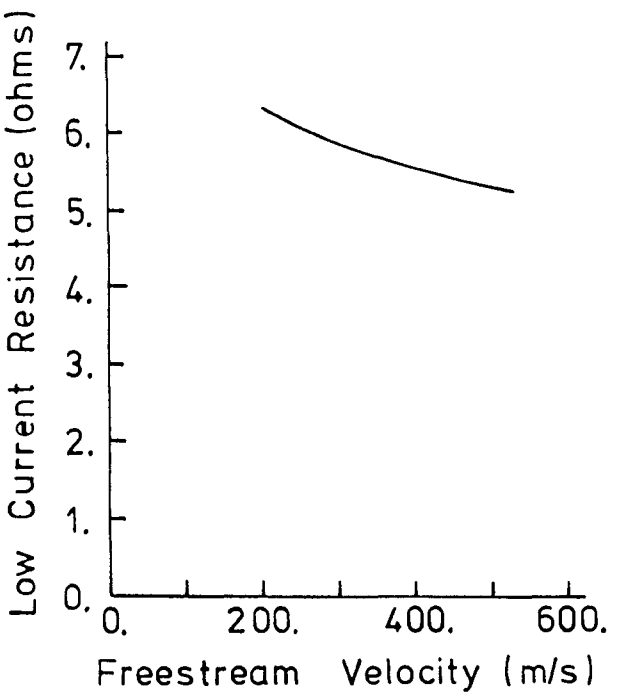

Figure 86a. Low current resistance as a function of freestream velocity. Conditions as specified in Table 13, except freestream velocity and insulator gap size (= 1.91 cm).

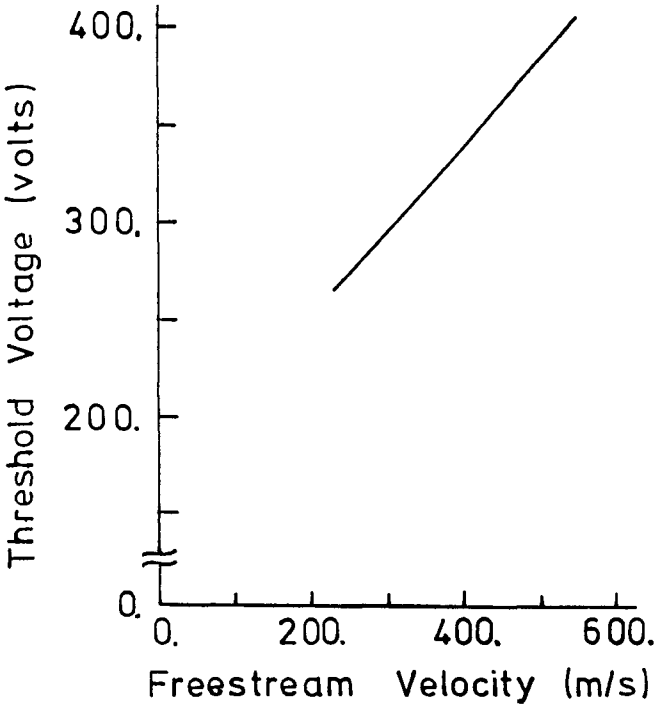

Figure 86b. Threshold voltage for planar plasma breakdown as a function of freestream velocity. Conditions as specified in Table 13, except freestream velocity and insulator gap size (= 1.91 cm).

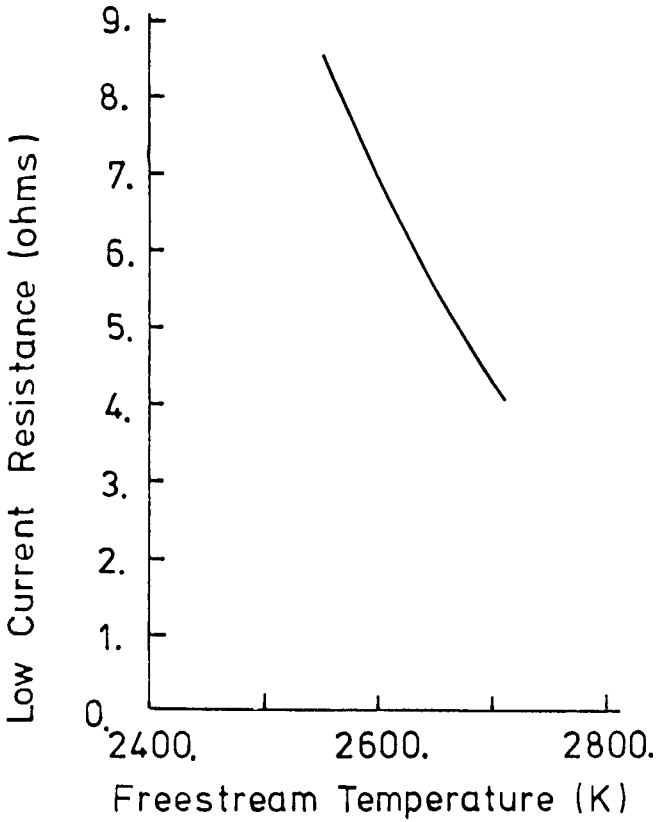

Figure 87a. Low current resistance as a function of freestream temperature. Conditions as specified in Table 13, except for freestream temperature and insulator gap size (= 1.91 cm).

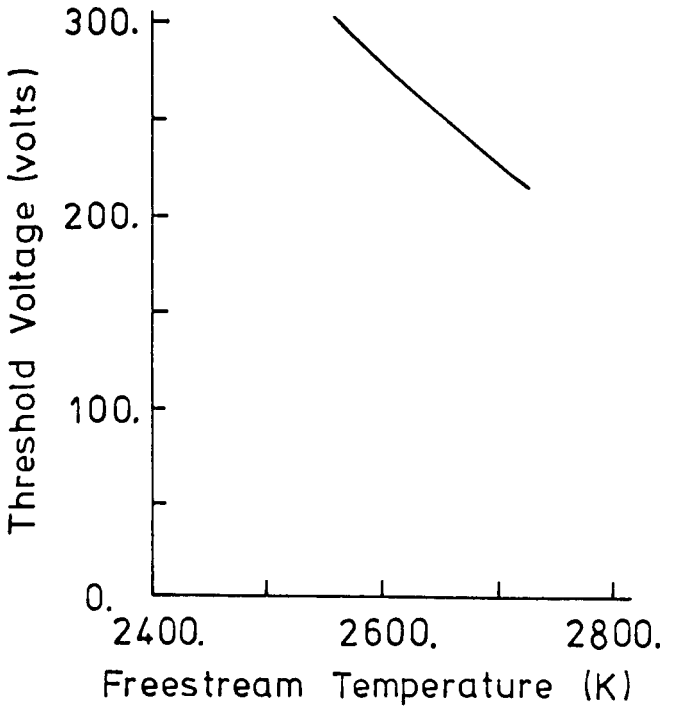

Figure 87b. Threshold voltage for planar plasma breakdown as a function of freestream temperature. Conditions as specified in Table 13, except freestream temperature and insulator gap size (= 1.91 cm).

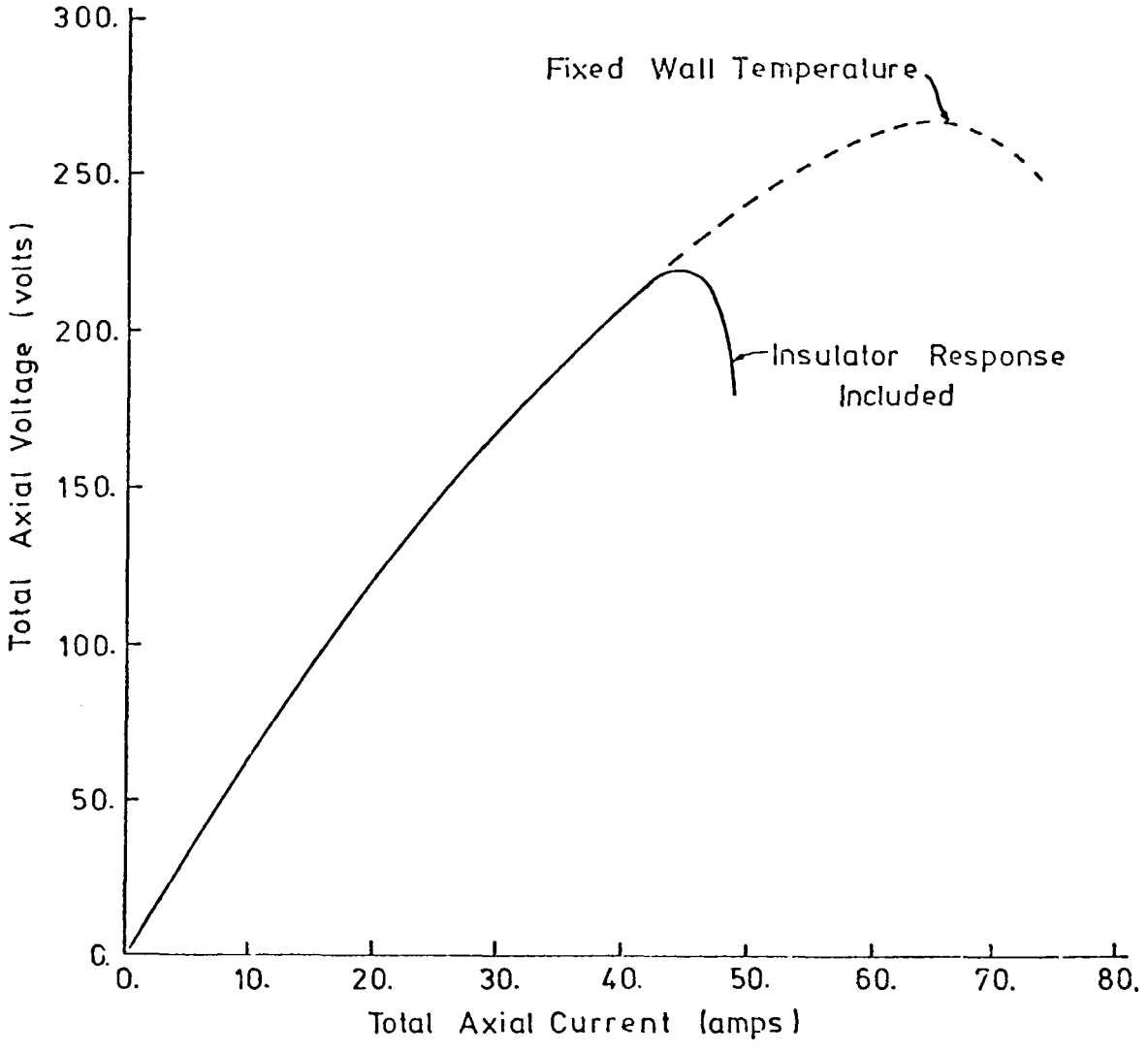

Figure 88. Steady-State total axial voltage versus total axial current including the transient response of the inter-electrode insulator. Voltage-current characteristic for fixed wall temperature is also shown in the figure. Anode and cathode surface-sheath voltage drops are not included in the calculation. Conditions used in the calculations are given in Table 14.

the region. The results displayed were obtained for a 1.91 cm gap at an initial inter-electrode insulator surface temperature of 1840 K and for plasma flow conditions typical of the experiments. The steady-state voltage-current characteristic for fixed wall temperature is displayed in the figure for comparison. Additional conditions used in the calculations are presented in Table 14. The voltage-current curve for variable insulator temperature follows the fixed temperature curve up to currents of ~ 40 amps indicating that the current transfer is predominantly through the plasma up to this point. A voltage maximum of ~ 220 volts is reached soon after the total insulator current becomes important and increases in current beyond the voltage maximum condition result in a decline in voltage maintained across the gap.

As in the fixed wall temperature situation the voltage maximum represents a threshold voltage for planar thermal breakdown, however for this case the breakdown occurs in the inter-electrode insulator rather than in the plasma. The thermal breakdown behavior can be illustrated by comparing the transient response of the inter-electrode region for two combinations of supply voltage and load resistance. The transient response of total voltage, total and insulator current and inter-electrode insulator surface temperature are displayed in Figure 89, with the steady-state voltage-current characteristic for the gap and the external voltage supply load lines shown for reference. The dashed curves, obtained for a supply voltage of 400 volts and a ballast resistance of 5 ohms, steady out after ~ 10 seconds, with voltage and current levels not extremely different from their initial levels. The solid curves, obtained for a supply voltage of 350 volts and a 3 ohms do not reach a steady-state but rather display a runaway behavior. A long delay time, tens of seconds, separates the initiation of current and the breakdown and the majority of the voltage decline occurs in a time of one or two seconds. Although it is the feedback between Joule heating and current conduction in the inter-electrode insulator that is directly responsible for the breakdown, the increase in heat flux to the wall resulting from Joule heating of plasma controls to a large extent the condition for which the thermal breakdown occurs. For example, a threshold voltage in excess of 550 volts is obtained for the same insulator if no seed is assumed to be present in the plasma; that is, if no Joule heating of the plasma occurs. Therefore, accurate modeling of insulator

Table 14. Base conditions for calculations presented in Figures 89-93. Conditions altered for particular calculations are stated in the figures.

Insulator Conditions:

Gap - 1.91 cm

Thickness - 1.25 cm

Width - 3.0 cm

Initial Surface Temperature - 1840 K

Rear Face Conductance - 900 w/m^2-K

Electrical Conductivity σ_{ref} - .12 mho/m

T_{ref} - 1900 K

A - 21.5

Plasma Conditions:

Free stream Temperature - 2630 K

Equivalent Radiative Conductance - 300 w/m^2-K

Plasma resistance and heat transfer coefficient specified (conditions for plasma prediction given in Table 13, except gap size which varies for some cases.)

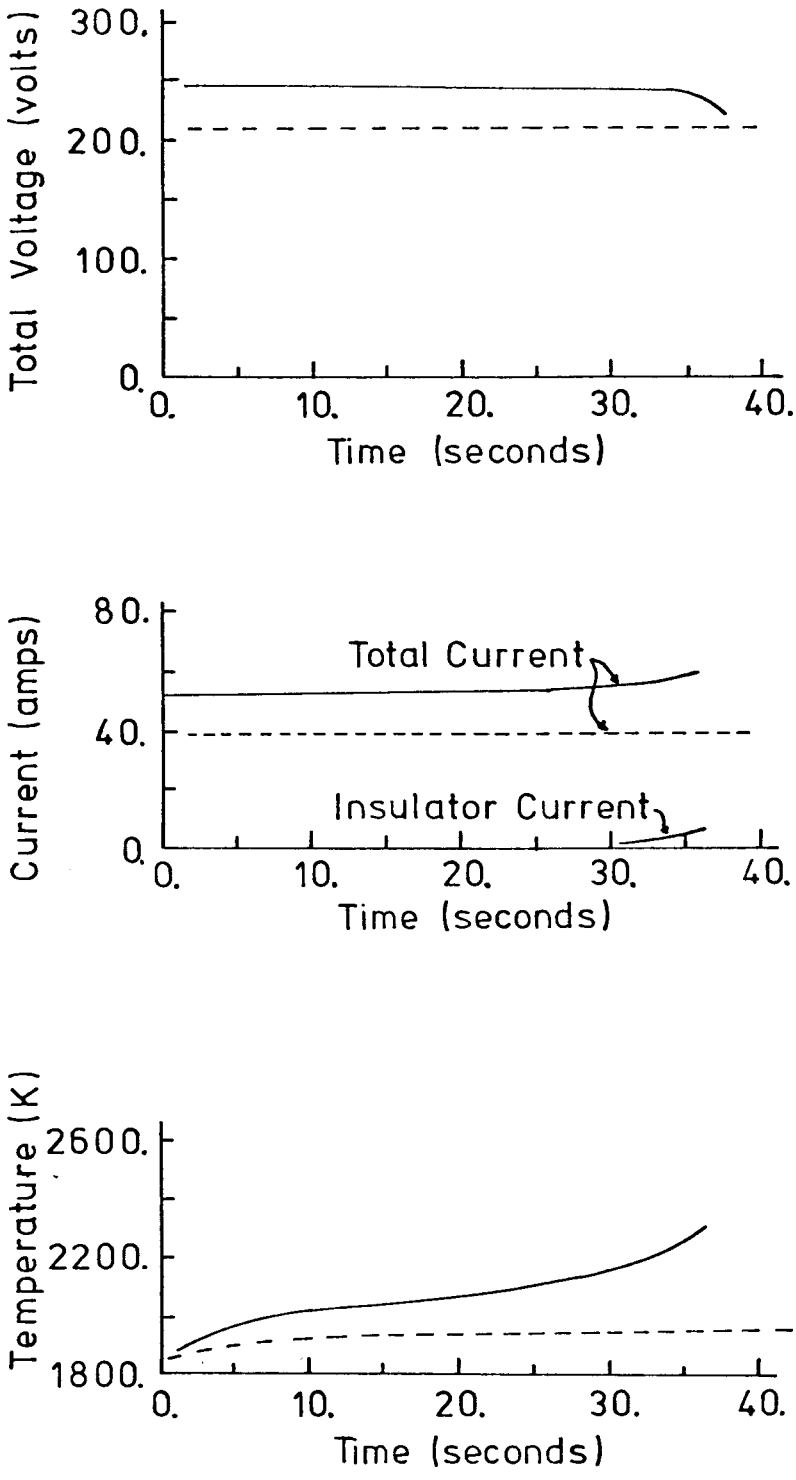

Figure 89. Transient response of inter-electrode region for variable wall temperature, for two combinations of supply voltage and ballast resistance. Figure shows total voltage, total and insulator current and insulator surface temperature as a function of time. Conditions as specified in Table 14.

thermal breakdown requires accurate modeling of the plasma, in particular the heat flux to the wall.

The influence of various parameters on the behavior of the inter-electrode region for variable wall conditions can be characterized by the resulting change in threshold voltage. The most important parameter is the insulator gap size, the influence of which can be observed in Figure 90. Neglecting the non-linearity, the threshold voltage for these conditions can be expressed approximately as

$$V_{threshold} = 150 \text{ volts} + 9.0 \frac{\text{volts}}{\text{mm}} \times \text{gap(in mm)} .$$

Although, lateral conduction is certainly of importance for gaps below ~ 1 cm, it is interesting to note that a non-zero theshold voltage is indicated for zero gap even for the one-dimensional case. It should be noted that the one-dimensional insulator model predicts a threshold electric field which would be the same for <u>any</u> insulator gap size provided that the plasma side heat transfer characteristics were the same for all gap sizes; it is then the variation in plasma behavior which is responsible for the threshold voltage with gap size behavior.

The effect of inter-electrode insulator initial surface temperature on threshold voltage is displayed in Figure 91. In the results presented, the rear face thermal resistance is adjusted as a means of fixing the insulator surface temperature; similar results would be expected if insulator thickness were adjusted to obtain different initial surface temperatures. As expected, the threshold voltage declines with increasing initial surface temperature. The influence of the constants A and σ_r of the insulator electrical conductivity temperature dependence ($\sigma = \sigma_{ref}[\exp(A(1-T_{ref}/T))]$) on the threshold voltage is indicated in Figures 92 and 93. Variation of A from ~22 to ~ 13 changes the threshold voltage by only ~20 volts and variation of σ_{ref} from 0.02 to 0.12 changes the threshold by ~ 40 volts. The above results represent the maximum uncertainty in the electrical properties of magnesium oxide.

The importance of axial variations in heat flux to the insulator is demonstrated by comparing the threshold voltage calculated using the heat transfer characteristics representative of the upstream half of the insulator, with the threshold voltage calculated using heat transfer characteristics

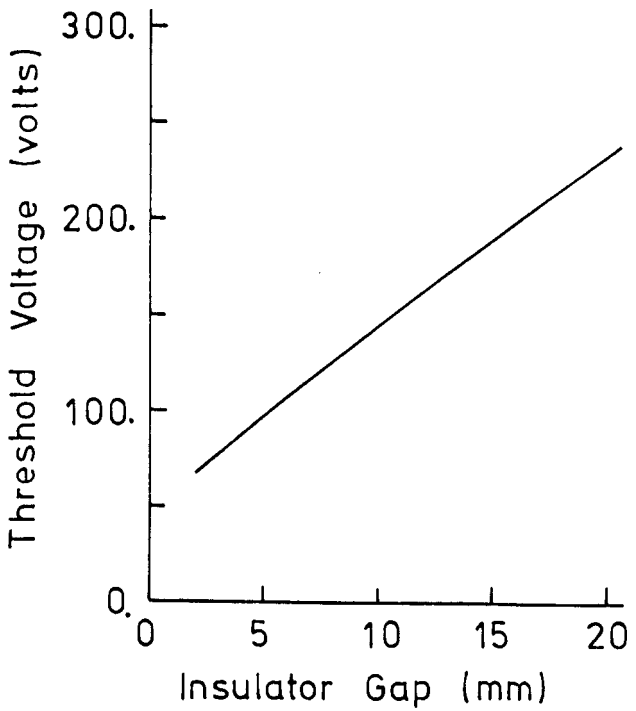

Figure 90. Threshold voltage for planar insulator breakdown as a function of insulator gap size. Conditions as specified in Table 14, except insulator gap size.

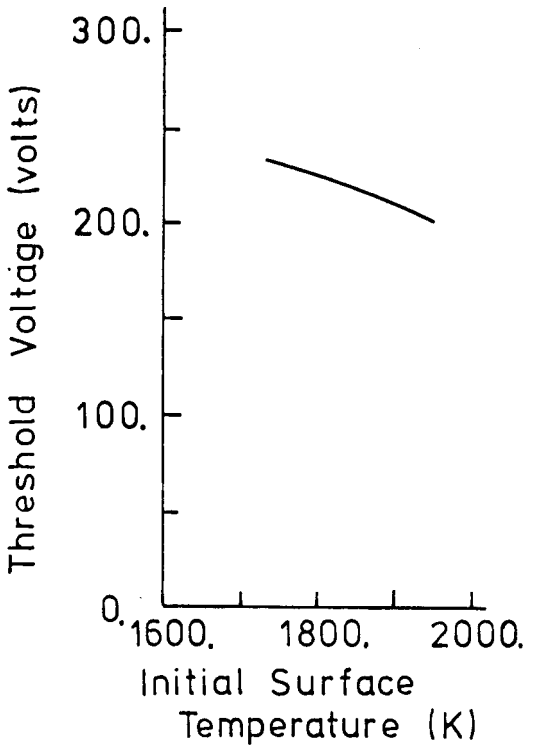

Figure 91. Threshold voltage for planar insulator breakdown as a function of initial surface temperature. Surface temperature adjusted by modifying the thermal resistance between the coolant and the insulator rear face. Conditions as specified in Table 14, except initial insulator surface temperature.

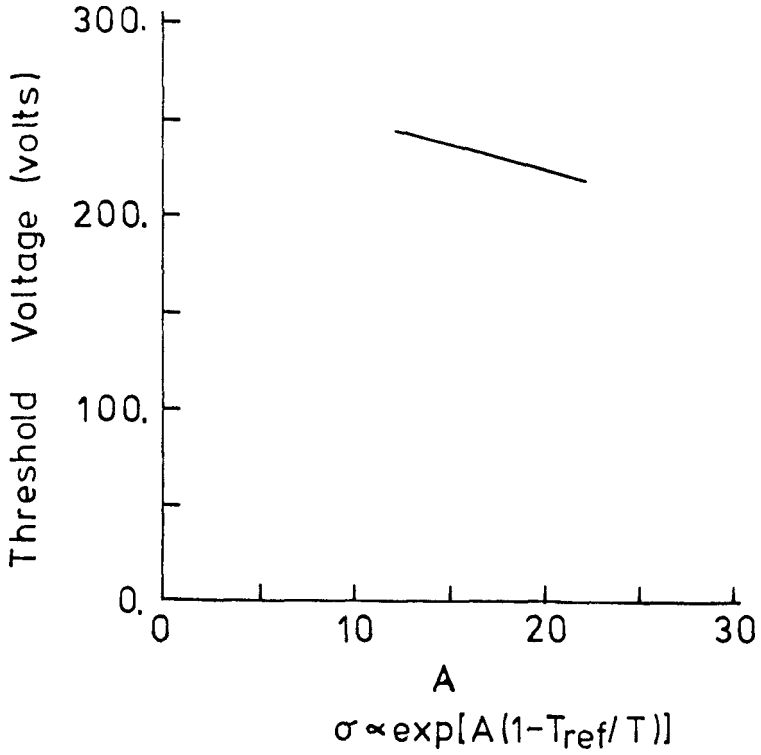

Figure 92. Threshold voltage for planar insulator breakdown as a function of assumed conductivity dependence on temperature. Temperature dependence varied by changing the constant A, where

$$\sigma = \sigma_{ref} \exp[A(1 - T_{ref}/T)].$$

Conditions as specified in Table 14.

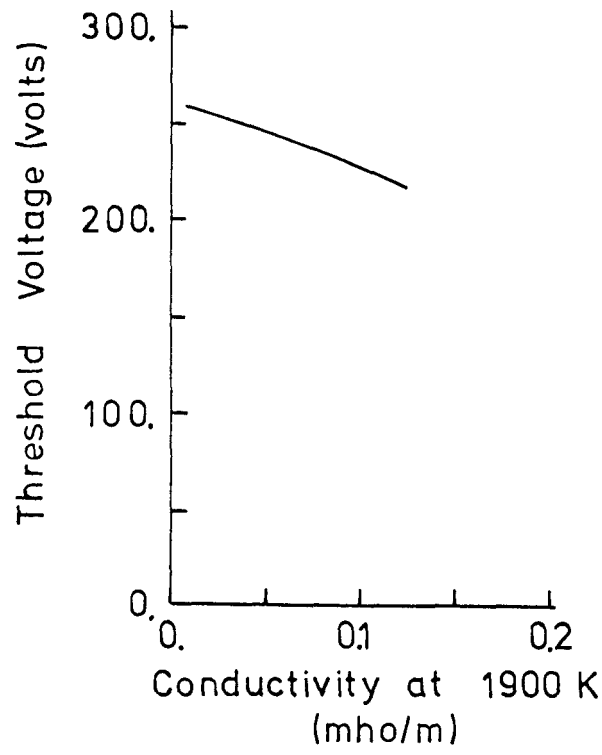

Figure 93. Threshold voltage for planar insulator breakdown as a function of assumed conductivity dependence on temperature. Temperature dependence varied by changing the constant σ_{ref}, where

$$\sigma = \sigma_{ref} \exp[A(1 - T_{ref}/T)].$$

Conditions as specified in Table 14.

at the insulator center-line. For a 1 cm gap, a threshold voltage of 125 volts is predicted using the heat transfer rates of the upstream half of the insulator, while a threshold of 150 volts is predicted using the center-line heat transfer rates.

In the calculations presented thus far, a constant effective radiative conductance has been assumed. A detailed consideration of radiation must include band radiation from the CO_2 and H_2O in the combustion products, line radiation from the potassium (and sodium seed) and net thermal radiation to the insulator from the other walls of the channel which may be operating at significantly different temperatures. The latter component will result in a higher heat flux for low plasma current (and thus lower insulator surface temperature), but will result in a quenching effect as the insulator surface temperature exceeds that of the surrounding walls. The plasma radiation components, however, should increase with increasing plasma current and should result in a reduced threshold voltage. While a detailed calculation of the radiative heat flux was not performed, an estimate of the importance of the heat transfer rates is demonstrated by assuming the radiative heat transfer coefficient to increase linearly with total axial current. For a 1 cm gap and with the radiative component doubling from a current of 0 amps to 30 amps a reduction of the threshold voltage by ~ 20% results. The preceeding estimates indicate the importance of including axial heat flux variations and radiative heat transfer in a more detailed model of insulator breakdown.

Behavior for Variable Insulator Temperature - Two-Dimensional Results. The results using the two-dimensional model are presented in Figure 94, where the threshold voltage is plotted as a function of insulator gap size. These calculations include heat conduction to the electrodes as well as conduction to the sidewalls of the channel. For the geometry considered, lateral heat conduction is significantly more important than conduction toward the sidewalls and threshold voltages for several degrees of lateral contact are presented. The pertinent thermal resistances and other conditions used in the calculations are presented in Table 15. As can be observed in Figure 94, improved lateral conduction increases the threshold voltage for insulator breakdown significantly. It should be noted that the best contact represented in the figure represents a 2% contact fraction with a void of ~ .4 mm and that at that contact the threshold voltage for

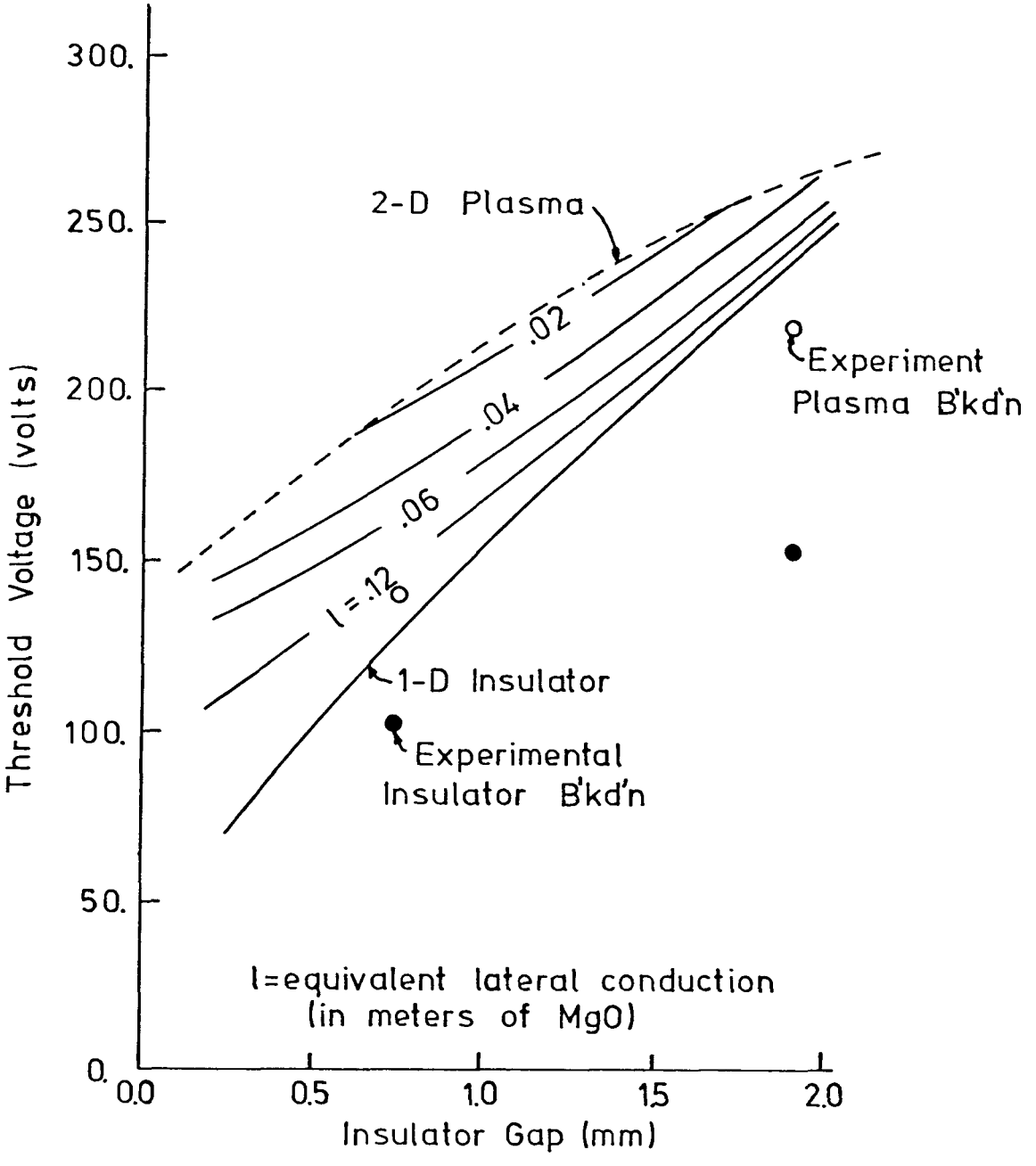

Figure 94. Threshold voltage for insulator initiated breakdown versus insulator gap size for various levels of thermal contact between the electrodes and the inter-electrode insulator. Thermal contact represented as an equivalent length of MgO. Calculations including the insulator behavior are two-dimensional except as labeled. Threshold voltage for plasma initiated breakdown also shown. Experimental threshold voltages are shown in the figure for comparison.

Table 15. Base conditions for Induced Field non-breakdown calculations presented in figures 96-102.

Generator Conditions (open circuit, at center of active region):

Mass Flow Rate	.23 kg/sec
Core Velocity	730 m/sec
Core Pressure	.98 bar
Core Temperature	2740 K
Core Conductivity	16 mho/m
Hall Parameter	1.6
Boundary Layer Thinkness	1.1 cm
Magnetic Field Strength	2.6 Tesla

Channel Dimensions:

Nozzle Exit to Electrode Centerline	46 cm
Channel Height	10 cm
Channel Width	3.1 cm

Electrode Wall Dimensions:

Electrode Length	1.9 cm
Electrode Pitch	3.8 cm

Wall Temperatures:

Electrodes	1400 K
Inter-electrode Insulators	1800 K
Side-wall Insulators	2200 K

insulator breakdown has been increased to approximately the same level as that for plasma breakdown. It should be stressed that as was indicated by the simple models presented in Section 4.2.2, an increased threshold voltage results when the two-dimensional (in the plane perpendicular to the applied electric field) effects are considered. The threshold voltages for insulator breakdown obtained assuming the temperature and current not to vary across the channel width should be considered as a lower bound on the actual threshold voltage rather than an upper bound as is generally accepted. The above results indicate the importance of lateral conduction for insulator sizes studied and show that if good thermal contact with relatively cold electrodes is maintained and the electrode temperature remains relatively constant as the current to the electrodes increases, small insulator gaps can maintain higher electric fields without suffering breakdown.

4.4 Modeling for the Induced Field Configuration

Modeling performed for the generator configuration is limited to (i) a quasi-one-dimensional model for predicting the generator behavior under conditions of no breakdown, and (ii) a coarse grid current distribution model developed primarily to determine the generator response after breakdown is well developed. No time-dependent calculations were performed for the generator configuration. The non-breakdown model and results are presented first and then the coarse grid model and results are discussed.

4.4.1 Non-Breakdown Generator Performance

The fluid mechanical and electrical behavior of the generator for non-breakdown conditions is described using a quasi-one-dimensional computer model. The fluid mechanics model follows a core-boundary layer approach assuming 1/7th power low turbulent boundary layers develop along the walls of the constant area channel. The inlet properties are provided using a separate program described in Appendix D. An electrical model is used to compute the retarding force $\vec{J} \times \vec{B}$ and the energy dissipation term $\vec{J} \cdot \vec{E}$ necessary for the fluid solution, and to predict the generator electrical performance. Included in the electrical model are an anode wall boundary layer voltage drop calculation, a correction factor for the sidewall boundary layers, an empirical cathode voltage drop, and specification of the axial component of current in the core of the flow by the coarse grid cur-

rent distribution model described later in this section. Thermal and electrical properties used in the calculations are curvefits to the equilibrium properties calculated for the particular combustion gas mixture used. Details of the model are given in Appendix D.

The predicted non-breakdown generator behavior for conditions typical of the experiments is displayed in Figure 95. As is evident in Figure 95, the Hall voltage rises relatively linearly with Faraday current and the pressure drop across the active region rises linearly with total Faraday current. The rapid decline of Faraday voltage with current at low Faraday current results from the assumed cathode voltage drop and, excepting this behavior, the Faraday voltage decreases almost linearly with Faraday current out to the highest currents. The negative Faraday voltages result from the augmentation of the Faraday current by external power supplies. The slight non-linearity in the Hall voltage and Faraday voltage curves at the higher currents results from small changes in properties caused by the increased pressure in the channel.

While this non-breakdown model is of limited utility in the interpretation of the breakdown results, the model greatly aided in the choice of conditions resulting in the highest Hall voltages, and in providing the overall conditions necessary for the coarse grid current distribution calculations.

4.4.2 Coarse Grid Current Distribution Model

A coarse grid current distribution model is used to determine the generator behavior for cases where breakdown has occurred. Periodic boundary conditions are applied to a series of three electrode pairs, as shown schematically in Figure 96, so that the model does not require breakdown across all gaps along an electrode wall. A mesh of 6 × 10 nodal points is used to cover the region and the resistance between each nodal point is adjustable such that breakdown can be simulated. The elements along the inter-electrode insulator surface are considered to represent the plasma in the region adjacent to the insulator and the insulator itself. The free-stream velocity, magnetic field strength, Hall parameter and external circuit parameters are specified and a solution is obtained for the potential at each nodal point and for the current passing between each pair of nodal points.

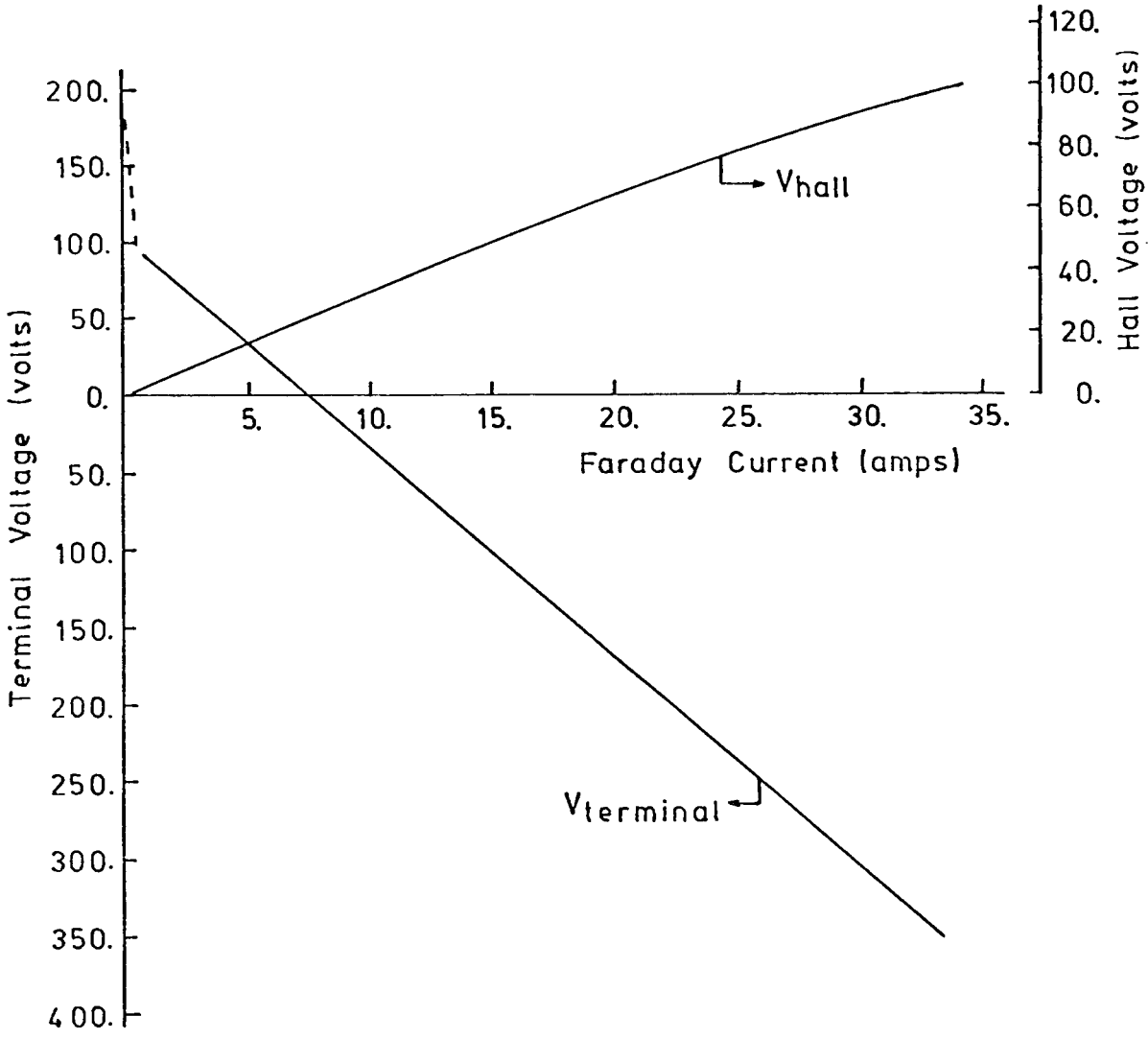

Figure 95a. Calculated terminal (Faraday) voltage and Hall voltage as a function of Faraday current. Conditions for calculations specified in Table 16.

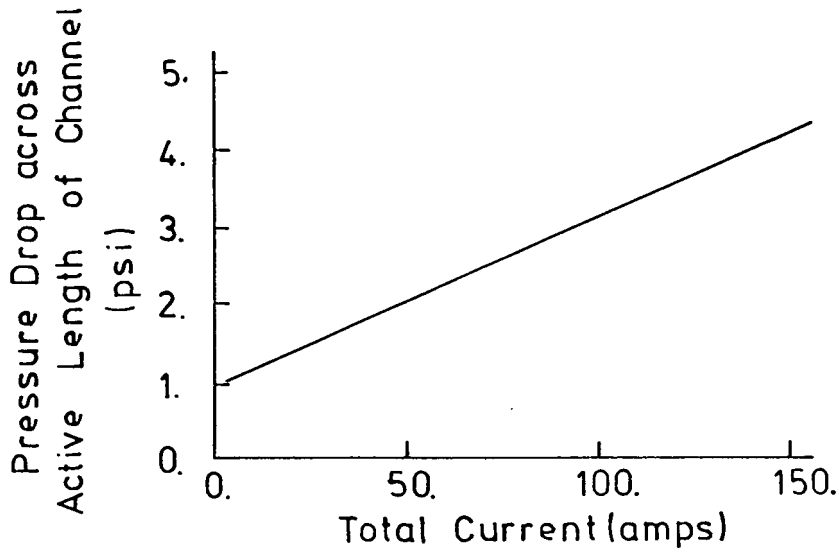

Figure 95b. Calculated pressure drop across active length of the generator as a function of total current through the generator. Conditions for calculations specified in Table 16.

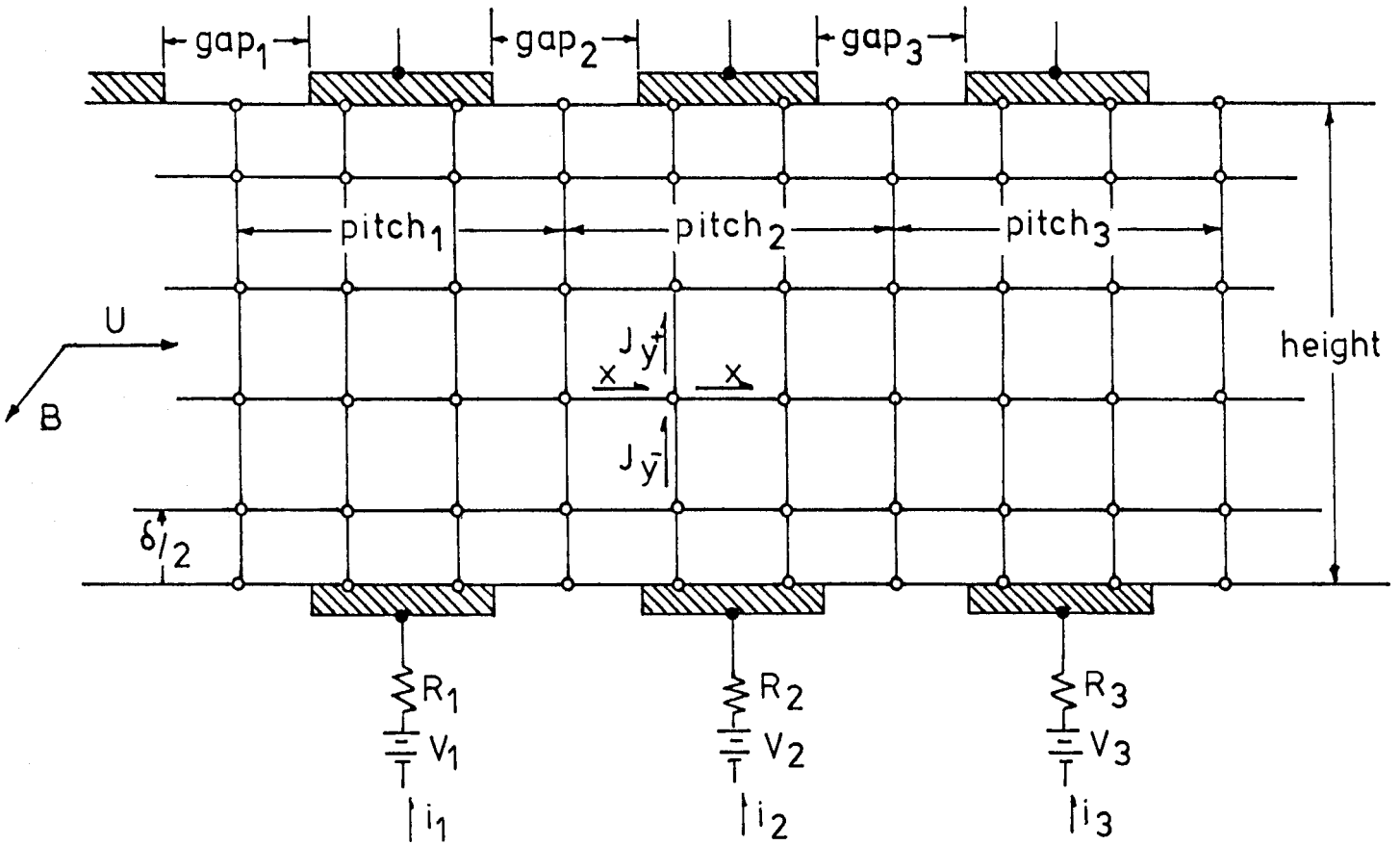

Figure 96. Sketch of grid and summary of equations used in coarse grid solution for induced field configuration. (Continued on next page.)

Unknowns: 60 nodal equations (ϕ_i)

1 Hall voltage (V_H)

Equations: 42 non-electrode nodal point equations of the form

$0 = J_{y+} + J_{y-} + J_{x+} + J_{x-}$, where the J_{y+} etc. are related to the nodal point potentials through averaged ohms law equations for example

$$J_{y+} = -\frac{1}{1+\beta^2}\left[\frac{\Delta V_y}{R_y} + \beta\frac{\Delta V_x}{R_x} + \frac{U\,\beta\,\Delta Y}{R_y}\right]$$

where

$$R_y = \left(\frac{1}{\sigma}\right)_y \Delta Y$$

and

$$R_x = \left(\frac{1}{\sigma}\right)_x \Delta X$$

6 electrode nodal point equations of the form

$$\phi_{\text{electrode left}} = \phi_{\text{electrode right}}$$

3 electrode current-load equations of the form

$$V_{B1} - i_{e1} R_{L1} = \phi_{\text{electrode}_{top}} - \phi_{\text{electrode}_{bottom}}$$

6 periodicity equations of the form

$$\phi_i + V_H = \phi_{i+54} \; ; \quad i = 1,6$$

1 relative potential equation

$$\phi_1 = 0$$

3 zero net x-current equations of the form

$$i_{\text{elect}_{bott}} = i_{\text{elect}_{top}}$$

Parameters: gap_i, $pitch_i$, U,B,β = constant, height, width, boundary layer thickness R_L, V_L

Figure 96. Sketch of grid and summary of equations used in coarse grid solution for induced field configuration.

The equations and boundary conditions for the problem are summarized in Figure 96. Gaussian elimination was used to obtain the solution. Prior to using the code to model breakdown conditions, predictions for non-breakdown conditions from the program were compared with non-breakdown results of Oliver [34] which are based on a fine grid current distribution model for relatively simple conductivity dependences. As expected, quantitative agreement is not especially good, however the coarse grid model does predict the proper trends. Further details of the numerical method and verification of the computer code are given in Appendix E.

To illustrate the results, the non-breakdown and simulated breakdown results are presented for conditions typical of the induced field experiments. Each electrode wall is configured such that a constant electrode pitch is maintained with every third inter-electrode gap set at 8 mm while the remaining gaps are 12 mm. Inter-nodal conductivities for non-breakdown conditions, electrode circuit identification and other pertinent conditions for the calculations are presented in Figure 97. The Faraday voltage and Hall voltage are plotted as a function of Faraday current for non-breakdown conditions in Figure 98. The sharp decline in Faraday voltage at small currents results from the assumed cathode voltage drop. The predicted Hall voltage across the 8 mm gaps is not significantly different from that across the other gaps and the Hall voltage curve shown in the figure represents the behavior of all gaps for non-breakdown behavior.

Breakdown is simulated by increasing the conductivity of inter-nodal elements representing the inter-electrode region. Consider first the breakdown of the 8 mm gap on the anode wall of the generator, simulated by increasing by a factor of 10 the inter-nodal resistances labeled a and b in Figure 97. The response of the Hall voltage maintained across four of the insulator gaps is shown in Figure 99, with results presented for initial Hall voltage levels of 140 volts per pair and 88 volts per pair. In preparing Figure 99 the Hall voltage maintained across a particular gap is plotted against the Faraday current which passes over that gap rather than by the average Faraday current in the circuits adjacent to the gap. The Hall voltage declines significantly across the gap for which breakdown is simulated, with the associated Faraday current increasing by a moderate amount. The Hall voltage across the gap opposite the breakdown gap decreases significantly; however, as can be seen in the figure, much of the

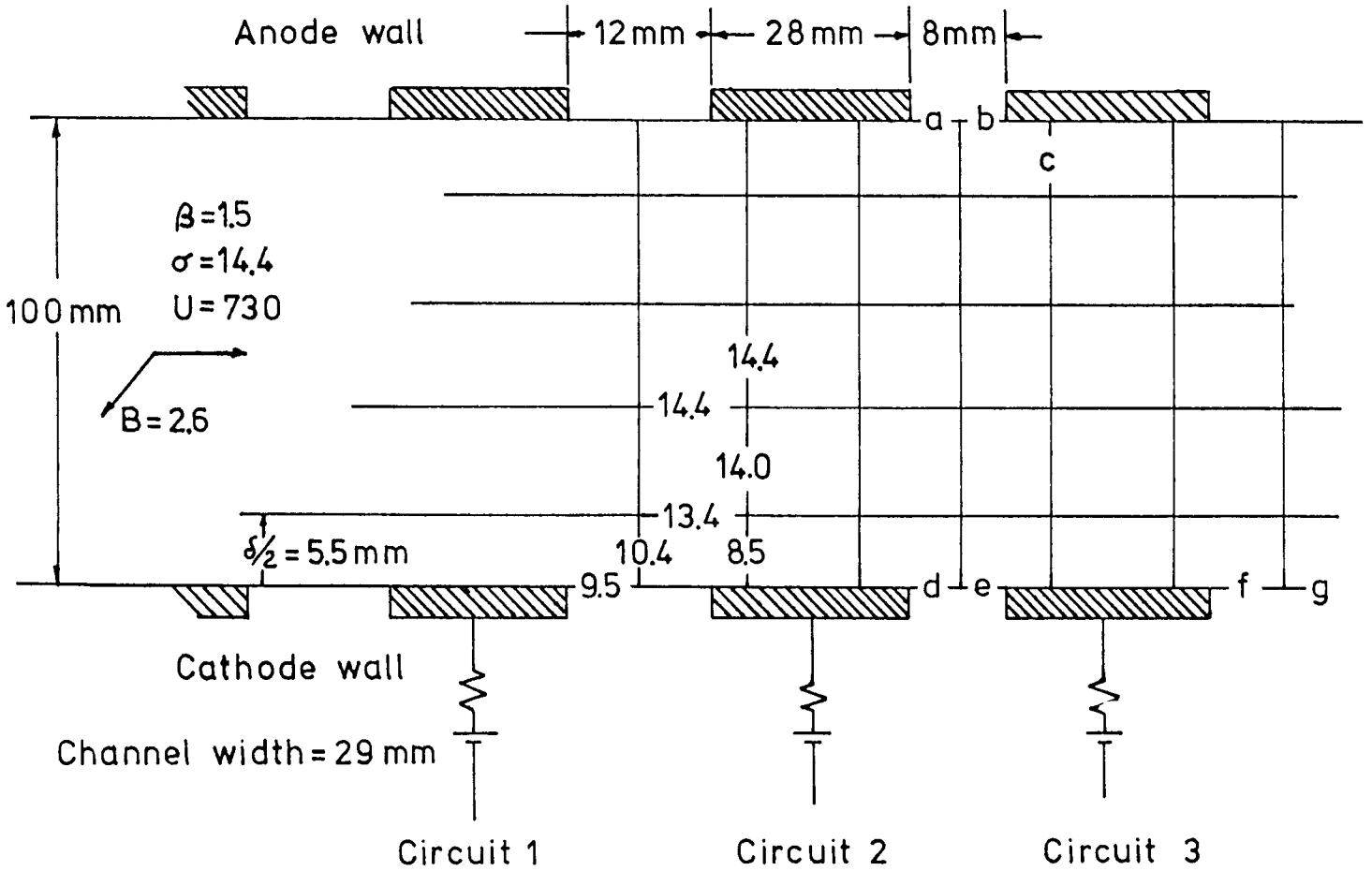

Figure 97. Schematic of coarse grid network for illustration of induced field breakdown. Inter-nodal conductivities (in mho/m) for non-breakdown conditions are indicated, geometry and core-flow conditions are shown and the circuits are identified. Inter-nodal elements altered to simulate breakdown are indicated by the letters a - g.

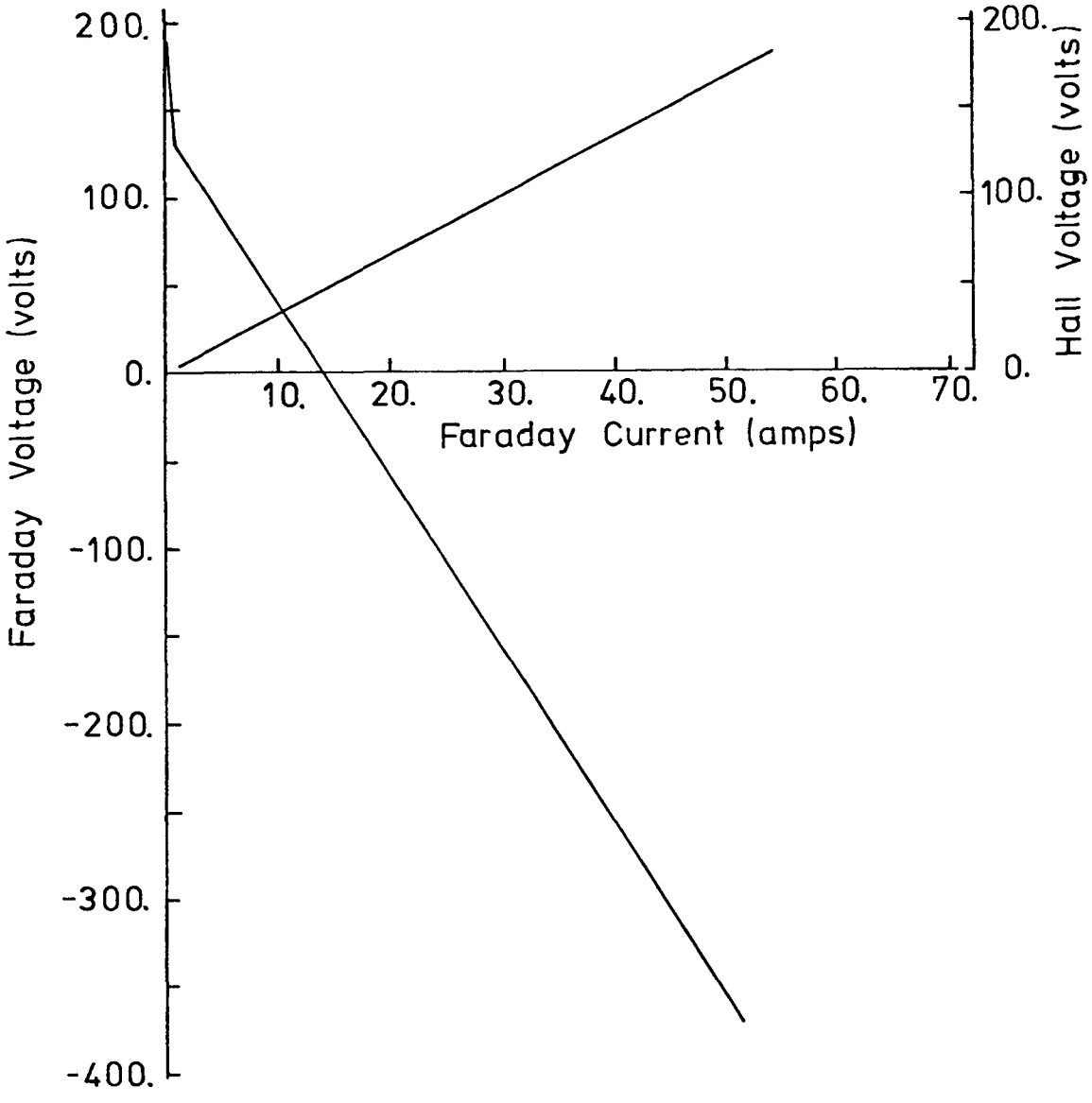

Figure 98. Calculated Faraday voltage and Hall voltage as a function of Faraday current for non-breakdown conditions. A near-cathode voltage drop of 50 volts has been assumed. Geometry and other pertinent conditions shown in Figure 98.

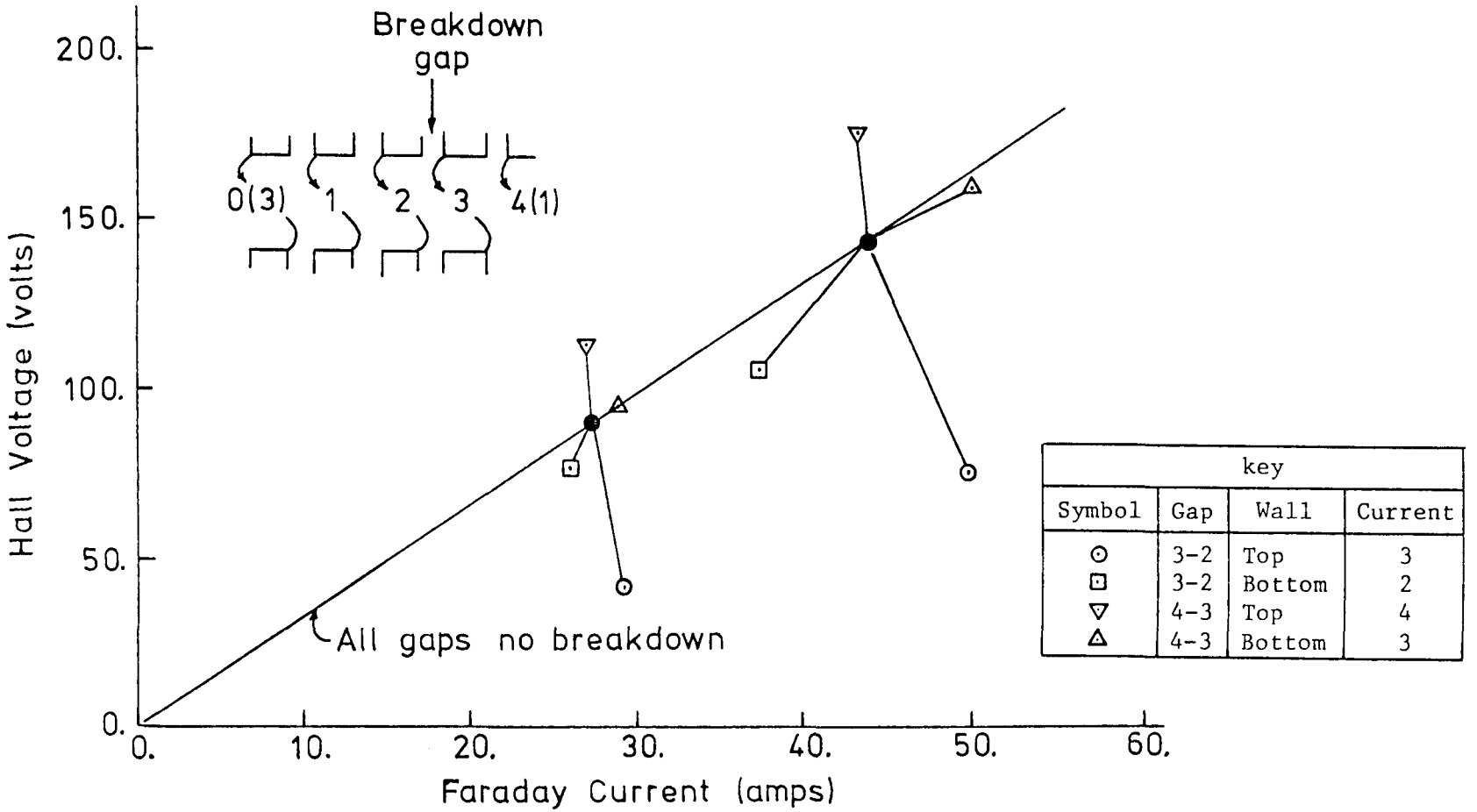

Figure 99. Hall voltage versus Faraday current displaying the response of the generator to a simulated Hall-voltage breakdown of a single anode wall gap. Sketch and key identify the gap voltages and circuits. Breakdown simulated by increasing the conductivity of inter-nodal elements "a" and "b" (see Figure 98) by a factor of 10.

decline can be attributed to the decline of the associated Faraday current. The Hall voltages maintained across the gaps downstream of the breakdown location rise to accommodate the decline at the breakdown gap and the overall generator response is little affected. Significant alteration of the current pattern in the vicinity of the inter-electrode insulator results from the breakdown and is displayed in Figures 100a and 100b. The axial component of current in the inter-electrode region increases dramatically when breakdown occurs, with a significant fraction of this axial current entering the adjacent electrode before being collected at the cathode.

Calculations for breakdown on the cathode wall of the generator yield similar results. The computer code can also be used to simulate the formation of a constriction in the Faraday current (with no increase in the conductivity of the inter-electrode insulator) by increase in the appropriate inter-nodal conductivity. The response of the Hall voltages of four gaps to a tenfold increase in conductivity of inter-nodal resistance "c" (see Figure 97) is shown in Figure 101 and indicates that a similar, but much less severe, perturbation to the generator, results from this Faraday current constriction as compared with that resulting from Hall voltage breakdown. As in the case of breakdown, the current pattern in the near electrode region changes significantly with the formation of a constriction of the Faraday current as can be observed in Figure 100c. In contrast to the breakdown situation, the Faraday current constriction does not lead to a significant current reversal in the adjacent electrode. Where breakdown to be preceeded, or caused, by a constriction in the Faraday current, transient records should indicate that a rapid increase in Faraday current should lead the formation of a current reversal at the adjacent electrode. This will be discussed in more detail when direct comparisons of calculations with the experimental results are made in Chapter 5.

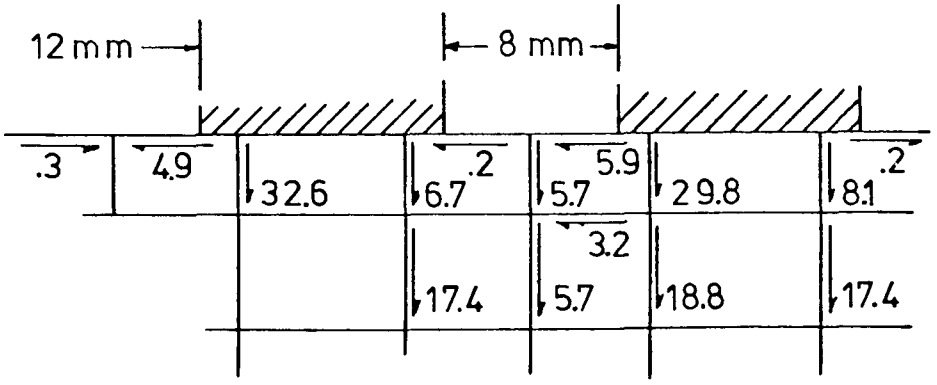

Figure 100a. Figure displays inter-nodal currents (in amps) for non-breakdown conditions.

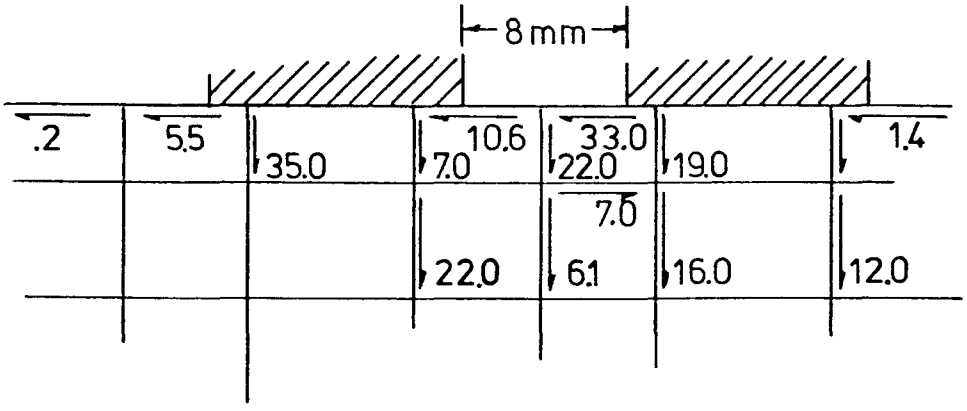

Figure 100b. Figure displays inter-nodal currents (in amps) for breakdown of an 8 mm anode wall gap.

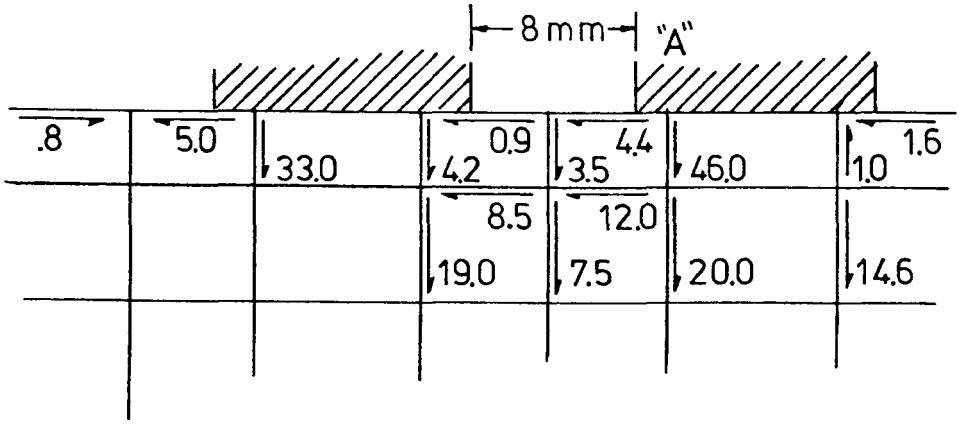

Figure 100c. Figure displays inter-nodal currents (in amps) for a simulated constriction in the Faraday current at the electrode edge labeled A.

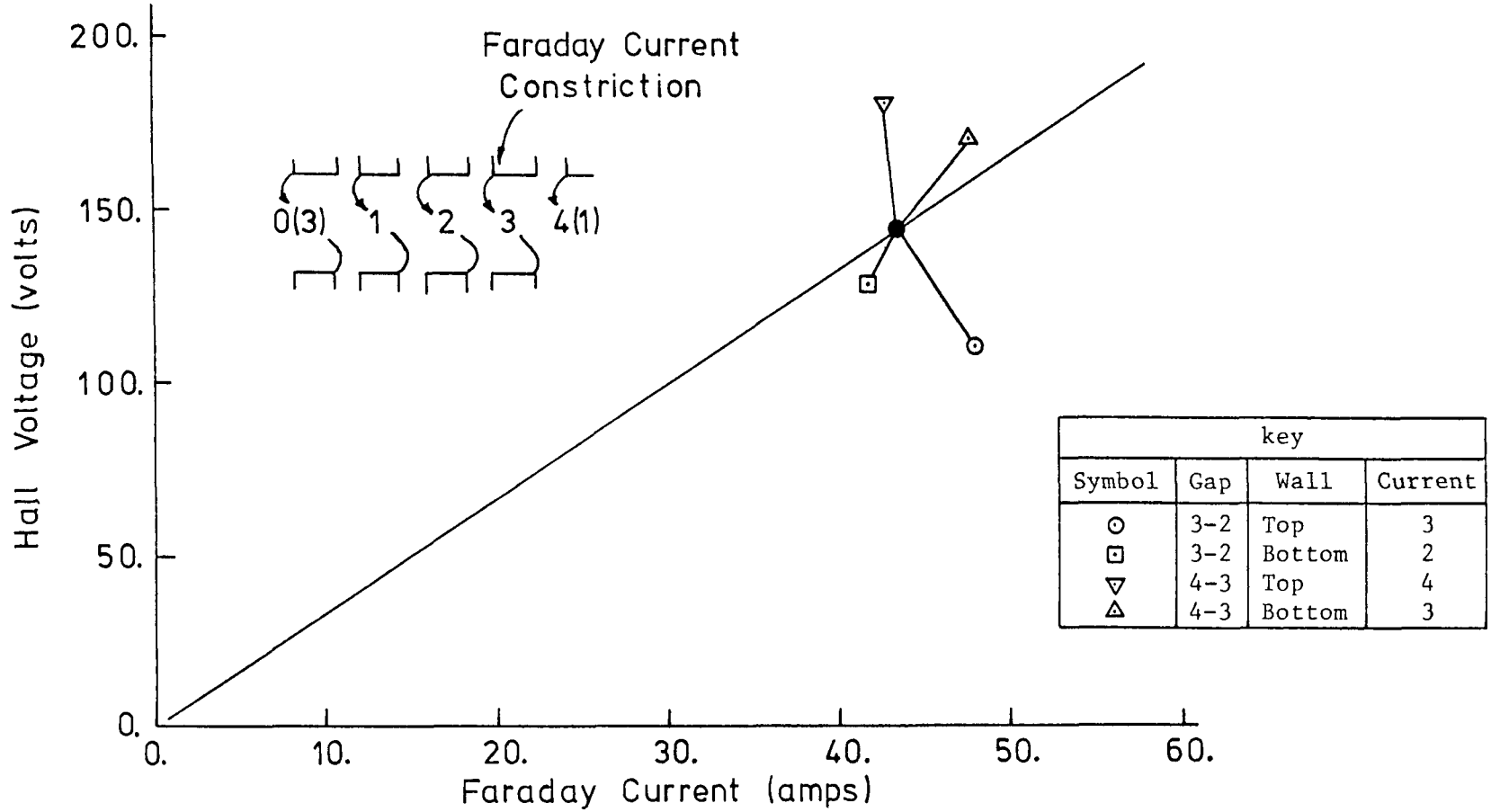

Figure 101. Hall voltage versus Faraday current displaying the response of the generator to a constriction of the Faraday current as it enters one of the electrodes. Sketch and key identify the gap voltages and circuits. The constriction in current is simulated by increasing the conductivity of inter-nodal element "c" (see Figure 98) by a factor of 10.

CHAPTER 5

COMPARISON OF THEORY AND EXPERIMENT

5.1 Introduction

In this chapter analytical results are presented for the conditions of the experiments and direct comparison of calculated and measured results are made. General agreement between theory and experiment is evident from comparison of the experimental results of Chapter 3 with the illustrative calculations of Chapter 4, however direct and detailed comparison is required to determine what aspects of the anslyses require refinement. Comparisons of the results for the applied field configuration are presented first and then the induced field results are discussed.

5.2 Applied Field Experiments and Theory

5.2.1 Pre-Breakdown and Incipient Breakdown for the Plasma

Calculations of pre-breakdown and incipient breakdown behavior were performed for conditions as close as possible to the conditions of four of the eight run series of the axial experiments. A summary of the important experimental conditions and the conditions used in the calculations is presented in Table 16. For each of the four run series, comparisons of predicted and measured values for

a) total axial voltage ("cathode-corrected") versus total axial current,

b) near-anode voltage drop versus total axial current, and

c) far-electrode voltage drop versus total axial current.

The surface-sheath behavior at the anode is included in these calculations. In addition, for Run series .75-A a comparison is made of predicted plasma temperature with plasma temperature inferred from the photodiode measurements. A comparison of predicted and measured current distribution in the axial direction and across the channel is also presented for Run series 1.9-B. It should be noted that excepting for the empirical removal of the cathode behavior (see Section 3.2.3) no attempt has been made to "adjust" parameters in the prediction code to better represent the data; as can be observed in Figures 102a-d, predicted values of total axial voltage are generally lower at a given current than the measured values. Further, the

Table 16. Comparison of actual experimental conditions with conditions used in the calculations for for the applied field configuration. Calculated core conditions use measured plenum pressure and measured combustor heat loss and are performed for the experimentally measured combustion properties. Properties used in main calculations are curve-fits for slightly different conditions as are detailed in the table.

	Run Series 1.9-B		Run Series .75-A		Run Series .75-B		Run Series .75-C	
Core Conditions:	Expt.	Calc.	Expt.	Calc.	Expt.	Calc.	Expt.	Cal.
Pressure (10^5 Pa)	1.013	1.013	1.013	1.013	1.013	1.013	1.013	1.013
Temperature (K)	n.a.	2650	n.a.	2660	n.a.	2593	n.a.	2542
Core Velocity (M/S)	n.a.	265	n.a.	281	n.a.	275	n.a.	428
Combustion Gas Properties:								
N/O by weight	.6	.5	.6	.6	.8	.6	1.1	1.1
Potassium by weight (%)	.92	.92	.95	.95	.86	.86	.76	.77
Equivalence Ratio	.95	1.0	1.0	1.0	1.0	1.0	1.0	1.0
Surface Temperatures:								
Upstream Insulator (K)	2190	2190	2060	2060	1900	1900	2030	2030
Anode (K)	1130	1400	1170	1400	980	1400	1100	1400
Inter-electrode Insulator (K)	n.a.	1800	n.a.	1800	n.a.	1800	n.a.	1800
Cathode (K)	830	1400	1100	1400	970	1400	1122	1400
Downstream Insulator (K)	n.a.	2190	n.a.	2060	n.a.	1900	n.a.	2030
Sidewall (K)	2100	2100	2000	2000	1900	1900	1970	1970

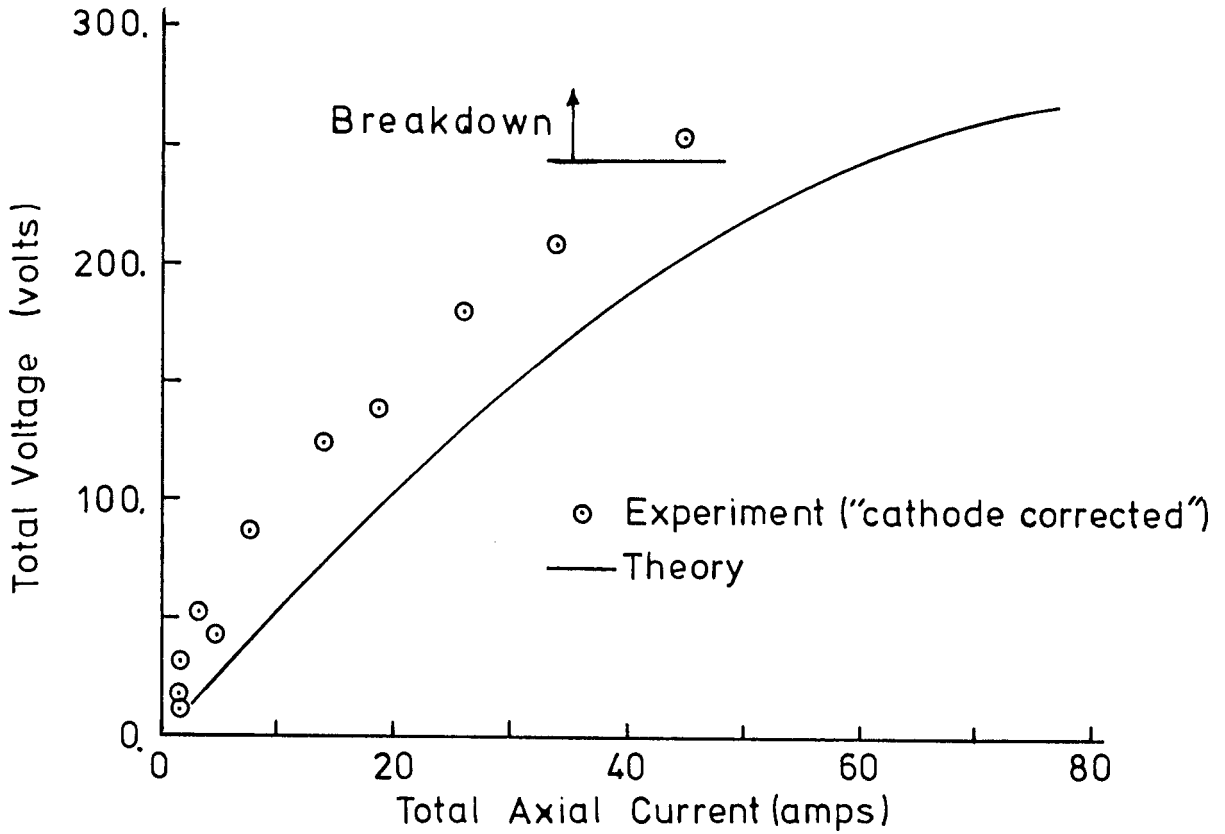

Figure 102a. Comparison of predicted and measured total axial voltage versus total axial current for experimental Run series 1.9-B. Conditions used in calculations compared with actual experiment conditions in Table 17. Experimental voltage is "cathode-corrected" as discussed in Section 3.3.2. Calculated curve includes anode surface-sheath voltage drop.

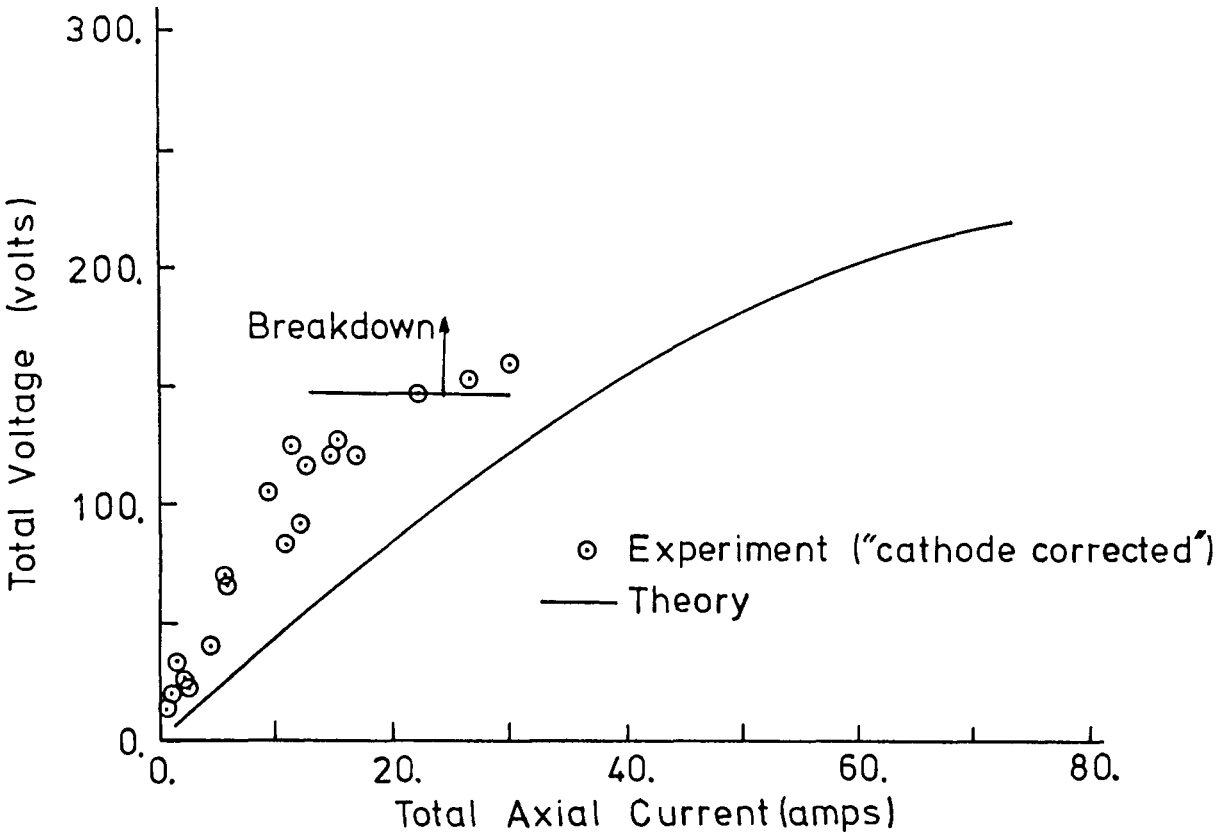

Figure 102b. Comparison of predicted and measured total axial current for experimental Run series .75-A. Conditions used in calculations compared in Table 17. Experimental voltage is "cathode-corrected" as discussed in Section 3.2.2. Calculated curve includes anode surface-sheath voltage drop.

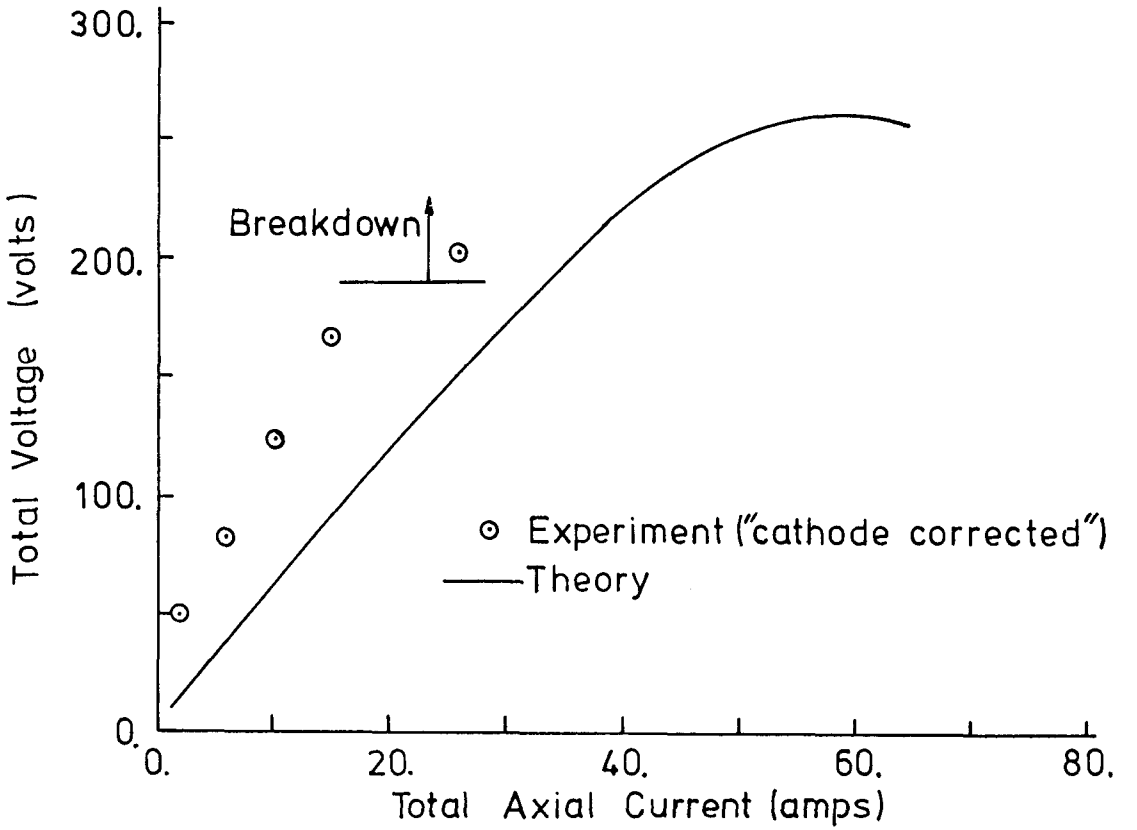

Figure 102c. Comparison of predicted and measured total axial voltage versus total axial current for experimental Run series .75-B. Conditions used in calculations compared with actual experimental conditions in Table 17. Experimental voltage is "cathode-corrected" as discussed in Section 3.2.2. Calculated curve includes anode surface-sheath voltage drop.

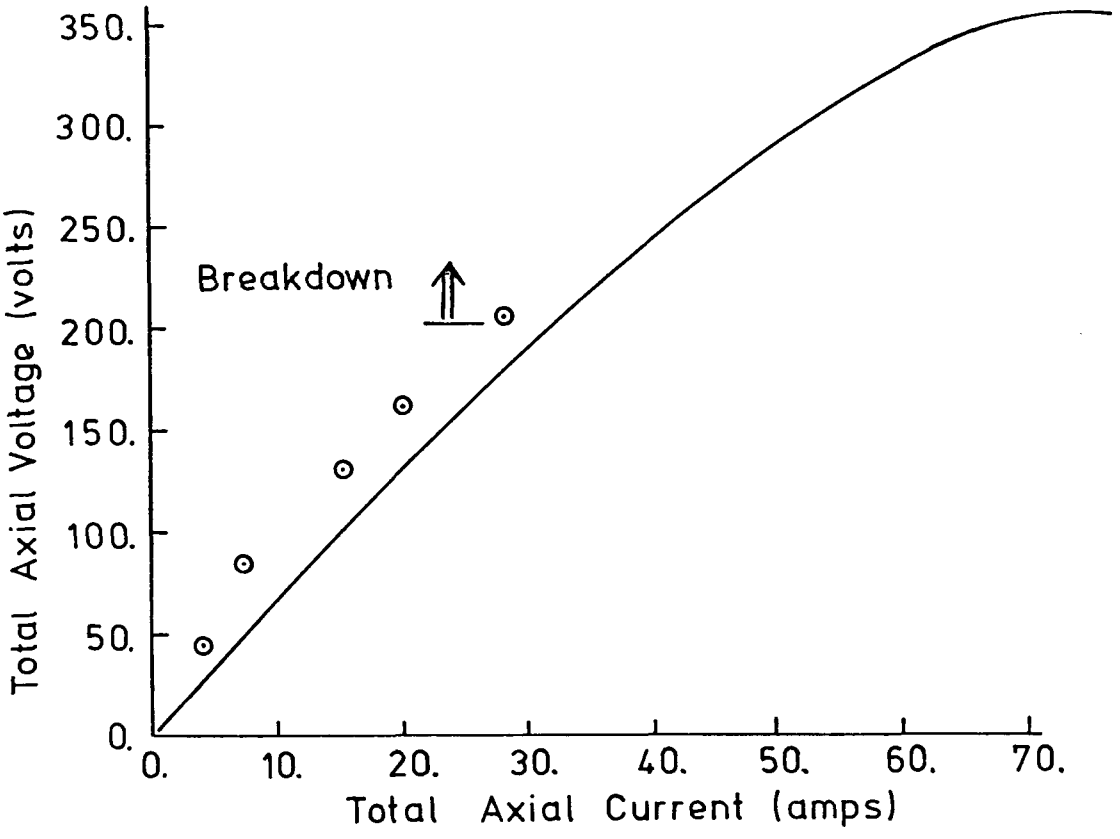

Figure 102d. Comparison of predicted and measured total axial voltage versus total axial current for experimental Run series .75-C. Conditions used in calculations compared with actual experimental conditions in Table 17. Experimental voltage is "cathode-corrected" as discussed in section 3.2.2. Calculated curve includes anode surface-sheath voltage drop.

predicted threshold voltage, as indicated by the peak voltage, is considerably higher than the measured breakdown threshold voltage and occurs for a significantly higher total axial current. Predicted and measured behavior in the region away from the electrodes is displayed in Figures 103a-d and again predicted voltages are lower than those measured. Predicted and measured behavior in the near-anode region is displayed in Figures 104a-d, excepting Run series 1.9-B, where agreement is excellent (and probably fortuitious), predicted values are significantly lower than measured values. Predicted and measured current distribution at the electrode surface for the axial and transverse direction are compared in Figure 105a and Figure 105b. Reasonable agreement is obtained for the axial current distribution for Run 1.0-B although the experimental data indicate greater current concentration at a given total current levels; this trend is repeated in comparisons for the other Run series. The predicted distribution across the channel width almost identical for all the Run series and as displayed in Figure 105b agrees reasonably well with data from Run 1.9-B. Agreement for other Run series is generally good although some anomolous results were obtained. A comparison of plasma temperature in the region above the inter-electrode insulator is represented in Figure 106, where the ratio of radiation emission intensity (for the potassium 4040 Å lines) with current to the intensity without current is plotted as a function of total axial current. The predicted values are determined from the calculated plasma temperature treating the gas as if it were optically thin to that radiation. As can be observed in the figure measured ratios are generally higher than predicted ratios although considerable scatter is displayed in the data.

Direct comparison of predicted and measured behavior for the plasma display only moderately good quantitative agreement, as indicated in Figures 102-106 and in summary Table 17. The comparisons indicate an under-prediction of the resistance at low currents and indicate that the effects of Joule heating are also under-predicted. The under-prediction of near-anode voltage drop might be ascribed to effects of resistive surface coatings on the electrodes, however the calculations also under-predict the voltage drop in the region away from the electrodes. The near-anode behavior, the axial current distribution behavior and the radiation intensity behavior all indicate that the effects of Joule heating are under predicted by the model. The under-prediction of the effects of Joule heating

Table 17. Comparison of measured and calculated dynamic resistances and breakdown threshold voltages for the applied field configuration. Calculation of two-dimensional insulator threshold voltages are taken directly from results in Chapter 4, for an equivalent lateral conductance of 0.4 m of MgO.

		Run Series			
		1.9-B	.75-A	.75-B	.75-C
Dynamic Resistances (ohms): Near Anode (low current)	Expt.	1.1	3.0	3.5	3.6
	Calc.	1.3	1.2	1.6	1.8
Near Anode (moderate current)	Expt.	0.5	1.3	2.0	1.7
	Calc.	1.0	1.3	1.6	1.0
Far Electrode	Expt.	4.6	1.9	3.3	2.6
	Calc.	3.2	1.5	2.3	2.7
Total ("cathode corrected") gap (moderate current)	Expt.	5.6	4.5	7.3	6.0
	Calc.	5.2	4.1	5.5	5.0
Breakdown Threshold Voltages: Plasma Initiated	Expt.	250	150	180	200
	Calc.	280	220	250	330
Insulator Initiated	Expt.	210*	140	130	170
	1-D calc.	230	130	n.a.	n.a.
	2-D calc.	250	170	n.a.	n.a.

* Run Series 1.9-D

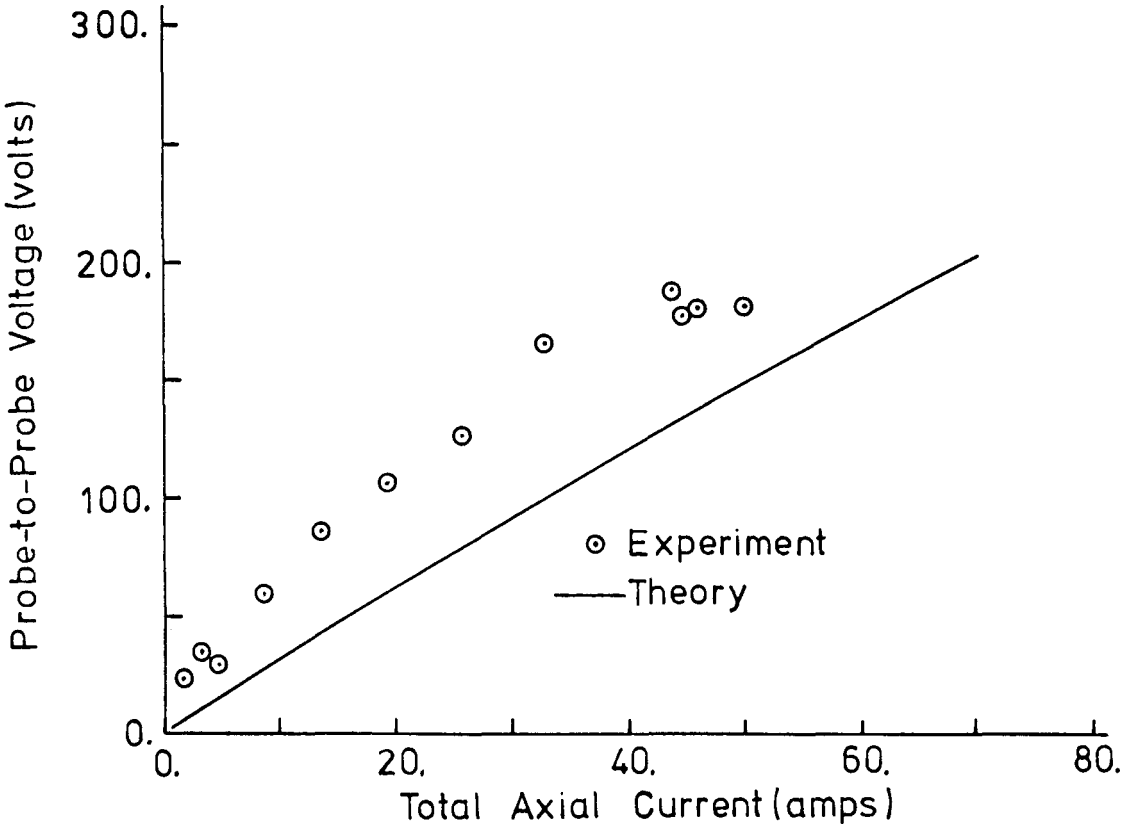

Figure 103a. Comparison of predicted and measured voltage difference between probes located away from the electrode wall as a function of total axial current for Run series 1.9-B. Conditions used in calculations compared with actual experimental conditions in Table 17.

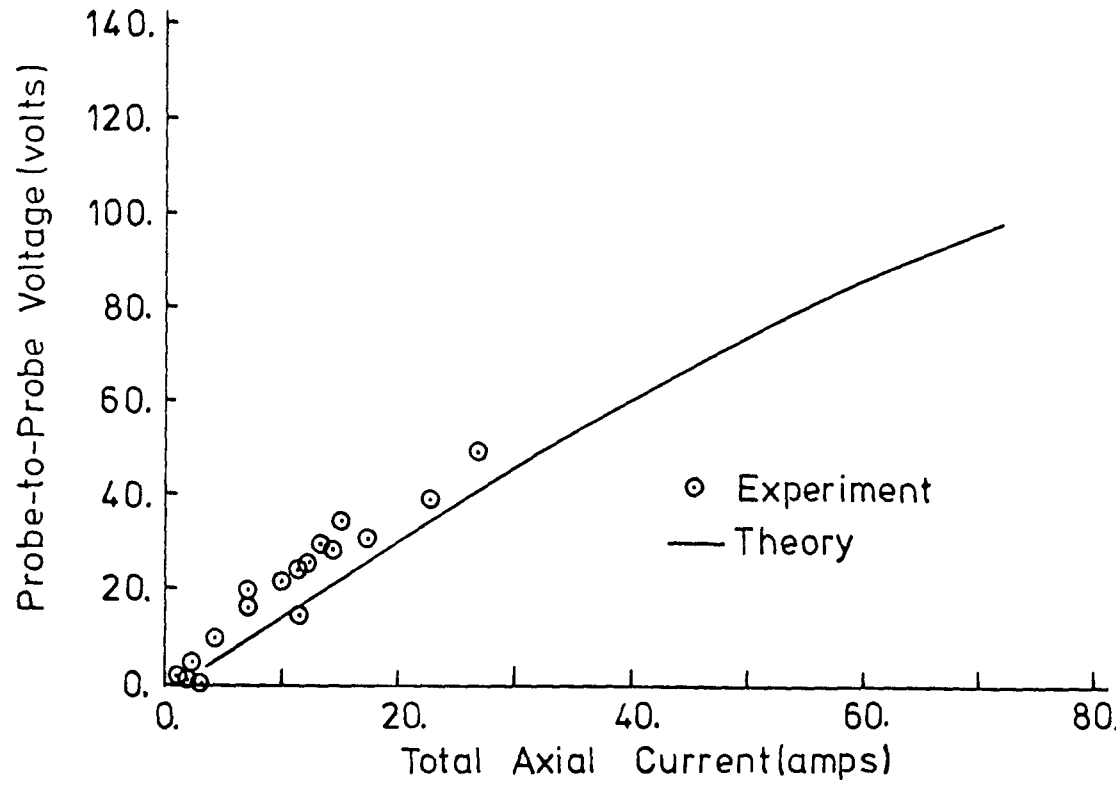

Figure 103b. Comparison of predicted and measured voltage difference between voltage probes located away from the electrode wall as a function of total axial current for Run series .75-A. Conditions used in calculations compared with actual experimental conditions in Table 17.

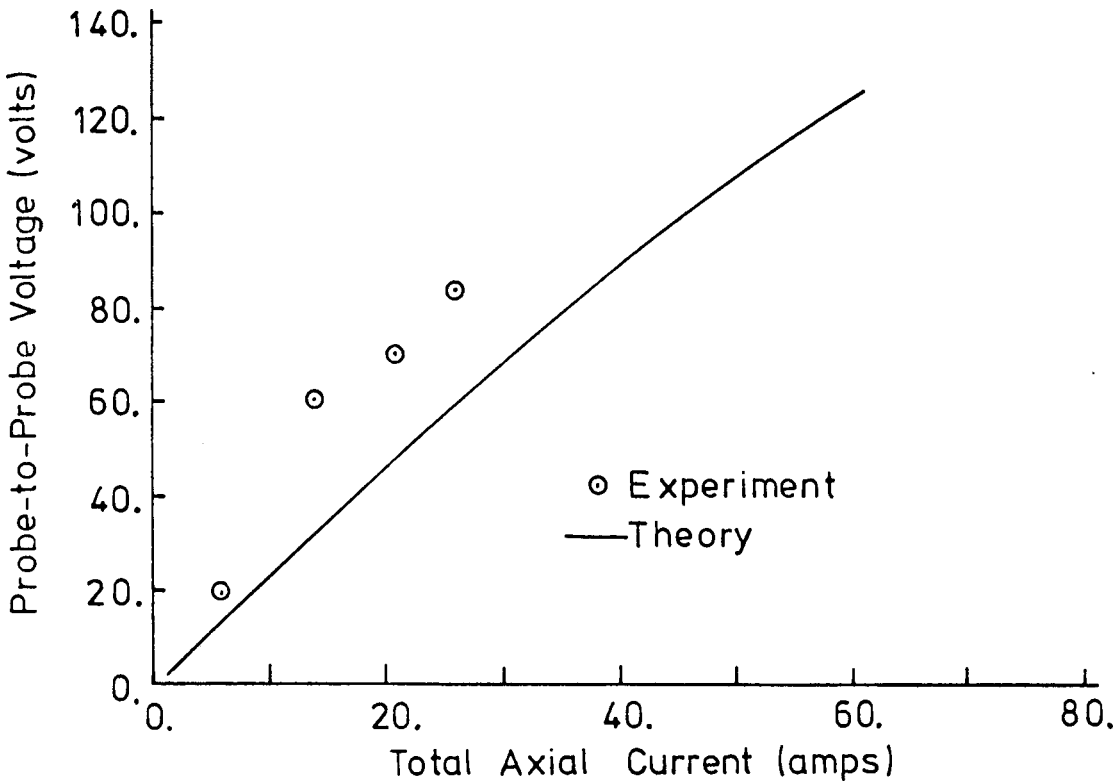

Figure 103c. Comparison of predicted and measured voltage difference between voltage probes located away from the electrode wall as a function of total axial current for Run series .75-B. Conditions used in calculations compared with actual experimental conditions in Table 17.

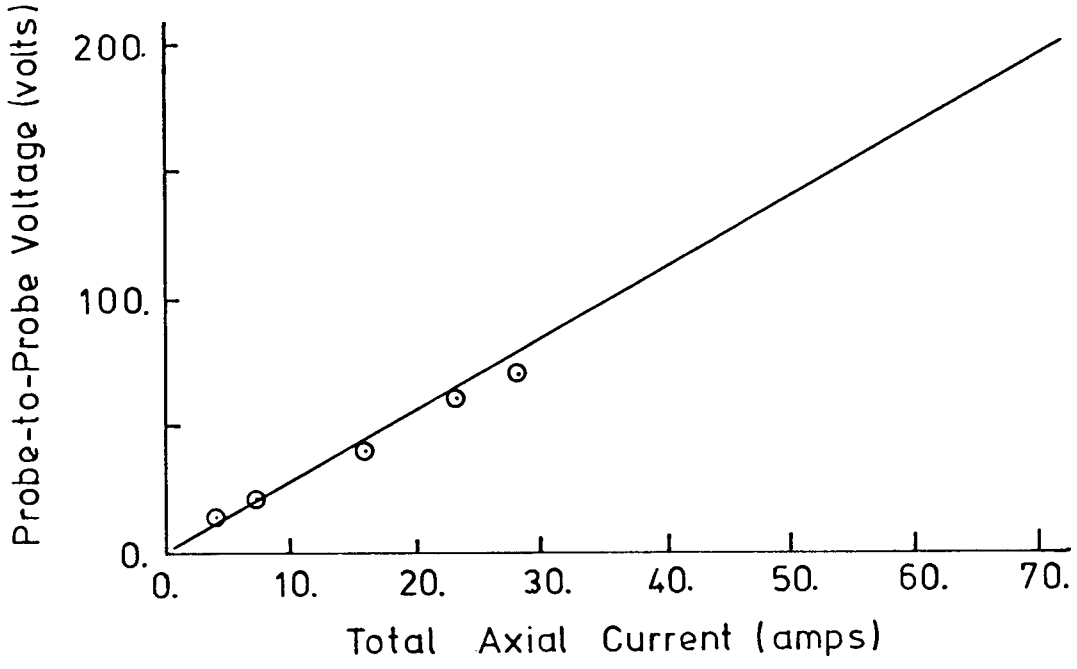

Figure 103d. Comparison of predicted and measured voltage difference between voltage probes located away from the electrode wall as a function of total axial current for Run series .75-C. Conditions used in calculations compared with actual experimental conditions in Table 17.

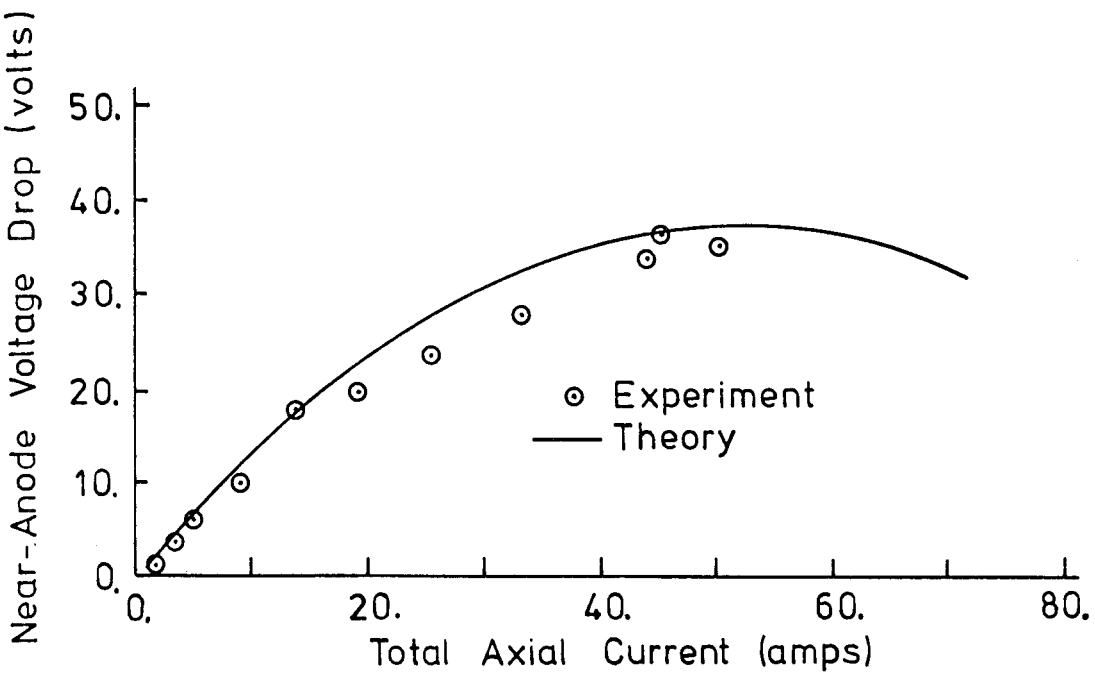

Figure 104a. Comparison of predicted and measured near-anode voltage drop as a function of total axial current for Run series 1.9-B. Conditions used in calculations in Table 17. Calculated curve includes anode surface sheath voltage drop.

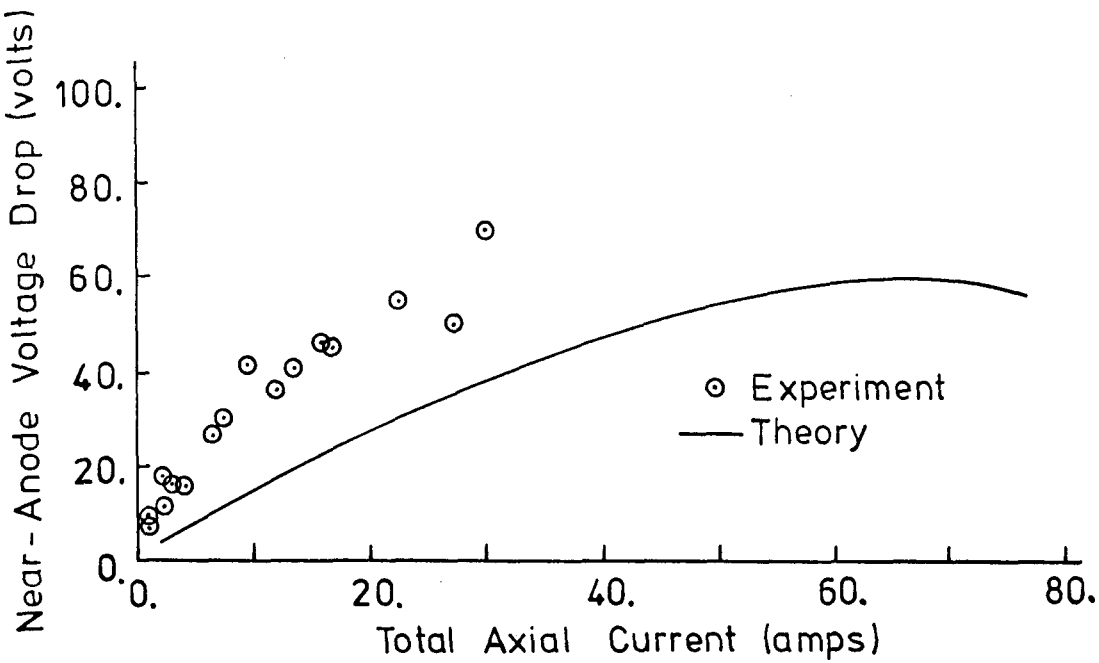

Figure 104b. Comparison of predicted and measured near-anode voltage drop as a function of total axial current for Run series .75-A. Conditions used in calculations compared with actual experimental conditions in Table 17. Calculated curve includes anode surface sheath voltage drop.

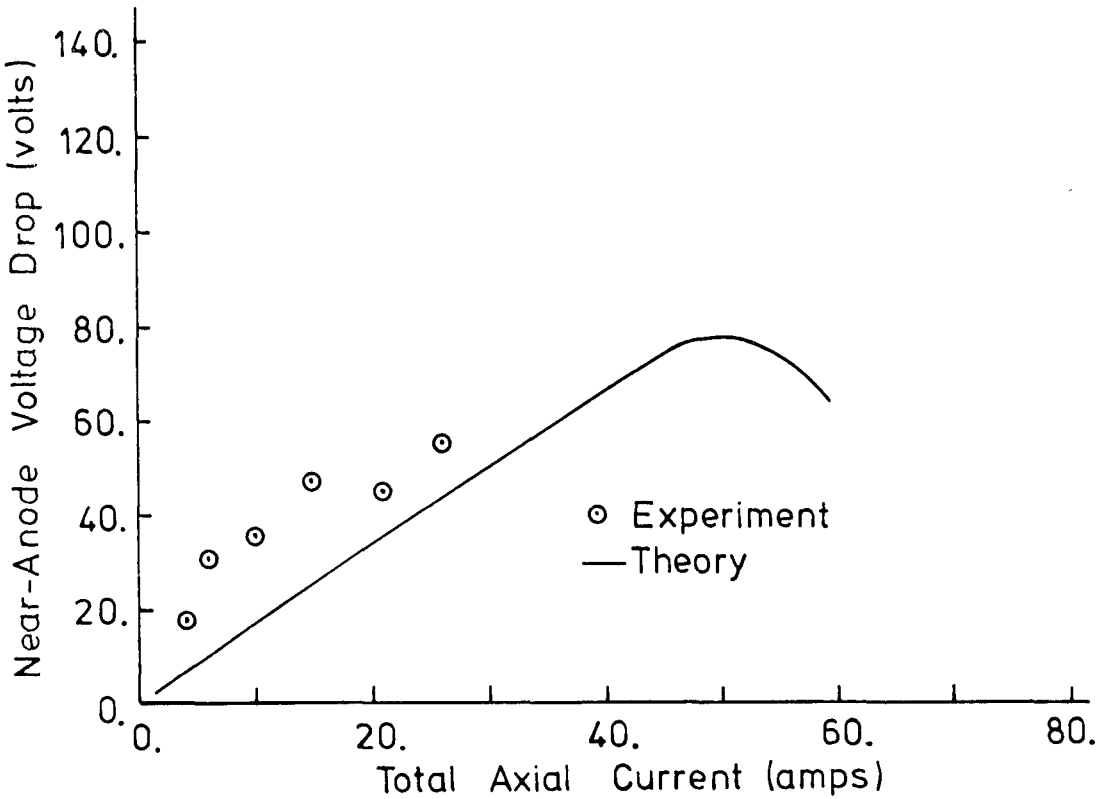

Figure 104c. Comparison of predicted and measured near-anode voltage drop as a function of total axial current for Run series .75-B. Conditions used in calculations compared with actual experimental conditions in Table 17. Calculated curve includes anode surface sheath voltage drop.

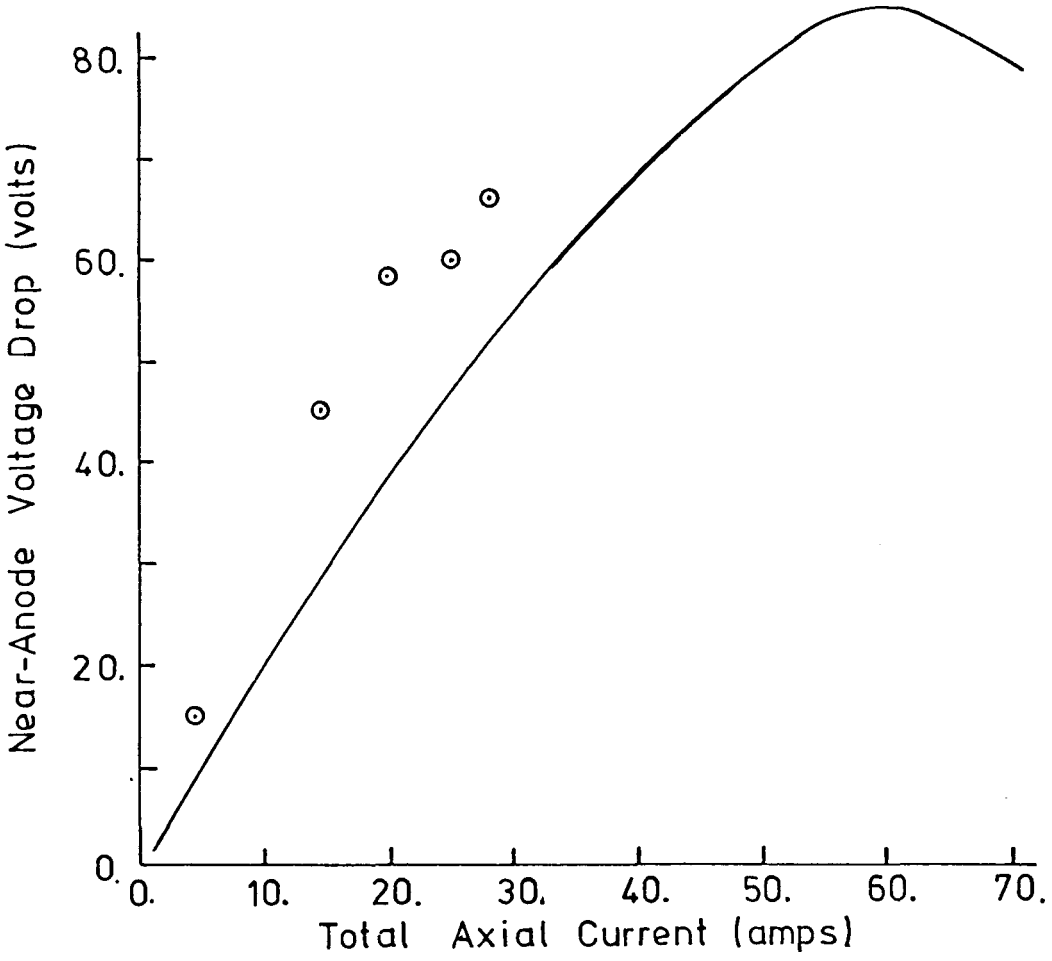

Figure 104d. Comparison of predicted and measured near-anode voltage drop as a function of total axial current for Run series .75-C. Conditions used in calculations compared with actual experimental conditions in Table 17. Calculated curve includes anode surface sheath voltage drop.

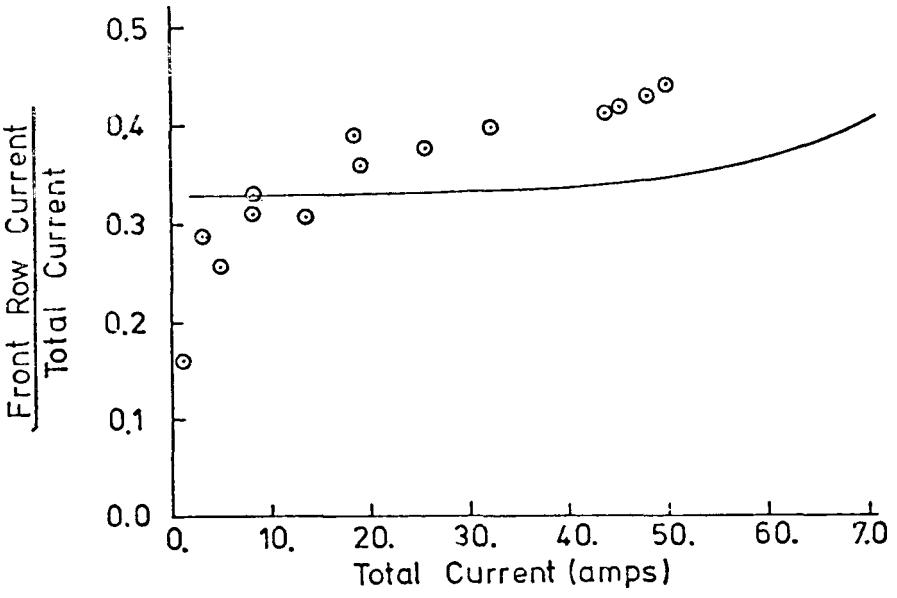

Figure 105a. Comparison of predicted and measured axial current distribution for Run 1.9-B. Axial current distribution represented by fraction of total electrode current which leaves the 1/4" portion of the electrode adjacent to the inter-electrode insulator.

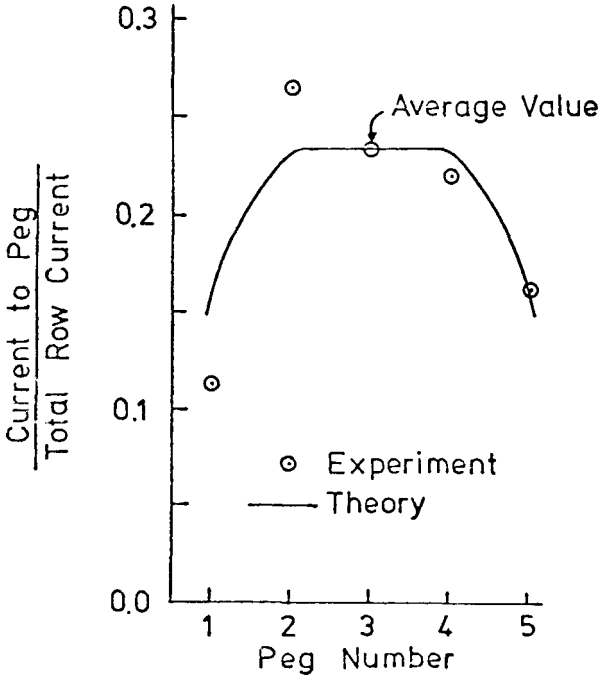

Figure 105b. Comparison of predicted and measured distribution of current across width for Run series 1.9-B. Current distribution represented by fraction of current leaving each of the five 1/4" segments of the electrode.

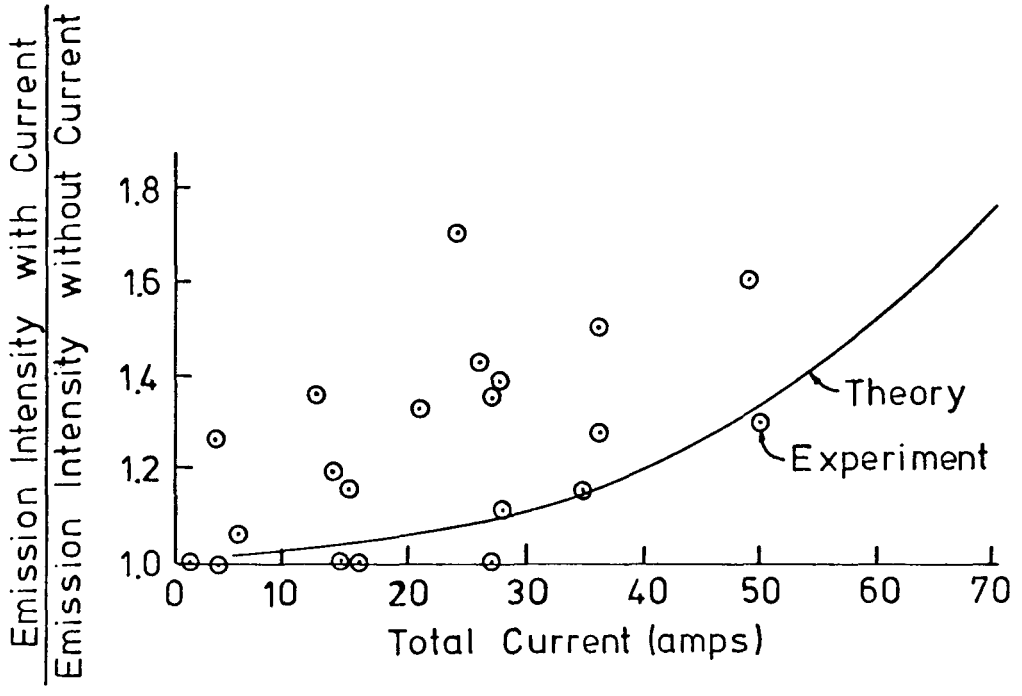

Figure 106. Comparison of predicted and measured radiation emission intensity for Run series .75-A. Measured values taken from photo-diode sighted along inter-electrode insulator centerline, approximately 2 mm from insulator surface; intensity presented as ratio of intensity with and without current. Calculated values determined from computed temperatures at same location, assuming the plasma to be optically thin to the radiation.

could easily be responsible for the over-prediction of the threshold voltage, although rapid heating of the inter-electrode insulator edges also probably contributes. It should also be noted that with fixed wall temperature, no delay time between initiation of current and breakdown is predicted by the model. It would appear that efforts to refine the plasma model (and extend it to the induced field configuration) should include further consideration of the physical processes important in the region near the electrodes.

With the above comments in mind, the comparison of theory and experiment shows that the proper trends are predicted by the model and that a reasonable first approximation to the threshold voltage for plasma initiated breakdown can be obtained using the model.

5.2.2 Threshold Predictions for Insulator Initiated Breakdown

Plasma-side heat transfer characteristics for the representative cases in Chapter 4 are close enough to those obtained for the more precise conditions used in Section 5.2.1, that the threshold voltage for insulator initiated breakdown will remain essentially as presented in Section 4.3.4. A comparison of measured and predicted threshold voltages is displayed in Table 17. As is evident in the Table predicted threshold voltages are generally higher than those measured in the experiment. The importance of axial variation in heat flux, precise relationship of the electrical conductivity with temperature and other effects have been demonstrated in Chapter 4 and these undoubtedly contribute to the discrepancy. However, the under-prediction of the effect of Joule heating in the plasma, as indicated by comparison of the plasma results, is likely the major factor.

Again, as with the plasma model, the insulator model proposed does indicate the proper trends and provides reasonable first approximations of the threshold voltage for insulator initiated breakdown.

5.3 Induced Field Experiments and Theory

Direct comparison of theory and experiment for the induced field configuration is limited to a comparison of calculated and measured non-breakdown behavior and simulated and measured breakdown behavior. The non-breakdown generator performance is treated first and then the breakdown response is discussed.

5.3.1 Non-Breakdown Generator Performance

The non-breakdown generator performance program was used to calculate the Hall voltage and Faraday voltage response with Faraday current for conditions of Run series .75-A and .75-C. In performing the calculations the measured plenum pressure, reactant flow rates, burner and plenum heat losses, and channel surface temperatures were used. A cathode voltage drop of 50 volts, typical of the experiments, was used and the slope of the current in the core was calculated by the coarse grid current distribution model for conditions of no breakdown. The calculated and measured Faraday voltage versus Faraday current response is displayed in Figure 107, and as can be observed the agreement is good. Calculated and measured Hall voltage versus Faraday current response for Run series .75-A is displayed in Figure 108 and as is evident in the figure the calculated values are close to the average values for the three gaps displayed. The slight non-linearity results from the increase in plenum (and channel) pressure with total current. The calculated and measured response of pressure drop across the active length with total Faraday current is displayed in Figure 109. Data from all run series are displayed in this figure and agreement is good, although the calculated pressure drop is slightly high.

The coarse-grid current distribution program was used to explore the cause of the different Hall voltage versus Faraday current response of different gaps as displayed for Run series .75-A in Figure 108. The core conditions (velocity, temperature and pressure) were provided by the generator performance program. A sketch of the region modeled is displayed in Figure 110 and indicates the inter-nodal conductances used in the calculations; the basic conditions for the calculations and experiments are given in Table 15. As can be observed in Figure 111, if the inter-nodal conductances corresponding to the .75 cm gap and the gap opposite are increased at higher Faraday currents, the Hall voltage versus Faraday current response for the three gaps is reasonably well modeled. It would appear that moderate increases (by a factor of 2 at the highest currents) in the conductance in the inter-electrode gap region (plasma or insulator) are responsible for the levelling out of the Hall voltage versus Faraday current curve.

Modeling of the Hall voltage versus Faraday current response for Run series 1.0-AP and 1.0-CP where the electrode pitch was doubled by pairing

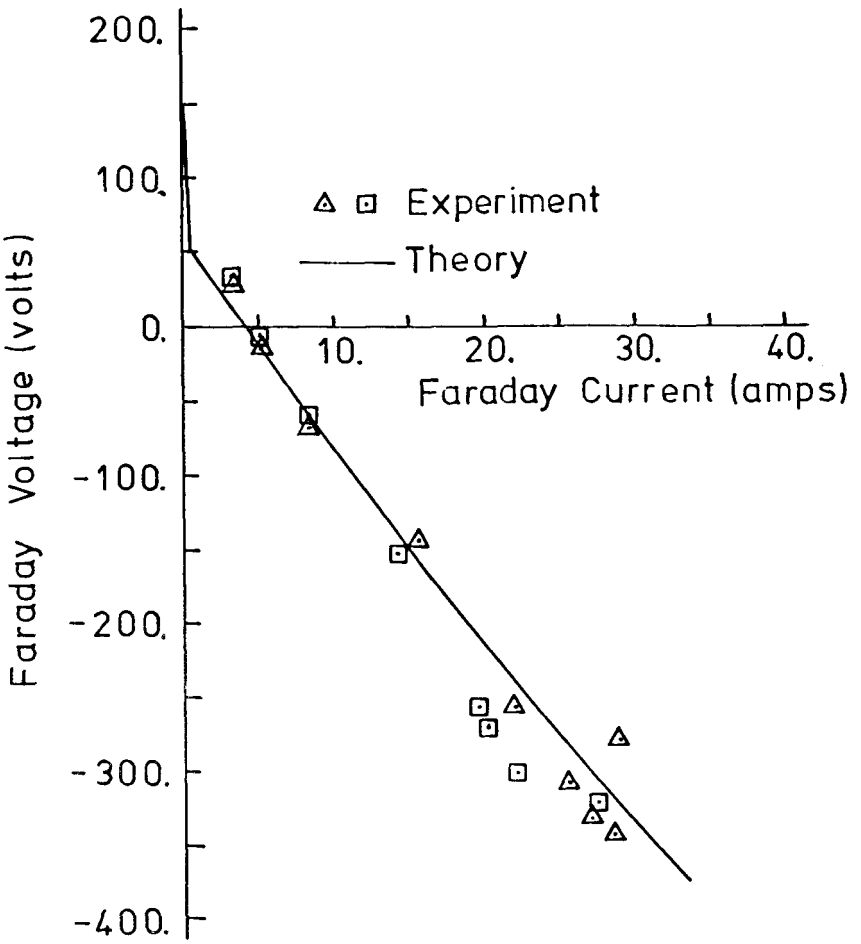

Figure 107. Comparison of calculated and measured generator load line (Faraday voltage versus Faraday current) for Run series .75-A and .75-C. Only data from the inner electrode pairs is shown. Conditions for the calculations are specified in Table 16.

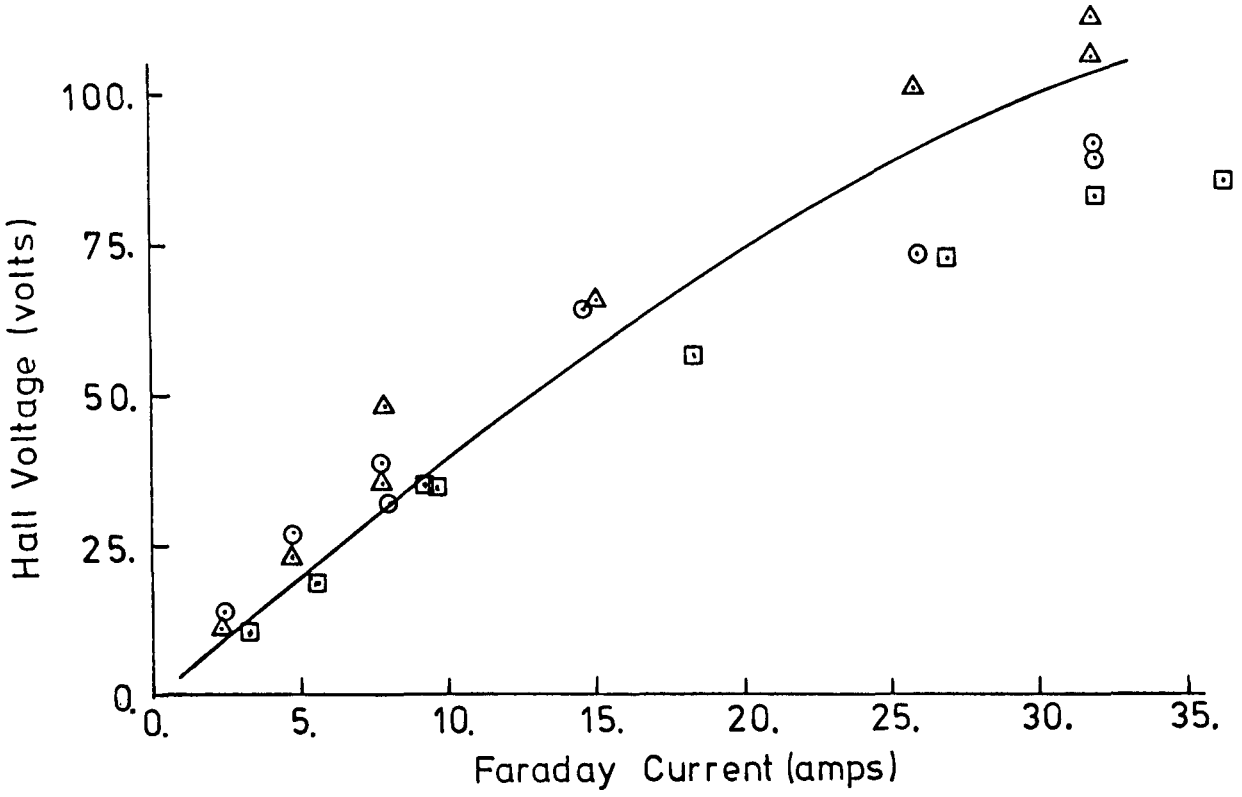

Figure 108. Comparison of calculated and measured non-breakdown Hall voltage versus Faraday current behavior. Data is taken from Run .75-A and represents the behavior of three inter-electrode gaps. Conditions used in the calculations are specified in Table 16.

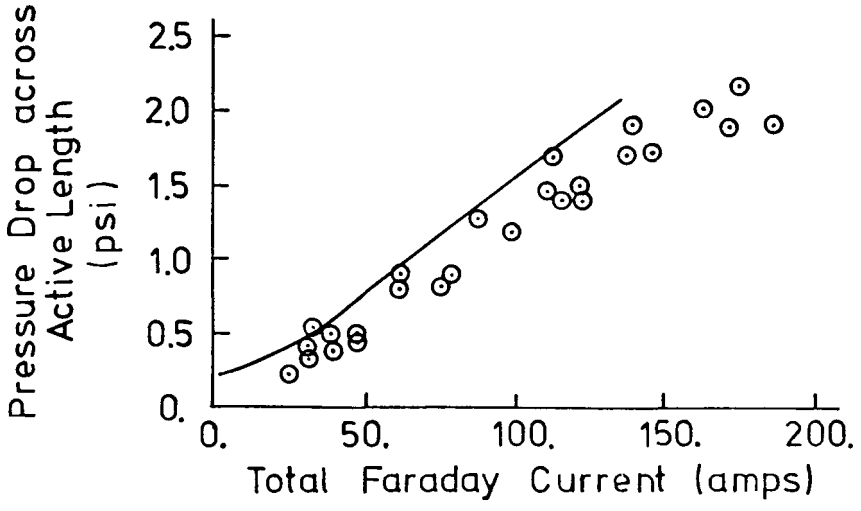

Figure 109. Comparison of calculated and measured pressure drop across active length of generator as a function of total Faraday current. Data from all Run series is displayed. Conditions for calculations specified in Table 16.

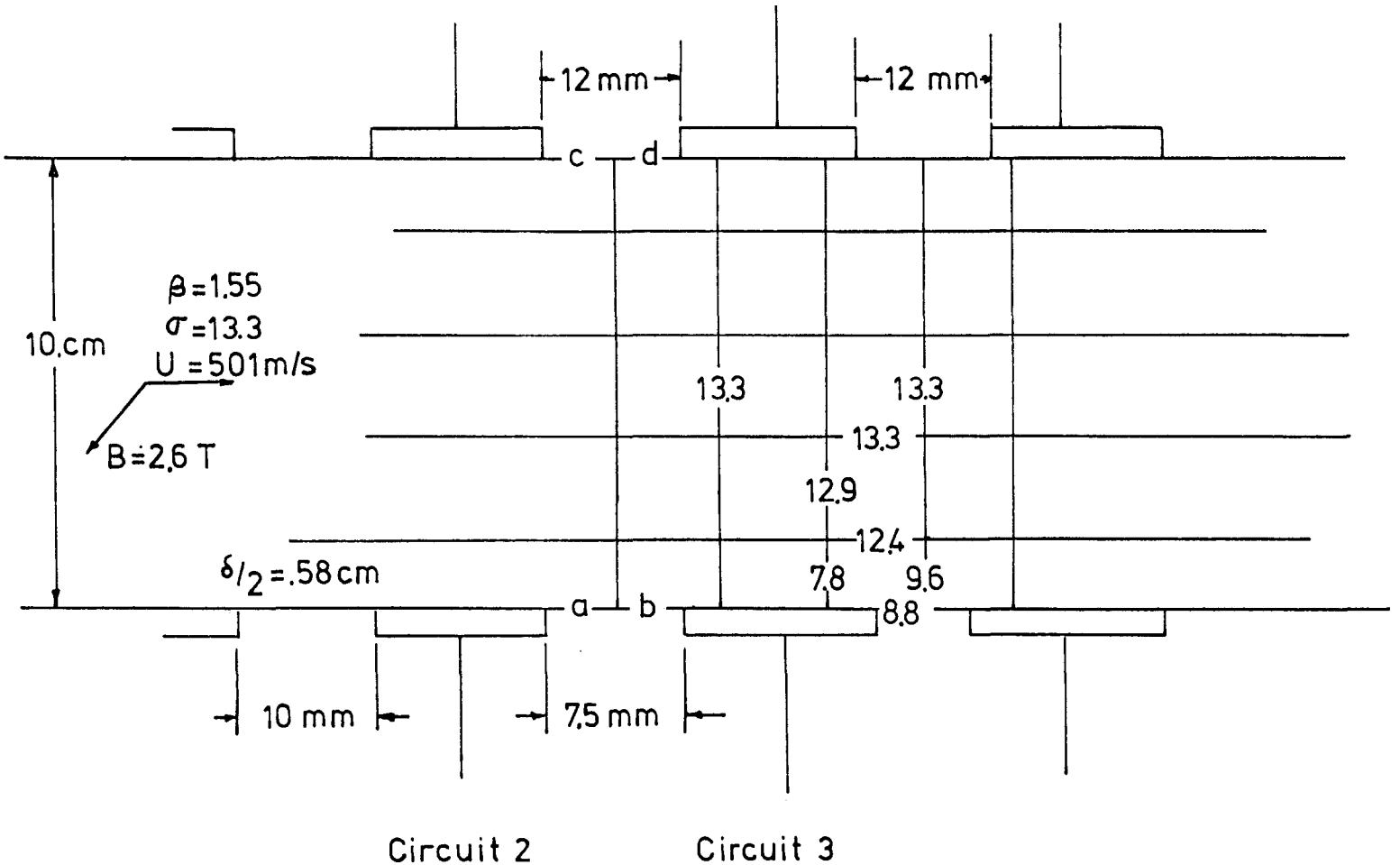

Figure 110. Schematic of region modeled using the coarse-grid generator model, showing values of the important parameters including the conductances used for representative inter-nodal regions.

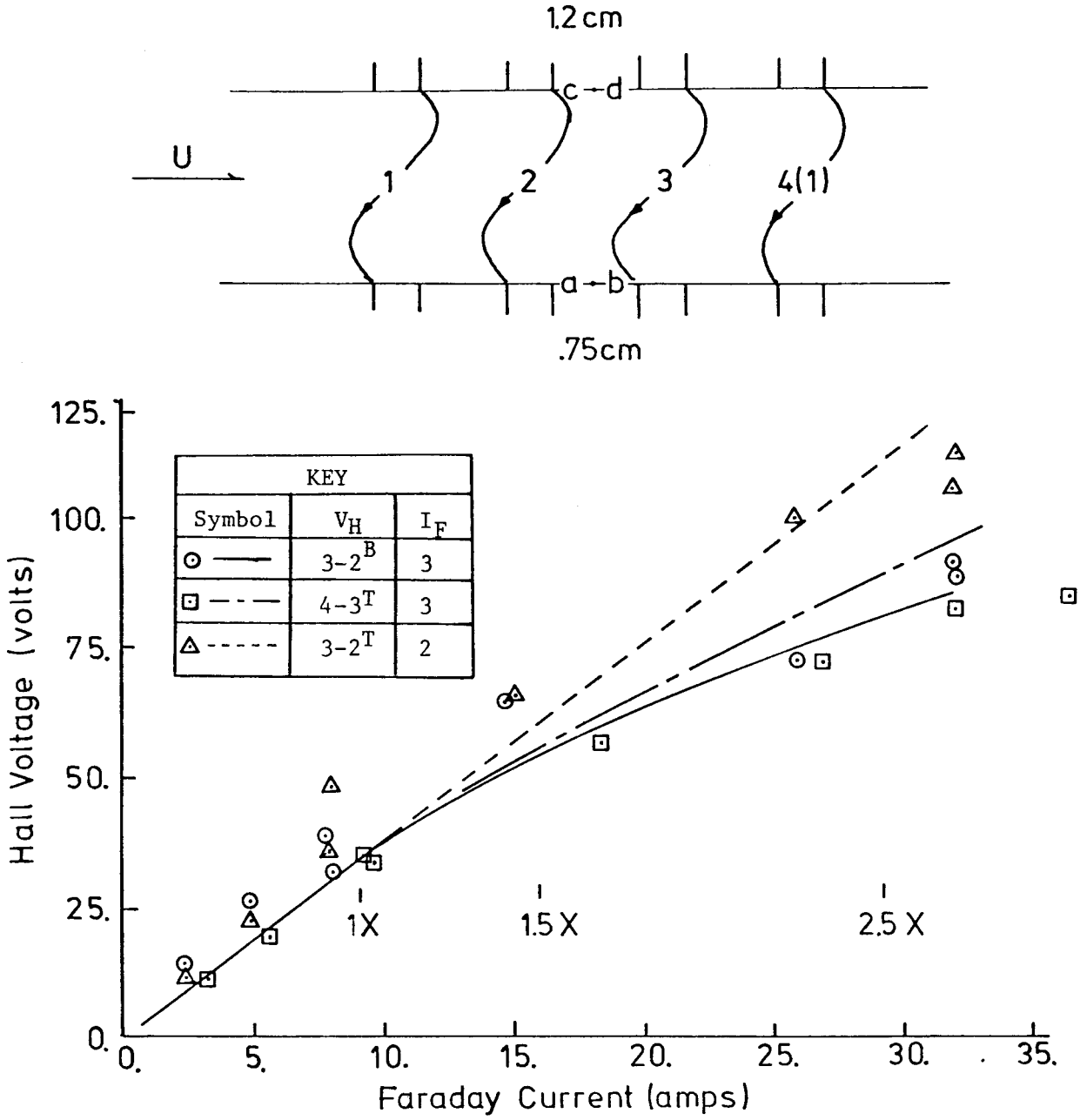

Figure 111. Comparison of simulated and measured non-breakdown Hall voltage versus Faraday current behavior for Run series .75-A. Internodal conductances a,b,c, and d (see sketch in Figure or Figure 111) were altered as indicated in the Figure to reporduce the behavior experimentally measured.

the electrodes adjacent to the 1.0 cm gap is not as good. A comparison of the calculated and measured Hall voltage response for Run series 1.0-CP is shown in Figure 112 and indicates that the behavior for large pitch to height ratio is not well modeled by the coarse grid model. The lack of close quantitative agreement is not surprising as is discussed in Appendix E.3. Nevertheless, some useful information can be obtained from comparisons of theory and experiment for conditions where breakdown is well developed.

The above comparisons demonstrate that the overall generator performance is well-modeled for non-breakdown conditions of these experiments and that the coarse grid current distribution model can be used to indicate the response in the near-insulator regions for moderate pitch to height ratios ($p/h \lesssim .4$).

5.3.2 Induced Field Breakdown Response

The coarse grid current distribution program was used to simulate a breakdown of Run series .75-A and a breakdown of Run series 1.0-CP. Calculated and measured Hall voltage versus Faraday current response for three inter-electrode gaps to a breakdown of the .75 cm anode wall gap is shown in Figure 113. The breakdown was simulated by increasing by a factor of eleven the inter-nodal conductances corresponding to the .75 cm gap. As can be observed in the figure the response of the Hall voltage for all three gaps is well represented. Applied field experiments would indicate a factor of 4 or 5 increase in average conductance to accompany breakdown; the larger increase required for good simulation by the coarse grid model is not unexpected. The development of the breakdown is represented in Figure 114 by presenting calculated results for successive increases in the inter-nodal conductances corresponding to the .75 cm gap. The calculated results are compared with the measured time response by arbitrarily associating a particular level of inter-nodal conductance with a time. As is evident in the figure, the measured response of Hall voltage and current to the electrode edges adjacent to the .75 cm gap can be well represented in this manner.

If the development of the breakdown is modeled with a constriction in the Faraday current preceeding the increase in inter-electrode conductance, a slight larger increase in current to the electrode edge downstream of the gap is predicted. Unfortunately the difference in response is not enough to clearly establish if a Faraday current constriction preceeds the breakdown.

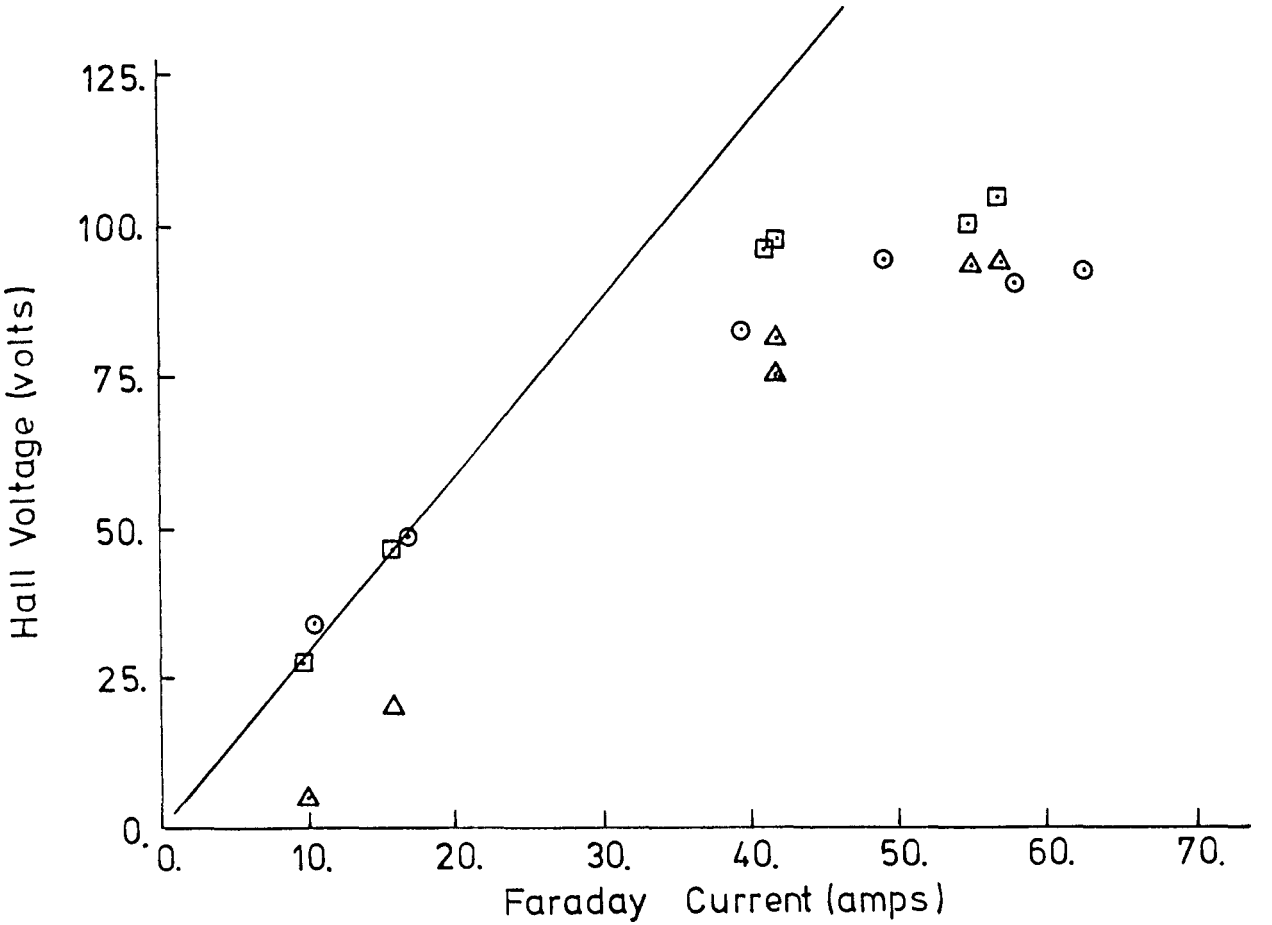

Figure 112. Comparison of calculated and measured non-breakdown Hall voltage versus Faraday current behavior. No attempt has been made to simulate the decline in slope measured experimentally. Conditions used in the calculations are specified in Table 16.

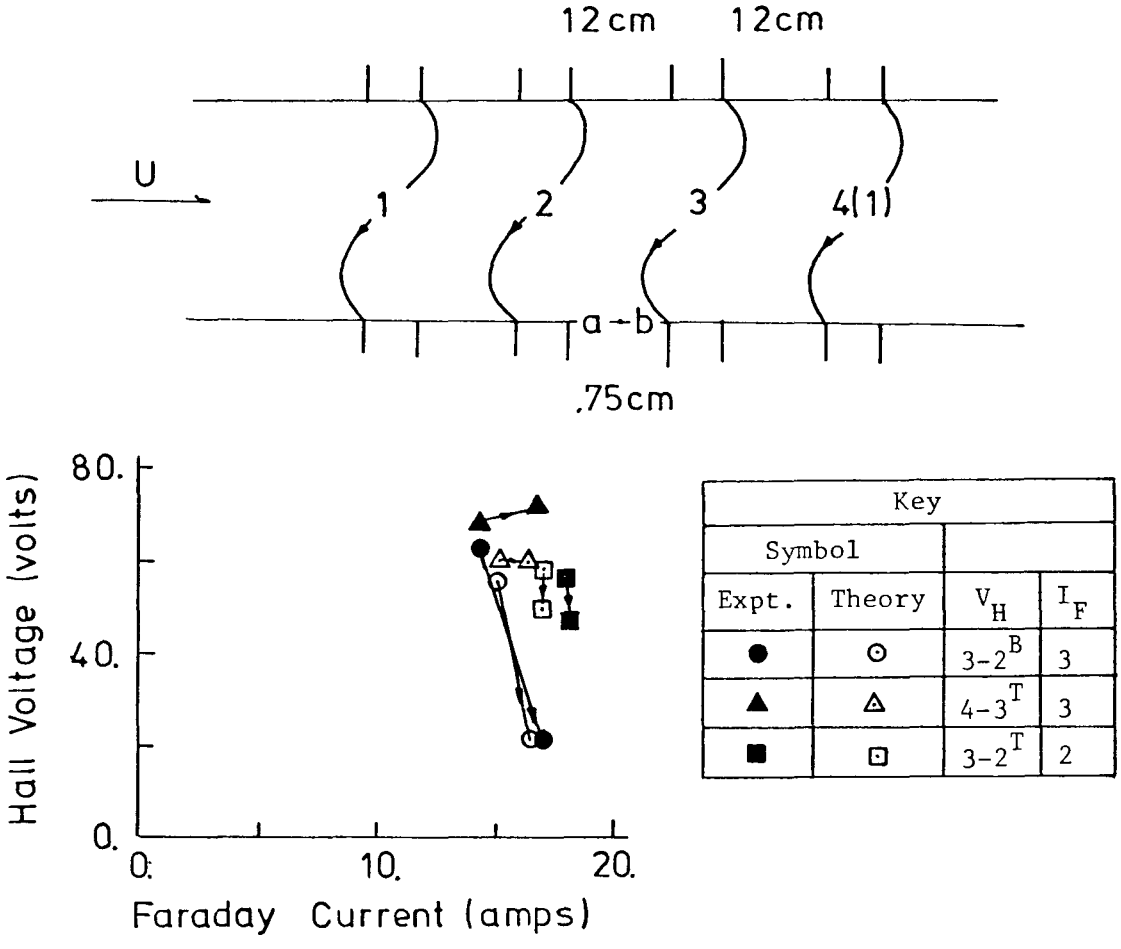

Figure 113. Comparison of simulated and measured Hall voltage and Faraday current response for a breakdown in Run series .75-A. Breakdown is simulated by increasing the internodal conductances corresponding to the .75 cm gap by a factor of 11. See Figure 111 for sketch of region and identification of the symbols.

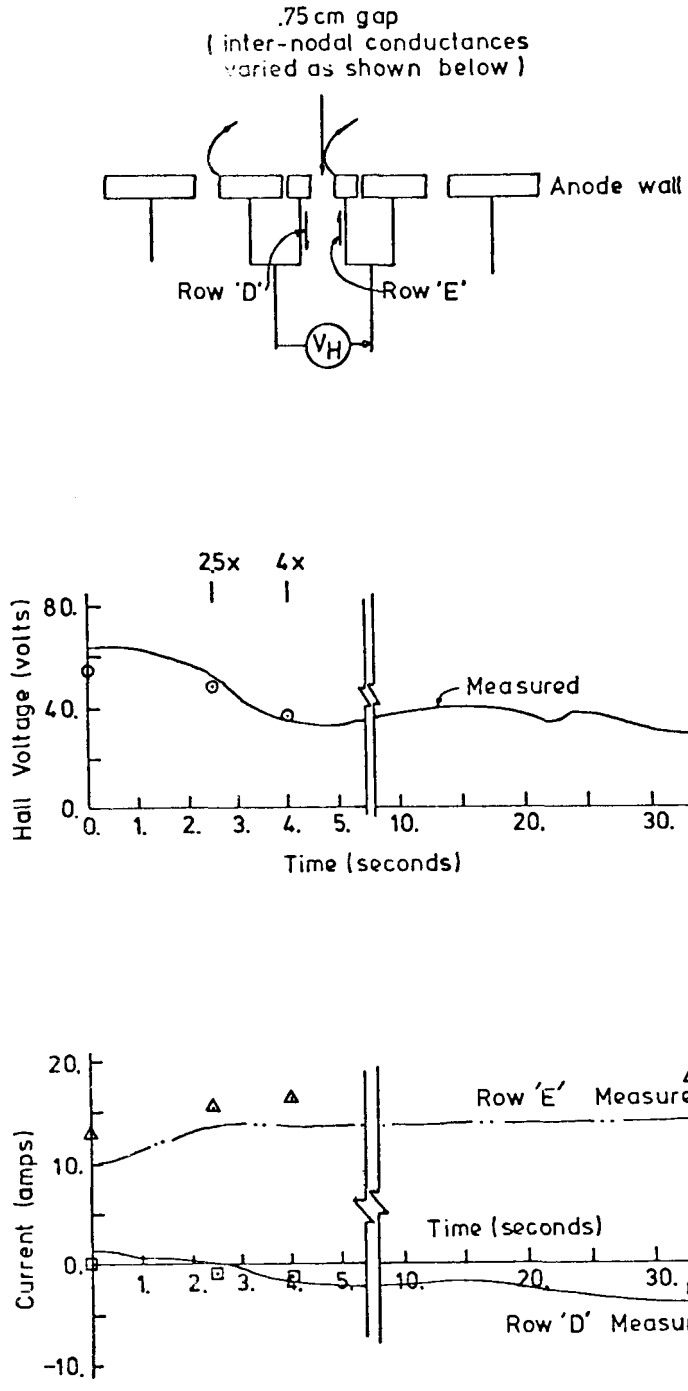

Figure 114. Comparison of measured and calculated response of Hall voltage and various currents in a simulated Hall voltage breakdown. The various stages of breakdown are simulated by incrementing the inter-nodal conductances corresponding to the gap suffering breakdown as indicated in the figure; the time scale for the calculations is arbitrary and has been adjusted to yield agreement with the measured response. Sketch identifies the current and voltage. Figure 111 shows the non-breakdown conditions.

Breakdown of a 1.0 cm cathode wall gap, followed by a breakdown of a second cathode wall gap was also simulated with the coarse-grid model. In this case, good qualitative agreement was obtained, however the quantitative agreement was poor. The poor quantitative agreement results from the inability of the coarse grid model to accurately predict the generator response for the large pitch to height ratios rather than the breakdown being poorly simulated.

The results presented indicate that the response of the generator to a simulated breakdown is well represented by a relatively coarse grid current distribution model. This suggests that modeling for the induced field configuration consider in detail only the inter-electrode region where breakdown occurs and use a relatively coarse grid (although less coarse than the one used in the present work) to represent the response of the generator. This approach removes the requirement that breakdown occurs at every gap as is required in the model of Oliver and at the same time removes the need to specify the overall behavior of the generator prior to computing the breakdown characteristics of the interelectrode region as been done in calculations for the Soviet channel using the model of Oliver.

CHAPTER 6

SUMMARY AND CONCLUSIONS

6.1 Summary of Present Investigation

An experimental and analytical investigation of axial field breakdown in non-slagging wall, combustion-driven MHD generators has been performed. Some experiments and analysis were performed for a segmented Faraday generator, however more detailed studies were performed for a simplified configuration in which a voltage was applied to a pair of adjacent electrodes in the absence of a magnetic field. Plasma conditions for both types of experiments were typical of expected central station power plant MHD applications. Breakdown was characterized by a rapid decline in axial voltage and a change in the mode of current transport from a relatively diffuse mode to a highly constricted mode. Dual filter cine-photographic records obtained for the simplified configuration demonstrated that breakdown could be initiated in the plasma or in the inter-electrode insulator; however, for breakdown initiated in the plasma, the insulator became the dominant breakdown current carrier within a few seconds. Plasma initiated and insulator initiated breakdown resulted only when a threshold voltage was exceeded, the threshold voltage increasing with increased insulator gap size. For the electrode wall configuration studied, the threshold voltage for plasma initiated breakdown was significantly higher than the threshold voltage for insulator initiated breakdown. Both threshold voltages were considerably in excess of the voltage maintained after breakdown was well developed. Little effect of freestream velocity, freestream temperature or electrode polarity was observed in the experiments with the simplified configuration. Insulator initiated breakdown observed in the generator experiments was qualitatively similar to the insulator initiated breakdown observed in the simplified configuration, although the threshold voltage for a particular insulator gap size was somewhat reduced in the generator experiments. No qualitative differences in the development of breakdown on an anode wall and on a cathode wall were observed.

Simple considerations indicated that thermal breakdown rather than field-induced breakdown was responsible for the behavior observed in the experiments. A computer model was developed to predict the non-breakdown

and incipient breakdown behavior for the inter-electrode insulator region for the simplified configuration. The two-dimensional model for the plasma included a solution of the unsteady (in the mean) turbulent boundary layer equations and a solution for the distribution of current. The electron-continuity equation was solved such that the effects of electron-ion kinetics were included. A separate analytical solution was obtained for the electrical behavior in the region near the anode where space-charge effects are important; similar effects in the region near the cathode were treated in an empirical fashion. The insulator was modeled by the heat conduction equation with the Joule heating evaluated using an electrical conduction model.

Calculated results for fixed insulator temperature displayed a thermal runaway behavior similar to the plasma initiated breakdowns observed in the experiments. The predicted threshold voltage was significantly higher than the measured threshold (30% to 50% higher), but the model predicted the proper variation of threshold voltage with insulator gap size. Detailed comparison of predicted and measured plasma behavior indicated that the model under predicts the plasma resistance at low current and under-predicts the effects of Joule heating in the inter-electrode region. Calculated results for variable insulator temperature displayed a thermal runaway behavior similar to the insulator initiated breakdowns observed in the experiments. Again, the predicted threshold voltage was significantly higher than the measured threshold, but the model predicted the proper variation of threshold voltage with insulator gap size. Under-prediction of the effect of Joule heating by the plasma model is likely responsible for the high threshold voltages predicted, although several other factors could also contribute. Results of a simplified analysis indicated that threshold voltages for planar and axi-symmetric thermal breakdown were comparable, with the threshold voltage for axi-symmetric breakdown higher than that for planar breakdown due to the improved cooling characteristics; results with the detailed insulator model also displayed a lower threshold voltage for planar breakdown.

A quasi-one-dimensional generator performance prediction code was used to predict the generator behavior for non-breakdown conditions. A coarse grid current distribution model was developed for the generator configuration and was used to simulate breakdown at one or more of the

insulator gaps. Measured overall generator behavior was well predicted by the quasi-one-dimensional performance code for non-breakdown conditions. Calculations to simulate breakdown showed that the effects of breakdown at an insulator gap on the generator performance could be moderately well described with the coarse grid model.

6.2 Implications in MHD Generator Design

Design philosophies regarding the problem of Hall voltage breakdown might be characterized as:

> Philosophy 1) Assume breakdown will occur and design the generator wall and generator electrical controls to minimize the damage to the generator, while introducing the minimum detrimental effect on generator power output and efficiency,
>
> and
>
> Philosophy 2) Design the generator wall and generator controls to prevent breakdown from occurring.

As stated above, it would appear the latter approach is more desirable; the choice of the first philosophy by most generator designers results from the lack of knowledge to effectively implement the second philosophy, or the belief that the second philosophy is not practically realizable. While the present study does not answer all questions regarding the prevention of breakdown it does provide some information to evaluate the gains by following the second philosophy and some indications of how to successfully prevent breakdown.

A channel designer has many parameters to choose, the most important of which, for breakdown considerations, might be:

a) electrode pitch
b) inter-electrode insulator gap
c) average axial (Hall) field (generator length and magnetic field strength)
d) electrode configuration (window frame, V-wall, etc.)
e) electrode wall component materials and design temperatures.

Design philosophy 1, as implemented at AVCO, has lead to

a) electrode configurations where the current which can be coupled to a single arc is limited

b) active electrical controls on the generator to limit the Hall voltage per pair to levels below the steady burning voltage of a breakdown arc, and

c) limits on the average Hall field commensurate with b)

For the relatively large gaps (7.5 mm and 19.1 mm) used in the present studies an electric field of ~ 40 volts/cm is exhibited by the well-developed breakdown; this value agrees well with the value advanced by AVCO. To first approximation, this result is roughly independent of electrode configuration, electrode wall materials, or component temperatures. Further, the steady-arcing field is not likely to be dependent on insulator material or whether or not the wall is covered with slag, as most insulator materials and slag have comparable high temperature properties. The main parameters available to the designer are the average electric field, the electrode pitch and insulator gap size. For a given average axial electric field in the core, the average field across the insulator will be

$$E_{x_{insulator}} \sim \left(\frac{pitch}{gap}\right) E_{x_{core}} .$$

Thus if the maximum electric field at the insulator is limited to the steady arcing value of 40 volts/cm,

$$E_{x_{core}} < \left(\frac{gap}{pitch}\right) E_{x_{\substack{insulator \\ maximum}}}$$

$$< 40 \text{ volts/cm} \left(\frac{gap}{pitch}\right) .$$

Thus, to a first approximation, the first design philosophy results in a limitation on the core axial field which depends only on the gap to pitch ratio. This indicates that improvements with respect to maximum Hall field can be achieved only with increases in average current density to the electrode. The desire to limit the maximum current to be coupled to a breakdown arc would indicate that a small pitch is desirable, although subdivision of the electrodes in the magnetic field direction and active controls would also seem required to limit damage.

The present study has demonstrated that a threshold voltage must be exceeded if breakdown is to occur, and that the threshold voltage is

considerably higher than the voltage maintained after breakdown is well developed. The threshold voltage for insulator breakdown was lower than that for plasma initiated breakdown, however it would appear that by careful thermal design insulator initiated breakdown could be prevented for clean wall generators. On the other hand, the experimentally measured threshold voltage for plasma initiated breakdown was only moderately affected by any of the parameters studied except gap size. The threshold electric field for plasma initiated breakdown increased with decreasing gap size in the applied field experiments and might be expressed as

$$E_{x_{\substack{\text{insulator} \\ \text{threshold}}}} = \frac{130 \text{ volts}}{\text{gap (in cm)}} + 70 \frac{\text{volts}}{\text{cm}} \left(\frac{\text{gap}}{\text{pitch}}\right) .$$

Note: Although data for only two gap sizes were obtained a linear variation of threshold voltage with gap size is indicated by the calculations and seems reasonable except for very small gap sizes. Also, while the threshold voltage for insulator induced breakdown was lower it displayed a similar behavior as the threshold for plasma initiated breakdown.

The maximum core axial electric field becomes

$$E_{x_{\substack{\text{core} \\ \text{threshold}}}} < \frac{130 \text{ volts}}{\text{pitch}} + 70 \frac{\text{volts}}{\text{cm}} \left(\frac{\text{gap}}{\text{pitch}}\right) .$$

For fixed gap/pitch ratio, that is for fixed average current density at the electrode, substantial increases in core axial field can be obtained by a reduction in electrode pitch. For example, at a gap to pitch ratio of .25, the maximum core field is 83 volts/cm at a 2 cm pitch and 148 volts/cm at a 1 cm pitch. Thus for the same average current density (gap/pitch = .25) and the same electrode pitch (pitch = 1 cm) the maximum allowable axial field based on the threshold level is ~ 150 volts/cm or ~ 15 times the value based on the steady arcing level. Although threshold voltage levels for plasma initiated breakdown are likely to be lower for the generator configuration than were measured for the applied field configuration the above estimates do indicate that substantial gains can be achieved by the prevention of breakdown.

Presence of a slag layer on the electrode wall could significantly alter the breakdown characteristics of the inter-electrode gap, as well as

lead to a long term degradation of the electrode wall components. While the present study does not consider such a layer, it would appear that the slag layer will behave much as the inter-electrode insulator and that in as much as the thermal state of the slag is more difficult to control, slag initiated breakdown may dominate the problem. Obviously, in view of the significant possible gains indicated above, analytical and experimental work relating to the slagging wall configuration is desirable.

6.3 Conclusions and Recommendations

An electro-thermal instability has been established as the principle cause of axial voltage breakdown in non-slagging wall, combustion-driven MHD generators. Experimental and analytical work has demonstrated that breakdown can be initiated either in the plasma or the inter-electrode insulator and has shown that breakdown occurs only when a threshold voltage is exceeded. Very simple arguments indicate that significant improvements in generator performance can result from prevention of breakdown. The present study indicates that by careful thermal design insulator initiated breakdown can be prevented and that for fixed gap/pitch ratio (fixed average current density) a smaller pitch should be more resistant to breakdown.

The investigation has demonstrated the utility of studies on a simplified, non-generator configuration. An analytical model for the thermal and electrical behavior of the plasma and inter-electrode insulator for such a simplified configuration predicts most of the qualitative features leading up to axial field breakdown and predicts threshold voltages comparable to those measured in the experiments. Detailed comparisons of theory and experiment indicate that even with the relatively sophisticated model utilized, including a detailed solution for the current distribution, only moderately good agreement is obtained.

The following recommendations for future work are suggested in order that detailed design strategies to prevent Hall voltage breakdown can be developed:

1) extend the detailed analytical model to the induced field configuration, including both the plasma and insulator behavior and allowing for breakdown at isolated insulator gaps,

2) evaluate the above analytical model by detailed comparison with induced field experiments,
3) extend the experimental and analytical work to the slagging wall situation, perhaps first concentrating on the simplified configuration,
4) improve the predictive capabilities for plasma fluid and electrical behavior, perhaps first concentrating on very simple discharge configurations, and
5) improve the inter-electrode insulator modeling to include effects of axial gradients in plasma side heat transfer and several other effects.

APPENDIX A

SEGMENTED ELECTRODE CONSTRUCTION

This appendix describes the design of the segmented electrodes used in the applied field and induced field experiments. The overall design is first discussed and the heat transfer calculations outlined. The technique developed for maintaining good thermal contact is then discussed and finally the electrical lead out designs for the induced field and applied field configurations are briefly discussed.

Overall Design. Current distribution measurements by electrode segmentation required a compact electrode design capable of maintaining a uniform surface temperature and maintaining adequate insulating characteristics at the operating conditions. The peg electrode design shown in Figure A.1 was found to meet the requirements as long as good thermal contact was maintained at the metal/ceramic interfaces. Cooling of the stainless steel pegs is predominantly through the alumina wafer to the water cooled copper backing piece; the air gap between the electrical lead and pin and the copper piece reduces the heat loss by the lead out pin heat loss to less than 5% of the total heat transfer. Thermal shorting of the end of the lead-out pin does not result in appreciable heat transfer. A one-dimensional heat conduction analysis was used to choose the component thickness to achieve the desired surface temperature at the design conditions. The gas-side heat transfer coefficient was calculated from simple turbulent boundary layer correlations. Figure A.1 indicates relative values of the various thermal resistances for typical conditions. In the induced field experiments where the overall height of the electrode was limited, thermal choking of the stainless steel pegs was used to achieve the desired surface temperature. Electrical insulation of the pegs from the copper piece is provided by the alumina wafers and insulation between the pegs is provided by the thin dense alumina wafers inserted between the electrode pegs.

Thermal Contact. Early experiments were performed without attaching the alumina wafers to the stainless steel pegs or to the copper backing, however poor thermal contact resulted in excessive surface temperatures and of more importance the thermal resistance varied considerably from peg to

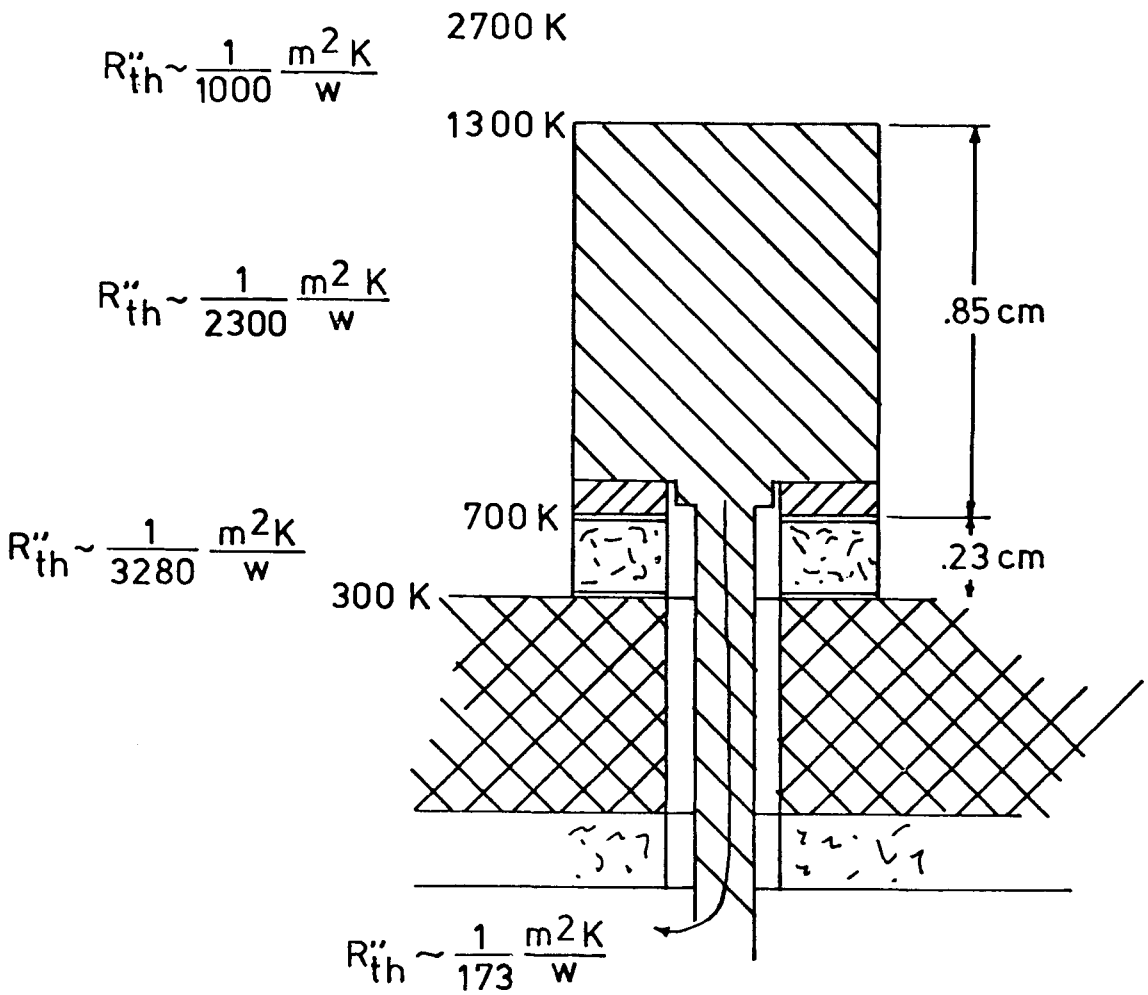

Figure A.1. Schematic of segmented electrode design indicating the thermal resistances of the important components.

peg. Although use of a softer material such as boron-nitride in place of the dense alumina and the addition of tension springs could alleviate the problem of variable thermal resistance it was decided that a metallizing approach would produce a more reliable and compact design. The major difficulties encountered were associated with the differential thermal expansion of the stainless steel peg and the alumina wafer and in the compatibility of the metallized surfaces with the braze and solder materials to be used. The design shown in Figure A.2 and the techniques described below are the result of an iterative process and represent the final design.

A nickel surface was prepared on both sides of the slab of alumina by R and W Products of Redwood City, California. The technique used was a standard molymanganese process followed by a nickel plating and sintering operation. The wafers were cut from the slabs of alumina using a diamond wheel and the center hole drilled using a diamond core drill. Attempts to bond the metallized wafers directly to the stainless steel pegs resulted in a shearing of the metallizing from the alumina due to the differential contraction of the two materials as they cooled. This problem was accentuated by the high temperature braze material required to form the bond with the stainless steel (in an inert furnace without flux) and by the stiffness of stainless steel. Further, it was difficult to form a good low temperature braze joint, or even a good solder joint, with the nickel plated surface. These problems were solved by brazing a thin (~ 30 mil) copper piece to the rear of the stainless steel peg and coating a very thin layer (~ 2-3 mil) of high temperature braze material (nickoral) over the nickel plating of the alumina wafers. The wafers and the pegs could then be silver brazed with no problems of shearing. Subsequent to the brazing operation the flux was boiled off such that it would not degrade the nickel to alumina joint. The second face of the alumina wafer was also coated with braze material resulting in a more reliable solder joint when final assembly of the pegs to the copper base was performed.

Electrical Leads. The stainless steel pin was used to conduct the current from the peg to the lead out wires to which the individual current shunts were attached. The pins are of a large enough diameter to accommodate 60 amps for a period of at least a minute; electro-plating of a thin layer of copper along the outside of the pin was considered however this seemed

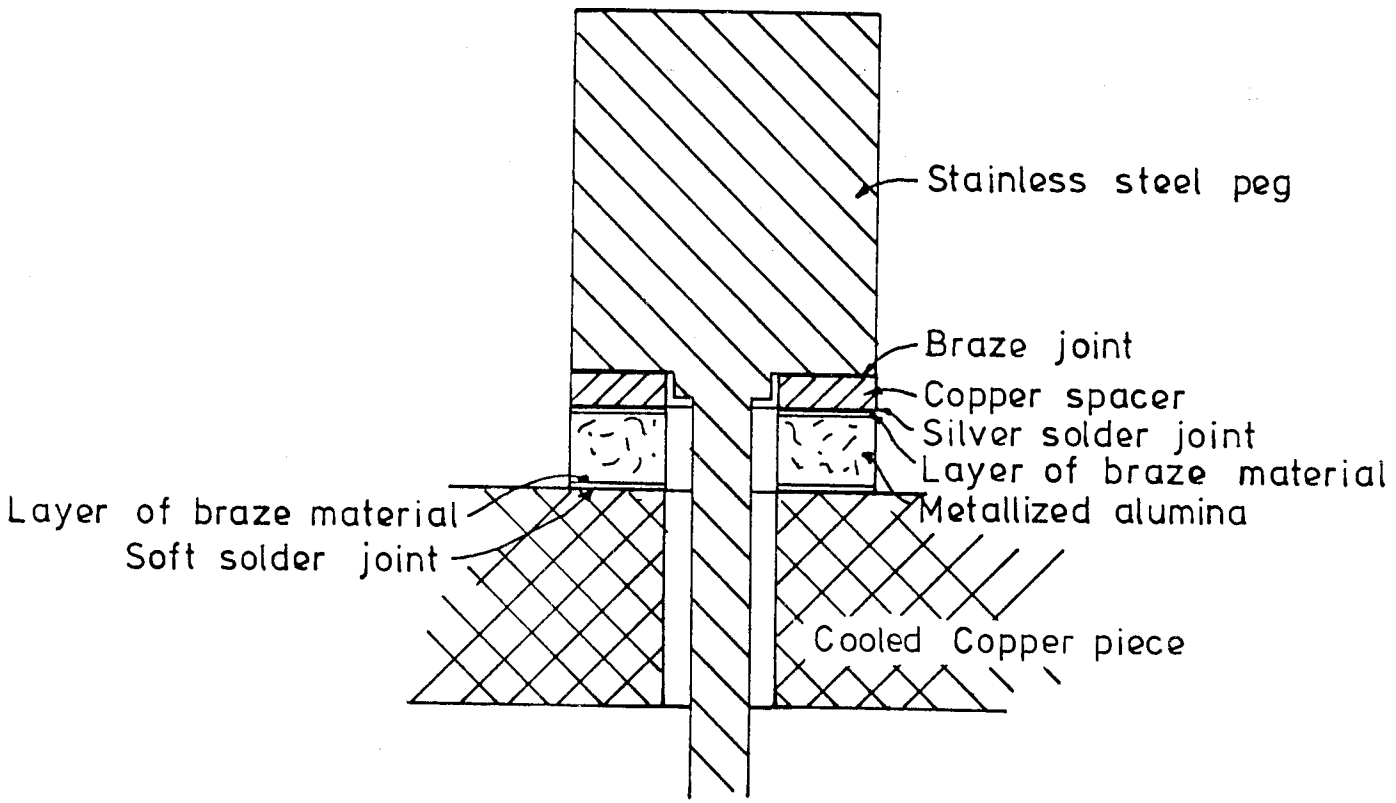

Figure A.2. Schematic of segmented electrode design detailing the components used in producing reliable metal-ceramic thermal and mechanical contact.

unnecessary for the present application. For the applied field configuration easy access to the rest of the electrode allowed a special plug to be used for quick connection of the pegs to the external circuit; limited access in the induced field configuration resulted in a less convenient electrical lead out design. In both cases care was exercised to provide sufficient conductor size and cooling to prevent overheating of the conductor cables.

APPENDIX B

DUAL FILTER PHOTOGRAPHY

This appendix presents details of the optical device used to obtain the dual filter photographic records. The optical train is first discussed and then the calibration techniques are presented. Calibration curves for the various components are included.

Optical Train. The schematic of the optical train shown in Figure B.1 details the light paths followed for formation of the various images on the film. Light from the channel is split at the first beam splitter with part of the light directed through the interference filter and part of the light directed through the red filter. The two beams are subsequently combined at beam splitter 2 and directed toward the camera by beam splitter 3. By proper adjustment of the mirrors and beam splitters the two images are formed side-by-side on the film with a minimum of vignetting. The third beam splitter is included such that light from an illuminated timer can be imaged on the film; the focusing lenses are required such that the timer image could be focused on the film although the film to timer distance was considerably shorter than the film to channel wall distance. In the actual set-up the light from the timer was "folded" to allow a more compact design. Light from the tungsten strip-lamp was focused by lens 1 on the five-region step filter as indicated in the sketch. Light from the step filter was split by a beam splitter 1 such that an image of the step filter is formed through each of the filters. The distance of the step filter from the camera was adjusted such that the step filter and the channel are in focus at the same time. All optical components are mounted on a single board such that most of the alignment procedure can be performed prior to installation of the channel itself. Final alignment is performed after the channel is completely assembled and installed.

Access to the channel was more difficult in the induced field experiments and required the use of an additional lens and several beam steering mirrors as is shown schematically in Figure B.2. Considerable distortion of the view resulted from the shallow viewing angle and the entire channel width could not be viewed.

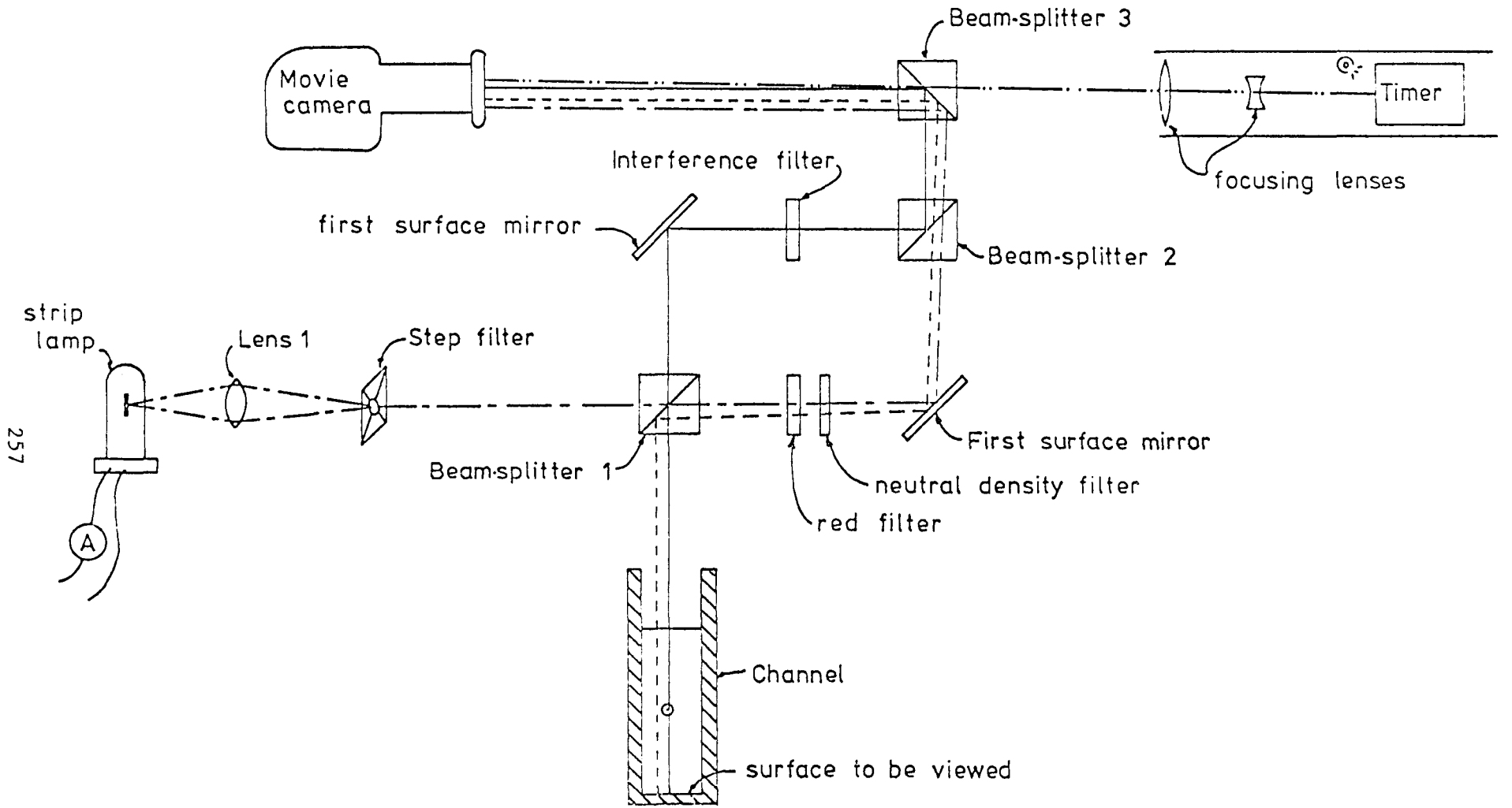

Figure B.1. Schematic of dual-filter photographic device, detailing the various light paths and components.

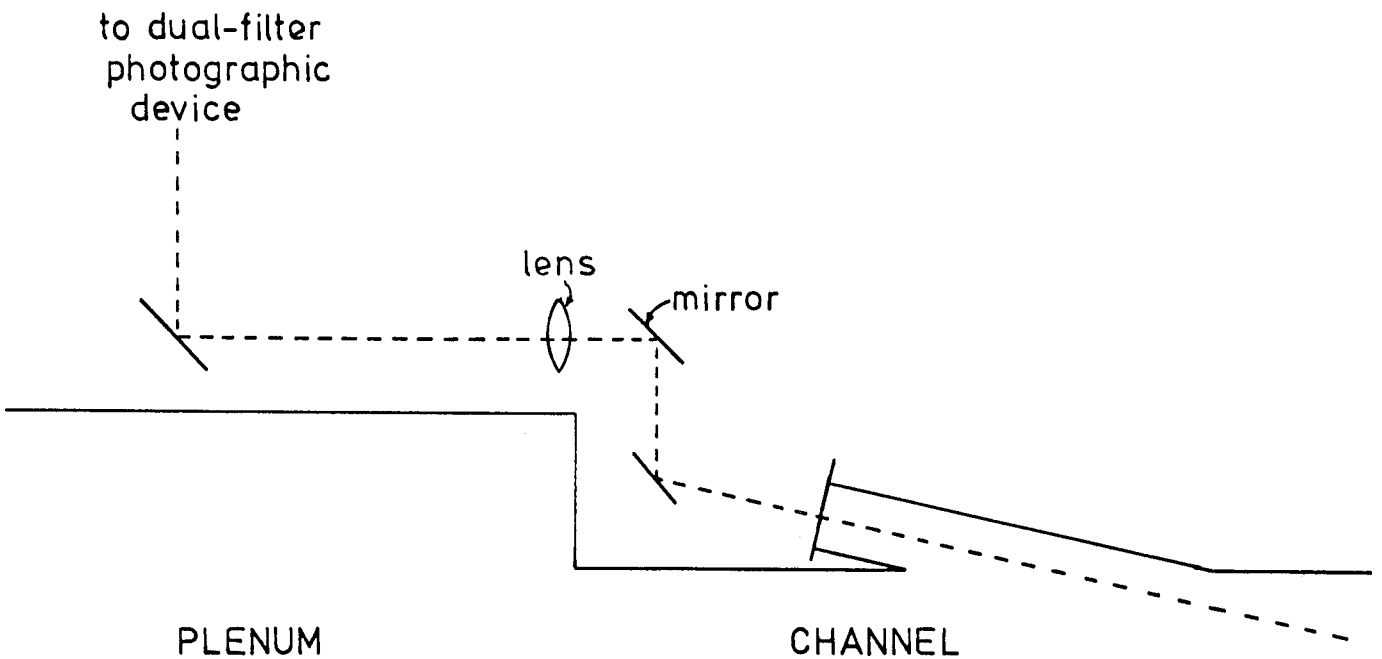

Figure B.2. Sketch of additional mirrors and lens required to obtain optical access to the generator wall.

Calibration Procedures. Semi-quantitative determination of the insulator surface temperature was performed by visual comparison of film exposure (of the red or "wall" image) of a region of the insulator, with the exposure of the regions of the step filter image formed through the red filter. Although not employed in the present study a microdensitometer could be used to make more accurate temperature measurements. Calibration of the device to allow the surface temperature determination is described in this section.

As is evident in the schematic, after passing through the first beam splitter, each step filter and channel wall image pair are formed through the same series of optical components. Thus, only the reflectance and transmittance characteristics of beam splitter 1 need be known in detail; since the step filter is used in only a qualitative manner in the "plasma" image, only the characteristics for the beam paths indicated in Figure B.3 are needed. The transmittance characteristics must also be known for the lens step filter region combination and the tungsten strip lamp brightness temperature versus lamp current response must be known. If the emissivity of the insulator material is known as well, the equivalent temperature of the five step filter regions can be calculated for a given lamp current.

The filament temperature versus lamp current was obtained using a Pyro Micro Optical Pyrometer, manufactured by the Pyrometer Instrument Co. Inc., measuring the brightness temperature for a series of lamp currents. The lamp was cured prior to the calibration to avoid aging transients exhibited by new filaments. The pryometer had been recently calibrated by the manufacturer against an NSB standard. Transmittance was determined by measuring, with the optical pyrometer, the apparent brightness temperature of the filament of the tungsten strip lamp with and without the component of interest in the optical path. The transmittance can be calculated from the two measured temperatures as

$$\ln \tau = \frac{1.44 \times 10^4}{\lambda(\text{microns})} \left(\frac{1}{T_{\text{without}}} - \frac{1}{T_{\text{with}}} \right)$$

where λ is the wavelength at which the pyrometric measurement is made. Center wavelength for the pyrometer used is .65 microns.

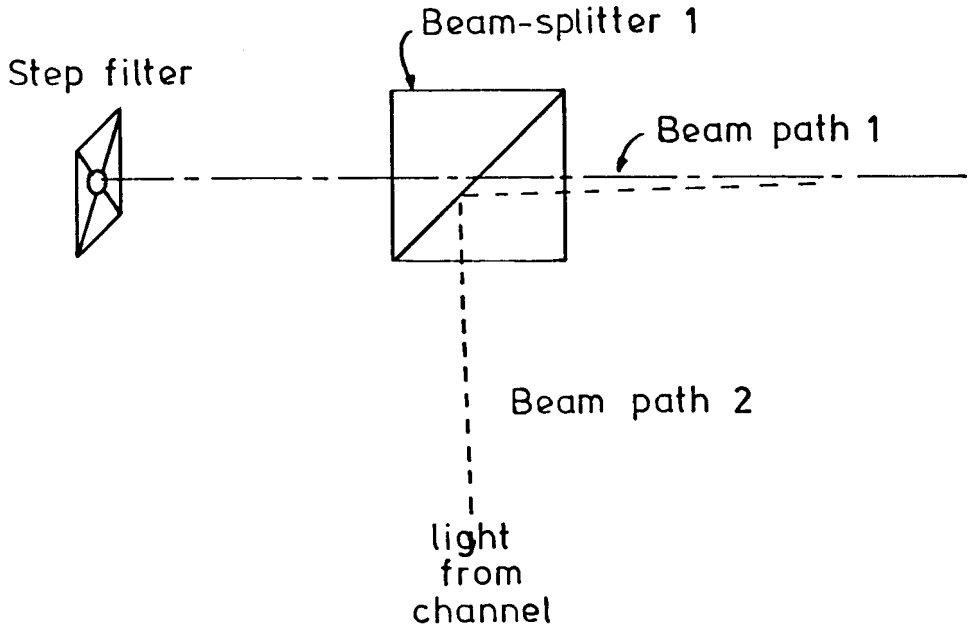

Figure B.3. Sketch of beam paths for which transmittance or reflection characteristics are required in order to obtain quantitative wall temperature measurements.

Spectral Characteristics of Various Filters. The wall image was formed through the red cutoff filter which together with the sensitivity of the film served to isolate a relatively narrow wavelength band at ~ 6500 Å. A gelatin filter (Kodak Wratten filter #29) or a red glass filter (Corning Glass Company, cutoff at 6450) was found suitable when used in combination with Kodak High Speed Ektachrome Super 8 movie film. The spectral characteristics of Kodak Wratten filter #29 can be found in Kodak Bulletin B-3; the spectral characteristics of the red forming dye of the film used can be found in Kodak Bulletin E-78. Spectral characteristics of the red glass filter can be obtained from the Corning Glass Company. A neutral density filter was also placed in the optical path of the wall image to allow a balancing of the intensity of the plasma and the wall images. Typically the intensity of the wall image was reduced by a factor of four using a glass neutral density filter.

As mentioned in the text, a very narrow bandpass filter is required to effectively isolate radiation from the plasma. Prior to receiving a special filter a wide band (~ 160 Å Half bandwidth) interference filter centered at 4040 Å was used, however as can be observed in Figure B.4a the central region of the step filter (corresponding to a wall temperature of ~ 2500 K) is significantly exposed in the plasma image. A ten angstrom bandwidth interference filter was supplied by the Corion Corporation of Waltham, Mass. and as can be observed in Figure B.4b, the central region of the step filter is barely exposed. The spectral characteristics of the interference filter supplied by the manufacturer are displayed in Figure B.5 along with a typical, predicted intensity versus wavelength behavior allowing for "radiative broadening" caused by optical thickness for potassium line radiation at 4044 Å.

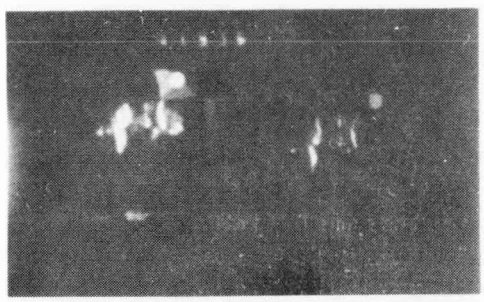

Wide-band
Taken from Run series 1.9-A

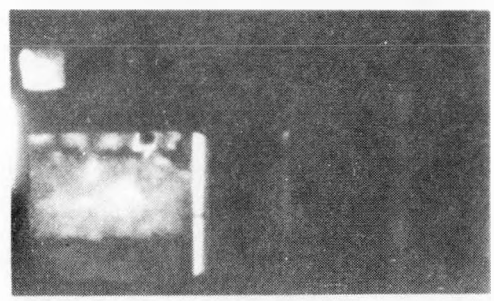

Narrow-band
Taken from Run series 1.9-C

Figure B.4 Frames of the movies showing the relative exposure of the step filter regions with the wide-band (160 A half-bandwidth) and the narrow-band (10 A half-bandwidth) filters. The circular region of the step filter corresponds to a temperature of ∿2500 K.

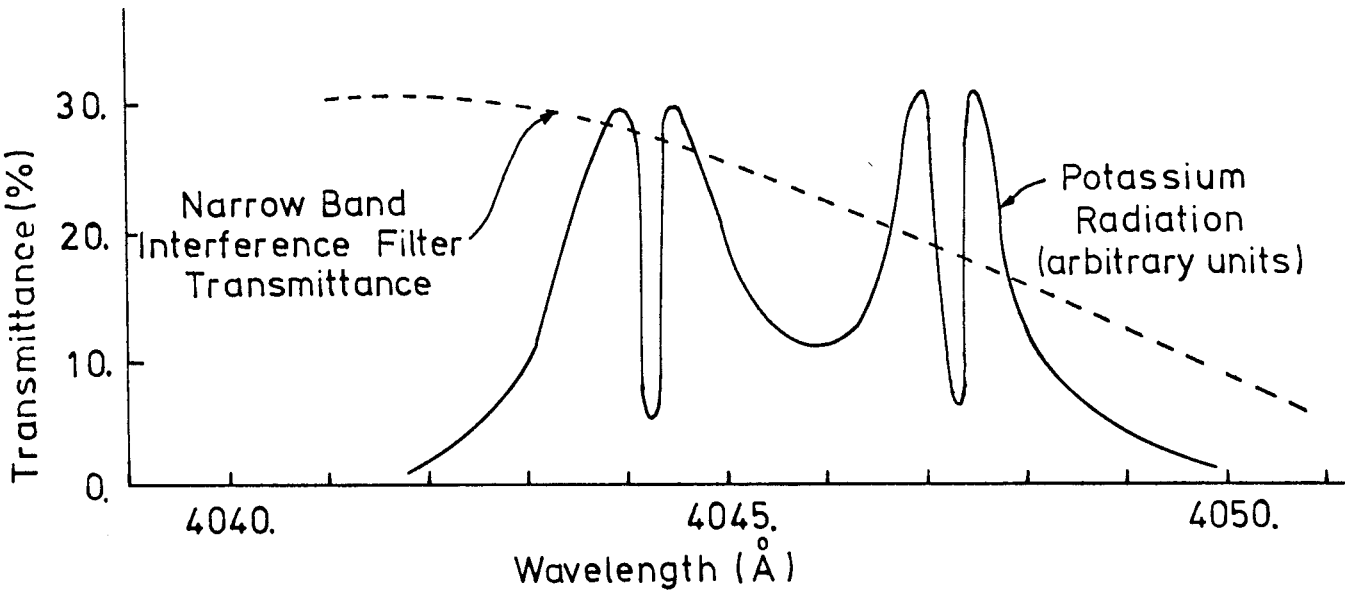

Figure B.5. Spectral transmission of narrow band interference filter ultimately used in dual-filter photographic device and calculated emission spectra for potassium 4044 Å doublet the filter was used to isolate. Emission spectra calculated by solution of the radiative transfer equation for typical conditions (T_∞ = 2700 K, T_{wall} = 2000 K).

APPENDIX C

PHOTO-DIODE INTENSITY MEASUREMENTS

This appendix presents details of the optical device used to obtain approximate plasma temperature measurements in the near-wall and far wall regions.

Detection Optics and Electronics. A schematic of the detector optics is shown in Figure C.1. This photodiode used was an EG&G SGD40B with an active area of 1 mm diameter, such that with the one-to-one optics used a spatial resolution of ~ 1 mm diameter at the focus was obtained. Choice of aperture size was a balance between spatial resolution and incident intensity; typically a 5 mm diameter opening was used. Care was exercised to make sure that the diode sighted nearest the insulator surface did not gather radiation from the wall.

Signal levels for the potassium doublet at 4044 Å are relatively weak and a current-to-voltage op-amp circuit was used. The amplifier circuit used in the experiments had a frequency response flat out to ~ 3 kHz and a gain of ~ 10^7 volts/watt of incident power. Dark signal (diode output signal with no incident light) and zero drift of the amplifier are a problem when absolute magnitudes of the incident light intensity are to be deduced. To avoid this problem a shutter was provided whereby the output of the diode-amplifier combination for no light input could be determined periodically. Typical amplifier output was ~ 40 mV for the sodium lines and 5 mV for the potassium lines.

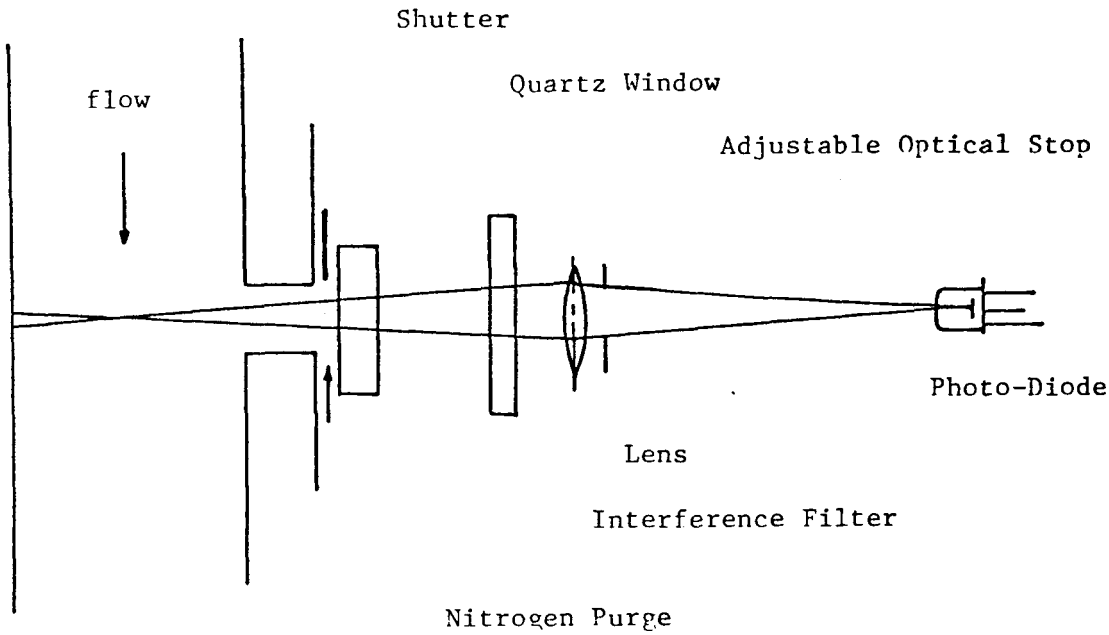

Figure C.1. Schematic of optical set-up used to make photo-diode intensity measurements in the plasma adjacent to the inter-electrode insulator.

APPENDIX D.1

CALCULATIONS OF COMBUSTOR EXIT CONDITIONS

The boundary layer computer codes and the generator performance model require as input the core conditions at the channel inlet. These inlet conditions are computed by performing an energy balance for the combustor-plenum system and then considering an isentropic expansion of the combustion products from the plenum pressure to the channel inlet pressure. Plenum pressure, reactant, fuel and seed flowrates, and combustor-plenum water cooling losses measured during the experiment are input to the computer program. An equilibrium chemical composition computer code is used to determine the combustion products properties [25].

APPENDIX D.2
GENERATOR PERFORMANCE MODEL

A quasi- one-dimensional fluid and electrical model was developed for calculation of generator performance for cases in which breakdown had not occurred. As indicated in Figure D.1, the model assumes that an inviscid core exists for the entire length of the channel. The fluid momentum equation for a streamline in the inviscid core is

$$\rho u \frac{du}{dx} + \frac{dp}{dx} = J_y B ,$$

where the $J_y B$ term is the so-called MHD body force. For the laboratory reference frame, the fluid energy equation for a streamline in the inviscid core is,

$$\rho u^2 \frac{du}{dx} + \rho u \frac{dh}{dx} = \dot{q}'''_{rad} + J_x E_x + J_y E_y$$

where $\dot{q}'''_{rad}$ is the volumetric energy loss due to radiation and the last terms in the equation result from the interaction of the fluid and the electric field. The continuity equation is satisfied in a global sense and it is through this equation that the viscous boundary layers and the channel geometry are included. The appropriate continuity equation is

$$\frac{1}{\rho} \frac{d\rho}{dx} + \frac{1}{u} \frac{du}{dx} = - \frac{1}{A_c} \frac{dA_c}{dx}$$

where ρ and u are the core density and velocity and A_c is interpreted as the core area, that is, the physical cross-sectional area of the channel minus the "blocked" area resulting from the viscous flow regions adjacent to the wall. The fluid is adequately described by the equilibrium properties and the thermal equation of state is expressed as

$$p = \rho R(\rho,T)T ,$$

where the function $R(\rho,T)$ is obtained using an equilibrium chemical

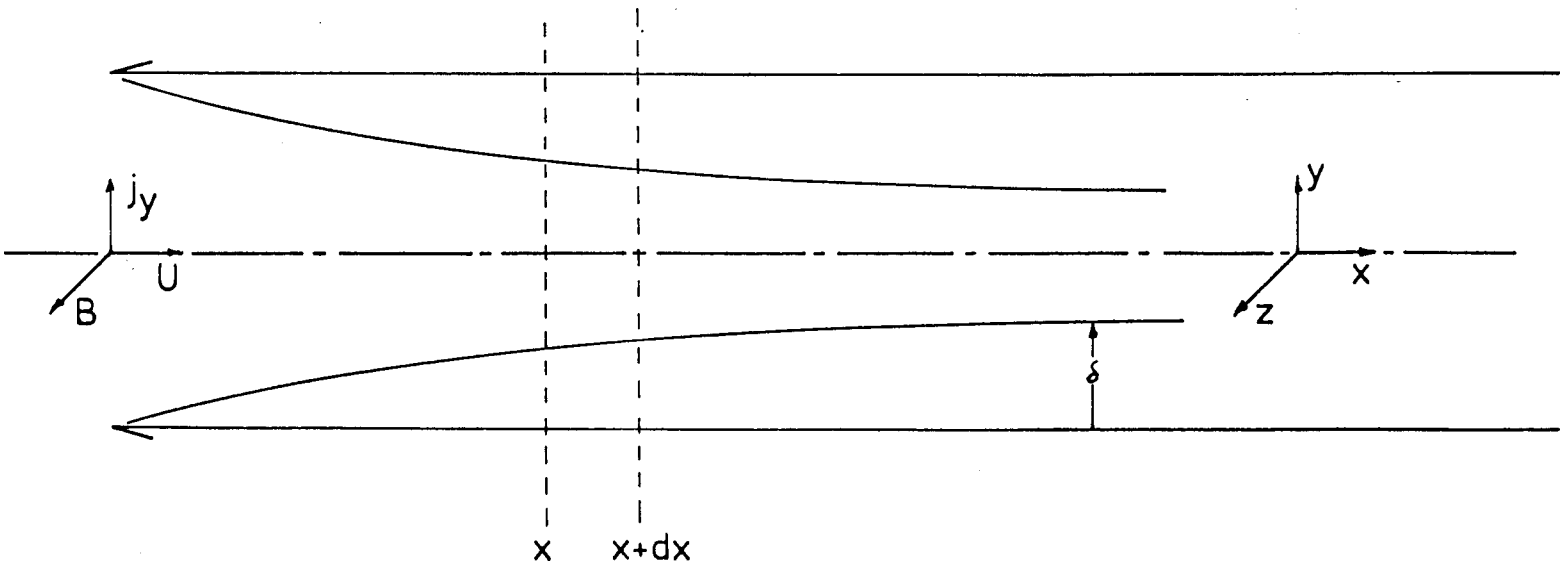

Figure D.1. Schematic of geometry and coordinate directions used in quasi-one-dimensional generator performance model.

composition and thermal properties computer solution [25]. With the further assumptions that the specific heat at constant pressure, c_p, and the specific heat at constant volume, c_v, are not functions of pressure, and that both c_p and c_v are weakly varying functions of temperature, the enthalpy can be eliminated in favor of ρ and p by use of the following expression:

$$\frac{dh}{dx} = \underbrace{\frac{\gamma}{\gamma-1}}_{c_p/R} \frac{1}{\rho} \frac{dp}{dx} - \frac{\gamma}{\gamma-1} \frac{p}{\rho^2} \frac{d\rho}{dx}$$

where the γ is based upon the "equilibrium" specific heats rather than on the frozen (or fixed chemical composition) specific heats. The continuity, momentum and energy equations are solved for the axial gradients of u, ρ and p, resulting in the following set of first-order ordinary differential equations:

$$\frac{du}{dx} = \frac{-\frac{p}{\rho A_c}\frac{dA_c}{dx} - \frac{J_y B}{\rho} - \frac{\ell}{\rho}}{Den}$$

$$\frac{d\rho}{dx} = \frac{\frac{p}{\rho u} J_y B + u\ell + \frac{\gamma-1}{\gamma} u J_v B + \frac{pu}{A_c}\frac{dA_c}{dx}}{Den}$$

$$\frac{dP}{dx} = \frac{\frac{\ell}{u} + \frac{\rho u}{\gamma A_c}\frac{dA_c}{dx} + \frac{J_y B}{u}}{Den}$$

where

$$\ell \equiv -\frac{\gamma-1}{\gamma}\rho\left(\frac{\dot{q}'''_{rad} + J_x E_x + J_y E_y}{\rho u}\right)$$

and

$$Den \equiv \frac{1}{\rho u}\left(p - \frac{1}{\gamma}\rho u^2\right) .$$

With the inlet conditions specified as described in Appendix D.1, the above equations are integrated down the channel using a fourth-order Runge-Kutta

integration scheme. The calculation of the quantities A_c, dA_c/dx, J_y, J_x, E_y, E_x and $\dot{q}'''_{rad}$ needed for each step forward in x are discussed in the paragraphs following.

The effective core area and its gradient are computed from the specified channel cross-sectional area through use of the boundary layer displacement thickness. Referring to Fig. D.2, the core area is

$$A_c = A_p - 2w\delta_1 - 2(h - 2\delta_1)\delta_1$$

and the gradient of the core area is

$$\frac{dA_c}{dx} \cong \frac{dA_p}{dx} - 2\frac{d\delta_1}{dx} - 2(h - 2\delta_1)\frac{d\delta_1}{dx} ,$$

where A_p is the cross-sectional area of the channel and δ_1 is the boundary layer displacement thickness. The cross-sectional area as a function of axial position is an input to the program. An empirical correlation, with corrections for compressibility and variable properties, suggested in Kays [31] is used to determine the displacement thickness for the turbulent boundary layers growing along the channel wall. The displacement thickness is given as

$$\delta_1 = \frac{.37}{8}\frac{x}{R^{*.2}}$$

and the gradient determined by differentiating the above expression is

$$\frac{d\delta_1}{dx} = .037\frac{1}{R^{*.2}} ,$$

where R^* is the Reynolds number based on axial position with the properties calculated at a reference state; that is,

$$R^* = \frac{\rho^* ux}{\mu^*} .$$

For moderate velocity and Prandtl numbers near unity, the reference state is evaluated approximately at the local pressure and the mean static enthalpy across the boundary layer [31]; that is,

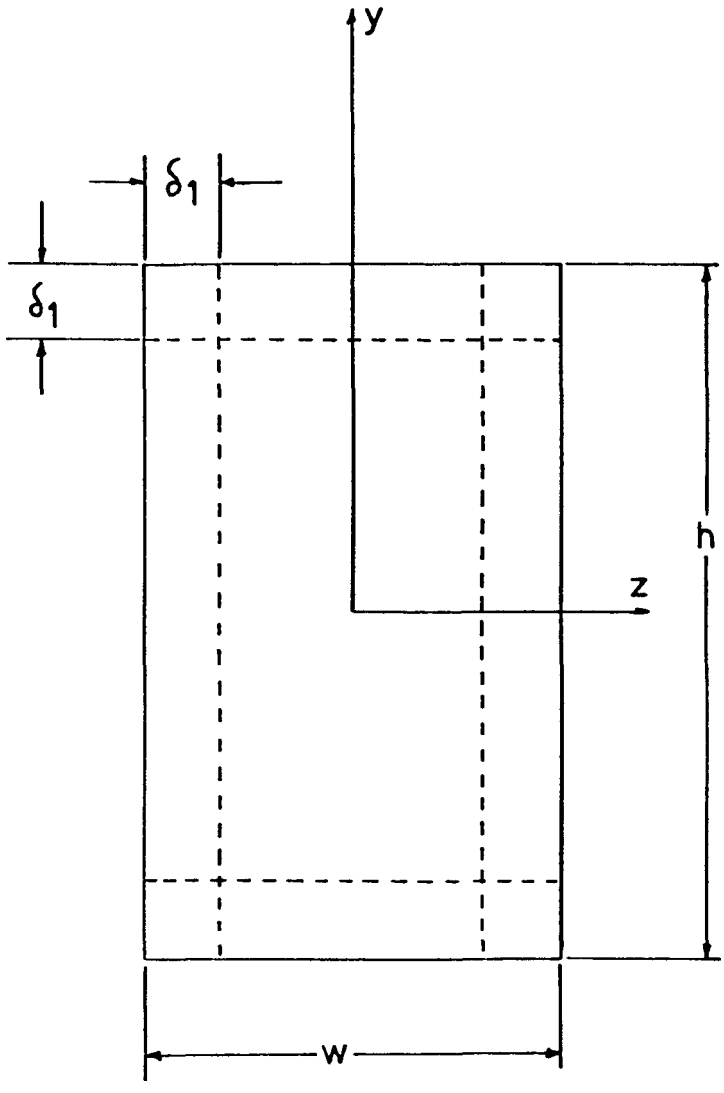

Figure D.2. Schematic of cross-section of channel identifying dimensions used in calculation of the core area.

$$h^* \simeq \frac{h_\infty + h_{wall}}{2} \quad .$$

Band radiation from carbon dioxide and water vapor and line radiation from the potassium seed are considered in the calculation of the radiative loss term $\dot{q}'''_{rad}$. The band radiation calculated from the standard gas radiation equation, using the total absorptivity and emissivities tabulated in Hottel [32]. Line radiation was determined using the radiation escape factor as described by MacGregor [33].

The electrical performance model is developed for the segmented Faraday configuration. For simplicity, the velocity and electrical conductivity are assumed to be of the form

$$\gamma(x,y,z) = \gamma_1(x,y) \cdot \gamma_2(x,z) \quad ,$$

resulting in the rectangular core region as shown schematically in Fig. D.3. Unfortunately, the above assumptions are not sufficient to allow a simple solution for the electrical behavior, except for the case of $B = 0$ or $u \neq u(z)$, and an approximate approach must be followed to determine the performance. The approach adopted is to first consider the variation in the magnetic field direction, neglecting the effects of the electrode wall boundary layers, and then to consider the electrode wall boundary layers using the average properties across the channel width. The approach is shown schematically in Fig. D.3.. The central region in the sketch is solved for first with the assumption that $u \neq u(y)$, $\sigma \neq \sigma(y)$ and that β, B and the slope of the current in the core, J_x/J_y, are uniform in z For these conditions, J_z and E_z are zero and E_y = constant = V_g/h. Ohms law can then be written as

$$J_y(x,z) = \frac{\sigma(x,z)(E_y(x) - u(x,z)B)}{(1 - \beta(J_x/J_y))} \quad .$$

Averaging over z yields

$$\langle J_y \rangle_z = \frac{E_y \langle \sigma \rangle_z - B\langle \sigma u \rangle_z}{(1 - \beta(J_x/J_y))} \quad ,$$

where $\langle\ \rangle_z$ denotes the spatial average across z. The slope of the current in the core, J_x/J_y, is determined using the coarse grid current

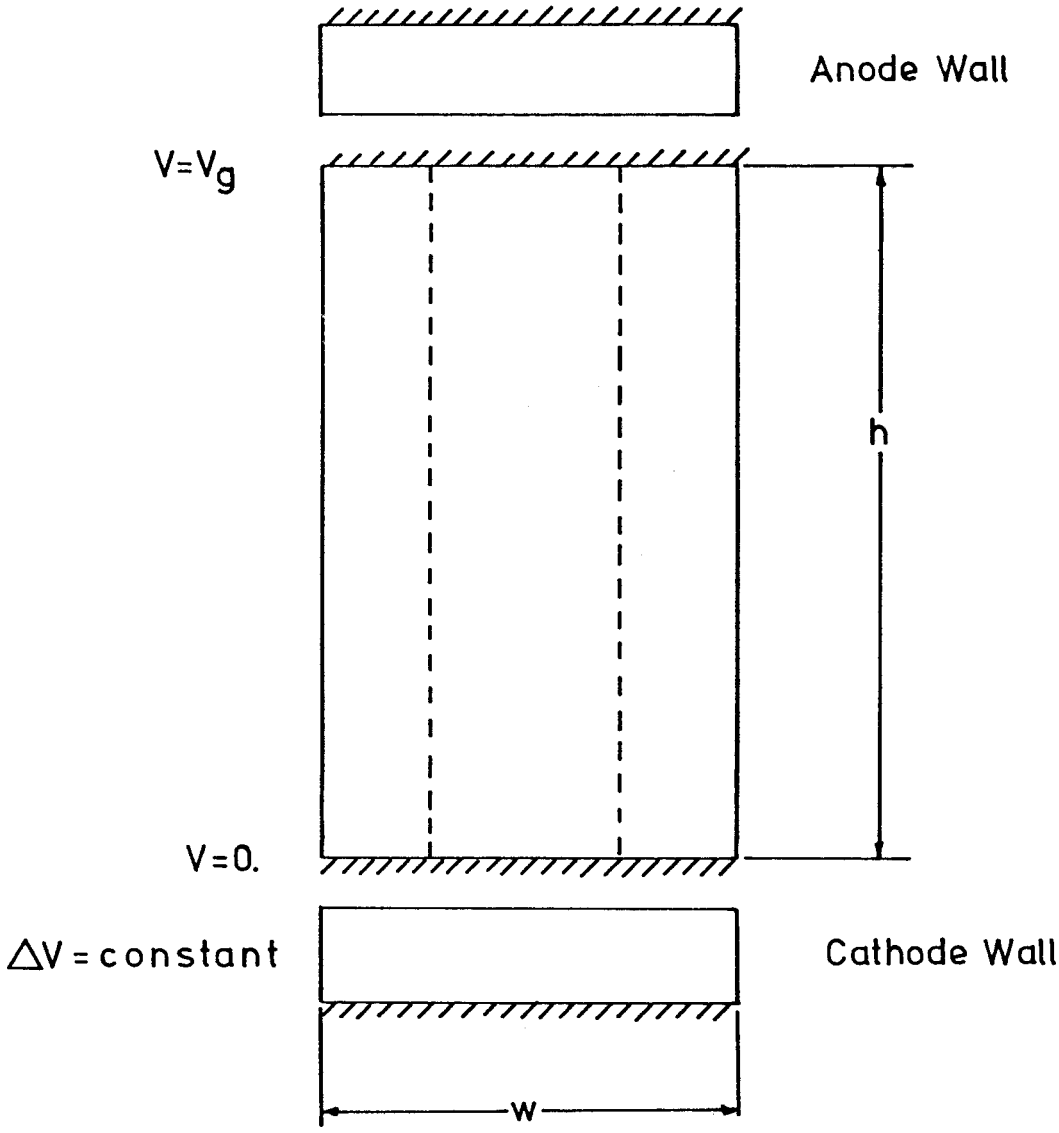

Figure D.3. Schematic of splitting of cross-sectional area for simplified electrical analysis.

distribution model described in Chapter 4. The effects of the anode wall boundary layer are cast in the form of an impedance in series with the generator load, and a constant voltage drop is assumed for the cathode. Neglecting the Hall effect and finite segmentation effects, the impedance through the anode boundary layer is simply

$$\int_{y_c}^{\delta} \frac{dy}{\sigma(y)} = \frac{\delta}{\sigma_{core}} \int_{\eta_c}^{1} \frac{d\eta}{(\sigma/\sigma_{core})} \quad ,$$

where $\eta_c = y_c/\delta$ is a cutoff to account for the sheath region. [Note: this simple voltage drop calculation has been shown to yield reasonable results, although, as discussed in Appendix F, the accuracy is somewhat fortuitous.] Including the geometric factors and the Hall effect and subtracting the contribution to the resistance already included in accounting for the z-variations, the anode wall boundary layer resistance can be expressed as

$$R^*_{anode} = \frac{\delta}{\sigma_{core}} (1 + .31\ \beta^2_{core}) \frac{\int_{\eta_o}^{1} \frac{d\eta}{(\sigma/\sigma_{core})}}{\text{length/pitch}} - 1 \quad ,$$

where $(1 + .31\ \beta^2_{core})$ is the effect of Hall parameter for geometries typical of the experiments (as determined using a two-dimensional current distribution program), and the $*$ denotes that the resistance is based upon a unit area. The external circuit includes a ballast resistance and an augmentation power supply; the overall electrical circuit is shown in Fig. D.4. The overall equation can be solved for the average current density, from which the quantities E_x, E_y, J_x and J_y at the centerline can be computed.

The properties used in the calculations are curve-fits to the equilibrium properties calculated for the gas mixture of interest. Curve-fit thermal properties are within $\lesssim$ 1% of the calculated values, and curve-fit electrical properties are within $\lesssim$ 5% of the calculated values over the temperature range from 1000 K to 3000 K.

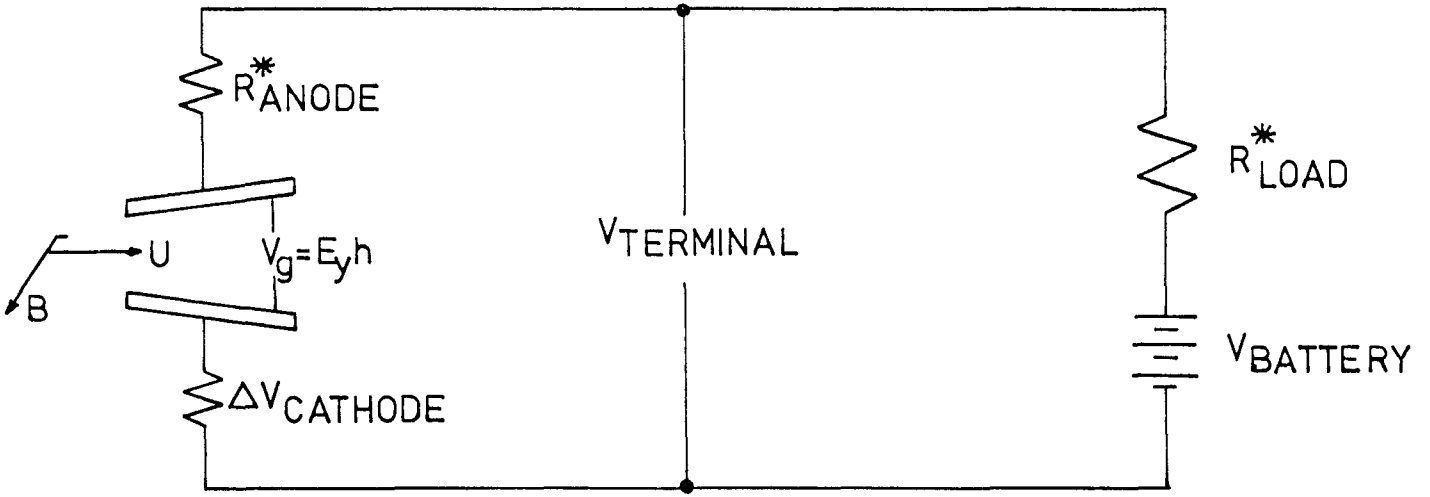

Figure D.4. Schematic of overall circuit used in quasi-one-dimensional generator performance model.

APPENDIX E

NUMERICAL TECHNIQUES AND COMPUTER CODE VERIFICATION

This appendix presents the important details of the numerical solutions performed in the present work and discusses the comparisons of predicted results with analytical, analog or previously predicted results for special circumstances as a means of verifying the computer code and the numerical method.

E.1 Electrical Solution for the Outer Region of the Plasma

Solution for the Streamfunction ψ

The formulation of the equations and boundary conditions for the current streamfunction is presented in Chapter 4. High resolution is desirable in the regions of large spatial gradients, notably the region close to the electrode surface and the regions adjacent to the electrode edges. A coordinate transformation is performed to provide such resolution, while maintaining the total number of grid points small and allowing a uniform grid to be used in formulating the difference equations. The transverse coordinate, y, is transformed as

$$y = b(e^{aY} - 1)$$

where Y is the transformed coordinate and $y = Y = 0$ corresponds to the electrode wall surface. The axial coordinate, x, is transformed as

$$x = cX^5 + dX^3 + eX$$

where X is the transformed coordinate and $x = X = 0$ corresponds to the center-line of the inter-electrode insulator. The constants a, b, c, d and e are chosen for the particular geometry and desired number of grid points in each direction. The equation for the streamfunction, ψ, is formed in terms of the transformed coordinates and, with the dummy time dependence introduced, becomes

$$\frac{\partial \psi}{\partial t} = A(Y)\left(\frac{\partial^2}{\partial Y^2} + B(X,Y)\,\frac{\partial}{\partial Y}\right)\psi + C(X)\left(\frac{\partial^2}{\partial X^2} + D(X,Y)\,\frac{\partial}{\partial X}\right)\psi$$

where

$$A(Y) = \frac{e^{-aY}}{a^2 b^2} ,$$

$$B(X,Y) = -a - \frac{\partial}{\partial X} (\ell n\ \sigma)\Big|_{(X,Y)} ,$$

$$C(X) = (5cX^4 + 3dX^2 + e)^{-2} ,$$

and

$$D(X,Y) = -\frac{(20cX^3 + 6dX)}{(5cX^4 + 3dX + e)} - \frac{\partial}{\partial X} (\ell n\ \sigma)\Big|_{(X,Y)}$$

The parabolic equation is time-split in a locally one-dimensional fashion such that a step forward in time (that is, an iteration) proceeds by taking a half step during which the governing equation for the interior region is

$$\frac{\partial \psi}{\partial t} = A(Y) \left(\frac{\partial^2}{\partial Y^2} + B(X,Y) \frac{\partial}{\partial Y} \right) \psi ,$$

and a second half-step during which the governing equation is

$$\frac{\partial \psi}{\partial t} = C(X) \left(\frac{\partial^2}{\partial X^2} + D(X,Y) \frac{\partial}{\partial X} \right) \psi$$

The finite-difference form of the above equations is obtained using the Crank-Nicolson implicit-difference operators together with the boundary conditions used to formulate the corresponding matrix problem. In matrix form, the iteration procedure is represented as

$$(\bar{I} + \alpha \bar{V}) \bar{\psi}^{t+\frac{1}{2}} = (\bar{I} - \alpha \bar{V}) \bar{\psi}^{t} + \bar{k}_1$$

$$(I + \alpha \bar{H}) \bar{\psi}^{t+1} = (\bar{I} - \alpha \bar{H}) \bar{\psi}^{t+\frac{1}{2}} + \bar{k}_2 ,$$

where $\bar{I}$ is the identity matrix, α is essentially the iteration parameter, $\bar{H}$ and $\bar{V}$ are determined from the governing equation and the difference operators used, and $\bar{k}_1$ and $\bar{k}_2$ result from the boundary conditions. In order that the matrices $(\bar{I} + \alpha \bar{V})$ and $(\bar{I} + \alpha \bar{H})$ are tridiagonal the derivative boundary conditions at the electrode surfaces are

handled only to accuracy $O(\Delta y)$, while the remainder of the difference scheme is $O(\Delta y^2)$ accurate. This restriction is most likely not serious, since coordinate stretching provides a very close grid spacing in the near-electrode region. The ordering of the equations for the grid points is also altered between the two half-steps to maintain the matrices in tri-diagonal form. Inclusion of the boundary conditions $\bar{k}_1$ and $\bar{k}_2$ is straightforward because only the steady-state solution is desired. The above iteration scheme can be shown to be unconditionally stable with the steady-state solution for the original elliptic equation given as

$$\psi = \lim_{t\to\infty} \left(\frac{\psi^t + \psi^{t+\frac{1}{2}}}{2} \right) .$$

Although the numerical method is unconditionally stable, restrictions on the conductivity gradients are imposed by the tridiagonal solution algorithm used; normally, these restrictions are not severe and are removed by adjusting the coordinate transformation constants. The convergence criterion used is to require that the residual at all grid points has been reduced to a specified level. Typically, with a crude initial ψ distribution, 50-150 iterations are required to reduce the maximum residual to less than ~.0005, while with a good initial guess only 5-10 iterations are required.

Solution for Current Density and Potential Distribution

The axial and transverse current density components, based on unit current per unit width, are obtained from the defining equations for the streamfunction set in finite-difference form. After calculating the resistance for unit current per unit width, the external circuit equations are employed to determine the actual current through the plasma and the current density components appropriately scaled.

The outer region electric potential, ϕ, is calculated from the current density by numerical integration of

$$\bar{\nabla} \cdot \phi = \bar{E} = \bar{J}/\sigma \quad . .$$

Integration proceeds first up along the inter-electrode insulator center-line, with the potential set to zero at the wall, and then upstream and downstream from the insulator center-line. The solution for ϕ is performed all the way to the wall although, as discussed in Chapter 4 and in Appendix F, the potential drop in the near electrode as computed by the outer region is incorrect and is replaced by the more detailed calculation at a later time. The resistance for unit current per unit width is determined from the potential difference between the electrodes.

Numerical Method and Computer Code Verification

To verify the numerical method and the computer code, predictions using the computer program were compared with solutions obtained using electrically resistive teledeltos paper. Values of ψ at the grid points agreed within the accuracy of the teledeltos solution (~7-8%). The computed and measured resistance between the electrodes also agreed within 8-9%. In addition, the computer code was used to approximate source-sink flow in a constant conductivity region and in a region in which the conductivity varies linearly in the direction perpendicular to the line joining the source and sink. Computed results compared favorably with theoretical results, except close to the singularities. In particular, as can be observed in Fig. E.1.1(a,b), the values of the axial current density at the center-line between the source and sink were in good agreement.

E.2 Time-Dependent Solution for the Plasma

Solution for u, v, h and c_e

The formulation of the equations, initial conditions and boundary conditions for the fluid solution are given in Chapter 4. High resolution is desirable near the wall to adequately model the laminar sublayer of the boundary layer and to provide high resolution in the regions of high spatial gradients of the energy source term, J^2/σ. For convenience, the fluid solution employs the same coordinate transformations and grid structure as are used for the electrical solution. The governing equations are reformulated in the transformed coordinate plane, and the corresponding finite-difference equations are formulated. An implicit-explicit differencing scheme is employed such that, in obtaining the solution, only

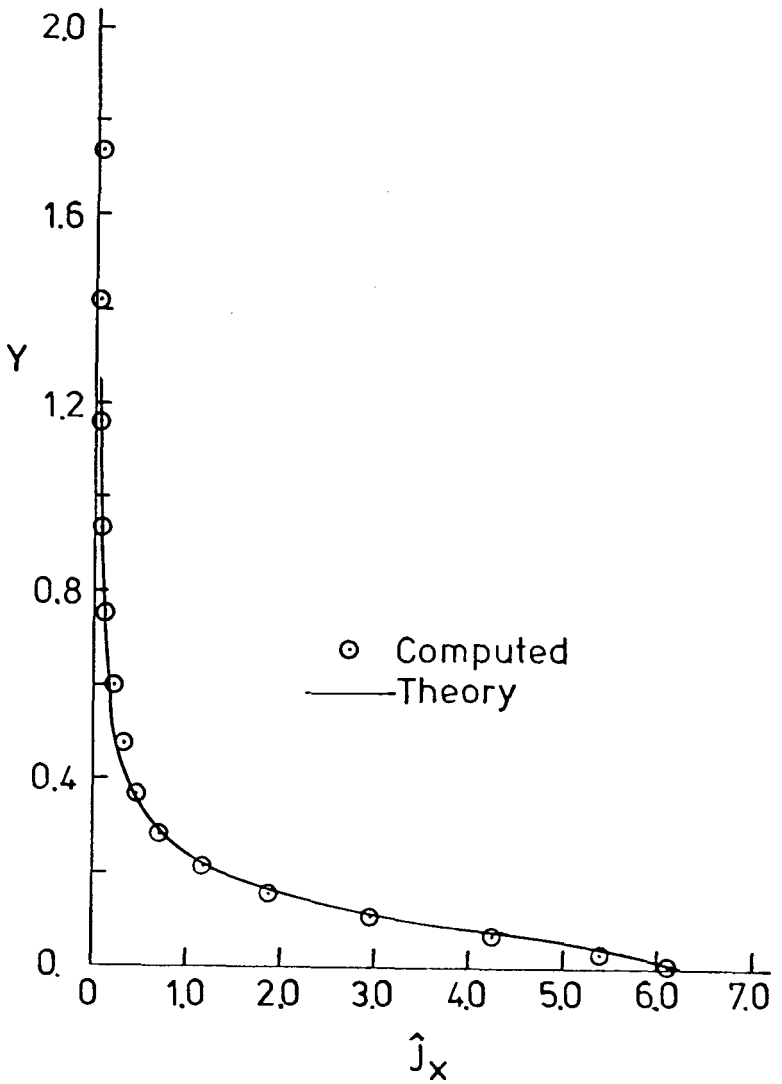

Figure E.1.1a. Comparison of calculated and analytical current density profile for source-sink flow in a region of uniform electrical conductivity. Comparison is made for centerline between the source and sink.

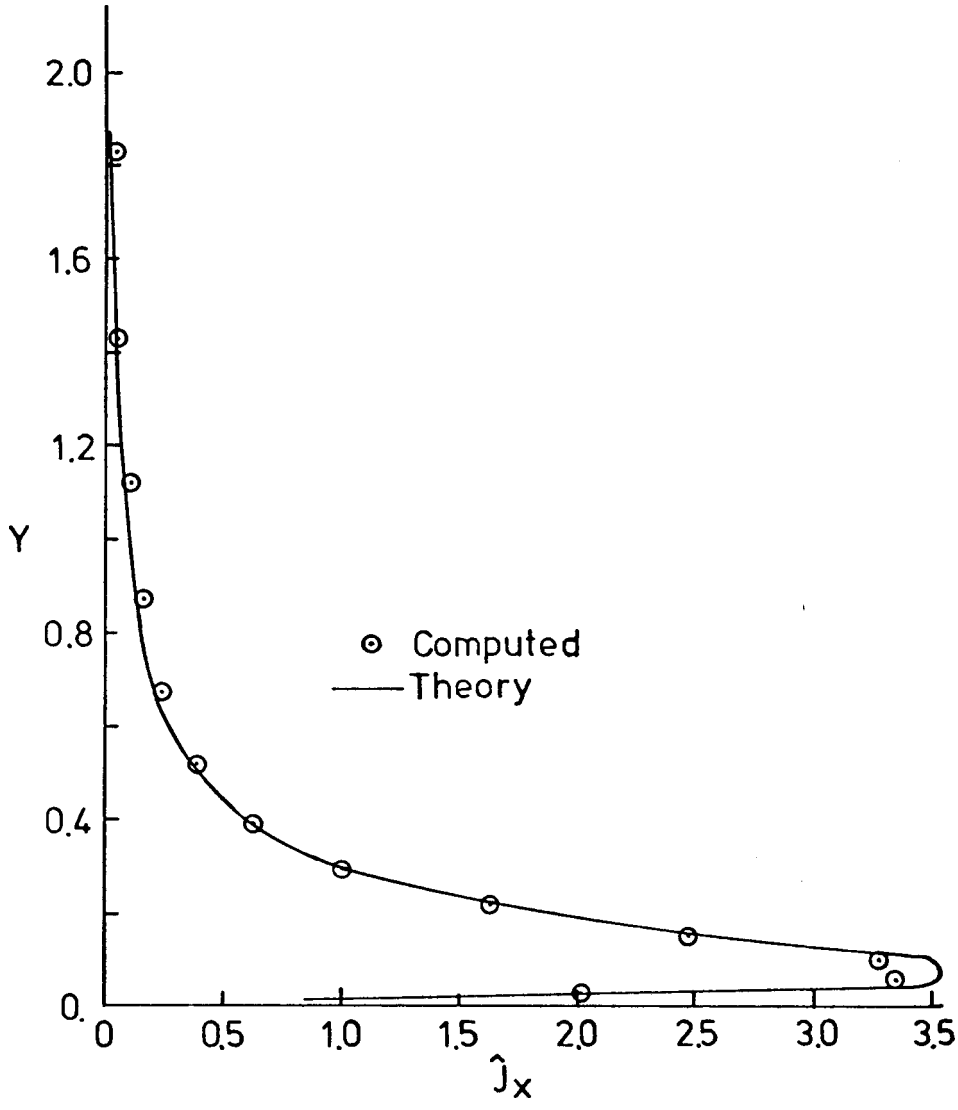

Figure E.1.1b. Comparison of calculated and analytical current density profile for source-sink flow in a region of non-uniform electrical conductivity. Conductivity varies as $\sigma \propto y$, where y is measured perpendicular to the line joining the source and sink. Comparison is made for the centerline between the source and sink.

tri-diagonal matrix inversions are required. The transverse diffusion and convection terms are handled implicitly, while the axial convection terms, the source terms and all fluid properties are handled explicitly. The explicit handling of the axial convection terms imposes a time-step restriction; however, since the source term cannot be considered implicitly, a difference scheme which considered the axial convection terms implicitly would have a time-step restriction associated with the accuracy desirable for the source term. The Crank-Nicolson implicit-difference operators are used for the transverse derivatives, and the upwind difference operator is used for the axial derivatives. For each time step the solution proceeds by marching downstream from the inlet location, solving the momentum, energy and electron continuity equations for each axial location.

Numerical Method and Computer Code Verification

To verify the numerical method and the computer code, steady-state results from the computer code were compared with results from a well-established boundary layer code, STAN5 [22]. Comparisons were made for a variety of conditions, including laminar and turbulent flows, constant and variable fluid-property flows, and zero and non-zero source terms, with satisfactory agreement obtained for all cases. For example, excellent agreement of the static enthalpy is displayed in Fig. E.2.1 for a turbulent, variable-property boundary layer with a variable energy source term. The computer code was also used to approximately model Stoke's first problem [30], and good agreement was obtained for the behavior of the time-dependent velocity profile.

E.3 Coarse Grid Model for the Induced Field Configuration

Electrical Solution

The equations and boundary conditions for the problem are presented in Chapter 4. Solution of the resulting equations is performed by the standard procedure of Gaussian elimination with row-pivoting.

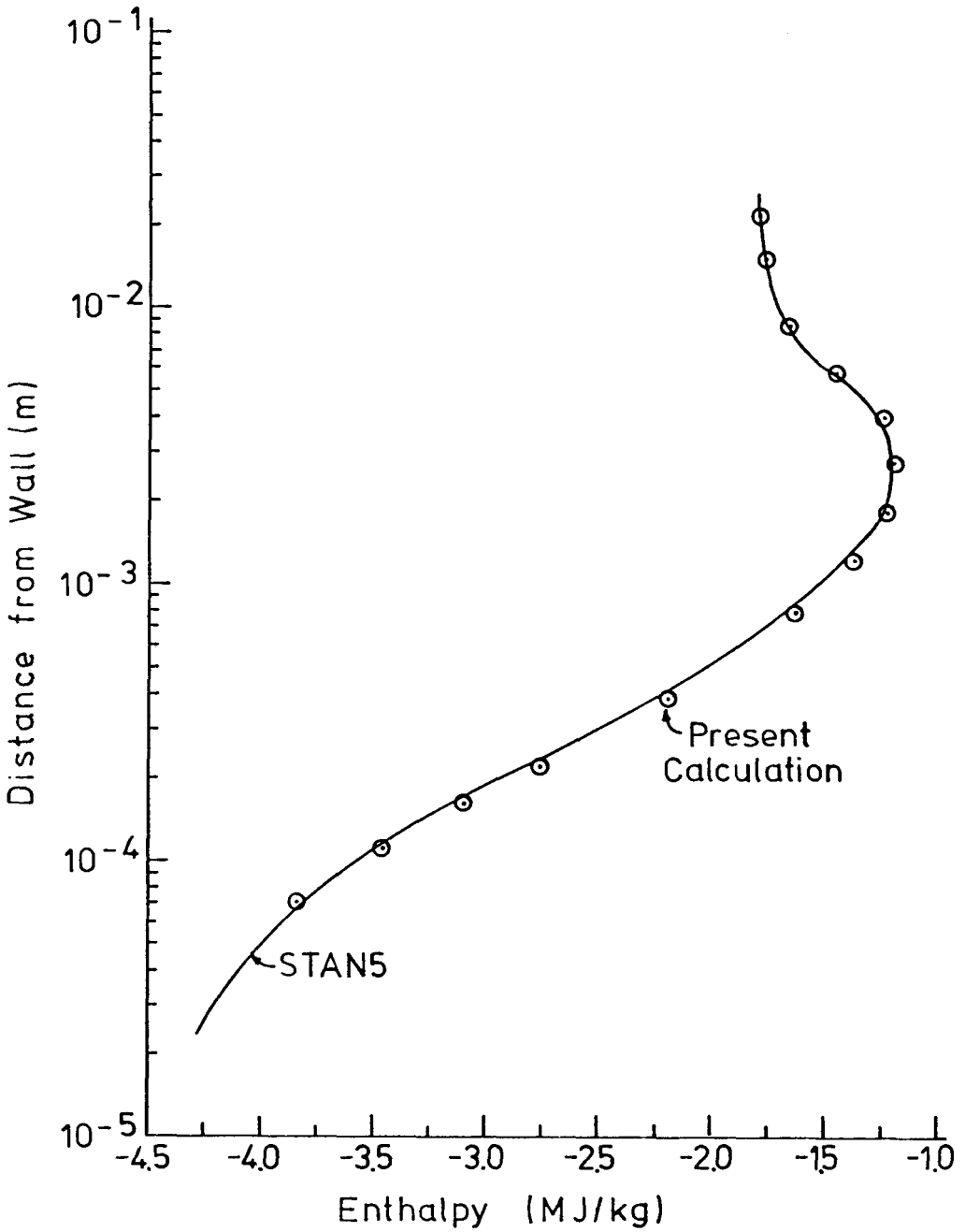

Figure E.2.1. Comparison of static enthalpy profile predicted by present computer code with the predicted profile of STAN5[22]. The flow is turbulent, has variable thermal properties and includes a Joule heating source term which is non-uniform in distance from the wall.

Verification

Prior to using the model to make predictions for conditions of interest, calculated results from the model were compared with previously calculated results of Oliver [34], to determine the extent to which the coarse grid model would be representative of actual generator behavior. Oliver calculated transverse resistances and Hall voltages for linear near-wall conductivity profiles using a fine mesh two-dimensional current distribution model. The geometry and assumed conditions for the comparisons are shown in Figs. E.3.1. The effect of wall-to-freestream-conductivity ratio, σ_w/σ_∞, on normalized Hall voltage is shown in Fig. E.3.2, for Hall parameters of 1 and 3. As expected, the coarse grid results are not in close quantitative agreement, but do indicate the proper trends; comparisons are better for low wall conductivities. The behavior of normalized transverse resistance with Hall parameter is displayed in Fig. E.3.3. The coarse grid results indicate an increasing resistance with increasing Hall parameter, in qualitative agreement with the detailed calculations; however, the influence of σ_w/σ_∞ is poorly predicted.

The above comparisons indicate that the coarse grid model is of some utility in determining generator behavior; however, significant quantitative differences should be expected.

Oliver defines

$$R_{yy} \triangleq \frac{V'_y}{I_y} \qquad (I_x = 0)$$

and

$$\bar{R}_T \triangleq \frac{R_{yy}}{R_{yy}(\beta=0)}$$

i.e., R_T represents effects of β or transverse impedence. Also we have

$$V'_x = R_H V'_y \qquad (I_x = 0)$$

and

$$\bar{V}_H = \frac{V'_x}{V'_x} \quad \sigma = \text{const.}$$

infinite segmentation

i.e., V_H represents effects of non-uniform conductivity on Hall voltage.

Oliver's geometry

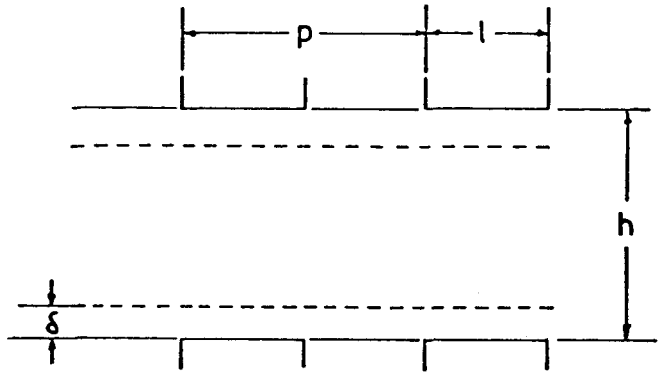

Model conductivity profiles:

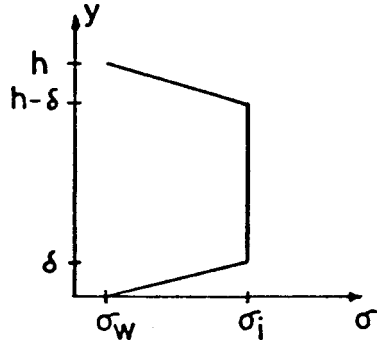

Calculations for $p/h = 1$, $\ell/p = 0.5$, $\delta/h = 0.2$

Figure E.3.1. Summary of geometry, profiles and terms used in comparison of coarse grid results with Oliver's fine grid results.

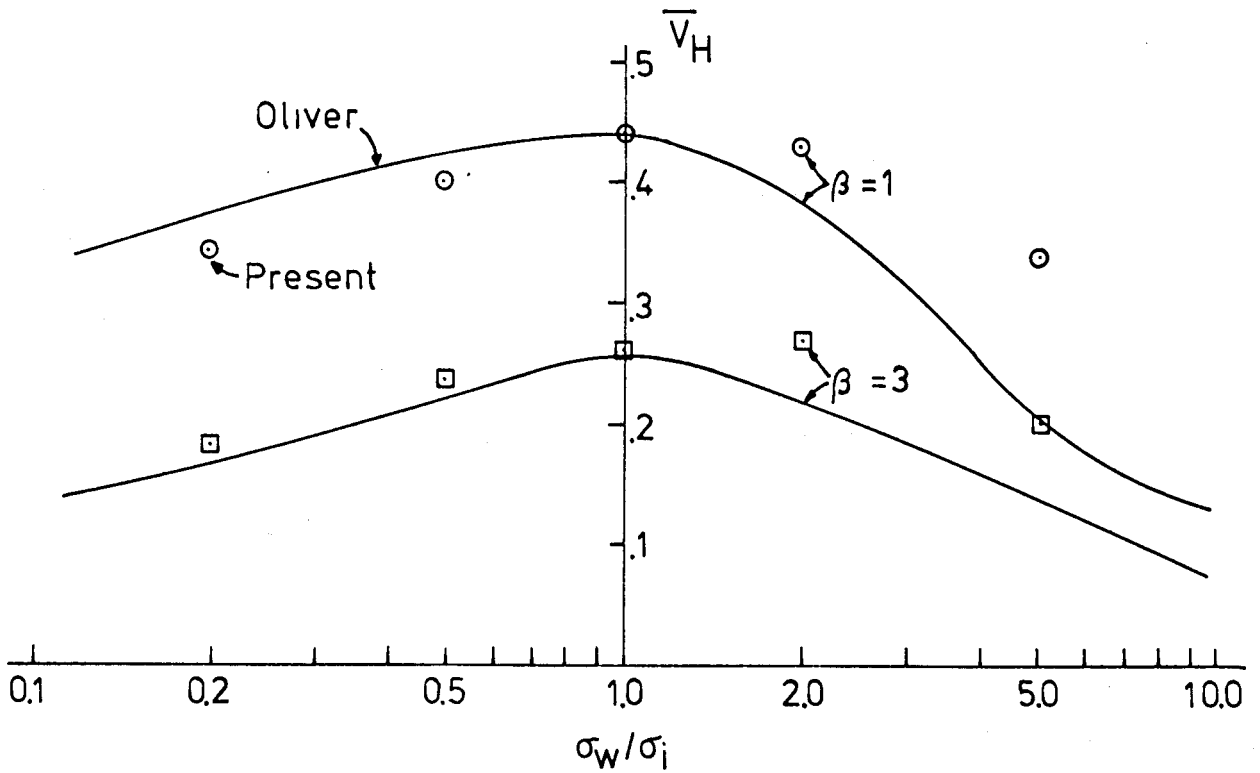

Figure E.3.2. Comparison of coarse grid results with fine grid results of Oliver [31]. Figure compares non-dimensional Hall voltage as a function of σ_w/σ_i, the ratio of wall conductivity to free-stream conductivity. Results shown for $\beta = 1.$ and $\beta = 3$. See Figure E.3.1 for description of terms.

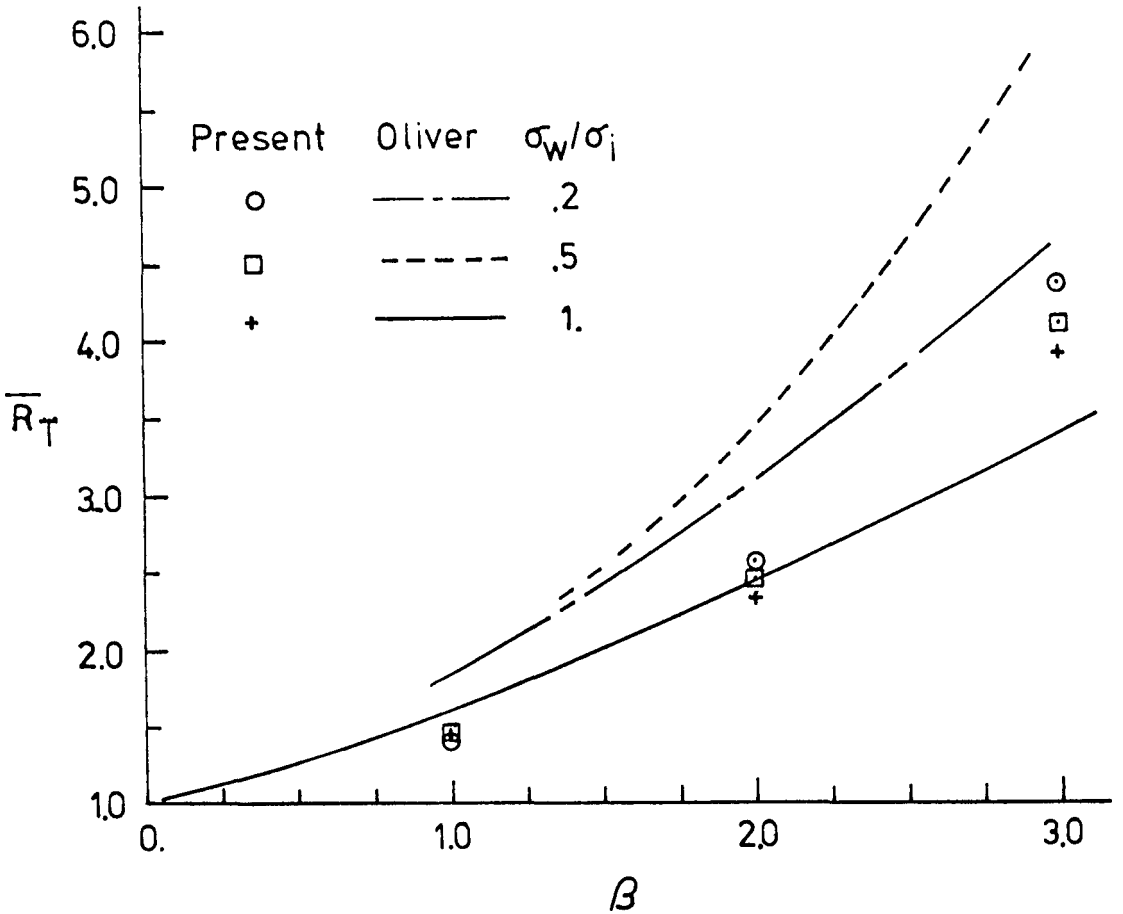

Figure E.3.3. Comparison of coarse grid results with fine grid results of Oliver [31]. Figure compares non-dimensional transverse resistance as a function of Hall parameter for three values of σ_w/σ_i, the ratio of wall conductivity to free-stream conductivity. See Figure E.3.1 for description of terms.

APPENDIX F

NEAR-ELECTRODE CURRENT TRANSPORT

This appendix presents a general discussion of the calculation procedure used to evaluate the potential distribution in the vicinity of the generator wall. Discussion is first directed toward calculations for the outer, or charge-neutral, region, and then the surface-sheath region is discussed. A simple discharge configuration is treated to display the physics of the problem rather than bringing out the geometrical complexities of flow and current distribution calculations. The surface-sheath model and, to some extent, the outer region model are preliminary in nature and in some respects serve only to point out areas where further and more detailed studies are required.

F.1 Introduction

For the purpose of illustrating the important features of the calculation of number density and potential distribution profiles, consider a one-dimensional discharge through the boundary layer formed over the electrode wall, as shown schematically in Fig. F.1. For this discussion, a typical clean combustion products flow is assumed and the electrode is assumed to be metallic and operating at a surface temperature in the range of 1000-1600 K. Immediately upstream of the electrode under consideration is a relatively hot (1800 K) insulating wall. These conditions are chosen to represent the conditions of the applied field experiments discussed in the text and are not fundamental restrictions imposed by the applicability of the theory. Current densities from zero to 10 amps/cm^2 are considered for both anodes and cathodes. For some conditions the main result of the theory will be a prediction of a maximum current density beyond which the one-dimensional discharge is not possible.

F.2 Outer Region

For the conditions stated, the majority of the gasdynamic boundary layer region is characterized by low electric field gradients and low thermal energy per particle. Little departure from charge neutrality can be supported for such conditions, and the electron and ion number densities

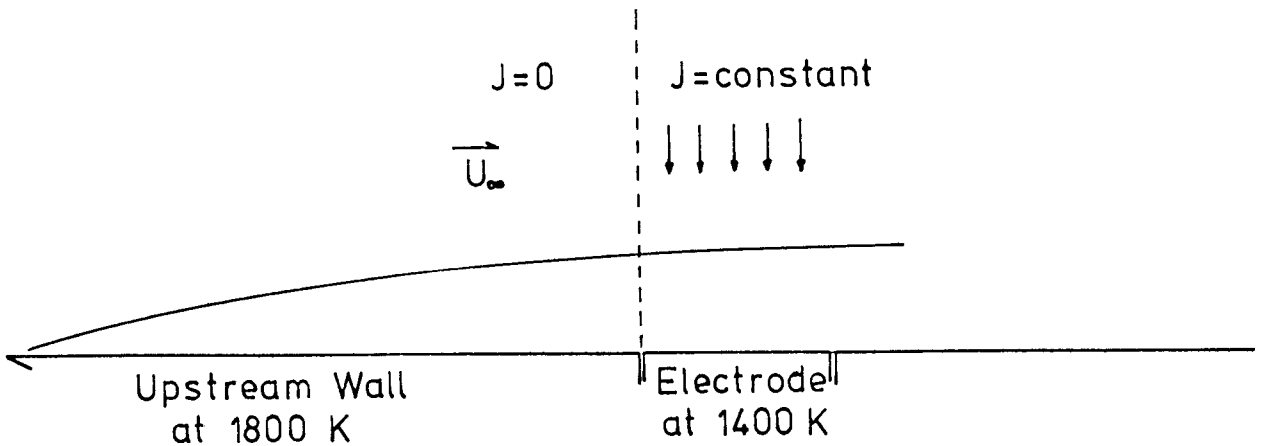

Figure F.1. Schematic of simplified discharge configuration used in general discussion of near-electrode voltage drops.

can be considered equal. The species conservation equations for electrons and ions can be combined, assuming $n_e \simeq n_i$, to form the ambipolar diffusion equation and to form a current conservation equation. The ambipolar diffusion equation for the mean electron concentration in the turbulent flow field is

$$u \frac{\partial c_e}{\partial x} + v \frac{\partial c_e}{\partial y} + \frac{1}{\rho} \frac{\partial}{\partial y} (\rho D_a + \rho \varepsilon_E) \frac{\partial c_e}{\partial y} + \frac{m_e}{\rho} \dot{n}_e \qquad (F.1)$$

where $c_e = n_e m_e / \rho$ is the electron concentration, D_a and ε_E are the ambipolar diffusion rates for molecular and turbulent transport, respectively, and $\dot{n}_e$ is the net ionization rate [23]. In the case where three-body (electron as the third body) recombination is the dominant recombination reaction, the net ionization rate can be given as

$$\dot{n}_e = 2.52 \times 10^{-33} n_e \exp(T/325) \left\{ n_e^{*2} - n_e^2 \right\} , \quad [21] \qquad (F.2)$$

where the $*$ denotes equilibrium and the temperature T is taken as the local mean temperature. With the electrons and heavy gas maintained close to equilibrium, the electron energy equation need not be solved, as the heavy particle continuity, momentum, energy and state equations, together with the electron continuity equation, determine the electron (and ion) number density profiles in the charge-neutral region. No explicit dependence upon current density appears in the electron continuity equation; however, a Joule heating term does appear in the heavy particle energy equation, and the current distribution in the region of interest must be determined simultaneously with the fluid solution. For this illustrative calculation, only the transverse current density, J_y, will be non-zero and it will be assumed constant along the electrode length and zero elsewhere. For this case the current conservation equation is

$$J_y = (\mu_e + \mu_i) e n_e \left\{ E_y + \frac{1}{n_e} \frac{d(n_e k T_e)}{dy} \right\} , \qquad (F.3)$$

where μ_e and μ_i are the electron and ion mobilities, respectively. The approximations $\mu_e >> \mu_i$ and $E_y >> 1/n \, (d(n_e k T_e)/dy$ reduce Eqn. (F.2) to

$$J_y = \sigma_e E_y \quad , \tag{F.4}$$

where $\sigma_e = n_e \mu_e e$ is the electron conductivity. The simple Ohm's law represented by Eqn. (F.4) indicates that current transfer is accomplished predominantly by the more mobile electrons. The electron and ion number density profiles, however, are controlled predominantly by the motion of the ions, as

$$D_a = \frac{2kT}{e} \frac{\mu_e \mu_i}{\mu_e + \mu_i} \simeq 2D_i \quad , \tag{F.5}$$

where D_i is the ion diffusion coefficient. The low mobility of the ions and insufficient energy per molecule to support significant charge separation prevents the depletion of electrons in the boundary layer; as will be exhibited later, a region exists close to the wall where electric field gradients are large enough to support significant departures from charge neutrality, and this inner, or sheath, region will have extremely different characteristics.

Before presenting detailed profile results, it is instructive to consider the limiting cases of infinite and negligible electron-ion reaction rates. The behavior for large reaction rates can be displayed by combining Eqns. (F.1) and (F.2) into the equation

$$\left| n_e^{*2} - n_e^2 \right| = \frac{\left| \rho u \frac{\partial c_e}{\partial x} + \rho v \frac{\partial c_e}{\partial y} - \frac{\partial}{\partial y} (\rho D_a + \rho \varepsilon_E) \frac{\partial c_e}{\partial y} \right|}{2.53 \times 10^{-33} \, n_e m_e \exp(T/325)} \quad . \tag{F.6}$$

As the reaction rate (the denominator in Eqn. (F.6)) becomes large, the number density is forced toward the equilibrium number density. In the limit of infinite reaction rates, the electron continuity equation need not be solved, as the electron number density can be viewed simply as a fluid property $n_e = n_e^*(p,T)$. The pressure and temperature are determined by the solution of the heavy particle continuity, momentum, energy and state equations, together with a solution for the current distribution. In the limit of the low reaction rates, the last term in Eqn. (F.1) can be neglected, and the electron number density is governed by the convective-diffusive equation,

$$\rho u \frac{\partial c_e}{\partial x} + \rho v \frac{\partial c_e}{\partial y} = \frac{\partial}{\partial y} (\rho D_a + \rho \varepsilon_E) \frac{\partial c_e}{\partial y} \quad . \tag{F.7}$$

The resulting "frozen" electron number density profile would have the same character as the axial velocity or total enthalpy profile; that is, the profile is determined by the balance of convection and diffusion. In fact, for turbulent and molecular Prandtl and Lewis numbers of unity, non-dimensional axial velocity profiles and non-dimensional electron concentration profiles would be the same. For these conditions, the non-dimensional total enthalpy profile would differ from the electron concentration and axial velocity profiles only as a result of Joule heating and viscous dissipation. The insensitivity of the major part of the electron concentration profile to the precise value of electron concentration at the wall (providing that the electron concentration at the wall is small relative to that at the freestream) can be seen by examining the non-dimensional profile shape, which can be represented as

$$\frac{c_e - c_{e,wall}}{c_{e,\infty} - c_{e,wall}} = \frac{c_e}{c_{e,\infty}} \frac{(1 - c_{e,wall}/c_e)}{(1 - c_{e,wall}/c_{e,\infty})} = f(y) \quad , \qquad (F.8)$$

where ∞ denotes freestream. For $c_{e,wall}/c_{e,\infty} \to 0$, Eqn. (F.8) becomes

$$\frac{c_e}{c_{e,\infty}} (1 - c_{e,wall}/c_e) = f(y) \quad ,$$

indicating that the level of $c_{e,wall}$ will be important only in the region very close to the wall, where $c_{e,wall}/c_e$ is not small. Since it will be shown that the assumption of charge neutrality fails as the wall is approached and a more detailed solution is employed in this near-wall region, the preceding discussion indicates that calculation of the profile in the charge-neutral region can proceed without precise knowledge of the inner-region behavior; this is considered further in the discussion of the surface-sheath modeling.

For conditions typical of MHD-generator operation, the boundary layer region is not well represented by either the frozen or equilibrium limits, as can be observed in Fig. F.2, where calculated profiles are presented. Conditions assumed in the preparation of the figure are presented in Table F.1. The number density profiles for the limiting cases of infinite and negligible reaction rates are shown in the figure, for comparison with the "kinetic" calculated curve. As is evident in the figure, the kinetic

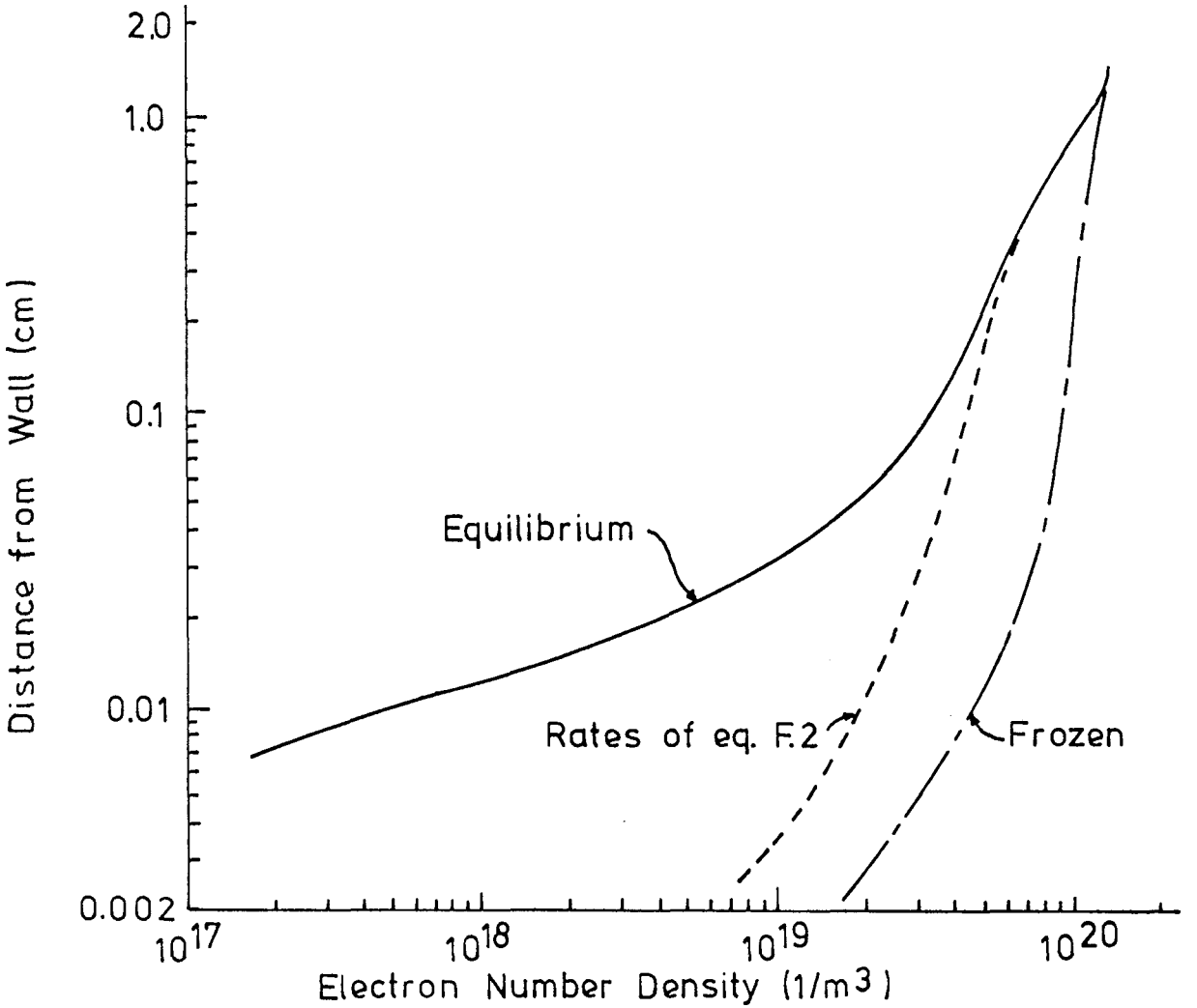

Figure F.2. Calculated electron number density profile for conditions of Table F.1. Number density profile for zero reaction rate and infinite reaction rate are shown for comparison.

Table F.1

CONDITIONS USED IN CALCULATIONS PRESENTED IN FIGURE F.2

Freestream Temperature = 2700°K

Freestream Velocity = 500 m/s

Freestream Pressure = 1 atm

Boundary Layer Thickness = 1.2 cm

Wall Temperature = 1400 K

Wall Electron Number Density =

$$n_e = n_e^*(1400\ K) = 1.1 \times 10^{15}\ /m^3$$

Transverse Current Density = 0 amp/cm^2

curve follows closely the equilibrium curve in the outer portion of the boundary layer, where the temperature (and thus the reaction rate) is high. Significant departure from equilibrium is evident at ~1 mm from the wall, and interior to this the reaction rates quickly become small and the electron number density profile takes on the characteristics of a "frozen" profile. The electron number density calculated assuming negligible reaction rates throughout the boundary layer is considerably higher than the kinetic calculated level throughout the boundary layer. The cumulative resistance for the profiles presented in Fig. F.2 is plotted as a function of non-dimensional distance from the wall in Fig. F.3. As expected, the total resistance, taken for this discussion as the resistance from the edge of the boundary layer to a distance close to the wall, varies considerably for the three profiles presented in Fig. F.2. (Note: as discussed later in the appendix, the solution presented to this point cannot be used for distances close to the wall.) The total resistance values for the cases are:

Profile	Resistance
Kinetic	1.1×10^{-3} ohm - m^2
Equilibrium	22.0×10^{-3} ohm - m^2
Frozen	$.34 \times 10^{-3}$ ohm - m^2

The importance of considering the kinetics in detail in the calculations for these conditions is clearly demonstrated. Increased wall temperature, decreased freestream velocity, and increased freestream temperature all result in a decrease of the difference between the kinetic and equilibrium electron number density profiles. For the freestream conditions of the preceding calculations, but for an electrode wall surface temperature ~ 1800 K (typical of slagging-wall generator operation), the kinetic and equilibrium total resistances still differ by ~40%. It is important to note that, even neglecting the region very close to the surface, the inner 1 mm of the boundary layer accounts for approximately half of the total boundary layer resistance. Thermal runaway, predicted by the time-dependent calculations presented in Chapter 4, results from the formation of a planar current sheet $\lesssim$ 1 mm from the surface, further indicating the importance of including the electron continuity equation in the calculation procedures designed to predict electrode wall phenomena. The importance of considering

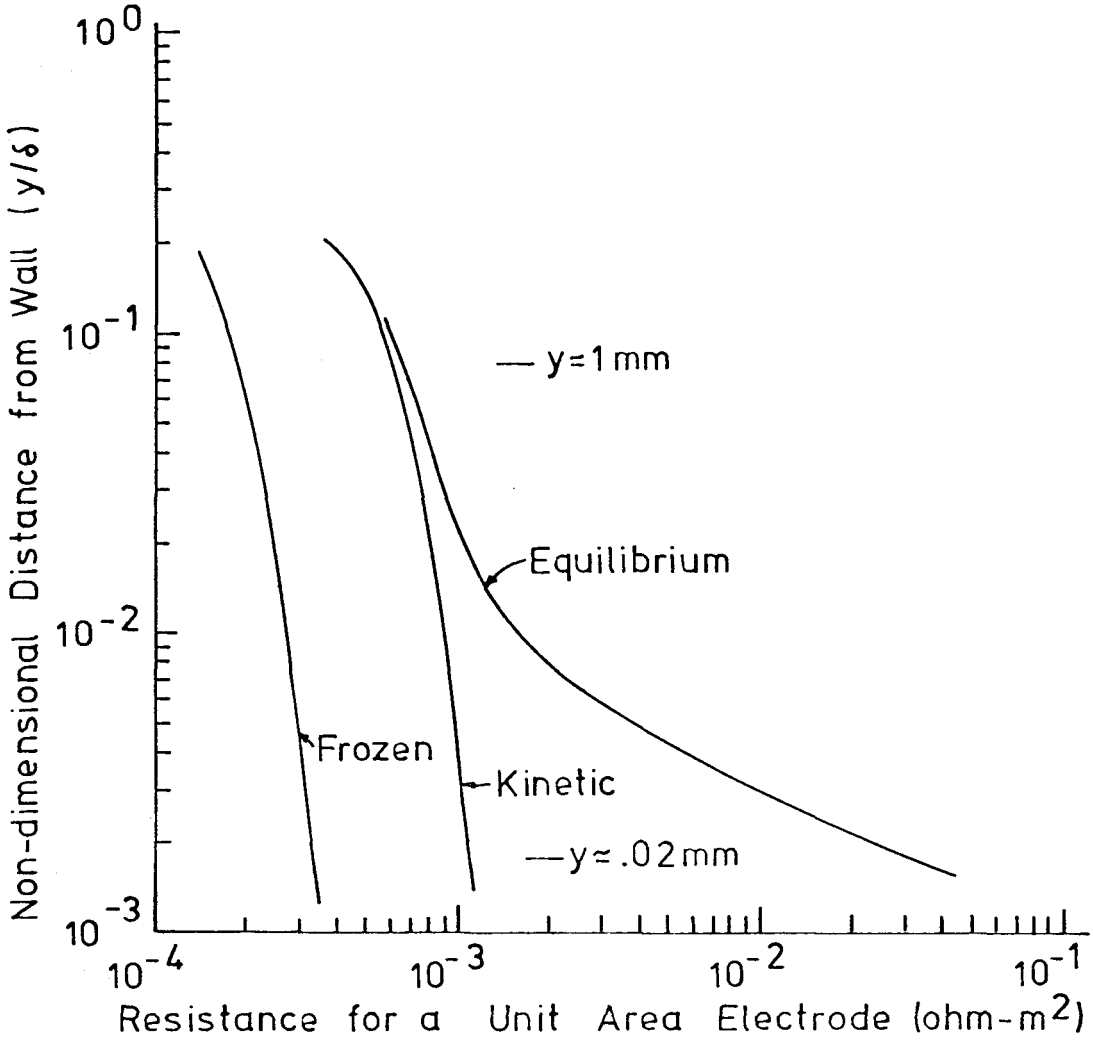

Figure F.3. Cumulative resistance as a function of non-dimensional distance from the electrode surface. Curves presented for the number density calculations considering finite electron-ion reaction rates with the limiting cases of frozen and equilibrium displayed for comparison.

the reaction processes is further demonstrated by examination of the equilibrium and calculated number density profiles for the same conditions as in Fig. F.2, but for a current density of 5 amps/cm^2. As is evident in Fig. F.4, the calculated number density is below the equilibrium number density at some locations from the wall, as reaction processes are insufficient to maintain the number density at equilibrium. Comparisons of predicted and measured electron number density profiles and boundary layer resistances under carefully controlled conditions are important in establishing the validity of the calculation procedure used for the charge neutral region. Some comparisons of predicted and measured electron number density profiles have been presented by Daily [23] and provide some confirmation of the calculation technique; however, further work is required to establish more clearly the validity of the calculation procedure.

Prior to discussing the limitations of the above calculation procedure in the near wall region, it is useful to discuss approximate methods of computing the electron number density profile and the resistance through the charge-neutral region which might be useful for generator performance models and other situations where the detailed response is not overly important. The simplest and most commonly used method is to assume a power law profile for the non-dimensional total enthalpy profile and to evaluate the electron number density from the resulting temperature profile assuming equilibrium. This procedure has been used with considerable success [42,15,17]; however, good agreement of the approximate theory and experiment is fortuitous. Calculated enthalpy and electron number density profiles for the conditions of Table F.1 are compared in Fig. F.5 with the profiles obtained assuming a 1/7th total enthalpy profile and equilibrium electron number density. The equilibrium electron number density profile for the calculated enthalpy profile is also shown in the figure. For the outer portion ($y \gtrsim 1$ mm for these conditions), where the electron number density remains close to the equilibrium and the enthalpy profile is reasonably well represented by the power law formula, the agreement is good. For the inner millimeter, good agreement is still obtained for the electron number density profile; however, the assumed power law enthalpy profile and the calculated enthalpy profile diverge. The divergence is not surprising, since $y \sim .8$ mm corresponds to the edge of the so-called buffer region inside which the empirically based power law profile would

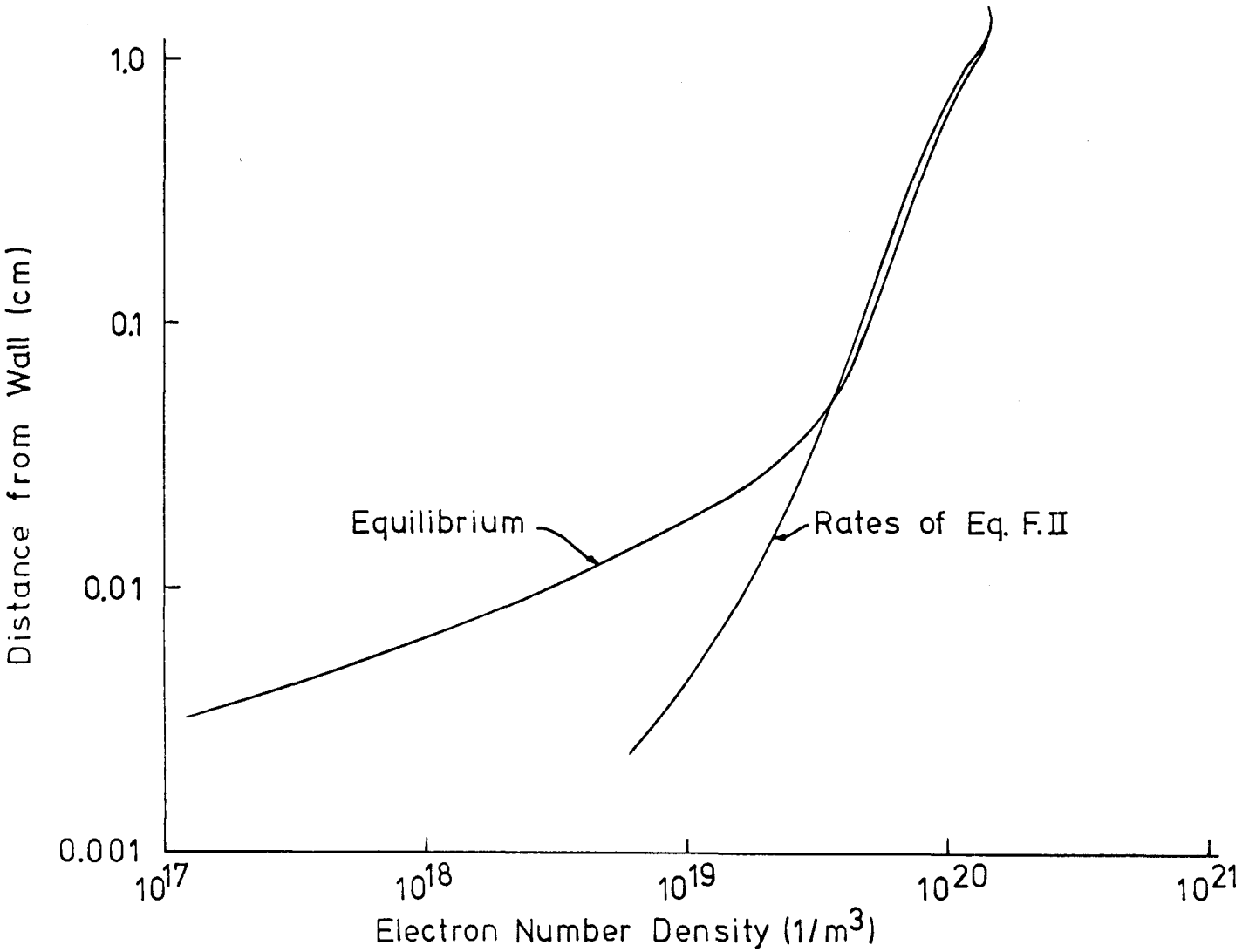

Figure F.4. Kinetic and equilibrium electron number density as a function of distance from the wall. Conditions as specified in Table F.1, except current density is 5 amp/cm^2.

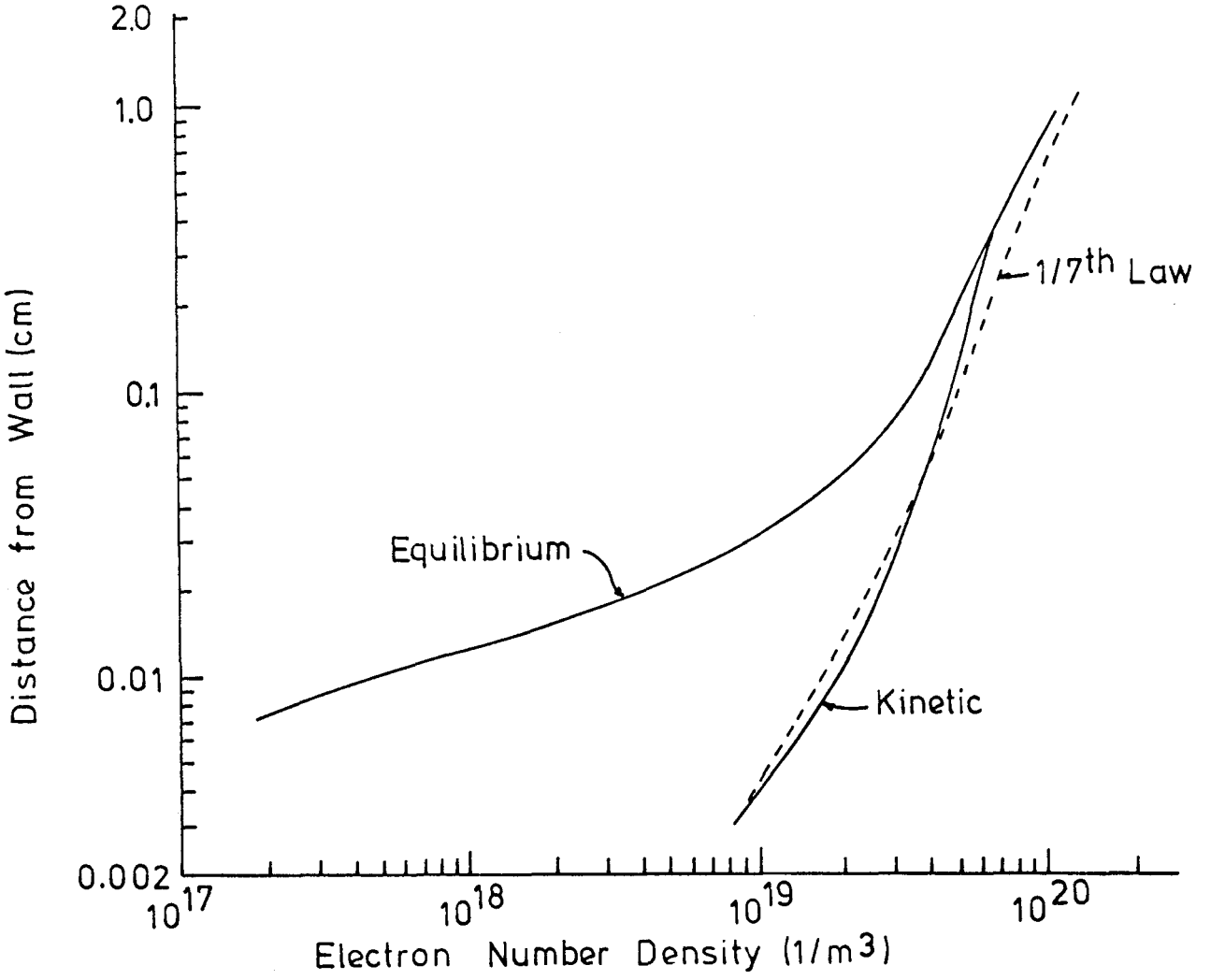

Figure F.5a. Comparison of calculated electron number density profile with profile computed from 1/7th law enthalpy profile assuming equilibrium. Equilibrium electron number density profile based on calculated enthalpy profile is also shown. Conditions for calculations specified in Table F.1.

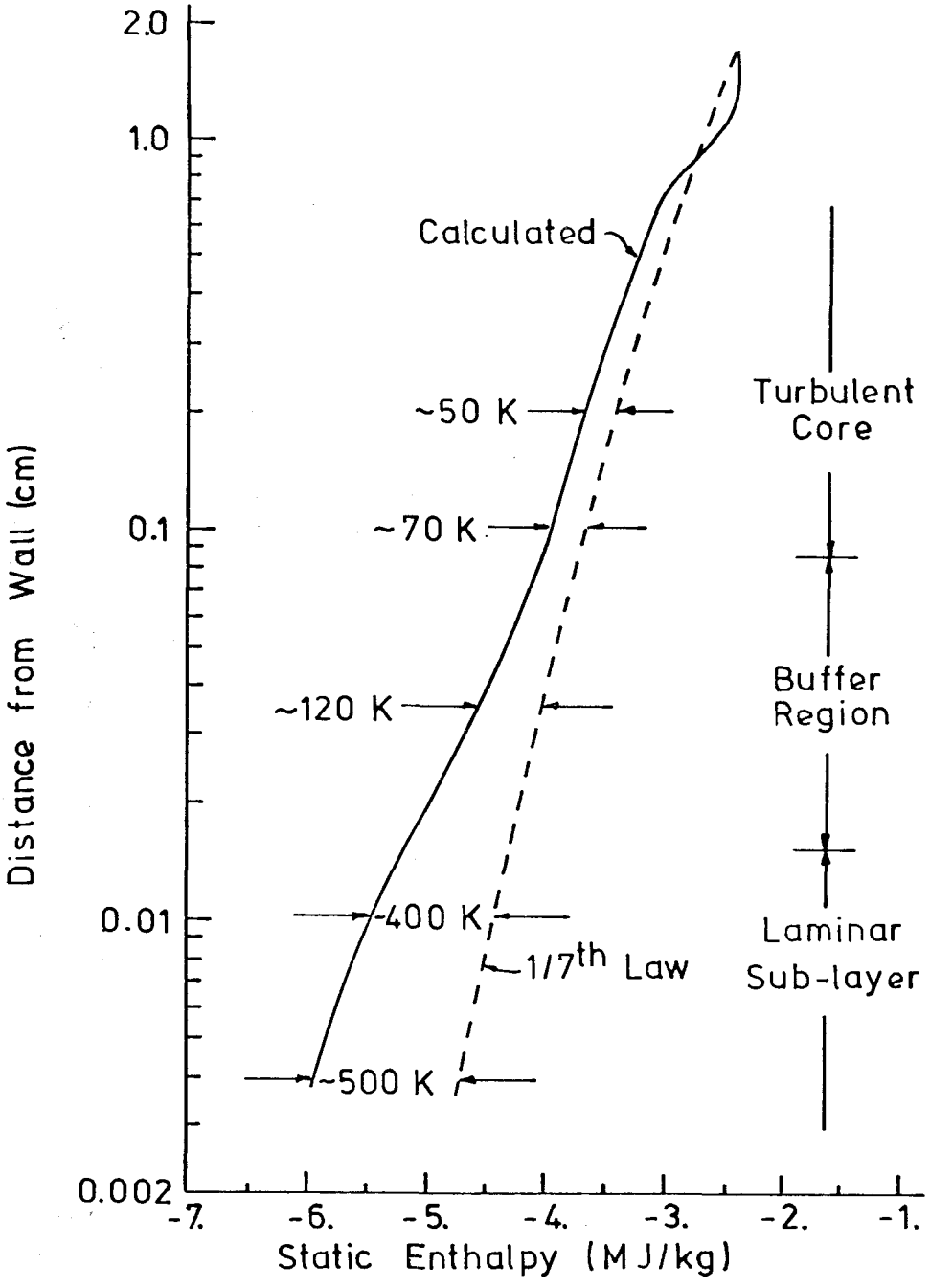

Figure F.5b. Comparison of calculated static enthalpy profile with 1/7 th law enthalpy profile. Extents of laminar sublayer, buffer region and turbulent core are indicated in the figure. Conditions for calculations specified in Table F.1.

not be expected to apply. The good agreement of the electron number density profiles is the result of the over-prediction of the temperature by the power law approximation, rather than the physics being well modeled. Improvements to a model based on the simplified calculation procedure outlined above to account for effects of Joule heating, for example, cannot be assumed to yield the proper behavior, at least as far as the inner portion of the boundary layer. Inasmuch as the inner portion accounts for half the transverse resistance (for the conditions presented above), results from such models should be accepted only with reservation.

The preceding discussion indicates that an improved approximate technique, which would more adequately represent the physics of the entire charge-neutral region but still require only minimal calculation time, is desirable. A more accurate enthalpy profile in the near-wall region can be obtained by employing a more sophisticated approximate profile, such as the three-layer model of Martinelli [35] with little increase in computation time. With an accurate enthalpy profile for the inner portion, equilibrium electron number density can no longer be assumed for the inner portion. The strong temperature dependence of the net electron-ion reaction rate (see Eqn. (F.2)) suggests that splitting of the boundary layer profile into an equilibrium region and a frozen region could be a useful approach. The same approximate profile shape used for the total enthalpy profile can be employed for the calculation of the electron concentration in the frozen region. The split location could be determined empirically from profiles calculated by the two-dimensional boundary layer code for conditions of interest, or perhaps the split location could be determined from an approximate evaluation of the relative importance of reactions, convection, and diffusion through the boundary layer. It seems probable that such a model could ultimately accommodate effects such as Joule heating and variable wall temperature in a physically reasonable (although perhaps empirically based) fashion. A preliminary evaluation of such an approach is represented by Figs. F.6a and F.6b, where calculated profiles and approximate profiles are compared for the conditions used in the previous calculations. As can be observed, reasonable agreement can be achieved with such a technique. Further work is obviously required to fully establish the utility of such an approach.

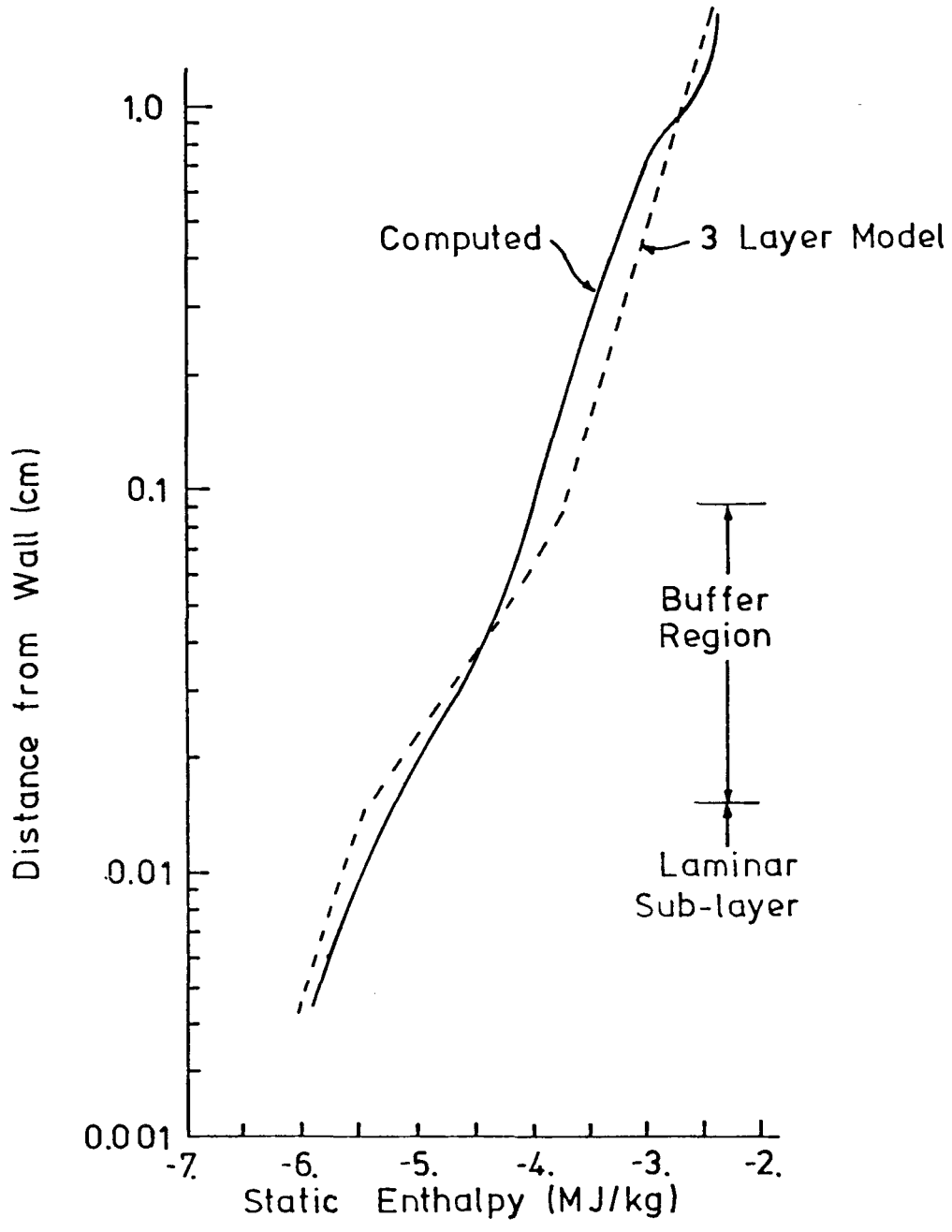

Figure F.6a. Comparison of calculated static enthalpy profile with 3-layer model of Martinelli. Conditions for calculations specified in Table F.1.

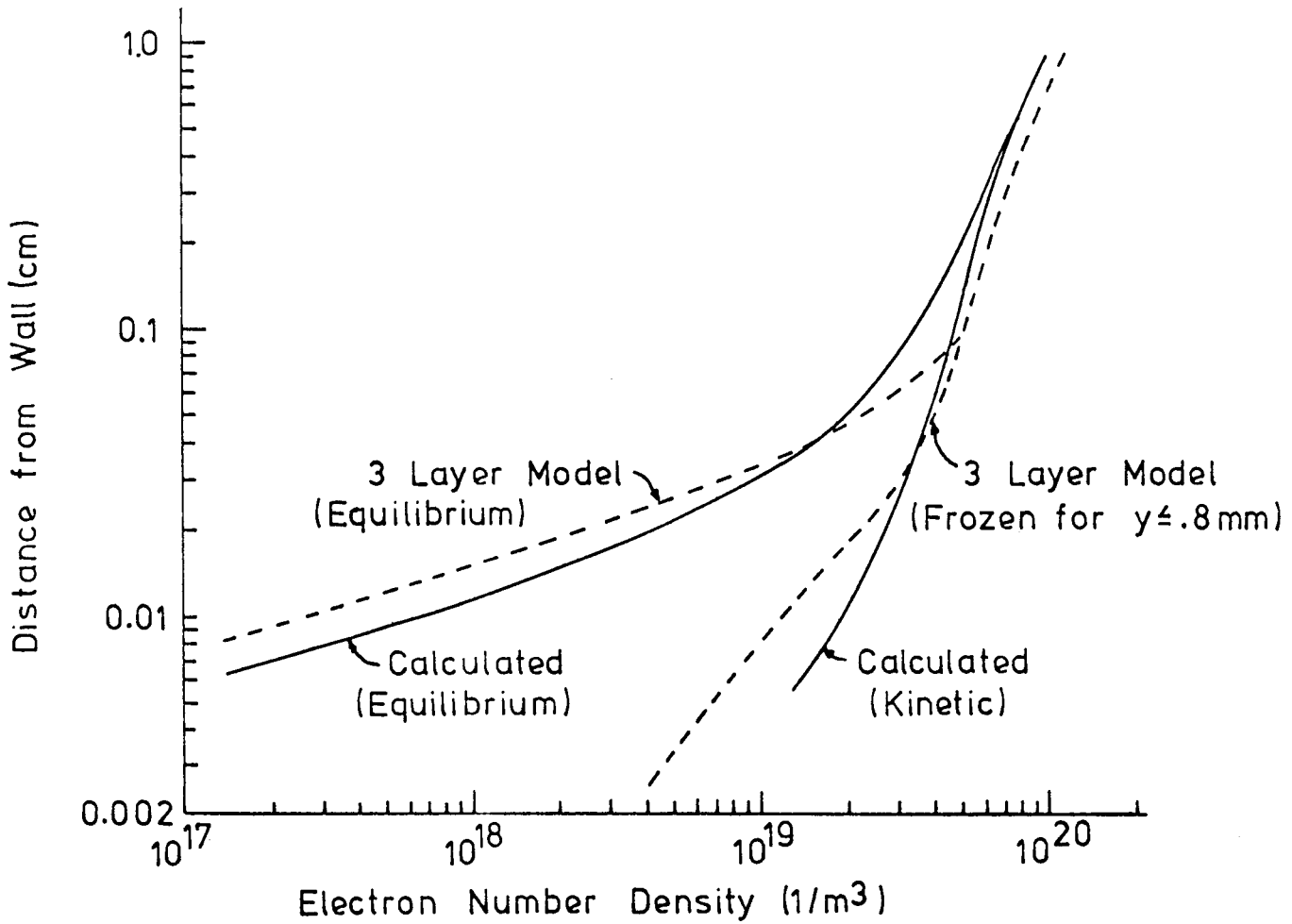

Figure F.6b. Comparison of calculated electron number density profile with approximate profile. Calculated equilibrium number density profile and equilibrium number density profile based on 3-layer enthalpy profile are also shown. Conditions for calculations specified in Table F.1.

F.3 Limitations of the Outer Solution

The calculation procedure presented in the previous section incorporates several assumptions and cannot be used to represent the behavior over the entire region of interest. In particular, extremely large electric field gradients and high Joule dissipation in the near-wall region predicted using the outer solution indicate that a more detailed physical description of this region is required. Space-charge effects are perhaps the most important limitation of the outer solution and are treated first. The outer solution is used to estimate the distance from the wall where space-charge effects must be included, and this distance is used as the dividing point for the inner and outer solutions. Some characteristics of the inner region are mentioned, although a detailed description of the model to be used is deferred to a later section. The electron pressure gradient term in the current conservation equation (F.3) and electron temperature non-equilibrium are discussed and their importance evaluated for the inner and outer regions.

Violation of Charge Neutrality

As suggested by Self [36], the solution obtained assuming equal electron and ion number densities is used to establish the distance from the wall where space-charge effects are first of importance. Poisson's equation relates the net charge density to the electric field gradient as

$$\nabla \cdot \vec{E} = \frac{\rho_c}{\varepsilon_o}$$

where $\rho_c = e(n_i - n_e)$ is the charge density. For a one-dimensional discharge and employing the simple Ohm's law (Eqn. (F.4)) as an expression for the departure from charge neutrality can be estimated as

$$\xi = \frac{n_i - n_e}{n_e} \simeq J_y \frac{\varepsilon_o}{e^2} \frac{1}{n_e} \frac{d}{dy} \frac{1}{\mu_e n_e} \quad .$$

The inner edge of applicability of the outer solution can be evaluated as the point at which the fraction ξ exceeds a specified level. The departure from charge neutrality ξ is plotted as a function of distance from the wall in Fig. F.7 for conditions of Table F.2 and for several current density levels. The indicated size of the inner region, as would

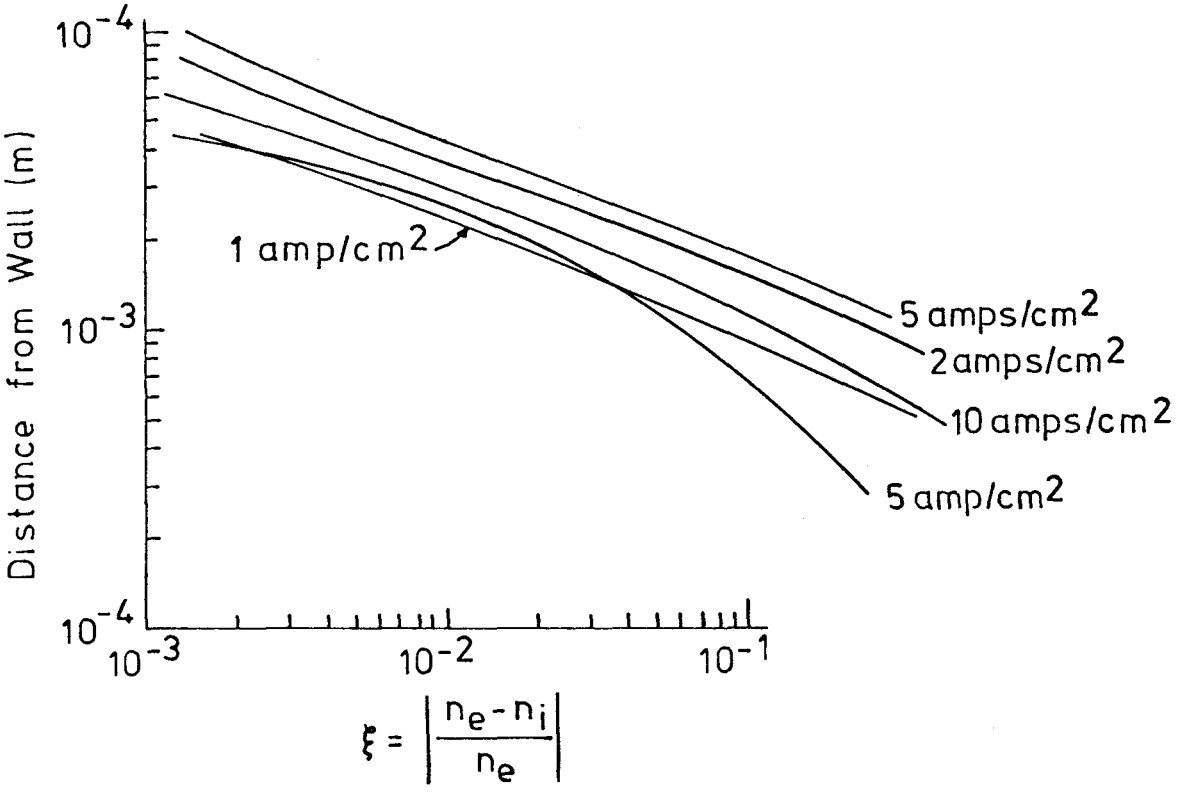

Figure F.7. Distance from the wall at which $\xi = |(n_e - n_i)/n_e|$ exceeds a certain fraction. Results shown for several values of current density.

Table F.2

CONDITIONS USED IN CALCULATIONS PRESENTED IN SECTION F.3

Freestream Temperature = 2629.1 K

Freestream Velocity = 250 m/s

Freestream Pressure = 1 atm

Boundary Layer Thickness = 7 mm

Wall Temperature = 1300°K

Wall Electron Number Density Used in Outer Region Calculations = $n_e = n_e^* = .6 \times 10^{15}\ /m^3$

Recombination Rate = .8 × rates of Eqn. (F.2)

be determined by choosing $\xi = 10\%$ and $\xi = 1\%$, is shown in Fig. F.8 for current density levels from .5 amp/cm^2 to 10 amp/cm^2. As can be observed, the size of the region where charge neutrality is violated increases with current density up to ~ 5 amp/cm^2 and then declines; a typical size is ~ 2×10^{-3} cm for $\xi = 10\%$ and ~ 8×10^{-3} cm for $\xi = 1\%$. The $\xi = 10\%$ point is taken in this analysis as defining the extent of the inner region for the purpose of calculating the properties in that region. The inner region solution is generally carried out to greater distances from the wall, typically to the $\xi = 1\%$ point.

A detailed discussion of the characteristics of the inner region is deferred until the next section; however, it is useful to mention some of the features of the region at this time. Examination of the electron number density profiles for these conditions indicates that reactions have ceased to be important inside ~ 1 mm of the surface and therefore the inner region can be considered completely frozen. A distance from the wall of ~ 10^{-2} cm corresponds to a distance of $y^+ \sim 5$ in so-called wall coordinates; that is, the inner region is mostly contained in the laminar sublayer of the boundary layer. Finally, with a typical mean free path of ~ 10^{-6} m, a collisional inner region is indicated.

Charge Transfer by Diffusion

For the one-dimensional discharge considered here, the current conservation equation is (Eqn. (F.3))

$$J_y = (\mu_e + \mu_i) e n_e E_y + \frac{1}{n_e e} \frac{d(n_e k T_e)}{dy} \quad .$$

The relative importance of current transport through the influence of the electric field and through diffusion is indicated in Fig. F.9 for several values of current density. For this estimate, the electron temperature has been taken equal to the gas temperature. As is evident in the figure, diffusion is responsible for less than 10% of the current transport in the outer region, for current density levels greater than .5 amp/cm^2. As indicated in the equation above, as $J_y \to 0$, $E_y \to \frac{1}{n_e e} (d(n_e k T_e))/dy$, and the diffusion term will in fact dominate. It would appear that neglect of

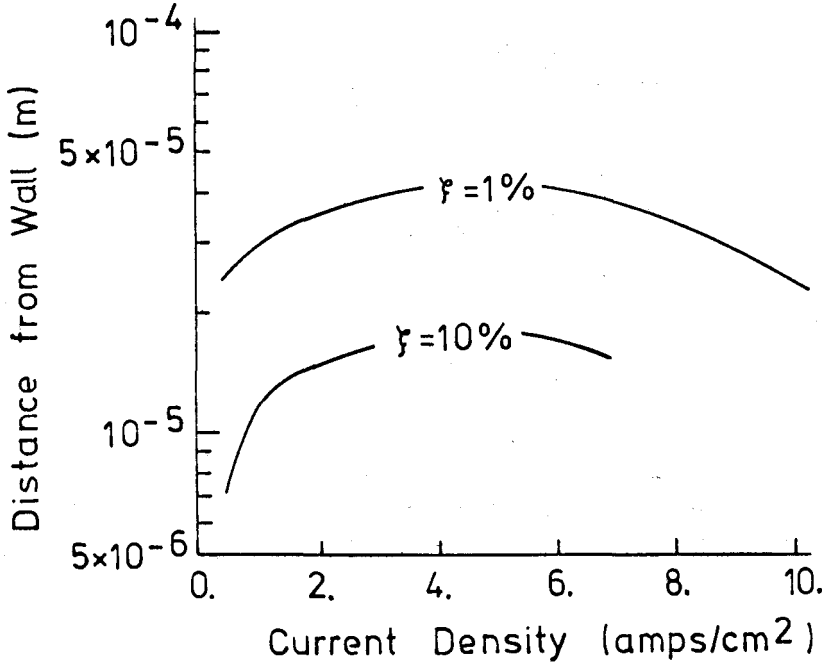

Figure F.8. Extent of inner region as a function of current density. Curves are presented for two levels of departure from charge neutrality.

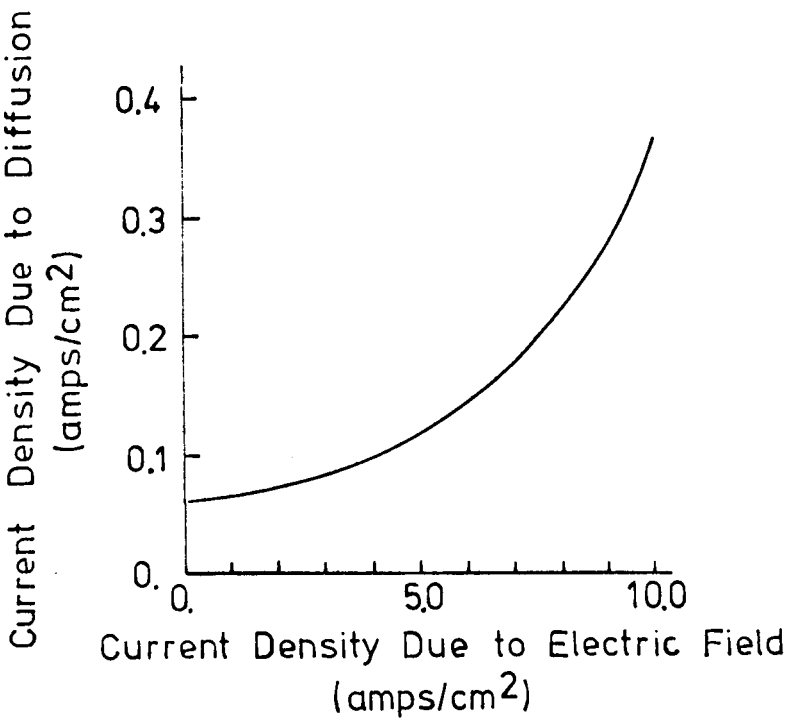

Figure F.9. Comparison of diffusion driven current density with electric field driven current density. Conditions for calculations specified in Table F.2.

the diffusion term in the current conservation equation for the outer region will not introduce serious error for the current densities generally of interest. Diffusion is of considerable importance in the inner region, where number density gradients can be extremely large, and is included in that model.

Electron Temperature Non-Equilibrium

For a combustion products plasma, inelastic collisional processes provide strong electron-heavy particle energy coupling, and the electron temperature is maintained close to the heavy particle temperature in the core region and throughout most of the boundary layer. In the region close to the wall, however, the electron number density is low, and for high enough current density, Joule dissipation in the electron gas may be sufficiently great to result in significant electron temperature elevation. If collisional loss to the heavy species is considered the dominant energy loss mechanism for the electrons, an estimate of the electron temperature elevation can be obtained by a balance of the collisional loss rate and the rate at which energy is imparted to the electrons by the electric field. That is, the electron temperature can be estimated from the equation

$$\frac{3}{2} k(T_e - T_h) \quad 2\delta \frac{m_e}{m_n} \bar{\nu}_{eH} = \frac{1}{n_e} \frac{J^2}{\sigma_e} , \qquad (F.9)$$

where $\bar{\nu}_{eH}$ is the electron-heavy particle collision frequency, T_e and T_h are the electron and heavy particle temperatures, respectively, and the quantity $(2\delta(m_e/m_h))$ represents the average fraction of energy loss per collision. The physics of the collisional processes is contained in the evaluation of the quantity δ, termed the energy loss factor. For a noble gas plasma, where elastic collisions are dominant, the energy loss factor is close to unity; however, calculation of the energy loss factor for combustion gas plasmas indicate that $\delta \sim 2000$ is typical [37]. Estimated electron temperature profiles for the conditions of Table F.2 and for $\delta = 2000$ are shown in Fig. F.10, for current densities from .5 amp/cm^2 to 10 amp/cm^2. In preparation of Fig. F.7, the outer region solution has been used to evaluate the quantities in Eqn. (F.9), and the heavy gas temperature profiles are shown in the figures for reference.

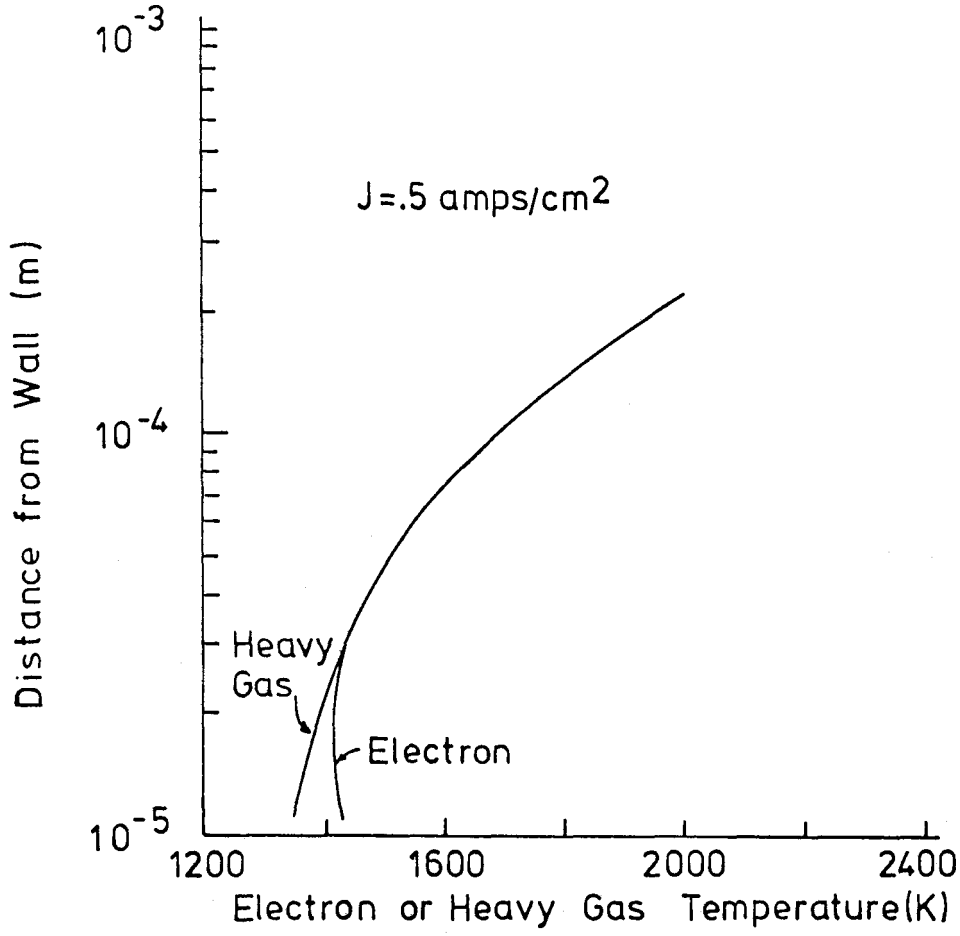

Figure F.10a. Electron and heavy gas temperatures in region near the wall for a current density of 0.5 amp/cm^2. Conditions for the calculations as specified in Table F.2 and with an energy loss factor, δ, of 2000. Estimated departure from charge neutrality is also indicated on figure.

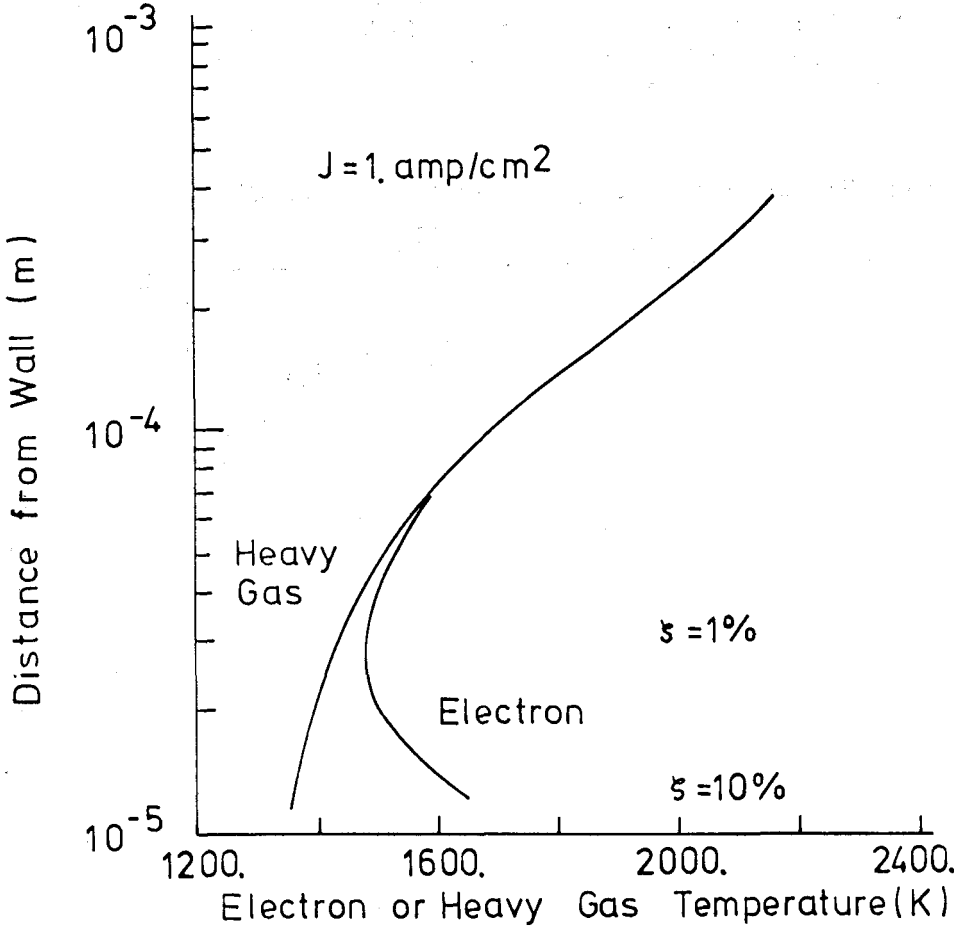

Figure F.10b. Electron and heavy gas temperatures in region near the wall for a current density of 1.0 amp/cm^2. Conditions for the calculations as specified in Table F.2 and with an energy loss factor, δ, of 2000. Estimated departure from charge neutrality is also indicated on figure.

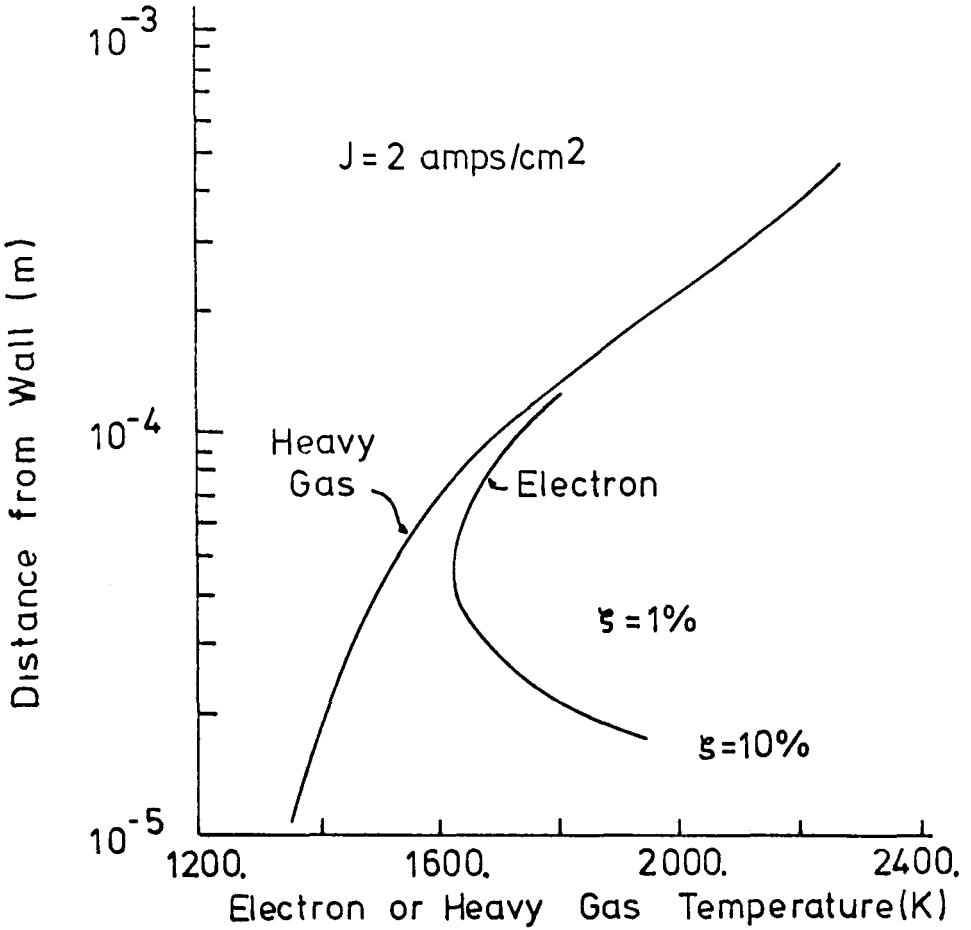

Figure F.10c. Electron and heavy gas temperatures in region near the wall for a current density of 2.0 amp/cm^2. Conditions for the calculations as specified in Table F.2 and with an energy loss factor, δ, of 2000. Estimated departure from charge neutrality is also indicated on figure.

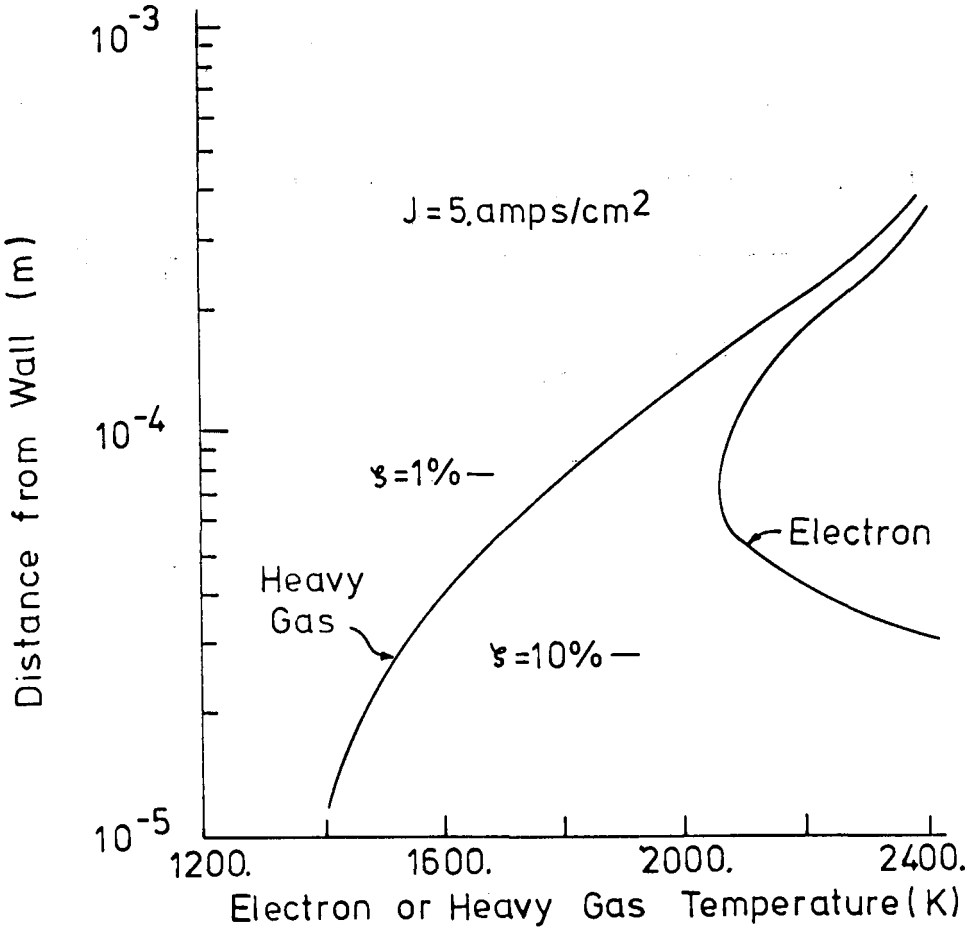

Figure F.10d. Electron and heavy gas temperatures in region near the wall for a current density of 5.0 amp/cm^2. Conditions for the calculations as specified in Table F.2 and with an energy loss factor, δ, of 2000. Estimated departure from charge neutrality is also indicated on figure.

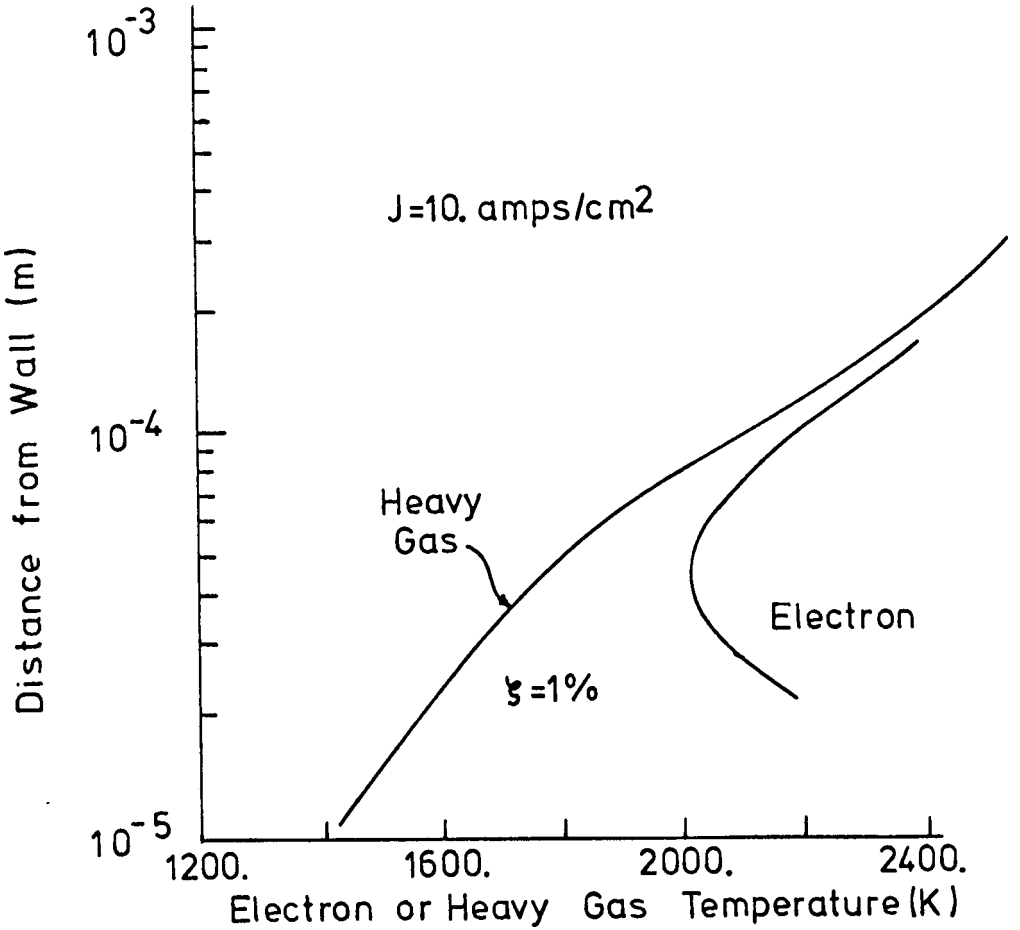

Figure F.10e. Electron and heavy gas temperature in region near the wall for a current density of 10.0 amp/cm^2. Conditions for the calculations as specified in Table F.2 and with an energy loss factor, δ, of 2000. Estimated departure from charge neutrality is also indicated on figure.

As can be observed in the figures, for all current densities the region of significant electron temperature elevation is confined to within $\lesssim 2 \times 10^{-4}$ m of the wall. Only for the highest current density does the electron temperature exceed the heavy gas temperature by more than 300°K (< 20%) outside the $\delta = 1\%$ point.

Evaluation of the importance of electron temperature non-equilibrium must consider its overall effect on the electron number density and on the current transport in the near-wall region. The equilibrium number density is, of course, a strong function of the electron temperature; however, as was established in the previous section, the electron number density is not maintained close to the equilibrium level in the near-wall region, due to low ionization-recombination rates. The increase in electron temperature indicated by the above calculation does not appear sufficient to make reactions important and will therefore have little effect on the electron number density in this manner. Increased electron temperature will also affect the electron pressure gradient term in the electron continuity equation and will alter the electron mobility. For the charge-neutral region, and in the spirit in which Eqn. (F.1) was derived, the principal effect of increased electron temperature would be to increase the molecular ambipolar diffusion coefficient by a factor of $(1+T_e/T_i)/2$. For the electron temperature elevation indicated for the charge-neutral refion, only a relatively small effect should result, and this effect is not included. The effect of electron temperature elevation on the diffusion characteristics is included in an approximate manner in the model for the inner region. The effect on current transport can be examined by considering the current conservation equation (F.3).

$$J_y = (\mu_e + \mu_i) e n_e E_y + \frac{1}{n_e e} \frac{d(n_e k T_e)}{dy}$$

The gradient term, which contains an explicit dependence on electron temperature, is relatively unimportant in the outer region (especially for the current densities where electron elevation is high), and the increased electron temperature will tend to further decrease its importance. For the inner region, the gradient term is of importance in determining the current density, and electron temperature elevation is included in an approximate fasion. In addition, simple considerations would suggest that

increased electron temperature will result in a decrease in the electron mobility. The electron mobility can be expressed as

$$\mu_e = \frac{e}{m_e \bar{\nu}_{eH}}$$

where $\bar{\nu}_{eH}$ is the electron-heavy particle collision frequency. Simple considerations yield

$$\bar{\nu}_{eH} = n_H \bar{C}_{eH} \bar{Q}_{eH}$$

where n_H is the heavy particle number density, $\bar{Q}_{eH}$ is the average collision cross section, and $\bar{C}_{eH}$ is the mean relative speed of the collision partners, which can be taken as approximately the mean electron speed. The electron mobility then varies as

$$\mu_e \propto \frac{1}{n_H \bar{C}_e}$$

or

$$\mu_e \propto \frac{1}{\sqrt{T_e}}$$

and the mobility should be corrected by a factor of $\sqrt{T_i/T_e}$. The effect of increased electron temperature is more complex than indicated, and, since the estimated effect is relatively small ($T_i/T_{e\ max} \sim 1.2$ for the outer region), the effect is not included for that region.

F.4 Inner Region

Continuum Sheath Model

Comparison of the estimated inner region size ($\sim 10^{-5}$ to 10^{-4} m) with the electron mean free path ($\sim 10^{-6}$ m) indicates that a collisional sheath model is required. Since the region can be considered reactionless and the flow laminar, the continuum sheath approach of Lam is appropriate. Temperature variation across the inner region is significant for the higher current densities (larger inner region thicknesses); however, for the present model, the electron and ion temperatures and mobilities will be assumed constant at their values at $\xi = 10\%$, as discussed in the previous section. The electron temperature at the $\xi = 10\%$ point is determined using the approximate form of the electron energy equation, as represented

by Eqn. (F.9). At the outer edge of the sheath region, the appropriate boundary condition is that $n_e \to n_i \to n_{\text{outer solution}}$ as $y \to \infty$. The collisional sheath model is assumed to apply to within a mean free path of the surface, and the electron and ion number densities at the inner edge are calculated from the Knudsen layer-surface layer model described later in this section.

Starting with the electron and ion conservation equations and Poisson's equation, the solution for the sheath region is formulated in terms of an equation for the non-dimensional electric field. The development of the equations for the sheath region is presented at the end of the appendix. Prior to discussion of the Knudsen layer-surface layer region, it is useful to discuss the characteristics of the sheath region, defined as the location where $|n_e - n_i|/n_i \sim .10$, as indicated from the outer solution. For a wall which does not emit electrons or ions, the sheath voltage drop versus current density relationship is shown in Fig. F.2. The conditions for the calculations are given in Table F.3. As is evident in Fig. F.11, a saturation current is observed for operation as an anode and for operation as a cathode. Saturation can be explained through an examination of the electron and ion number fluxes for different current densities. For the sheath model used here, the number fluxes are constant through the sheath and can be expressed as

$$\Gamma_i = - D_e \frac{d\hat{n}}{d\hat{y}} \beta(x + \varepsilon) \tag{F.10a}$$

and

$$\Gamma_e = - D_e \frac{d\hat{n}}{d\hat{y}} (1 - x) \quad , \tag{F.10b}$$

where $d\hat{n}/d\hat{y}$ is the slope of the number density at the inner edge of the ambipolar region and x is the non-dimensional total current given by

$$x = \frac{1 - \varepsilon\beta}{1 + \beta} - \frac{J_t}{D_e(1 + \beta)e\ (d\hat{n}/d\hat{y})} \tag{F.10c}$$

For a cathode x is always positive, while for an anode x decreases from $\frac{1 - \varepsilon\beta}{1 + \beta}$ (~ 1) and for significantly high current density becomes negative. For zero current density, both number fluxes are negative; that is,

Table F.3

CONDITIONS USED IN CALCULATIONS PRESENTED IN SECTION F.4

Freestream Temperature = 2630 K

Freestream Velocity = 250 m/sec

Freestream Pressure = 1 atm

Boundary Layer Thickness ~ 1 cm

Electrode Temperature = 1300 K

Upstream Wall Temperature = 1800 K

Length of Upstream Wall = 20 cm

Electrode Length = 1 cm

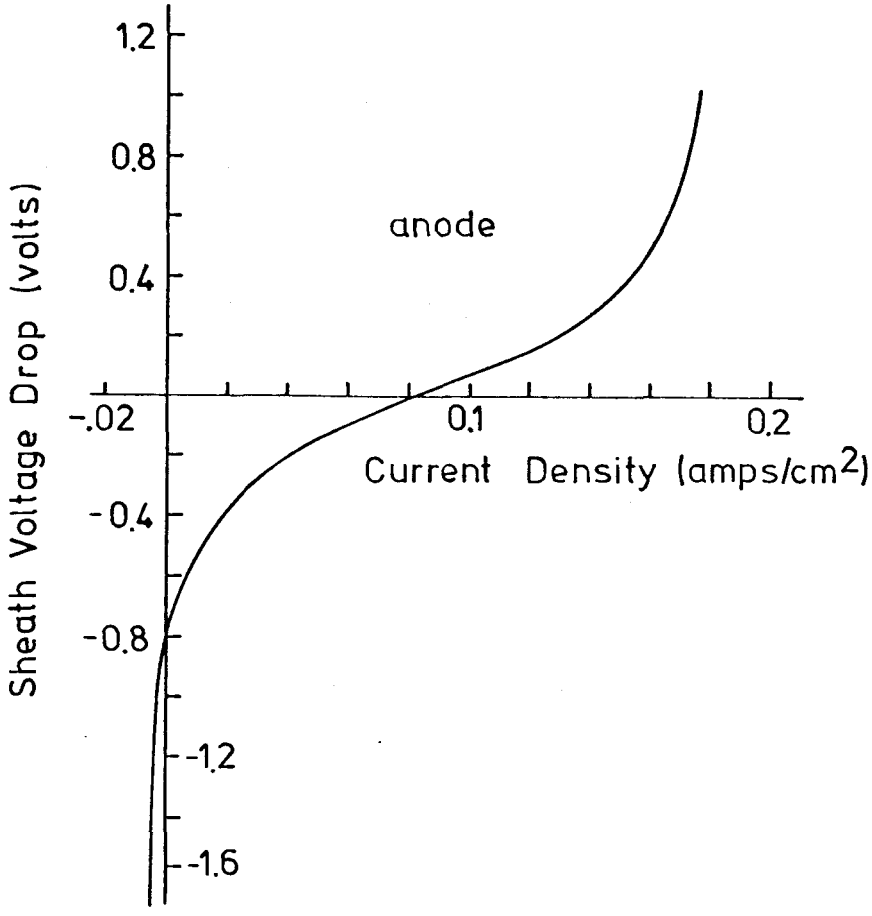

Figure F.11. Sheath voltage-current characteristic for a non-emitting electrode and for conditions of Table F.2.

electrons and ions both diffuse toward the walls. For a cathode, increases in current density result in a decline in $|\Gamma_e|$ such that as $x \to 0$, $\Gamma \to 0$. For $x > 1$, the electron number flux is positive, indicating that electron emission from the electrode is required; thus, for a non-emitting cathode, saturation will occur as $x \to 1$. A similar effect occurs for a non-emitting anode, in that as $x \to -\varepsilon$ ion emission would be required. The saturation current densities for non-emitting electrodes are

$$J_{\substack{\text{saturation} \\ \text{anode} \\ \text{no emission}}} = D_e(1+\varepsilon)e \frac{d\hat{n}}{d\hat{y}}$$

and

$$J_{\substack{\text{saturation} \\ \text{cathode} \\ \text{no emission}}} = -\beta D_e(1+\varepsilon)e \frac{d\hat{n}}{d\hat{y}} = -\beta \times J_{\substack{\text{saturation} \\ \text{anode} \\ \text{no emission}}}$$

As expected, the high mobility of the electrons results in a lower saturation current density for a cathode. As saturation is approached, significant space charge results in the sheath due to the depletion of either electrons or ions. This behavior is displayed for an anode in Figs. 12a-c, where the ion number density is shown to decrease dramatically as saturation occurs. For the conditions of Table F.3,, saturation current densities of $\sim 10^{-3}$ amps/cm^2 for a cathode and $\sim 10^{-1}$ amps/cm^2 for an anode are indicated for non-emitting electrodes; a typical average current density of ~ 1 amp/cm^2 would be expected for typical MHD operating conditions. In the absense of saturation, sheath voltage drops of a few kT_e or $\tilde{<} 1$ volt are indicated. As saturation is approached, electric field gradients become large and several effects not included in this model can become of importance. For the conditions used in the calculations of Table F.3, the electric field at $y = \lambda_{mfp} \sim 10^{-6}$ m increases from 1.5×10^4 volts/m at a current density of .1 amp/cm^2 to $\sim 5 \times 10^4$ volts/m as the saturation current density is approached. The most significant effect of the high electric field at the surface is that a transition to an arc can result; in fact, to the extent that the sheath is well modeled, the saturation current

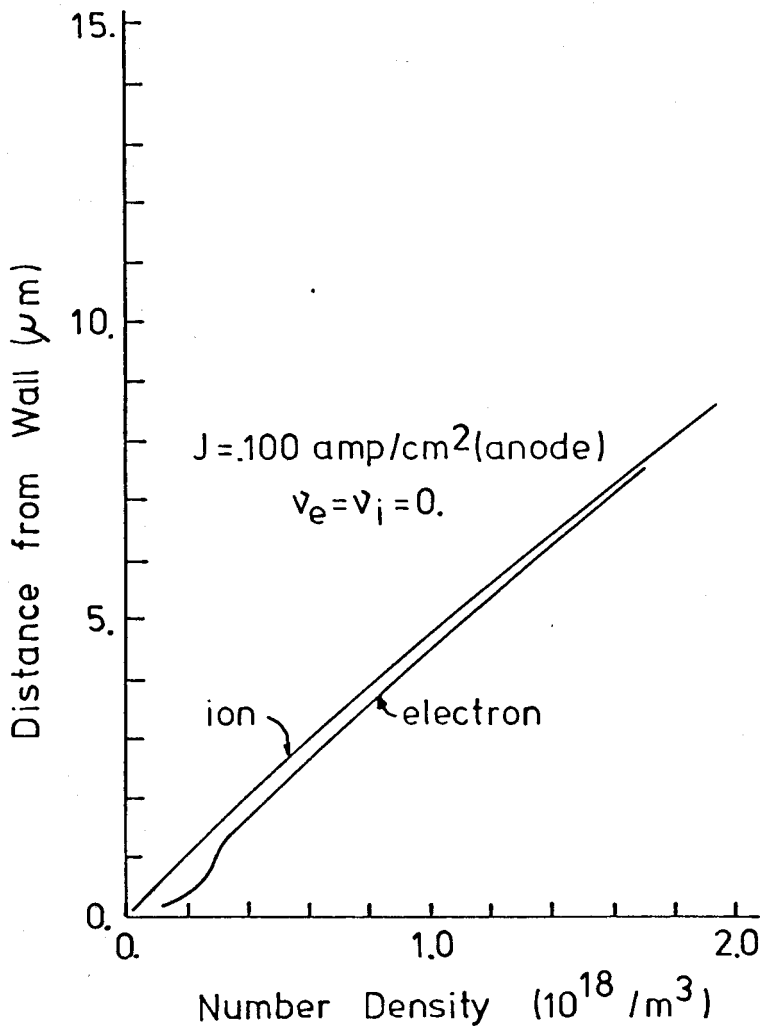

Figure F.12a. Electron and ion number density profiles in the sheath region. Conditions for the calculations are presented in Table F.2. Current density is .1 amp/cm^2 and the electrode is non-emitting and operating as an anode.

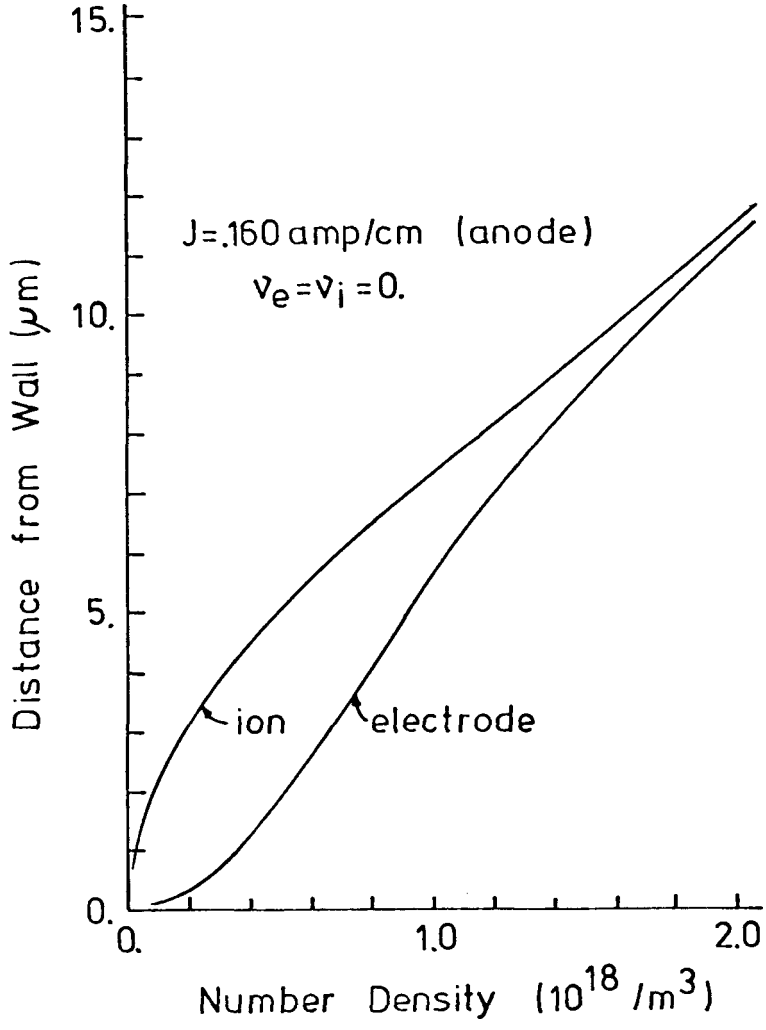

Figure F.12b. Electron and ion number density profiles in the sheath region. Conditions for the calculations are presented in Table F.2. Current density is .160 amp/cm^2 and the electrode is non-emitting and operating as an anode.

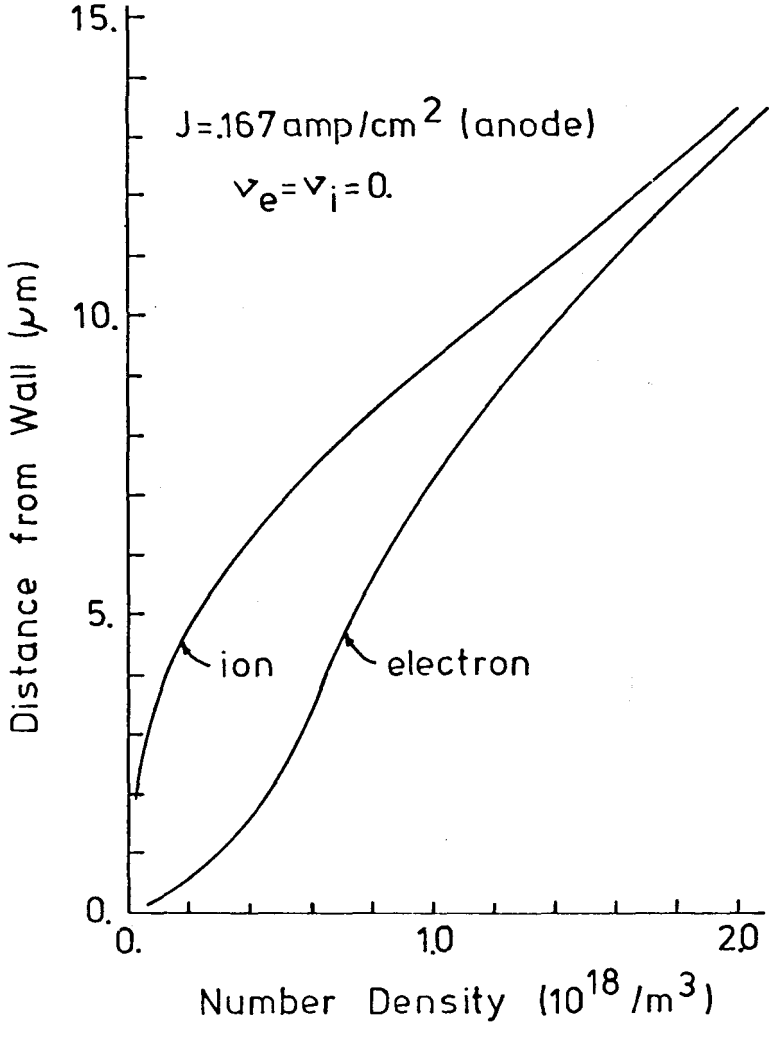

Figure F.12c. Electron and ion number density profiles in the sheath region. Conditions for the calculations are presented in Table F.2. Current density is .167 amp/cm^2 and the electrode is non-emitting and operating as an anode.

density predicted under the assumption of a diffuse discharge can be viewed as a threshold current density for transition to the arc mode.

Knudsen Layer-Surface Layer

The Knudsen layer-surface layer model of Koester [38] is employed to provide the inner boundary values for n_e and n_i. For this purpose, a region of extent $y \simeq \lambda_{mfp}$ immediately adjacent to the wall is considered as indicated in Fig. 13. The electron and ion number fluxes, Γ_e and Γ_i, respectively, are constant through the sheath and given by Eqns. (F.10a) and (F.10b). The surface emission fluxes for electrons and ions, ν_e and ν_i, respectively, are specified by the surface model of Gyftopoulos and Levine, or are considered as parameters. The model of Koester characterizes the incoming particles by a displaced Maxwellian velocity distribution such that the number densities at the inner edge of the sheath can be related to the wall emission and the total flux as

$$\hat{n}_{i_{\substack{\text{inner edge}\\ \text{of sheath}}}} = \frac{\nu_i}{c_i} F(\Gamma_i/\nu_i)$$

and

$$n_{e_{\substack{\text{inner edge}\\ \text{of sheath}}}} = \frac{e}{c_e} F(\Gamma_e/\nu_e) \quad ,$$

where F is a known function (see Koester [38], page 18) and $F(1) = 0$.

Prior to discussing the probable behavior of ν_e and ν_i, it is useful to discuss the effect of ν_e and ν_i on the voltage-current characteristics of the sheath region, in particular their effect on the saturation current densities. The voltage-current curves for the conditions of Table F.3 and several values of ν_e and ν_i are displayed in Fig. 14a and 14b. As expected, ion emission from an anode and electron emission from a cathode increase the saturation current densities. Following the arguments of the preceding section, saturation at the anode should occur when $\Gamma_i \to \nu_i$, while saturation at a cathode should occur when $\Gamma_e \to \nu_e$. The corresponding saturation currents with emission can be expressed as

$$J_{\substack{\text{saturation}\\ \text{anode}\\ \text{ion emission}}} \sim J_{\substack{\text{saturation}\\ \text{anode}\\ \text{no emission}}} \times \left(1 + \frac{\nu_i}{\Gamma_e} \frac{1}{\beta}\right)$$

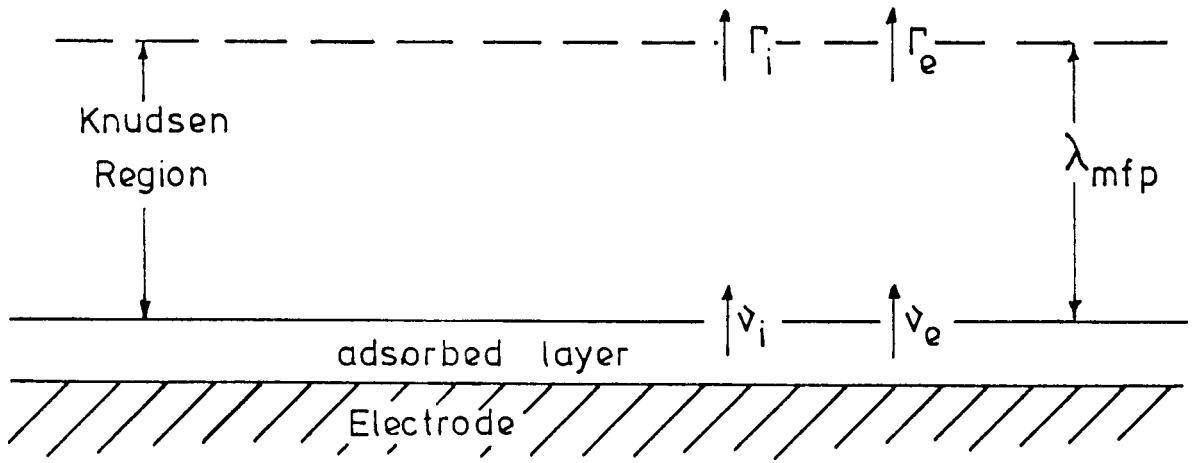

Figure F.13. Sketch of Knudsen layer, specifying some of the terminology.

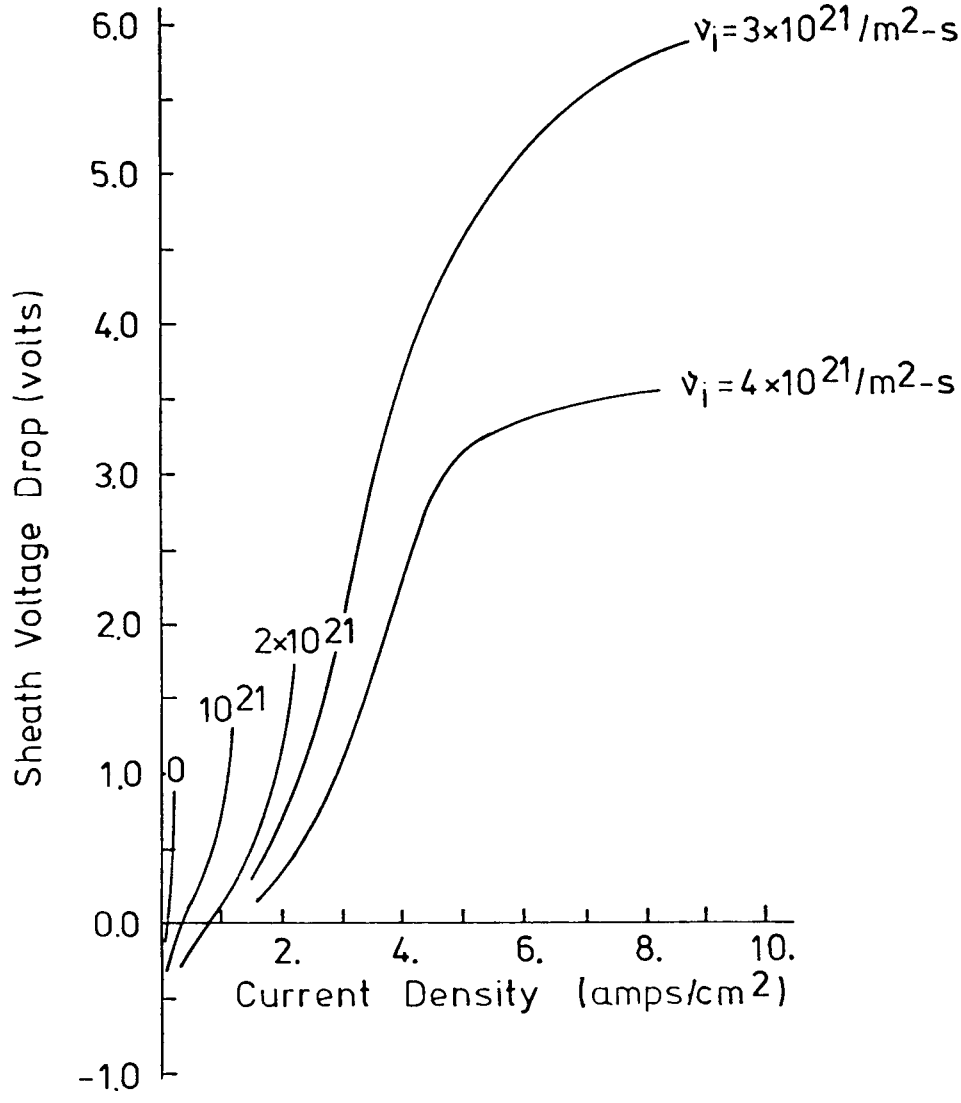

Figure F.14a. Voltage-current characteristics for sheath region for various levels of ion emission at the surface. Electrode is operating as an anode. Electron emission is zero; other conditions are specified in Table F.2.

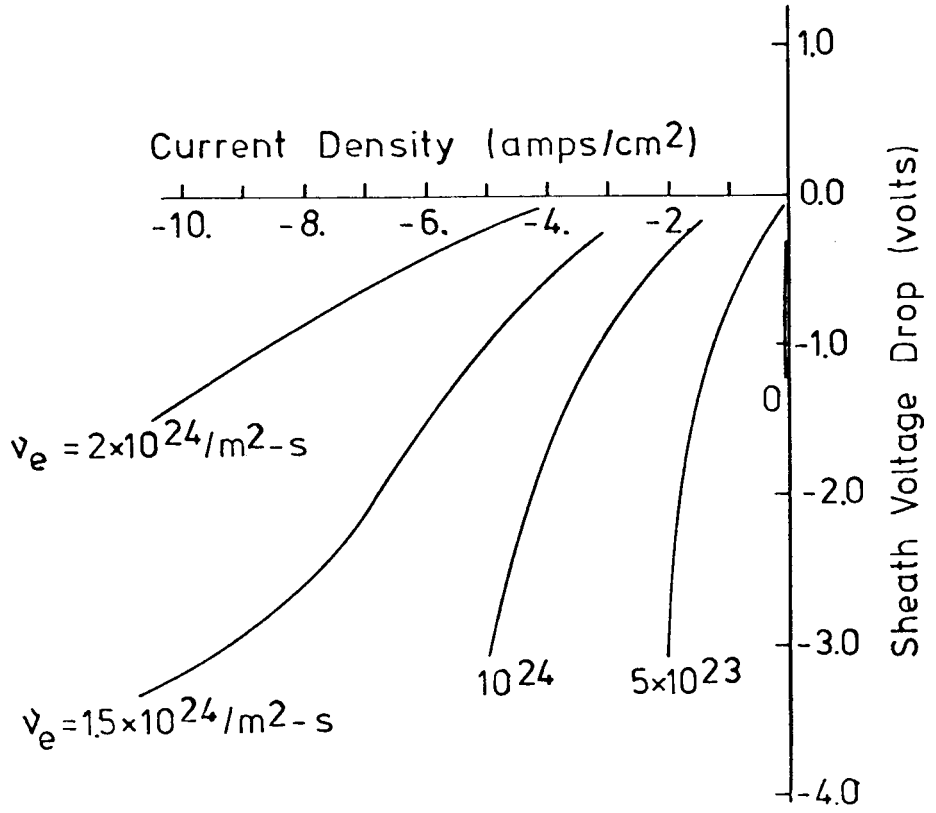

Figure F.14b. Voltage-current charactersitics for sheath region for various levels of electron emission at the surface. Electrode is operating as a cathode. Ion emission is zero; other conditions are specified in Table F.2.

and

$$J_{\substack{\text{saturation}\\ \text{cathode}\\ \text{electron emission}}} \sim J_{\substack{\text{saturation}\\ \text{cathode}\\ \text{no emission}}} \times \left(1 + \frac{\nu_e}{\Gamma_e}\right)$$

As can be observed above, increases in the cathode saturation current require significantly higher electron emission levels than the ion emission levels required for a significant increase in the anode saturation current density. For the conditions considered, ion emissions of $\sim 4 \times 10^{21}/m^2$-sec are required to raise the anode saturation current to a level of $\tilde{>} 5$ amps/cm^2. The lack of saturation in the anode voltage current curves for $\nu_i = 4 \times 10^{21}$ and 3×10^{21} results from changes in the outer solution due to the extremely high Joule heating. For the conditions considered, electron emission of $\sim 2 \times 10^{23}/m^2$-sec is required to prevent cathode saturation at current densities as high as 5 amps/cm^2. In the absence of saturation, voltage drops of less than ~ 6 volts are obtained for all current density levels.

Electron and ion emission at the electrode surface can result from several mechanisms. For electrons, thermionic emission, perhaps assisted by large electric fields at the electrode surface, might be expected to be the main mechanism for the non-arc mode. For some conditions, adsorbed layers of potassium on the electrode surface can lower the effective work function of the surface and dramatically increase the electron emission. Emission of positive ions of electrode material is likely to be low; however, for certain conditions adsorbed layers of potassium can result in significant ion emission from the surface. Theoretical modeling of adsorbed alkali-metals on transition metal electrodes has been developed by Levine and Gyftopoulos [39,40,41] and has been used with success by Koester for his cesium on tungsten situation in clean flow (not combustion products).

The model of Levine and Gyftopoulos predicts, for a particular substrate and absorbed specie combination, the electron and ion emission fluxes as a function of surface temperature, T_{wall}, and the fraction of the surface covered by the adsorbed layer. An atom balance at the surface is required to determine the fraction covered. The dependence of the emission fluxes, ν_e and ν_i, on the coverage fraction, θ, are shown in Fig. F.15a and F.15b for potassium on nickel and for several surface

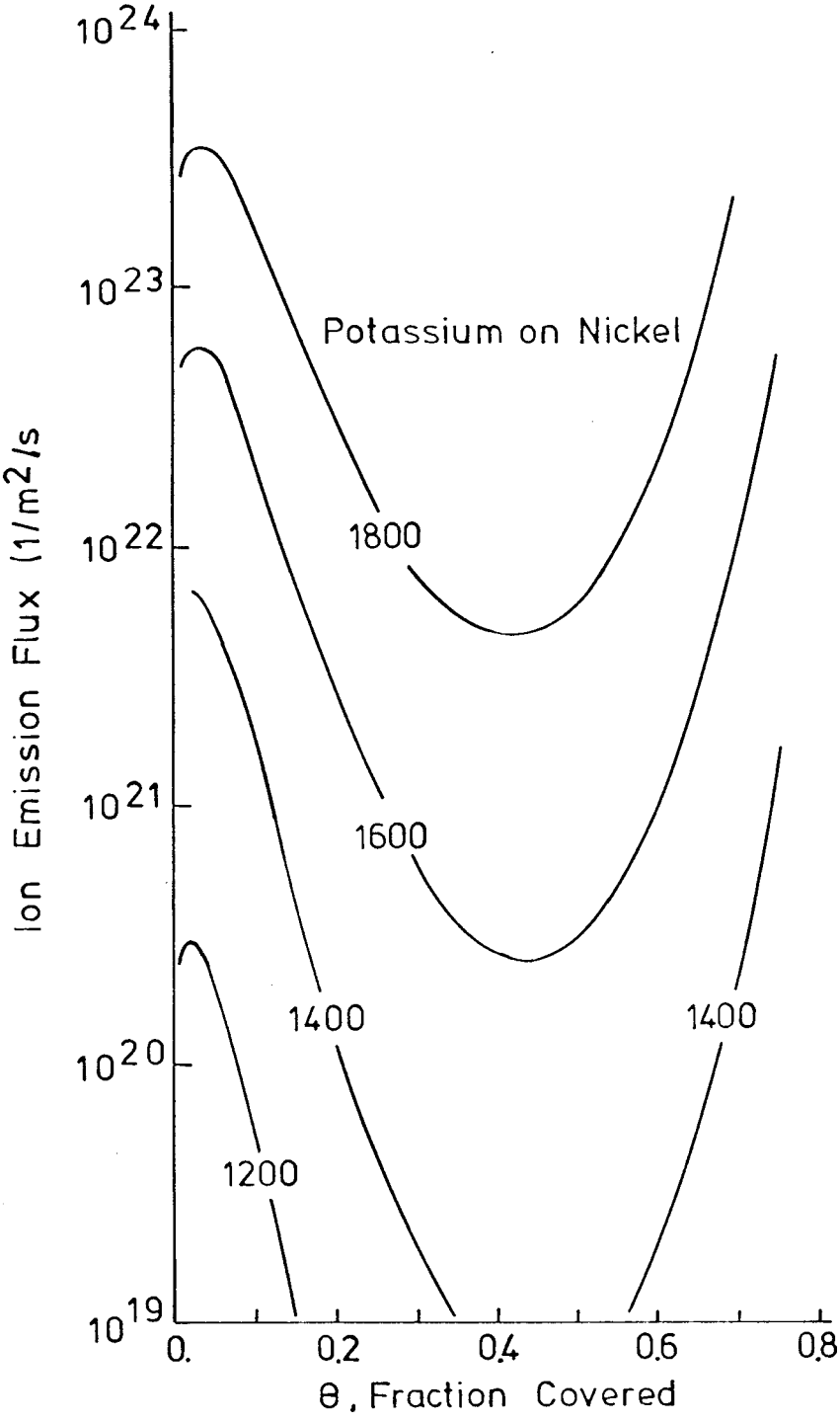

Figure F.15a. Plot of ion emission surface as a function of coverage fraction for Potassium adsorbed on pure nickel. Results for various temperatures are shown.

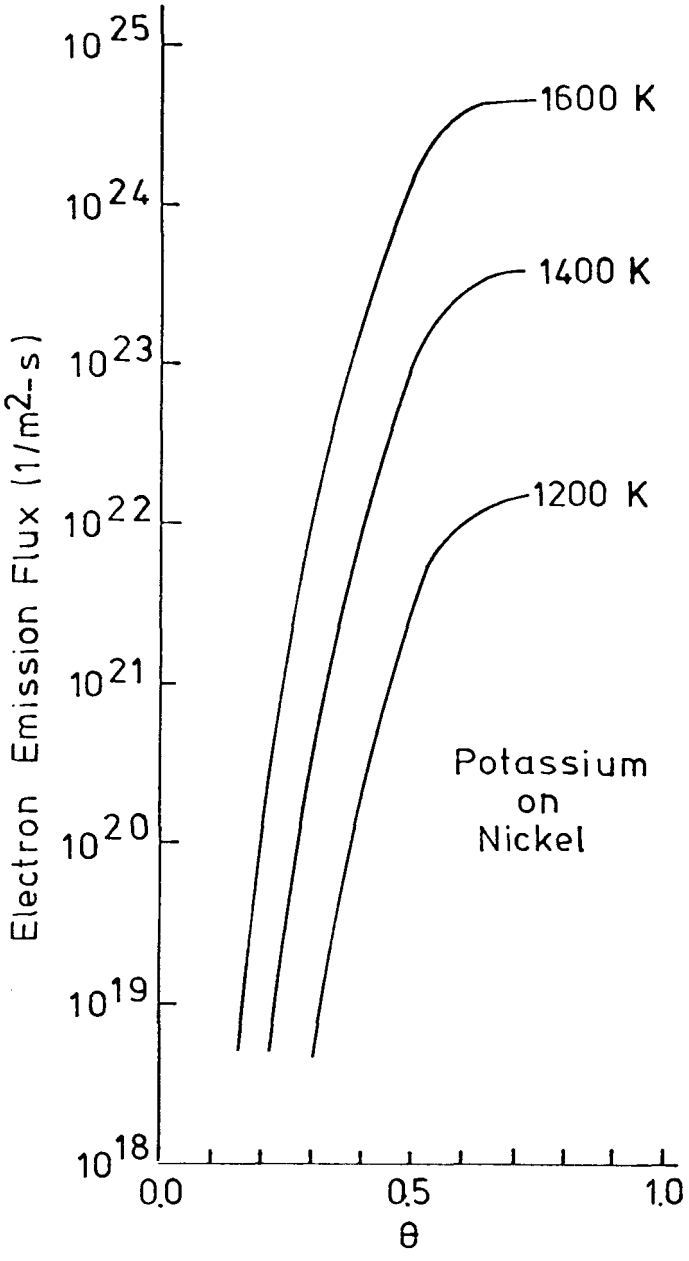

Figure F.15.b. Electron emission flux as a function of coverage fraction for potassium adsorbed on pure nickel. Results for various temperatures are shown.

temperatures. As can be observed in Fig. F.15a, the ion emission peaks at low coverage (< 10%) and is a minimum at $\theta \sim 50\%$. At low coverage, the effective work function is close to that of the bare metal. If the work function of the bare metal exceeds the ionization potential of the absorbed species, the majority of the potassium atoms desorbed from the surface will be stripped of an electron. For this case, a mass balance at the surface requires that the ion-emission flux be approximately equal to the rate of arrival of atoms. Electron emission increases from extremely low levels at low coverage to a peak level at $\theta \sim .6\text{-}.7$. As with ion emission, the electron-emission levels increase dramatically with surface temperature.

Although the surface physics theory is well developed and, with care, the atom balance for the surface could be performed, the characterization of the surface of the metal electrodes for MHD conditions is extremely difficult; characterization of a slagging wall surface is even more difficult. For stainless steel electrodes operating in the range of interest, a scale material forms over the surface. Post-test examination of the scale indicates that the material is slightly magnetic and probably contains a significant amount of ferrous-oxide. Chromic-oxide is also expected to form. The required physical constants are not available for either of these materials. Further, the presence of adsorbed oxygen on the surface can dramatically alter the characteristics, increasing ion emission and decreasing electron emission. Within the limitation of the above comments, an order-of-magnitude estimate of the atom-arrival rate for the conditions of Table F.3 is $\sim 10^{22}$ atoms/m^2-sec. This indicates that ion-emission rates of the order of $2\text{-}5 \times 10^{21}$ ions/m^2-sec, which are required to prevent saturation at an anode for the higher current densities (~ 10 A/cm^2), are quite possible. Observation of the anodes in the experiments revealed no evidence of arcing, even at the highest currents (until breakdown developed), generally confirming the analytical results; further work is obviously required if a full understanding of anode current transport is to be obtained. Examination of Fig. 15b indicates that sufficient electron emission to prevent saturation at current densities of ~ 10 A/cm^2 would be possible for a pure nickel electrode operating at a surface temperature $\gtrsim 1400$ K and at high coverage ($\sim 70\%$).

Cathode temperatures were typically less than ~ 1100 K, and arc spots were observed to form at the lowest current densities drawn in the experiments. Again, further work is required if a full understanding of the cathode current transport is to be obtained.

F.5 Limitations of Inner Solution

Setting aside for the moment the problems in characterizing the surface of the electrodes, it is important to consider the limitations of the model that has been used for the sheath region.

Electric Field at Surface

As indicated in the previous section, the electric field at the electrode surface can become quite high, especially if saturation is approached. A high surface electric field has several effects, the most notable of which are:

a) alteration of the emission characteristics,

b) acceleration of the particles leaving or approaching the surface.

The electric field alters the emission characteristics by effectively increasing or decreasing the energy required to eject a charged particle from the surface. Consider, for example, an anode approaching saturation such that a negative space charge exists in the vicinity of the electrode. The electric field for this situation tends to accelerate the + ions from the electrode surface, increasing the ion emission and delaying saturation. A similar effect would occur for the cathode, and the effect is referred to as field-induced emission. In the experiments of Koester, field-induced emission was responsible for as much as ~ 25% of the electron emission. Field-induced emission can be included in the surface physics model without serious difficulties.

If the electric field at the electrode surface is large enough that a significant fraction of the charged particles leaving the surface are accelerated to speeds close to or exceeding the thermal speed before collision, the simple description of the charged particles at the inner edge of the sheath may need to be improved. In particular, the particles accelerated from the electrode surface may cause ionization of a neutral atom, and this effect must be considered if the near electrode field becomes too

high. In addition, the high energies attained by charged particles traveling toward the electrode and the resulting highly energetic collisions with the surface may result in increased emission from the surface. For conditions of Table F.3 and for conditions in which saturation does not occur, the electric field at the inner edge of the sheath is $\lesssim .5 \times 10^6$ v/m for an anode operation at 10 amp/cm^2. If the electron-heavy gas collision frequency is used to evaluate the electron mean free path, the energy gain in crossing the Knudsen region $E\lambda_{mfp} \sim .5 \times 10^6$ v/m $\times .2 \times 10^{-6}$ m = .1 v, that is, about equal to the thermal energy at the inner edge of the sheath (with the electron and heavy gas temperatures equal). For lower current densities, the $E\lambda_{mfp}$ is somewhat smaller, while as saturation is approached the energy gained in crossing the Knudsen region could become extremely high. A more detailed evaluation of the energy distribution in the inner region would appear appropriate, especially if the behavior near saturation is to be studied.

Although the inner edge of the sheath region is expected to be the most severe in this respect, the concern about the energy gain between collisions applies not only to the inner edge of the sheath, but also to the outer portion of the sheath and to the outer region as well. Comparison of drift velocity with mean thermal speed for the outer region indicates that $u_d < .2\bar{C}_e$ for current densities as high as 10 amps/cm^2.

Prior to summarizing the results, it must again be stressed that the analysis of the inner region presented in this appendix is by no means a complete model, but rather an initial model to be used as a starting place for a more detailed analysis, and as such it is very useful.

F.6 Summary

In this appendix the near-electrode current transport characteristics have been discussed and a calculation procedure presented for a simple one-dimensional discharge configuration. Although many effects are considered in an extremely simple fashion, the model includes the effects of

- turbulent transport,
- finite electron ion reaction rates,
- electron-temperature non-equilibrium,
- space charge, and
- surface electron and ion emission.

The results demonstrate the importance of each of these effects. Results indicate that diffuse operation of anodes at current densities as high as 10 amps/cm^2 is possible, with sufficient ion emission provided by adsorbed potassium on the electrode surface; this result is in general agreement with experimental observations of anodes. For conditions where saturation does not result, the surface-sheath voltage drop is relatively small. The voltage-current characteristic for an anode with sufficient ion emission to prevent saturation at 10 amp/cm^2 is shown in Fig. F.16. The contributions of the various regions is indicated in the figure. For conditions of these calculations, the outer portion of the boundary layer ($y \gtrsim 1$ mm), where the electron number density is maintained close to the equilibrium level, accounts for roughly 2/3 of the total voltage drop. The remainder of the charge-neutral region, that is, the roughly reactionless region from $y \sim 1$ mm to the sheath edge, accounts for most of the remainder of the voltage drop at moderate current densities, with the voltage drop across the sheath becoming significant at higher current density levels. Although somewhat more difficult to assess, it would appear that sufficient electron emission to prevent saturation is not possible for the electrode surfaces and temperatures typical of the experiments; this is in general agreement with observation of cathodes, where arcs are observed at extremely low current densities. Although the results appear reasonable and generally agree with available data, detailed and direct comparison between experiment and theory is required to check this simple model and guide further development. Initial attempts at developing simplified calculation techniques for the outer region behavior are encouraging.

Collision-Dominated Sheath Equations

Although development of the equations for the collisional sheath model are presented elsewhere [38], details are included in this section for completeness and to establish the nomenclature used in the discussion. The equations employed for the sheath region (in dimensional form) are as follows:

Ion conservation:

$$\hat{u}\frac{\partial \hat{n}_i}{\partial \hat{x}} + \hat{v}\frac{\partial \hat{n}_i}{\partial \hat{y}} - \frac{\partial}{\partial \hat{y}}\left(\mu_i \hat{n}_i \frac{\partial \hat{\phi}}{\partial \hat{y}} + \frac{\mu_i k T_i}{e}\frac{\partial \hat{n}_i}{\partial \hat{y}}\right) = 0$$

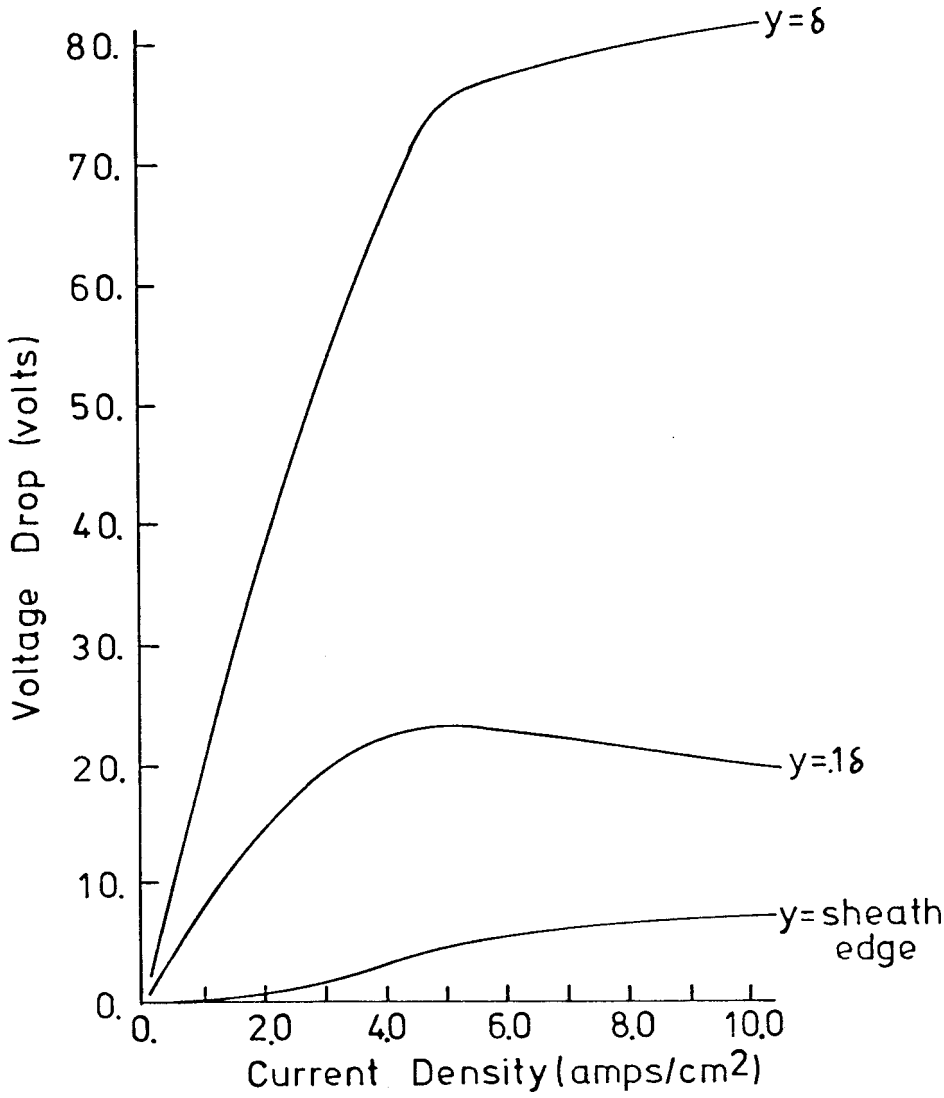

Figure F.16. Voltage drop in near-electrode region for anode operation without saturation. Conditions as specified in Table F.2. Electron emission flux = 0; ion emission flux = 2 x $10^{21}/m^2$ - sec.

Electron conservation:

$$\hat{u}\frac{\partial \hat{n}_e}{\partial \hat{x}} + v\frac{\partial \hat{n}_e}{\partial y} - \frac{\partial}{\partial \hat{y}}\left(-\mu_e \hat{n}_e \frac{\partial}{\partial \hat{y}} + \frac{\mu_e kT_e}{e}\frac{\partial \hat{n}_e}{\partial \hat{y}}\right) = 0 \quad .$$

Poisson's Equation:

$$\frac{\partial^2 \hat{\phi}}{\partial \hat{y}^2} = -\frac{n_i - n_e}{\varepsilon_o/e} \quad .$$

Einstein relations:

$$\mu_i = D_i e/kT_i \quad ; \qquad \mu_e = D_e e/kT_e \quad .$$

The quantities $\hat{u}$, $\hat{v}$, $\hat{n}_i$, $\hat{n}_e$, and $\hat{\phi}$ are non-dimensionalized as

$$u = \hat{u}/u_\infty \quad ; \qquad v = \hat{v}/u_\infty \quad ;$$

$$x = \hat{x}/L \quad ; \qquad y = \hat{y}/L \quad ;$$

$$n_e = \hat{n}_e/n_{e\infty} \quad ; \qquad n_i = \hat{n}_i/n_{e\infty} \quad ;$$

and

$$\phi = -\hat{\phi}/(kT_e/e)$$

where for convenience the $\hat{}$ has been used to denote the dimensional quantities, the ∞ denotes the free stream or outer properties, and L is a characteristic axial length scale. In terms of the non-dimensional quantities, the above equations become:

Ion conservation:

$$R\left(u\frac{\partial n_i}{\partial x} + v\frac{\partial n_i}{\partial y}\right) - \frac{\partial}{\partial y}\left(-n_i\frac{\partial \phi}{\partial y} + \varepsilon\frac{\partial n_i}{\partial y}\right) = 0 \qquad \text{(F.11a)}$$

Electron conservation:

$$\beta R\left(u\frac{\partial n_e}{\partial x} + v\frac{\partial n_e}{\partial y}\right) - \frac{\partial}{\partial y}\left(n_e\frac{\partial \phi}{\partial y} + \frac{\partial n_e}{\partial y}\right) = 0 \qquad \text{(F.11b)}$$

Poisson's equation:

$$\alpha^2 \frac{\partial^2 \phi}{\partial y^2} = n_i - n_e \qquad \text{(F.11c)}$$

where

$$\beta = \frac{D_i}{D_e} \frac{T_e}{T_i} ,$$

$$R = \frac{u_\infty L}{D_i} \frac{T_i}{T_e} ,$$

$$\varepsilon = \frac{T_i}{T_e} ,$$

and

$$\alpha^2 = \frac{\varepsilon_o k T_e}{n_{e\infty} e^2} \frac{1}{L^2} = \left(\frac{\lambda_{D\infty}}{L} \right)^2 .$$

Introducing the coordinate $\eta = R^{1/2} y$, where η is an order unity quantity, Eqns. (F.11a-c) become

$$\left\{ u \frac{\partial n_i}{\partial x} + R^{1/2} v \frac{\partial n_i}{\partial \eta} \right\} - \frac{\partial}{\partial \eta} \left\{ -n_i \frac{\partial \phi}{\partial \eta} + \varepsilon \frac{\partial n_i}{\partial \eta} \right\} = 0 \qquad \text{(F.12a)}$$

$$\beta \left\{ u \frac{\partial n_e}{\partial x} + R^{1/2} v \frac{\partial n_e}{\partial \eta} \right\} - \frac{\partial}{\partial \eta} \left\{ n_e \frac{\partial \phi}{\partial \eta} + \frac{\partial n_e}{\partial \eta} \right\} = 0 \qquad \text{(F.12b)}$$

$$R\alpha^2 \frac{\partial^2 \phi}{\partial \eta^2} = n_i - n_e . \qquad \text{(F.12c)}$$

The electron number density, n_e, is eliminated from the above equations, and the resulting equations are then re-scaled such that the inertia terms can be properly treated. Eliminating n_e from Eqn. (F.12b) using Eqn. (F.12c) and adding the result to Eqn. (F.12a), the following is obtained:

$$(1+\beta) \left\{ u \frac{\partial n_i}{\partial x} + R^{1/2} v \frac{\partial n_i}{\partial y} \right\} - \frac{\partial}{\partial \eta} \left\{ (1+\varepsilon) \frac{\partial n_i}{\partial \eta} \right\} = R\alpha^2 \left\{ \beta \left(u \frac{\partial^3}{\partial x \partial \eta^2} + R^{1/2} v \frac{\partial^3 \phi}{\partial \eta^3} \right) - \frac{\partial}{\partial \eta} \left(\frac{\partial \phi}{\partial \eta} \frac{\partial^2 \phi}{\partial \eta^2} + \frac{\partial^3 \phi}{\partial \eta^3} \right) \right\} \qquad \text{(F.13a)}$$

A second equation for the unknowns ϕ and n_i is obtained by multiplying Eqn. (F.12a) by β, subtracting it from Eqn. (F.12b), and again eliminating n_e using Eqn. (F.12c). Following the above procedure, the result obtained is

$$-\frac{\partial}{\partial\eta}\left\{(1+\beta)\, n_i \frac{\partial\phi}{\partial\eta} + (1-\beta\varepsilon)\frac{\partial n_i}{\partial\eta}\right\} = R\alpha^2\left\{\beta\left(u\frac{\partial^3\phi}{\partial x\partial\eta^2} + R^{1/2}v\frac{\partial^3\phi}{\partial\eta^3}\right) - \frac{\partial}{\partial\eta}\left(\frac{\partial\phi}{\partial\eta}\frac{\partial^2\phi}{\partial\eta^2} + \frac{\partial^3\phi}{\partial\eta^3}\right)\right\} \tag{F.13b}$$

Eqn. (F.13a) and (F.13b) are rescaled such that the new transver coordinate t is order unity at the edge of the sheath. Defining

$$\eta = (R\alpha^2/I)^{1/3}\, t - n_o/I \quad ,$$

$$n_i = (R\alpha^2 I^2)^{1/3}\, K(t) \quad ,$$

$$n_e = (R\alpha^2 I^2)^{1/3}\, G(t) \quad ,$$

where I and n_o are dimensionless quantities related to the boundary condition to be defined later, Eqns. (F.13a,b) become

$$(1-\beta)\frac{\partial}{\partial t}K\frac{\partial\phi}{\partial t} + (1-\beta\varepsilon)\frac{\partial^2 K}{\partial t^2} = -\frac{(\alpha^2 R)^{1/3}}{I^{4/3}}R\alpha^2\left\{\text{r.h.s. of (F.13b)}\right\} \tag{F.14a}$$

and

$$(1+\varepsilon)\frac{\partial^2 K}{\partial t^2} = (1+\beta)\left(\frac{R\alpha^2}{I}\right)^{2/3}\left\{u\frac{\partial K}{\partial x} + vR^{1/2}\left(\frac{I}{R\alpha^2}\right)^{1/3}\frac{\partial K}{\partial t}\right\} - \frac{(\alpha^2 R)^{1/3}}{I^{4/3}}\frac{R\alpha^2}{I}\left\{\text{r.h.s. of (F.13b)}\right\} \tag{F.14b}$$

with

$$\frac{(\alpha^2 R)^{1/3}}{I^{4/3}}R\alpha^2\left\{\text{r.h.s.}\right\} = \frac{\partial}{\partial t}\left(\frac{\partial\phi}{\partial t}\frac{\partial^2\phi}{\partial t^3}\right) - \beta\left(\frac{\alpha^2 R}{I}\right)^{2/3}\left\{u\frac{\partial^3\phi}{\partial x\partial t^2} + R^{1/2}v\left(\frac{I}{R\alpha^2}\right)^{1/3}\frac{\partial K}{\partial t}\right\} \tag{F.14c}$$

Neglecting terms of order $(\alpha^2 R/I)^{2/3}$ in Eqns. (F.14a-c), the final differential equations for the sheath region obtained are

$$(1+\beta)\frac{d}{dt}K\frac{d\phi}{dt} + (1-\varepsilon\beta)\frac{d^2K}{dt^2} = \frac{d}{dt}\left(\frac{d\phi}{dt}\frac{d^2\phi}{dt^2} + \frac{d^3\phi}{dt^3}\right) \qquad \text{(F.15a)}$$

and

$$(1+\varepsilon)\frac{d^2K}{dt^2} = \frac{d}{dt}\left(\frac{d\phi}{dt}\frac{d^2\phi}{dt^2} + \frac{d^3\phi}{dt^3}\right) . \qquad \text{(F.15b)}$$

Equation (F.15b) is integrated twice to obtain

$$(1+\varepsilon)K = \frac{1}{2}\left(\frac{d\phi}{dt}\right)^2 + \frac{d^2\phi}{dt^2} + C_1(t+C_2) . \qquad \text{(F.16)}$$

The boundary condition imposed on the outer edge is that the number densities n_e and n_i approach the ambipolar number density η as $t \to \infty$. The a mbipolar solution is represented as

$$\hat{n}_i = \hat{n}_e = \hat{n}_o + \frac{d\hat{n}_o}{d\hat{y}}\hat{y} ,$$

where $\left.\frac{d\hat{n}}{d\hat{y}}\right|_{\text{sheath edge}}$ and $\hat{n}_o$ are defined from the ambipolar solution where the sheath edge is defined as the point where $(\hat{n}_e-\hat{n}_i)/\hat{n}_i$ is estimated to be 10%. In the non-dimensional coordinates, the boundary condition is

$$K \to t \quad \text{as} \quad t \to \infty .$$

The outer solution also specifies the potential to which the sheath solution must asymptote as for the one-dimensional discharge:

$$J_t = \text{constant} = e\hat{n}_e\mu_e\left(1+\frac{\mu_i}{\mu_e}\right)\frac{d\hat{\phi}}{d\hat{y}} + \mu_e kT_e\frac{d\hat{n}_e}{d\hat{y}} - \mu_i kT_i\frac{d\hat{n}_i}{d\hat{y}} .$$

Non-dimensionalizing the equation and solving for the non-dimensional potential gradient, the following is obtained:

$$\frac{d\phi}{dt} \to \left(\frac{J_t L}{n_{e\infty}D_e(1+\beta)eR^{1/2}I} - \frac{(1-\beta\varepsilon)}{1+\beta}\right)\frac{1}{K} \quad \text{as} \quad t \to \infty$$

The constants C_1 and C_2 in Eqn. (F.13) are determined using the boundary conditions resulting in

$$(1+\varepsilon)(K-t) = \frac{1}{2}\left(\frac{d\phi}{dt}\right)^2 + \frac{d^2\phi}{dt^2} \quad . \tag{F.17a}$$

Combining Eqns. (F.12a) and (F.12b) and integrating once, a second equation for K and ϕ is obtained.

$$\varepsilon \frac{dK}{dt} = K \frac{d\phi}{dt} + \frac{(1+\varepsilon)}{(1+\beta)} - Q \quad , \tag{F.17b}$$

where

$$Q = \frac{J_t L}{n_{e\infty} D_e (1+\beta) e\, R^{1/2} I} \quad . \tag{F.17c}$$

Proceeding now to eliminate K in favor of ϕ and its derivaties, Eqns. (F.14a-c) become, after some manipulation,

$$\varepsilon \frac{d^3\phi}{dt^3} - t(1+\varepsilon) \frac{d\phi}{dt} + (\varepsilon-1) \frac{d^2\phi}{dt^2} \frac{d\phi}{dt} - \frac{1}{2}\left(\frac{d\phi}{dt}\right)^3 = (1+\varepsilon)X \tag{F.18a}$$

where

$$X = \left(\frac{1-\varepsilon\beta}{1+\beta} - Q\right) \quad . \tag{F.18b}$$

The inner-edge boundary conditions can be expressed as

$$K(t) = K_w \quad \text{at} \quad t_w \quad ,$$

$$G(t) = G_w \quad \text{at} \quad t_w \quad .$$

Introducing the quantity

$$w = \frac{d\phi}{dt} \quad ,$$

Eqn. (F.15a) becomes

$$\varepsilon \frac{d^2w}{dt^2} - t(1+\varepsilon)\, w - (\varepsilon-1)\, w \frac{dw}{dt} - \frac{1}{2} w^3 = -(1+\varepsilon)X \tag{F.19a}$$

and the boundary conditions can be expressed as

$$\left.\frac{dw}{dt}\right|_{t=t_w} = G_w - K_w \equiv B \tag{F.19b}$$

$$W^2\Big|_{t=t_w} = 2(\varepsilon K_w + G_w) - 2t_w(1+\varepsilon) \tag{F.19c}$$

and

$$W \to \frac{X}{t} \quad \text{as} \quad t \to \infty \quad . \tag{F.19d}$$

The equation (F.19a) can be solved for W and the number density profiles, potential distribution and overall sheath potential drop can be calculated from W as

$$\hat{n}_i = n_{e\infty}\left(\frac{\lambda D_\infty}{n_{e\infty}}\frac{d\hat{n}}{d\hat{y}}\right)^{2/3}\left(t + \frac{W^2}{2(1+\varepsilon)} - \frac{1}{(1+\varepsilon)}\frac{dw}{dt}\right) ,$$

$$\hat{n}_e = n_{e\infty}\left(\frac{\lambda D_\infty}{n_{e\infty}}\frac{d\hat{n}}{d\hat{y}}\right)^{2/3}\left(t + \frac{W^2}{2(1+\varepsilon)} + \frac{1}{(1+\varepsilon)}\frac{dw}{dt}\right) ,$$

$$t = \left(\frac{d\hat{n}}{d\hat{y}}\frac{1}{n_{e\infty}\lambda_{D\infty}^2}\right)^{1/3}\left(\hat{y} + \frac{\hat{n}_o}{d\hat{n}/d\hat{y}}\right) ,$$

and

$$\Delta\hat{\phi} = \frac{kT_e}{e}\int_{t_w}^{t_{\substack{\text{sheath}\\\text{edge}}}} w\, dt \quad .$$

APPENDIX G
OPTICAL ACCESS

A schematic of the design developed for providing optical access to various portions of the channel for clean fuel operation is shown in Fig. G.1. The precise geometry of the window assembly is dictated by size and location of the port and by space requirements exterior to the channel; however, the overall design was similar for the top view and side view access ports. The window, usually clear quartz, is mounted back from the flow and is purged by a stream of clean nitrogen. The purge serves to provide a thin layer of protective gas over the entire window surface and to keep the port clear of absorbing species and condensible materials. The purge flow rate is kept low, at least less than ~ 1% of the total channel flowrate, and the purge inlet is designed to give a uniform and, if possible, laminar flow of gas. The purge inlet operates essentially as a diffuser, so considerations of stall are of special importance. Design of the port size and flow direction of the purge is important and should result in the purge gas mixing easily into the main flow as it exits the port region, rather than promoting the formation of eddies in the port area; beveling of the edge downstream of the port, as shown in the schematic, is helpful in this respect. A metal shutter is provided to give additional protection for the window when the window is not in use, especially during preheat and postheat stages, when water condensation is a more severe problem. It is also desirable that the window operate warm, as this reduces the problem of water and, to a lesser extent, seed condensation. Finally, it is important that the port be designed such that the window can be easily cleaned between experiments.

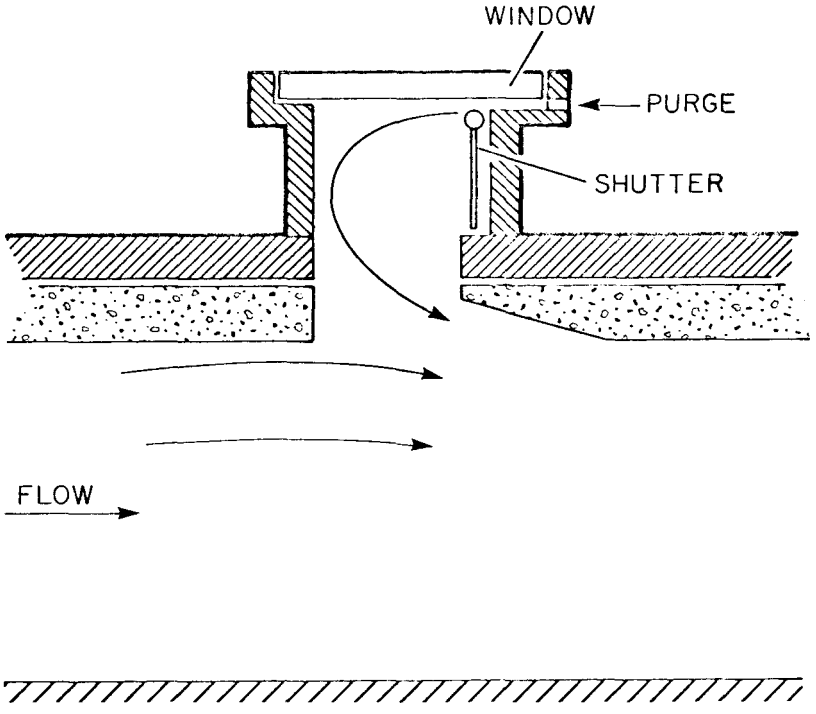

Figure G.1. A schematic of the design development for providing optical access to the channel for clean fuel operation.

APPENDIX H

HIGH TEMPERATURE GASDYNAMICS LABORATORY MHD TEST FACILITY GENERAL SYSTEM DESCRIPTION

by Marion K. Jenkins

The High Temperature Gasdynamics Laboratory MHD Test Facility has the following major parts:

1. OPERATING CONSOLE AND CONTROL PANEL
2. MHD CHANNEL (INCLUDING COMBUSTOR)
3. EXHAUST SYSTEM
4. MAGNET
5. DIAGNOSTICS AND INSTRUMENTATION
6. DATA ACQUISITION HARDWARE AND SOFTWARE

General system descriptions of the MHD system, at least as it existed in the past, are contained in the theses of Reseck [14], Kessler [40], and Rubin [15].

H.1 Operation Console and Control Panel

The control panel and operating console allow the operator to monitor the operation of the experiment from a room adjacent to the test bay itself. In this control room is contained the data acquisition system and most of the data collection equipment. It is necessary for someone to enter the test bay only to attend to special diagnostic equipment or to examine the condition of the channel or cooling water lines. Most functions pertaining to the experiment are performed in the control room.

Communication between the control room and the test bay and among the many test personnel is made possible with a 3-channel intercom system. Aircraft type headsets with boom microphones allow the various personnel to communicate and coordinate activities. All voice communications are recorded on cassette tapes for critical event documentation and for later review if necessary. The control panel also contains a digital run time clock and run number display so that all personnel in the control room can know the state of the experiment by checking the run number display and run time with the predetermined run plan. A second run number display is located in the test bay.

The control panel contains all necessary equipment to monitor and control the reactant flowrates to the combustor. The panel also contains a fuel selection valve making it possible to switch fuels while maintaining a given stoichiometry. Fuels used are ethanol, RP-1, propane, and a pulverized coal-ethanol slurry (up to 40% by weight coal). Pure gaseous oxygen is used as a oxidant and gaseous nitrogen is used as a diluent to vary the flame temperature within the combustor. Ethanol is stored in underground tanks and may be used directly, or pumped into 55 gallon drums and mixed with KOH pellets which supply the "seed" material. Different types of pulverized coal may be added to the alcohol to form a slurry for coal slag experiments. Several drums of seeded alcohol or coal slurry (with or without seed) may be used in a single run. Oxygen and nitrogen are stored as gases in storage tanks at a maximum pressure of 2200 psi. The reactants are monitored by standard rotameters and swirlmeters and flowrates can be adjusted manually during the experiment to match predetermined run conditions. Bourdon-type pressure gauges on the control panel measure oxygen and nitrogen supply pressures and combustor nozzle pressure.

At nominal run conditions of a total reactant flowrate of .5 lbm/sec. stoichiometric combustion, diluent/oxidant mass ratio of .5, there is sufficient oxygen and nitrogen to run for approximately 3.5 hours. Assuming running with strictly seeded fuel, an experiment of this duration would require about 4.5 55 gallon drums of seeded fuel.

Also present on the control panel is the necessary safety circuitry to signal hazardous operating conditions. A flame viewer senses the presence of a flame in the combustor by ultra-violet detection. If the flame goes out the oxygen and fuel control valves are automatically closed and a nitrogen purge begun. This is done to prevent any unburned fuel and oxidant mixture which may be present in the channel from being reignited by the hot ceramic liner of the channel. Other conditions which cause automatic shutdown and a warning signal to appear on the control panel are: plenum overpressure, indicating a possible flow obstruction in the channel; plenum underpressure, indicating a hole in the plenum or channel wall; cooling water inlet underpressure, indicating loss of cooling water. The plenum overpressure is adjustable and is checked before each experiment. A panic switch located on the control panel, and another

in the test bay, allow immediate manual shutdown by any of the test personnel in the event of dangerous conditions. Safety considerations prevent personnel from being in the test bay during major changes in run conditions, such as startup, shutdown, and transition between principal run and preheat or postheat phases of the experiment.

Cooling water and channel pressure gauges also alert the operator to other conditions of the channel. Static pressure taps located at various places within the channel are connected to gauges on the control panel for monitoring. Cooling water inlet manifold pressure gauges on the control panel provide a check on coolant water flowrates. These rarely change during a test or from one test to another, but are routinely monitored as a precautionary measure and also for later heat loss calculations.

Electrode circuitry comprises a major portion of the control panel. This consists of 13 identical circuits for selecting and monitoring the loads and augmentation voltage to 13 pairs of electrodes. Switching these circuits on and off can be done remotely although load selection and battery selection is manual. Silicon controlled rectifier (SCR) circuitry allows 6 electrode circuits to be switched on or off at precisely controlled times (30 μsec).

A large patch panel allows switching to several different generator configurations during an experiment. It is possible to operate a channel in segmented Faraday, continuous Faraday, diagonal Faraday, and segmented Hall configuration. By means of a large knife switch, it is also possible to reverse the direction of magnetic field, which reverses the current flow within the generator. In addition, 13 banks each consisting of 10 12 volt automobile batteries allow augmentation of current to levels otherwise not achievable to study certain phenomena at high current densities, such as arcing and breakdown and MHD boundary layer studies. This also can be used to study current behavior in the channel without utilizing the magnet at all.

Each electrode circuit contains its own voltmeter and ammeter, the range and polarity of which may be selected at the control panel. These are also scanned by the Vidar (data acquisition system) but constant monitoring is necessary to avoid excessive breakdown damage to the channel during high current runs. Each electrode circuit has a 12-position

resistance selector switch to choose the desired load resistance for that particular circuit. Resistance values from 1.7 ohms to 411 ohms can be selected, plus open and short circuit cases. The electrode circuits are rated at 60 amps. Opening the resistance selector switch on the panel opens a larger contacter switch behind the panel which actually breaks the circuit. Closing the control panel switch after selecting the desired resistance then closes the contacter switch and completes the circuit.

Nine additional electrode circuits are available for the M-8 channel, which as 22 pairs of electrodes. These nine circuits can only operate in open circuit or short circuit mode, or with a load of 7 ohms. The patch panel for these additional 9 electrodes is similar to the other 13. However, there are no voltmeters on the control panel for these additional 9 electrodes.

Electrode circuit meters and reactant pressures are also scanned by the data acquisition system. Redundancy, where it exists, is useful for cross-checking and trouble-shooting and allows the computer to be free for certain types of on-line data reduction.

It is sometimes desirable to conduct an experiment without utilizing the magnet. For example, slag layer fluid mechanics have been investigated without any electrical effects present. Slag layer electrical behavior has been investigated without utilizing the magnet by using external current supplies. These experiments not utilizing the magnet are run in what is usually referred to as the slag test bay. Experiments utilizing the magnet are conducted in what is usually referred to as the magnet test bay. Both the magnet and slag test bays are physically located in the same room, and each has circuitry to the control room patch panel and reactant supply and exhaust system connections, making each test bay relatively independent. This minimizes time between experiments and allows more efficient scheduling of tests.

H.2 MHD Channel

The "MHD Channel" here referred to is defined as the entire assembly of combustor, plenum, test section(s), and transfer section or diffuser. These components can be arranged to fit the needs of a particular experiment. Many times the needs of a particular experiment dictate that a special test

section be placed upstream or downstream of the magnet where the main test section is located. Other times, (e.g. flow nonuniformities, slag layer tests, etc.) the magnet may be bypassed entirely and the test section contain no current-carrying electrodes at all. It is also possible to use a special upstream or downstream test section to provide optical access to the test section actually containing the electrodes. These have been used, for example, to study MHD boundary layers, plasma fluctuations, electrode-insulator behavior, and Hall-field breakdown.

Usually the channel assembly--combustor, plenum, test section and diffuser are assembled in the buildup area and handled as a single unit. The channel is usually pressurized and leak checked, and checked electrically. It is then transported to the test bay as a single unit and installed in the magnet. After electrode and cooling lines are attached it is usually checked again for shorting out of channel parts to instrumentation leads.

There are two combustor-plenum assemblies currently in use in the HTGL. They are designated the M-2 and M-8, corresponding to the nominal input of 2 and 8 thermal megawatts, respectively. Each combustor has its own plenum and independent reactant, cooling and instrumentation hookups, which minimizes time between different experiments. There are also two main channels used for power generation experiments, also designated the M-2 and M-8 channels, depending on which combustor they were designed to operate with. Other smaller test sections may be run in conjunction with or instead of one of these power generation channels. In this way it is sometimes possible to obtain several different types of data from a single experiment. With the exception of dissimilarities in combustor-plenum assemblies and particular test sections being used, the two channels are similar enough that the term MHD channel used in the context of this document may well refer to either one.

The M-2 combustor is a cylindrical double-walled stainless steel shell with MgO liner. The inside diameter without MgO liner is 8.9 cm (3.5 in) and its length in the flow direction is 33 cm (13.5 in). It is designed to run with a maximum flow rate of .32 kg/sec (.71 lbm/sec) and a maximum pressure of 4 atm. The upstream end of the combustor is a plate containing the fuel nozzle, igniter, UV radiation detecting flame viewer, and a pressure tap. Connected to this plate is a swirl-type oxygen manifold with

four slots of approximately 5 cm (2 in) length for tangential injection of of oxygen to the combustor. Near the downstream end of the combustor is an external nitrogen manifold which supplies gaseous nitrogen in a tangential direction that partially cancels the swirl induced by the injection of the oxygen.

The M-2 plenum is basically a double-walled stainless steel box lined with MgO brick. The purpose of the plenum is to allow more time for the completion of the combustion process, smooth out some flow nonuniformities, and hold the nozzle which accelerates the flow prior to its entry into the test section. The approximate size of the M-2 plenum with brick in place is 23 cm high by 16.5 cm wide by 44.5 cm long in the flow direction (9 in x 6.5 in x 17.5 in). The plenum can be separated into upstream and downstream halves for refurbishment of the brick liner, which usually lasts several tests. The nozzle is also normally made of MgO brick and requires replacement more often than the main part of the plenum brick. The maximum design temperature for the plenum is 3000 K (5400R).

The M-2 channel is a linear channel with 13 pairs of segmented electrodes with a 3.81 cm (1.5 in) pitch. When bricked in its usual fashion the flow area is 3.18 cm x 10.16 cm (1.5 in x 4 in). Electrode length in the flow direction is normally 1.9 cm (.75 in). Maximum values of electrical parameters are: open circuit voltage = 250 volts, short circuit current density = 2.1 amps/cm^2, axial Hall voltage = 800 volts. Design exit Mach number is .9.

The M-8 combustor is basically a scale-up of the M-2 combustor. It is a 12.7 cm (5 in) by 30.5 cm (12 in) long cylindrical double-walled water cooled chamber lined with MgO brick. It is designed to run satisfactorily at a flow rate of .91 kg/sec (2 lbm/sec) at a maximum pressure of 6 atm. The approximate maximum flame temperature is 3400 K (6120R). Fuel is injected in a conical spray at the upstream end, and oxygen is injected tangentially. Nitrogen is injected tangentially at the downstream end in a direction opposite to the oxygen injection.

The M-8 plenum is cylindrical and is basically a double walled stainless steel tube lined with MgO brick. The inside dimensions without brick are 30.5 cm (12 in) diameter and 62 cm (24 in) in length. The brick liner is typically 3 to 5 cm thick (1 to 2 in).

The M-8 channel is a constant Mach number channel having 22 pairs

of segmented electrodes with a spacing of 3 cm (1.2 in). It has a special nozzle section available for operating supersonically. The flow area is 4.6 cm x 9 cm (1.8 in x 3.5 in) at the inlet and 6.4 cm x 9 cm (2.5 in x 3.5 in) at the exit with an exit Mach number of 1.9. Electrode length in the flow direction is 2.2 cm (.87 in). Maximum values of electrical parameters are: open circuit voltage = 380 volts, short circuit current density = 3.6 amps/cm^2, axial Hall voltage = 1600 volts.

After the combustion gases flow from the plenum through the actual test section there is usually some sort of diffuser or transfer section. The design of this component is dictated by the needs of a particular experiment, and may range from a water-cooled double-walled stainless steel duct with ceramic liner to an uncooled transite box with holes cut into the sides to allow for optical access or sampling probe sweep clearance. The flow then passes to a horizontal transfer tube in which the flow is usually quenched. This tube conducts the gas from the exit of the MHD channel to the exhaust system.

H.3 Exhaust System

The flow enters the exhaust system horizontally and is deflected upwards through a counterflow water quenching spray. It then enters a .77 M (2.5 ft) deep packed tower containing 5 cm dia. (2 in) ceramic saddles. A second counterflow water quenching spray forced down through the packed tower causes the flow to give up its particulate load (seed and ash particles) by impaction. The water which is not flashed to steam is drained at the bottom of the tower at a rate of about 50 gpm. A roof blower-smokestack assembly conducts the cleaned and cooled exhaust into the atmosphere.

In the near future it is planned to install an Air Pollution Systems Scrub-E electrostatic scrubber system. After the exhaust leaves the packed tower it will flow through a pre-ionizer, which will induce an electrostatic charge on the particles into a wet venturi which will provide water droplets to which the charged particles will attach themselves, and then into a centrifugal spearator where the water droplets containing the particles will be removed. The cleaned gas will then pass to the roof blower and stack.

H.4 Magnet

The magnet used in linear generator experiments is a conventional iron-core saddle-coil magnet with water-cooled copper conductor. This magnet can produce a fairly uniform magnetic induction of 2.7 tesla with a gap size of about 10 cm (4 in) and a magnet excitation current of 1150 amps. The magnetic field is fairly constant over the entire length of the 13 electrodes of the M-2 channel. The magnet is H-shaped; one half of the magnet is movable hydraulically on two lubricated ways. This movement is necessary in order to install the MHD channel within the magnet. Several mild steel spacers are available for cases when the channel size or optical access does not allow the magnet to be fully closed. The nominal cooling water requirement for the magnet is 30 gpm at 1150 amp excitation current. Filtered drinking water stored in a 1000 gal storage tank is pumped through the magnet for cooling. This allows about 1.25 hours of continuous magnet operation. The magnet power is supplied by four series connected banks of d.c. arc welder rectifiers, each bank consisting of three rectifiers connected in parallel. Each rectifier is rated at 1000 amps at 40 volts.

The magnet is regulated manually from its own control panel located in the main control room adjacent to the test bay. The magnet control panel contains excitation current controls and ammeter, cooling water pump control and water storage tank level indicator. Safety circuitry automatically shuts off the magnet current for magnet overcurrent, or excessive magnet temperature, or loss of coolant water.

H.5 Diagnostics and Instrumentation

Diagnostic techniques offer perhaps the greatest challenge of experimental work in MHD. High temperatures and the presence of corrosive seed materials and coal slag particles make conventional sampling using probes (such as hot wires, stagnation probes, etc.) very difficult. In addition, the presence of electric and magnetic fields dictates that a good deal of shielding of instrumentation is necessary. The physical limitations because of channel cooling and electrical connections, as well as the presence of the magnet, allow only very limited access to the channel. Various optical windows and probe access ports have been designed, with complicated purging necessary to maintain a clear path.

Diagnostics depend a great deal on the objectives of a particular experiment. However, many experiments have common needs in measuring such things as plasma and channel component temperatures, plasma and reactant static pressures, reactant flow rates, and electrode currents and voltages. These may be called basic instrumentation, and use more or less standard techniques, modified somewhat for the MHD environment.

Measurement of channel component temperature and heat loss rates are usually made with standard thermocouples. Copper-constantan thermocouples connected differentially are used to determine channel heat loss rates. Chromel-alumel thermocouples are used in stainless steel and ceramic parts which are subjected to high operating temperatures. High common mode voltages present on electrode thermocouples are eliminated by optically coupled amplifiers, allowing the actual thermocouple signal to be measured. Plasma-side wall temperatures can sometimes be obtained by optical pryometry where optical access is possible. Reactant static pressures and plasma static pressures at various channel locations are displayed on the control panel on bourdon-type pressure gauges. Temperature corrected measurements of the oxygen and nitrogen supply static pressures are also measured using pressure transducers and are used to update reactant flowrates during the experiment. Reactant flowrates are monitored on standard rotameters and swirlmeters, which are displayed on the operating console. Electrode voltages and currents are monitored using conventional voltmeters and current shunts within each electrode circuit, and are also scanned by the computer data acquisition system. Electrical behavior within the plasma is obtained with sidewall mounted voltage probes.

More advanced diagnostic methods have been investigated and are continuously being improved as more experience is gained in the hostile environment of a combustion MHD plasma. These advanced diagnostics may be differentiated from basic instrumentation discussed above as varying widely from one experiment to another, and usually requiring elaborate hardware and software for signal conditioning and data reduction. Phenomena which may be included in this category are measurements of core or boundary layer electrical conductivity, electron number density, gas temperatures, velocities, and pressures, as well as high frequency fluctuations of temperature, velocity, and pressure. Some items confined almost exclusively

to coal-fired experiments are determination slag layer thickness, velocity, and build-up rate, slag layer and core gas chemical composition, and particle size distribution and chemical composition.

Most of these items will not be considered in detail here; indeed the solution to some of these problems has been and is the basis for a major portion of several students' theses. An interesting and rather thorough review of the present state of the art as well as brief explanations of various advanced diagnostics techniques is found in Self and Kruger, "Diagnostic Methods in Combustion MHD Flows", Journal of Energy, Vol. 1, No. 1, 1977, pp 25-43. More detailed information is contained in various reports and theses, most of which are referenced by Self and Kruger.

Plasma electrical conductivity may be measured with a four-pin conductivity probe, either mounted in the channel wall or swept through the plasma stream. Inductive coil (RF) probes have also been used to obtain conductivity data. Electrical conductivity can also be deduced from electron number density data. Electron number densities have been measured using langmuir probes, swept through the plasma. Studies are now under way using emission spectroscopy of high-lying sodium lines to determine the electron number density.

Sodium line reversal techniques are being developed for determination of plasma temperature. Gas temperature fluctuations have been measured using simple photodiode radiation emission sensors. Laser-Doppler velocimetry (LDV) can be used to measure velocity profiles, and is capable of scanning into the boundary layer very close to the wall. It can also be used to measure the turbulence intensity of the plasma. High frequency pressure fluctuations associated with magnetoacoustic instabilities are obtained with pressure transducers placed in the channel wall, and recorded on a seven channel tape recorder, or digitized on-line with an A/D converter and stored on magnetic tape.

Optical techniques are being developed to measure coal slag layer behavior. Current work in this area is on measurement of slag layer thickness, temperature, velocity, and growth rate. Other techniques are being evaluated to determine the slag particle size within the plasma itself. Various sampling techniques are being investigated to determine particle size and chemical composition, as well as core gas chemical composition

and slag layer chemical composition. Current methods being evaluated for slag layer composition studies include scanning electron microscopy, electron beam microprobe and X-ray diffraction maps of cross section of frozen slag layers, all of which are done after an experiment. Slag layer fluid mechanics behavior, as well as electrode behavior such as arcing and breakdown, can be recorded by cinephotography.

H.6 Data Acquisition Hardware and Software

The digital data acquisition system is built around an HP-2100 minicomputer, a Vidar model 610 low level scanner and model 520 integrating digital voltmeter (IDVM), and a Preston model GMAD-1 16-channel analog to digital converter. An eight channel strip chart recorder is used to record data with long-term fluctuations. This is also used to take routine thermal data to free the computer for on-line data reduction, and is useful to quickly see the time-dependent behavior of slowly varying parameters. Other strip chart recorders and high speed oscillographs are used as well as oscilloscopes. A seven channel tape recorder (FM modulation) is also available for recording d.c. or fluctuating (up to 10 kHz) data. Slag layer phenomena and arcing behavior are recorded in cine cameras. This system provides flexibility and speed in monitoring, recording, and reducing experimental data. Unless otherwise indicated, the term HP-Vidar system will refer to the HP-2100 and Vidar scanner and IDVM as a single unit. Communications and input for the computer during an experiment is usually on an infoton CRT terminal, which is referred to as the system console.

The HP 2100 has a 32K word memory, with disc drive, paper tape punch and reader, Versatec electrographic printer (500 lines/minute), and HP 1600 BPI 9 track magnetic tape drive unit. The Preston analog to digital converter has a maximum sampling rate of 500 kHz. The Vidar 610 scanner has a maximum scan rate of 40 channels per second, and has random access capability. The model 520 IDVM has both manual and computer-controlled range, function, and resolution selection. The HP-Vidar system can scan 200 channels from a unit permanently located in the control room, plus another 200 channels from a remote location.

A thorough description of the HP-Vidar data acquisition program is

contained in a document by that name in the laboratory office. Inputs into the program set up the channel numbers to be scanned, the appropriate function for that channel number (i.e., isolator thermocouples--frequency, regular thermocouples--voltage), set the range and resolution of the IDVM, and other parameters relating to the time between scans and the type of transducers being sampled by the Vidar. A set of such inputs is referred to as a program set. Up to five program sets may be used during an experiment to sample different types of data at different times during the run.

The data acquisition program, known as HPVD, contains a main driver program plus one or more data reduction routines. These routines enable certain types of on-line data reduction during an experiment, and are modified to fit the needs of particular user. For instance, it may be desired to sample only thermal data (channel temperatures and heat loss rates) during the early portion of a run to establish the thermal integrity of the channel, and then sample a different type of data, such as LDV or line reversal data, and reduce it on-line if feasible. Crucial thermal data is then monitored on strip chart recorders, and a different program set and data reduction routine is selected at the console. It is therefore possible to change the type of data to be taken and the type of data reduction to be performed during the experiment. It is also possible to sample data more or less constantly from a single channel.

The raw data is stored on magnetic disc and magnetic or paper tape for further data reduction and storage. Analog data is reduced utilizing the analog to digital converter system. On-line data reduction may be displayed on the system console or on the line printer if hard copy is desired, or both. In addition, an oscilloscope plotter makes it possible to display data on an oscilloscope. This is particularly useful to monitor certain crucial temperatures, where actual temperature readings of predetermined channels may be displayed at one-second intervals on the oscilloscope.

The HPVD program also calculates flowmeter settings for given run conditions. The inputs to this program are: total flowrate, stoichiometry, seed fraction, and diluent/oxidant ratio. Several coal slurry fuels can also be handled by this program. Flowmeter settings are usually calculated prior to the experiment but they can be updated during the test itself. The Vidar can scan the oxygen and nitrogen supply pressures and

temperatures and can calculate new flowmeter settings from actual conditions, rather than nominal or average supply pressures and room temperature.

It is also possible to trigger or sequence events with the use of 16 relay registers tied into the HP-Vidar system. These may be used to turn on or off recorders, cameras, or trigger oscilloscope traces, or other data scans, as well as turn on or off the main electrode circuits.

Critical events during the experiment are recorded by the computer operator and also on the strip chart, which are stored and reviewed as necessary. The voice recorder may be reviewed for further event documentation. Pages 35-38 of Reseck's thesis indicate the level of success of many MHD experiments. The hostile environment of combustion MHD experiments causes many failures of electrodes, ceramics, and diagnostic hardware. Channel disassembly, inspection, and refurbishment is usually necessary every 2 or 3 tests to replace parts damaged during operation. The accurate storage of data and dilligent recording of crucial events often aids in explaining the channel condition upon disassembly, and helps in avoiding repeated mistakes.

REFERENCES

[1] Louis, J. F., et al., "Detailed Theoretical and Experimental Study on a Large MHD Generator," AVCO Report No. 174, March 1964.

[2] Mattson, et al., "Performance of a Self-Excited MHD Generator," AVCO Report No. 238, October 1965.

[3] Teno, J., et al., "Studies with a Hall Configuration MHD Generator," Proceedings of the Tenth Symposium on Engineering Aspects of Magnetohydrodynamics, Massachusetts Institute of Technology, Cambridge, Massachusetts, March 1969.

[4] Sonju, O. K., J. Teno, "Experimental and Analytical Research on a Two Megawatt High Performance MHD Generator, Technical Report AFAPL TR-72-98, October 1972.

[5] Oliver, D. A., and M. Mitchner, "Nonuniform Electrical Conduction in MHD Channels," AIAA Journal, 5, (1968).

[6] Crown, J. C., "Analysis of Magnetohydrodynamic Generators Having Segmented Electrodes and Anisotropic Conductivity," United Aircraft Corporation Report R-1852-2.

[7] Petty, S., R. Rosa and G. Enos, "Developments of the Mark VI Long-Duration MHD Generator," Proceedings of the Sixth International Conference on Magnetohydrodynamic Power Generation, Washington, D.C., June 1975.

[8] Petty, S., et al., "Progress on the Mark VI Long-Duration MHD Generator," Proceedings of the Fifteenth Symposium on Engineering Aspects of Magnetohydrodynamics, University of Pennsylvania, Philadelphia, Pennsylvania, May 1976.

[9] Cutting, J. C., "Axial Current Leakage in Segmented MHD Generators," Technical Report AFAPL-TR-71-73, January 1971.

[10] Oliver, D. A., "The Prediction of Interelectrode Breakdown in Magnetohydrodynamic Generators," MIT GTL Report #116, March 1974.

[11] Burenkov, D. K., et al., "Investigation of the Inter-Electrode Breakdown in a Channel of MHD Generator of the U-02 Installation," Proceedings of the Second Joint Soviet-American Colloquium on the Problems of MHD Power Generation, Washington, D.C., June 1975.

[12] Burenkov, D. K., et al., "Study of the Maximum Hall Voltages and Interelectrode Breakdown in the Channel of an Open-Cycle MHD Generator: A Joint U.S.-U.S.S.R. Experiment on the UØ2 Facility MHD Generator," Proceedings of the Sixteenth Symposium on Engineering Aspects of Magnetohydrodynamics, University of Pittsburgh, Pittsburgh, Pennsylvania, May 1977.

[13] Koester, J. K. and W. Unkel, "Performance and Hall Field Limitation Studies in the Stanford M-8 MHD Generator," Proceedings of the Fourteenth Symposium on Engineering Aspects of Magnetohydrodynamics, University of Tennessee Space Institute, Tullahoma, Tennessee, April 1974.

[14] Reseck, K. G., "Performance Characteristics of a Combustion-Driven Magnetogasdynamic Power Generator," Stanford University Institute for Plasma Research Report No. 87, August 1966.

[15] Rubin, E. S., "Effects of Electrode Size on the Performance of a Combustion-Driven MHD Generator," Technical Report AFAPL-TR-69-72, August 1969.

[16] Hohnstreiter, G. F., "Spectroscopic Investigation of Electron Temperature Distribution in a Non-equilibrium Partially Ionized Flowing Plasma," Stanford University Institute for Plasma Research Report No. 212, December 1967.

[17] Unkel, W., C. H. Kruger and J. K. Koester, "Axial Field Limitations in MHD Generators," Proceedings of the Sixth International Conference on Magnetohydrodynamic Power Generation, Washington, D.C., June 1975.

[18] Cobine, J. D., Gaseous Conductors, Dover Publications, Inc., New York, 1958.

[19] Whitehead, S., Dielectric Breakdown of Solids, Oxford at the Clarendon Press, 1951.

[20] Solbes, Albert, "Instabilities in Non-equilibrium M.H.D. Plasmas, A Review," AIAA Paper No. 70-40, AIAA 8th Aerospace Sciences Meeting, New York, January 1970.

[21] Curry, W. P., "Collisional Radiative Recombination in Hydrogen Plasmas and in Alkali Plasmas," Physical Review A, 1, 1970.

[22] Crawford, M. E., W. M. Kays, "STAN5 - A Program for Numerical Computation of Two-Dimensional Internal/External Boundary Layer Flows," Stanford University, Thermosciences Division Report No. HMT-23, December 1975.

[23] Daily, J. W., "Boundary Layer Phenomena in Combustion Driven MHD Power Generators," HTGL Report #102, December 1975, Stanford University, Stanford, California.

[24] Rankin, R. R., S. A. Self and R. H. Eustis, "A Study of the MHD Insulating Wall Boundary Layer," Addendum to Proceedings of the Sixteenth Symposium on Engineering Aspects of Magnetohydrodynamics, University of Pittsburgh, Pittsburgh, Pennsylvania, May 1977.

[25] Pepper, J. W., "Effect of Nitric Oxide Control on MHD-Steam Power Plant Economics and Performance," Stanford University Institute for Plasma Research Report No. 614, December 1974, Stanford, California.

[26] Goldsmith, A., T. E. Waterman and H. J. Hirschhorn, Handbook of Thermophysical Properties of Solid Materials Volume 3: Ceramics, MacMillan Co., New York, 1961.

[27] "Final Report, Investigation of Magnetohydrodynamic Power Generation. Volume IV: Materials," Pratt and Whitney Aircraft Division of United Aircraft Corporation Report PWA-2125. DDC Document RADC-TDR-62-464, Volume IV, December 1962.

[28] Sonju, O. K., "Viscous Magentohydrodynamic Flows," Stanford University Institute for Plasma Research Report No. 245, July 1968, Stanford, California.

[29] "Mechanical and Electrical Properties of AlSiMag R Ceramics," American Lava Corporation Chart No. 711, Chattanooga, Tennessee.

[30] Schlicting, H., Boundary Layer Theory, McGraw-Hill Book Company, New York, 1960.

[31] Kays, W. M., Convective Heat and Mass Transfer, McGraw-Hill Book Company, New York, 1966.

[32] Hottel, H. C., Chapter 2 of Heat Transmission (by W. C. McAdams), McGraw-Hill Book Company, New York, 1954.

[33] McGregor, D. D., "Electronic Nonequilibrium in a Supersonic Expansion of Ionized Gas, Appendix H; Radiation Escape Parameter," Stanford University Institute for Plasma Physics Research, Report No. 474, July 1972.

[34] Oliver, D. A., "Nonuniform Electrical Conduction in Magnetohydrodynamic Channels," Stanford University Institute for Plasma Research Report No. 163, May 1967, Stanford, California.

[35] Martinelli, R. C., Transactions of the A.S.M.E., 69, 1947.

[36] Eustis, R. H., et al., "Limiting Mechanisms in MHD Generator Performance," Final Report AFAPL-TR-76-21, December 1975, Section 6.2.

[37] Argyropoulos, G. S., et al., "Electron Nonequilibrium in Open-Cycle MHD Generators," Proceedings of the Thirteenth Symposium on Engineering Aspects of Magnetohydrodynamics, Stanford University, Stanford, California, March 1973.

[38] Koester, J. K., "Analytical and Experimental Studies of Thermionically Emitting Electrodes in Contact with Dense, Seeded Plasmas," Ph.D. Thesis, California Institute of Technology, Pasadena, California, 1970.

[39] Levine, J. D. and Gyftopoulos, E. P., "Adsorption Physics of Metallic Surfaces Partially Covered by Metallic Particles. I. Atom and Ion Desorption Energies," Surface Science, Vol. 1, 1964.

[40] Levine, J. D. and Gyftopoulos, E. P., "Adsorption Physics of Metallic Surfaces Partially Covered by Metallic Particles. II. Desorption Rates of Atoms and Ions," Surface Science, Vol. 1, 1964.

[41] Levine, J. D. and Gyftopoulos, E. P., "Adsorption Physics of Metallic Surfaces Partially Covered by Metallic Particles. III. Equations of State and Electron Emission S-Curves," Surface Science, Vol. 1, 1964.

[42] Kessler, R., "Effects of Electrode Temperature on MHD Generator Performance," Stanford University Institute for Plasma Research Report No. 239, June 1968, Stanford, California.

☆U.S. GOVERNMENT PRINTING OFFICE: 1979-640-092/504